

AJNR

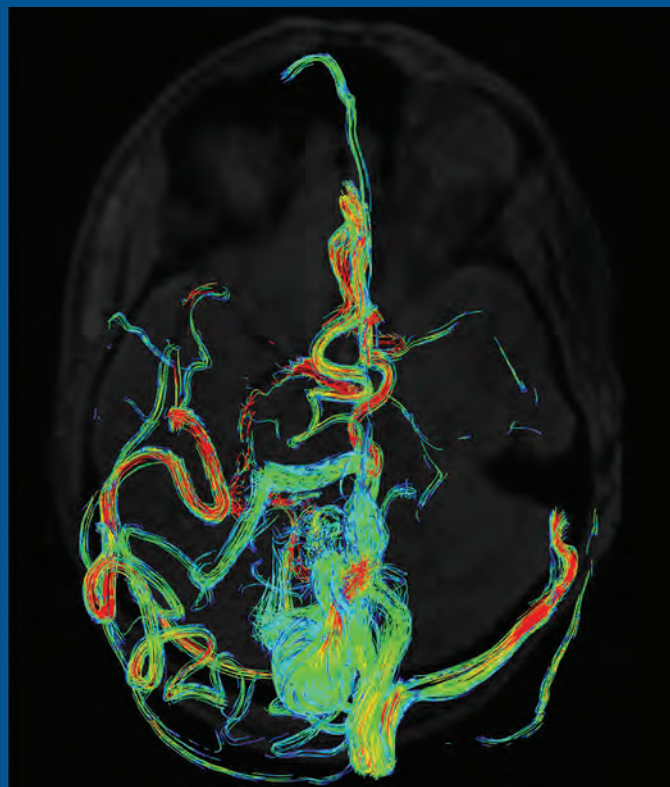
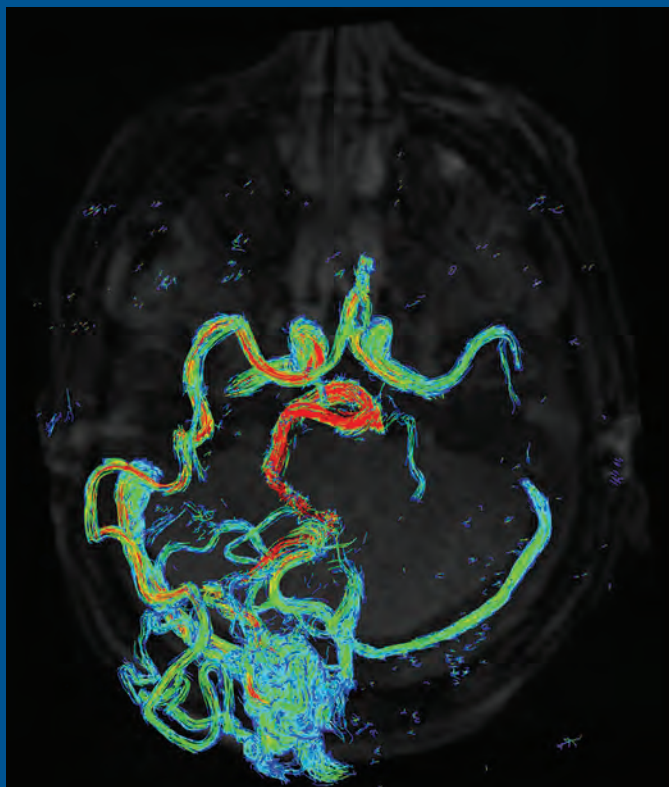
AMERICAN JOURNAL OF NEURORADIOLOGY

JUNE 2015
VOLUME 36
NUMBER 6
WWW.AJNR.ORG

THE JOURNAL OF DIAGNOSTIC AND
INTERVENTIONAL NEURORADIOLOGY

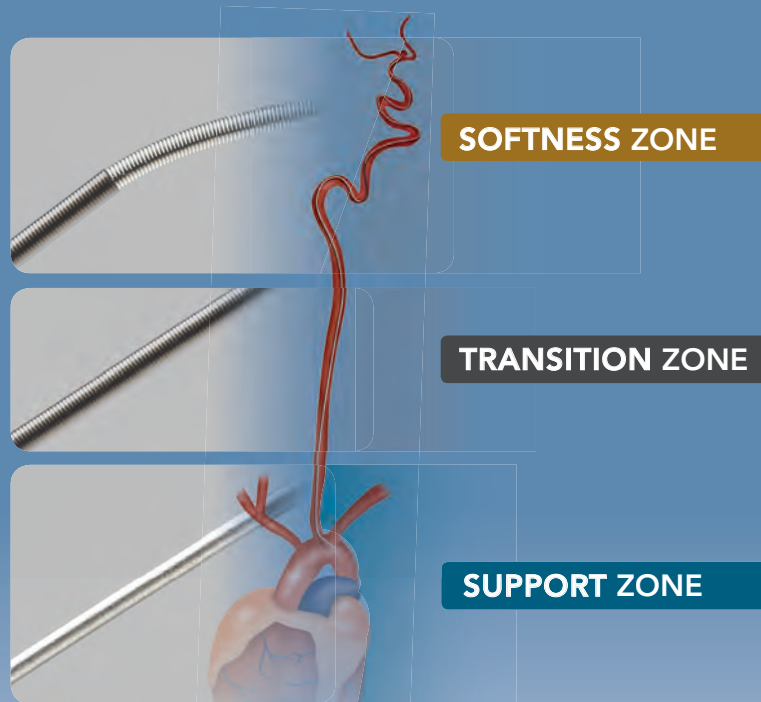
CNS infections as weapons of mass destruction
Mesenchymal cell transplantation in stroke
Noninvasive brain thermometry in stroke

Official Journal ASNR • ASFNR • ASHNR • ASPNR • ASSR



Advanced

by MicroVention



ENHANCED CONTROL TO MAXIMIZE COIL PERFORMANCE

The V-Trak® Advanced Coil System, the next generation to power the performance of our most technically advanced line of coils. Offering the optimal combination of support and flexibility.

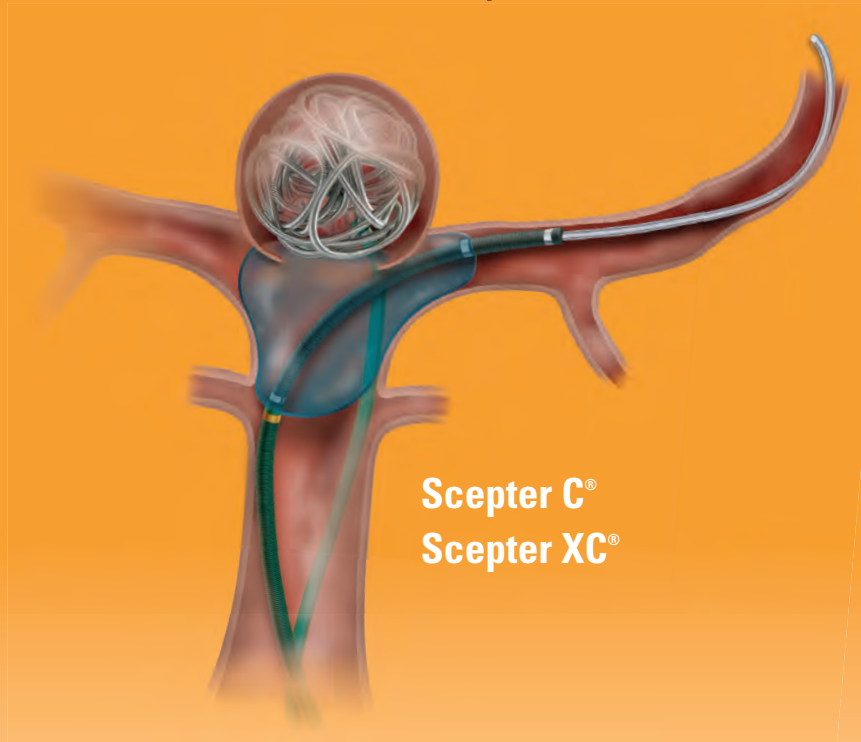
microvention.com

MICROVENTION, V-Trak, Scepter C, Scepter XC and Headway are registered trademarks of MicroVention, Inc. Scientific and clinical data related to this document are on file at MicroVention, Inc. Refer to Instructions for Use, contraindications and warnings for additional information. Federal (USA) law restricts this device for sale by or on the order of a physician. © 2015 MicroVention, Inc. 5/15

CE
0297

Versatility

by MicroVention



Scepter C[®]
Scepter XC[®]

Scepter
Occlusion Balloon
Catheter

REDEFINING DELIVERABILITY, VERSATILITY AND CONTROL

MicroVention has developed two occlusion balloon catheters. **Scepter C[®]** compliant balloon is designed for reliable vessel occlusion yet conforms to vessel anatomy. **Scepter XC[®]** x-tra compliant balloon conforms to extremely complex anatomies where neck coverage is more challenging.

• Used with

Headway
Microcatheter

For more information or a product demonstration,
contact your local MicroVention representative:

 **MicroVention[®]**
TERUMO

MicroVention, Inc.

Worldwide Headquarters

1311 Valencia Avenue

Tustin, CA 92780 USA

MicroVention UK Limited

MicroVention Europe, S.A.R.L.

MicroVention Deutschland GmbH

PH +1.714.247.8000

PH +44 (0) 191 258 6777

PH +33 (1) 39 21 77 46

PH +49 211 210 798-0

COILING OPTIMIZED



NOW AVAILABLE

**BARRICADE COMPLEX
FINISHING COIL**

- ◆ Extremely soft profile of The Barricade Finishing coil now in a complex shape
- ◆ Excellent microcatheter stability for confident coil placement
- ◆ Available in a size range of 1mm-5mm

BARRICADE™ COIL SYSTEM



MADE IN AMERICA

The Barricade Coil System is intended for the endovascular embolization of intracranial aneurysms and other neurovascular abnormalities such as arteriovenous malformations and arteriovenous fistulae. The System is also intended for vascular occlusion of blood vessels within the neurovascular system to permanently obstruct blood flow to an aneurysm or other vascular malformation and for arterial and venous embolizations in the peripheral vasculature. Refer to the instructions for use for complete product information.

18 TECHNOLOGY DRIVE #169, IRVINE CA 92618

p: 949.788.1443 | f: 949.788.1444

WWW.BLOCKADEMEDICAL.COM

MKTG-031 Rev. A



BLOCKADE
M E D I C A L

AJNR

AMERICAN JOURNAL OF NEURORADIOLOGY

JUNE 2015
VOLUME 36
NUMBER 6
WWW.AJNR.ORG

Publication Preview at www.ajnr.org features articles released in advance of print. Visit www.ajnrblog.org to comment on AJNR content and chat with colleagues and AJNR's News Digest at <http://ajnrdigest.org> to read the stories behind the latest research in neuroimaging.

EDITORIAL

PERSPECTIVES

- 1015 **Do You Need a Coach? I Do** *M. Castillo*

REVIEW ARTICLES

-   1018 **Armies of Pestilence: CNS Infections as Potential Weapons of Mass Destruction** *B.L. Hart and L. Ketai*
-    1026 **4D-CTA in Neurovascular Disease: A Review** *H.G.J. Kortman, E.J. Smit, M.T.H. Oei, R. Manniesing, M. Prokop, and F.J.A. Meijer*

EDITORIAL PERSPECTIVES

-  1034 **Screening for Self-Plagiarism in a Subspecialty-versus-General Imaging Journal Using iThenticate** *A.U. Kalnins, K. Halm, and M. Castillo*

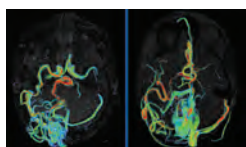
RESEARCH PERSPECTIVES

-  1039 **Evidence Levels for Neuroradiology Articles: Low Agreement among Raters** *J.N. Ramalho, G. Tedesqui, M. Ramalho, R.S. Azevedo, and M. Castillo*

BRAIN

-    1043 **White Matter Alterations in the Brains of Patients with Active, Remitted, and Cured Cushing Syndrome: A DTI Study** *P. Pires, A. Santos, Y. Vives-Gilabert, S.M. Webb, A. Sainz-Ruiz, E. Resmini, I. Crespo, M. de Juan-Delago, and B. Gómez-Anson*
-  1049 **Fast Contrast-Enhanced 4D MRA and 4D Flow MRI Using Constrained Reconstruction (HYPRFlow): Potential Applications for Brain Arteriovenous Malformations** *W. Chang, Y. Wu, K. Johnson, M. Loecher, O. Wieben, M. Edjlali, C. Oppenheim, P. Roca, J. Hald, B. Aagaard-Kienitz, D. Niemann, C. Mistretta, and P. Turski*
- 1056 **Predictors of Reperfusion in Patients with Acute Ischemic Stroke** *A.D. Horsch, J.W. Dankbaar, J.M. Niesten, T. van Seeters, I.C. van der Schaaf, Y. van der Graaf, W.P.Th.M. Mali, and B.K. Velthuis; on behalf of the Dutch Acute Stroke Study Investigators*
-  1063 **Qualitative and Quantitative Analysis of MR Imaging Findings in Patients with Middle Cerebral Artery Stroke Implanted with Mesenchymal Stem Cells** *C.P. Wanamaker, S. Fakhran, and L.M. Alhilali*
- 1069 **Multimodal CT Provides Improved Performance for Lacunar Infarct Detection** *T. Das, F. Settecase, M. Boulos, T. Huynh, C.D. d'Esterre, S.P. Symons, L. Zhang, and R.I. Aviv*
-   1076 **Statin Therapy Does Not Affect the Radiographic and Clinical Profile of Patients with TIA and Minor Stroke** *N. Asdaghi, J.I. Coulter, J. Modi, M.C. Camden, A. Qazi, M. Goyal, T. Rundek, and S.B. Coutts*

-  Indicates Editor's Choices selection
-  Indicates Fellows' Journal Club selection
-  Indicates open access to non-subscribers at www.ajnr.org
-  Indicates article with supplemental on-line table
-  Indicates article with supplemental on-line photo
-  Indicates article with supplemental on-line video
-  Indicates Evidence-Based Medicine Level 1
-  Indicates Evidence-Based Medicine Level 2



4D flow pathlines show AVM venous drainage in red.



Trevo[®] XP

PROVUE RETRIEVER

Take Control. Capture More.

The newly designed Trevo[®] XP ProVue Retriever takes proven Trevo Retriever performance to new levels for **easy delivery, easy placement, and easy visualization.**

When you're in control, it's amazing what you can capture.

stryker[®]
Neurovascular

-  **1081 Optimal MRI Sequence for Identifying Occlusion Location in Acute Stroke: Which Value of Time-Resolved Contrast-Enhanced MRA?** *A. Le Bras, H. Raoult, J.-C. Ferré, T. Ronzière, and J.-Y. Gauvrit*
-   **1089 SWI or T2*: Which MRI Sequence to Use in the Detection of Cerebral Microbleeds? The Karolinska Imaging Dementia Study** *S. Shams, J. Martola, L. Cavallin, T. Granberg, M. Shams, P. Aspelin, L.O. Wahlund, and M. Kristoffersen-Wiberg*
-  **1096 Progression of Microstructural Damage in Spinocerebellar Ataxia Type 2: A Longitudinal DTI Study** *M. Mascalchi, N. Toschi, M. Giannelli, A. Ginestroni, R. Della Nave, E. Nicolai, A. Bianchi, C. Tessa, E. Salvatore, M. Aiello, A. Soricelli, and S. Diciotti*
-  **1102 Usefulness of Quantitative Susceptibility Mapping for the Diagnosis of Parkinson Disease** *Y. Murakami, S. Kakeda, K. Watanabe, I. Ueda, A. Ogasawara, J. Moriya, S. Ide, K. Futatsuya, T. Sato, K. Okada, T. Uozumi, S. Tsuji, T. Liu, Y. Wang, and Y. Korogi*
-  **1109 Evaluating the Effects of White Matter Multiple Sclerosis Lesions on the Volume Estimation of 6 Brain Tissue Segmentation Methods** *S. Valverde, A. Oliver, Y. Díez, M. Cabezas, J.C. Vilanova, L. Ramió-Torrentà, À. Rovira, and X. Lladó*
-  **1116 Enhanced Axonal Metabolism during Early Natalizumab Treatment in Relapsing-Remitting Multiple Sclerosis** *O.T. Wiebenga, A.M. Klauser, M.M. Schoonheim, G.J.A. Nagtegaal, M.D. Steenwijk, J.A. van Rossum, C.H. Polman, F. Barkhof, P.J.W. Pouwels, and J.J.G. Geurts*
- 1124 Quiet PROPELLER MRI Techniques Match the Quality of Conventional PROPELLER Brain Imaging Techniques** *I. Corcuera-Solano, A. Doshi, P.S. Pawha, D. Gui, A. Gaddipati, and L. Tanenbaum*

FUNCTIONAL

-  **1128 Proton Resonance Frequency Chemical Shift Thermometry: Experimental Design and Validation toward High-Resolution Noninvasive Temperature Monitoring and In Vivo Experience in a Nonhuman Primate Model of Acute Ischemic Stroke** *S. Dehkharghani, H. Mao, L. Howell, X. Zhang, K.S. Pate, P.R. Magrath, F. Tong, L. Wei, D. Qiu, C. Fleischer, and J.N. Oshinski*

INTERVENTIONAL

- 1136 HydroCoils Reduce Recurrence Rates in Recently Ruptured Medium-Sized Intracranial Aneurysms: A Subgroup Analysis of the HELPS Trial** *W. Brinjikji, P.M. White, H. Nahser, J. Wardlaw, R. Sellar, H.J. Cloft, and D.F. Kallmes*
-   **1142 Evaluation of 4D Vascular Flow and Tissue Perfusion in Cerebral Arteriovenous Malformations: Influence of Spetzler-Martin Grade, Clinical Presentation, and AVM Risk Factors** *C. Wu, S.A. Ansari, A.R. Honarmand, P. Vakil, M.C. Hurley, B.R. Bendok, J. Carr, T.J. Carroll, and M. Markl*
- 1150 Endovascular Treatment of Wide-Neck Anterior Communicating Artery Aneurysms Using WEB-DL and WEB-SL: Short-Term Results in a Multicenter Study** *D.N. Gherasim, B. Gory, R. Sivan-Hoffmann, L. Pierot, H. Raoult, J.-Y. Gauvrit, H. Desal, X. Barreau, D. Herbreteau, R. Riva, F. Ambesi Impiombato, X. Armoiry, and F. Turjman*
-  **1155 The FRED Flow-Diverter Stent for Intracranial Aneurysms: Clinical Study to Assess Safety and Efficacy** *M.A. Möhlenbruch, C. Herweh, L. Jestaedt, S. Stampfl, S. Schönerberger, P.A. Ringleb, M. Bendszus, and M. Pham*
- 1162 Retrieval of Migrated Coils with Stent Retrievers: An Animal Study** *O. Nikoubashman, R. Pjontek, M.-A. Brockmann, R. Tolba, and M. Wiesmann*
- 1167 Fenestrations of Intracranial Arteries** *S.B.T. van Rooij, R.S. Bechan, J.P. Peluso, M. Sluzewski, and W.J. van Rooij*



American Society of Spine Radiology

2016 Annual Symposium • February 18-21, 2016

Hyatt Regency Coconut Point • Bonita Springs, FL

- Stillwater Spa with 18 treatment rooms, Watsu pool, and beauty salon
- Big Hickory Island Beach
- Spectacular waterfalls and pool features, as well as a spacious sundeck
- Family pool with 140-foot corkscrew water slide and hot tub, heated adult pool with hot tub, cold-plunge pool with waterfall
- 18-hole Raymond Floyd designed Raptor Bay golf course and club
- 24-hour Hyatt StayFit gym with cardio theater
- Bicycle and kayak rentals
- Dolphin watch eco-tours and sunset cruises
- Video arcade
- Har-Tru clay tennis courts
- Camp Hyatt®



A tropical paradise centrally located between Fort Myers and Naples, Florida in the upscale community of Bonita Springs. With stunning views of the Gulf Coast, Hyatt Regency Coconut Point Resort and Spa offers casual elegance and southern style hospitality, personalized service and attention to detail at every turn.

SAVE THE DATE

EXTRACRANIAL VASCULAR

-  1171 **MR Imaging–Detected Carotid Plaque Hemorrhage Is Stable for 2 Years and a Marker for Stenosis Progression** *R.J. Simpson, S. Akwei, A.A. Hosseini, S.T. MacSweeney, D.P. Auer, and N. Altaf*
- 1176 **Changes of Time-Attenuation Curve Blood Flow Parameters in Patients with and without Carotid Stenosis** *C.-J. Lin, F.-C. Chang, W.-Y. Guo, S.-C. Hung, C.-B. Luo, J. Beilner, M. Kowarschik, and W.-F. Chu*

HEAD & NECK

- 1182 **Imaging Appearance of Dextranomer/Hyaluronic Acid Copolymer Implant Injections for Treatment of Velopharyngeal Insufficiency** *W. Brinjikji, S.A. Cofer, and J.I. Lane*
- 1188 **Comparison of Fine-Needle Aspiration and Core Needle Biopsy under Ultrasonographic Guidance for Detecting Malignancy and for the Tissue-Specific Diagnosis of Salivary Gland Tumors** *H.-J. Eom, J.H. Lee, M.-S. Ko, Y.J. Choi, R.G. Yoon, K.J. Cho, S.Y. Nam, and J.H. Baek*
-    1194 **Different Spectral Hounsfield Unit Curve and High-Energy Virtual Monochromatic Image Characteristics of Squamous Cell Carcinoma Compared with Nonossified Thyroid Cartilage** *R. Forghani, M. Levental, R. Gupta, S. Lam, N. Dadfar, and H.D. Curtin*

1201 SOCIETY PRESIDENT BIOGRAPHIES

ONLINE FEATURES (www.ajnr.org)

WHITE PAPER

-  E41 **ASFNR Recommendations for Clinical Performance of MR Dynamic Susceptibility Contrast Perfusion Imaging of the Brain** *K. Welker, J. Boxerman, A. Kalnin, T. Kaufmann, M. Shiroishi, and M. Wintermark; for the American Society of Functional Neuroradiology MR Perfusion Standards and Practice Subcommittee of the ASFNR Clinical Practice Committee*

E52 ERRATUM

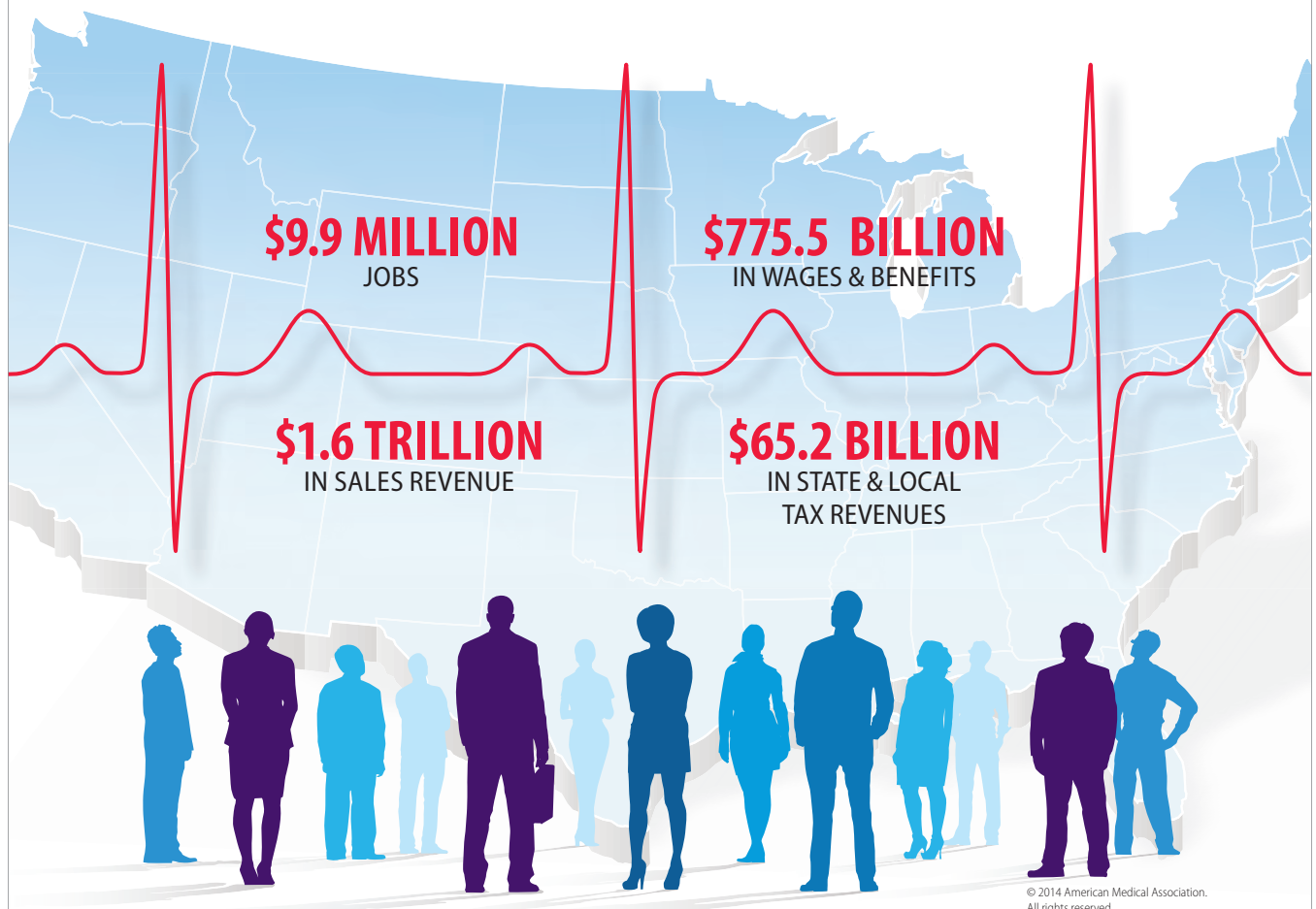
LETTERS

- E53 **Parent Artery Occlusion: A Well-Established Technique** *C.M. Benson, D.M. Pelz, and S.P. Lownie*
- E54 **Reply** *M.A. Labeyrie, J.P. Saint-Maurice, and E. Houdart*

BOOK REVIEWS *R.M. Quencer, Section Editor*

Please visit www.ajnrblog.org to read and comment on Book Reviews.

PHYSICIANS BOOST THE ECONOMY.



© 2014 American Medical Association. All rights reserved.

See the effects across the nation.

The American Medical Association 2014 Economic Impact Study shows how much physicians add to the economic health of our nation.

Check the effect physicians have on the U.S. economy by viewing the entire national report from the AMA Advocacy Resource Center at ama-assn.org/go/eis.



Please activate your 2015 AMA membership by calling (800) 262-3211 or visit ama-assn.org/go/join.

Official Journal:

American Society of Neuroradiology
American Society of Functional Neuroradiology
American Society of Head and Neck Radiology
American Society of Pediatric Neuroradiology
American Society of Spine Radiology

EDITOR-IN-CHIEF

Mauricio Castillo, MD

Professor of Radiology and Chief, Division of Neuroradiology, University of North Carolina, School of Medicine, Chapel Hill, North Carolina

SENIOR EDITORS

Harry J. Cloft, MD, PhD

Professor of Radiology and Neurosurgery, Department of Radiology, Mayo Clinic College of Medicine, Rochester, Minnesota

Nancy J. Fischbein, MD

Professor of Radiology, Otolaryngology-Head and Neck Surgery, Neurology, and Neurosurgery and Chief, Head and Neck Radiology, Department of Radiology, Stanford University Medical Center, Stanford, California

Jeffrey S. Ross, MD

Staff Neuroradiologist, Barrow Neurological Institute, St. Joseph's Hospital, Phoenix, Arizona

Pamela W. Schaefer, MD

Clinical Director of MRI and Associate Director of Neuroradiology, Massachusetts General Hospital, Boston, Massachusetts, and Associate Professor, Radiology, Harvard Medical School, Cambridge, Massachusetts

Charles M. Strother, MD

Professor of Radiology, Emeritus, University of Wisconsin, Madison, Wisconsin

Jody Tanabe, MD

Professor of Radiology and Psychiatry, Chief of Neuroradiology, University of Colorado, Denver, Colorado

EDITORIAL BOARD

Ashley H. Aiken, *Atlanta, Georgia*
A. James Barkovich, *San Francisco, California*
Walter S. Bartynski, *Charleston, South Carolina*
Barton F. Branstetter IV, *Pittsburgh, Pennsylvania*
Jonathan L. Brisman, *Lake Success, New York*
Julie Bykowski, *San Diego, California*
Donald W. Chakeres, *Columbus, Ohio*
Alessandro Cianfoni, *Lugano, Switzerland*
Colin Derdeyn, *St. Louis, Missouri*
Rahul S. Desikan, *San Diego, California*
Richard du Mesnil de Rochemont, *Frankfurt, Germany*
Clifford J. Eskey, *Hanover, New Hampshire*
Massimo Filippi, *Milan, Italy*
David Fiorella, *Cleveland, Ohio*
Allan J. Fox, *Toronto, Ontario, Canada*
Christine M. Glastonbury, *San Francisco, California*

John L. Go, *Los Angeles, California*
Wan-Yuo Guo, *Taipei, Taiwan*
Rakesh K. Gupta, *Lucknow, India*
Lotfi Hacein-Bey, *Sacramento, California*
David B. Hackney, *Boston, Massachusetts*
Christopher P. Hess, *San Francisco, California*
Andrei Holodny, *New York, New York*
Benjamin Huang, *Chapel Hill, North Carolina*
Thierry A.G.M. Huisman, *Baltimore, Maryland*
George J. Hunter, *Boston, Massachusetts*
Mahesh V. Jayaraman, *Providence, Rhode Island*
Valerie Jewells, *Chapel Hill, North Carolina*
Timothy J. Kaufmann, *Rochester, Minnesota*
Kenneth F. Layton, *Dallas, Texas*
Ting-Yim Lee, *London, Ontario, Canada*
Michael M. Lehl, *Erlangen, Germany*
Michael Lev, *Boston, Massachusetts*
Karl-Olof Lovblad, *Geneva, Switzerland*
Franklin A. Marden, *Chicago, Illinois*
M. Gisele Matheus, *Charleston, South Carolina*
Joseph C. McGowan, *Merion Station, Pennsylvania*
Kevin R. Moore, *Salt Lake City, Utah*
Christopher J. Moran, *St. Louis, Missouri*
Takahisa Mori, *Kamakura City, Japan*

Suresh Mukherji, *Ann Arbor, Michigan*
Amanda Murphy, *Toronto, Ontario, Canada*
Alexander J. Nemeth, *Chicago, Illinois*
Laurent Pierot, *Reims, France*
Jay J. Pillai, *Baltimore, Maryland*
Whitney B. Pope, *Los Angeles, California*
M. Judith Donovan Post, *Miami, Florida*
Tina Young Poussaint, *Boston, Massachusetts*
Joana Ramalho, *Lisbon, Portugal*
Otto Rapalino, *Boston, Massachusetts*
Álex Rovira-Cañellas, *Barcelona, Spain*
Paul M. Ruggieri, *Cleveland, Ohio*
Zoran Rumboldt, *Rijeka, Croatia*
Amit M. Saindane, *Atlanta, Georgia*
Erin Simon Schwartz, *Philadelphia, Pennsylvania*
Aseem Sharma, *St. Louis, Missouri*
J. Keith Smith, *Chapel Hill, North Carolina*
Maria Vittoria Spampinato, *Charleston, South Carolina*
Gordon K. Sze, *New Haven, Connecticut*
Krishnamoorthy Thamburaj, *Hershey, Pennsylvania*
Kent R. Thielen, *Rochester, Minnesota*
Cheng Hong Toh, *Taipei, Taiwan*
Thomas A. Tomsick, *Cincinnati, Ohio*
Aquilla S. Turk, *Charleston, South Carolina*
Willem Jan van Rooij, *Tilburg, Netherlands*
Arastoo Vossough, *Philadelphia, Pennsylvania*
Elysa Widjaja, *Toronto, Ontario, Canada*
Max Wintermark, *Charlottesville, Virginia*
Ronald L. Wolf, *Philadelphia, Pennsylvania*
Kei Yamada, *Kyoto, Japan*

EDITORIAL FELLOW

Asim F. Choudhri, *Memphis, Tennessee*

YOUNG PROFESSIONALS ADVISORY COMMITTEE

Asim K. Bag, *Birmingham, Alabama*
Anna E. Nidecker, *Sacramento, California*
Peter Yi Shen, *Sacramento, California*

HEALTH CARE AND SOCIOECONOMICS EDITOR

Pina C. Sanelli, *New York, New York*

Founding Editor

Juan M. Taveras

Editors Emeriti

Robert I. Grossman, Michael S. Huckman,
Robert M. Quencer

Special Consultants to the Editor

Sandy Cheng-Yu Chen, Juan Pablo Cruz,
Girish Fatterpekar, Ryan Fitzgerald,
Katherine Freeman, Yvonne Lui,
Sapna Rawal, Greg Zaharchuk

Managing Editor

Karen Halm

Electronic Publications Manager

Jason Gantenberg

Executive Director, ASNR

James B. Gantenberg

Director of Communications, ASNR

Angelo Artemakis

AJNR (Am J Neuroradiol) ISSN 0195-6108 is a journal published monthly, owned and published by the American Society of Neuroradiology (ASNR), 800 Enterprise Drive, Suite 205, Oak Brook, IL 60523. Annual dues for the ASNR include \$170.00 for journal subscription. The journal is printed by Cadmus Journal Services, 5457 Twin Knolls Road, Suite 200, Columbia, MD 21045; Periodicals postage paid at Oak Brook, IL and additional mailing offices. Printed in the U.S.A. POSTMASTER: Please send address changes to American Journal of Neuroradiology, P.O. Box 3000, Denville, NJ 07834, U.S.A. Subscription rates: nonmember \$380 (\$450 foreign) print and online, \$305 online only; institutions \$440 (\$510 foreign) print and basic online, \$875 (\$940 foreign) print and extended online, \$365 online only (basic), extended online \$790; single copies are \$35 each (\$40 foreign). Indexed by PubMed/Medline, BIOSIS Previews, Current Contents (Clinical Medicine and Life Sciences), EMBASE, Google Scholar, HighWire Press, Q-Sensei, RefSeek, Science Citation Index, and SCI Expanded. Copyright © American Society of Neuroradiology.





49th Annual Meeting | American Society of

Head & Neck Radiology

Comprehensive Head and Neck Imaging

September 9 - 13, 2015

Naples Grande Beach Resort
Naples, Florida

27.5 AMA PRA Category 1 Credit(s)TM

Certain sessions of the meeting program
will be submitted for SAM qualification.

**Hands-on US and US-Guided Biopsy Seminar
Friday, September 11, 2015**

Separate Registration Required

Registration is Limited to 20 Attendees Per Session.

Not accredited for AMA PRA Category 1 Credit(s)TM

Call for Abstracts at www.ashnr.org • Deadline: July 16, 2015

Do You Need a Coach? I Do

 M. Castillo, *Editor-in-Chief*

I recently reached an anniversary of sorts; during the 2015 Symposium Neuroradiologicum in Istanbul, Turkey, I gave my 900th invited lecture. Those who were there witnessed what I think were 2 unexceptional lectures. Why? I practiced each about 10 times before the meeting and thought I knew them well. The truth is that sadly, I am not a natural speaker. When I think about gifted speakers, Drs Thomas Naidich and Anne Osborn immediately come to mind. We participate in several events every year, and many times I have seen Dr. Naidich sitting in the first row, building his next conference and immediately thereafter delivering it flawlessly. I will never be able to do that; for me “practice makes perfect” and sometimes as in the Symposium, it does not. Because I think that I know my conference topics well, perhaps my delivery needs work. Maybe I talk too fast (yes, I am certain of that), maybe my body posture needs adjustment (not sure about this but gesticulating does keep nervousness at bay), or maybe I do not make enough eye contact with the audience. A million things can go wrong, but how to improve the most urgent ones is not clear to me. Would coaching help? I think that it would be helpful if someone were to film me and then constructively criticize how my lectures went. When one lectures as much as I do and feels the responsibility of representing one’s institution, journal, and professional societies, one worries about the usual stuff public figures do, but the difference is that most (and other not-so-public figures) have coaches who help them refine their deliveries and image.

In his essay “Personal Best,” Dr Atul Gawande begins with the following quotation (credited to Barry Blitt, an author and illustrator for the *New Yorker* magazine): “No matter how well trained people are, few can sustain their best performance on their own. That is where coaching comes in.”¹ Dr Gawande stated that after 8 years as a surgeon, his performance in the operating room (OR) reached a plateau, so he decided to try a coach. He contacted a surgeon he admired and asked him to evaluate his OR behavior. The coach pointed out several needed improvements, and once implemented, Gawande asked to be re-assessed. He also recorded his operations and later watched them with his coach. Of course, I imagine Gawande to be very self-assured and not easily hurt by criticisms. However, regardless of how he felt at the time of his coaching, he concluded that his OR skills improved.

If surgeons, athletes, musicians, singers, chess players, and public speakers, among others, have coaches, why not we radiologists? Today, excellence reigns among musicians, and the word “genius” has lost most of its importance. Most musicians and most professional athletes are excellent at what they do, and the difference between the excellent and truly great is not visible to the untrained like me. Coaching is about self-improvement and

achieving perfection; thus, it may be a lifetime activity for the coach and coachee. Coaching strives to make us better without the addition of drugs, implants, and other “enhancements.” Coaching is also a highly specialized activity often requiring not 1 individual but a team of professionals. For athletes, their coaching teams are formed by scientists, physicians, nutritionists, administrators, journalists, engineers, stylists, and many more.² Because winning in sports is nowadays a matter of milliseconds, every little bit counts. Coaching also prevents bad habits from forming and those already there from becoming routine, but coaching is not mentoring. Mentoring is defined as “the relationship between an older more experienced individual with a younger less experienced person with the goal of developing the career of the latter.”³ Mentoring seldom involves payments, while coaching does, and I think that mentoring is a much more complex and difficult relationship (not to say overall less successful).

Let me now discuss some elements of coaching. The International Coaching Federation (<http://www.coachfederation.org/>) counts over 20,000 members (coaches) and offers several levels of certification (associate, professional, master, and so forth). Most of its activities, but not all, are at the executive levels and have spun considerable data. What follows is a summary of some of that literature (in the financial world, performance and profitability before and after coaching are easily measured indicators). Coaching is akin to psychotherapy as far as human contact goes, but it differs from it by being highly focused and concentrating on the present and future rather than the past.³ While a patient generally pays a therapist, in coaching, an organization generally handles the costs, thus inserting at least a third person into the relationship. Both coaching and psychotherapy, however, try to change behavior. Coaching results in improved performance, commitment, efficacy, and leadership. An effective coach-coachee relationship depends on good mutual communication, trust, collaboration, and commitment to the process. After an initial observation stage, the coach provides feedback on performance and potential. These evaluations continue throughout the coach-coachee relationship and thus constantly serve to refine it. The second stage is implementation, and though the coachee ceases to be under constant observation, he or she continues to meet regularly with the coach to discuss obstacles and successes, thus learning to exert some control over the items that need improvement. As if all of this is not complex enough, we need to bring back into the scene the third person previously mentioned. A coach-coachee relationship in which a supervisor (or, in general, the working environment) is not actively invested in the process is bound to fail. For coaching to succeed, the supervisor must believe from the start that it will and encourage both coach and coachee when improvements and changes are achieved.

Many academic radiology programs have some type of mentorship program, and from what I know about them, most are failures. With the help of American Society of Neuroradiology (ASNR) and the American Roentgen Ray Society (ARRS), this

year we started 2 mentoring pilot projects trying to match senior and junior individuals in both societies. Although the final data are not in, the ASNR part has been only moderately successful and its ARRS counterpart less so. While one does not have to admire a coach, I feel that one must admire a mentor for the relationship to work. Self-choosing a mentor is critical, and that is why our pilots with ASNR and ARRS have not worked well (for the ASNR one, I attempted to match mentors with mentees). Therefore, here is my first proposal: Ask our larger organizations to establish coaching programs akin to what the financial institutions do. One or more senior radiologists could observe our senior residents, fellows, and attendings (at all levels) at work and coach them to become better radiologists. Alternatively, this could be done by using video capture. Real work situations could be evaluated for knowledge, safety, quality, education, collegiality, and efficacy and take the place of the complex general and specialty certifications and all that is needed to maintain them as valid. Scheduled visits, evaluations, and feedback could take the place of re-certifications; my feelings are that the current requirements to obtain these certifications really do not make us better radiologists because we all tend to keep up with knowledge, while at the same time, we design very poor-quality improvement programs, which in the end are of no use to anyone.

Coaching may also be useful beyond our clinical practices. After my significant involvement with 2 scientific societies (ASNR and ARRS), I have come to perceive succession for their key positions as a great challenge. If we think of our nonprofit organizations as families, perhaps it would be helpful to look at how coaching helps in the succession of family businesses. Difficulties found in our organizations are similar to those of family-run businesses: competition, ego, and jealousy, just to mention a few. However, we also share many positive features: values, commitment, legacy, and a desire to survive. Using data from 630 family-owned and -run companies, a study concluded that coaching had a greater influence on the performance of these businesses than mentoring.⁴ In these situations, short and focused coaching was cheaper than mentoring and showed immediate changes in professional performance and skill development. Individuals who were coached also performed successfully when they took over those businesses. My second proposal is that once our larger scientific societies have identified those individuals who eventually will become their leaders, why not hire coaches for them? The current process of mentoring those individuals and making them spend years (sometimes decades) as members of boards and councils does not always work; we are all aware of many chosen nonprofit leaders who were not prepared for the jobs.

Now back to where I started. I do not believe that public speaking coaching is for everyone. If you only give occasional lectures and most are case presentations to your residents, there is no need to go overboard and try to find a coach. However, if you are, like me, delivering some 50 invited lectures per year and still unsure if you are doing it well, some help may be useful. Public speaking coaches will rapidly tell you 2 things: Lecturing is a fact of life for most people (especially educators), and yes, most people are afraid of it (admittedly I still get nervous sometimes but have not

been able to identify what triggers it). I Googled “coaching for public speakers” and got more than 15 million hits. Reading the material found in the first 3 pages just confused me; many feel that coaching is essential (the opinion of most who sell those services), and some feel that it is not (these generally recommend recording your voice and image and self-coaching). The same did not happen when I Googled “vocal coaching” with emphasis on opera singers (they have consistently and reliably used coaches for a very long time). Opera coaching strives to extend vocal range and add projection to the voice (I like the part about adding “projection” because I feel that the voices of most academic lecturers do not project well), smooth out vocal wobbles and cracks (I have been trying to do this with the help of a glass of water on the podium), prepare for concerts, sing without straining, and other more technical stuff that does not apply to us (adding squillo, removing vibrato, and so forth) as well as recovering your voice after trauma. Some coaches (especially those residing in other countries) offer coaching via Skype. Coaching opera is difficult because the science of voice and the art of performance are intermingled. Yet that is exactly what I do when I get up to the podium to lecture, a combination of voice and person. Voice and performance are the 2 main factors by which any public speaker is judged. To those, one has to add knowledge when judging our academic lecturers. To me, there is no simple way of self-evaluating these 3 aspects, so does it make sense that at least some of us would benefit from coaching?

REFERENCES

1. Gawande A. **Personal best: top athletes and singers have coaches—Should you?** *New Yorker*. October 3, 2011. <http://www.newyorker.com/magazine/2011/10/03/personal-best>. Accessed November 19, 2014
2. Surowiecki J. **Better all the time: how the “performance revolution” came to athletics—and beyond.** *New Yorker*. November 10, 2014. <http://www.newyorker.com/magazine/2014/11/10/better-time>. Accessed November 19, 2014
3. Baron L, Morin L. **The coach-coachee relationship in executive coaching: a field study.** *Hum Resource Dev Q* 2009;20:85–106
4. Utrilla Nuñez-Cacho P, Torraleja FA. **The importance of mentoring and coaching for family businesses.** *J Manag Organ* 2013;19:386–404

Exit and Thanks

By the time this short note appears, I will be at the threshold of the exit door, nearly completing my 8-year tenure as the Editor-in-Chief of the *American Journal of Neuroradiology* (*AJNR*). I would be remiss not to thank at least some key individuals who have helped and labored with me during this period.

Two equally important teams deserve my appreciation: my support at headquarters: Karen Halm (managing editor), Jason Gentenberg (electronic publications manager), and now retired, Mary Harder (editorial assistant); and the second team, my Senior Editors: Harry Cloft, Nancy Fischbein, Jeff Ross (new *AJNR* Editor-in-Chief), Pam Schaefer, Charlie Strother, Jody Tanabe, Lucien Levy (now deceased), and Bill Dillon. My eternal gratitude goes to both teams. I am proud of the state of the journal, and they should be, too.

My mentors, Drs. Bob Quencer, Tom Naidich, Michael Huckman, and Joe Lee, have always offered support and constructive criticisms. All 4 of them and their families are dear to my heart.

It is simply impossible to thank everyone, that being the reason why this note is short (if I did, I doubt I could stop). To those who

are not mentioned here, you are not forgotten and I thank you for all you did for *AJNR*.

Last, I thank my family and especially Hortensia, who have been very patient while I spent countless hours together with *AJNR* (disappearing into a “black hole” as it is known at home).

Armies of Pestilence: CNS Infections as Potential Weapons of Mass Destruction

B.L. Hart and L. Ketai



ABSTRACT

SUMMARY: Infectious agents have been investigated, developed, and used by both governments and terrorist groups as weapons of mass destruction. CNS infections, though traditionally considered less often than respiratory diseases in this scenario, may be very important. Viruses responsible for encephalitides can be highly infectious in aerosol form. CNS involvement in anthrax is ominous but should change treatment. Brucellosis, plague, Q fever, and other bacteria can uncommonly manifest with meningoencephalitis and other findings. Emerging diseases may also pose threats. We review infectious agents of particular concern for purposes of biowarfare with respect to CNS manifestations and imaging features.

God omnipotent is mustering in his clouds on our behalf armies of pestilence.

Richard II, Act 3, Scene 3

Shakespeare had Richard II threaten his enemies with “armies of pestilence” from the clouds—a prospect that seems more plausible in our time when incidents involving anthrax, smallpox, and hemorrhagic fevers continue to make headlines. Many infectious agents have been developed during the past century for potential military use. By their nature, these are unconventional weapons more effective against unprotected, civilian targets than against soldiers; this attribute may make them attractive to terrorists. Among those organisms, some target the central nervous system. For others more commonly considered pulmonary or systemic agents, significant CNS effects may still result. Below, we review the historical background, some of the organisms considered at high risk for potential biowarfare or bioterrorism with a focus on neurologic implications, and potential future threats.

Background: Public Health in Reverse

Infections have accompanied warfare throughout history and have often caused more deaths than trauma.¹ Occasional attempts

were made to spread illness among enemies as a tool of warfare. One of the most notorious examples was giving blankets from smallpox victims to American Indians. Such effort, though reprehensible, in retrospect had limited impact in comparison with the widespread, natural impact of new diseases through the Americas. It is estimated that 95% of the American Indian population may have died as a result of exposure to smallpox, measles, and other European diseases.² This demonstrates the potentially lethal effect of infectious diseases on an immunologically naïve population.

With the establishment of the scientific basis of germ theory, major improvement in public health followed. Clean water and sanitation had huge effects, and vaccines were developed. With scientific understanding, though, came the potential for what one general later termed “public health in reverse.”² With the exception of some effort to spread illness among animals, there was little attempt in this direction during World War I. However, revulsion at the results of gas warfare led to the Geneva Protocol after the war, which banned the use of not only gas but also germ warfare. Despite this ban, biologic warfare became a reality during World War II. The Japanese army did extensive research on several infectious agents, made numerous human tests on prisoners of war, and released weaponized plague against civilians in cities. Under air attack and fearing the potential use of anthrax, Great Britain began investigating anthrax as a potential weapon and enlisted the additional help of the United States. Aerosolized anthrax spread by an explosive device was tested on a flock of sheep on a small Scottish island. The lethal feasibility of this agent was established—and the island was considered contaminated and off-limits for >40 years; final decontamination in-

From the Department of Radiology, University of New Mexico, Albuquerque, New Mexico.

Paper previously presented in part at: Annual Meeting of the American Society of Neuroradiology and the Foundation of the ASNR Symposium, May 17–22, 2014; Montreal, Quebec, Canada.

Please address correspondence to Blaine L. Hart, MD, Department of Radiology, MSC10 5530, 1 University of New Mexico, Albuquerque, NM 87131-0001; e-mail: bhart@unm.edu

Indicates open access to non-subscribers at www.ajnr.org

<http://dx.doi.org/10.3174/ajnr.A4177>

volved removal of some soil and spraying the entire island with formaldehyde.³

The Cold War accelerated work by both the United States and the Union of Soviet Socialist Republics. The United States developed 5 infectious agents: anthrax, tularemia, brucellosis, Q fever, and Venezuelan equine encephalitis, in addition to toxins of biologic origin: botulinum and staphylococcal enterotoxin B. Information on the Union of Soviet Socialist Republics work is less available, but reportedly anthrax, plague, tularemia, glanders, brucellosis, smallpox, Venezuelan equine encephalitis, and Marburg virus were all weaponized.^{2,4} US research during the Korean War included tests on conscientious objectors in addition to animal experiments. Human exposures resulted in illness but no deaths.⁵ The United States announced a unilateral, complete end to all biologic weapons work in 1969, and all existing stocks were destroyed by 1973. Furthermore, it supported an international biologic weapons protocol, which has since been signed by 170 nations. A major limitation of this treaty, however, is the absence of any inspection or enforcement provision. A dramatic illustration of the dangers of such weapons came when anthrax was accidentally released from a Soviet military facility in Sverdlovsk in 1979.⁶⁻⁸ At least 66 deaths resulted, perhaps many more. Clandestine development of biologic weapons by other nations remains a concern because these weapons of mass destruction are both cheaper and less technologically challenging to produce than nuclear weapons.

Infections are also of concern as instruments of terrorism. Preparing and delivering such agents does require some technical expertise, but the potential is demonstrated by relatively recent history. The perpetrators of the sarin attack on the Japanese subway system in 1995 were found to have anthrax and Ebola cultures in their possession and had made earlier unsuccessful attempts at aerosolized anthrax attacks.⁹ Most notably, in October 2001, there was a domestic terrorist attack in the United States by anthrax sent through the mail.^{10,11} Twenty-two cases of anthrax resulted in 5 deaths.

What Makes an Organism a Weapon?

Certain characteristics make micro-organisms of special interest for these purposes:

They Can Be Grown. Not all organisms are easily grown. Viruses in particular vary considerably in ease of culture.

They Can Be Stored. For those nations that seek to develop these potential weapons of mass destruction, some “shelf life” is desirable. Hardy organisms or those that have a sporelike form have been especially sought.

They Can Be Delivered to a Population. Aerial delivery, the most likely delivery mechanism, and dispersion may involve significant force, and not all organisms could survive.

They Can Be Infective and Harmful. For most agents, infectivity involves entry via the respiratory system. “Weaponization” of these agents has involved preparing organisms or a medium to maximize the likelihood of causing infection. For example, anthrax spores in nature often clump together, resulting in a size too large to reach the alveoli. Laboratory-prepared, weaponized an-

thrax is designed to deliver individual spores that are small enough to reach the alveoli.

Harmful agents may not be lethal. Lethal infections may have obvious advantages for military or terrorist purposes, but some infections, “incapacitating agents,” may be effective at tying up military resources or spreading panic among civilian populations.

A limited list of infectious agents meets all or some of these criteria for use as a weapon. Some of these agents have occasional CNS effects, while others more specifically target the CNS.

Anthrax

Anthrax is the arch villain of biowarfare, hardy and lethal. *Bacillus anthracis* is an encapsulated, Gram-positive bacterium, found naturally in soil, most commonly affecting herbivorous animals (cattle, sheep, and goats).^{12,13} Anthrax endospores are resilient and can survive for decades in the soil. Endospores that enter the body are phagocytized by macrophages. Germination causes activation to vegetative bacteria, with subsequent potential septicemia. The 3 peptides secreted by *B anthracis* combine to form exotoxins: edema toxin and lethal toxin.¹² Human exposure can occur through the skin, ingestion, or inhalation. A fourth route of infection has been described more recently in heroin users.¹⁴⁻¹⁶

Most anthrax cases in the world, up to 95%, are cutaneous forms.¹³ The characteristic lesion is a painless, pruritic papule that develops a vesicle. Central necrosis results in a classic black eschar that gives the name to the disease, from the Greek for coal or charcoal. Although the lesions may be self-limiting, antibiotic treatment is recommended. Severe edema can infrequently result.

Ingestion of contaminated meat results in gastrointestinal anthrax. Manifestations include ulcerations, edema, fever, abdominal pain, constipation or diarrhea, and ascites. An uncommon form is oropharyngeal anthrax. Although oropharyngeal is usually less serious than gastrointestinal anthrax, cervical edema and lymphadenopathy can cause respiratory distress and dysphagia.

Inhalational anthrax is uncommon in nature but often fatal. It is also one of the most investigated and feared forms of potential biowarfare. The 1- to 2- μm size of the spores lends itself to inhalation and deposition in the alveoli. Rather than causing a primary pneumonia, inhaled spores are transported by macrophages to mediastinal lymph nodes, where they germinate and release toxins. Hemorrhagic mediastinitis and septicemia follow. The clinical illness is classically biphasic, an initial nonspecific phase of fever, nonproductive cough, and myalgia followed several days later by fulminant illness and death. Sometimes, but not always, there is a brief intervening respite before the fulminant phase.¹⁷ Mediastinal widening is present on chest radiographs or CT, and effusions are often seen. CT can show high attenuation within hemorrhagic nodes.^{10,18}

A new type of infection, injectional, was described as a result of an unusual outbreak of anthrax in Scotland, England, and Germany in 2009 and 2010 among heroin users.^{14,15,19} Soft-tissue infections were characterized by disproportionate edema, less pain than that seen in necrotizing fasciitis, and relative lack of prominence of fever. Among 119 cases (47 considered confirmed and 72 probable or possible), 14 deaths occurred. A smaller, similar outbreak occurred in 2012–2013 in heroin users in Europe.¹⁶

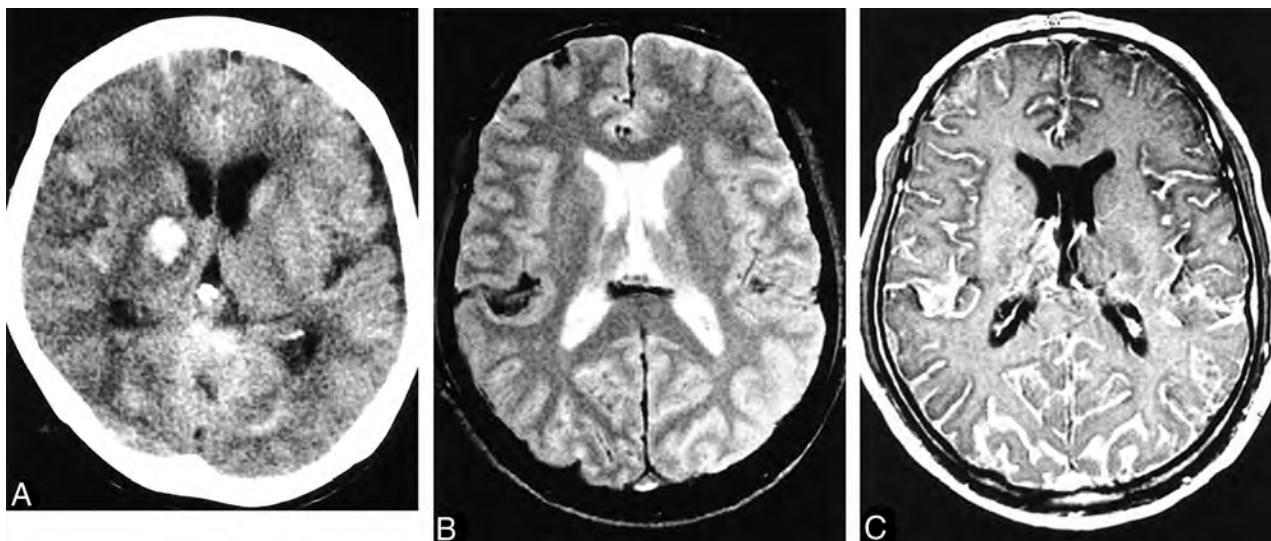


FIG 1. Anthrax meningoencephalitis. Noncontrast CT (A) of a patient with gastrointestinal anthrax shows subarachnoid, intraventricular, and parenchymal hemorrhage. MR imaging of a different patient shows subarachnoid hemorrhage on axial T2 gradient-recalled (B) imaging and diffuse leptomeningeal enhancement after gadolinium administration (C). Reprinted with permission from Kim et al.²¹

It is suspected that heroin may have been contaminated during transportation to Western Europe.

Meningitis may occur as a complication of any of these forms, most likely from hematogenous spread.^{12,20} Anthrax meningitis is usually fatal. CSF may contain large amounts of blood and organisms, and pathologic postmortem examination shows hemorrhagic meningitis, severe edema, and inflammatory infiltrates.^{7,12} The few reports of imaging describe subarachnoid hemorrhage and leptomeningeal enhancement on CT and MR imaging and sometimes intraventricular and parenchymal hemorrhage (Fig 1).^{21,22} Leptomeningeal enhancement helps distinguish meningitis from other causes of subarachnoid hemorrhage. Although anthrax meningitis has been described as rare in naturally acquired cases, examination of the 3 large outbreaks mentioned above reveals a different picture. Years after the Sverdlovsk outbreak, results of postmortem examinations were published. Half of the 42 reported cases had hemorrhagic meningitis.⁷ One of the 5 patients who died in the US mail bioterrorism attack had hemorrhagic meningitis.^{10,11} Of the 13 deaths in confirmed anthrax cases in the Scottish outbreak, 4 resulted from hemorrhagic meningitis.^{19,23} This 20%–50% rate of meningitis in fatal cases shows the ominous prognosis of anthrax meningitis and a higher rate in these outbreaks than reported in the past in sporadic cases. Guidelines for the management of anthrax from a Centers for Disease Control and Prevention expert panel published in February 2014 make the presence or suspected presence of meningitis a key decision point in treatment.²⁴ If meningitis is suspected, 3 drugs are recommended, including high-CNS-penetration drugs, and antitoxin therapy and steroids may be of benefit (though data are limited). Detection of hemorrhagic meningitis should thus trigger specific and aggressive treatment.

Nightmares from the Past

Two of the major pestilences from the past are of concern as potential weapons of mass destruction. Smallpox, caused by the DNA virus Variola, was a cause of enormous devastation. Highly

infectious, it caused approximately 30% mortality in unvaccinated subjects. The fact that humans are the only host made possible its elimination from nature by an unprecedented public health vaccination program.²⁵ The only known remaining samples are held under tight security in strict laboratory conditions in the United States and Russia (though a forgotten sample was recently found in a laboratory freezer and quickly moved). That very success, however, means that much of the world now has little or no immunity against smallpox. The potential for terrorist or rogue state use of smallpox has led to contentious and continuing debate about the fate of the remaining laboratory stores, the course of research, and the appropriate timetable for destruction of those samples. Clinical manifestations of smallpox are primarily cutaneous and pulmonary, not neurologic.

Plague, on the other hand, still exists in nature and causes disease.²⁶ *Yersinia pestis*, a nonmotile, Gram-negative bacillus, was the cause of several great pandemics, including the Black Death that killed a third of the population of Europe in the 14th century.²⁷ Bubonic plague occurs when infected fleas, part of an enzootic cycle with a rodent population, bite a human and cause regional lymphadenitis. Secondary pneumonia or septicemia may occur, with serious or fatal consequences. Primary septicemic plague, without bubo formation, has a high mortality. Pneumonic plague is uncommon in nature but is the form to be expected in a deliberate aerosol attack. Early treatment would be critical for survival. Some 5–15 cases of plague per year, mostly bubonic, occur in the United States, most in the Southwest. A review of >100 cases in the United States found that 6% had plague meningitis.²⁸ Most of these were patients with bubonic plague, presumably with hematogenous spread to the meninges. Primary plague meningitis probably does not occur. There have been suggestions that meningitis is more likely to occur with axillary or cervical buboes, though statistical evidence is not strong.²⁸ There is better evidence that patients with inadequate early treatment are at higher risk of developing meningitis.^{28–30}

Other Bacterial Agents

Tularemia was weaponized by the United States and the Union of Soviet Socialist Republics² and is among the agents to which volunteers were exposed during development in the Cold War.⁵ *Francisella tularensis*, a small Gram-negative intracellular coccobacillus, is the cause of tularemia and is found naturally in animals, including infected rabbits (whence the term “rabbit fever”). Humans can become infected by direct contact with animals, through ingestion, through contaminated ticks, or by inhalation. Human-to-human transmission is not reported. Naturally acquired cases are most commonly ulceroglandular, resulting in fever, chills, and a cutaneous ulcer with lymphadenopathy. Less common forms include typhoidal, oropharyngeal, and pneumonic. Tularemia can cause significant morbidity and mortality. Aerosolized delivery is the greatest concern for biowarfare use. The disease is highly infectious from as few as 10 inhaled bacteria. Pulmonary tularemia has occurred in a number of landscape workers in Martha’s Vineyard and elsewhere. Typical features are bilateral bronchopneumonia, sometimes with cavitation, and lymphadenopathy and pleural effusions in about one-third of patients.¹⁸ Meningitis or cerebral abscesses are rare complications of tularemia.^{31–33} There are no specific imaging features reported for tularemic meningitis, but notable laboratory aspects are mononuclear predominance in the CSF and sometimes delay in diagnosis because of difficulty of culture.³¹

Q fever is caused by *Coxiella burnetii*, an obligate intracellular, rickettsia-like organism found worldwide, which is highly infectious and produces a resistant, sporelike form.³⁴ Unlike anthrax, however, Q fever causes few deaths but prolonged, incapacitating illness. Acute Q fever can cause nonspecific febrile illness, pneumonia, hepatitis, or meningoencephalitis. Meningitis can occur without pneumonia.³⁵ Chronic forms are uncommon but serious and include endocarditis, chronic hepatitis, and osteomyelitis. A review of 121 cases of acute Q fever found >40% with neurologic symptoms, most commonly headache and confusion.³⁶ Clinical meningitis is less common.^{36,37} The laboratory picture of *C burnetii* meningitis is similar to that of aseptic meningitis, generally a mild lymphocytic pleocytosis, with the important distinction that it is treatable with antibiotics. CT and MR imaging findings are usually normal, but there are reported cases of encephalitis findings on imaging.³⁷

Brucellosis is caused by facultative intracellular bacteria of the *Brucella* genus, most commonly *Brucella melitensis*, which infects sheep, goats, cattle, swine, and dogs. Humans are infected by contact with infected animals or food, especially unpasteurized dairy products, but the disease is readily spread by aerosol, with a number of laboratory infections known.^{38,39} *Brucella* species were previously adapted for military biowarfare and are considered a possible bioterrorism agent. The reticuloendothelial system is the usual target, but granulomatous disease can occur in many organs. Clinical manifestations include acute febrile illness; chronic, undulant fevers; bone or joint disease in approximately one-third of patients, which can include spondylitis; genitourinary infections; hepatitis; lung infection; endocarditis, which, though rare, is responsible for most deaths; and neurologic disease in approximately 5%–10% of cases. Both peripheral and central nervous systems can be affected, and sensorineural hearing loss is com-

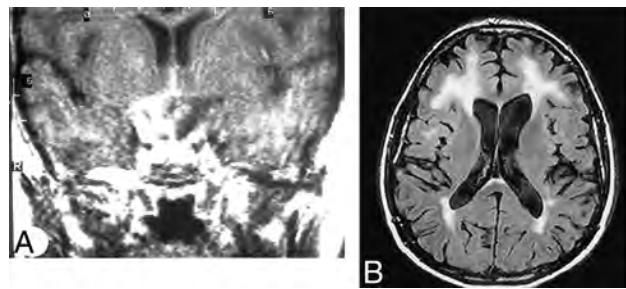


FIG 2. Neurobrucellosis. Coronal postgadolinium MR imaging (A) shows sellar and suprasellar thickening and enhancement, presumed granuloma formation. Abnormalities resolved after treatment. Axial FLAIR (B) of a different patient shows extensive white matter hyperintensities in a 50-year-old patient. White matter changes in brucellosis may be due to demyelination, perhaps from autoimmune reaction. Meningeal enhancement and vascular changes are also reported in brucellosis. Reprinted with permission from Al-Sous et al.⁴¹

mon. Effective treatment of CNS disease requires months of triple drug therapy. CNS disease can be the first or predominant presentation.⁴⁰ Imaging findings can be normal in many cases^{40,41}; a review found 10 of 23 MR imaging studies with normal findings. Observed abnormal findings include the following: inflammation with dural, leptomeningeal, or lumbar nerve root enhancement, and suprasellar granuloma formation; white matter changes, focal or diffuse, likely due to demyelination; and vascular findings, lacunes, or small hemorrhages (Fig 2).⁴¹ Endocarditis may also lead to embolic disease or mycotic aneurysms.

Viruses: Encephalitis and Hemorrhagic Fevers

A number of viruses most known for causing encephalitis are considered potential tools for deliberate attack.⁴² Most viral encephalitides are arboviruses transmitted in nature by mosquitoes but are also transmissible by aerosolization, which would most likely be implemented by a bioweapon. Hemorrhagic fever viruses also are potential bioweapon agents. Many of these illnesses result in nonspecific imaging findings, and for others, there is limited information available on imaging findings. We review here some candidate viruses with notable imaging or clinical features; the list is not exhaustive.

The most common cause of viral encephalitis is Japanese encephalitis, a flavivirus common in eastern and southern Asia and the Pacific Rim transmitted by mosquitoes.^{43,44} Other neurotropic flaviviruses cause St Louis encephalitis, West Nile virus, and Murray Valley encephalitis. As with other viruses in this family, many subclinical infections occur. In addition to nonspecific febrile illness, aseptic meningitis, encephalitis, and acute flaccid paralysis from anterior horn cell involvement may occur. Movement disorders are common. There is a strong predilection for involvement of the thalamus (Fig 3). A review of 42 patients with Japanese encephalitis found abnormal CT findings in 55% of patients and abnormal MR imaging findings in all patients. The thalami were abnormal in 94% of MR images.⁴⁵

West Nile virus has gained considerable attention since arriving in the United States several years ago. Many West Nile infections are asymptomatic or only mildly symptomatic, and

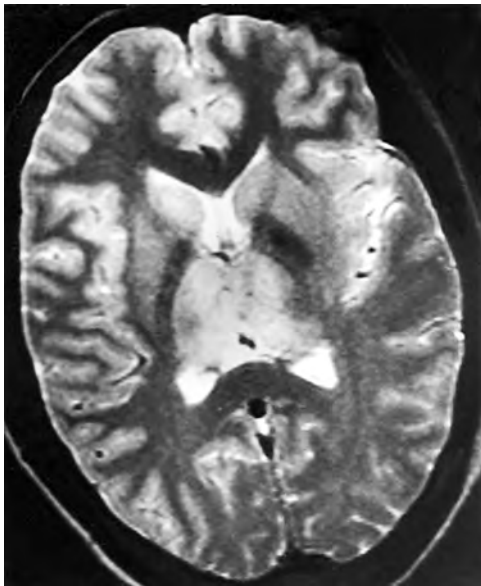


FIG 3. Japanese encephalitis. Axial T2-weighted MR imaging shows bilateral hyperintensity in the thalami and basal ganglia. Reprinted with permission from Kalita et al⁴⁴ Copyright © 2003, American Medical Association. All rights reserved.

a minority of patients develop fever, myalgias, headache, lymphadenopathy, and rash. Clinical encephalitis is serious, with a worse outcome in the elderly. Imaging features of West Nile encephalitis are nonspecific and range from normal to diffusion-only abnormalities to scattered T2 hyperintensities and, less commonly, parenchymal or meningeal enhancement. Normal and diffusion-only patterns appear to correlate with better clinical outcome, while more extensive abnormalities are associated with worse clinical outcome.⁴⁶ In addition to encephalitis, West Nile infection can result in myelitis, causing a polioliike illness.^{47,48} Imaging abnormalities in the spine can include spinal cord or nerve T2 hyperintensity or enhancement.⁴⁶

Equine encephalitis viruses, of which there are 3 major types in the Western hemisphere, have been of special interest for biowarfare. These alphaviruses are fairly readily grown, highly infectious by aerosol (>100 accidental laboratory infections have occurred), and relatively stable.⁴⁹ Venezuelan equine encephalitis was weaponized or investigated by several nations, including the United States and the Union of Soviet Socialist Republics. Venezuelan equine encephalitis results in a high rate of illness but a fairly low rate of encephalitis. There is relatively little information on imaging findings, to our knowledge. Most cases of Western encephalitis virus infection cause only mild symptoms. The development of frank encephalitis, however, as in any of the equine encephalitides, often causes major morbidity. Eastern encephalitis has a lower symptomatic infection rate but more frequently causes clinical encephalitis, with an especially high case fatality rate (50%–75%).⁵⁰ Eastern encephalitis also has more specific imaging features than most viral encephalitides. Most reports note early basal ganglia and thalamic involvement, which is a distinguishing feature from herpes simplex encephalitis (Fig 4).^{50–52} In all of these equine viral encephalitides, the elderly and very young are affected most severely.

Hemorrhagic fever viruses are RNA viruses that attack the vas-

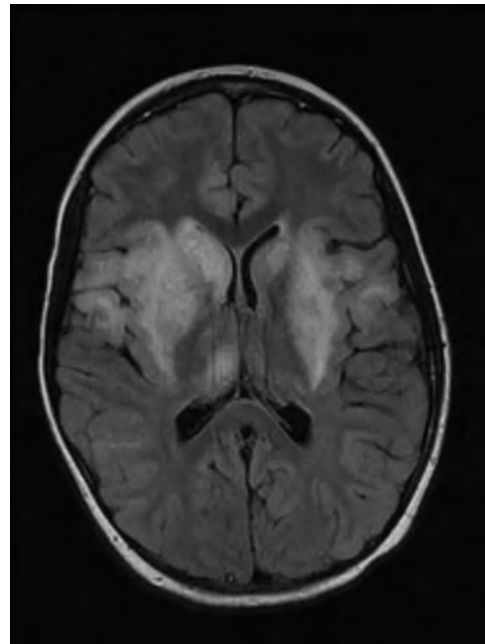


FIG 4. Eastern equine encephalitis. FLAIR image illustrates basal ganglia involvement typical in this disease and involvement of the thalami, insula, and more peripheral cortex. Reprinted with kind permission from Springer Science and Business Media from Lury and Castillo.⁵¹

culature. Increased blood permeability leads to hypovolemia and shock, with variations in specific organ involvement among the different viruses. For example, Rift Valley and yellow fever virus frequently cause hepatitis. Encephalitis has been reported as a rare complication of Rift Valley fever.^{18,53} Hemorrhagic complications are more common with the *Filoviridae* family. These include the Ebola virus, center of much attention and fear, and the Marburg virus, which was weaponized by the Union of Soviet Socialist Republics and also causes severe illness. Mortality rates from both viruses are in the range of 60%–90%. Information on imaging findings is sparse.

Although often mild or asymptomatic, dengue virus can cause hemorrhagic fever. There have been controversial allegations regarding the use of dengue as a biowarfare agent. Dengue is a widespread problem, with an estimated 100 million cases of symptomatic infection annually. Also a flavivirus, it is endemic in tropical and subtropical countries. Infection can be asymptomatic but can also result in dengue fever, with fever, headache, abdominal pain, and muscle, bone and joint pain; dengue hemorrhagic fever, with thrombocytopenia, increased vascular permeability, and hemorrhagic complications; and dengue shock syndrome.⁵⁴ Because of the sometimes severe hemorrhagic or metabolic complications, there is a variety of possible causes of dengue encephalopathy other than direct CNS infection. These include liver or renal damage, dehydration, and electrolyte imbalances. In addition, dengue viral encephalitis can occur, and separating secondary encephalopathy (in dengue hemorrhagic fever) from dengue viral encephalitis may be difficult.⁵⁵ Imaging findings are nonspecific but include T2 hyperintensities in a variety of locations.^{55,56} Intracranial hemorrhage can be seen, and encephalopathy or shock may be accompanied by imaging findings of ischemic injury (Fig 5).

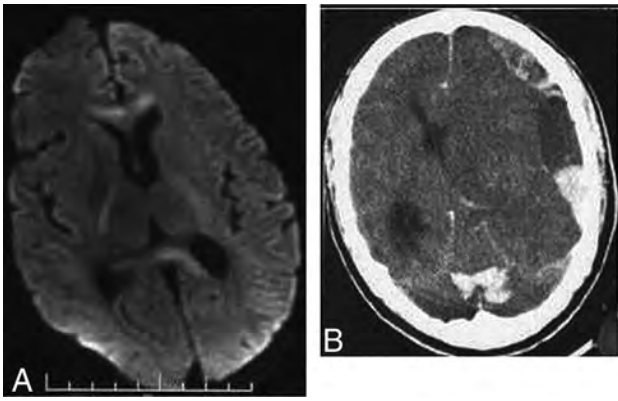


FIG 5. Dengue. DWI (A) shows increased signal in the genu and splenium of the corpus callosum and posterior limbs of the internal capsules in a patient with dengue encephalopathy. Areas of edema or restricted diffusion in dengue encephalopathy are nonspecific and variable. Noncontrast CT of a different patient (B), with dengue shock syndrome, shows subdural and parenchymal hemorrhage. Intracranial hemorrhage is uncommon in dengue, even in those with systemic and cutaneous hemorrhagic complications. Reprinted from Bhoi et al⁵⁵ with permission from Elsevier.

New or Emerging Diseases

New infectious disease threats are a constant possibility for a variety of reasons. New viruses are still being discovered, usually following an outbreak. Serious, frightening illnesses such as those due to coronaviruses bring extensive public concern. Pulmonary hantavirus came to attention in 1993 when multiple patients in the US Southwest presented with noncardiogenic pulmonary edema and respiratory failure, with high mortality. The responsible hantavirus was previously unrecognized. Other hantaviruses in Asia and Europe typically affect the kidneys.

Mutations change the infectious nature of organisms. Influenza virus, for example, is particularly notorious for constant change. Influenza, though most commonly causing pulmonary disease, can sometimes have serious neurologic consequences.

Diseases can also change or become serious when environments change. An example of an emerging disease with major CNS consequences is Nipah encephalitis. The responsible agent is a paramyxovirus for which fruit bats constitute the natural reservoir. An outbreak in Malaysia in 1999 caused >200 cases of human infection, with nearly 40% mortality.⁵⁷ The generally accepted reason for the sudden outbreak of human infection relates to the expansion of pig farming in or near orchards or the jungle. The likely pathway ensued when bats dropped partially eaten fruit contaminated with the virus, pigs would eat the fruit and become infected, and humans, in turn, became infected from pigs. Subsequent investigation has shown human infections from other intermediate animals, occurring without intermediate animal hosts, and also human-to-human transmission.⁵⁸ Pathologic findings include endothelial infection of small blood vessels in the CNS, with thrombotic occlusion and microinfarction. Imaging findings in acute Nipah encephalitis include multiple small, discrete lesions on MR imaging, likely the result of vasculitis (Fig 6). Spinal cord lesions may occur.⁵⁹ Chronic or recurrent forms can also occur, with a more confluent appearance of T2 hyperintensity in the cortex.^{59,60}

Chikungunya, caused by an alphavirus, is re-emerging after

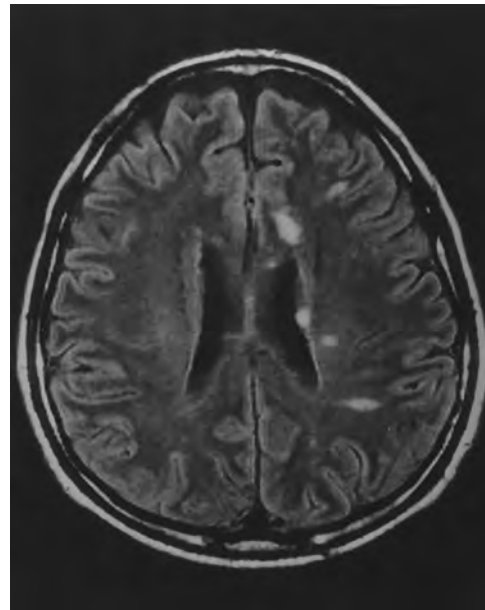


FIG 6. Nipah encephalitis, acute findings. Multiple discrete lesions on FLAIR are consistent with vasculitis reported on pathologic studies. Reprinted from Sarji et al⁶⁰ with permission from the American Journal of Roentgenology.

decades of quiescence. Natural spread is by mosquitos, especially the same *Aedes* species that carry dengue. Epidemics exploded around the Indian Ocean in 2005. A different strain appears to be responsible for the recent outbreak in the Western hemisphere in 2013.⁶¹ Local transmission in the United States began in the summer of 2014. Chikungunya infection is characterized by fever, rash, headache, and, most notably, polyarthralgias, which can be debilitating and chronic.⁶² Encephalopathy, meningoencephalitis, flaccid paralysis, and Guillain-Barré syndrome are uncommon manifestations.⁶³ Vertical (mother-to-child) transmission can cause encephalopathy in the child, with areas of restricted diffusion on MR imaging during the acute phase.⁶⁴

The likelihood of emerging infections used for purposes of biowarfare is unknown, but some of these viruses can be highly infectious and harmful. Such traits may be enticing for nefarious purposes.⁶⁵ Moreover, there is greater potential than ever before for deliberate genetic manipulation of infectious agents. Such manipulation could result in greater virulence or resistance to antibiotics or vaccines. There are reports that Soviet biowarfare research included attempts to create chimera viruses combining smallpox with virulence genes from the Ebola virus, for example.²⁵

CONCLUSIONS

Armies of pestilence have been used for both military and terrorist purposes in the past and remain a threat. Several potential biowarfare infections cause abnormalities relevant to neuroimaging. Hemorrhagic meningitis should suggest anthrax. Although carrying a grim prognosis, hemorrhagic meningitis in anthrax should change treatment. Meningitis can also occur in several unusual diseases, including plague, Q fever, and tularemia, and is treatable with appropriate antibiotics. CNS findings in brucellosis are protean and can include inflammatory changes, demyelination, and

vascular disease. Among the many different forms of viral encephalitis, Eastern equine and Japanese are notable for deep gray matter predilection. New or changed diseases remain a constant threat. In the appalling event of deliberate use, prompt recognition would be especially important.

Disclosures: Blaine L. Hart—UNRELATED: Grants: National Institutes of Health grant: U54 NS065705. Loren Ketai—UNRELATED: Grants: National Institutes of Health grant: R01AT007171.

REFERENCES

- Martin JW, Christopher GW, Eitzen EM. **History of biological weapons: from poisoned darts to intentional epidemics.** In: Dembek ZF, ed. *Medical Aspects of Biological Warfare.* Washington, DC: Borden Institute; 2007:1–20
- Croddy E. *Chemical and Biological Warfare: A Comprehensive Survey for the Concerned Citizen.* New York: Copernicus Books; 2002
- Manchee RJ, Broster MG, Stagg AJ, et al. **Formaldehyde solution effectively inactivates spores of *Bacillus anthracis* on the Scottish island of Gruinard.** *Appl Environ Microbiol* 1994;60:4167–71
- Cook MS, Woolf AF. **Preventing proliferation of biological weapons: US assistance to the former Soviet states.** Published April 10, 2002. <http://oai.dtic.mil/oai/oai?verb=getRecord&metadataPrefix=html&identifier=ADA454722>. Accessed August 1, 2014
- PBS: American Experience. *The Living Weapon.* <http://www.pbs.org/wgbh/americanexperience/features/transcript/weapon-transcript/>. Accessed August 1, 2014
- Meselson M, Guillemin J, Hugh-Jones M, et al. **The Sverdlovsk anthrax outbreak of 1979.** *Science* 1994;266:1202–08
- Abramova FA, Grinberg LM, Yampolskaya OV, et al. **Pathology of inhalational anthrax in 42 cases from the Sverdlovsk outbreak of 1979.** *Proc Natl Acad Sci U S A* 1993;90:2291–94
- Ragg V. **Russia: anthrax in the Urals.** *Lancet* 1992;339:419–20
- Takahashi H, Keim P, Kaufmann AF, et al. ***Bacillus anthracis* bioterrorism incident, Kameido, Tokyo, 1993.** *Emerg Infect Dis* 2004;10:117–20
- Jernigan JA, Stephens DS, Ashford DA, et al. **Bioterrorism-related inhalational anthrax: the first 10 cases reported in the United States.** *Emerg Infect Dis* 2001;7:933–44
- Jernigan DB, Raghunathan PL, Bell BP, et al. **Investigation of bioterrorism-related anthrax, United States, 2001: epidemiologic findings.** *Emerg Infect Dis* 2002;8:1019–28
- Dixon TC, Meselson M, Guillemin J, et al. **Anthrax.** *N Engl J Med* 1999;341:815–26
- Purcell BK, Worsham PL, Friedlander AM. **Anthrax.** In: Dembek ZF, ed. *Medical Aspects of Biological Warfare.* Washington, DC: Borden Institute; 2007:69–90
- Ramsay CN, Stirling A, Smith J, et al. **An outbreak of infection with *Bacillus anthracis* in injecting drug users in Scotland.** *Euro Surveill* 2010;15:pii:19465
- Palmateer NE, Ramsay CN, Browning L, et al. **Anthrax infection among heroin users in Scotland during 2009–2010: a case-control study by linkage to a national drug treatment database.** *Clin Infect Dis* 2012;55:706–10
- Abbara A, Brooks T, Taylor GP, et al. **Lessons for control of heroin-associated anthrax in Europe from 2009–2010 Outbreak Case Studies, London, UK.** *Emerg Infect Dis* 2014;20:1115–22
- Brachman PS. **Inhalation anthrax.** *Ann N Y Acad Sci* 1980;353:83–93
- Ketai L, Alrajhi AA, Hart B, et al. **Radiologic manifestations of potential bioterrorist agents of infection.** *AJR Am J Roentgenol* 2003;180:565–75
- National Services Scotland on behalf of the National Anthrax Outbreak Control Team. **An outbreak of anthrax among drug users in Scotland, December 2009 to December 2010.** December 2011. <http://www.documents.hps.scot.nhs.uk/giz/anthrax-outbreak/anthrax-outbreak-report-2011-12.pdf>. Accessed April 2, 2014
- Tahernia AC, Hashemi G. **Survival in anthrax meningitis.** *Pediatrics* 1972;50:329–33
- Kim HJ, Jun WB, Lee SH, et al. **CT and MR findings of anthrax meningoencephalitis: report of two cases and review of the literature.** *AJNR Am J Neuroradiol* 2001;22:1303–05
- Yildirim H, Kabakus N, Koc M, et al. **Meningoencephalitis due to anthrax: CT and MR findings.** *Pediatr Radiol* 2006;36:1190–93
- Booth MG, Hood J, Brooks TJ, et al. **Anthrax infection in drug users.** *Lancet* 2010;375:1345–46
- Hendricks KA, Wright ME, Shadomy SV, et al. **Centers for Disease Control and Prevention expert panel meetings on prevention and treatment of anthrax in adults.** *Emerg Infect Dis* 2014;20 doi: 10.3201/eid2002.130687
- Tucker JB. *Scourge: The Once and Future Threat of Smallpox.* New York: Atlantic Monthly Press; 2001
- Inglesby TV, Dennis DT, Henderson DA, et al. **Plague as a biological weapon: medical and public health management—Working Group on Civilian Biodefense.** *JAMA* 2000;283:2281–90
- Bray RS. *Armies of Pestilence: The Impact of Disease on History.* Cambridge: James Clarke and Co; 2004
- Becker TM, Poland JD, Quan TJ, et al. **Plague meningitis: a retrospective analysis of cases reported in the United States, 1970–1979.** *West J Med* 1987;147:554–57
- Martin AR, Hurtado FP, Plessala RA, et al. **Plague meningitis: a report of three cases in children and review of the problem.** *Pediatrics* 1967;40:610–16
- Jawetz E, Meyer KF. **The behaviour of virulent and avirulent *P. pestis* in normal and immune experimental animals.** *J Infect Dis* 1944;74:1–13
- Hofinger DM, Cardona L, Mertz GJ, et al. **Tularemia meningitis in the United States.** *Arch Neurol* 2009;66:523–27
- Lovell VM, Cho CT, Lindsey NJ, et al. **Francisella tularensis meningitis: a rare clinical entity.** *J Infect Dis* 1986;154:916–18
- van de Beek D, Steckelberg JM, Marshall WF, et al. **Tularemia with brain abscesses.** *Neurology* 2007;68:531–31
- Anderson A, Bijlmer H, Fournier PE, et al. **Diagnosis and management of Q fever—United States, 2013: recommendations from CDC and the Q Fever Working Group.** *MMWR Recomm Rep* 2013;62(RR-03):1–30
- Schattner A, Kushnir M, Zhornicky T, et al. **Lymphocytic meningitis as the sole manifestation of Q fever.** *Postgrad Med J* 1993;69:636–37
- Kofteridis DP, Mazokopakis EE, Tselentis Y, et al. **Neurological complications of acute Q fever infection.** *Eur J Epidemiol* 2004;19:1051–54
- Bernit E, Pouget J, Janbon F, et al. **Neurological involvement in acute Q fever: a report of 29 cases and review of the literature.** *Arch Intern Med* 2002;162:693–700
- Pappas G, Akritidis N, Bosilkovski M, et al. **Brucellosis.** *N Engl J Med* 2005;352:2325–36
- Purcell BK, Hoover DL, Friedlander AM. **Brucellosis.** In: Dembek ZF, ed. *Medical Aspects of Biological Warfare.* Washington, DC: Borden Institute; 2007:185–98
- Bilen Ş, Güneş HN, Saka M, et al. **Four different clinical manifestations of neurobrucellosis (case reports).** *Eur J Intern Med* 2008;19:e75–e77
- Al-Sous MW, Bohlega S, Al-Kawi MZ, et al. **Neurobrucellosis: clinical and neuroimaging correlation.** *AJNR Am J Neuroradiol* 2004;25:395–401
- Bossi P, Tegnell A, Baka A, et al. **BICHAT guidelines for the clinical management of viral encephalitis and bioterrorism-related viral encephalitis.** *Euro Surveill* 2004;9:E21–22
- Misra UK, Kalita J. **Overview: Japanese encephalitis.** *Prog Neurobiol* 2010;91:108–20
- Kalita J, Misra UK, Pandey S, et al. **A comparison of clinical and radiological findings in adults and children with Japanese encephalitis.** *Arch Neurol* 2003;60:1760–64
- Kalita J, Misra UK. **Comparison of CT scan and MRI findings in the diagnosis of Japanese encephalitis.** *J Neurol Sci* 2000;174:3–8

46. Ali M, Safriel Y, Sohi J, et al. **West Nile virus infection: MR imaging findings in the nervous system.** *AJNR Am J Neuroradiol* 2005;26:289–97
47. Leis AA, Stokic DS, Polk JL, et al. **A poliomyelitis-like syndrome from West Nile virus infection.** *N Engl J Med* 2002;347:1279–80
48. Sejvar JJ, Leis AA, Stokic DS, et al. **Acute flaccid paralysis and West Nile virus infection.** *Emerg Infect Dis* 2003;9:788–93
49. Steele KE, Reed DS, Glass PJ, et al. **Alphavirus encephalitis.** In: Dembek ZF, ed. *Medical Aspects of Biological Warfare*. Washington, DC: Borden Institute; 2007:241–70
50. Deresiewicz RL, Thaler SJ, Hsu L, et al. **Clinical and neuroradiographic manifestations of eastern equine encephalitis.** *N Engl J Med* 1997;336:1867–74
51. Lury K, Castillo M. **Eastern equine encephalitis: CT and MRI findings in one case.** *Emerg Radiol* 2004;11:46–48
52. Silverman MA, Misasi J, Smole S, et al. **Eastern equine encephalitis in children, Massachusetts and New Hampshire USA, 1970–2010.** *Emerg Infect Dis* 2013;19:194–201
53. Alrajhi AA, Al-Semari A, Al-Watban J. **Rift Valley fever encephalitis.** *Emerg Infect Dis* 2004;10:554–55
54. Carod-Artal FJ, Wichmann O, Farrar J, et al. **Neurological complications of dengue virus infection.** *Lancet Neurol* 2013;12:906–19
55. Bhoi SK, Naik S, Kumar S, et al. **Cranial imaging findings in dengue virus infection.** *J Neurol Sci* 2014;342:36–41
56. Cam BV, Fonsmark L, Hue NB, et al. **Prospective case-control study of encephalopathy in children with dengue hemorrhagic fever.** *Am J Trop Med Hyg* 2001;65:848–51
57. Chua KB. **Nipah virus: a recently emergent deadly paramyxovirus.** *Science* 2000;288:1432–35
58. Luby SP, Gurley ES, Hossain MJ. **Transmission of human infection with Nipah virus.** *Clin Infect Dis* 2009;49:1743–48
59. Lim CCT, Lee WL, Leo YS, et al. **Late clinical and magnetic resonance imaging follow up of Nipah virus infection.** *J Neurol Neurosurg Psychiatry* 2003;74:131–33
60. Sarji SA, Abdullah BJ, Goh KJ, et al. **MR imaging features of Nipah encephalitis.** *AJR Am J Roentgenol* 2000;175:437–42
61. Morens DM, Fauci AS. **Chikungunya at the door: déjà vu all over again?** *N Engl J Med* 2014;371:885–87
62. Burt FJ, Rolph MS, Rulli NE, et al. **Chikungunya: a re-emerging virus.** *Lancet* 2012;379:662–71
63. Economopoulou A, Dominguez M, Helynck B, et al. **Atypical chikungunya virus infections: clinical manifestations, mortality and risk factors for severe disease during the 2005–2006 outbreak on Réunion.** *Epidemiol Infect* 2009;137:534–41
64. Gérardin P, Barau G, Michault A, et al. **Multidisciplinary prospective study of mother-to-child chikungunya virus infections on the island of La Reunion.** *PLoS Med* 2008;5:e60
65. Whitehouse CA, Schmaljohn AL, Dembek ZF. **Emerging infectious diseases and future threats.** In: Dembek ZF, ed. *Medical Aspects of Biological Warfare*. Washington, DC: Borden Institute; 2007:579–607

4D-CTA in Neurovascular Disease: A Review

H.G.J. Kortman, E.J. Smit, M.T.H. Oei, R. Manniesing, M. Prokop, and  F.J.A. Meijer



ABSTRACT

SUMMARY: CT angiography is a widely used technique for the noninvasive evaluation of neurovascular pathology. Because CTA is a snapshot of arterial contrast enhancement, information on flow dynamics is limited. Dynamic CTA techniques, also referred to as 4D-CTA, have become available for clinical practice in recent years. This article provides a description of 4D-CTA techniques and a review of the available literature on the application of 4D-CTA for the evaluation of intracranial vascular malformations and hemorrhagic and ischemic stroke. Most of the research performed to date consists of observational cohort studies or descriptive case series. These studies show that intracranial vascular malformations can be adequately depicted and classified by 4D-CTA, with DSA as the reference standard. In ischemic stroke, 4D-CTA better estimates thrombus burden and the presence of collateral vessels than conventional CTA. In intracranial hemorrhage, 4D-CTA improves the detection of the “spot” sign, which represents active ongoing bleeding.

ABBREVIATIONS: dAVF = dural arteriovenous fistula; TI-CTA = timing-invariant CTA

Multidetector row CT angiography has enabled rapid noninvasive evaluation of the intracranial vasculature for acute neurologic conditions such as subarachnoid hemorrhage or ischemic stroke. While the anatomic evaluation is excellent, the evaluation of flow dynamics is limited with CTA because information is obtained from only 1 single time point during the passage of a contrast bolus.^{1,2}

Diagnostic catheter-based digital subtraction angiography has been widely replaced by CTA as a diagnostic procedure but retains its value if very high spatial resolution is required or the flow dynamics of a cerebral vascular abnormality need to be assessed. Remaining indications for DSA include work-up of vascular malformations or the evaluation of collateral vessels in obstructive arterial disease. In addition, DSA is considered the criterion standard for the detection of aneurysms in nontraumatic subarachnoid hemorrhage. Drawbacks of DSA are the relatively time-consuming procedure, high cost, radiation exposure for both patient and operator,^{3,4} a low but nonnegligible risk of transient or permanent neurologic complications,⁵⁻⁷ and an even higher risk of silent embolic events.⁸

Dynamic CTA has been developed in recent years as a technique that combines the noninvasive nature of CTA with the dynamic acquisition of DSA. The technique is also referred to as 4D-CTA and enables the noninvasive evaluation of flow dynamics of the intracranial vasculature by multiple subsequent CT acquisitions or a continuous volume CT acquisition for a period of time.

The value of 4D-CTA compared with CTA and DSA has been the subject of an increasing number of publications within the past decade. This article provides a description of the 4D-CTA techniques and reviews the current literature on the application of cranial 4D-CTA in hemorrhagic and ischemic stroke and the evaluation of intracranial arteriovenous malformations and arteriovenous fistulas.

Imaging Technique

Data Acquisition. Various approaches have been developed to provide whole-brain coverage of 4D-CTA: a toggling-table technique, shuttle mode scanning, or volume mode (Fig 1). The width of the CT detector determines which acquisition mode can be used to ensure coverage of the whole brain.

The most versatile option is a volume mode, which allows complete or partial coverage of the whole brain during 1 rotation. Detector configurations that cover the whole brain with 16-cm coverage are now available from 2 major vendors and have been implemented as 320×0.5 mm or 256×0.625 mm collimations. Scanners with 4- to 8-cm coverage acquire smaller portions of the cerebral vascular system, usually including the region of the circle of Willis and above.⁹

From the Department of Radiology and Nuclear Medicine, Radboud University Nijmegen Medical Center, Nijmegen, the Netherlands.

Please address correspondence to Frederick J.A. Meijer, MD, Geert Grooteplein 10, 6500 HB Nijmegen, the Netherlands; e-mail: Anton.Meijer@radboudumc.nl

 Indicates open access to non-subscribers at www.ajnr.org

 Indicates article with supplemental on-line table.

 Indicates article with supplemental on-line video.

<http://dx.doi.org/10.3174/ajnr.A4162>

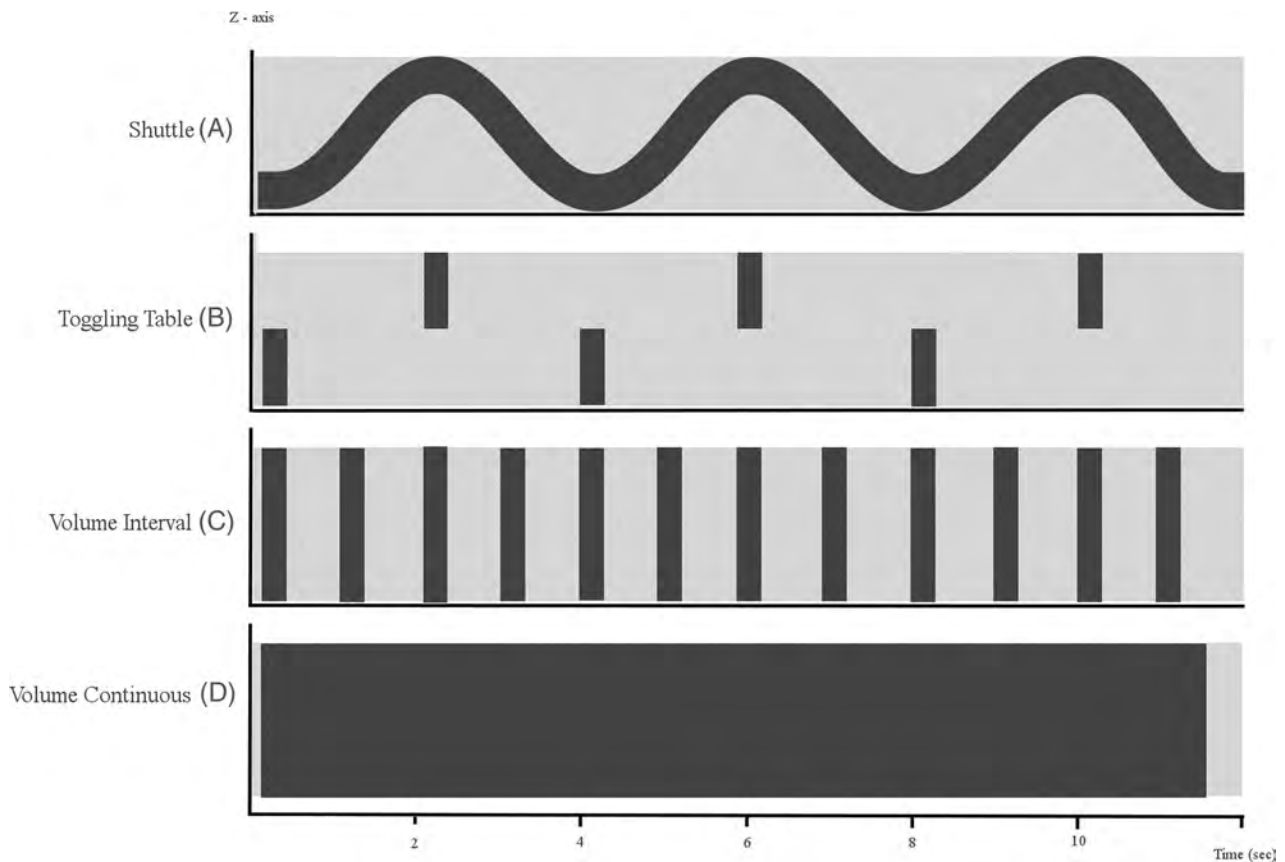


FIG 1. Schematic diagram of 4D-CTA imaging techniques. The x-axis represents the time domain. The y-axis represents the z-dimension. The light-gray horizontal bar represents the area that needs to be covered in the z-dimension. *A*, Shuttle mode: the sinus represents continuous table movement back and forth in the z-axis dimension to provide adequate coverage of the region of interest at multiple points in time. Notice that the temporal resolution is a function of the speed of table movement, typically 2–4 seconds depending on coverage. *B*, Toggling-table technique: the bars represent table repositioning in the z-axis dimension to provide adequate coverage of the region of interest at multiple points in time. Notice that the temporal resolution is a function of the speed of table repositioning, typically 3–4 seconds. *C*, Volume scanning: complete coverage of the region of interest (horizontal bar) with 1 gantry rotation. Notice that the temporal resolution is a function of the scanning interval settings because each rotation provides full coverage. Volume CT scanning enables (*D*) continuous volume scanning. Temporal resolution is limited by the gantry rotation speed.

Dynamic acquisitions with this volume mode can be performed discontinuously or continuously, depending on the required temporal resolution. The sequence of 3D datasets acquired with the discontinuous acquisition mode is sampled according to preset fixed or variable temporal intervals, usually in the range of 1- to 4-seconds. True 4D-datasets from the continuous scanning mode are acquired continuously during a period of time. These continuously acquired data can then be retrospectively reconstructed at any time interval. While the reconstructed time interval can be as little as 20 ms, the data for each reconstructed 3D volume are sampled during one-half to 1 gantry rotation, usually on the order of 0.275–0.5 seconds. In the case of continuous volume acquisitions and narrow temporal reconstruction intervals, the reconstructed data overlap in the temporal domain, very similar to overlapping data created from helical scanning in the spatial domain.¹⁰ Continuous scanning is possible only in volume mode.

The toggling-table technique increases coverage by continuously switching between adjacent regions with fast table movement.¹¹ The minimum time intervals between subsequent acquisitions of each of the 2 regions is limited by the detector width and the speed of table movement. The temporal resolution typically allows a scan interval in the range of 2–4 seconds.¹² One has to be

aware, however, that the enhancement curve of the cerebral vasculature is sampled differently for both scan regions, with an interleaving sampling pattern. Artifacts at the interface between regions may arise because enhancement differs between consecutive scans; this difference could impair the evaluation of flow dynamics or the detection of steno-occlusive vessel disease. A detector width of approximately 8 cm is required to image the entire brain in 2 acquisitions. For scanners with smaller detector widths, shuttle mode scanning is preferred to obtain whole-brain coverage because the temporal resolution will be significantly reduced with the toggling-table technique.

In shuttle mode scanning, a continuous helical acquisition is performed while the table moves smoothly to and fro to cover the desired scan range. This is the preferred mode for all scanners that cannot cover the whole area within 1 volume. Compared with the toggling-table technique, the shuttle mode is more flexible with regard to the length of coverage and does not create artifacts at the border between adjacent regions. However, temporal sampling intervals are only constant for the center of the scan range. Further to the periphery of the scan range, sampling intervals alternate between progressively shorter and longer periods (Fig 1).

Radiation Dose. The cumulative dose of 4D-CTA is the sum of the radiation doses of the individual acquisitions. Even if each of these acquisitions uses a lower dose than conventional CTA, the cumulative dose of 4D-CTA is usually substantially higher than that in conventional CTA.^{13,14} Reducing the dose of individual acquisitions further will lead to excessive image noise. This needs to be counterbalanced by image filtering or iterative reconstruction. Proper image filtering will allow substantial dose reduction with preservation of or even increase in diagnostic image quality.^{15,16} The use of iterative reconstructions has enabled a radiation-dose reduction with preserved image quality.¹⁷

The radiation dose becomes larger as the number of acquisitions during 4D-CTA or the dose per acquisition is increased. Continuous scanning delivers the highest dose. A faster gantry rotation time at identical milliamperes-second settings will reduce the dose but increase the noise. The cumulative milliamperes-second values are a good relative indicator of radiation exposure. At a setting of 200 mAs and a rotation time of 0.275 ms, each rotation delivers 55 mA. If for 40 seconds, an acquisition is performed every 2 seconds for a total of 20 acquisitions, the cumulative exposure becomes $55 \text{ mA} \times 20 = 1100 \text{ mA}$, which is identical to a continuous acquisition of 5.5 seconds ($5.5 \text{ seconds} \times 200 \text{ mA} = 1100 \text{ mAs}$).

Comparison of the radiation dose between CTA and DSA is challenging because of different geometries of the x-ray beam. In addition, radiation exposure is reported by using different units of measurement.¹⁸ An effective radiation dose, however, can be compared but varies greatly depending on the scanning technique for 4D-CTA and the complexity of the procedure and the number of contrast runs during DSA. Effective doses of 5–6 mSv have been reported for 4D-CTA and 2–4.5 mSv for diagnostic cerebral DSA.^{3,18,19} Doses reported for therapeutic interventions are substantially higher. Skin doses of $>10,000 \text{ mGy}$ may be accumulated during complex procedures.^{20,21}

Image Processing. 4D-CTA generates a large amount of data that depends on the number of reconstructed 3D volumes and the reconstruction increment of each 3D volume. For example, a shuttle acquisition that covers 150 mm and uses 10 passes to and fro creates 2×10 datasets. If each dataset is reconstructed as a 1-mm section with a 1-mm increment, the total number of CT images is $20 \times 150 = 3000$. If overlapping reconstruction with a 0.5-mm increment is used, the number of images doubles to 6000. A discontinuous volume acquisition consisting of 20 scans with $320 \times 0.5 \text{ mm}$ detector collimation reconstructed as 0.5-mm sections with a 0.5-mm increment will create $320 \times 20 = 6400$ images. If the increment is reduced to 0.25 mm, which provides high-quality isotropic imaging, the number doubles to 12,800 images. A continuous-volume CT acquisition with $320 \times 0.5 \text{ mm}$ collimation during 10 seconds reconstructed at a frame rate of 10 per second and 0.5-mm increments results in $320 \times 10 \times 10 = 32,000$ images. These numbers increase when additional image planes are reconstructed.

This huge number of images requires powerful workstations and optimized data postprocessing. Viewing the data as thin sections is possible but very ineffective, given the total number of images to be reviewed. This mode is reserved for problem solving.

Maximum intensity projections provide a much better over-

view of the vasculature and are the standard mode of viewing 4D data. Because of superimposing bone, usually thin slabs of 10–20 mm are viewed interactively. Small vascular structures are better evaluated in multiplanar reconstructions.

Alternatively, bone subtraction can be performed. The various 3D datasets should be aligned by rigid or nonrigid registration to compensate for patient motion during the 4D acquisition. If a patient moves during an acquisition, the dataset becomes slightly distorted and rigid registration leads to artifacts in the moving areas. These problems can be avoided by nonrigid approaches.

Bone subtraction then can be performed by subtracting the nonenhanced scan from each subsequent acquisition. This procedure, however, substantially increases image noise. Therefore, bone masking is frequently performed. This technique identifies bones as high-attenuation objects on the nonenhanced scan and removes these from the subsequent contrast-enhanced 4D sequence (On-line Videos).

MIP of these bone-subtracted data creates DSA-like images that can be viewed as a temporal sequence that shows contrast inflow and washout. As an alternative to MIP, volume-rendering, which provides more morphologic detail of the vessel lumen, can be performed.

The vascular morphology can best be evaluated if the whole 4D dataset is condensed into a 3D dataset by using temporal MIP, which displays the brightest voxel across all time points. If one filters the data in the temporal domain, spatial resolution remains intact while image noise is reduced and image quality is substantially improved. The resulting so-called timing-invariant CTA (TI-CTA) creates a high-quality timing-insensitive MIP of the vascular tree.²²

Several studies reported inferior or comparable image quality of 4D-CTA and conventional CTA.^{13,14,19} TI-CTA, on the other hand, was shown to have a 43% higher contrast-to-noise ratio and a 28% lower image noise compared with conventional CTA.¹⁶ In addition, TI-CTA was rated as having less vascular noise, better vascular contour, better detail visibility of medium arteries, better detail visibility of small arteries, and better overall image quality than conventional CTA and 4D-CTA.¹⁶

Choice of Acquisition Technique. The choice between a continuous or noncontinuous 4D-CTA acquisition depends on the available scanning modes and is limited to noncontinuous acquisitions in case of toggling-table or shuttle modes. In patients suspected of having a high-flow vascular malformation, such as a dural AVF (dAVF) or AVM, the detection of abnormal early filling of venous structures requires a high temporal resolution of 4D-CTA. These cases profit from continuous acquisition (Fig 2). When collateral flow in case of an arterial occlusion needs to be evaluated, a lower temporal resolution will be sufficient.

Review of Literature on 4D-CTA in Neurovascular Disease

Vascular Malformations. An arteriovenous malformation is an abnormal communication between an artery and a vein with a network of abnormal intervening vessels, referred to as a nidus. An arteriovenous fistula is an abnormal communication between an artery and a venous structure without a nidus. For planning endovascular or surgical treatment, various grading systems have

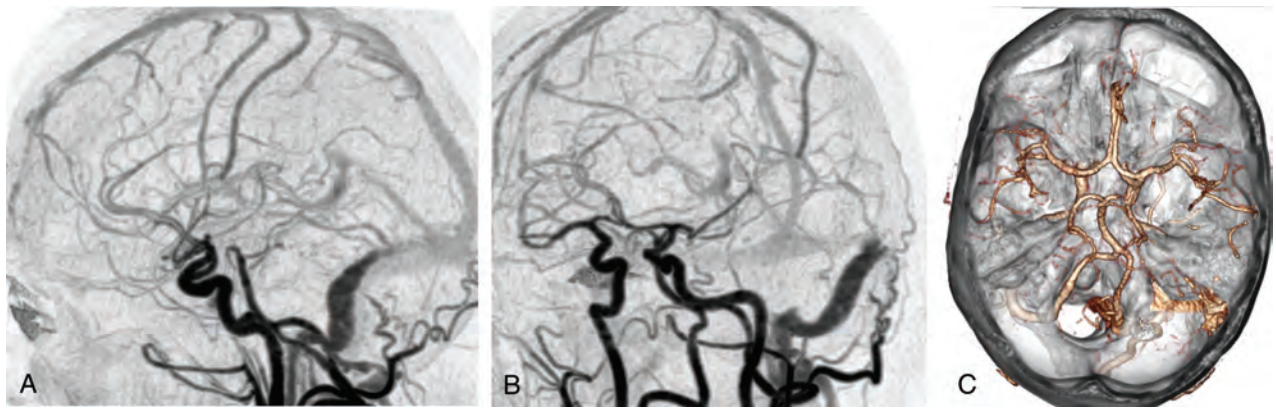


FIG 2. 4D-CTA demonstrating a Borden type I dural arteriovenous fistula of the left sigmoid sinus. Selected 4D-CTA subtraction MIP images of a continuous 4D-CTA volume acquisition (320–detector row CT) in lateral (A) and oblique (B) projections in a patient presenting with left-sided tinnitus. Branches of the occipital artery are identified as arterial feeders of the dAVF. There is normal antegrade venous return. The 3D image (C) demonstrates the advantage of 4D-CTA to study vessels in relation to surrounding structures.

Classification of arteriovenous malformations and arteriovenous fistulas

Pathology	AVM	AVF
Distinguishing feature	Presence of a nidus	No nidus
Grading system	Spetzler-Martin classification	Cognard classification Borden classification
Classification	Spetzler-Martin AVM grading scale Size Small (<3 cm) = 1 Medium (3–6 cm) = 2 Large (>6 cm) = 3 Eloquence of adjacent brain Noneloquent = 0 Eloquent = 1 Venous drainage Superficial only = 0 Deep component = 1	Cognard classification: Grade I: in sinus wall; normal antegrade venous drainage Grade IIa: in sinus; reflux to sinus, not cortical veins Grade IIb: retrograde drainage (reflux) to cortical veins Grade III: direct cortical venous drainage; no venous ectasia Grade IV: direct cortical venous drainage and venous ectasia Grade V: Spinal perimedullary venous drainage Borden classification: Type I: dural arterial supply with antegrade venous drainage Type Ia: simple dAVF with single meningeal arterial supply Type Ib: complex dAVF with multiple meningeal arteries Type II: retrograde cortical venous drainage Type III: dural arteries drain into cortical veins

been developed on the basis of imaging characteristics. Features include the location of the lesion, presence and size of a nidus, number and size of the feeding arteries, and the patterns of venous drainage (Table). The most commonly used grading system for AVMs is the Spetzler-Martin system.²³ The Cognard classification and Borden classification are most commonly used for dAVFs.^{24,25} These classification systems were originally developed on the basis of DSA but can also be applied to 4D-CTA.

Adequate depiction of the angioarchitectural features of intracranial vascular malformations is essential for hemorrhage risk assessment and treatment planning.^{23–25} The high temporal and spatial resolution required could, until recently, only be provided by DSA. Studies that compare 4D-CTA with DSA for the evaluation of brain AVMs and AVFs include descriptive case series and observational cohort studies (On-line Table). Because none of these exceed level 3 evidence, further research is warranted to assess the role of 4D-CTA in the work-up of craniospinal vascular malformations.

Wang et al²⁶ compared 4D-CTA and DSA examinations for diagnosing AVMs in 17 patients. They found that 4D-CTA was consistent with DSA in all cases for AVM location, size, and vascular structures. Compared with DSA, 4D-CTA could distinguish the main feeding arteries and successfully identify all draining veins in all patients. In 1/17 patients, however, there were discrepan-

cies in the identification of smaller and specific arterial branches. Good correlation of 4D-CTA with DSA for the detection and grading of cerebral AVMs was also found by Willems et al.²⁷ In 17 patients, all AVMs were detected by 4D-CTA. With regard to the Spetzler-Martin grade, 4D-CTA disagreed with DSA in 1 patient in whom deep venous drainage was missed.

In a study comparing 4D-CTA and DSA in patients with a variety of cerebrovascular pathology, physiologic and abnormally shortened cerebral circulation times were comparable for 4D-CTA and DSA.²⁸

Abnormal venous drainage is the hallmark of classifying a dAVF. Retrograde venous flow in cortical veins, which is associated with increased risk of hemorrhage,²⁴ can be visualized by using 4D-CTA.²⁴ Performance of 4D-CTA was similar to that of DSA for the diagnosis and grading of dAVFs. Fujiwara et al²⁹ compared 4D-CTA with DSA in 29 patients for diagnosis, classification, and follow-up of dAVFs. DSA depicted 33 dAVFs in 28 cases (in 1 subject the dAVF was resolved after endovascular treatment). By consensus reading, 4D-CTA correctly detected 32/33 dAVFs in 27 cases and properly graded 31/33 lesions by using the Cognard classification.²⁴ Spinal venous drainage was missed by both readers on 4D-CTA in a case with a Cognard type V dAVF. In 1 case, 1 reader missed cortical venous reflux on 4D-CTA.

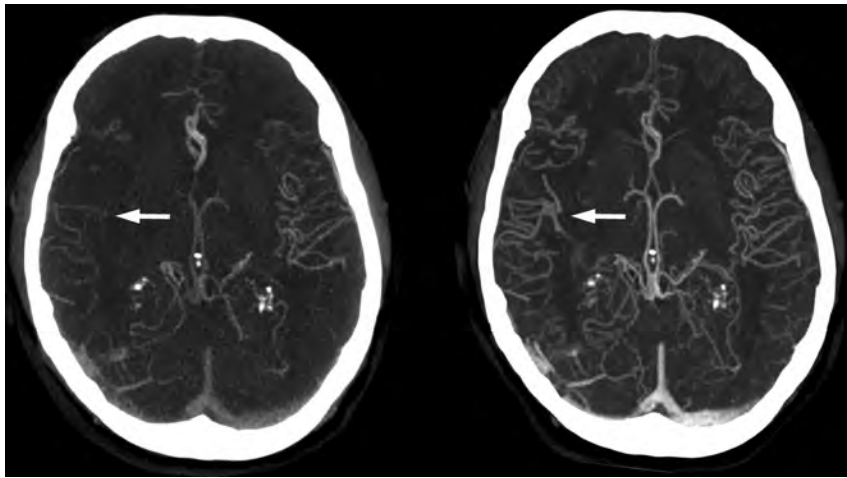


FIG 3. Timing-invariant CTA better estimates the extent of collateral circulation in a patient with right middle cerebral artery occlusion. The *left* image is a conventional CTA showing poor collateral circulation and suggests a poor prognosis. The *right* image is a TI-CTA image from a 4D-CTA acquisition (ie, temporal MIP), which shows good collateral filling and suggests a good prognosis. In this case, the patient had a good recovery.

Intermodality agreement for the presence and classification of dAVFs was excellent ($\kappa = 0.955$ and 0.921 , respectively). 4D-CTA detected 77 of 109 feeding arteries (71%) in 25 cases. In 3 cases with a dAVF located at the cavernous sinus, neither reader could detect any feeding arteries. The intermodality agreement for the number of feeding arteries of dAVFs was good ($\kappa = 0.713$). Prior studies support the accuracy of 4D-CTA for the diagnosis and classification of dAVFs with DSA as the reference standard.³⁰⁻³³

A single report evaluated spinal dAVFs and compared 4D-CTA with MRA and DSA.³⁴ 4D-CTA could detect the perimedullary veins and the location of the AVF in 3/4 cases. The direction of venous flow was correctly assessed in all cases. The authors, however, used a high-dose technique in the thoracolumbar region with a reported effective dose of >40 mSv. Because the evaluation of the spine for the detection of a vascular malformation requires coverage of a large area, the use of 4D-CTA as a first screening tool is probably limited. Thus, 4D-MRA has the advantage of extended coverage and lack of radiation exposure.

Hemorrhagic Stroke. In patients with intracranial hemorrhage, CTA is used to evaluate potential underlying neurovascular pathology such as aneurysms or vascular malformations. Another application is to detect extravasation of contrast material, also termed the “spot” sign. The spot sign is associated with hematoma expansion and increased mortality.^{35,36} In a prospective evaluation, Sun et al³⁷ found the spot sign to be present throughout the arterial-to-venous phases on 4D-CTA studies of 112 patients and it was an independent predictor of hematoma progression. In comparison with conventional CTA, the spot sign on 4D-CTA had a higher predictive value for hematoma expansion; therefore, 4D-CTA seems to be more accurate for estimating prognosis. The false-negative results of CTA can be explained by the time it takes for contrast extravasation to manifest, so the single acquisition of conventional CTA may be too early.

Ischemic Stroke. In the work-up of patients presenting with ischemic stroke, 4D-CTA demonstrated added value over conven-

tional CTA for the evaluation of the extent and dynamics of collateral flow.³⁸

The length and location of the thrombus burden in case of intracranial vessel occlusion have been used to predict therapy response, with larger proximal thrombus considered more resistant to intravenous thrombolytic therapy.³⁹ Frölich et al⁴⁰ found better demarcation of thrombus burden in patients with anterior circulation occlusion by using 4D-CTA compared with conventional CTA due to better visualization of collateral circulation.

For endovascular procedures, the angiographic appearance of the occlusion site has been used as a predictor of recanalization success.^{41,42} In particular, angiographic demonstration of delayed antegrade contrast opacification distal to the occlusion site referred to as

the “clot outline” sign has been linked to improved recanalization rates after intra-arterial thrombolytic therapy.⁴³ 4D-CTA has been comparable with DSA in discriminating antegrade and retrograde flow across a cerebral artery occlusion.⁴⁴ The presence of antegrade flow on 4D-CTA is associated with an increased chance of early vessel recanalization by using intravenous thrombolysis.⁴⁴

The extent of infarcted brain tissue generally depends on the location of the vessel occlusion and the time to recanalization.⁴⁵ In recent years, it has become clear that the extent of collateral circulation is an important independent factor for the extent of infarction and clinical outcome.⁴⁶ Collateral blood flow is also an independent prognostic factor for successful thrombolytic therapy.^{47,48} In accordance with these findings, collateral grading on CTA has been shown to be a strong and independent prognostic factor for clinical outcome after acute stroke.⁴⁹ In particular, the absence of leptomeningeal collaterals has been shown to be highly predictive for poor clinical outcome.⁵⁰ However, the absence of collaterals on conventional CTA may not be a correct representation of true collateral blood supply: The acquisition may be too early to display collaterals with delayed filling.³⁸ Absence of collaterals on 4D-CTA should be a better measure because delayed enhancement can be captured during the acquisition sequence. As a result, 4D-CTA should also be a stronger predictor of patient outcome after stroke.⁵¹ In a prospective cohort study in 40 subjects, Smit et al²² compared CTA with TI-CTA calculated from 4D-CTA data in patients presenting with ischemic stroke. Patients with poor collateral circulation on conventional CTA were still found to have good clinical outcome in 31% of cases. On TI-CTA, this subgroup of patients was found to have good collaterals (Fig 3). Conversely, all patients with poor collateral status on TI-CTA also showed poor clinical outcome. Another recent study supports these findings.⁴⁰

Whole-brain perfusion maps can be calculated from 4D-CTA data, which enables the correlation between parenchyma perfusion deficits and the detection of vessel occlusions.⁵²

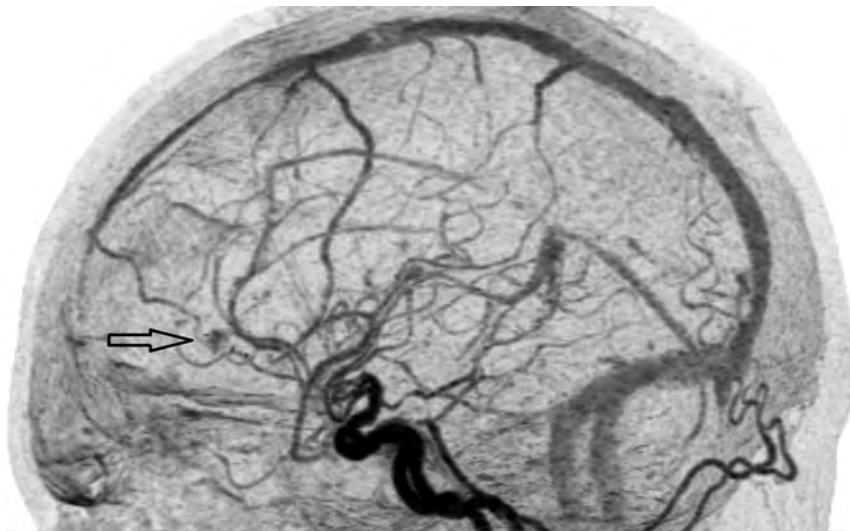


FIG 4. 4D-CTA image demonstrating recurrence of an arteriovenous malformation. The *arrow* indicates the nidus, which is fed by arterial feeders from the anterior cerebral artery. There is cortical venous drainage toward the rostral superior sagittal sinus.

Chronic Arterial Disease. In case of proximal vascular stenotic or occlusive disease, 4D-CTA can be used to study altered flow dynamics of the intracranial vasculature, for example, to evaluate collateral flow via the circle of Willis. In a retrospective study with 25 patients with proximal vessel occlusion, Menon et al⁵³ could differentiate distinct patterns of collaterals. These patterns consisted of posterior cerebral artery–MCA dominant collateralization, intratentorial leptomeningeal collaterals, and variability in size, extent, and retrograde filling time in pial arteries.

Discussion

4D-CTA has enabled noninvasive evaluation of flow dynamics of neurovascular pathology. High temporal resolution for the detection and classification of intracranial AVMs and AVFs can be achieved by a continuous volume acquisition, though for whole-brain coverage, a wide detector is required. In case of smaller detector width, the toggling-table technique or shuttle mode scanning enables 4D-CTA with extended coverage in which a lower temporal resolution seems to be acceptable for the evaluation of ischemic or hemorrhagic stroke. The main challenge for routine clinical use of 4D-CTA is to keep the radiation dose at bay, which strongly depends on the acquisition parameters used. Because dose-reduction techniques such as iterative reconstruction and noise-reduction filters already have reduced the radiation dose dramatically, the challenge now is to bring the radiation dose of 4D-CTA down to the level of conventional CTA so that the clinical application can be extended. To achieve consistent high image quality, image registration and filtering techniques should be further improved. This change can result in better depiction of small, clinically important vascular structures on 4D-CTA. DSA is still superior to 4D-CTA with respect to spatial resolution and the possibility of selective vessel contrast injection.

Future Perspectives and Clinical Implementation. Detection of the main arterial feeders and patterns of venous drainage by 4D-CTA seems to be sufficient in most cases to correctly identify and classify brain AVMs and AVFs. This can be used for treatment

planning, which would save the patient a preinterventional invasive DSA. In addition, 4D-CTA could replace an invasive DSA in the follow-up of intracranial vascular malformations (Fig 4). The advantage of a noninvasive procedure is evident, and the decrease in spatial resolution does not seem to change clinical management for most patients. However, this needs to be addressed in larger cohort studies. In ischemic stroke, 4D-CTA or timing-invariant CTA displays the presence and extent of collateral vessels and thrombus burden more reliably than conventional CTA. This difference has important implications for prognosis assessment and treatment decision-making. The spot sign in intracranial hemorrhage is an indicator of acute contrast extravasation and is better detected by 4D-CTA than by conventional

CTA. It is an independent predictor of outcome that may guide early surgical or endovascular treatment.

Currently, whole-brain coverage can be achieved with different dynamic CT techniques. However, additional evaluation of the cervical vessels is commonly necessary in the diagnostic work-up of stroke. An additional CTA of the neck would result in an additional contrast bolus and radiation exposure with already opacified venous structures as a result of the first contrast bolus. With the use of a wide detector, a volume neck CTA acquisition combined with dynamic volume acquisitions of the head is technically feasible,⁵⁴ though clinical application of this technique needs to be further evaluated.

CONCLUSIONS

There is increasing evidence that 4D-CTA has added value over conventional CTA for the diagnosis, treatment planning, and follow-up of different neurovascular disorders because 4D-CTA enables evaluation of flow dynamics. However, because level 3 evidence is mainly available, additional prospective clinical cohort studies are necessary, taking the scanning technique used into account. In addition, the radiation dose of 4D-CTA should be further reduced by improved filtering and registration techniques. Improved filtering and registration should result in improved image quality with better depiction of small vascular structures.

Appendix: Search Strategy

Methods. A systematic search was performed in the following data bases: MEDLINE by using PubMed, Cochrane Central Register of Controlled Trials, Web of Science (formerly ISI Web of Knowledge), and EMBASE via OvidSP. During the search, no restrictions were made with regard to language or date of publication. Reference and citation tracking of selected articles were included in the search. All abstracts were read, and relevant articles were selected.

Search. (“Stroke” [Medical Subject Headings or MeSH] OR “Intracranial Arteriovenous Malformations” [MeSH] OR “Central Nervous System Vascular Malformations” [MeSH] OR “Arteriovenous Fistula” [MeSH] OR “Subarachnoid Hemorrhage” [MeSH] OR “Aneurysm, Intracranial Berry, 1” [Supplementary Concept] OR Arteriovenous Malformation* [tiab] OR AVM* [tiab] OR AVF* [tiab] OR dAVF* OR Subarachnoid Hemorrhage* [tiab] OR Subarachnoid Bleed* [tiab] OR SAH* [tiab] OR SAB [tiab] OR SABs [tiab] OR Aneurysm* [tiab] OR Vascular Malformation* [tiab] OR Vascular Anomal* [tiab] OR Arteriovenous Fistula* [tiab] OR CVA* [tiab] OR Cerebrovascular [tiab] OR Neurovascular [tiab] OR Stroke* [tiab] OR Intracranial collateral* [tiab] OR Leptomeningeal collateral* OR Moyamoya [tiab])

OR

“Angiography, Digital Subtraction” [MeSH] OR Digital Subtraction Angiograph* [tiab] OR DSA [tiab] OR Subtraction Angiograph* [tiab] OR Cerebral Angiograph* [tiab] OR Spinal Angiograph* [tiab] OR cerebral angiograph* [tiab] OR “Cerebral Angiography” [MeSH])

AND

(Four Dimensional Computed Tomograph* [tiab] OR Whole brain CT* [tiab] OR Dynamic angiograph* [tiab] OR 4D Computed Tomograph* [tiab] OR 4D CT [tiab] OR Four Dimensional CAT [tiab] OR Four Dimensional CATs [tiab] OR Four Dimensional CT* [tiab] OR 4D CAT [tiab] OR 4D CATs [tiab] OR 4D CT* [tiab] OR 4DCT* [tiab] OR Time resolved 3D [tiab] OR Time resolved 4D [tiab] OR Dynamic 3D [tiab] OR Dynamic three dimensional [tiab] OR Dynamic CT* [tiab] OR Time resolved CT* [tiab] Or Time invariant CT* [tiab] OR Timing invariant CT* [tiab] OR “Four-Dimensional Computed Tomography” [MeSH]).

Results. We retrieved 328 articles.

Two reviewer authors independently selected the articles from the list of identified references. Consensus was sought, but when no consensus could be reached, a third review author was consulted. If relevance could not be ascertained on the basis of the abstract, the complete article was reviewed. The final decision of inclusion was then made on review of the full text.

Disclosures: Ewoud J. Smit—UNRELATED: Payment for Lectures (including service on Speakers Bureaus); Toshiba Medical Systems (Speakers Bureau). Rashindra Mani—RELATED: Grant: Toshiba Medical Systems*; UNRELATED: Grants/Grants Pending: Dutch Technology Foundation (STW)*; Mathias Prokop—RELATED: Grant: Philips Healthcare*; UNRELATED: Grants/Grants Pending: Philips Healthcare*; Toshiba Medical Systems*; Payment for Lectures (including service on Speakers Bureaus); Bracco, Toshiba Medical Systems, Bayer-Schering, CME Science; Travel/Accommodations/Meeting Expenses Unrelated to Activities Listed: Toshiba Medical Systems, Philips Healthcare, European School of Radiology, CME Science. Frederick J.A. Meijer—UNRELATED: Payment for Lectures (including service on Speakers Bureaus); Toshiba Medical Systems (Speakers Bureau). *Money paid to the institution.

REFERENCES

- Klingebl R, Siebert E, Diekmann S, et al. **4-D imaging in cerebrovascular disorders by using 320-slice CT: feasibility and preliminary clinical experience.** *Acad Radiol* 2009;16:123–29
- Schellinger PD, Richter G, Kohrmann M, et al. **Noninvasive angiography (magnetic resonance and computed tomography) in the di-**

- agnosis of ischemic cerebrovascular disease: techniques and clinical applications.** *Cerebrovasc Dis* 2007;24(suppl 1):16–23
- Alexander MD, Oliff MC, Olorunsola OG, et al. **Patient radiation exposure during diagnostic and therapeutic interventional neuroradiology procedures.** *J Neurointerv Surg* 2010;2:6–10
- James RF, Wainwright KJ, Kanaan HA, et al. **Analysis of occupational radiation exposure during cerebral angiography utilizing a new real time radiation dose monitoring system.** *J Neurointerv Surg* 2014 May 14. [Epub ahead of print]
- Willinsky RA, Taylor SM, terBrugge K, et al. **Neurologic complications of cerebral angiography: prospective analysis of 2,899 procedures and review of the literature.** *Radiology* 2003;227:522–28
- Cloft HJ, Joseph GJ, Dion JE. **Risk of cerebral angiography in patients with subarachnoid hemorrhage, cerebral aneurysm, and arteriovenous malformation: a meta-analysis.** *Stroke* 1999;30:317–20
- Kaufmann TJ, Huston J, Mandrekar JN, et al. **Complications of diagnostic cerebral angiography: evaluation of 19,826 consecutive patients.** *Radiology* 2007;243:812–19
- Bendszus M, Koltzenburg M, Burger R, et al. **Silent embolism in diagnostic cerebral angiography and neurointerventional procedures: a prospective study.** *Lancet* 1999;354:1594–97
- Morhard D, Wirth CD, Fesl G, et al. **Advantages of extended brain perfusion computed tomography: 9.6 cm coverage with time resolved computed tomography-angiography in comparison to standard stroke-computed tomography.** *Invest Radiol* 2010;45:363–69
- Hoogenboom TC, van Beurden RM, van Teylingen B, et al. **Optimization of the reconstruction interval in neurovascular 4D-CTA imaging: a technical note.** *Interv Neuroradiol* 2012;18:377–79
- Roberts HC, Roberts TP, Smith WS, et al. **Multisection dynamic CT perfusion for acute cerebral ischemia: the “toggling-table” technique.** *AJNR Am J Neuroradiol* 2001;22:1077–80
- Youn SW, Kim JH, Weon YC, et al. **Perfusion CT of the brain using 40-mm-wide detector and toggling table technique for initial imaging of acute stroke.** *AJR Am J Roentgenol* 2008;191:W120–26
- Saake M, Goelitz P, Struffert T, et al. **Comparison of conventional CTA and volume perfusion CTA in evaluation of cerebral arterial vasculature in acute stroke.** *AJNR Am J Neuroradiol* 2012;33:2068–73
- Yang CY, Chen YF, Lee CW, et al. **Multiphase CT angiography versus single-phase CT angiography: comparison of image quality and radiation dose.** *AJNR Am J Neuroradiol* 2008;29:1288–95
- Mendrik AM, Vonken EJ, van Ginneken B, et al. **TIPS bilateral noise reduction in 4D CT perfusion scans produces high-quality cerebral blood flow maps.** *Phys Med Biol* 2011;56:3857–72
- Smit EJ, Vonken EJ, van der Schaaf IC, et al. **Timing-invariant reconstruction for deriving high-quality CT angiographic data from cerebral CT perfusion data.** *Radiology* 2012;263:216–25
- Lin CJ, Wu TH, Lin CH, et al. **Can iterative reconstruction improve imaging quality for lower radiation CT perfusion? Initial experience.** *AJNR Am J Neuroradiol* 2013;34:1516–21
- Manninen AL, Isokangas JM, Karttunen A, et al. **A comparison of radiation exposure between diagnostic CTA and DSA examinations of cerebral and cervicocerebral vessels.** *AJNR Am J Neuroradiol* 2012;33:2038–42
- Siebert E, Bohner G, Dewey M, et al. **320-slice CT neuroimaging: initial clinical experience and image quality evaluation.** *Br J Radiol* 2009;82:561–70
- Moskowitz SI, Davros WJ, Kelly ME, et al. **Cumulative radiation dose during hospitalization for aneurysmal subarachnoid hemorrhage.** *AJNR Am J Neuroradiol* 2010;31:1377–82
- Vano E, Fernandez JM, Sanchez RM, et al. **Patient radiation dose management in the follow-up of potential skin injuries in neuroradiology.** *AJNR Am J Neuroradiol* 2013;34:277–82
- Smit EJ, Vonken EJ, van Seeters T, et al. **Timing-invariant imaging of collateral vessels in acute ischemic stroke.** *Stroke* 2013;44:2194–99
- Spetzler RF, Martin NA. **A proposed grading system for arteriovenous malformations.** *J Neurosurg* 1986;65:476–83
- Cognard C, Gobin YP, Pierot L, et al. **Cerebral dural arteriovenous**

- fistulas: clinical and angiographic correlation with a revised classification of venous drainage. *Radiology* 1995;194:671–80
25. Borden JA, Wu JK, Shucart WA. **A proposed classification for spinal and cranial dural arteriovenous fistulous malformations and implications for treatment.** *J Neurosurg* 1995;82:166–79
 26. Wang H, Ye X, Gao X, et al. **The diagnosis of arteriovenous malformations by 4D-CTA: a clinical study.** *J Neuroradiol* 2014;41:117–23
 27. Willems PW, Taeshineetanakul P, Schenk B, et al. **The use of 4D-CTA in the diagnostic work-up of brain arteriovenous malformations.** *Neuroradiology* 2012;54:123–31
 28. Siebert E, Diekmann S, Masuhr F, et al. **Measurement of cerebral circulation times using dynamic whole-brain CT-angiography: feasibility and initial experience.** *Neurol Sci* 2012;33:741–47
 29. Fujiwara H, Momoshima S, Akiyama T, et al. **Whole-brain CT digital subtraction angiography of cerebral dural arteriovenous fistula using 320-detector row CT.** *Neuroradiology* 2013;55:837–43
 30. Brouwer PA, Bosman T, van Walderveen MA, et al. **Dynamic 320-section CT angiography in cranial arteriovenous shunting lesions.** *AJNR Am J Neuroradiol* 2010;31:767–70
 31. Salomon EJ, Barfett J, Willems PWA, et al. **Dynamic CT angiography and CT perfusion employing a 320-detector row CT: protocol and current clinical applications.** *Klin Neuroradiol* 2009;19:187–96
 32. Willems PW, Brouwer PA, Barfett JJ, et al. **Detection and classification of cranial dural arteriovenous fistulas using 4D-CT angiography: initial experience.** *AJNR Am J Neuroradiol* 2011;32:49–53
 33. Beijer TR, van Dijk EJ, de Vries J, et al. **4D-CT angiography differentiating arteriovenous fistula subtypes.** *Clin Neurol Neurosurg* 2013;115:1313–16
 34. Yamaguchi S, Takeda M, Mitsuhashi T, et al. **Application of 4D-CTA using 320-row area detector computed tomography on spinal arteriovenous fistulae: initial experience.** *Neurosurg Rev* 2013;36:289–96; discussion 296
 35. Demchuk AM, Dowlathshahi D, Rodriguez-Luna D, et al. **Prediction of haematoma growth and outcome in patients with intracerebral haemorrhage using the CT-angiography spot sign (PREDICT): a prospective observational study.** *Lancet Neurol* 2012;11:307–14
 36. Becker KJ, Baxter AB, Bybee HM, et al. **Extravasation of radiographic contrast is an independent predictor of death in primary intracerebral hemorrhage.** *Stroke* 1999;30:2025–32
 37. Sun SJ, Gao PY, Sui BB, et al. **“Dynamic spot sign” on CT perfusion source images predicts haematoma expansion in acute intracerebral haemorrhage.** *Eur Radiol* 2013;23:1846–54
 38. Frölich AM, Wolff SL, Psychogios MN, et al. **Time-resolved assessment of collateral flow using 4D CT angiography in large-vessel occlusion stroke.** *Eur Radiol* 2014;24:390–96
 39. Riedel CH, Zimmermann P, Jensen-Kondering U, et al. **The importance of size: successful recanalization by intravenous thrombolysis in acute anterior stroke depends on thrombus length.** *Stroke* 2011;42:1775–77
 40. Frölich AM, Schrader D, Klotz E, et al. **4D CT angiography more closely defines intracranial thrombus burden than single-phase CT angiography.** *AJNR Am J Neuroradiol* 2013;34:1908–13
 41. Pillai JJ, Lanzieri CF, Trinidad SB, et al. **Initial angiographic appearance of intracranial vascular occlusions in acute stroke as a predictor of outcome of thrombolysis: initial experience.** *Radiology* 2001;218:733–38
 42. Suarez JJ, Sunshine JL, Tarr R, et al. **Predictors of clinical improvement, angiographic recanalization, and intracranial hemorrhage after intra-arterial thrombolysis for acute ischemic stroke.** *Stroke* 1999;30:2094–100
 43. Christoforidis GA, Mohammad Y, Avutu B, et al. **Arteriographic demonstration of slow antegrade opacification distal to a cerebrovascular thromboembolic occlusion site as a favorable indicator for intra-arterial thrombolysis.** *AJNR Am J Neuroradiol* 2006;27:1528–31
 44. Frölich AM, Psychogios MN, Klotz E, et al. **Antegrade flow across incomplete vessel occlusions can be distinguished from retrograde collateral flow using 4-dimensional computed tomographic angiography.** *Stroke* 2012;43:2974–79
 45. Ringelstein EB, Biniek R, Weiller C, et al. **Type and extent of hemispheric brain infarctions and clinical outcome in early and delayed middle cerebral artery recanalization.** *Neurology* 1992;42:289–98
 46. McVerry F, Liebeskind DS, Muir KW. **Systematic review of methods for assessing leptomeningeal collateral flow.** *AJNR Am J Neuroradiol* 2012;33:576–82
 47. Miteff F, Levi CR, Bateman GA, et al. **The independent predictive utility of computed tomography angiographic collateral status in acute ischaemic stroke.** *Brain* 2009;132(pt 8):2231–38
 48. Kucinski T, Koch C, Eckert B, et al. **Collateral circulation is an independent radiological predictor of outcome after thrombolysis in acute ischaemic stroke.** *Neuroradiology* 2003;45:11–18
 49. Maas MB, Lev MH, Ay H, et al. **Collateral vessels on CT angiography predict outcome in acute ischemic stroke.** *Stroke* 2009;40:3001–05
 50. Souza LC, Yoo AJ, Chaudhry ZA, et al. **Malignant CTA collateral profile is highly specific for large admission DWI infarct core and poor outcome in acute stroke.** *AJNR Am J Neuroradiol* 2012;33:1331–36
 51. Tan IY, Demchuk AM, Hopyan J, et al. **CT angiography clot burden score and collateral score: correlation with clinical and radiologic outcomes in acute middle cerebral artery infarct.** *AJNR Am J Neuroradiol* 2009;30:525–31
 52. Orrison WW, Snyder KV, Hopkins LN, et al. **Whole-brain dynamic CT angiography and perfusion imaging.** *Clin Radiol* 2011;66:566–74
 53. Menon BK, O'Brien B, Bivard A, et al. **Assessment of leptomeningeal collaterals using dynamic CT angiography in patients with acute ischemic stroke.** *J Cereb Blood Flow Metab* 2013;33:365–71
 54. Oei M, Manniesing R, Meijer FJ, et al. **One-step-stroke imaging: does an interleaved acquisition of cerebral CT perfusion and CTA of the carotids affect CTP values.** In: *Proceedings of the European Congress of Radiology*, Vienna, Austria. March 6–10, 2014

Screening for Self-Plagiarism in a Subspecialty-versus-General Imaging Journal Using iThenticate

A.U. Kalnins, K. Halm, and  M. Castillo



ABSTRACT

BACKGROUND AND PURPOSE: Self-plagiarism is a form of research misconduct that can dilute the credibility and reputation of a scientific journal, as well as the represented specialty. Journal editors are aware of this problem when reviewing submissions and use on-line plagiarism-analysis programs to facilitate detection. The *American Journal of Neuroradiology* (*AJNR*) uses iThenticate to screen several submitted original research manuscripts selected for review per issue and retrospectively assesses 3 issues per year. The prevalence of self-plagiarism in *AJNR* was compared with that in *Radiology*; the necessity and cost of more extensive screening in *AJNR* were evaluated.

MATERIALS AND METHODS: The self-duplication rate in *AJNR* original research articles was compared with that in *Radiology*, a general imaging journal that screens all submitted original research manuscripts selected for review by using iThenticate. The rate of self-duplication in original research articles from 2 randomly selected 2012 *AJNR* issues was compared with the rate in the prior year to gauge the need for more extensive screening. A cost analysis of screening all submitted original research manuscripts selected for review by using iThenticate was performed.

RESULTS: Using an empiric 15% single-source duplication threshold, we found that the rate of significant self-plagiarism in original research articles was low for both journals. While *AJNR* had more articles exceeding this threshold, most instances were insignificant. Analyzing 2 randomly chosen issues of *AJNR* for single-source duplication of >15% in original research articles yielded no significant differences compared with an entire year. The approximate annual cost of screening all submitted original research manuscripts selected for review was US \$6800.00.

CONCLUSIONS: While the rate of self-plagiarism was low in *AJNR* and similar to that in *Radiology*, its potential cost in negative impact on *AJNR* and the subspecialty of neuroradiology justifies the costs of broader screening.

ABBREVIATIONS: *AJNR* = *American Journal of Neuroradiology*; ORA = original research article; SORMSR = submitted original research manuscript selected for review

The appropriation of previously published ideas or words without proper credit is known as “plagiarism” and is considered a major breach of ethics in scientific publications. In 2005, the National Science Foundation identified plagiarism in nearly 66% of suspected cases of fraud.¹ The same institution implemented a plagiarism checking system and discovered that 1.5% of the nearly 8000 grants accepted in 2011 contained significant plagiarism.² The recognized significance of plagiarism has merited its inclu-

sion in the federal definition of “research misconduct,” defined as, “fabrication, falsification, or plagiarism in proposing, performing, or reviewing research, or in reporting research results.”³ While plagiarism may involve the use of the work of others, the use of one’s own work without acknowledging its source is known as “redundant publication” or “self-plagiarism” and is no less significant.⁴ The pressure of academic productivity as measured by the number of one’s publications or how often one is cited creates an incentive for authors to publish a greater volume of work, which may increase the likelihood of self-plagiarism.^{5,6}

The presence of sporadic phrases reproduced from an author’s own prior work, particularly from “Materials and Methods” sections of manuscripts based on similar research methodologies, may be acceptable at the discretion of an editor and not necessarily suspected as intentional duplication.⁷ However, copying entire sections or illustrations of one’s own prior work without appropriate attribution is not acceptable and constitutes self-plagia-

Received September 20, 2014; accepted after revision November 13.

From the Department of Radiology (A.U.K.), Stanford University Medical Center, Stanford, California; *American Journal of Neuroradiology* (K.H., M.C.), Oak Brook, Illinois; and Department of Radiology (M.C.), University of North Carolina at Chapel Hill, Chapel Hill, North Carolina.

Please address correspondence to Mauricio Castillo, MD, FACR, University of North Carolina at Chapel Hill, Department of Radiology, Room 3326, Old Infirmary Building, Manning Dr, Chapel Hill, NC 27599-75; e-mail: Castillo@med.unc.edu; @AleksKalnins

<http://dx.doi.org/10.3174/ajnr.A4234>

ism. While there are various different classifications for self-plagiarism, a well-accepted one developed by Miguel Roig defines 4 distinct types: recycling of text, copyright infringement, “salami slicing” or dividing 1 study into multiple publications with the intent of apparently increasing productivity, and duplicate publication.⁸⁻¹⁰

Editors of scientific journals are aware of the potential of self-plagiarism when reviewing submissions, and the use of electronic plagiarism analysis software has greatly facilitated its detection. Widely used plagiarism-analysis programs are iThenticate (<http://www.ithenticate.com>) in scientific publications and Turnitin (<http://turnitin.com>) in general education.¹¹ These programs are similar in their comparison of selected documents with data bases of published or submitted articles including “CrossCheck” for iThenticate and “OriginalityCheck” for Turnitin.^{12,13} The iThenticate data base enables manuscripts to be compared with >37 billion Web pages, >92 million published works from on-line and off-line research publications and data bases, and >37 million scholarly articles through the “CrossCheck” data base, the largest comparison data base of scientific, technical, and medical publications in the world.^{14,15} Analysis of documents by one of these programs generates an overall “similarity index” with works in the data base as well as an interactive summary of individual sources with which a document demonstrates sameness.^{16,17} In one study, plagiarism was detected in 3% of assignments submitted by adult learners when manually evaluated for significant overlap, but when evaluated with Turnitin, plagiarism was identified in 13%.¹⁸

Given the awareness of the practice of plagiarism and self-plagiarism as well as the ease of use and availability of electronic plagiarism analysis, it is convenient for scientific journals to use it for evaluation. At the time of this study, *Radiology* used iThenticate to screen all manuscripts for the presence of duplications since February 2013 (D. Levine, MD, personal e-mail communication, October 2014), and the *American Journal of Neuroradiology* (*AJNR*) selectively used the iThenticate service for approximately 3 submitted original research manuscripts selected for review (SORMSRs) per issue since 2012. *AJNR* publishes about 300–350 original articles per year, and of these, 3 issues are now randomly retrospectively selected for review with iThenticate to evaluate the presence of duplication. In addition, all manuscripts originating from authors who have been associated with previous fraudulent behavior are prospectively assessed with iThenticate before undergoing the peer review process, representing approximately 3 SORMSRs per issue.

When one analyzes manuscript submissions by using electronic plagiarism software, the acceptable percentage of similarity between scientific publications is not well-defined. According to the Turnitin Web site instructions for the interpretation of the “similarity index,” there are no clear rules that define when plagiarism has taken place. However, the company previously disseminated guidelines to academic institutions suggesting a 15% “similarity index” for alerting to the possibility of plagiarism.^{16,19-22} Organizations involved in promoting ethics and best practices of scientific editing (International Committee of Medical Journal Editors, International Society of Managing and Technical Editors, Committee on Publication Ethics) do not define a specific numeric “cutoff” for the identification of plagiarism.²³⁻²⁵

While *AJNR* has adopted the 15% guideline, other journals set it as low as 10%.⁷

In this study, we first sought to evaluate the rate of duplications in published *AJNR* original research articles to see if it is comparable with that in the general radiology literature and to evaluate whether screening all SORMSRs versus a random sample is sufficient. We also performed an analysis of the costs of screening all SORMSRs for potential duplication with iThenticate to assess the economic impact on *AJNR*.

MATERIALS AND METHODS

Part 1

We selected articles published in *AJNR* and *Radiology* in 2011 under the heading of “Original Research.” Review articles, editorials, commentaries, vignettes, case reports, clinical reports, and so forth were excluded because these do not constitute most articles in an imaging journal and were thought to be more susceptible to differences in opinion regarding the significance of flagged content. All “Original Research” articles published in *Radiology* and *AJNR* in 2011 were uploaded into iThenticate in a .pdf format, and an analysis was run. iThenticate parameters were set to exclude quotations and bibliographic entries from comparison and to ignore single-source duplications of $\leq 3\%$, given the likelihood of random similarity at or below this threshold. The 15% single-source “similarity index” threshold was set for flagging manuscripts needing further evaluation.^{16,19-22} When an article exceeded this 15%, 2 individuals (Editor-in-Chief, Managing Editor) separately assessed the duplications and rated them as being significant or insignificant. The presence of plagiarism and self-plagiarism was evaluated by comparing the authors of the SORMSRs with the authors of prior publications that were identified by the iThenticate program as having >15% total similarity. If any author of the SORMSR was an author of the flagged prior publication, self-plagiarism was suspected and the manuscript was further assessed for significance. The presence of sporadic phrases from prior works was ignored, while the presence of large blocks of text was further judged as significant or insignificant.

A significant duplication was characterized as duplicate publication of the same article with no or minor modifications or unreasonable duplication of large or small blocks of text from any portion of the manuscript without appropriate modification or citation of the prior publication. This characterization was consistent with published recommendations for classification of significant (major or minor) duplications.^{26,27} When differences occurred between the 2 evaluators in the judgment of duplication as significant or insignificant, these were resolved by consensus. Total significant single-source duplications of original research articles (ORAs) in *AJNR* and *Radiology* were compared by using the Mann-Whitney *U* test, with the null hypothesis that there is no difference between the ranks of the significant single-source duplications of ORAs in *AJNR* and *Radiology*. Statistical analysis was performed by using MedCalc for Windows, Version 14.10.2, 64-bit (MedCalc Software, Mariakerke, Belgium).

Part 2

We assessed the value of analyzing all versus a small sample of submitted manuscripts for the presence of duplication by evalu-

Table 1: Duplication in ORAs, AJNR 2011 and Radiology 2011

	AJNR 2011	Radiology 2011
Issues (No.)	11	12
ORAs (No.)	302	343
ORAs per issue (mean)	27.5	28.6
ORAs per issue (SD)	2.73	1.31
With >15% duplication (No.)	54	12
With >15% duplication (% of total)	17.9	3.5
With >15% duplication from a single source (No.)	12	2
With >15% duplication from a single source (% of total ORAs)	4	0.6
With >15% duplication from a single source (significant) (No.)	2	1
With >15% duplication from a single source (significant) (% of total ORAs)	0.7	0.3

Table 2: Results of the Mann-Whitney U test to compare the difference between total significant (>15%) single-source duplications of ORAs in AJNR and Radiology in 2011

Group	No.	Rank Average	Sum of Ranks	U	Z	P
AJNR 2011	11	12.59	138.5	59.5	0.61	.545
Radiology 2011	12	11.46	137.5			

Note:—U indicates the Mann-Whitney U test.

ating all “Original Research” articles in 2 randomly selected issues of *AJNR* in 2012 (March and September) and comparing the results with those obtained for an entire year (2011).

Part 3

An analysis was performed to assess the total current and potential future annual cost of using iThenticate to evaluate all SORMSRs for self-plagiarism, factoring in the fixed costs (iThenticate annual subscription fee) and variable costs (iThenticate manuscript analysis fee and time of the *AJNR* staff) of screening.

RESULTS

Part 1

In 2011, *AJNR* was published 11 times and contained a total of 302 original research articles ($\bar{x} = 27.5$ per issue, $\sigma = 2.73$), while *Radiology* was published monthly with a total of 343 original research articles ($\bar{x} = 28.6$ per issue, $\sigma = 1.31$) (Table 1).

In *AJNR*, iThenticate found 54 articles (17.9%) that showed >15% duplication rates, while 12 (3.5%) such articles were found in *Radiology*. In *AJNR*, 12 articles (4%) were found to have duplication rates above 15% from a single source, while in *Radiology*, only 2 (0.6%) such articles were found. After individual evaluations of these articles, only 2 in *AJNR* and 1 in *Radiology* were judged by consensus agreement to contain significant “single-source” duplications consistent with self-plagiarism. In *AJNR*, this finding led the editors to contact the authors and request explanations, concluding that most duplication arose from similarities in the “Materials and Methods.”

The total number of identified “single-source” duplications in original research articles in both journals was compared (Table 2).

Table 2 reveals the results of Mann-Whitney U test for the number of significant single-source duplications in original research articles published in *AJNR* and *Radiology* in 2011, which did not show any statistical difference ($Z = 0.606$; $P = .5447$). The rank average of the number of single-source duplications in original research articles published in *AJNR* was 12.59, and in *Radiology*, it was 11.45. The similar rank averages demonstrate that the number of significant single-source duplications

in original research articles in *AJNR* and *Radiology* was nearly equal.

Part 2

Two *AJNR* issues from 2012, selected at random (March and September), contained 25 and 27 original research articles each. In these 2 issues, 5 and 4 articles surpassed our 15% duplication threshold, respectively, compared with an average of 4.9 ($\sigma = 1.92$) articles in all of 2011. The fact that this value was within the SD led us to believe that the rate of articles surpassing the 15% minimum threshold is likely constant throughout the year. The number of articles in which the 15% duplication rate originated from a single source was 3 in March and 1 in September ($\bar{x} = 1.09$ per

issue in 2011, $\sigma = 1.04$). Individual evaluation of these 4 articles demonstrated no significant self-plagiarism that accounted for the duplication rate above the 15% threshold.

Part 3

We evaluated the cost of analyzing an entire year of submitted manuscripts, factoring in the financial cost of using iThenticate and wage hours spent by *AJNR* staff to perform this task (Table 3).

In 2013, an average of 3 articles per issue (36 articles per year) were prospectively flagged for evaluation by using iThenticate due to previous duplication problems with authors at an annual cost of US \$840.72. If *AJNR* were to evaluate all submitted articles by using iThenticate, the annual cost would rise by US \$5963.76 to a total of US \$6804.48.

DISCUSSION

In comparing *AJNR* and *Radiology*, our results indicate that both journals published about the same number of articles under the category of “Original Research” per issue but that the rate of non-significant duplication was higher in *AJNR*. When the origin of the nonsignificant duplications was evaluated in *AJNR*, it was found to be mostly secondary to similarities in research methodologies used in previously published research by the same authors, and the discrepancy between the 2 journals may reflect differences in journal standards regarding screening of SORMSRs for the presence of self-duplication and re-publication of nonsignificant duplication of research methodologies. When these articles were individually studied for significant duplications, only 2 in *AJNR* and 1 in *Radiology* were considered exceeding the 15% threshold (0.66% of articles in *AJNR* and 0.29% of articles in *Radiology*). As a result of identified duplications, *AJNR* editors contacted the authors and requested an explanation (M. Castillo, MD, *AJNR* e-mail correspondence with manuscript authors regarding duplication, 2012). After careful deliberation by an internal committee, it was concluded that most similarities arose mostly from the “Materials and Methods” and matters were not pursued further.

In cases of proven self-plagiarism, the Committee on Publication Ethics guidelines recommends taking further action, which

Table 3: 2013 AJNR iThenticate cost analysis of SORMSRs

Cost Estimate Variable	Cost
Annual iThenticate subscription fee	\$550.00
Annual iThenticate administrative fee	\$110.00
Total annual fixed cost to use iThenticate (\$550.00 subscription fee + \$110.00 administrative fee)	\$660.00
iThenticate cost per analyzed manuscript	\$0.75
Hourly rate of AJNR administrative staff	\$25.64
Average time to submit manuscript to iThenticate (min)	10
Average staff cost to submit manuscript to iThenticate	\$4.27
Total variable cost to submit a single manuscript to iThenticate (\$0.75 cost per article + \$4.27 AJNR staff time cost per manuscript)	\$5.02
Number of AJNR issues per year	12
Current No. of SORMSRs analyzed by iThenticate per issue	3
Total current annual cost to use iThenticate (\$660.00 annual fixed cost + [\$5.02 time cost/manuscript × 3 manuscripts/issue × 12 issues/year])	\$840.72
Total current cost per issue to use iThenticate (\$840.72 per year/12 issues)	\$70.06
Average No. of SORMSRs per issue	102
Total potential annual cost to use iThenticate to analyze all SORMSRs (\$660.00 annual fixed cost + [\$5.02 time cost/manuscript × 102 manuscripts/issue × 12 issues/year])	\$6804.48
Total potential cost per issue to use iThenticate to analyze all SORMSRs (\$6804.48 per year/12 issues)	\$567.04
Additional potential annual cost to use iThenticate for all SORMSRs (\$6804.48 annual cost of iThenticate for all SORMSRs, \$840.72 annual cost of iThenticate for 3 SORMSRs/issue)	\$5963.76

may lead to informing the author's institution (chairperson, dean of the medical school, institutional review board, and so forth), flagging the authors, scrutinizing their future submissions, and/or potentially prohibiting them from publishing in that journal for a time or indefinitely, and even retracting the article in question from PubMed.^{28,29} The economic costs of dealing with research misconduct are nonnegligible; while iThenticate has reported an estimate of between \$10,000 and \$50,000 in capital losses due to incidents of research misconduct in nearly 200 organizational clients surveyed, the direct costs of an investigation of a case of research misconduct have been estimated to approach \$525,000.^{30,31} The additional costs of published research misconduct are characterized by broader detrimental effects on the credibility and reputation of a scientific journal and the specialty that it represents.³² While these effects are difficult to quantify in monetary terms, their potentially long-standing and irreversible effects may be devastating.

Ideally, this sequence of events could be avoided by prospectively checking for duplications when articles are initially received. This may, however, delay the review process and be financially impossible for smaller journals and, in the case of *AJNR*, would result in checking about 75%–80% of SORMSRs that are ultimately rejected. Because of this, the second question we sought to answer was whether randomly studying a sample of published articles yields similar results to studying all articles published in 1 year.

In 2012, *AJNR* published an average of 27.45 original articles in each of its 11 issues. The average number of articles per issue surpassing the 15% duplication rate was 4.91, which nearly matched the number of articles in the same category in the 2 months randomly chosen (March: 5 and September: 4). Overall, the average monthly number of articles containing a >15% overlap from a single source (1.09) also nearly matched that found in the 2 individual months (March: 3 and September: 1). Therefore, in our study, sampling only 2 randomly selected months yields similar results to analyzing an entire year.

While the financial and time costs of prospectively evaluating

all *AJNR* submissions (approximately US \$6800 per annum) may not seem feasible for smaller journals or justified by the low rate of duplication identified in this study, these are relatively low compared with the potential economic costs of dealing with incidents of research misconduct, broader detrimental effects on journal credibility and reputation, and the professional and public perception and trust of the represented subspecialty, which may be long-standing and irreversible.

CONCLUSIONS

Using the suggested empiric duplication threshold of 15%, which is used by *AJNR*, the number of original articles found to have significant duplicated content was low for *AJNR* and *Radiology*. While *AJNR* had a greater number of articles showing >15% overlap compared with *Radiology*, most duplications were not considered significant. When these articles were individually studied, self-plagiarism was found to account for all of the duplicated content, and most of it arose from the "Materials and Methods" and was ultimately considered unimportant. Last, analyzing 2 randomly chosen issues of *AJNR* yielded no significant differences in articles with duplications of >15% compared with those published during an entire year. However, in light of the potentially enormous economic cost of dealing with incidents of research misconduct and adverse effects on the credibility of the journal, its reputation, and perception and trust of its represented subspecialty, more extensive screening of SORMSRs may provide a cost-effective safeguard.

REFERENCES

1. Roig M. **Plagiarism in the sciences: conference highlights.** *Science Editor* 2006;29:48–49
2. Mervis J. **NSF audit of successful proposals finds numerous cases of alleged plagiarism.** *Science Insider*. March 8, 2013. <http://news.sciencemag.org/2013/03/nsf-audit-successful-proposals-finds-numerous-cases-alleged-plagiarism>. Accessed November 23, 2013
3. Department of Health and Human Services. **Public Health Service Policies on Research Misconduct: Final Rule.** CFR Parts 50 and 93.

- Federal Register*. Vol 70. No. 94. May 17, 2005:28386. Washington: Department of Health and Human Services
4. Bird SJ. **Self-plagiarism and dual and redundant publications: what is the problem? Commentary on 'seven ways to plagiarize: handling real allegations of research misconduct.'** *Science and Engineering Ethics* 2002;8:543–44
 5. Hirsch JE. **An index to quantify an individual's scientific research output.** *Proc Natl Acad Sci U S A* 2005;102:16569–72
 6. Marnet A. H-index: what it is and how to find yours. 2010. <http://www.benchfly.com/blog/h-index-what-it-is-and-how-to-find-yours/>. Accessed November 23, 2013
 7. Berquist TH. **Scientific integrity: has CrossCheck made a difference?** *AJR Am J Roentgenol* 2013;201:703
 8. Roig M. **Recycling portions of text from the same author's previously published papers in psychology: an exploratory study.** In: *Proceedings of the Conference of the Second Office of Research Integrity*. Bethesda, Maryland. November, 16–18, 2002
 9. Roig M. Avoiding plagiarism, self-plagiarism, and other questionable writing practices: a guide to ethical writing. August 2006. <http://ori.hhs.gov/sites/default/files/plagiarism.pdf>. Accessed November 24, 2013
 10. Scanlon PM. *Song From Myself: An Anatomy of Self-Plagiarism*. Ann Arbor: Michigan University Library; 2007:57–66
 11. iParadigms. <http://www.iparadigms.com/>. Accessed November 10, 2013
 12. Crosscheck. <http://www.crossref.org/crosscheck/index.html>. Accessed November 10, 2013
 13. Turnitin. Reduce plagiarism. http://turnitin.com/en_us/features/originalitycheck. Accessed November 10, 2013
 14. iThenticate. <http://www.ithenticate.com/content>. Accessed November 13, 2013
 15. iThenticate. Prevent plagiarism in published works. <http://www.ithenticate.com/>. Accessed November 3, 2013
 16. Turnitin. Instructor training about OriginalityCheck. http://turnitin.com/en_us/training/instructor-training/about-originalitycheck. Accessed November 10, 2013
 17. iThenticate. Text-only reports. <http://www.ithenticate.com/training/text-only>. Accessed November 10, 2013
 18. Jocoy CL, DiBiase D. **Plagiarism by adult learners online: a case study in detection and remediation.** *International Review of Research in Open and Distance Learning* 2006;7:1–15
 19. The University of the West Indies. Guidelines for staff and students on plagiarism. October 2010. http://sta.uwi.edu/resources/documents/postgrad/guidelines_staff_students_plagiarism.pdf. Accessed November 3, 2013
 20. University of Stellenbosch Business School. Contract conditions for ad hoc Faculty teaching on USB-ED programmes, December 2013. Policy Annexure B: Interpreting Turnitin Results. 2013. <http://www.usb-ed.com/content/Downloadable%20documents/Faculty%20Contract%20Conditions%20USB%20ED%202014.pdf>. Accessed November 17, 2013
 21. Syracuse University answers. Turnitin and Blackboard. Interpreting Turnitin originality reports. August 28, 2013. <https://answers.syr.edu/display/blackboard01/Interpreting+Turnitin+Originality+Report>. Accessed November 17, 2013
 22. Tennessee University E-learning @ Tees Staff. Interpreting Turnitin originality reports. November 2013. <https://eat.scm.tees.ac.uk/bb8content/resources/recipes/interpretTurnitin.pdf>. Accessed November 17, 2013
 23. Committee on Publication Ethics. Serial plagiarism by an experienced author. 2012. <http://publicationethics.org/case/serial-plagiarism-experienced-author>. Accessed November 10, 2013
 24. Meddings K. **CrossCheck plagiarism screening: what's the magic number.** *Editorial Office News*. August 2011. <http://www.ismte.org/File/Aug11CrossCheck.pdf>. Accessed November 10, 2013
 25. International Committee of Medical Journal Editors. Recommendations for the conduct, reporting, editing and publication of scholarly work in medical journals. December 2013. <http://www.icmje.org/icmje-recommendations.pdf>. Accessed November 24, 2013
 26. Wager E. Committee on Publication Ethics. What to do if you suspect redundant (duplicate) publication. 2008. http://publicationethics.org/files/u2/01A_Redundant_Submitted.pdf. Accessed August 24, 2014
 27. Editors at BioMed Central. Committee on Publication Ethics. Text recycling guidelines. <http://publicationethics.org/text-recycling-guidelines>. Accessed August 24, 2014
 28. Bankier AA, Levine D, Sheiman RG, et al. **Redundant publications in Radiology: shades of gray in a seemingly black-and-white issue.** *Radiology* 2008;247:605–07
 29. Committee on Publication Ethics. What to do if you suspect plagiarism: (a) suspected plagiarism in a submitted manuscript. <http://publicationethics.org/files/u7140/plagiarism%20A.pdf>. Accessed November 10, 2013
 30. iThenticate. White paper. True costs of research misconduct. <http://www.ithenticate.com/resources/papers/research-misconduct>. Accessed August 17, 2012
 31. Michalek AM, Hutson AD, Wicher CP, et al. **The costs and underappreciated consequences of research misconduct: a case study.** *PLoS Med* 2010;7:e1000318
 32. Hoover GA. **A game-theoretic model of plagiarism.** *Atlantic Economic Journal* 2006;34:449–54

Evidence Levels for Neuroradiology Articles: Low Agreement among Raters

J.N. Ramalho, G. Tedesqui, M. Ramalho, R.S. Azevedo, and  M. Castillo



ABSTRACT

BACKGROUND AND PURPOSE: Because evidence-based articles are difficult to recognize among the large volume of publications available, some journals have adopted evidence-based medicine criteria to classify their articles. Our purpose was to determine whether an evidence-based medicine classification used by a subspecialty-imaging journal allowed consistent categorization of levels of evidence among different raters.

MATERIALS AND METHODS: One hundred consecutive articles in the *American Journal of Neuroradiology* were classified as to their level of evidence by the 2 original manuscript reviewers, and their interobserver agreement was calculated. After publication, abstracts and titles were reprinted and independently ranked by 3 different radiologists at 2 different time points. Interobserver and intraobserver agreement was calculated for these radiologists.

RESULTS: The interobserver agreement between the original manuscript reviewers was -0.2283 (standard error = 0.0000; 95% CI, -0.2283 to -0.2283); among the 3 postpublication reviewers for the first evaluation, it was 0.1899 (standard error = 0.0383; 95% CI, 0.1149–0.2649); and for the second evaluation, performed 3 months later, it was 0.1145 (standard error = 0.0350; 95% CI, 0.0460–0.1831). The intraobserver agreement was 0.2344 (standard error = 0.0660; 95% CI, 0.1050–0.3639), 0.3826 (standard error = 0.0738; 95% CI, 0.2379–0.5272), and 0.6611 (standard error = 0.0656; 95% CI, 0.5325–0.7898) for the 3 postpublication evaluators, respectively. These results show no-to-fair interreviewer agreement and a tendency to slight intrareviewer agreement.

CONCLUSIONS: Inconsistent use of evidence-based criteria by different raters limits their utility when attempting to classify neuroradiology-related articles.

ABBREVIATIONS: *AJNR* = *American Journal of Neuroradiology*; EBM = evidence-based medicine; R = reviewer; SE = standard error

Basic and clinical research has been essential in medicine for a long time; however, until recently, the process by which research results were incorporated into medical decisions was highly subjective. To make decisions more objective and more reflective of evidence from research, in the early 1990s, a group of physician-epidemiologists developed a system known as “evidence-based medicine.”^{1,2} Thereafter, the definition of evidence-based medicine was consolidated and redefined by the Evidence-Based Medicine Working Group at McMaster University in Hamilton, Ontario, Canada, as “the integration of current best

evidence with clinical expertise and patient values.”^{3,4} Since then, evidence-based medicine (EBM) has developed and has been applied to many medical disciplines, including imaging.⁵ The major goal of EBM in radiology is to bridge the gap between research and clinical practice and ensure that decisions regarding diagnostic imaging and interventions in patient groups or individual patients are based on the best current evidence.⁶

Finding the best current evidence is challenging, particularly due to the rapidly expanding volume of medical knowledge. In this setting, independent and critical appraisal of the literature is essential.^{6–12}

Medical literature may be classified into different levels of evidence on the basis of the study design and methodology. Haynes et al¹³ described the “evidence pyramid” in which the literature is ranked and weighted in 4 levels: 1) primary, 2) syntheses (evidence-based reviews, critically appraised topics, and systematic reviews with meta-analysis), 3) synopses, and 4) information systems. Primary literature includes original studies and represents

Received October 20, 2014; accepted after revision December 10.

From the Departments of Neuroradiology (J.N.R., G.T., M.C.) and Radiology (M.R.), University of North Carolina Hospital, Chapel Hill, North Carolina; Centro Hospitalar de Lisboa Central (J.N.R.), Lisbon, Portugal; Hospital Garcia de Orta (M.R.), Almada, Portugal; and Faculdade de Medicina da Universidade de São Paulo (R.S.A.), São Paulo, Brazil.

Please address correspondence to Joana Ramalho, MD, 302Q Copperline Dr, Chapel Hill, NC 27516; e-mail: Joana-Ramalho@netcabo.pt

<http://dx.doi.org/10.3174/ajnr.A4242>

the base of the pyramid. The upper 3 levels are secondary literature. Evidence identified at higher echelons of the pyramid is scientifically better than that at lower levels, and if the evidence answers a question or fills a knowledge gap, searching for it at the base of the pyramid is considered redundant.¹¹ Unfortunately, in radiology, there is often little secondary evidence available about any given topic,¹¹ and the quality of research is variable and frequently difficult to evaluate.¹⁴

Methods for reviewing the evidence have matured during the years as investigators have gained experience in developing evidence-based guidelines. For some years, the standard approach to evaluating the quality of individual studies was based on a hierarchical grading system of research design, in which randomized controlled trials received the highest scores. More recently, the Centre for Evidence-Based Medicine (University of Oxford, Oxford, England) developed a classification applicable to diagnostic, therapeutic, or prognostic articles, which ranks articles in 5 main levels of evidence.¹⁵ The *American Journal of Neuroradiology (AJNR)*, a peer-reviewed imaging journal with a current 5-year impact factor of 3.827, implemented, 4 years ago, a classification system of levels of evidence for all submitted articles, highlighting in its “Table of Contents” those articles corresponding to levels 1 and 2. *AJNR* initially adopted the modified criteria suggested by the US Preventive Services Task Force.¹⁶ Nevertheless, in that time, we have noticed a wide variation of peer-reviewer evidence-based classifications; and to our knowledge, no study has previously evaluated the reproducibility of the levels-of-evidence classification system in medical imaging-related publications. Thus, the purpose of our study was to determine whether the classification used by *AJNR* is reproducible and allows consistent identification of the levels of evidence of articles published.

MATERIALS AND METHODS

We used the *AJNR* reviewer data base between January 5, 2012, and June 19, 2012, to randomly select 100 consecutive published original research articles. We excluded all other types of articles.

As part of the standard, prepublication, double-blind peer-review process, the 2 individuals who initially evaluated the manuscripts were asked to classify these articles according to their level of evidence (here called “prepublication reviewers”). The levels of evidence defined by *AJNR* were as follows: level I, evidence obtained from at least 1 properly designed randomized controlled trial; level II, evidence obtained from well-designed controlled trials without randomization; level III, evidence obtained from a well-designed cohort or case-control analytic study, preferably from >1 center or research group; level IV, evidence obtained from multiple time-series with or without the intervention, such as case studies. Dramatic results in uncontrolled trials might also be regarded as level IV. Level V was opinions of respected authorities, based on clinical experience, descriptive studies, or reports of expert committees.¹⁶ These levels were modified for ease of use from those proposed by the US Preventive Services Task Force.

Thereafter, titles and abstracts for all 100 articles were printed and assigned to 3 different neuroradiologists (here called “post-publication reviewers” 1–3), respectively, with 24, 9, and 5 years of experience in neuroradiology, who were asked to independently classify the articles according to the levels of evidence.

Inter- and intraobserver agreement

Agreement
1) Interobserver agreement (R1, R2, and R3) Agreement among 3 raters: Slight agreement for both reading sessions (Fleiss κ : 0.18 and 0.11) Agreement between R1 and R2, R2 and R3, and R1 and R3 for 2 sessions: Slight agreement R1 \times R2 (Cohen κ unweighted = 0.20 and 0.04) Fair agreement R2 \times R3 (Cohen κ unweighted = 0.27 and 0.30) Slight agreement R1 \times R3 (Cohen κ unweighted = 0.12 and 0.07)
2) Interobserver agreement (prepublication reviewers) No agreement (Cohen κ unweighted = -0.22)
3) Intraobserver agreement (R1, R2, and R3) R1 fair agreement (Cohen κ : 0.23) R2 fair agreement (Cohen κ : 0.38) R3 substantial agreement (Cohen κ : 0.66)

While the first reviewer is an editor with experience in research methods and EBM, the other 2 did not have any formal training in research methods, EBM, or health services research. The articles were assigned in random order for each reviewer and blinded to the ratings given by the 2 prepublication reviewers. These evaluations were performed twice. In an attempt to reduce potential biases that could result from recall, the second session was performed 3 months later, in a random order different from that in the first evaluation.

Statistical Analyses

Interobserver agreement among the 3 postpublication reviewers was calculated by using the Fleiss κ for each of the 2 rating sessions. Interobserver agreement between reviewer (R)1 and R2, R1 and R3, and R2 and R3 for each of the 2 rating sessions and interobserver agreement between the ratings of the prepublication reviewers were calculated by using the unweighted Cohen κ . Intraobserver agreement (R1, R2, and R3) was calculated by using the unweighted Cohen κ to evaluate the concordance between the same reviewers with time.

Because the levels of evidence are considered categorical variables, there are no recognized relations between them, thus only the unweighted κ was used.

RESULTS

The summary of the results is shown in the Table.

Interobserver agreement among the 3 postpublication reviewers (R1, R2, and R3) for the first evaluation was 0.1899 (standard error [SE] = 0.0383; 95% CI, 0.1149–0.2649); and for the second evaluation performed 3 months later, it was 0.1145 (SE = 0.0350; 95% CI, 0.0460–0.1831).

Interobserver agreement between R1 and R2 was 0.2015 (SE = 0.0733; 95% CI, 0.0579–0.3451) and 0.0488 (SE = 0.0585; 95% CI, -0.0659 – 0.1636); between R2 and R3, it was 0.2730 (SE = 0.0784; 95% CI, 0.1193–0.4267) and 0.3022 (SE = 0.0768; 95% CI, 0.1516–0.4527); and between R1 and R3, it was 0.1230 (SE = 0.0726; 95% CI, -0.0193 – 0.2652) and 0.0721 (SE = 0.0615; 95% CI, -0.0484 – 0.1926) for each evaluation session.

Interobserver agreement between the prepublication reviewers was -0.2283 (SE = 0.0000; 95% CI, -0.2283 to -0.2283).

Intraobserver agreement was 0.2344 (SE = 0.0660; 95% CI, 0.1050–0.3639), 0.3826 (SE = 0.0738; 95% CI, 0.2379–0.5272), and 0.6611 (SE = 0.0656; 95% CI, 0.5325–0.7898) for R1, R2, and R3, respectively.

DISCUSSION

The rapidly expanding volume of medical publications and physicians' limited training in appraising the quality of scientific literature represent a major obstacle to finding the best current evidence. One strategy to solve this drawback is to assign a level of evidence for each published article.¹¹ Theoretically, when faced with a question, it would be sufficient to read the article with the highest level of evidence to answer it, making the best use of our time.¹⁴

During the manuscript evaluation, *AJNR* asked its reviewers to assign each submission a level of evidence by using the *AJNR* criteria. Theoretically, these criteria should allow raters to quickly assign a level of evidence to each article, and the classification should be clear and objective enough to be reproducible among raters. However, on the basis of empiric experience, we have noticed a wide variation of reviewer grades.

To assess this observation, we decided to retrospectively compare the level of evidence attributed to different articles among manuscript reviewers (prepublication reviewers) and among 3 neuroradiologists with varying degrees of experience (postpublication reviewers).

Our results showed overall no agreement to fair interreviewer agreement and a tendency to slight intrareviewer agreement. Most interesting, 1 reviewer (R3) had substantial intrarater agreement. This might be related to increased recall bias from the first reading or, alternatively, to increased knowledge of the EBM classification by this reviewer despite his lack of formal training in this area; however, despite this good intrarater agreement, the overall intra- and interreviewer agreement remained very low. This means that there was no uniform agreement among different reviewers and among the same reviewers with time. According to these results, we may assume that the definitions of levels of evidence used by *AJNR* did not allow consistent article classification.

The levels of evidence defined by the Centre for Evidence-Based Medicine to assess study design and methodology¹⁵ are currently accepted as the gold standard criteria. This classification is freely available, conceptually easy to understand and to apply, and internationally recognized as robust. The *AJNR* criteria do not exactly reproduce the Centre for Evidence-Based Medicine levels of evidence criteria. For example, the Centre for Evidence-Based Medicine Levels of Evidence classification subdivides the studies by type, including studies of diagnosis, differential diagnosis, and prognosis, which are evaluated slightly differently. In addition, the criteria of *AJNR* do not take into account different optimal study designs according to the type of question being addressed; therefore, it is reasonable to expect that these criteria might be more difficult to apply. Most of the original research articles evaluated in our study dealt with diagnostic and interventional neuroradiology, which should probably be appraised in different categories.

Another possible explanation is the incorrect interpretation of the *AJNR* criteria by raters, suggesting that it might be necessary to promote adequate training to understand their meaning and use them properly. Although there was no specific training in evidence-based research methods, the slight-to-fair agreement seen among postpublication reviewers in contrast to the no agreement perceived in prepublication reviewers may reflect the inherent learning necessary to perform this study. A further possibility is that the nature of neuroradiology literature requires additional criteria specifically designed for its appraisal. *AJNR* implemented the use of these criteria in the beginning because of their simplicity and presumably ease of use; on the basis of the results here presented, it has switched to the more complex Centre for Evidence-Based Medicine criteria, which will be similarly evaluated when more data are accumulated.

It has been suggested that diagnostic, therapeutic, and interventional articles should be appraised applying additional evidence-based criteria. For example, some pertinent questions that can be added in the evaluation of diagnostic studies include the following: 1) Was there an independent, blinded comparison with a reference standard of diagnosis? 2) Was the diagnostic test evaluated in an appropriate spectrum of patients (like those for whom it would be used in practice)? 3) Was the reference standard applied regardless of the diagnostic test result? 4) Was the test (or a cluster of tests) validated in a second, independent group of patients?^{4,11}

Given the nature of radiology publications, some investigators have suggested that they should also be assessed from a radiologist's perspective, and other considerations may be pertinent, including the following: 1) Has the imaging method been described in sufficient detail for it to be reproduced in one's own department? 2) Has the imaging test been evaluated and the reference test been performed to the same standard of excellence? 3) Have "generations" of technology development within the same technique (eg, conventional versus helical, single-detector row versus multidetector row CT) been adequately considered in the study design and discussion? 4) Has radiation exposure been considered? (The concept of justification and optimization has assumed prime importance in radiation protection to patients.) 5) Were MR and/or CT images reviewed on a monitor or as film (hard copy) images?^{11,17}

Given the limitations found when assessing evidence-based levels for imaging articles, alternative methods may have to be considered.¹¹ The Standards for Reporting of Diagnostic Accuracy Initiative attempts to implement consistency in study design by providing a 25-item checklist to construct epidemiologically sound diagnostic research.¹⁸ Recently, Smidt et al¹⁹ evaluated English language articles published in 2000 in biomedical journals with an Impact Factor of >4 , regarding the number of the Standards for Reporting of Diagnostic Accuracy Initiative items present in each publication. The authors found that only 41% of articles included $>50\%$ of the 25-item checklist and no article reported $>80\%$ of these items.¹¹

The supporters of evidence-based medicine often point out the many biases and weaknesses found in traditional narrative reviews favoring that evidence-based articles represent the best literature to identify evidence that should be assimilated into clin-

ical practice.^{20,21} Weeks and Wallace²² evaluated 110 research articles and concluded that almost all were extremely difficult to read, which eventually may also hamper their evidence-based classification.

Our study has some limitations. One limitation was the use of only the title and abstracts to rank the articles a posteriori instead of the complete “Material and Methods” and “Results” sections. We, however, assumed that the abstracts published in *AJNR* follow a format that describes the essential aspects of an investigation and that the information contained should be enough to closely reflect the content of the articles and thus is sufficient to assign them a level of evidence. Another limitation is the lack of a “criterion standard” with which to evaluate the accuracy of each reviewer. From our results, we found that it is difficult to expect good accuracy in evidence-based grading from pre- and postpublication reviewers, because we found only slight overall intrareviewer agreement. Moreover, our purpose was to determine whether the classification used by *AJNR* is reproducible among different readers and not to determine its accuracy.

CONCLUSIONS

The results of our study show that the levels-of-evidence criteria adopted in our subspecialty journal did not allow consistent manuscript classification between readers and even by the same reader at 2 time points. Alternative methods for appraisal of neuroradiology articles and/or adequate training of reviewers should be considered.

REFERENCES

1. Evidence-Based Medicine Working Group. **Evidence-based medicine: a new approach to teaching the practice of medicine.** *JAMA* 1992; 268:2420–25
2. Howick JH. *The Philosophy of Evidence-Based Medicine.* Hoboken: John Wiley & Sons; 2011:15
3. Sackett DL, Rosenberg WM, Gray JA, et al. **Evidence based medicine: what it is and what it isn't.** *BMJ* 1996;312:71–72
4. Sackett DL, Strauss SE, Richardson WS, et al. *Evidence Based Medicine: How to Practice and Teach EBM.* 2nd ed. Edinburgh: Churchill Livingstone; 2000:1–12
5. The Evidence-Based Radiology Working Group. **Evidence-based radiology: a new approach to the practice of radiology.** *Radiology* 2001;220:566–75
6. Malone DE. **Evidence-based practice in radiology: an introduction to the series.** *Radiology* 2007;242:12–14
7. Budovec JJ, Kahn CE. **Evidence-based radiology: a primer in reading scientific articles.** *AJR Am J Roentgenol* 2010;195:W1–4
8. Malone DE. **Evidence-based practice in radiology: what color is your parachute?** *Abdom Imaging* 2008;33:3–5
9. Kelly AM. **Evidence-based radiology: step 1—ask.** *Semin Roentgenol* 2009;44:140–46
10. Kelly AM. **Evidence-based practice: an introduction and overview.** *Semin Roentgenol* 2009;44:131–39
11. Dodd JD. **Evidence-based practice in radiology: steps 3 and 4—appraise and apply diagnostic radiology literature.** *Radiology* 2007; 242:342–54
12. Malone DE, Staunton M. **Evidence-based practice in radiology: step 5 (evaluate)—caveats and common questions.** *Radiology* 2007; 243:319–28
13. Haynes RB. **Of studies, summaries, synopses, and systems: the “4S” evolution of services for finding best current evidence.** *Evid Based Ment Health* 2001;4:37–39
14. Staunton M. **Evidence-based radiology: steps 1 and 2—asking answerable questions and searching for evidence.** *Radiology* 2007;242: 23–31
15. Levels of evidence. Oxford Centre for Evidence-Based Medicine Web site. <http://www.cebm.net/oxford-centre-evidence-based-medicine-levels-evidence-march-2009/>. Accessed March 2014
16. Harris RP, Helfand M, Woolf SH, et al. **Current methods of the U.S. Preventive Services Task Force: a review of the process.** *Am J Prev Med* 2001;20:21–35
17. Maher MM, McNamara AM, MacEaney PM, et al. **Abdominal aortic aneurysms: elective endovascular repair versus conventional surgery—evaluation with evidence-based medicine techniques.** *Radiology* 2003;228:647–58
18. Bossuyt PM, Reitsma JB, Bruns DE, et al. **Towards complete and accurate reporting of studies of diagnostic accuracy: the STARD Initiative.** *Radiology* 2003;226:24–28
19. Smidt N, Rutjes AW, van der Windt DA, et al. **Quality of reporting of diagnostic accuracy studies.** *Radiology* 2005;235:347–53
20. Loke YK, Derry S. **Does anybody read “evidence-based” articles?** *BMC Med Res Methodol* 2003;3:14
21. Moher D, Cook DJ, Eastwood S, et al. **Improving the quality of reports of meta-analyses and randomised controlled trials: the QUOROM statement.** *Lancet* 1999;354:1896–900
22. Weeks WB, Wallace AE. **Readability of British and American medical prose at the start of the 21st century.** *BMJ* 2002;325:1451–52

White Matter Alterations in the Brains of Patients with Active, Remitted, and Cured Cushing Syndrome: A DTI Study

P. Pires, A. Santos, Y. Vives-Gilabert, S.M. Webb, A. Sainz-Ruiz, E. Resmini, I. Crespo, M. de Juan-Delago, and B. Gómez-Anson



ABSTRACT

BACKGROUND AND PURPOSE: Cushing syndrome appears after chronic exposure to elevated glucocorticoid levels. Cortisol excess may alter white matter microstructure. Our purpose was to study WM changes in patients with Cushing syndrome compared with controls by using DTI and the influence of hypercortisolism.

MATERIALS AND METHODS: Thirty-five patients with Cushing syndrome and 35 healthy controls, matched for age, education, and sex, were analyzed through DTI (tract-based spatial statistics) for fractional anisotropy, mean diffusivity, axial diffusivity, and radial diffusivity (general linear model, family-wise error, and threshold-free cluster enhancement corrections, $P < .05$). Furthermore, the influence of hypercortisolism on WM DTI changes was studied by comparing 4 subgroups: 8 patients with Cushing syndrome with active hypercortisolism, 7 with Cushing syndrome with medication-remitted cortisol, 20 surgically cured, and 35 controls. Cardiovascular risk factors were used as covariates. In addition, correlations were analyzed among DTI values, concomitant 24-hour urinary free cortisol levels, and disease duration.

RESULTS: There were widespread alterations (reduced fractional anisotropy, and increased mean diffusivity, axial diffusivity, and radial diffusivity values; $P < .05$) in patients with Cushing syndrome compared with controls, independent of the cardiovascular risk factors present. Both active and cured Cushing syndrome subgroups showed similar changes compared with controls. Patients with medically remitted Cushing syndrome also had reduced fractional anisotropy and increased mean diffusivity and radial diffusivity values, compared with controls. No correlations were found between DTI maps and 24-hour urinary free cortisol levels or with disease duration.

CONCLUSIONS: Diffuse WM alterations in patients with Cushing syndrome suggest underlying loss of WM integrity and demyelination. Once present, they seem to be independent of concomitant hypercortisolism, persisting after remission/cure.

ABBREVIATIONS: AD = axial diffusivity; CS = Cushing syndrome; FA = fractional anisotropy; MD = mean diffusivity; RD = radial diffusivity; UFC = urinary free cortisol

Cushing syndrome (CS) is a rare endocrine disease with a prevalence of approximately 40 cases per million inhabitants,¹ in which diagnosis and, therefore, treatment are often delayed for months or years. It is caused by excessive cortisol exposure due to an adrenocorticotropin-secreting pituitary adenoma (Cushing disease), an adrenal adenoma, or an ectopic secretion of adreno-

corticotropin by tumors in other organs.² It causes a range of physical and psychological symptoms, including depression and apathy.³ The so-called glucocorticoid cascade hypothesis, based on animal models, associates the harmful effects of glucocorticoid excess on the structure, function, and vitality of brain cells.⁴ Excessive exposure to glucocorticoid leads to changes in plasticity, reduced neurogenesis, and cell loss in the hippocampus.⁵ Besides, cortisol induces myelin loss around axons in postnatal rats,⁶ and more recent evidence indicates that prolonged exposure to ele-

Received October 11, 2014; accepted after revision December 14.

From the Asociación para la Innovación en Análisis, Gestión y Procesamiento de Datos Científicos y Tecnológicos (P.P., Y.V.-G.), Barcelona, Spain; Departments of Endocrinology/Medicine (P.P., A.S., S.M.W., E.R., I.C.), Hospital Sant Pau, IIB-Sant Pau, Instituto de Salud Carlos III, and Universitat Autònoma de Barcelona, Barcelona, Spain; Port d'Informació Científica (Y.V.-G., A.S.-R.), Bellaterra, Barcelona, Spain; Institut de Física d'Altes Energies (A.S.-R.), Barcelona, Spain; and Neuroradiology Unit (M.d.J.-D., B.G.-A.), Hospital Sant Pau, IIB-Sant Pau, Universitat Autònoma de Barcelona, Barcelona, Spain.

This work was supported by grants from the Instituto de Salud Carlos III, Spanish Ministry of Science and Innovation (MICINN, FIS080302 and FIS 070770), and the European Commission (ERCUSYN PHP800200).

Please address correspondence to: Beatriz Gómez-Ansón, MD, PhD, FRCR, Neuro-radiology Unit, Hospital Sant Pau, C/San Antoni Maria Claret 167, 08025 Barcelona, Spain; e-mail: BGomezA@santpau.cat

Indicates open access to non-subscribers at www.ajnr.org

Indicates article with supplemental on-line appendix and tables.

Indicates article with supplemental on-line photo.

Evidence-Based Medicine Level 2.

<http://dx.doi.org/10.3174/ajnr.A4322>

Demographic and clinical characteristics of healthy controls and patients with active, remitted, and cured CS^a

	Healthy Controls	Patients with Active CS	Patients with Remitted CS	Patients with Cured CS	F/ χ^2	P Value
Age (yr)	42.3 ± 10.4	41.9 ± 8.7	47.1 ± 10.0	41.4 ± 10.0	5.9	NS
Sex (M/F)	6:29	1:7	1:6	4:16	0.3	NS
Years of education	13.5 ± 3.4	14.4 ± 3.0	12.9 ± 2.3	13.4 ± 3.1	0.3	NS
24-Hour urinary free cortisol	133 ± 52	543 ± 307	152 ± 74	122 ± 75	26.3	<.001 ^b
Smoking status (nonsmoker/smoker/ex-smoker)	12/12/11	7/1/0	2/4/1	9/5/6	10.4	NS
Disease duration (mo)	NA	77.6 ± 77.4	44.6 ± 21.9	64.6 ± 34.0	0.99	NS
Origin (pituitary/adrenal/ectopic/AIMAH)	NA	5/3/0/0	3/2/1/1	17/2/0/0	10.8	NS
Hypertension (no/yes)	35/0	4/4	3/4	13/7	20.9	<.001 ^c
Hypercholesterolemia (no/yes)	31/4	7/1	7/0	17/3	1.2	NS
Hypertriglyceridemia (no/yes)	29/6	6/2	3/4	9/11	10.5	.015 ^d
Central obesity (no/yes)	25/10	2/6	0/7	9/11	15.6	.001 ^e
Body mass index ^g (no/overweight/obesity)	22/11/2	2/5/1	1/3/3	8/9/3	12.6	.049 ^f

Note:—NS indicates not significant; AIMAH, ACTH-independent macronodular adrenal hyperplasia.

^a Data are expressed as mean ± SD.

^b Healthy controls vs active CS (<.001); active CS vs remitted CS (<.001); active CS vs cured CS (<.001).

^c Healthy controls vs active CS (<.001); healthy controls vs remitted CS (<.001); healthy controls vs cured CS (<.001).

^d Healthy controls vs remitted CS (.043); healthy controls vs cured CS (.006).

^e Healthy controls vs active CS (.015); healthy controls vs remitted CS (.001).

^f Healthy controls vs remitted CS (.015).

^g Body mass index: normal, ≤25; overweight, 25–30; obesity, >30.

vated glucocorticoid may alter oligodendrocyte-mediated myelination.^{7,8} Thus, cortisol excess most likely alters the microstructure of cerebral white matter, targeting the myelinated axonal tracts in the brains of patients with CS. Moreover, hypercortisolism frequently determines diabetes mellitus, central obesity, and thrombophilia, which increase cardiovascular disease,⁹ the main cause of mortality in CS, even after biochemical cure.¹⁰ These comorbidities may also affect cerebral WM microstructure in CS.¹¹

A few imaging studies have investigated brain structures in patients with CS.^{12,13} Starkman et al,¹⁴ using MR imaging, found a relationship among hippocampal volume reduction, memory dysfunction, and elevated cortisol levels in CS. More recent studies, including CT and MR imaging, have described loss of brain volume in CS.¹⁵ With MR imaging and automated volumetry, hippocampal volume reductions were found in patients with CS with severe memory deficits.¹⁶ A more recent study investigated WM with DTI in patients in long-term remission of Cushing disease and observed widespread abnormalities. The authors also observed a loss of integrity of the uncinate fasciculus, which was related to the severity of depression.¹⁷ They concluded that structural changes in WM integrity in the brain persisted after hypercortisolism cure¹⁷; but patients with active disease were not included, and cardiovascular risk factors were not reported.

DTI is an MR imaging technique that allows noninvasive, in vivo study of the brain by assessing the motion of water molecules along and across neural axons.^{18,19} Different DTI maps show the WM architecture²⁰ and can depict microstructural WM abnormalities. Fractional anisotropy (FA) reflects WM integrity, while increases in mean diffusivity (MD) may be caused by demyelination or edema.²¹ Decreases in axial diffusivity (AD) indicate axonal loss,²² while increased radial diffusivity (RD) is related to demyelination.²¹

The aim of this study was to investigate cerebral WM microstructure in patients with CS compared with healthy controls by using DTI. It was hypothesized that WM integrity in the brain of patients with CS was altered, reflecting microstructural changes, and that these alterations persisted after remission or cure of hypercortisolism.

A first DTI analysis was performed comparing patients with CS with healthy controls, followed by a second analysis in which patients were separated into active CS, remitted CS, and cured CS. Comorbidities known to increase cardiovascular risk were investigated as covariates. Correlations of WM changes with 24-hour urinary free cortisol (UFC) values and the duration of hypercortisolism were also investigated.

MATERIALS AND METHODS

Participants

Thirty-five patients with CS and 35 healthy control volunteers matched for sex, age (±3 years), and years of education (±3 years) were included. Eight patients had active hypercortisolism, 7 had remitted hypercortisolism on medical therapy, and 20 were cured after surgery (Table). Remission of hypercortisolism was considered when patients achieved adrenal insufficiency or morning cortisol suppression (<50 nmol/L, <1.8/μg/dL) after 1 mg dexamethasone overnight and had repeatedly normal 24-hour UFC levels (<280 nmol/24 hours). Disease duration, 24-hour UFC levels, and clinical variables related to cardiovascular risk (smoking, hypertension, dyslipidemia, central obesity, and increased body mass index) were collected (Table). Disease duration was defined by the endocrinologist in charge as the time from symptom onset until remission of hypercortisolism after treatment. At diagnosis, duration of hypercortisolism was estimated by personal interview and detailed review of medical records and photographs of patients. All information was written or kept in clinical records, together with biochemical data. Patients with diabetes mellitus were excluded because it is known to affect WM.²³

All subjects were right-handed and signed an informed consent after approval of the study by the ethics committee of the hospital. No subject had brain injury or clinical cerebrovascular disease.

Image Processing

DTI processing was performed at the computing of Port d'Informació Científica in Barcelona through a designed, portal-based platform, including fMRI of the Brain Software Library

(FSL; Version 4.1.4; <http://www.fmrib.ox.ac.uk/fsl>).²⁴ Images were first corrected for head motion and eddy currents by an affine registration. The first 3D volume was extracted as the image reference by using the Brain Extraction Tool (<http://fsl.fmrib.ox.ac.uk/fsl/fslwiki/BET>).²⁵ Voxelwise images of FA, MD, AD, and RD maps were generated by using the fMRI of the Brain Diffusion Toolbox (<http://www.fmrib.ox.ac.uk/fsl/fdt/index.html>) by fitting diffusion tensors at each voxel. Next, the tract-based spatial statistics package (<http://fsl.fmrib.ox.ac.uk/fsl/fslwiki/TBSS>)²⁶ was applied for a voxelwise statistical analysis. First, the fMRI of the Brain Linear Image Registration Tool (FLIRT; <http://www.fmrib.ox.ac.uk/>) was used to align all FA images into a standard space (fMRI of the Brain 58-FA). Then, a mean skeleton of all FA images was built by selecting the main WM tracts, thinned with a 0.2 threshold value (excluding all FA voxels of <0.2) to increase consistency. MD, AD, and RD maps followed the same Tract-Based Spatial Statistics procedure of nonlinear warps and skeleton projection to obtain estimated vectors for each.

MR imaging acquisition and statistical analysis are detailed in the On-line Appendix.

RESULTS

Analysis 1: Comparison between Patients with CS and Controls

Demographic and Clinical Variables. Because of the matched study design, no differences in age, sex, or years of education between patients with CS and controls were present. Differences were found for comorbidities: hypertension (0 controls/15 patients with CS; $P < .001$), hypertriglyceridemia (6 controls/17 patients with CS; $P = .004$), central obesity (10 controls/24 patients with CS; $P < .001$), and body mass index (22, healthy, <25; 11 overweight, between 25 and 30; and 2 obese, >30 controls versus 11 healthy, 17 overweight, and 7 obese patients with CS; $P = .019$). To correct for these differences, we included these comorbidities as covariates in the DTI analysis. No differences in smoking (12 nonsmokers, 12 smokers, and 11 ex-smokers among controls versus 18 nonsmokers, 10 smokers, and 7 ex-smokers in patients with CS) or in the prevalence of hypercholesterolemia (4 healthy controls versus 4 patients with CS) were observed between groups.

DTI Analysis

The Figure shows widespread FA decreases (A) and MD (B), AD (C), and RD (D) increases in all patients with CS compared with controls ($P < .05$). No differences were found in the reverse comparisons (ie, controls had neither lower FAs nor higher MD, AD, or RDs than patients with CS).

Analysis 2: Comparison between Patients with Active, Remitted, and Cured CS and Controls

Demographic and Clinical Characteristics. No differences were found in age, sex, or years of education between controls and any of the CS subgroups. Twenty-four-hour UFC levels in patients with active CS were higher than in those in the other 3 groups. The prevalence of hypertension, hypertriglyceridemia, central obesity, and increased body mass index differed among groups, so they

were analyzed as covariates in DTI analysis (Table). Smoking and hypercholesterolemia did not differ among groups. No differences in disease duration or etiology among the CS groups were found.

DTI Analysis

On-line Fig 1 shows voxels/regions having decreased FA (A) and increased MD (B), AD (C), and RD (D) values in patients with active CS compared with controls ($P < .05$). No differences were found in the reverse contrasts (ie, controls had neither lower FA nor higher MD, AD, or RD values than patients with active CS).

On-line Fig 2 shows voxels/regions having decreased FA (A) and increased MD (B) and RD (C) values ($P < .05$) in patients with remitted CS compared with controls. No differences were found in the reverse contrasts (ie, controls had neither lower FA nor higher MD or RD values than patients with active CS). No differences in AD values among groups were seen.

On-line Fig 3 shows voxels/regions having decreased FA (A) and higher MD (B), AD (C), and RD (D) values ($P < .05$) in patients with cured CS compared with controls. No differences were found in the reverse contrasts (ie, controls had neither lower FA nor higher MD, AD, or RD values than patients with cured CS).

No differences were found in any DTI maps/values (FA, MD, AD, or RD) among the 3 subgroups of patients with CS (active, remitted, and cured).

Correlation Analysis

No correlations were found for any DTI maps (FA, MD, AD, and RD) with the 24-hour UFC levels of healthy controls ($n = 28$) or patients with CS ($n = 34$) or with disease duration in patients with CS.

DISCUSSION

This study demonstrates widespread WM alterations on DTI in the brains of patients with CS compared with healthy controls, which persist after controlling for cardiovascular risk factors (hypertension, dyslipidemia, and obesity). The pattern of WM involvement, with decreased FA and increased MD, AD, and RD, suggests an underlying loss of WM integrity and predominant demyelination. The subgroup analysis demonstrates this same pattern of WM involvement in patients with active, remitted, and cured CS, without any correlation among DTI values, concomitant 24-hour UFC levels, or disease duration. These results imply that WM damage does not depend on current hypercortisolism because it persists after remission/cure of CS. These findings support the recent concept that once WM damage has occurred after early exposure to hypercortisolism, it is not completely reversible, despite successful treatment with surgery or medical therapy. It adds to the growing body of evidence that residual morbidity persists after endocrine control of CS.¹⁷

Although most DTI studies refer to FA values, the other DTI maps/parameters provide additional information on WM microstructure that expands the understanding of WM integrity. Reduced FA values indicate loss of fiber coherence and therefore of WM integrity. An increase in overall water diffusion in all directions (MD) may reflect demyelination²⁷ or edema²¹; more specif-

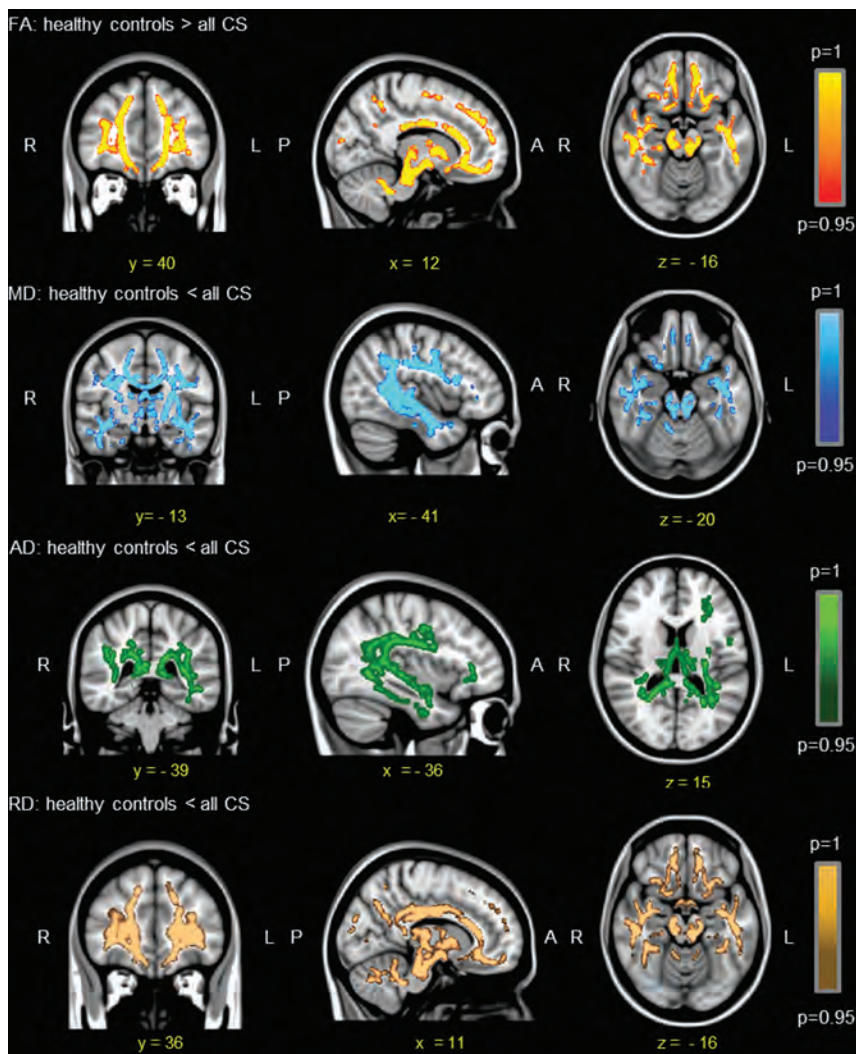


FIGURE. Differences ($P < .05$) in DTI maps among all patients with CS and controls by using hypertension, hypertriglyceridemia, central obesity, and body mass index as covariates.

ically, radial diffusivity measures diffusion perpendicular to the tract and relates to myelin sheath integrity,²⁸ so it is increased in demyelination.^{21,29} The overall local magnitude of diffusion parallel to the tract (axial diffusivity) provides information on axonal integrity, so reduced AD values indicate axonal loss.²² Nevertheless, any microstructural features of WM inferred from DTI maps are indirect measures of the real biologic structure and should be interpreted with caution.^{30,31}

Our study demonstrates widespread WM damage throughout the brains of patients with CS, with reduced FA and increased diffusivities, including RD, which persist after controlling for cardiovascular risk factors and clinical variables that may also alter WM (including hypertension, dyslipidemia, and obesity). These microstructural changes in the WM of patients with CS reflect loss of integrity mainly due to demyelination but not to axonal loss. Our results are similar to those obtained in a recent DTI study of 22 patients with CS in long-term remission (11 years) after surgery, by using a similar DTI methodology.¹⁷ These authors reported findings similar to ours, with patients with CS having widespread reduced FA values in WM, including the corpus callosum, bilateral cingulate gyrus, and bilateral uncinate fasciculus.

They also found increased RD values, similar to our results, indicating predominant underlying demyelination in altered WM tracts. The observed increases in RD should, nevertheless, be interpreted with caution, especially in regions containing white matter tract crossings, as has been previously reported.³¹ Our results expand the findings not only to patients in long-term remission but also in those with active hypercortisolism and those with remitted CS on medical therapy. Furthermore, cardiovascular risk factors, which may also damage the brain WM, were controlled for in our study. Evidence indicates that glucocorticoid may contribute to brain aging⁵ and produce WM changes on DTI³² similar to those found in CS. The pattern of WM involvement in aging has been termed “chronic WM degeneration” and includes increased extracellular volume (edema) and lower membrane attenuation as a consequence of myelin loss, smaller axonal ratio volume, higher axonal interspace, and reductions in extracellular tortuosity.³³ These microstructural WM changes are similar to the DTI changes observed in patients with CS in our study.

Some studies have reported a certain degree of reversibility of brain³⁴ and hippocampal volume loss³⁵ after hypercortisolism correction. However, metabolic abnormalities in the hippocampi of patients with cured CS, namely persistent neuronal dysfunction/loss and glial proliferation, have recently been observed,³⁶ which agree with the DTI alterations we have now observed in patients with remitted and cured CS. Most interesting, it has been suggested that chronic exposure to glucocorticoid in the central nervous system could cause inflammation,³⁷ which may trigger WM microstructure damage in patients with CS, as found in the present study. Moreover, high cortisol levels are known to increase the prevalence of cardiovascular risk factors^{9,11} such as hypertension, dyslipidemia, and obesity, which could also affect WM microstructure. Therefore, we corrected for these cardiovascular risk factors, which differed among groups of patients with CS; but WM damage was observed independent of the existence or absence of these comorbidities. We excluded patients and controls with diabetes, another disease known to damage brain WM. Our results lead us to hypothesize that exposure to hypercortisolism plays the major role, possibly mediated by inflammation,³⁷ and is responsible for the persistence of WM damage in remitted/cured patients with CS.³⁸

Our study has some limitations: first, the small sample of subjects included, which is difficult to overcome in a rare endocrine

disease like CS. Compared with controls, patients with remitted CS showed decreased FA and increased MD and RD only, with no changes in AD, these results being different from those observed in patients with active and cured CS; this lack of change in AD may be due to the small sample size. Second, the DTI study, although methodologically robust, is cross-sectional and includes patients with CS in different stages of the disease (active, remitted, and cured). To clearly define the influence of hypercortisolism on WM alterations, larger longitudinal studies are desirable. Finally, our study did not address the functional significance of WM alterations and whether they relate to psychology.

CONCLUSIONS

WM damage on DTI in the brains of patients with CS suggests widespread integrity loss and predominant demyelination. These alterations seem to be independent of concomitant hypercortisolism and the presence or absence of other cardiovascular risk factors like hypertension, dyslipidemia, and obesity, and they persist despite remission/cure. When they occur and the mechanisms and the potential modifiers involved remain unclear.

ACKNOWLEDGMENTS

We thank patients and healthy volunteers who participated in the current study for their kind cooperation.

Disclosures: Patricia Pires—RELATED: Grant: Spanish Ministry of Science and Innovation (FIS080302, FIS 070770).* Alicia Santos—RELATED: Grant: Ministerio de Ciencia y educación.* Comments: Public Spanish grant FIS080302. Susan M. Webb—RELATED: Grant: Instituto de Salud Carlos III, Ministry of Economy and Competitiveness, and Ministry of Health, Spain.* Comments: This was a public competitive grant for which I am the principal investigator. Eugenia Resmini—RELATED: Grant: Ministerio de Ciencia e Innovación (FIS 080302).* Iris Crespo—RELATED: Grant: FIS 080302 “Neuroradiological, Neuropsychological and Clinical Study in Endogenous Hypercortisolism: Comparison between Cushing’s Syndrome and Chronic Major Depressive Disorder”; funding agency: Instituto de Salud Carlos III; duration of the project: from 2009 to 2011, Principal Investigator: Susan M. Webb.* Money paid to the institution.

REFERENCES

- Newell-Price J. Cushing’s syndrome. *Clin Med* 2008;8:204–08
- Hatipoglu BA. Cushing’s syndrome. *J Surg Oncol* 2012;106:565–71
- Guaraldi F, Salvatori R. Cushing syndrome: maybe not so uncommon of an endocrine disease. *J Am Board Fam Med* 2012;25:199–208
- Sapolsky RM, Krey LC, McEwen BS. The neuroendocrinology of stress and aging: the glucocorticoid cascade hypothesis. *Endocr Rev* 1986;7:284–301
- Goosens KA, Sapolsky RM. Stress and glucocorticoid contributions to normal and pathological aging. In Riddle DR, ed. *Brain Aging: Models, Methods, and Mechanisms*. Boca Raton: CRC Press; 2007:305–22
- Bohn MC, Friedrich VL Jr. Recovery of myelination in rat optic nerve after developmental retardation by cortisol. *J Neurosci* 1982;2:1292–98
- Alonso G. Prolonged corticosterone treatment of adult rats inhibits the proliferation of oligodendrocyte progenitors present throughout white and gray matter regions of the brain. *Glia* 2000;31:219–31
- Miyata S, Koyama Y, Takemoto K, et al. Plasma corticosterone activates SGK1 and induces morphological changes in oligodendrocytes in corpus callosum. *PLoS One* 2011;6:e19859

- Fallo F, Sonino N. Should we evaluate for cardiovascular disease in patients with Cushing’s syndrome? *Clin Endocrinol* 2009;71:768–71
- Aulinas A, Valassi E, Webb SM. Prognosis of patients treated for Cushing syndrome. *Endocrinol Nutr* 2014;61:52–61
- Miljic P, Miljic D, Cain JW, et al. Pathogenesis of vascular complications in Cushing’s syndrome. *Hormones (Athens)* 2012;11:21–30
- Trethowan WH, Cobb S. Neuropsychiatric aspects of Cushing’s syndrome. *AMA Arch Neurol Psychiatry* 1952;67:283–309
- Cope O, Raker JW. Cushing’s disease: the surgical experience in the care of 46 cases. *N Engl J Med* 1955;253:119–27
- Starkman MN, Gebarski SS, Berent S, et al. Hippocampal formation volume, memory dysfunction, and cortisol levels in patients with Cushing’s syndrome. *Biol Psychiatry* 1992;32:756–65
- Simmons NE, Do HM, Lipper MH, et al. Cerebral atrophy in Cushing’s disease. *Surg Neurol* 2000;53:72–76
- Resmini E, Santos A, Gómez-Anson B, et al. Verbal and visual memory performance and hippocampal volumes, measured by 3-Tesla magnetic resonance imaging, in patients with Cushing’s syndrome. *J Clin Endocrinol Metab* 2012;97:663–71
- van der Werff SJ, Andela CD, Nienke Pannekoek J, et al. Widespread reductions of white matter integrity in patients with long-term remissions of Cushing’s disease. *Neuroimage Clin* 2014;4:659–67
- Johansen-Berg H, Rushworth MF. Using diffusion imaging to study human connective anatomy. *Annu Rev Neurosci* 2009;32:75–94
- Le Bihan D, Breton E, Lallemand D, et al. MR imaging of intravoxel incoherent motions: application to diffusion and perfusion in neurologic disorders. *Radiology* 1986;161:401–07
- Le Bihan D. Looking into the functional architecture of the brain with diffusion MRI. *Nat Rev Neurosci* 2003;4:469–80
- Alexander AL, Lee JE, Lazar M, et al. Diffusion tensor imaging of the brain. *Neurotherapeutics* 2007;4:316–29
- Budde MD, Xie M, Cross AH, et al. Axial diffusivity is the primary correlate of axonal injury in the experimental autoimmune encephalomyelitis spinal cord: a quantitative pixelwise analysis. *J Neurosci* 2009;29:2805–13
- Hsu JL, Chen YL, Leu JG, et al. Microstructural white matter abnormalities in type 2 diabetes mellitus: a diffusion tensor imaging study. *Neuroimage* 2012;59:1098–105
- Smith SM, Jenkinson M, Woolrich MW, et al. Advances in functional and structural MR image analysis and implementation as FSL. *Neuroimage* 2004;23(suppl 1):S208–19
- Smith SM. Fast robust automated brain extraction. *Hum Brain Mapp* 2002;17:143–55
- Smith SM, Jenkinson M, Johansen-Berg H, et al. Tract-based spatial statistics: voxelwise analysis of multi-subject diffusion data. *Neuroimage* 2006;31:1487–505
- Horsfield MA, Jones DK. Applications of diffusion-weighted and diffusion tensor MRI to white matter diseases: a review. *NMR Biomed* 2002;15:570–77
- Beaulieu C. The basis of anisotropic water diffusion in the nervous system: a technical review. *NMR Biomed* 2002;15:435–55
- Song SK, Yoshino J, Le TQ, et al. Demyelination increases radial diffusivity in corpus callosum of mouse brain. *Neuroimage* 2005;26:132–40
- Wheeler-Kingshott CA, Cercignani M. About “axial” and “radial” diffusivities. *Magn Res Med* 2009;61:1255–60
- Jones DK, Knösche TR, Turner R. White matter integrity, fiber count, and other fallacies: the do’s and don’ts of diffusion MRI. *Neuroimage* 2013;73:239–54
- Minati L, Grisoli M, Bruzzone MG. MR spectroscopy, functional MRI, and diffusion-tensor imaging in the aging brain: a conceptual review. *J Geriatr Psychiatry Neurol* 2007;20:3–21
- Burzynska AZ, Preuschhof C, Bäckman L, et al. Age-related differences in white matter microstructure: region-specific patterns of diffusivity. *Neuroimage* 2010;49:2104–12

34. Bourdeau I, Bard C, Noël B, et al. **Loss of brain volume in endogenous Cushing's syndrome and its reversibility after correction of hypercortisolism.** *J Clin Endocrinol Metab* 2002;87:1949–54
35. Starkman MN, Giordani B, Gebarski SS, et al. **Decrease in cortisol reverses human hippocampal atrophy following treatment of Cushing's disease.** *Biol Psychiatry* 1999;46:1595–602
36. Resmini E, Santos A, Gómez-Anson B, et al. **Hippocampal dysfunction in cured Cushing's syndrome patients, detected by (1) H-MR-spectroscopy.** *Clin Endocrinol (Oxf)* 2013;79:700–07
37. Sorrells, Sapolsky RM. **An inflammatory review of glucocorticoid actions in the CNS.** *Brain Behav Immun* 2007;21:259–72
38. Barahona MJ, Sucunza N, Resmini E, et al. **Persistent body fat mass and inflammatory marker increases after long-term cure of Cushing's syndrome.** *J Clin Endocrinol Metab* 2009;94:3365–71

Fast Contrast-Enhanced 4D MRA and 4D Flow MRI Using Constrained Reconstruction (HYPRFlow): Potential Applications for Brain Arteriovenous Malformations

W. Chang, Y. Wu, K. Johnson, M. Loecher, O. Wieben, M. Edjlali, C. Oppenheim, P. Roca, J. Hald, B. Aagaard-Kienitz, D. Niemann, C. Mistretta, and P. Turski



ABSTRACT

BACKGROUND AND PURPOSE: HYPRFlow is a novel imaging strategy that provides fast, high-resolution contrast-enhanced time-resolved images and measurement of the velocity of the entire cerebrovascular system. Our hypothesis was that the images obtained with this strategy are of adequate diagnostic image quality to delineate the major components of AVMs.

MATERIALS AND METHODS: HYPRFlow and 3D TOF scans were obtained in 21 patients with AVMs with correlative DSA examinations in 14 patients. The examinations were scored for image quality and graded by using the Spetzler-Martin criteria. Mean arterial transit time and overlap integrals were calculated from the dynamic image data. Volume flow rates in normal arteries and AVM feeding arteries were measured from the phase contrast data.

RESULTS: HYPRFlow was equivalent to 3D-TOF in delineating normal arterial anatomy, arterial feeders, and nidus size and was concordant with DSA for AVM grading and venous drainage in 13 of the 14 examinations. Mean arterial transit time on the AVM side was 0.49 seconds, and on the normal contralateral side, 2.53 seconds with $P < .001$. Across all 21 subjects, the mean arterial volume flow rate in the M1 segment ipsilateral to the AVM was 4.07 ± 3.04 mL/s; on the contralateral M1 segment, it was 2.09 ± 0.64 mL/s. The mean volume flow rate in the largest feeding artery to the AVM was 3.86 ± 2.74 mL/s.

CONCLUSIONS: HYPRFlow provides an alternative approach to the MRA evaluation of AVMs, with the advantages of increased coverage, 0.75-second temporal resolution, 0.68-mm isotropic spatial resolution, and quantitative measurement of flow in 6 minutes.

ABBREVIATIONS: CE-VIPR = contrast-enhanced time-resolved vastly undersampled isotropic radial projection reconstruction; HYPR LR = highly constrained projection reconstruction using a local reconstruction convolution kernel; PC-VIPR = phase-contrast MRA using vastly undersampled isotropic radial projection reconstruction; HYPRFlow = highly constrained projection reconstruction using PC-VIPR flow images for the constraint

Many MR angiography techniques have been used for the imaging of arteriovenous malformations with various levels of efficacy. 3D-TOF imaging is capable of imaging arterial components of AVMs with high spatial resolution.^{1,2} However, it does not routinely visualize venous structures, which are important in

assessing AVMs, and does not acquire relevant hemodynamic information. 4D contrast-enhanced MRA has been reported to be of value for pre- and posttreatment assessment of AVMs by using Cartesian acquisitions, partial-Fourier encoding, and multicoil parallel imaging.³ However, because acquisition time increases proportionally with matrix size, obtaining an FOV and spatial resolution sufficient to visualize arteriovenous malformations can be challenging. Furthermore, low temporal resolution can also make delineation of small arterial feeders and venous drainage difficult with these techniques.³⁻⁹

Recent progress in constrained reconstruction techniques has suggested that it may be possible to overcome many of the limitations in temporal resolution, spatial resolution, and signal-to-noise ratio encountered by using conventional reconstruction schemes for time-resolved contrast-enhanced MRA. In such techniques, assumptions are made regarding the sparsity of images in time and space, and a priori information is used to guide or “constrain” the reconstruction. The assumptions are enforced during reconstruction using a nonlinear reconstruction. Unfortunately,

Received July 23, 2014; accepted after revision September 29.

From the Department of Radiology (W.C.), University of California, Los Angeles, Los Angeles, California; Departments of Radiology (B.A.-K., P.T.), Neurosurgery (D.N.), and Medical Physics (Y.W., K.J., M.L., O.W., C.M.), University of Wisconsin School of Medicine, Madison, Wisconsin; Department of Radiology (M.E., C.O., P.R.), Université Paris-Descartes, Paris, France; and Department of Radiology (J.H.), Rikshospitalet, Oslo, Norway.

This work was supported by the National Institutes of Health RO1NS066982.

Paper previously presented in part at: Annual Meeting of the American Society of Neuroradiology and the Foundation of the ASNR Symposium, April 21–26, 2012; New York, New York.

Please address correspondence to Patrick A. Turski, MD, University of Wisconsin Hospital, Radiology MC 3252, 600 Highland Ave, Madison, WI 53792; e-mail: pturski@uwhealth.org

Indicates open access to non-subscribers at www.ajnr.org

<http://dx.doi.org/10.3174/ajnr.A4245>

the utility of many such techniques has been limited by long reconstruction times due to the iterative nature of the reconstruction process.^{10,11}

In this work, we investigated the utility of a noniterative constrained acquisition and reconstruction scheme, HYPRFlow (highly constrained projection reconstruction using PC-VIPR flow images for the constraint), for the assessment of AVMs. The basis of HYPRFlow is that temporal resolution and spatial resolution are separated into 2 scans, a dynamic contrast-enhanced examination and a highly accelerated 3D phase-contrast angiogram. The 3D phase-contrast scan not only serves as a high-quality constraining image for the dynamic contrast-enhanced images but also provides velocity maps of the entire cerebrovascular system. While it is not presently realized clinically, this detailed flow information has the potential to improve characterization of AVMs and to assess treatment efficacy.^{12,13}

MATERIALS AND METHODS

Volunteer patient studies were performed in compliance with the Health Insurance Portability and Accountability Act regulations and by using a protocol approved by the local institutional review board. Subjects were recruited from patients undergoing clinical assessment for known brain arteriovenous malformations. Twenty-one adult subjects (14 women, 7 men) ranging from 27 to 69 years of age were imaged by using a 3T MR imaging system (Discovery 750; GE Healthcare, Milwaukee, Wisconsin) with an 8-channel head coil (HD Brain Coil; GE Healthcare).

Methods: Acquisition Strategy

A key element of HYPRFlow is the use of undersampled 3D radial trajectories to speed the acquisition (3D radial readout = vastly undersampled isotropic projection reconstruction [VIPR]). Radial imaging eliminates the time-consuming phase-encoding used in Cartesian acquisitions. Acceptable radial images can be generated from substantially fewer readouts than conventional Cartesian encoding, providing whole-brain imaging in a fraction of the imaging time. However, as the number of radial trajectories decreases, undersampling artifacts become apparent in the images. The undersampling artifacts can be removed or dramatically reduced by the constraining process.

Dynamic Scan. Fast serial 3D radial scans are obtained of the entire brain during the passage of a contrast agent by using only a small number of readouts. This dynamic acquisition is termed CE-VIPR (contrast-enhanced time resolved vastly undersampled isotropic radial projection reconstruction). Very fast temporal resolution can be achieved providing a whole-head 3D acquisition every 0.5 seconds.

Static Scan. High-resolution phase-contrast vastly undersampled radial projection reconstruction (PC-VIPR) angiograms and velocity measurements are acquired by using a 5-point flow-encoding strategy that increases the velocity-to-noise ratio.¹⁴ The phase-contrast angiograms are well-suited for highly constrained projection and local reconstruction (HYPR LR) because the stationary background tissue is subtracted out and the remaining vascular structures are sparse in the imaging volume.

Methods: Constrained Image Reconstruction Using HYPR LR

The reconstruction of HYPRFlow images by using HYPR LR¹⁵ can be formulated as follows:

$$I_H(t) = I_w^t \times I_C = \frac{I_t \times K}{I_C \times K} \times I_C,$$

where I_t is a reconstructed timeframe image from the dynamic scan, I_C is the phase-contrast constraint (PC-VIPR), and K is a $10 \times 10 \times 10$ (pixels) convolution kernel. To compensate for the signal variations due to the high undersampling, we applied a tornado-shaped filter with 0.5 seconds at the center of a k -space and 0.75 seconds at the cutoff frequency of the local kernel being applied. The result is a time-series of high-spatial-resolution MR angiographic images (voxel size, 0.68 mm³) with the contrast kinetic features of high temporal resolution (0.75 seconds). The PC-VIPR velocity data can also be used for flow analysis. The entire acquisition is obtained in a clinically acceptable imaging time of 6 minutes. Reconstruction time for the HYPRFlow images ranged from 30 to 45 minutes. The strategy of combining rapid contrast-enhanced serial 3D radial imaging (CE-VIPR), phase-contrast radial imaging (PC-VIPR), and highly constrained projection reconstruction (HYPR LR) is termed "HYPRFlow" (Fig 1).¹²

By including both a dynamic series for the display of contrast kinetics and a phase-contrast acquisition to measure flow features, we anticipated that this strategy would be useful for the evaluation of high-flow conditions such as brain arteriovenous malformations. Our primary hypothesis is that the images obtained with this novel strategy are of adequate diagnostic quality to delineate the major components of AVMs.

HYPRFlow Imaging Protocol

Imaging parameters for the dynamic contrast-enhanced multi-echo 3D radial scan (CE-VIPR) were the following: FOV = $22 \times 22 \times 22$ cm³, TR/TE = 3.0/0.4 ms, bandwidth = 125 kHz, 64 points from the center to the edge of the k -space for each projection, frame rate = 0.5 seconds, spatial resolution = $1.7 \times 1.7 \times 1.7$ mm. Gadobenate dimeglumine (MultiHance; Bracco Diagnostics, Princeton, New Jersey) was injected at 3 mL/s, and the contrast dose was 0.1 mL/kg followed by a 20-mL saline flush.

After the dynamic acquisition, a high-resolution 3D radial phase-contrast (PC-VIPR) examination is performed. The phase-contrast scan, in principle, could be acquired in any trajectory. However, to achieve high-spatial-resolution and whole-brain coverage within a reasonable scan time, a 3D radial trajectory is used to speed the phase-contrast acquisition.^{14,16,17}

Scanning parameters for postcontrast PC-VIPR were the following: FOV = 22 cm³, TR/TE = 8.1/2.8 ms, velocity encoding = 80 cm/s, bandwidth = 62.5 kHz. The readout matrix was 320 points per projection, and the spatial resolution for the phase-contrast study was 0.68 mm³. Seven thousand radial projections were acquired within approximately 5 minutes. For comparison of spatial resolution, 3D TOF examinations were obtained by using 4–5 overlapping slabs (TR/TE = 25/2.5 ms, FOV = 24 cm, Cartesian encoding, zero-filling, voxel size = 0.5-mm isotropic).

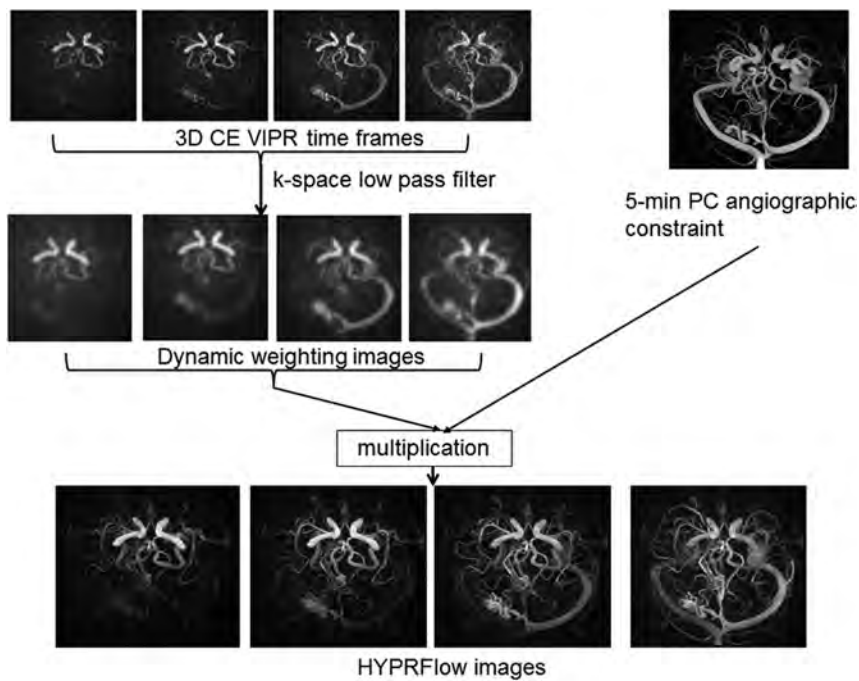


FIG 1. HYPRFlow image reconstruction. Top row: 60 whole-brain 3D radial scans are obtained every 0.5 seconds and reconstructed by using a 0.75-second acquisition window during the first passage of the contrast bolus. Four scans are displayed from this time-series (3D CE-VIPR time-frames). Top right: following the dynamic scan, a 3D radial phase-contrast MRA is obtained (5-minute PC-VIPR MRA used as the vascular constraint). Middle row: temporal weighting images are produced by using a low-pass filter. Bottom row: HYPR LR multiplication and reconstruction are performed by using the phase-contrast angiographic data to constrain the dynamic weighting images. Four HYPRFlow images from the 60-image time-series are displayed, demonstrating improved SNR and spatial resolution following HYPR LR reconstruction.

3D-TOF was included to allow comparison of the arterial anatomy with the highest resolution MRA method commercially available. The DSA studies were obtained within 8 weeks of the HYPRFlow scans by using an Artis zee biplane system (Siemens, Erlangen, Germany) with multiple projections, supplemented by 3D imaging and microcatheter-selective injections using imaging frame rates of 4–8 frames per second. DSA was considered the criterion standard for analysis.

Image Quality and Anatomic Analysis

HYPRFlow arterial and venous phase images and TOF images and DSA arterial and venous phase images were scored by 2 experienced neuroradiologists (with >25 years in practice) for image quality in the M2/M3 branches for all 3 modalities. Deep and superficial venous image quality was also scored for HYPRFlow and DSA.

The examinations were presented by using a clinical PACS workstation. Source and MIP images were reviewed. The MR imaging research coordinator randomized the examinations, attended each review session, and entered the data into the score sheet. Images were scored from 1–4 (scale: 1, poor visualization; 2, visualized but not of diagnostic quality; 3, good visualization of diagnostic quality; 4, excellent visualization and of excellent diagnostic quality). The largest diameter of the nidus was measured for all 3 modalities. In addition to scoring the venous image quality, the venous drainage pattern of each AVM was recorded as

superficial, deep, or mixed. The AVMs were graded by using the Spetzler-Martin scoring system.¹⁸

Flow Analysis

Quantitative measurement of the separation of arteries and veins for the time-resolved contrast-enhanced HYPRFlow images was assessed by generating contrast time curves obtained from the proximal middle cerebral artery and the vein of Trolard (or an analogous large cortical vein) ipsilateral and contralateral to the AVM. The overlap integral was calculated as the area of the overlapped region between arterial and venous contrast kinetic curves. The description of this approach for the evaluation of time-resolved contrast-enhanced MRA has been previously reported.^{19,20} A smaller overlap integral implies better arterial and venous separation. The overlap integrals were compared by using a 2-sample *t* test. In addition, mean arterial transit time and the vein of Trolard (contralateral to the AVM) and the main feeding artery trunk (A1, M1, P1) and the earliest filling cortical vein (ipsilateral to the AVM).

The flow analysis of the PC-VIPR velocity data was performed by using a commercial software program (EnSight; CEI, Apex, North Carolina). Volume flow rates were measured in the proximal middle cerebral artery (ipsilateral and contralateral to the AVM) and the largest arterial feeder to the AVM.

Statistical Analysis

Image quality values for HYPRFlow were compared with both TOF and DSA. TOF was also directly compared with DSA by using the Wilcoxon rank sum test. A *P* value < .05 was considered a significant difference between modalities. Maximum nidus diameter was measured for all 3 modalities, and the Wilcoxon rank sum test was used to compare the results.

RESULTS

Anatomic Analysis

When we compared M2/M3 arterial branches, there was no significant difference between the mean image quality scores of HYPRFlow (3.18) and TOF (3.26) (*P* > .05), but there were very significant differences between the image quality of both HYPRFlow and TOF compared with DSA (3.94) with *P* < .002 and .004, respectively. DSA deep and superficial venous image quality (3.82) was significantly better than HYPRFlow (3.08) (*P* < .005) (Figs 2–4).

Differences in the maximum diameter of the nidus were not significant between HYPRFlow (mean diameter, 32.4 mm) and DSA (mean diameter, 34.3 mm) (Wilcoxon rank sum test, *P* = .11). How-

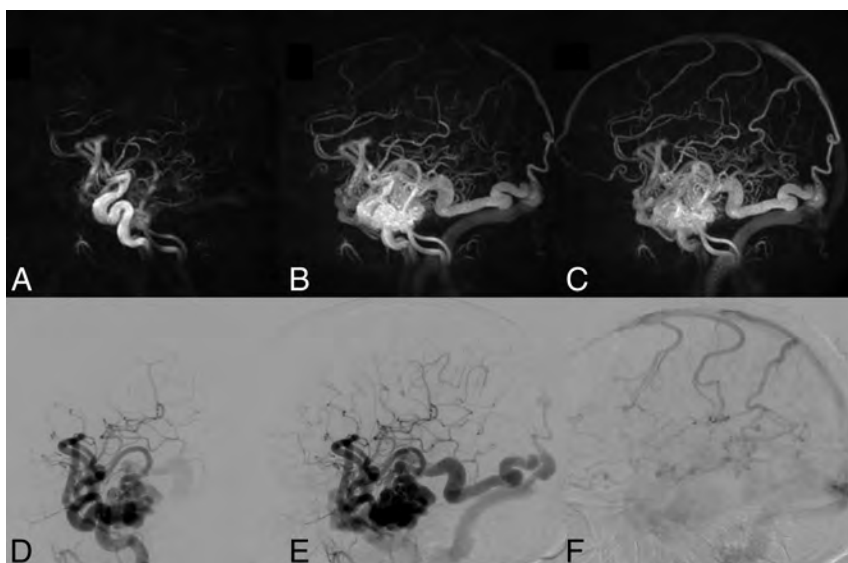


FIG 2. Right temporal lobe AVM. Top row: 3 HYPRFlow images from the 60-image dynamic series. Arterial (A), mixed (B), and venous phase (C) images are displayed. Bottom row: corresponding DSA arterial (D), mixed (E), and venous phase (F) images. The HYPRFlow images demonstrate the cortical venous drainage similar to the DSA.

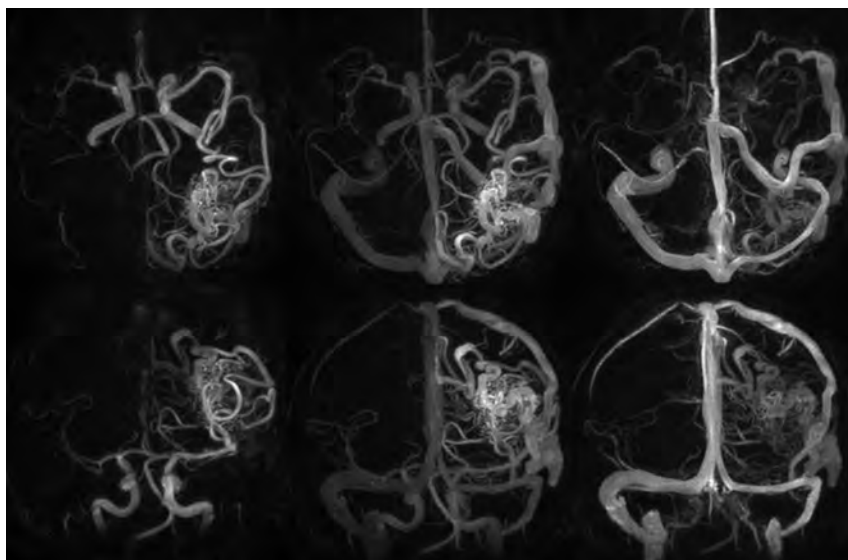


FIG 3. HYPRFlow images of a left parietal occipital AVM, demonstrating whole-brain coverage and isotropic 0.68-mm resolution. Top row: axial HYPRFlow MIP images left to right: arterial, mixed, and venous phase. Bottom row: the same image data projected into the coronal plane, left to right: arterial, mixed, and venous phase images.

ever, there was a statistically significant difference ($P = .016$) when TOF (mean diameter, 30.2 mm) was compared with DSA.

The Spetzler-Martin grades and number of patients in each category based on DSA were grade I ($n = 2$), grade II ($n = 4$), grade III ($n = 3$), grade IV ($n = 3$), and grade V ($n = 2$) (Figs 2–4). There was 1 instance in which very small deep medullary draining veins were not identified on the HYPRFlow examination, resulting in disagreement with the DSA Spetzler-Martin grade (Fig 5); otherwise HYPRFlow and DSA were in concordance.

Flow Analysis

A 2-sample t test revealed a significant difference between the mean arterial transit time on the AVM side (0.49 seconds) com-

pared with the normal contralateral side (2.53 seconds) with $P < .001$. A 2-sample t test revealed a significant difference between the overlap integral of the AVM (0.92) compared with the normal side (0.82) with $P < .001$. The mean arterial volume flow rate in the M1 ipsilateral to the AVM across all subjects was 4.07 ± 3.04 mL/s, the contralateral mean arterial volume flow rate was 2.09 ± 0.64 mL/s, and the mean volume flow rate measured in the largest feeding artery to the AVM was 3.86 ± 2.74 mL/s.

DISCUSSION

Evaluation of cerebral arteriovenous malformations is challenging with existing MRA methods because AVMs can be extensive, requiring a large FOV but also containing very small features that require high spatial resolution. The rapid flow and arteriovenous shunting intrinsic to AVMs demands high temporal resolution. The criterion standard for the evaluation of arteriovenous malformations is digital subtraction angiography, which has extremely high temporal and spatial resolution. However, DSA provides limited physiologic information, exposes patients to ionizing radiation, uses iodinated contrast agents carrying a risk of renal injury or allergic reaction, and is an invasive procedure with a risk of iatrogenic stroke.²¹ 4D CT angiography is another technique that has high spatial and temporal resolution, accurately delineates the vascular components of AVMs, but also exposes patients to iodinated contrast agents and ionizing radiation.²² The advantages of combining MR imaging and MRA have led to continued interest in the use of MR angiography in the study of AVMs. Although time-resolved contrast-enhanced MRA using Cartesian phase en-

coding has a wide safety margin, the risk of nephrogenic systemic fibrosis must be considered in patients with renal failure.²³ TOF MRA has spatial resolution approaching that of CT angiography, displays arterial elements with excellent image quality, and has clinically acceptable acquisition times.²⁴ However, it does not routinely provide assessment of the venous drainage and dynamic information on vessel filling or arteriovenous shunts. Phase-contrast MRA (4D flow MR imaging) has been used to visualize AVMs, provide flow analysis of AVMs, and monitor treatment effects.^{13,25} Multiple studies have demonstrated that Cartesian-based 4D time-resolved contrast-enhanced MRA using Cartesian phase encoding can characterize the major components of AVMs.

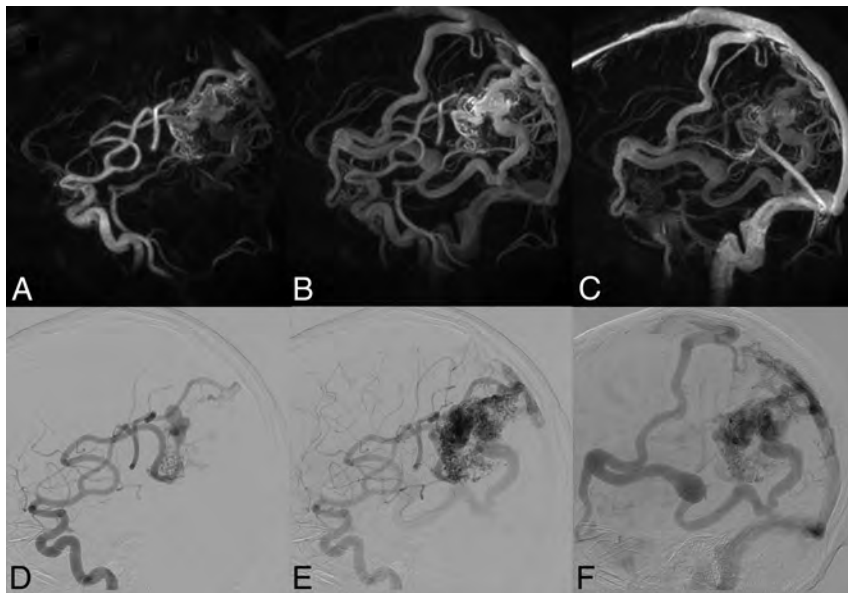


FIG 4. The same patient as shown in Fig 3. Top row: HYPRFlow images in the sagittal plane: arterial (A), mixed (B), and venous phase (C). Bottom row: corresponding DSA images: arterial (D), mixed (E), and venous phase (F). Note the excellent correlation of the arterial supply and venous drainage pattern.

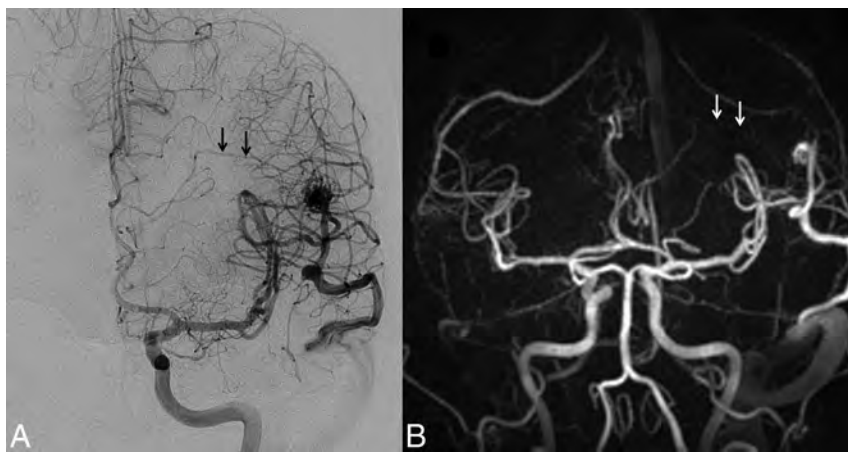


FIG 5. Left posterior frontal AVM. A, The DSA examination demonstrates a small deep medullary vein (arrows), which drains into the straight sinus. The AVM nidus was in close proximity to the Broca area and was scored as Spetzler-Martin grade III. B, Coronal HYPRFlow late arterial phase image with poor delineation of the deep medullary vein (arrows), resulting in incorrect classification of the AVM as Spetzler-Martin grade II.

Current Cartesian encoding methods use variable k -space sampling, parallel imaging, and temporal correlations to accelerate the acquisition and improve resolution, but these methods are typically limited in coverage.^{3,4,7-9,26} Noncontrast 4D arterial spin-labeling methods provide excellent temporal resolution and arterial imaging; venous imaging with these methods can be limited due to transit-time signal decay.²⁷⁻²⁹ Radial encoding without constrained reconstruction has been successfully used to accelerate acquisition and imaging of AVMs but has SNR limitations.³⁰ The advantage of combining radial encoding and constrained reconstructions to increase SNR has been previously demonstrated in healthy subjects³¹ and patients with AVMs.³²

HYPRFlow is a highly innovative approach that overcomes many of the limitations of previous methods. Whole-brain

coverage for both the dynamic CE-VIPR and static PC-VIPR scans allows a global assessment of the entire cerebrovascular system, enabling characterization of the AVM and alterations in flow in adjacent vascular territories. HYPRFlow is well-suited to study AVMs because in addition to the global anatomic coverage, the dynamic series can be used to measure contrast kinetics such as contrast arrival time, time to peak, overlap integral, and transit time. Our results show that transit time can be quantitated and that it is dramatically shortened compared with the contralateral analogous vessels. We further estimated the magnitude of the arteriovenous shunting by measuring the overlap integral for the largest artery supplying the AVM and compared this value with the analogous contralateral vessels. The analysis of contrast kinetics is augmented by the addition of flow encoding of the entire cerebrovascular system. Our flow analysis results demonstrate that flow measurements can be easily accomplished in primary arterial segments (A1, M1, and P1 segments) and major arterial branches supplying the AVM. Although we performed a limited flow analysis for this report, the HYPRFlow velocity data can be used to generate flow path lines,¹³ estimate wall shear stress,³³ measure pulsatility, quantitate velocity/flow,²⁵ and identify pressure gradients.³⁴

One of the appealing features of HYPRFlow is the ability to image both the venous drainage of the AVM and the global venous drainage of the entire cerebrovascular system. The dynamic contrast-enhanced images provide detailed anatomic depiction of the venous drainage and have adequate resolution to identify venous stenosis and varices. The anatomic images can then be used

to guide the flow analysis by using the PC-VIPR velocity data. For example, with the velocity data, venous outflow can be quantified and pressure gradients can be measured across regions of venous outflow obstruction. Risk stratification for patients with AVMs remains a challenge, and continued investigation of both anatomic features and hemodynamics is warranted because there are few well-established criteria to identify high-risk populations.³⁵⁻³⁷

Limitations

While this study demonstrates that HYPRFlow is well-suited to assess AVMs, there are still multiple challenges. Patient motion may result in misregistration of the dynamic and static scans, resulting in image blurring after constrained reconstruction. Un-

undersampling artifacts may also be a concern; however, the artifacts are limited by the sparsity of neurovascular structures in the imaging volume and the location of the artifacts predominantly outside the ROI. The sample size of patients is small, limiting generalization of the findings. The flow analysis was limited to major arterial structures, and no hemodynamic measurements were made of the venous components. There may also be vascular signal loss in the PC-VIPR data due to spin-dephasing from complex flow. The impact of hemosiderin and other blood products on the image quality of the HYPRFlow images was not systematically reviewed. However, signal loss due to blood products would fall under the general class of artifacts related to susceptibility phase dispersion and subsequent signal loss. Susceptibility-based signal loss was a major aspect of our analysis. The short TE of the PC-VIPR sequence reduces but does not eliminate signal loss due to susceptibility effects.

Another limitation is the challenge related to detecting aneurysms within and remote from the nidus. Previous reports have shown that aneurysms can be accurately identified when a portion of the signal from the contrast-enhanced magnitude dataset (the contrast-enhanced 3D radial T1-weighted component of the phase-contrast acquisition) is combined with the flow images.³⁸ However, this approach was not used in this investigation due to the large size of the datasets and the lack of automated processing tools. Consequently, systematic analysis of aneurysm detection was not performed. The velocity dependence of PC-VIPR may result in loss of signal in very slow-flow structures, though this is reduced by the use of contrast enhancement and 5-point flow encoding and can be overcome by including a component of the magnitude data in the reconstruction.³⁸ Finally, reconstruction by using HYPRFlow takes 30–45 minutes and requires noncommercial software.

CONCLUSIONS

This study demonstrates that HYPRFlow compares favorably with 3D-TOF for the evaluation of arterial feeders and AVM nidus size. There was no significant difference in the measurement of the maximum diameter of the nidus between HYPRFlow and DSA, and there was only 1 discrepancy in assessing venous drainage. HYPRFlow provides a more comprehensive evaluation of AVMs, delineating the arterial supply, nidus size, and venous drainage and offers contrast kinetics and hemodynamic information.

Disclosures: Kevin Johnson—*RELATED: Grant:* National Institutes of Health*; *UNRELATED: Patents (planned, pending or issued):* US patent pending, *Comments:* Contrast-Enhanced MRA with Highly Constrained Backprojection Reconstruction Using Phase Contrast Composite Image, US Patent No. 7991452. Under our agreements, I may be entitled to a portion of the licensing fees if this technology were put into a commercial product; *Royalties:* US Patent Royalties; *Other:* research support from GE Healthcare.* Pauline Roca—*RELATED: Grant:* GE Healthcare.* *Comments:* I had a postdoctoral position funded by GE Healthcare from June 1, 2011, to May 31, 2013. Beverly Aagaard-Kienitz—*RELATED: Grant:* GE Healthcare.* *Comments:* GE Healthcare provides support to the University of Wisconsin MR imaging research program. The investigators do not receive any direct funding. Charles Mistretta—*RELATED: Grant:* National Institutes of Health*; *Support for Travel to Meetings for the Study or Other Purposes:* National Institutes of Health*; *UNRELATED: Grants/Grants Pending:* National Institutes of Health, *Comments:* 4D DSA and 4D fluoroscopy; *Payment for Lectures (including service on Speakers Bureaus):* various universities, *Comments:* typical visiting professor lectures; *Patents (planned, pending or issued):* I have several recent patents related to x-ray work; *Royalties:* Wisconsin Alumni

Research Foundation. *Comments:* royalties on several MR imaging patents. Patrick Turski—*RELATED: Grant:* National Institutes of Health ROI NS066982.* *Comments:* National Institutes of Health ROI NS066982 provides support for development of accelerated MRA techniques; *UNRELATED: Other:* GE Healthcare.* *Comments:* GE Healthcare provides support to the University of Wisconsin MR imaging research program. The investigators do not receive any direct funding. *Money paid to the institution.

REFERENCES

- Heidenreich JO, Schilling AM, Unterharnscheidt F, et al. **Assessment of 3D-TOF-MRA at 3.0 Tesla in the characterization of the angio-architecture of cerebral arteriovenous malformations: a preliminary study.** *Acta Radiol* 2007;48:678–86
- Loy DN, Rich KM, Simpson J, et al. **Time-of-flight magnetic resonance angiography imaging of a residual arteriovenous malformation nidus after Onyx embolization for stereotactic radiosurgery planning: technical note.** *Neurosurg Focus* 2009;26:E13
- Hadizadeh DR, Kukuk GM, Steck DT, et al. **Noninvasive evaluation of cerebral arteriovenous malformations by 4D-MRA for preoperative planning and postoperative follow-up in 56 patients: comparison with DSA and intraoperative findings.** *AJNR Am J Neuroradiol* 2012;33:1095–101
- Gauvrit JY, Leclerc X, Oppenheim C, et al. **Three-dimensional dynamic MR digital subtraction angiography using sensitivity encoding for the evaluation of intracranial arteriovenous malformations: a preliminary study.** *AJNR Am J Neuroradiol* 2005;26:1525–31
- Gauvrit JY, Oppenheim C, Nataf F, et al. **Three-dimensional dynamic magnetic resonance angiography for the evaluation of radiosurgically treated cerebral arteriovenous malformations.** *Eur Radiol* 2006;16:583–91
- Hadizadeh DR, von Falkenhausen M, Gieseke J, et al. **Cerebral arteriovenous malformation: Spetzler-Martin classification at subsecond-temporal-resolution four-dimensional MR angiography compared with that at DSA.** *Radiology* 2008;246:205–13
- Taschner CA, Gieseke J, Le Thuc V, et al. **Intracranial arteriovenous malformation: time-resolved contrast-enhanced MR angiography with combination of parallel imaging, keyhole acquisition, and k-space sampling techniques at 1.5 T.** *Radiology* 2008;246:871–79
- Petkova M, Gauvrit JY, Trystram D, et al. **Three-dimensional dynamic time-resolved contrast-enhanced MRA using parallel imaging and a variable rate k-space sampling strategy in intracranial arteriovenous malformations.** *J Magn Reson Imaging* 2009;29:7–12
- Oleaga L, Dalal SS, Weigele JB, et al. **The role of time-resolved 3D contrast-enhanced MR angiography in the assessment and grading of cerebral arteriovenous malformations.** *Eur J Radiol* 2010;74:e117–21
- Mistretta CA. **Undersampled radial MR acquisition and highly constrained back projection (HYPR) reconstruction: potential medical imaging applications in the post-Nyquist era.** *J Magn Reson Imaging* 2009;29:501–16
- Wu Y, Chang W, Johnson KM, et al. **Fast whole-brain 4D contrast-enhanced MR angiography with velocity encoding using undersampled radial acquisition and highly constrained projection reconstruction: image-quality assessment in volunteer subjects.** *AJNR Am J Neuroradiol* 2011;32:E47–50
- Velikina JV, Johnson KM, Wu Y, et al. **PC-HYPR flow: a technique for rapid imaging of contrast dynamics.** *AJNR Am J Neuroradiol* 2010;31:447–56
- Ansari SA, Schnell S, Carroll T, et al. **Intracranial 4D flow MRI: toward individualized assessment of arteriovenous malformation hemodynamics and treatment-induced changes.** *AJNR Am J Neuroradiol* 2013;34:1922–28
- Johnson KM, Markl M. **Improved SNR in phase contrast velocimetry with five-point balanced flow encoding.** *Magn Reson Med* 2010;63:349–55
- Johnson KM, Velikina J, Wu Y, et al. **Improved waveform fidelity using local HYPR reconstruction (HYPR LR).** *Magn Reson Med* 2008;59:456–62

16. Gu T, Korosec FR, Block WF, et al. **PC VIPR: a high-speed 3D phase-contrast method for flow quantification and high-resolution angiography.** *AJNR Am J Neuroradiol* 2005;26:743–49
17. Johnson KM, Francois C, Lum D, et al. **Rapid comprehensive evaluation of luminography and hemodynamic function with 3D radially undersampled phase contrast imaging MRI.** *Conf Proc IEEE Eng Med Biol Soc* 2009;2009:4057–60
18. Spetzler RF, Martin NA. **A proposed grading system for arteriovenous malformations.** *J Neurosurg* 1986;65:476–83
19. Cashen TA, Jeong H, Shah MK, et al. **4D radial contrast-enhanced MR angiography with sliding subtraction.** *Magn Reson Med* 2007;58:962–72
20. Wu Y, Johnson K, Kecskemeti SR, et al. **Time resolved contrast enhanced intracranial MRA using a single dose delivered as sequential injections and highly constrained projection reconstruction (HYPR CE).** *Magn Reson Med* 2011;65:956–63
21. Willinsky RA, Taylor SM, TerBrugge K, et al. **Neurologic complications of cerebral angiography: prospective analysis of 2,899 procedures and review of the literature.** *Radiology* 2003;227:522–28
22. Wang H, Ye X, Gao X, et al. **The diagnosis of arteriovenous malformations by 4D-CTA: a clinical study.** *J Neuroradiol* 2014;41:117–23
23. Sadowski EA, Bennett LK, Chan MR, et al. **Nephrogenic systemic fibrosis: risk factors and incidence estimation.** *Radiology* 2007;243:148–57
24. Buis DR, Bot JC, Barkhof F, et al. **The predictive value of 3D time-of-flight MR angiography in assessment of brain arteriovenous malformation obliteration after radiosurgery.** *AJNR Am J Neuroradiol* 2012;33:232–38
25. Markl M, Wu C, Hurley MC, et al. **Cerebral arteriovenous malformation: complex 3D hemodynamics and 3D blood flow alterations during staged embolization.** *J Magn Reson Imaging* 2013;38:946–50
26. Willinek WA, Hadizadeh DR, von Falkenhausen M, et al. **4D time-resolved MR angiography with keyhole (4D-TRAK): more than 60 times accelerated MRA using a combination of CENTRA, keyhole, and SENSE at 3.0T.** *J Magn Reson Imaging* 2008;27:1455–60
27. Yu S, Yan L, Yao Y, et al. **Noncontrast dynamic MRA in intracranial arteriovenous malformation (AVM), comparison with time of flight (TOF) and digital subtraction angiography (DSA).** *Magn Reson Imaging* 2012;30:869–77
28. Raoult H, Bannier E, Maurel P, et al. **Hemodynamic quantification in brain arteriovenous malformations with time-resolved spin-labeled magnetic resonance angiography.** *Stroke* 2014;45:2461–64
29. Wu H, Block WF, Turski PA, et al. **Noncontrast dynamic 3D intracranial MR angiography using pseudo-continuous arterial spin labeling (PCASL) and accelerated 3D radial acquisition.** *J Magn Reson Imaging* 2014;39:1320–26
30. Eddleman CS, Jeong HJ, Hurley MC, et al. **4D radial acquisition contrast-enhanced MR angiography and intracranial arteriovenous malformations: quickly approaching digital subtraction angiography.** *Stroke* 2009;40:2749–53
31. Chang W, Landgraf B, Johnson KM, et al. **Velocity measurements in the middle cerebral arteries of healthy volunteers using 3D radial phase-contrast HYPRFlow: comparison with transcranial Doppler sonography and 2D phase-contrast MR imaging.** *AJNR Am J Neuroradiol* 2011;32:54–59
32. Jeong HJ, Cashen TA, Hurley MC, et al. **Radial sliding-window magnetic resonance angiography (MRA) with highly-constrained projection reconstruction (HYPR).** *Magn Reson Med* 2009;61:1103–13
33. Chang W, Loecher MW, Wu Y, et al. **Hemodynamic changes in patients with arteriovenous malformations assessed using high-resolution 3D radial phase-contrast MR angiography.** *AJNR Am J Neuroradiol* 2012;33:1565–72
34. Moftakhar R, Aagaard-Kienitz B, Johnson K, et al. **Noninvasive measurement of intra-aneurysmal pressure and flow pattern using phase contrast with vastly undersampled isotropic projection imaging.** *AJNR Am J Neuroradiol* 2007;28:1710–14
35. Stapf C, Mast H, Sciacca RR, et al. **Predictors of hemorrhage in patients with untreated brain arteriovenous malformation.** *Neurology* 2006;66:1350–55
36. Mohr JP, Kejda-Scharler J, Pile-Spellman J. **Diagnosis and treatment of arteriovenous malformations.** *Curr Neurol Neurosci Rep* 2013;13:324
37. van Beijnum J, van der Worp HB, Buis DR, et al. **Treatment of brain arteriovenous malformations: a systematic review and meta-analysis.** *JAMA* 2011;306:2011–19
38. Kecskemeti S, Johnson K, Wu Y, et al. **High resolution three-dimensional cine phase contrast MRI of small intracranial aneurysms using a stack of stars k-space trajectory.** *J Magn Reson Imaging* 2012;35:518–27

Predictors of Reperfusion in Patients with Acute Ischemic Stroke

A.D. Horsch, J.W. Dankbaar, J.M. Niesten, T. van Seeters, I.C. van der Schaaf, Y. van der Graaf, W.P.Th.M. Mali, and B.K. Velthuis;
on behalf of the Dutch Acute Stroke Study Investigators

ABSTRACT

BACKGROUND AND PURPOSE: Ischemic stroke studies emphasize a difference between reperfusion and recanalization, but predictors of reperfusion have not been elucidated. The aim of this study was to evaluate the relationship between reperfusion and recanalization and identify predictors of reperfusion.

MATERIALS AND METHODS: From the Dutch Acute Stroke Study, 178 patients were selected with an MCA territory deficit on admission CTP and day 3 follow-up CTP and CTA. Reperfusion was evaluated on CTP, and recanalization on CTA, follow-up imaging. Reperfusion percentages were calculated in patients with and without recanalization. Patient admission and treatment characteristics and admission CT imaging parameters were collected. Their association with complete reperfusion was analyzed by using univariate and multivariate logistic regression.

RESULTS: Sixty percent of patients with complete recanalization showed complete reperfusion (relative risk, 2.60; 95% CI, 1.63–4.13). Approximately one-third of patients showed some discrepancy between recanalization and reperfusion status. Lower NIHSS score (OR, 1.06; 95% CI, 1.01–1.11), smaller infarct core size (OR, 3.11; 95% CI, 1.46–6.66; and OR, 2.40; 95% CI, 1.14–5.02), smaller total ischemic area (OR, 4.20; 95% CI, 1.91–9.22; and OR, 2.35; 95% CI, 1.12–4.91), lower clot burden (OR, 1.35; 95% CI, 1.14–1.58), distal thrombus location (OR, 3.02; 95% CI, 1.76–5.20), and good collateral score (OR, 2.84; 95% CI, 1.34–6.02) significantly increased the odds of complete reperfusion. In multivariate analysis, only total ischemic area (OR, 6.12; 95% CI, 2.69–13.93; and OR, 1.91; 95% CI, 0.91–4.02) was an independent predictor of complete reperfusion.

CONCLUSIONS: Recanalization and reperfusion are strongly associated but not always equivalent in ischemic stroke. A smaller total ischemic area is the only independent predictor of complete reperfusion.

ABBREVIATIONS: DUST = Dutch Acute Stroke Study; RR = relative risk

Patients with acute ischemic stroke presenting within 4.5 hours are treated with IV-rtPA to dissolve the thrombus and achieve revascularization.¹ A recent consensus meeting on stroke imaging research (Acute Stroke Imaging Research Roadmap II) suggests that revascularization is a combination of 3 different mechanisms: 1) recanalization, referring to arterial patency; 2) reperfusion,

which refers to antegrade microvascular perfusion; and 3) collateralization, which refers to microvascular perfusion via pial arteries or other anastomotic arterial channels that bypass the primary site of vessel occlusion.² Recanalization, reperfusion, and collateralization can be evaluated by CTA and CTP, which are frequently used in dedicated stroke imaging protocols. An important reason to look at the revascularization mechanisms separately is the concept that recanalization of an arterial occlusion, as visualized on CTA, does not necessarily lead to complete reperfusion and improved clinical outcome.^{3,4} Furthermore, reperfusion can also occur without afferent vessel recanalization through collateralization of the ischemic area by collateral flow.^{5,6}

Many previous studies, including those investigating intra-arterial therapy, consider recanalization to be synonymous with reperfusion.^{7–10} Other articles suggest that this assumption is not justified and found reperfusion to be a better predictor of follow-up infarct volume and clinical outcome than recanalization.^{5,8,9,11–15}

Received August 11, 2014; accepted after revision December 11.

From the Department of Radiology (A.D.H., J.W.D., J.M.N., T.v.S., I.C.v.d.S., W.P.Th.M.M., B.K.V.), University Medical Center Utrecht, Utrecht, the Netherlands; Department of Radiology (A.D.H.), Rijnstate Hospital, Arnhem, the Netherlands; and Julius Center for Health Sciences and Primary Care (Y.v.d.G.), Utrecht, the Netherlands.

This work was supported by grants from the Netherlands Heart Foundation (2008 T034 and 2012 T061) and the Nuts Ohra Foundation (0903-012).

Please address correspondence to Alexander D. Horsch, MD, MRCS, University Medical Center Utrecht, Heidelberglaan 100, HP E01.132, 3584 CX Utrecht, the Netherlands; e-mail: alexanderhorsch@gmail.com

<http://dx.doi.org/10.3174/ajnr.A4283>

Although recanalization correlates well with improved reperfusion rates, it is unclear which other clinical and imaging factors influence reperfusion.^{5,6,11,12,16} Knowing which factors, available before treatment decisions, predict complete reperfusion could aid in decision-making. Treatment with IV-rtPA, good collateral scores and lesion geography (location of the infarct relative to penumbra), and structure (solitary or multiple infarct areas) have been related to reperfusion status assessed with CT or MR imaging.^{5,15,17-19}

The aim of this study was to evaluate the relationship between reperfusion and recanalization and to investigate which clinical and CT imaging parameters, available on admission, can help predict complete reperfusion in patients with acute ischemic stroke.

MATERIALS AND METHODS

Study Design

The Dutch Acute Stroke Study (DUST) is a large prospective multicenter cohort study, which aims to assess the additional value of CTP and CTA in predicting the outcome of patients with acute ischemic stroke.

The study protocol has been published previously.²⁰ In brief, inclusion criteria for this study were 18 years of age or older, suspected acute ischemic stroke of <9 hours' duration, and an NIHSS score of ≥ 2 (or 1 if an indication for IV-rtPA was present). Exclusion criteria were known renal failure, contraindications to iodinated contrast material, and the presence of another diagnosis on admission NCCT that explained the symptoms. This study was approved by the local institutional ethics review boards of the participating centers. All patients or family gave signed informed consent unless a patient died before consent could be obtained. In that case, the need for consent was waived by the medical ethics committee.²⁰

Patient Selection

From the DUST data base, a consecutive series of patients included between May 2009 and August 2012 was selected from 9 centers. Additional inclusion criteria for this study were the following: 1) perfusion deficit in the MCA territory on admission CTP, and 2) available admission and follow-up CTP and CTA. Exclusion criteria were the following: 1) poor-quality CTP or CTA, 2) absence of 1 of the 2 ASPECTS levels on admission CTP, or 3) use of intra-arterial treatment. The inclusion process is clarified in the flow chart (Fig 1).

Predictor Selection

Clinical variables that were collected included age, sex, history of stroke, admission NIHSS score, IV-rtPA treatment, and time from symptom onset to treatment. Admission imaging variables included the following: infarct core size and total ischemic area from CTP ASPECTS levels and clot burden (clot burden score), thrombus location (ICA, MCA-M1 segment, MCA-M2 segment, and >M2), and collateral score from CTA.

Imaging Protocol

NCCT, CTP, and CTA of the cervical and cerebral vessel were performed on admission. Multidetector CT scanners were used, with the number of detectors ranging from 40 to 320 (Brilliance 40, Brilliance 64, Brilliance iCT 256; Philips Healthcare, Best, the Netherlands; Sensation 64; Siemens, Erlangen, Ger-

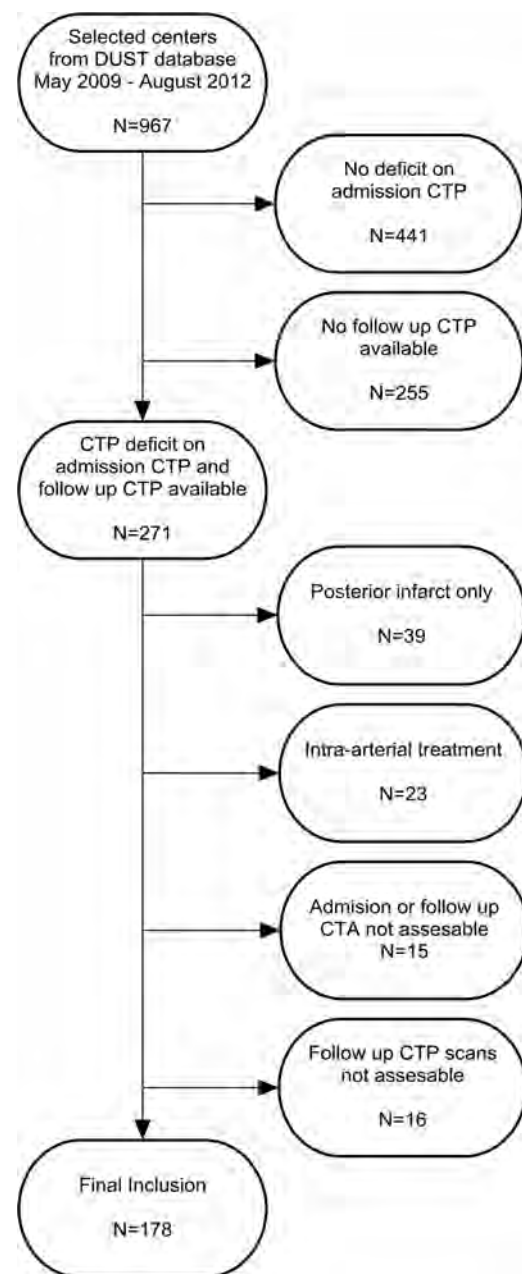


FIG 1. Inclusion flow chart.

many; Aquilion ONE; Toshiba Medical Systems, Tokyo, Japan). NCCT was performed with 120 kV, 300–375 mAs, and a section thickness of 5 mm.²⁰

The CTP, performed with 80 kV and 150 mAs, involved successive gantry rotations in cine mode during intravenous administration of 40 mL of nonionic contrast material followed by 40 mL of saline with a flow of 6 mL/s.²⁰ CTP coverage included at least the level of the basal ganglia to the lateral ventricles to be able to assess both ASPECTS levels.²¹

CTA was acquired from the aortic arch to the vertex with 50–70 mL of contrast followed by 40 mL of saline, both with a flow of 6 mL/s. The individual CTA scan delay after intravenous injection was calculated from time-to-peak arterial enhancement on CTP or by trigger-based Hounsfield unit threshold measurement of contrast enhancement in the aortic arch.²⁰

Imaging Analysis

CTP. CBF, CBV, MTT, and time-to-peak were automatically calculated from CTP data using commercially available CTP software (Extended Brilliance Workstation 4.5; Philips Healthcare). The nonoccluded ICA or anterior cerebral artery was chosen as the arterial input function.²² The superior sagittal sinus was used as the venous output function. The presence of a perfusion deficit on admission was defined as a focal asymmetry on the CBF, CBV, MTT, or time-to-peak map, matching a part or the whole of the MCA flow territory. The total ischemic area was defined with an MTT threshold of 145% compared with the nonaffected side. Within this area, a CBV value of <2.0 mL/100 g was used to define the infarct core.²³ Infarct core size and total size of the ischemic area were calculated at ASPECTS levels 1 and 2 on admission CTP. The degree of axial CTP coverage was different between scanners because CTP was performed with CT scanners ranging from 40-detector to 320-detector. This range could potentially underestimate the initial ischemic area or the degree of reperfusion. For this reason, we only used the ASPECTS levels to compare patients, to exclude major bias from the difference in the number of detectors.

The presence of reperfusion was analyzed by visual comparison of the admission CTP parameter maps (CBF, CBV, MTT, and time-to-peak) with the follow-up parameter maps. Reperfusion outcome was classified into 2 categories (complete and incomplete reperfusion). Complete reperfusion was defined as the absence of a perfusion deficit on follow-up CTP in the presence of a deficit on admission. All remaining deficits on follow-up CTP, which were not considered to be caused by artifacts, ipsilateral carotid stenosis, or focal hemorrhage, were categorized as incomplete reperfusion. Hyperperfusion was included in the complete reperfusion group, and an enlarged or new perfusion deficit, in the incomplete reperfusion group.

Differences in blood pressure between admission and follow-up CTP have not been taken into account in the assessment of reperfusion status because this assessment was done in a qualitative fashion by visual comparison of the 4 CTP maps and not on image-based quantitative thresholds. It was not expected that potential small differences in the size of the CTP deficit would have changed the category of reperfusion status.

CTA. Admission CTA provided data on clot burden score, collateral score, and intracranial thrombus location. Intracranial thrombus location was divided into 3 groups (intracranial ICA, MCA-M1 segment, and MCA-M2 or more distal occlusion).^{24–26} Thrombus location was classified to the most proximal site of occlusion unless there was a combined extracranial ICA occlusion and a more distal MCA occlusion with an open ICA-top (tandem lesion), which was classified at the level of the MCA occlusion.²⁷ Recanalization status was defined qualitatively on follow-up CTA scans as complete or incomplete recanalization. All imaging data were evaluated by 1 of 3 observers (I.C.v.d.S., B.K.V., and J.W.D.), all with at least 5 years of experience in stroke imaging. Only the side of symptoms was provided for the evaluation.

Statistical Analysis

For all analyses, the complete reperfusion group was compared with the incomplete reperfusion group. Similarly, the complete recanalization group was compared with the incomplete recanalization group. To analyze the relation between complete recanalization and complete reperfusion, absolute and relative risks (RRs) were calculated. Potential determinants of complete reperfusion were tested with univariate and multivariate binary logistic regression analysis, and 95% confidence intervals were calculated. To reduce the potential influence of non-normal distributions, we recorded the following variables into categories on the basis of tertiles: time to treatment (<60 minutes, 60–120 minutes, and ≥ 120 minutes), infarct core size (<300 mm², 300–1400 mm², and ≥ 1400 mm²), and total ischemic area (<2000 mm², 2000–5000 mm², and ≥ 5000 mm²).

For analysis, patients without visible occlusion on CTA were included in the MCA-M2 or more distal occlusion group. All significant predictors in univariate analysis ($P < .05$) were used in stepwise backward-elimination multivariate regression analysis. Statistical computations were performed by using SPSS 19.0 (IBM, Armonk, New York).

RESULTS

Inclusion criteria for this study were met in 178 patients (Fig 1). Not all patients in the DUST study received follow-up due to very rapid recovery and discharge before follow-up could be done, poor condition of the patient, impaired renal function, or absence of permission for follow-up. No significant difference in admission NIHSS score was found between patients with or without follow-up CTP and CTA, which suggests that no major preselection occurred.

Baseline clinical and imaging characteristics for the 2 reperfusion groups are summarized in Table 1. Mean age was 68 years, 39% were female, median NIHSS score was 9, and 68% received IV-rtPA. The infarct core size (479 versus 985 mm²) and total ischemic area size (2352 versus 4587 mm²) were significantly smaller in the complete reperfusion group compared with the incomplete reperfusion group. In addition, the clot burden was significantly lower in the complete reperfusion group (clot burden score, 9 versus 8), and the thrombus was located more distally (M2 or >M2 in 62% versus 42%, respectively). A good collateral score was also significantly more frequent in the complete reperfusion group (86% versus 69%). No ipsilateral ICA-top occlusion was found on admission in the complete reperfusion group versus 15% in the incomplete reperfusion group.

Table 2 shows the relation between reperfusion status and recanalization in 152 patients with a visible occlusion and the reperfusion status in 26 patients without a visible occlusion on admission CTA. Complete reperfusion was found in 60% of patients with complete recanalization and in 23% in the incomplete-recanalization group (RR, 2.60; 95% CI, 1.63–4.13). Approximately one-third of patients (32%) showed some discrepancy between recanalization and reperfusion status. Remarkably, complete reperfusion was found with incomplete recanalization (16 patients), and incomplete reperfusion was found despite complete recanalization (33 patients). Two illustrative cases are shown in Fig 2. In the 26 patients without a

Table 1: Baseline clinical and imaging characteristics

	All Patients (n = 178)	Incomplete Reperfusion (n = 92, 52%)	Complete Reperfusion (n = 86, 48%)	P Value
Clinical parameters				
Age (yr) (mean) (SD)	68 (13)	68 (14)	67 (13)	.92
Female sex (No.) (%)	69 (39)	34 (37)	35 (41)	.61
Prior stroke (No.) (%)	35 (20)	15 (16)	20 (23)	.24
NIHSS score (median) (IQR)	9 (5–15)	12 (5–16)	8 (4–13)	.06
Treatment				
rtPA (No.) (%)	121 (68)	61 (66)	60 (70)	.62
Time to treatment ^a (min) (median) (IQR)	100 (73–130)	105 (75–127)	99 (70–151)	.89
Imaging parameters				
Time to admission scan (min) (median) (IQR)	105 (66–170)	105 (71–157)	105 (61–187)	.62
Time to follow-up (day) (mean) (SD)	3.2 (1.3)	3.3 (1.3)	3.1 (1.2)	.19
CTP				
Size of infarct core ^b (mm ²) (median) (IQR)	630 (187–1758)	985 (293–2659)	479 (115–1332)	.002 ^c
Size of total ischemic area ^b (mm ²) (median) (IQR)	3629 (1551–5605)	4587 (2848–6248)	2352 (734–4328)	.0005 ^c
CTA				
Clot burden score (median) (IQR)	8.0 (6.0–9.0)	8.0 (6.0–9.0)	9.0 (7.0–9.0)	.003 ^c
Thrombus location, ^d ICA (No.) (%)	13 (9)	13 (15)	0	.01 ^c
Thrombus location, ^d M1 (No.) (%)	62 (41)	37 (43)	25 (38)	.01 ^c
Thrombus location, ^d M2 or >M2 (No.) (%)	77 (51)	36 (42)	41 (62)	.01 ^c
Good collateral score (No.) (%) ^e	137 (77)	63 (69)	74 (86)	.005 ^c

Note:—IQR indicates interquartile range.

^a Only 121 patients received IV-rtPA.

^b Size of infarct core and total ischemic area at both ASPECTS levels combined.

^c Significant.

^d Only 152 cases because 26 patients had no visible occlusion on admission CTA.

^e All patients without visible artery occlusion on admission CTA had a good collateral score.

Table 2: Outcome summary—relation between reperfusion and recanalization^a

	Incomplete Reperfusion	Complete Reperfusion	Total
Reperfusion and recanalization (n = 152)			
Incomplete recanalization	53 (77)	16 (23)	69 (100)
Complete recanalization	33 (40)	50 (60)	83 (100)
Total	86 (57)	66 (43)	152 (100)
Reperfusion without visible occlusion on admission CTA (n = 26)			
No occlusion on admission	6 (23)	20 (77)	26 (100)

^a Data are No. (% in rows).

visible occlusion on admission CTA, most patients (77%) showed complete reperfusion.

The univariate logistic regression analysis is shown in Table 3. Lower NIHSS score (OR, 1.06; 95% CI, 1.01–1.11), smaller infarct core size (OR, 3.11; 95% CI, 1.46–6.66; and OR, 2.40; 95% CI, 1.14–5.02), smaller total ischemic area (OR, 4.20; 95% CI, 1.91–9.22; and OR, 2.35; 95% CI, 1.12–4.91), lower clot burden (OR, 1.35; 95% CI, 1.14–1.58), distal thrombus location (OR, 3.02; 95% CI, 1.76–5.20), and good collateral score (OR, 2.84; 95% CI, 1.34–6.02) significantly increased the odds of complete reperfusion. Age, sex, or IV-rtPA treatment did not influence complete reperfusion. In multivariate analysis, a smaller total ischemic area (OR, 6.12; 95% CI, 2.69–13.93; and OR, 1.91; 95% CI, 0.91–4.02) was the only independent predictor of complete reperfusion (not shown in the Tables).

DISCUSSION

This study shows that although reperfusion is strongly related to recanalization in acute ischemic stroke, reperfusion and recanalization do not always occur in unison. An important finding is that

none of the patients with an ipsilateral intracranial ICA occlusion showed complete reperfusion. Factors that help predict complete reperfusion are lower NIHSS score on admission, lower clot burden, more distal thrombus location and a good collateral score (on CTA), and smaller infarct core and smaller total ischemic area (on CTP). In multivariate analysis, only total ischemic area was an independent predictor of complete reperfusion.

Recanalization versus Reperfusion

The proportion of complete recanalization and complete reperfusion in our study compares with values described in the literature, 22%–60% for recanalization and 26%–79% for reperfusion.^{15–18} Our data confirm the suggestion that recanalization and reperfusion are closely related but not interchangeable. The discrepancy of incomplete reperfusion in the presence of complete recanalization can be caused by either the break-up of the primary clot into fragments leading to distal embolization of smaller vasculature not visible on CTA, reversible incomplete microcirculatory reperfusion, or the irreversible no-reflow phenomenon.^{3,28–30} Reperfusion without recanalization of the proximal occlusion is thought to be mediated by collateralization (through pial arteries or other anastomotic channels).² Patients without an identifiable occlusion on admission CTA had higher complete reperfusion rates in comparison with patients with a visible occlusion. Undetected microthrombi in distal vessels may account for this higher rate because they are more likely to dissolve.

Predictors of Reperfusion

Thrombus location was a predictor of complete reperfusion in our study. Distal MCA occlusions showed better reperfusion rates on follow-up compared with more proximal MCA or ICA-top occlusions. A positive relation between distal thrombus location

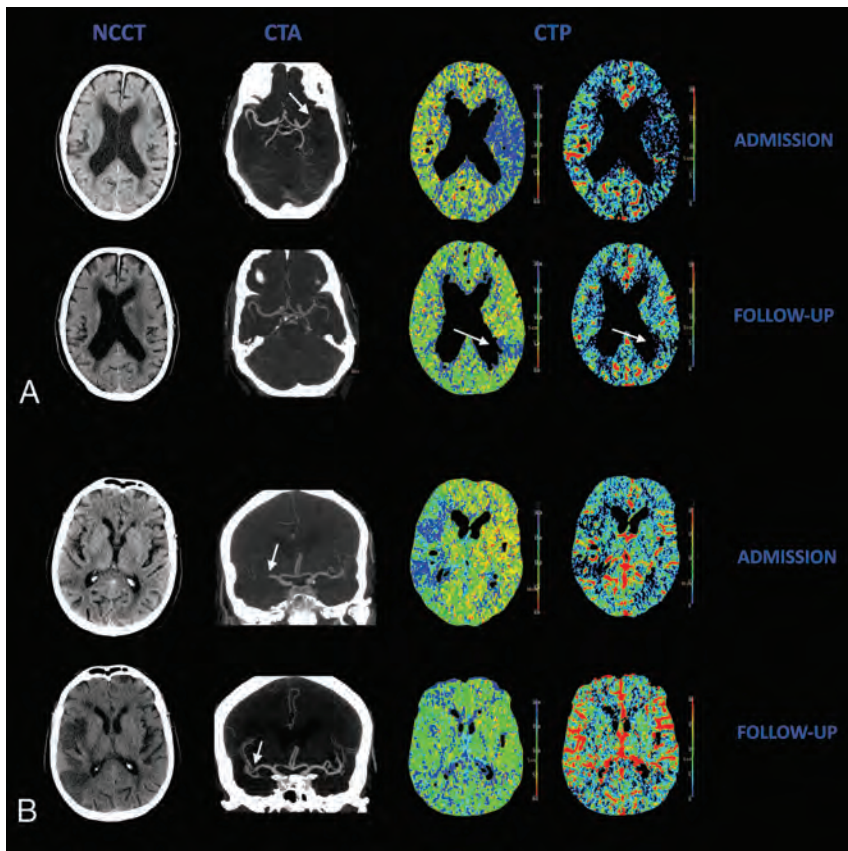


FIG 2. Relation between recanalization and reperfusion. *A*, A patient with complete recanalization without complete reperfusion. Admission NCCT shows no early CT signs. Follow-up NCCT shows infarction of the basal ganglia. Admission CTA shows occlusion of the M1 segment (arrow). Follow-up CTA shows complete recanalization; no distal M3 occlusion could be found. Admission CTP shows a large area of decreased MTT and CBV in ASPECTS M5 and M6. Follow-up CTP shows a residual perfusion deficit ASPECTS M6 on the MTT and CBV maps (arrow). *B*, A patient with incomplete recanalization but complete reperfusion. Admission NCCT shows some early CT signs in the MCA territory. Admission CTA shows an occlusion in the M1 and M2 segments of the MCA. Follow-up CTA shows a short residual occlusion in an M2 segment (arrows). Admission CTP shows a large area of decreased MTT and CBV in ASPECTS M1–M3, which has completely resolved on follow-up.

Table 3: Predictors of complete reperfusion (N = 178)

	OR	95% CI	P Value
Clinical parameters			
Age (yr)	1.00	0.98–1.02	.86
Female sex	1.17	0.64–2.14	.61
NIHSS score	1.06	1.01–1.11	.03 ^a
rtPA	1.17	0.62–2.21	.62
Time to treatment, ^b 60–120 min versus <60 min	0.54	0.17–1.69	.29
Time to treatment, ^b ≥120 min versus <60 min	0.78	0.23–2.61	.68
Imaging parameters			
Size infarct core, ^c <300 versus ≥1400 mm ²	3.11	1.46–6.66	.003 ^a
Size infarct core, ^c 300–1400 versus ≥1400 mm ²	2.40	1.14–5.02	.02 ^a
Size total ischemic area, ^c <2000 vs ≥5000	4.20	1.91–9.22	.004 ^a
Size total ischemic area, ^c 2000–5000 versus ≥5000 mm ²	2.35	1.12–4.91	.02 ^a
Clot burden score	1.35	1.14–1.58	.001 ^a
Thrombus location, ICA, M1 or M2, and >M2	3.02	1.76–5.20	.006 ^a
Good collateral score ^d	2.84	1.34–6.02	.01 ^a

^a P < .05 is significant.

^b Only 121 patients received IV-rtPA.

^c Size of infarct core and total ischemic area at both ASPECTS levels combined.

^d All patients without visible artery occlusion on admission CTA had a good collateral score.

and recanalization has been found in multiple studies.^{7,31–33} In contrast, Lemmens et al³⁴ found no relation between distal occlusion and recanalization, though they did find a better clinical

response with increased reperfusion. Moreover, none of our patients with an intracranial carotid occlusion showed complete reperfusion (despite complete recanalization in 15% and 54% receiving IV-rtPA in this patient group of 13 patients). These findings suggest that those specific patients may need intra-arterial thrombolysis or mechanical thrombectomy. A recent review showed that stent placement and mechanical thrombectomy in patients with an intracranial ICA occlusion are associated with higher recanalization rates and better functional outcome.³⁵

Few articles describe predictors of brain tissue reperfusion. The most frequently found imaging predictor of reperfusion was recanalization in both CT and MR imaging studies.^{5,6,11,16,17,36} However, recanalization is not a variable that can be assessed before treatment. Good collateral scores, treatment with alteplase or tenecteplase, older age, and lesion geography and structure were also associated with better reperfusion.^{5,15,17–19,37}

Only total ischemic area was an independent predictor of complete reperfusion in our study. This is not surprising because a smaller size of the total ischemic area is the result of a more distal thrombus location and good collateral status. The effect of these variables is therefore most likely represented by the total ischemic area in our multivariate analysis.

It is unclear why we could not demonstrate a significant relation between IV-rtPA treatment and complete reperfusion. Christoforidis et al³⁸ suggested no benefit from thrombolysis in patients with poor collaterals and a more distal occlusion site, but in our population, we did not find a worse reperfusion rate in the patient group treated with IV-rtPA. Another reason could be a difference in population characteristics between treated and nontreated patients, with a higher admission NIHSS score in the IV-rtPA-treated patients.

Although some predictors of reperfusion (size of the infarct core, size of the total ischemic area) have not been related to recanalization, most reperfusion predictors (NIHSS score, clot burden score, thrombus location, collateral score) have been established for recanalization.^{7,16,24,32,39–45} In addition, several articles describing predictors of reperfusion or recanalization showed a good correlation between these predic-

tive factors and outcome (final infarct size and mRS at 3 months).^{6,11,16} This is not surprising because reperfusion is a parameter situated between recanalization and outcome. Our data confirm that these relations are already established at day 3, relatively early in the clinical course. This finding suggests that follow-up reperfusion data could be used as a surrogate end point.

There are some limitations to this study. First, our patient group is seemingly different from those in many previous stroke articles because of a shorter time to scan, lower NIHSS scores, and higher IV-rtPA treatment rate. However, with improved stroke awareness and faster stroke protocols, our population is probably more representative of the current stroke populations.

Second, the time to follow-up was approximately 3 days. Most brain cells die early in ischemic conditions, but recanalization is known to continue even after the focal areas have infarcted. Timely and clinically meaningful recanalization and reperfusion may be better demonstrated when follow-up is performed at an earlier time point.

Third, assessment of both recanalization and reperfusion was not done quantitatively but in a 2-point scale, a method also previously used.⁴⁶⁻⁴⁸ The predictive value can improve with more quantitative assessment, but small lesions are prone to measurement errors.¹⁵ Moreover, qualitative assessment is easier and shows good agreement in clinical practice, especially with limited lesion coverage.⁴⁹

Fourth, the 26 patients with a peripheral perfusion deficit, who did not show an occlusion on CTA, were included in the M2-MCA/distal occlusion group. It was assumed that the peripheral perfusion deficit in these patients was caused by a distal occlusion, not detectable on CTA. Possibly, some of these distal occlusions may have resulted from fragmentation of a larger thrombus and thus (partial) recanalization before the initial imaging. However, this cause seems unlikely because the median time to treatment in our study was only 100 minutes, which leaves little time for early recanalization to occur.

CONCLUSIONS

This study confirms that recanalization and reperfusion outcomes in ischemic stroke are significantly related but are not always interchangeable. Lower NIHSS scores, smaller size of the infarct core, smaller total ischemic area, lower clot burden, more distal intracranial thrombus location, and good collateral scores have been identified as predictors of complete reperfusion. A smaller total ischemic area is the only independent predictor of complete reperfusion.

APPENDIX

The following are the DUST investigators: Academic Medical Center, Amsterdam, the Netherlands (C.B. Majoie, Y.B. Roos); Catharina Hospital, Eindhoven, the Netherlands (L.E. Duijm, K. Keizer); Erasmus Medical Center, Rotterdam, the Netherlands (A. van der Lugt, D.W. Dippel); Gelre Hospitals, Apeldoorn, the Netherlands (K.E. Droogh-de Greve, H.P. Bienfait); Leiden University Medical Center, Leiden, the Netherlands (M.A. van Walderveen, M.J. Wermer); Medical Center Haaglanden, The Hague, the Netherlands (G.J. Lycklama à Nijeholt, J. Boiten); Onze Lieve Vrouwe Gasthuis, Amsterdam, the Netherlands (D. Duyndam,

V.I. Kwa); Radboud University Nijmegen Medical Center, Nijmegen, the Netherlands (F.J. Meijer, E.J. van Dijk); Rijnstate Hospital, Arnhem, the Netherlands (F.O. Kesselring, J. Hofmeijer); St. Antonius Hospital, Nieuwegein, the Netherlands (J.A. Vos, W.J. Schonewille); St. Elisabeth Hospital, Tilburg, the Netherlands (W.J. van Rooij, P.L. de Kort); St. Franciscus Gasthuis, Rotterdam, the Netherlands (C.C. Pleiter, S.L. Bakker); VU Medical Center, Amsterdam, the Netherlands (J. Bot, M.C. Visser); University Medical Center Utrecht, Utrecht, the Netherlands (B.K. Velthuis, I.C. van der Schaaf, J.W. Dankbaar, W.P. Mali, T. van Seeters, A.D. Horsch, J.M. Niesten, G.J. Biessels, L.J. Kappelle, M.J. Luitse, Y. van der Graaf).

Disclosures: Jan W. Dankbaar—RELATED: Grant: Netherlands Heart Foundation (No. 2012T61). Birgitta K. Velthuis—RELATED: Grant: Netherlands Heart Foundation,* Nuts Ohra Foundation.* Comments: This study was supported by grants from the Netherlands Heart Foundation (2008 T034 and 2012 T061) and the Nuts Ohra Foundation (0903-012).

REFERENCES

1. Hacke W, Donnan G, Fieschi C, et al. **Association of outcome with early stroke treatment: pooled analysis of ATLANTIS, ECASS, and NINDS rt-PA stroke trials.** *Lancet* 2004;363:768–74
2. Wintermark M, Albers GW, Broderick JP, et al; for the Stroke Imaging Research (STIR) and Virtual International Stroke Trials Archive (VISTA)-Imaging Investigators. **Acute Stroke Imaging Research Roadmap II.** *Stroke* 2013;44:2628–39
3. Dalkara T, Arsava EM. **Can restoring incomplete microcirculatory reperfusion improve stroke outcome after thrombolysis?** *J Cereb Blood Flow Metab* 2012;32:2091–99
4. Zaidat OO, Yoo AJ, Khatri P, et al. **Recommendations on angiographic revascularization grading standards for acute ischemic stroke: a consensus statement.** *Stroke* 2013;44:2650–63
5. Soares BP, Tong E, Hom J, et al. **Reperfusion is a more accurate predictor of follow-up infarct volume than recanalization: a proof of concept using CT in acute ischemic stroke patients.** *Stroke* 2010;41:e34–40
6. Albers GW, Thijs VN, Wechsler L, et al. **Magnetic resonance imaging profiles predict clinical response to early reperfusion: the diffusion and perfusion imaging evaluation for understanding stroke evolution (DEFUSE) study.** *Ann Neurol* 2006;60:508–17
7. Murphy A, Symons SP, Hopyan J, et al. **Factors influencing clinically meaningful recanalization after IV-rtPA in acute ischemic stroke.** *AJNR Am J Neuroradiol* 2013;34:146–52
8. Furlan AJ, Eyding D, Albers GW, et al. **Dose Escalation of Desmoteplase for Acute Ischemic Stroke (DEDAS): evidence of safety and efficacy 3 to 9 hours after stroke onset.** *Stroke* 2006;37:1227–31
9. Hacke W, Albers G, Al-Rawi Y, et al. **The Desmoteplase in Acute Ischemic Stroke Trial (DIAS): a phase II MRI-based 9-hour window acute stroke thrombolysis trial with intravenous desmoteplase.** *Stroke* 2005;36:66–73
10. Fiehler J, Remmele C, Kucinski T, et al. **Reperfusion after severe local perfusion deficit precedes hemorrhagic transformation: an MRI study in acute stroke patients.** *Cerebrovasc Dis* 2005;19:117–24
11. Eilaghi A, Brooks J, d'Este C, et al. **Reperfusion is a stronger predictor of good clinical outcome than recanalization in ischemic stroke.** *Radiology* 2013;269:240–48
12. De Silva DA, Fink JN, Christensen S, et al. **Assessing reperfusion and recanalization as markers of clinical outcomes after intravenous thrombolysis in the Echoplanar Imaging Thrombolytic Evaluation Trial (EPITHET).** *Stroke* 2009;40:2872–74
13. Yoo AJ, Chandra RV, Lev MH. **Revascularization grading: the devil is in the details.** *Radiology* 2013;269:6–7
14. Soares BP, Chien JD, Wintermark M. **MR and CT monitoring of recanalization, reperfusion, and penumbra salvage: everything that recanalizes does not necessarily reperfuse!** *Stroke* 2009;40:S24–27

15. Davis SM, Donnan GA, Parsons MW, et al. **Effects of alteplase beyond 3 h after stroke in the Echoplanar Imaging Thrombolytic Evaluation Trial (EPITHET): a placebo-controlled randomised trial.** *Lancet Neurol* 2008;7:299–309
16. Derex L, Nighoghossian N, Hermier M, et al. **Influence of pretreatment MRI parameters on clinical outcome, recanalization and infarct size in 49 stroke patients treated by intravenous tissue plasminogen activator.** *J Neurol Sci* 2004;225:3–9
17. Parsons M, Spratt N, Bivard A, et al. **A randomized trial of tenecteplase versus alteplase for acute ischemic stroke.** *N Engl J Med* 2012;366:1099–107
18. Ogata T, Christensen S, Nagakane Y, et al. **The effects of alteplase 3 to 6 hours after stroke in the EPITHET-DEFUSE combined dataset: post hoc case-control study.** *Stroke* 2013;44:87–93
19. Olivot JM, Mlynash M, Thijs VN, et al. **Geography, structure, and evolution of diffusion and perfusion lesions in Diffusion and perfusion imaging Evaluation For Understanding Stroke Evolution (DEFUSE).** *Stroke* 2009;40:3245–51
20. van Seeters T, Biessels GJ, van der Schaaf IC, et al. **Prediction of outcome in patients with suspected acute ischaemic stroke with CT perfusion and CT angiography: the Dutch Acute Stroke Trial (DUST) study protocol.** *BMC Neurol* 2014;14:37
21. Barber PA, Demchuk AM, Zhang J, et al. **Validity and reliability of a quantitative computed tomography score in predicting outcome of hyperacute stroke before thrombolytic therapy.** *Lancet* 2000;355:1670–74
22. Niesten JM, van der Schaaf IC, Riordan AJ, et al. **Optimisation of vascular input and output functions in CT-perfusion imaging using 256 (or more)-slice multidetector CT.** *Eur Radiol* 2013;23:1242–49
23. Wintermark M, Flanders AE, Velthuis B, et al. **Perfusion-CT assessment of infarct core and penumbra: receiver operating characteristic curve analysis in 130 patients suspected of acute hemispheric stroke.** *Stroke* 2006;37:979–85
24. Tan IYL, Demchuk AM, Hopyan J, et al. **CT angiography clot burden score and collateral score: correlation with clinical and radiologic outcomes in acute middle cerebral artery infarct.** *AJNR Am J Neuroradiol* 2009;30:525–31
25. Tan JC, Dillon WP, Liu S, et al. **Systematic comparison of perfusion-CT and CT-angiography in acute stroke patients.** *Ann Neurol* 2007;61:533–43
26. Puetz V, Dzialowski I, Hill MD, et al. **Intracranial thrombus extent predicts clinical outcome, final infarct size and hemorrhagic transformation in ischemic stroke: the clot burden score.** *Int J Stroke* 2008;3:230–36
27. El-Mitwalli A, Saad M, Christou I, et al. **Clinical and sonographic patterns of tandem internal carotid artery/middle cerebral artery occlusion in tissue plasminogen activator-treated patients.** *Stroke* 2002;33:99–102
28. Molina CA, Alvarez-Sabin J. **Recanalization and reperfusion therapies for acute ischemic stroke.** *Cerebrovasc Dis* 2009;27(suppl 1):162–67
29. del Zoppo GJ. **Virchow's triad: the vascular basis of cerebral injury.** *Rev Neurol Dis* 2008;5(suppl 1):S12–21
30. Wong CH, Crack PJ. **Modulation of neuro-inflammation and vascular response by oxidative stress following cerebral ischemia-reperfusion injury.** *Curr Med Chem* 2008;15:1–14
31. Mendonça N, Rodriguez-Luna D, Rubiera M, et al. **Predictors of tissue-type plasminogen activator nonresponders according to location of vessel occlusion.** *Stroke* 2012;43:417–21
32. Bhatia R, Hill MD, Shobha N, et al. **Low rates of acute recanalization with intravenous recombinant tissue plasminogen activator in ischemic stroke: real-world experience and a call for action.** *Stroke* 2010;41:2254–58
33. Yeo LL, Paliwal P, Teoh HL, et al. **Timing of recanalization after intravenous thrombolysis and functional outcomes after acute ischemic stroke.** *JAMA Neurol* 2013;70:353–58
34. Lemmens R, Mlynash M, Straka M, et al. **Comparison of the response to endovascular reperfusion in relation to site of arterial occlusion.** *Neurology* 2013;81:614–18
35. Kappelhof M, Marquering HA, Berkhemer OA, et al. **Intra-arterial treatment of patients with acute ischemic stroke and internal carotid artery occlusion: a literature review.** *J Neurointerv Surg* 2015;7:8–15
36. Marks MP, Olivot JM, Kemp S, et al. **Patients with acute stroke treated with intravenous tPA 3–6 hours after stroke onset: correlations between MR angiography findings and perfusion- and diffusion-weighted imaging in the DEFUSE study.** *Radiology* 2008;249:614–23
37. Lansberg MG, Thijs VN, Bammer R, et al. **The MRA-DWI mismatch identifies patients with stroke who are likely to benefit from reperfusion.** *Stroke* 2008;39:2491–96
38. Christoforidis GA, Mohammad Y, Kehagias D, et al. **Angiographic assessment of pial collaterals as a prognostic indicator following intra-arterial thrombolysis for acute ischemic stroke.** *AJNR Am J Neuroradiol* 2005;26:1789–97
39. Shhadeh A, Garg A, Hassan AE, et al. **Recanalization following various endovascular modalities for treatment of anterior circulation acute ischemic strokes.** *J Vasc Interv Neurol* 2012;5:10–16
40. Tandberg Askevold E, Naess H, Thomassen L. **Predictors for recanalization after intravenous thrombolysis in acute ischemic stroke.** *J Stroke Cerebrovasc Dis* 2007;16:21–24
41. Saqqur M, Uchino K, Demchuk AM, et al. **Site of arterial occlusion identified by transcranial Doppler predicts the response to intravenous thrombolysis for stroke.** *Stroke* 2007;38:948–54
42. Legrand L, Naggara O, Turc G, et al. **Clot burden score on admission T2*-MRI predicts recanalization in acute stroke.** *Stroke* 2013;44:1878–84
43. Nam HS, Kim EY, Kim SH, et al. **Prediction of thrombus resolution after intravenous thrombolysis assessed by CT-based thrombus imaging.** *Thromb Haemost* 2012;107:786–94
44. Zangerle A, Kiechl S, Spiegel M, et al. **Recanalization after thrombolysis in stroke patients: predictors and prognostic implications.** *Neurology* 2007;68:39–44
45. Nambiar V, Sohn SI, Almekhlafi MA, et al. **CTA collateral status and response to recanalization in patients with acute ischemic stroke.** *AJNR Am J Neuroradiol* 2014;35:884–90
46. Bivard A, Spratt N, Levi C, et al. **Perfusion computer tomography: imaging and clinical validation in acute ischaemic stroke.** *Brain* 2011;134:3408–16
47. Kloska SP, Dittrich R, Fischer T, et al. **Perfusion CT in acute stroke: prediction of vessel recanalization and clinical outcome in intravenous thrombolytic therapy.** *Eur Radiol* 2007;17:2491–98
48. Olivot JM, Mlynash M, Thijs VN, et al. **Relationships between cerebral perfusion and reversibility of acute diffusion lesions in DEFUSE: insights from RADAR.** *Stroke* 2009;40:1692–97
49. Luby M, Ku KD, Latour LL, et al. **Visual perfusion-diffusion mismatch is equivalent to quantitative mismatch.** *Stroke* 2011;42:1010–14

Qualitative and Quantitative Analysis of MR Imaging Findings in Patients with Middle Cerebral Artery Stroke Implanted with Mesenchymal Stem Cells

C.P. Wanamaker, S. Fakhran, and L.M. Alhilali



ABSTRACT

BACKGROUND AND PURPOSE: Mesenchymal stem cells have potential as a regenerative therapy in ischemic stroke. We sought to determine MR imaging findings after mesenchymal stem cell implantation in chronic middle cerebral artery infarcts and to compare brain volume changes in patients with mesenchymal stem cells with those in age-matched healthy controls and controls with chronic stable MCA infarcts.

MATERIALS AND METHODS: We retrospectively identified 5 patients receiving surgical mesenchymal stem cell implantation to an MCA infarct from January 1, 2005, to July 1, 2013, with MR imaging immediately and 1 year postimplantation. Images at both time points were evaluated for any postimplantation complications. Structural image evaluation using normalization of atrophy software was used to determine volume changes between time points and compare them with those in healthy and age- and sex-matched controls with chronic, stable MCA infarcts by using Kruskal-Wallis and Mann-Whitney *U* tests.

RESULTS: Susceptibility signal loss and enhancement at the implantation site were seen. No teratoma, tumor, or heterotopia was identified. Volumetric analysis showed a trend toward less overall volume loss after mesenchymal stem cell implantation (0.736; 95% CI, -4.15–5.62) compared with that in age- and sex-matched controls with chronic, stable MCA infarcts (-3.59; 95% CI, -12.3 to -5.21; *P* = .09), with a significantly greater growth-to-loss ratio in infarcted regions (1.30 and 0.78, respectively, *P* = .02). A trend toward correlation of growth-to-loss ratio with improvement in physical examination findings was seen (*r* = 0.856, *P* = .06).

CONCLUSIONS: Postoperative changes consistent with stereotactic implantation were seen, but no teratoma, tumor, or heterotopia was identified. Initial findings suggest a trend toward less volume loss after mesenchymal stem cell implantation compared with that in age- and sex-matched controls with chronic, stable MCA infarcts, with a significantly greater growth-to-loss ratio in the infarcted tissue.

ABBREVIATIONS: %BVC = percentage brain volume change; GLR = growth-to-loss ratio; MCAI controls = age- and sex-matched controls with chronic, stable MCA infarcts; MSC = mesenchymal stem cells; SIENA = structural image evaluation using normalization of atrophy; ST = section thickness

Stroke is a leading cause of morbidity and mortality in the United States,¹ with an estimated 50% of patients surviving at 90 days demonstrating pronounced long-term disability.² Unfortunately, the only approved drug therapy for ischemic stroke, recombinant tissue plasminogen activator, has a limited therapeutic window.³ Given the limited therapeutic options, research into methods to decrease the morbidity associated with ischemic

stroke has gained pronounced interest. Although rehabilitation has been shown to help functional recovery after stroke, recovery is usually limited.⁴ Cell-based regenerative therapies have been shown to reduce infarct size and improve functional outcomes in animal models of stroke and offer hope of restoring function in patients with fixed neurologic disability following ischemic stroke.^{5–8}

Among cell-based therapies, mesenchymal stem cells (MSC) are adult nonhematopoietic pluripotent cells derived from almost all tissues of the body.⁹ These have received considerable attention as a possible regenerative therapy for ischemic stroke due to their multilineage potential,¹⁰ secretion of trophic factors for neural tissue,¹¹ ease of collection,¹² lack of ethical issues,¹³ efficacy in animal models,^{14,15} and safety in multiple clinical trials.^{16,17}

Methods for introducing MSC to an infarct include intravenous, intra-arterial, and intracerebral.¹⁸ IV and intra-arterial methods both have certain drawbacks that may be ameliorated by using direct intracerebral implantation. Specifically, IV adminis-

Received August 20, 2014; accepted after revision December 5.

From the Department of Radiology, Division of Neuroradiology, University of Pittsburgh Medical Center, Pittsburgh, Pennsylvania.

Preliminary data previously presented at: American Society of Neuroradiology Annual Meeting and the Foundation of the ASNR Symposium, May 17–20, 2014; Montreal, Quebec, Canada.

Please address correspondence to Lea M. Alhilali, MD, Department of Radiology, Division of Neuroradiology, University of Pittsburgh Medical Center, 8th Floor, 8 North, Presby South Tower, 200 Lothrop St, Pittsburgh, PA 15213; e-mail: alhilalilm@upmc.edu

Indicates article with supplemental on-line table.

<http://dx.doi.org/10.3174/ajnr.A4232>

tration results in first-pass trapping of stem cells in the lung and liver, while intra-arterial administration risks compromise of regional blood flow and MCA occlusion.¹⁸ Stereotactic implantation is more invasive than either IV or intra-arterial methods. However, it lacks their limitations and offers potentially greater efficacy due to direct delivery of the MSC to infarcted tissues. Intracerebral delivery has been used with success in animal models, demonstrating decreased apoptosis, increased angiogenesis, and neuroprotective effects.^{19,20}

Evaluations of the effectiveness of MSC for stroke have mainly focused on changes in clinical function,^{6,8} with only 1 clinical trial evaluating changes on imaging as a possible marker of efficacy following IV administration.⁷ Despite the relative paucity of data on imaging findings after MSC administration, imaging assessment remains important because clinical testing may be undermined by additional neuropsychological factors. For example, symptoms related to comorbidities, such as depression, may clinically mimic persistent neurologic dysfunction, while poor motivation and ulterior motives may undermine the accuracy of clinical tests. However, if concomitant imaging findings can be matched with clinical testing, this matching may provide a quantitative anatomic biomarker to confirm clinical findings.

A prior clinical trial has evaluated changes in infarct T2 hyperintensity after MSC intravenous administration⁷; however, no control patients were evaluated, and it remains unclear whether observed changes in T2 hyperintensity merely represented the natural history of the infarcted tissue or response to MSC. The purpose of our study was to determine MR imaging findings after MSC implantation in patients with chronic MCA infarcts and to compare global and regional brain volume changes in patients with MSC implants with age-matched healthy controls and controls with chronic stable MCA infarcts (MCAI controls).

MATERIALS AND METHODS

Patient Selection and Image Acquisition

Our institutional review board approved this study, with a waiver of informed consent. All studies included were performed as part of a research protocol, and results were retrospectively reviewed.

We searched our electronic medical record to identify MR imaging studies performed on patients who had undergone implantation of MSC for MCA infarction. Stem cell implantation is performed surgically at our institution as part of a research protocol on a small number of study patients by using a Leksell Coordinate Frame G stereotactic head frame (Elekta Instruments, Stockholm, Sweden). We make 3 target selections: an anterior, mid, and posterior target for the medial wall of each infarct, regardless of infarct size. The xyz coordinates are calculated, and stem cells are verified and loaded. The 3 targets are then used, and 20 μ L is injected to each target point in a single burr-hole trajectory, with small volumes injected each time for several minutes.

MR imaging reports from January 1, 2005, to July 1, 2013, were searched by using the keywords "stem cell." Inclusion criteria were the following: age, 18–75 years; MCA ischemic infarct with no prior infarcts; 6- to 60-month intervals between the infarct and imaging; no further improvement from physical therapy after at least 6 months; initial MR imaging within 1 day of MSC implantation; and follow-up MR imaging 10–14 months after implanta-

tion. Exclusion criteria were the following: sufficient motion degradation to preclude volumetric analysis as determined by a neuroradiologist with >3 years of experience with quantitative imaging analysis, lack of follow-up imaging, any other major neurologic disease, any malignancy except squamous or basal cell carcinoma of the skin, contraindication to MR imaging, pregnancy, or lactation. Demographic data recorded included patient age and sex. The location of the infarct, infarct etiology, and physical examination findings initially and >10 months post-MSC implantation by either a primary care physician or neurologist were likewise recorded.

Patient recovery was graded by a recovery score, with a point system determined as follows:

1) We recorded preimplantation deficits in the following categories: facial sensation (1) and strength (2), upper extremity sensation (3) and strength (4), lower extremity sensation (5) and strength (6), visual acuity (7), and language (8).

2) If there was a deficit in a given category that demonstrated improvement, then the patient received a score of 1 in that category. If there was no change, the score was zero. If there was deterioration, the score was -1. If there was no initial deficit in a category, the patient received no score for the given category.

3) The total number of points for all categories was summed and divided by the total number of categories scored. The resulting number was termed the "total recovery score."

Age- and sex-matched controls were obtained by using an individual matching method in which each control was within 5 years of age of the individual matched subject. Controls were found by searching the electronic medical record for MR imaging examinations by using the keywords "unremarkable" and "within normal limits." Controls were excluded if there was any infarct detected on imaging as determined by a fellowship-trained radiologist, any evidence of vasculopathy, a history of any other major neurologic disease, lack of follow-up imaging within 10–14 months, interval infarct, hemorrhage or other neurologic disease process, or sufficient motion degradation to preclude volumetric analysis. Reasons for MR imaging examinations in controls were memory loss (3 patients) and dizziness (2 patients).

Age- and sex-matched control subjects with chronic, stable MCA encephalomalacia (referred to as MCAI controls) were also obtained by using an individual matching method in which each MCAI control was within 5 years of age of the individual matched stem-cell subject. MCAI controls were found by searching the electronic medical record for MR imaging examinations by using the keywords "middle cerebral artery," "stroke," "infarct," and "encephalomalacia." Inclusion criteria for MCAI controls were the following: ischemic middle cerebral artery infarct between 6 and 60 months of age based on review of the electronic medical record and follow-up imaging between 10 and 14 months of the initial MR imaging. MCAI controls were excluded if there was sufficient motion degradation to preclude volumetric analysis. Comparison of the time interval between initial and follow-up imaging between subjects with MSC implants and the MCAI controls was determined with the Mann Whitney *U* test.

All subjects and controls underwent MR imaging at 2 time points (initial imaging and 10–14 months after initial imaging) on a 1.5T system (Signa; GE Healthcare, Milwaukee, Wisconsin)

with a standard head coil. Sequences included sagittal and axial T1-weighted (TR, 600 ms; TE, minimum; section thickness [ST], 5 mm; NEX, 1), fast spin-echo axial proton-attenuation (TR, 2000–2500 ms; TE, minimum; ST, 5 mm; NEX, 1), T2-weighted (TR, 2000–2500 ms; TE, 84–102 ms; ST, 5 mm; NEX, 1), fluid-attenuated inversion-recovery (TR, 9000–10,000 ms; TE, 149 ms; TI, 2200 ms), and diffusion-weighted (single-shot echo-planar; TR, 10,000 ms; TE, minimum; ST, 5 mm; matrix, 128). Either T2* gradient recalled-echo (TR/TE/NEX/flip angle, 4400 ms/21 ms/1/90°; ST, 3 mm), susceptibility-weighted (TR/TE/NEX/flip angle, 37 ms/23 ms/1/15°; ST, 2.4 mm), or echo-spoiled gradient-echo imaging (TR/TE/NEX, 25 ms/3 ms/1; ST, 1.0 mm; matrix, 256 × 256) was performed. The FOV ranged from 200 to 240 mm. Contrast-enhanced echo-spoiled gradient-echo images were obtained with 0.1-mmol/kg gadolinium-based contrast material (gadobenate dimeglumine, MultiHance; Bracco Diagnostics, Princeton, New Jersey) by using parameters as described above, performed immediately (<1 minute) after contrast administration.

Evaluation for Imaging Findings Associated with MSC Implantation

MR images from both imaging time points in all patients with MSC implants were reviewed by 2 fellowship-trained neuroradiologists (S.F., L.M.A.) for the following findings at both imaging time points: 1) interval infarction or hemorrhage remote from the MSC implantation site, 2) any neoplasm—especially teratoma—or heterotopia, 3) qualitative evaluation of any edema (mild, moderate, severe), and 4) the presence or absence of any enhancement. Differences were resolved by consensus.

Quantitative Volumetric Analysis

Percentage Brain Volume Change. Comparison of the percentage of brain volume change (%BVC) between the 2 time points for patients with MSC implants, controls, and MCAI controls was performed with the Structural Image Evaluation using Normalization of Atrophy (SIENA) software (fMRI of the Brain Software Library, Version 3.2 software suite; <http://www.fmrib.ox.ac.uk/fsl>).^{21,22} SIENA determines the %BVC in the following steps: 1) The brain is segmented from nonbrain tissue, and the skull surface is estimated from the anatomic images; 2) this segmentation is then used to coregister the 2 images at each time point and normalize for changes in geometric shape; and 3) local changes in brain volume are determined on the basis of movement associated with image edges (Fig 1A, -B). Calculated volumetric changes are presented as %BVC between the 2 imaging time points.

Although several automated methods are available for measurements of brain volume change—SIENA, Unified Segmentation (SPM5; <http://www.fil.ion.ucl.ac.uk/spm/software/spm5>), and k-Nearest Neighbor–based probabilistic segmentation being the most popular—SIENA was chosen due to its previously reported high accuracy in the evaluation of longitudinal changes in brain volume,²² and its superior performance in direct comparisons.²³ The principal limitation to all of these methods is variability in results when multiple scanners are used, particularly with differing field strengths and at different centers.^{23,24}

Comparison of %BVC among the 3 groups (patients with MSC implants, controls, and MCAI controls) was performed with

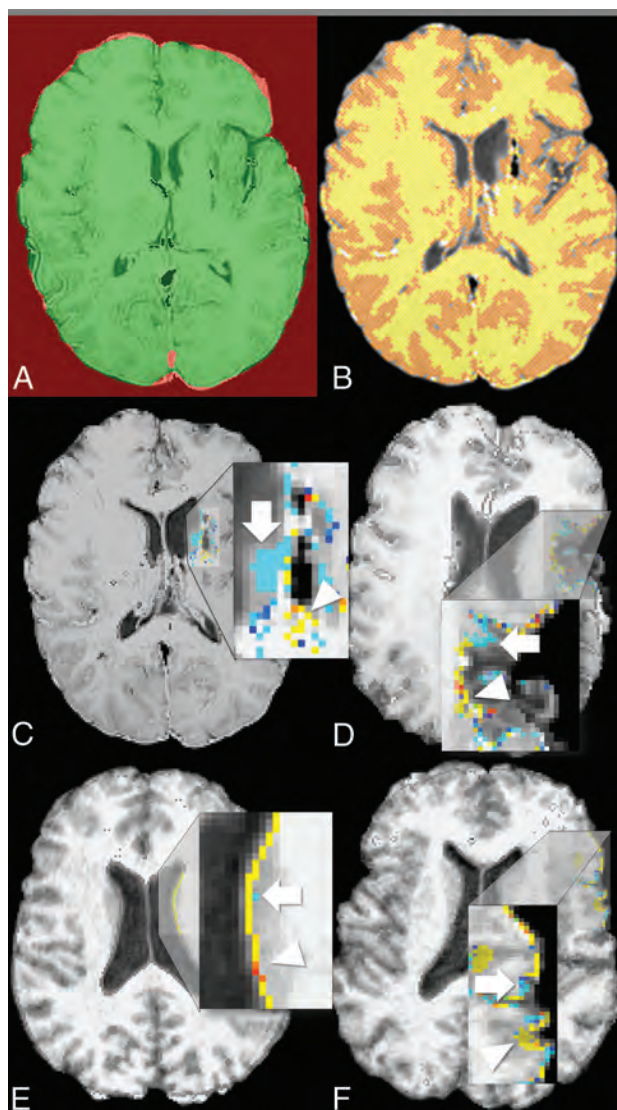


FIG 1. Calculation of percentage brain volume change and growth-to-loss ratio. **A**, Brain and skull images are initially each extracted from whole-head input data from the 2 separate time points for each individual subject. The 2 images (1 at each time point) are aligned to each other by using the skull images to constrain registration scaling at each time point. Green shows the intersection of the 2 standard space brain masks. Red demonstrates the perpendicular edge displacement at the brain/nonbrain boundary between the 2 time points is estimated, and the mean edge displacement is converted in the estimate of the percentage brain volume change between the 2 points. **C** and **D**, The growth-to-loss ratio is calculated in 2 different patients with mesenchymal stem cell implants from the color-rendered image of edge motion superimposed on a half-way image, created by aligning the 2 brain images from the 2 time points to each other by using the skull images to constrain the registration scaling. Red-yellow indicates brain volume increase (white arrowhead), while blue-light blue indicates brain volume decrease (“atrophy”) (white arrow). Regions of growth (red-yellow) are seen to be predominantly at the medial margin of the infarct, where the stem cells are implanted. **E** and **F**, Comparable periventricular and cortical regions are shown in healthy controls, demonstrating more red-yellow voxels in similar areas in healthy controls compared with the infarcted regions in patients with MSC implants. The GLR is calculated by tabulating the ratio of the total number of red-yellow voxels (growth areas) to the total number of blue-light blue voxels (areas of volume loss) in the region of the infarct.

a Kruskal-Wallis test, followed by pair-wise analysis by using a Mann-Whitney *U* test.

Regional Brain Volume Change. Regional brain volume changes in regions of infarction were assessed for patients with MSC implants and MCAI controls by using color maps of voxelwise change in brain volume generated by SIENA. Voxels demarcating a region of brain volume loss were color-coded blue or light blue, while voxels indicating a region of brain volume increase were color-coded yellow or red. Voxels in which volume remained unchanged were color-coded gray. The total number of blue–light blue and yellow/red voxels for each infarct was separately tabulated by a fellowship-trained neuroradiologist with >3 years of image analysis experience (L.M.A.), blinded to the clinical findings. The ratio of yellow/red to blue–light blue voxels was calculated to create a growth-to-loss ratio (GLR), to compare volume changes in infarcted tissue between the 2 groups, controlling for infarct size (Fig 1C, -D). Comparison of the GLR between patients with MSC implants and MCAI controls was performed with a Mann-Whitney *U* test. Correlation of GLR with the total recovery score was performed with the Pearson correlation coefficient.

RESULTS

Patient Selection and Image Acquisition

Six patients underwent MSC implantation. One patient was excluded because appropriate follow-up imaging had not been performed. The remaining 5 patients were included in this study (3 men, 2 women; mean age, 62 years; range, 53–77 years). All patients underwent initial MR imaging within 1 day of MSC implantation and had a follow-up MR imaging 12 months after the initial imaging. No patients were lost to follow-up. The average time interval from stroke to MSC implantation was 23 months (range, 6–36 months). The patient demographics, etiology of the infarcts, initial physical examination findings, and physical examination findings post-MSC implantation are shown in the On-line Table.

Five age- and sex-matched controls were included (3 men, 2 women; mean age, 59 years; range, 51–76 years). The average time between imaging was 10.4 months (range, 10–11 months).

Five age- and sex-matched MCAI controls were included (3 men, 2 women; mean age, 64 years; range, 48–82 years). The average time between imaging was 12.4 months (range, 11–14 months). No significant difference was seen in the imaging time interval between MCAI controls and patients with MSC implants ($P = .67$, $U = 10$).

Evaluation for Imaging Findings Associated with Stem Cell Implantation

The immediate postprocedural findings corresponded well with known complications post-stereotactic biopsy.²⁵ One patient had a small subdural collection immediately post-MSC implantation deep to the burr-hole site measuring approximately 6 mm. No new infarct was identified in any patient.

Three patients had mild edema along the operative tract, while 2 had moderate edema. No edema persisted on follow-up imaging. All patients had enhancement at the implantation site, and 2

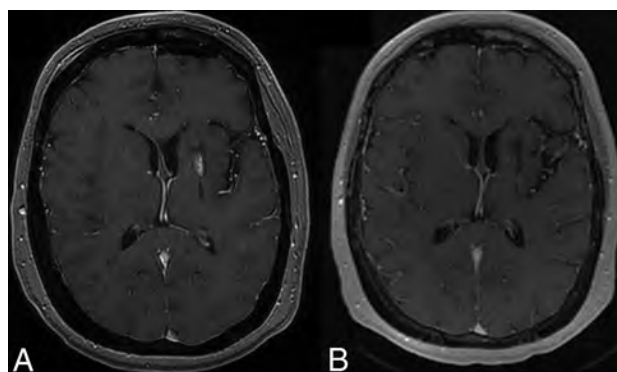


FIG 2. Resolution of enhancement at the implantation site on follow-up imaging. Postcontrast axial echo-spoiled gradient-echo sequence images in a 54-year-old woman status post stem cell implantation demonstrate initial enhancement at the implantation site immediately postoperatively (A), which resolved on 1-year follow-up imaging (B).

Kruskal-Wallis analysis of %BVC among healthy controls, patients with stem cell (MSC) implantation, and MCAI controls

	Healthy Controls	MSC Implantation	MCAI Controls
%BVC	2.00	0.736	–3.59
95% CI	–1.58–5.58	–4.15–5.62	–12.3 to –5.21
<i>P</i> value compared with healthy controls ^a	NA	.38	.06
<i>P</i> value compared with patients with MSC	.38	NA	.09
<i>P</i> value compared with MCAI controls	.06	.09	NA

Note:—NA indicates not applicable.

^a *P* values from a post hoc pair-wise analysis using the Mann-Whitney *U* test of the Kruskal-Wallis analysis results.

had enhancement along the implantation tract. No enhancement persisted on follow-up imaging (Fig 2). All patients had punctate susceptibility signal loss along both the implantation tract and site, suggestive of hemosiderin staining, which persisted at follow-up imaging.

No neoplasm or sign of heterotopia was detected in any patient.

Quantitative Volumetric Analysis

%BVC. Mean %BVC among controls, MCAI controls, and subjects with MSC implants (Table) was significantly different ($P = .046$, H value = 6.14). Post hoc analysis found that MCAI controls trended toward greater volume loss than healthy controls ($P = .06$). No significant difference in volume loss was seen between patients with MSC implants and healthy controls ($P = .14$). However, patients with MSC implants trended toward less volume loss compared with MCAI controls ($P = .09$).

Regional Brain Volume Change. The GLR for patients with MSC implants (mean, 1.30; range, 0.92–1.42) was significantly higher than that for MCAI controls (mean, 0.78; range, 0.56–1.05; $P = .02$). There was a trend toward correlation of GLR with a higher total recovery score ($P = .06$, $r = 0.856$). The total recovery score did not correlate with time from stroke to implantation ($P = .42$, $r = -0.477$).

DISCUSSION

Implantation of MSC results in typical imaging changes seen after stereotactic intervention, with an additional finding of transient enhancement at the implantation site. No complications unique to MSC, such as a teratoma or heterotopia, were detected. Most important, MSC implantation after stroke resulted in a trend toward overall less volume loss and more regions of growth at the infarct site compared with controls with infarcts who did not receive MSC.

While currently use of MSC is essentially limited to clinical trials, the growing body of evidence of their safety in humans⁶⁻⁸ suggests that imaging of patients who have received MSC will only become more common in the future. It is, therefore, important for the interpreting radiologist to be aware of the expected imaging findings and their time course. Previous studies have looked at changes in the appearance of the treated stroke after implantation but have not evaluated changes related to the implantation itself.⁷ Our study evaluated MSC administered via stereotactic implantation. While enhancement and edema may be seen immediately after any stereotactic intervention,²⁵ these findings resolved on follow-up imaging in all our patients. Therefore, on the basis of our preliminary findings, persistent enhancement or edema may possibly indicate a secondary process, though further studies are needed to confirm the natural history of the imaging findings.

The most feared complications associated with MSC implantation, including teratoma formation and heterotopias, were not seen in our patients, similar to findings in previous studies.²⁶ Although our follow-up was only 1 year, previous animal experiments have suggested that neoplastic complications typically appear within 1 month of treatment.^{27,28} Similarly, although MSC may induce an inflammatory reaction,^{29,30} no progressive enhancement or edema was seen in our cohort. This may be because MSC also have immunomodulatory properties³¹ that may suppress an inflammatory reaction. This finding bodes well for the efficacy of MSC in the treatment of stroke because the immunosuppressive properties of MSC are key to their regenerative capacity. Immune/inflammatory cells play a key role in tissue injury in patients with stroke.¹⁴ MSC combats this inflammatory cascade and promotes tissue regeneration/repair by secreting growth factors suppressing these inflammatory cytokines, resulting in enhanced angiogenesis, decreased leukocyte transmigration, and greater stem cell differentiation.³² Larger studies to confirm lack of an inflammatory response should be a goal of future research.

Our preliminary findings support the effectiveness of MSC in promoting tissue regeneration through these described mechanisms. While our cohort was small, we found a trend toward less brain volume loss and significantly greater growth at the infarct site in the transplanted cohort compared with the MCAI cohort. This finding is encouraging because the therapeutic action of the implanted MSC is believed to be related to the secretion of trophic factors that would stimulate neuronal survival and differentiation of native stem cells.³³ Notably, this greater GLR after implantation trended toward a correlation with improved clinical findings in our patients, suggesting that the imaging findings may be used as a marker of clinical improvement that can assist in further clinical trials. Previous stroke studies have correlated the volume of diffusion abnormality³⁴ or the final infarct volume³⁵ with clin-

ical outcomes after intervention with thrombolysis, and perhaps the GLR may serve as a similar predictor of clinical outcome after intervention with MSC. However, future studies are needed to confirm this trend toward improved clinical function with greater growth on imaging.

Our assessment of MR imaging findings after MSC implantation is limited by our small number of patients and short follow-up interval. However, larger cohorts are difficult to amass, given the current relatively limited use of stem cells. It will also be important to correlate imaging findings with objective stroke scales before and after implantation, to quantify any clinical benefit. Additional imaging of white matter tracts would be another avenue to explore the effects of MSC implantation on new white matter tracts and brain plasticity.

CONCLUSIONS

Initial findings after MSC implantation demonstrate expected postprocedural changes after a stereotactic procedure and no unique complications such as teratoma, tumor, or heterotopia. A significantly greater growth-to-loss ratio in infarcted tissue was seen in patients receiving MSC compared with patients who did not receive MSC, which trended toward a correlation with an improvement in physical examination findings.

REFERENCES

1. Roger VL, Go AS, Lloyd-Jones DM, et al; for the American Heart Association Statistics Committee and Stroke Statistics Subcommittee. **Heart disease and stroke statistics: 2012 update—a report from the American Heart Association.** *Circulation* 2012;125:e2-220
2. Johnston SC, Mendis S, Mathers CD. **Global variation in stroke burden and mortality: estimates from monitoring, surveillance, and modelling.** *Lancet Neurol* 2009;8:345-54
3. Adeoye O, Hornung R, Khatri P, et al. **Recombinant tissue-type plasminogen activator use for ischemic stroke in the United States: a doubling of treatment rates over the course of 5 years.** *Stroke* 2011;42:1952-55
4. Hong KS, Ali LK, Selco SL, et al. **Weighting components of composite end points in clinical trials: an approach using disability-adjusted life-years.** *Stroke* 2011;42:1722-29
5. Friedrich MA, Martins MP, Araújo MD, et al. **Intra-arterial infusion of autologous bone marrow mononuclear cells in patients with moderate to severe middle cerebral artery acute ischemic stroke.** *Cell Transplant* 2012;21(suppl 1):S13-21
6. Lee JS, Hong JM, Moon GJ, et al. **A long-term follow-up study of intravenous autologous mesenchymal stem cell transplantation in patients with ischemic stroke.** *Stem Cells* 2010;28:1099-106
7. Honmou O, Houkin K, Matsunaga T, et al. **Intravenous administration of auto serum-expanded autologous mesenchymal stem cells in stroke.** *Brain* 2011;134(pt 6):1790-807
8. Bhasin A, Srivastava MV, Mohanty S, et al. **Stem cell therapy: a clinical trial of stroke.** *Clin Neurol Neurosurg* 2013;115:1003-08
9. Glover LE, Tajiri N, Weinbren NL, et al. **A step-up approach for cell therapy in stroke: translational hurdles of bone marrow-derived stem cells.** *Transl Stroke Res* 2012;3:90-98
10. Mezey E, Chandross KJ, Harta G, et al. **Turning blood into brain: cells bearing neuronal antigens generated in vivo from bone marrow.** *Science* 2000;290:1779-82
11. Phinney DG, Prockop DJ. **Concise review: mesenchymal stem/multipotent stromal cells: the state of transdifferentiation and modes of tissue repair—current views.** *Stem Cells* 2007;25:2896-902
12. Mohal JS, Taylor HD, Khan WS. **Sources of adult mesenchymal stem cells and their applicability for musculoskeletal applications.** *Curr Stem Cell Res Ther* 2012;7:103-09

13. Ikegame Y. **Among mesenchymal stem cells: for the best therapy after ischemic stroke.** *Stem Cell Res Ther* 2013;4:9
14. Tatarishvili J, Oki K, Monni E, et al. **Human induced pluripotent stem cells improve recovery in stroke-injured aged rats.** *Restor Neurol Neurosci* 2014;32:547–58
15. Tornero D, Wattananit S, Grønning Madsen M, et al. **Human induced pluripotent stem cell-derived cortical neurons integrate in stroke-injured cortex and improve functional recovery.** *Brain* 2013; 136(pt 12):3561–77
16. Burns TC, Steinberg GK. **Stem cells and stroke: opportunities, challenges and strategies.** *Expert Opin Biol Ther* 2011;11:447–61
17. Bang OY, Lee JS, Lee PH, et al. **Autologous mesenchymal stem cell transplantation in stroke patients.** *Ann Neurol* 2005;57:874–82
18. Hao L, Zou Z, Tian H, et al. **Stem cell-based therapies for ischemic stroke.** *Biomed Res Int* 2014;2014:468748
19. Bao X, Feng M, Wei J, et al. **Transplantation of Flk-1+ human bone marrow-derived mesenchymal stem cells promotes angiogenesis and neurogenesis after cerebral ischemia in rats.** *Eur J Neurosci* 2011;34:87–98
20. Li J, Zhu H, Liu Y, et al. **Human mesenchymal stem cell transplantation protects against cerebral ischemic injury and upregulates interleukin-10 expression in Macaca fascicularis.** *Brain Res* 2010; 1334:65–72
21. Smith SM, De Stefano N, Jenkinson M, et al. **Normalized accurate measurement of longitudinal brain change.** *J Comput Assist Tomogr* 2001;25:466–75
22. Smith SM, Zhang Y, Jenkinson M, et al. **Accurate, robust, and automated longitudinal and cross-sectional brain change analysis.** *Neuroimage* 2002;17:479–89
23. de Bresser J, Portegies M, Leemans A, et al. **A comparison of MR based segmentation methods for measuring brain atrophy progression.** *Neuroimage* 2011;54:760–68
24. Durand-Dubief F, Belaroussi B, Armspach JP, et al. **Reliability of longitudinal brain volume loss measurements between 2 sites in patients with multiple sclerosis: comparison of 7 quantification techniques.** *AJNR Am J Neuroradiol* 2012;33:1918–24
25. Hall WA. **The safety and efficacy of stereotactic biopsy for intracranial lesions.** *Cancer* 1998;82:1749–55
26. Eckert MA, Vu Q, Xie K, et al. **Evidence for high translational potential of mesenchymal stromal cell therapy to improve recovery from ischemic stroke.** *J Cereb Blood Flow Metab* 2013;33:1322–34
27. Aldahmash A, Atteya M, Elsafadi M, et al. **Teratoma formation in immunocompetent mice after syngeneic and allogeneic implantation of germline capable mouse embryonic stem cells.** *Asian Pac J Cancer Prev* 2013;14:5705–11
28. Yamamoto M, Cui L, Johkura K, et al. **Branching ducts similar to mesonephric ducts or ureteric buds in teratomas originating from mouse embryonic stem cells.** *Am J Physiol Renal Physiol* 2006; 290:F52–60
29. Inoue S, Popp FC, Koehl GE, et al. **Immunomodulatory effects of mesenchymal stem cells in a rat organ transplant model.** *Transplantation* 2006;81:1589–95
30. François M, Romieu-Mourez R, Stock-Martineau S, et al. **Mesenchymal stromal cells cross-present soluble exogenous antigens as part of their antigen-presenting cell properties.** *Blood* 2009;114:2632–38
31. Ren G, Su J, Zhang L, et al. **Species variation in the mechanisms of mesenchymal stem cell-mediated immunosuppression.** *Stem Cells* 2009;27:1954–62
32. Ma S, Xie N, Li W, et al. **Immunobiology of mesenchymal stem cells.** *Cell Death Differ* 2014;21:216–25
33. Liu X, Ye R, Yan T, et al. **Cell based therapies for ischemic stroke: from basic science to bedside.** *Prog Neurobiol* 2014;115:92–115
34. Turc G, Aguetaz P, Ponchelle-Dequatre N, et al. **External validation of the MRI-DRAGON score: early prediction of stroke outcome after intravenous thrombolysis.** *PLoS One* 2014;9:e99164
35. Yoo AJ, Chaudhry ZA, Nogueira RG, et al. **Infarct volume is a pivotal biomarker after intra-arterial stroke therapy.** *Stroke* 2012;43: 1323–30

Multimodal CT Provides Improved Performance for Lacunar Infarct Detection

T. Das, F. Settecase, M. Boulos, T. Huynh, C.D. d'Esterre, S.P. Symons, L. Zhang, and R.I. Aviv

ABSTRACT

BACKGROUND AND PURPOSE: Lacunar infarcts account for approximately 25% of acute ischemic strokes. Compared with NCCT alone, the addition of CTP improves sensitivity for detection of infarcts overall. Our aim was to systematically evaluate the diagnostic benefit and interobserver reliability of an incremental CT protocol in lacunar infarction.

MATERIALS AND METHODS: Institutional review board approval and patient consent were obtained. One hundred sixty-three patients presenting with a lacunar syndrome ≤ 4.5 hours from symptom onset were enrolled. Images were reviewed incrementally by 2 blinded readers in 3 separate sessions (NCCT only, NCCT/CTA, and NCCT/CTA/CTP). Diagnostic confidence was recorded on a 6-point scale with DWI/ADC as a reference. Logistic regression analysis calculated differences between actual and observed diagnoses, adjusted for confidence. Predictive effects of observed diagnostic accuracy and confidence score were quantified with the entropy r^2 value. Sensitivity, specificity, and confidence intervals were calculated accounting for multiple readers. Receiver operating characteristic analyses were compared among diagnostic strategies. Interobserver agreement was established with Cohen κ statistic.

RESULTS: The final study cohort comprised 88 patients (50% male). DWI/ADC-confirmed lacunar infarction occurred in 59/88 (67%) with 36/59 (61%) demonstrating a concordant abnormal finding on CTP. Sensitivity for definite or probable presence of lacunar infarct increased significantly from 9.3% to 42.4% with incremental protocol use, though specificity was unchanged (range, 91.9%–95.3%). The observed diagnosis was significantly related to the actual diagnosis after adjusting for CTP confidence level ($P = .04$) and was 5.1 and 2.4 times more likely to confirm lacunar infarct than NCCT or CTA source images. CTP area under the curve (0.77) was significantly higher than that of CTA source images (0.68, $P = .006$) or NCCT (0.55, $P < .001$).

CONCLUSIONS: CTP offers an improved diagnostic benefit over NCCT and CTA for the diagnosis of lacunar infarction.

ABBREVIATIONS: AIC = Akaike information criterion; CTA-SI = CT angiographic–source images; IQR = interquartile range; LI = lacunar infarct

Lacunar infarcts (LIs) account for approximately 25% of all acute ischemic strokes.¹ These small subcortical infarcts are typically located in the basal ganglia, thalamus, internal capsule, corona radiata, or brain stem.² Although single perforating artery occlusion is the dominant pathophysiology, lacunar syndromes may be secondary to large-artery disease and cardioembolic

causes in up to 10% of cases.³ The National Institutes of Neurological Disorders and Stroke study showed the benefit of thrombolytic use on functional outcome across all stroke subtypes, including small-vessel infarcts characterized at baseline.⁴ Although conflicting findings have been reported,^{5,6} a general consensus favors thrombolytic use in lacunar infarction.⁷ Anecdotally, thrombolysis treatment of an acute LI was associated with MR imaging perfusion and DWI deficit reversal, with good clinical recovery.⁸ Inaccuracy of the LI diagnosis is present in approximately 30% of stroke presentations by using clinical and NCCT findings alone.⁹ CTP is increasingly used during acute stroke work-up due to its cost effectiveness, ease, availability, speed, and tolerability.¹⁰ CTP significantly improves sensitivity for detection of infarcts overall compared with NCCT alone.^{11,12} Perfusion abnormality associated with LI is clinically important and may be associated with early clinical deterioration, infarct growth, or resolution.^{8,13–15} No prior study has systematically evaluated the performance of CTP for LI, to our knowledge. The purpose of

Received August 11, 2014; accepted after revision December 11.

From the Department of Radiology (T.D.), Cambridge University Hospitals NHS Foundation Trust, Addenbrooke's Hospital, Cambridge, UK; Department of Neurology (C.D.d.), University of Calgary, Calgary Stroke Program, Foothills Medical Centre, Calgary, Alberta, Canada; Departments of Medical Imaging (F.S., T.H., R.I.A., S.P.S., L.Z.) and Neurology (M.B.), Sunnybrook Health Sciences Centre, Toronto, Ontario, Canada; and University of Toronto (M.B., T.H., S.P.S., R.I.A.), Toronto, Ontario, Canada.

Paper previously presented in part as an oral presentation at: American Society of Neuroradiology Annual Meeting and the Foundation of the ASNR Symposium, May 18–23, 2013; San Diego, California.

Please address correspondence to Richard I. Aviv, MD, Sunnybrook Health Sciences Centre, 2075 Bayview Ave, Room AG-31E, Toronto, ON, M4N 3M5, Canada; e-mail: Richard.aviv@sunnybrook.ca

<http://dx.doi.org/10.3174/ajnr.A4255>

this study was to evaluate the diagnostic benefit and interobserver reliability of an incremental CT protocol in the diagnosis of LI.

MATERIALS AND METHODS

Study Cohort

All study procedures and medical chart reviews were approved by the local institutional research ethics board. Patients were retrospectively selected from a prospectively acquired database of consecutive patients presenting to a tertiary stroke center between March 2011 and February 2013, admitted under a code stroke designation to the emergency department <4.5 hours after symptom onset. Inclusion criteria were presentation with an acute code stroke designation with a clinical lacunar syndrome¹⁶ determined at admission by the attending stroke neurologists (5–10 years' experience) and undergoing the admission CT stroke protocol (NCCT, CT angiographic–source images [CTA-SI], and CTP) and follow-up MR imaging, with or without restriction in a LI distribution on DWI/ADC and no vessel occlusion. Patients with both cortical and lacunar infarcts were excluded from review ($n = 44$). Of 163 patients presenting with a clinical lacunar syndrome, we excluded the following: 11 patients with stroke mimic (cavernous malformation, aneurysm, venous thrombosis, seizure, migraine, 5.3%) and 64 with delayed follow-up MR imaging (>30 days from presentation) or MR imaging performed following repatriation and not available for review (30.9%). A 30-day DWI limit was applied, because this represents an accepted time for DWI to remain sensitive for infarct detection in patients with acute ischemic stroke.^{11,17} LI was defined as solitary, subcortical lesions, ≤ 20 mm in greatest diameter as previously defined,¹⁵ recommended,¹⁸ and clinically applied.^{19,20} The final study cohort comprised 88 patients.

Imaging Protocol

CT stroke protocol, performed on a 64-section CT scanner (VCT; GE Healthcare, Milwaukee, Wisconsin), includes a pre- and post-contrast head CT with the following parameters: 120 kV(peak), 340 mA, 8×5 mm collimation, 1 s/rotation, and table speed of 15 mm/rotation. CTA was performed from the aortic arch to the vertex with the following parameters: 0.7-mL/kg iodinated contrast agent up to a maximum of 90 mL (iohexol, Omnipaque 300 mg iodine/mL; GE Healthcare, Piscataway, New Jersey), 5- to 10-second delay, 120 kVp, 270 mA, 1 s/rotation, 1.25-mm-thick sections, and table speed of 3.7 mm/rotation. Biphasic CT perfusion included a 45-second scan reconstructed at 0.5-second intervals followed by 6 further acquisitions 15 seconds apart for an additional 90 seconds. CTP scan parameters were the following: 80 kVp, 100 mA, 0.5-mL/kg (maximum, 50 mL) iodinated contrast agent injected at 4 mL/s with a 3- to 5-second delay.¹¹ Sections were selected to cover either the infra- or supratentorium, depending on clinical suspicion of infarct location by an attending neurologist. In all cases, the first supratentorial and last infratentorial CTP sections included the inferiormost portion of the frontal horn of the lateral ventricle. Follow-up MR imaging comprised at least DWI (TR = 8125 ms/minimum TE, 26-cm FOV, 128×128 matrix, 5-mm section thickness, no intersection gap) and FLAIR sequences (TR = 8000 ms/TE = 120 ms/TI = 200 ms,

22-cm FOV, 320×224 matrix, 5-mm section thickness, 1-mm intersection gap). Effective doses of individual components of CT stroke protocol were NCCT, 1.2 mSv; CTA, 2.4 mSv; and CTP, 2.5 mSv. Lifetime attributable risk of cancer for NCCT at the median age of the included cohort is 0.01%.²¹

Image Processing

CT Perfusion 4 (GE Healthcare) was used to calculate parametric maps as described previously.¹¹ Briefly, arterial input and venous time-attenuation curves were generated, after manually selecting regions of interest in the anterior cerebral artery ipsilateral to the side of the infarct and the superior sagittal sinus, respectively. PACS postprocessing of CTA-SI (4 mm thick with a 2-mm gap and aligned to match the NCCT) was performed by CT technologists at the CT operator console.

Review Protocol

The review protocol simulated the usual order in which stroke studies are reviewed in our practice, beginning with NCCT images, followed by CTA and CTA-SI and CTP color maps. The 2 reviewers were a recently trained neuroradiologist and an experienced neuroradiology fellow (1-years' experience in a high-volume stroke center). Before review, 3 anonymized DICOM folders were prepared and stored on a secure server. The first folder contained only NCCT images; the second, NCCT and CTA-SI; and the third, NCCT, CTA-SI, and CTP color maps (CBF, CBV, and MTT). Only 1 folder was available to a reader at a time, and each completed folder was removed following completion. A minimum 2-week interval separated each review to minimize recall bias. Images were reviewed with a Windows-based PACS (K-PACS, version 1.6.0; <http://www.k-pacs.de>). Reviewers were blinded to all clinical information including the affected side. For each patient, the reviewers scored both hemispheres for the presence or absence of LI and assigned a 6-point level of confidence score to each side (1, stroke definitely present; 2, stroke probably present; 3, equivocal but leaning to positive; 4, equivocal but leaning to negative; 5, stroke probably absent; 6, stroke definitely absent). For studies with positive findings, the precise location of the infarct was recorded. For CTP, color maps were evaluated initially in combination to generate a combined score. Separate scores were also assessed for each CTP map. The total number of scores generated for each technique was 352 (88 patients, 2 sides and 2 readers). The final observed diagnosis was established on DWI/ADC coregistered to baseline imaging by an experienced neuro-radiologist (9 years' experience) (SPM 8; <http://www.fil.ion.ucl.ac.uk/spm/software>). True-positive studies required a confidence score of 1–3 and identification of the correct infarct location. Incorrect location with scores of 1–3 constituted a false-positive response.

Statistical Analysis

Analyses were performed with SAS (Version 9.1; SAS Institute, Cary, North Carolina). Results were expressed as either the mean \pm SD or median and interquartile range (IQR) for quantitative variables and as proportions for categorical findings. Comparisons of demographic features were performed by using an unpaired samples t test and Mann-Whitney U and χ^2 tests.

Table 1: Comparison of baseline demographic features of 88 patients presenting with acute stroke symptoms with and without lacunar infarct^a

	Lacunar Infarct Present (n = 59)	Lacunar Infarct Absent (n = 29)	P Value
Mean age (yr) (SD)	72 (13.4)	68 (17.5)	.30
Median NIHSS (IQR)	6.5 (5)	2 (5)	.16
Median days to follow-up (IQR)	2.5 (3)	2 (5.5)	.60
Male sex	33 (56%)	11 (38%)	.17
Cardiovascular risk factors			
Hypertension	39 (66%)	12 (41%)	.04 ^b
Diabetes	15 (25%)	1 (3%)	.02 ^b
Atrial fibrillation	8 (14%)	1 (3%)	.26
Coronary artery disease	13 (22%)	4 (14%)	.40
Hyperlipidemia	23 (39%)	6 (21%)	.10
Smoking	6 (10%)	1 (3%)	.27

^a All values are No. (%) unless otherwise specified.

^b Statistically significant.

Table 2: Distribution of confidence scores for infarct presence by modality for 2 readers for a total of 352 observations

Confidence Score		NCCT	NCCT + CTA-SI	NCCT + CTA-SI + CTP
1	Definitely present	5 (1.4%)	16 (4.5%)	42 (11.9%)
2	Probably present	25 (7.1%)	26 (7.4%)	27 (7.7%)
3	Equivocal, possibly present	83 (23.6%)	68 (19.3%)	18 (5.1%)
4	Equivocal, possibly absent	4 (1.1%)	2 (0.6%)	18 (5.1%)
5	Probably absent	78 (22.2%)	89 (25.3%)	131 (37.2%)
6	Definitely absent	157 (44.6%)	151 (42.9%)	116 (33.0%)

Logistic regression analysis was used to predict the actual from observed diagnosis for the incremental protocol, adjusting for confidence score. The combined predictive effects of the observed diagnostic performance and the confidence score in the model were quantified with the entropy r^2 value calculated as $r^2 = (L_O - L_M)/L_O$, where L_O and L_M represent the log-likelihood (maximized-2) of the null and the fitted model, respectively. The Akaike information criterion (AIC) was calculated as $AIC = L_M + 2n$, (where n is the number of parameters) and was used to compare models among the 3 modalities. Diagnostic performance of the incremental protocols was evaluated with a receiver operating characteristic curve, and the area under the curve was compared according to DeLong et al.²²

To analyze correlated data from readers, we used generalized estimating equations to assess actual from observed stroke diagnosis after adjusting for the confidence score by using a generalized linear model with a binomial distribution (logit link function). The quasilielihood information criterion was applied to fit the models. Individual sensitivity (Se_i) and specificity (Sp_i) were calculated as follows:

$$Se = \frac{\sum_{i=1}^n N_i Se_i}{\sum_{i=1}^n N_i}$$

and

$$Sp = \frac{\sum_{i=1}^n N_i Sp_i}{\sum_{i=1}^n N_i}$$

where N_i indicates the total number of diagnoses considered for each patient and found positive at the time the actual diagnosis was made and n indicates the total number of patients. The esti-

mate of sensitivity and specificity and their variances were derived.²³ To compare sensitivity and specificity among the 3 modalities, we performed a regression model of the natural log of Se_i/Sp_i . Interobserver agreement was calculated by the Cohen κ statistic and considered moderate, substantial, and near-perfect (κ values = 0.41–0.60, 0.61–0.80, and 0.81–1.00, respectively). To test the equality of the correlated Cohen κ statistics, we performed a weighted least-squares approach.²⁴ $P < .05$ was considered significant.

RESULTS

Of 88 included patients ($n = 44$, 50% male; cohort median age, 73.5 years; IQR = 60–82 years), acute LI was demonstrated in 59 (67%) MR imaging studies. The median time to CTP was 150 minutes (IQR = 87–196 minutes). The median time to follow-up MR imaging was 2 days (IQR, 1–4.25 days). The distribution of LI was lenticulostriate, 34 (57.6%); thalamus/posterior internal capsule, 11 (18.6%); and pons, 14 (23.7%). Patients with LI were more likely to have hypertension and diabetes compared with those without ($P = .04$; $P = .02$, respectively; Table 1). The median NIHSS score was 6.5 (IQR = 4–9) in patients with LI compared with 5 (IQR = 2–7) in those without, but it did not reach significance. Sixteen patients (18.2%) received a mean dose of 73 ± 27 mg of IV rtPA. Perfusion abnormality was seen in 36/59 (61%) LIs. No significant difference in age, sex, cardiovascular risk factors, and rtPA use or side of infarct was present between patients with and without a perfusion abnormality. Patients with a perfusion abnormality had a higher NIHSS score of 7.5 (IQR = 4.8–12.0) versus 4.8 (IQR = 2–7, $P < .01$) and tended to present earlier (101 minutes, IQR = 70–163 minutes versus 168 minutes IQR = 120–203 minutes, $P = .09$). Median mRS scores (3, IQR = 0.8–4.0 versus 1, IQR = 0–2.5; $P = .40$), and the likelihood of early clinical deterioration (19.4% versus 4.3%, $P = .38$) were higher in the presence of a perfusion abnormality than without it, but these did not reach clinical significance.

Table 2 demonstrates the confidence scores for each technique, showing a reduction of equivocal studies from 24.7% with NCCT to 19.9% and 10.2% with CTA-SI and CTP, respectively. Confidence for the presence and absence of infarct increased incrementally with multimodal assessment. Significant correlation between the observed and actual diagnoses for CTA-SI and CTP modalities versus NCCT was demonstrated. Best fit was demonstrated for the multimodal approach including CTP (Table 3); progressive entropy r^2 values increased from 0.015 to 0.329 and AIC was reduced (451.1 to 357.3) with the incremental protocol. The observed diagnosis was significantly related to the actual diagnosis after adjusting for confidence level for CTP ($P = .04$) and was 5.1 and 2.4 times more likely to confirm LI than NCCT or

Table 3: Progressive increase of multiple entropy r^2 value and decrease of AIC with the incremental protocol^a

	Logistic Regression Model				GEEs Method	
	r^2	AIC	P Value	Odds Ratio (95% CI)	AIC	P Value
NCCT						
Model fit statistics	0.015	451.1			451.3	
Observed diagnosis (yes vs no)			.28	1.68 (0.65–4.41)		.29
Observed confidence score			.90	1.03 (0.67–1.58)		.90
NCCT + CTA-SI						
Model fit statistics	0.170	409.2			408.7	
Observed diagnosis (yes vs no)			.59	0.78 (0.31–1.94)		.57
Observed confidence score			<.001 ^b	0.46 (0.31–0.68)		<.001 ^b
NCCT + CTA-SI + CTP						
Model fit statistics	0.329	357.3			357.1	
Observed diagnosis (yes vs no)			.04 ^b	0.33 (0.11–0.95)		.05
Observed confidence score			<.001 ^b	0.30 (0.20–0.44)		<.001 ^b

Note:—GEEs indicates generalized estimating equations.

^a With logistic regression analysis and the GEEs method, the actual stroke diagnosis was modelled on different observed diagnoses (NCCT alone, NCCT + CTA-SI, NCCT + CTA-SI + CTP) when adjusting for the corresponding confidence score. OR < 1 indicates that patients with a positive diagnosis on MRI are more likely to have a lower level of confidence (1 = definitely present, 2 = probably present, 3 = possibly present, 4 = possibly absent, 5 = probably absent, 6 = definitely absent).

^b Statistically significant.

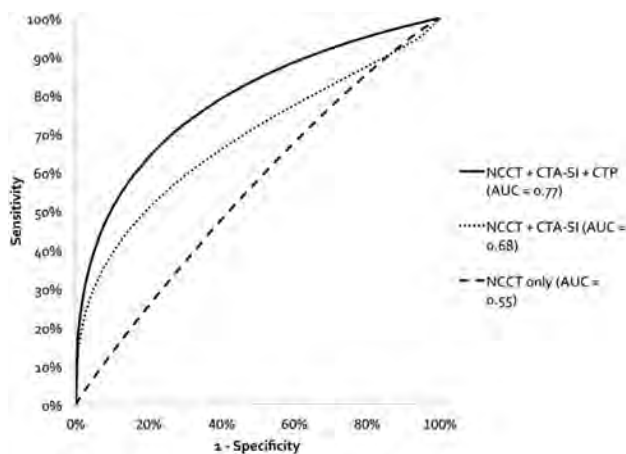


FIG 1. Receiver operating characteristic curves show the diagnostic performance of the incremental CT protocol in the detection of lacunar infarction, without adjusting for multiple readers. There is a statistically significant increase in the area under the curve with each incremental protocol (CTP versus CTA, $P < .006$, and CTP versus NCCT, $P < .001$). The dashed line indicates NCCT only; the dotted line, NCCT and CTA-SI; and the solid line, NCCT, CTA-SI, and CTP.

CTA-SI, respectively. Incremental protocol use was associated with a correlation coefficient increase of -0.09 (95% CI, -0.20 – 0.01 ; $P = .08$), -0.35 (95% CI, -0.44 to -0.26 ; $P < .001$), and -0.48 (95% CI, -0.55 to -0.39 ; $P < .001$). When one considers the 3 CTP maps separately, MTT demonstrated the best model fit and overall performance ($r^2 = 0.320$, AIC = 360.3), while CBV performance was the poorest ($r^2 = 0.265$, AIC = 378.0).

Receiver operating characteristic analysis (Fig 1) demonstrated higher area under the curve for CTP (0.77; 95% CI, 0.72–0.81) than CTA-SI (0.68; 95% CI, 0.63–0.73; $P = .006$) or NCCT alone (0.55; 95% CI, 0.50–0.60; $P < .001$). The difference between CTA-SI and NCCT alone was also statistically significant ($P < .001$).

Diagnostic performance improved with incremental protocol use (Table 4). Although interobserver agreement increased with the incremental protocol (poor-to-moderate), this was not statistically significant (Table 5).

DISCUSSION

Our results demonstrate a significantly improved area under the curve and confidence for correct diagnosis, with fewer equivocal scan outcomes by using a multimodal approach. Similarly, increased interobserver reliability is demonstrated compared with conventional NCCT with a fair overall performance.

A recent study evaluating the efficacy of a newly established incremental CTP protocol found that 10% of false-negative CTP studies in patients with clinical stroke were attributable to LI.¹² The false-negative rate is multifactorial and reflects a learning curve in LI CTP pattern identification^{2,16,25} but also variability in the size of perfusion abnormality in the context of LI.¹⁵ Traditionally, studies have focused on identifying larger hemispheric perfusion defects with or without concurrent deep abnormalities. In the absence of cortical involvement, pure LIs are often overlooked because of their smaller size and inattention to a typical lacunar pattern of perfusion abnormality within the perforator territories including brain stem, basal ganglia, and thalamus. In our experience, LIs are poorly detected with NCCT and CTA. CTP significantly improves detection but requires careful evaluation of the perforator locations for small perfusion defects in the absence of a larger perfusion abnormality (Figs 2 and 3).

The frequency and significance of perfusion abnormality in LI was previously addressed in several small series.^{26–28} One of the largest studies (22 patients) demonstrated MTT abnormality in 68.2% of LIs, comparing favorably with 61% in the present series. Other smaller studies report perfusion abnormality in 0%^{26,28} to 100%¹⁴ of cases. Clinically, perfusion abnormality in LI was previously shown to be associated with the persistence of symptoms beyond 24 hours.¹³ In the present study, analysis of CTP-positive and CTP-negative findings of LI showed a higher NIHSS score, shorter time to scanning, and poorer outcome in patients with a perfusion abnormality. Pathophysiologic differences may explain the variability of perfusion abnormality in the context of LI. LIs associated with perfusion defects may be secondary to atherothrombotic occlusion of several perforator branches rather than single 40- to 200- μ m lipohyalinotic perforator occlusions. In support, we found both hypertension and diabetes to be associated with LI overall, but neither were significantly different between

Table 4: Diagnostic performance for stroke detection with incremental study review using receiver operating characteristic–determined thresholds for level of confidence

	Sensitivity		Specificity	
	Se% (95% CI)	P Value ^a	Sp% (95% CI)	P Value ^a
Level of confidence ≥ 5 vs < 5				
1) NCCT	40.7 (30.8–50.6)	1 vs 2: .174	70.5 (64.4–76.7)	1 vs 2: .088
2) NCCT + CTA-SI	51.7 (40.9–62.5)	1 vs 3: .048 ^b	78.2 (72.2–84.2)	1 vs 3: .002 ^b
3) NCCT + CTA-SI + CTP	55.9 (45.6–66.3)	2 vs 3: .536	83.3 (78.3–88.3)	2 vs 3: .155
Level of confidence ≤ 2 vs < 2				
1) NCCT	9.3 (4.3–14.3)	1 vs 2: .009 ^b	91.9 (88.5–95.2)	1 vs 2: .130
2) NCCT + CTA-SI	26.3 (17.3–35.3)	1 vs 3: $< .001$ ^b	95.3 (92.5–98.1)	1 vs 3: .691
3) NCCT + CTA-SI + CTP	42.4 (30.6–54.2)	2 vs 3: .030 ^b	91.9 (88.4–95.4)	2 vs 3: .264

Note:—Se indicates sensitivity; Sp, specificity.

^a P value was obtained by a linear regression model of natural log(Se) or log(Sp) for each modality.

^b Statistically significant.

Table 5: Interobserver variability between 2 readers for lacunar infarction detection with incremental protocol

	Cohen κ (95% CI) for Each Sequence		
	NCCT	NCCT + CTA-SI	NCCT + CTA-SI + CTP
Reader 1 vs 2	0.25 (0.11–0.39)	0.47 (0.34–0.61)	0.50 (0.35–0.64)

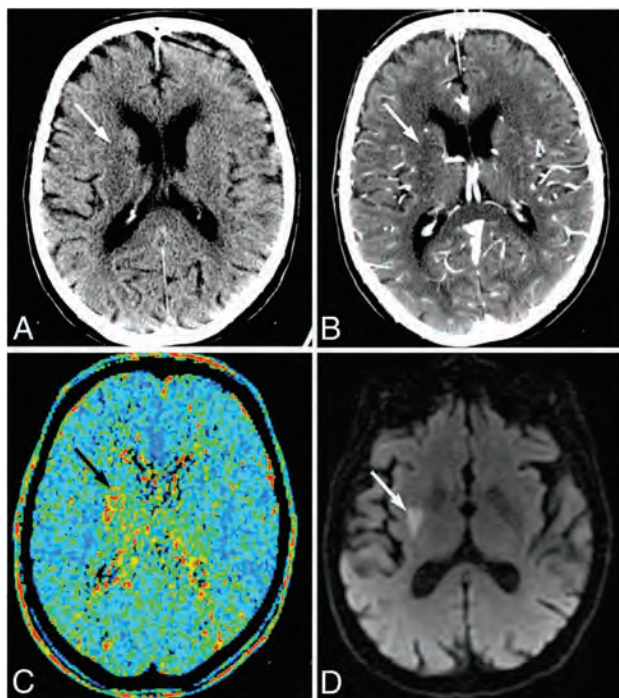


FIG 2. Images of a 72-year-old man who presented with left-sided weakness (NIHSS score, 9), scanned 85 minutes after symptom onset. NCCT (A) and CTA-SI (B) show subtle hypoattenuation, inconclusive for acute infarction (white arrows). C, The MTT map demonstrates a perfusion deficit in the right lentiform nucleus (black arrow). The patient received intravenous thrombolysis. D, Follow-up DWI confirms lacunar infarction in the right lentiform nucleus (white arrow).

patients with and without a perfusion defect. These results mirror a large community-based prospective cohort study of 15,792 middle-aged adults in whom both hypertension and diabetes were associated with smaller (but not large) infarcts.²⁵

The utility of CTP in the context of LI has been previously studied.^{8,13,14} Early clinical deterioration occurs in 27%–62% of LI cases and is not reliably predicted clinically.^{26,28} Perfusion abnormality absence was highly predictive of clinical stability in 1

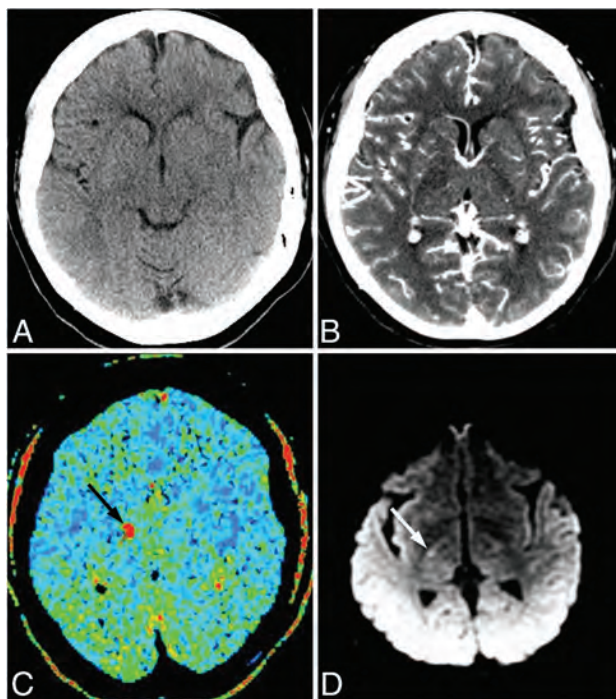


FIG 3. Images of a 55-year-old man who presented with left-sided weakness. A, No abnormality is evident on NCCT. B, CTA-SI shows a possible hypoattenuation in the posterior limb of the right internal capsule or thalamus. C, MTT map demonstrates a focus of increased MTT in the region of the internal capsule (black arrow). The patient received intravenous thrombolysis. D, Follow-up DWI confirms focal hyperintensity consistent with recent lacunar infarction in the posterior limb of the right internal capsule (white arrow).

study, while one-third of patients with perfusion abnormality experienced clinical deterioration.¹⁴ Yamada et al¹³ demonstrated higher MTT ratios and lower CBF ratios in patients experiencing clinical deterioration. The reported reversal of a matched right thalamostriate perfusion and diffusion abnormality following thrombolysis suggests a potential role for perfusion imaging in the management of LI.⁸ Although thrombolysis in LI is controversial, growing evidence supports its use. Lacunar strokes treated with IV rtPA in the National Institutes of Neurological Disorders and Stroke study demonstrated more favorable outcomes compared with a placebo group (63% versus 40%; mRS, ≤ 1).⁴ Similarly, a Canadian Stroke Network Registry study of 11,503 patients showed equal benefit after thrombolysis for lacunar and total anterior circulation strokes.²⁹ Patients with thrombolysis-treated

ischemic stroke with small-vessel infarcts showed better clinical outcome and lower hemorrhagic complications than those secondary to other etiologies.^{30,31}

Justifiable concern remains regarding the radiation dose from CTP, conferring an effective dose of ~2.5 mSv. The total dose of the CT protocol is 6.1 mSv by the International Commission on Radiological Protection 103 criteria. Thus, the relative incremental CTP dose is small but conferring the benefit of increased confidence of diagnosis. A recent study has shown that this could be reduced by 50% by using 50 mA instead of 100 mA.³² Furthermore, due to scan obliquity, no significant lens dose exposure was experienced. The largest contributor to dose remains the CTA component, due to spatial coverage and exposure to the thyroid and lenses. MR imaging in acute ischemic stroke is considered a reference standard³³ and indeed provides superior infarct core delineation. Unfortunately, the overwhelming majority of tertiary stroke centers and other hospitals receiving patients with acute ischemic stroke do not have acute MR imaging access. Therefore, although MR imaging triage is recommended by consensus, this is usually after a decision to treat based on NCCT.³³ We argue simply that CTA and CTP use improves initial detection over NCCT without precluding subsequent MR imaging use according to institutional resource availability. Dose is important in terms of overall population burden, and conscientious effort should be made to conform to “as low as reasonably achievable” principles and to reduce the dose in all patients. While MR imaging has the advantage of not conferring any radiation dose, the biologic effect of CT dose in an elderly population is small.²¹

Limitations include a retrospective study design. Although relatively small in sample size, the study does constitute one of the largest imaged lacunar cohorts. Readers were blinded to clinical information but were aware of the nature of the study; this circumstance introduced potential bias. It could also be argued that selection of particular CTP sections biases CTP detection by limiting the number of sections to a region of interest and unblinds readers. While CTP scans were directed to the posterior fossa or supratentorium by the attending neurologist, depending on the clinical presentation, standard protocol–mandated anatomic landmarks were used for every acquisition. While neuroanatomic localization may be useful in lesion detection, exact lesion determination is frequently not possible and the requirement of both a positive score and correct location reduces the possibility of bias. Prior strategies in acute stroke work-up necessitate MR imaging within a week of ictus in the context of a clinically significant vessel stenosis, placing pressure on limited and costly resources in busy acute stroke centers. A CTP study with positive findings may circumvent this need. CTP studies with negative findings will still require early MR imaging for carotid endarterectomy planning, but the number of patients requiring MR imaging should be reduced by 16%–33% compared with NCCT and CTA approaches, respectively. LI classification using DWI/ADC may potentially miss patients due to the known reduced DWI sensitivity for posterior fossa infarcts leading to both false-positive and -negative studies. However, the bias is systematic, applying equally to all sequences. Although the readers were still within their fellowship period, they had significant experience in stroke imaging due to

high-volume exposure at a tertiary stroke center, allowing generalizability to other readers.

CONCLUSIONS

Multimodal CT including CTP has an estimated sensitivity of 42% in the detection of LI and increases the diagnostic performance 5.1- and 2.4-fold over NCCT and/or CTA-SI.

ACKNOWLEDGMENTS

We gratefully acknowledge our radiographic technicians without whom this work would not be possible.

Disclosures: Mark Boulos—UNRELATED: Other: clinical research fellowship in stroke and sleep medicine, Comments: The clinical research fellowship was funded by the Canadian Institutes of Health Research, the Heart and Stroke Foundation, and the Canadian Stroke Network. Sean P. Symons—UNRELATED: Grants/Grants Pending: Brain Tumour Foundation of Canada*; Payment for Lectures (including service on Speakers Bureaus): Biogen (MS lectures). *Money paid to the institution.

REFERENCES

1. Kolominsky-Rabas PL, Weber M, Gefeller O, et al. **Epidemiology of ischemic stroke subtypes according to TOAST criteria: incidence, recurrence, and long-term survival in ischemic stroke subtypes: a population-based study.** *Stroke* 2001;32:2735–40
2. Wardlaw JM, Smith C, Dichgans M. **Mechanisms of sporadic cerebral small vessel disease: insights from neuroimaging.** *Lancet Neurol* 2013;12:483–97
3. Norrving B. **Long-term prognosis after lacunar infarction.** *Lancet Neurol* 2003;2:238–45
4. National Institute of Neurological Disorders and Stroke rt-PA Stroke Study Group. **Tissue plasminogen activator for acute ischemic stroke.** *N Engl J Med* 1995;333:1581–87
5. IST-3 collaborative group. **The benefits and harms of intravenous thrombolysis with recombinant tissue plasminogen activator within 6 h of acute ischaemic stroke (the third International Stroke Trial [IST-3]): a randomised controlled trial.** *Lancet* 2012;379:2352–63
6. Fuentes B, Martínez-Sánchez P, Alonso de Leciana M, et al. **Efficacy of intravenous thrombolysis according to stroke subtypes: the Madrid Stroke Network data.** *Eur J Neurol* 2012;19:1568–74
7. Pantoni L, Fierini F, Poggesi A. **Thrombolysis in acute stroke patients with cerebral small vessel disease.** *Cerebrovasc Dis* 2014;37:5–13
8. Chalela JA, Ezzeddine M, Latour L, et al. **Reversal of perfusion and diffusion abnormalities after intravenous thrombolysis for a lacunar infarction.** *J Neuroimaging* 2003;13:152–54
9. Wessels T, Röttger C, Jauss M, et al. **Identification of embolic stroke patterns by diffusion-weighted MRI in clinically defined lacunar stroke syndromes.** *Stroke* 2005;36:757–61
10. Young KC, Benesch CG, Jahromi BS. **Cost-effectiveness of multimodal CT for evaluating acute stroke.** *Neurology* 2010;75:1678–85
11. Hopyan J, Ciarallo A, Dowlatshahi D, et al. **Certainty of stroke diagnosis: incremental benefit with CT perfusion over noncontrast CT and CT angiography.** *Radiology* 2010;255:142–53
12. Campbell BCV, Weir L, Desmond PM, et al. **CT perfusion improves diagnostic accuracy and confidence in acute ischaemic stroke.** *J Neurol Neurosurg Psychiatry* 2013;84:613–18
13. Yamada M, Yoshimura S, Kaku Y, et al. **Prediction of neurologic deterioration in patients with lacunar infarction in the territory of the lenticulostriate artery using perfusion CT.** *AJNR Am J Neuroradiol* 2004;25:402–08
14. Poppe AY, Coutts SB, Kosior J, et al. **Normal magnetic resonance perfusion-weighted imaging in lacunar infarcts predicts a low risk of early deterioration.** *Cerebrovasc Dis* 2009;28:151–56
15. Gerraty RP, Parsons MW, Barber PA, et al. **Examining the lacunar**

- hypothesis with diffusion and perfusion magnetic resonance imaging. *Stroke* 2002;33:2019–24
16. Fisher CM. **Lacunae: small, deep cerebral infarcts.** *Neurology* 1965;15:774–84
 17. Lansberg MG, Thijs VN, O'Brien MW, et al. **Evolution of apparent diffusion coefficient, diffusion-weighted, and T2-weighted signal intensity of acute stroke.** *AJNR Am J Neuroradiol* 2001;22:637–44
 18. Potter GM, Marlborough FJ, Wardlaw JM. **Wide variation in definition, detection, and description of lacunar lesions on imaging.** *Stroke* 2011;42:359–66
 19. Doege CA, Kerskens CM, Romero BI, et al. **Assessment of diffusion and perfusion deficits in patients with small subcortical ischemia.** *AJNR Am J Neuroradiol* 2003;24:1355–63
 20. Restrepo L, Jacobs MA, Barker PB, et al. **Etiology of perfusion-diffusion magnetic resonance imaging mismatch patterns.** *J Neuroimaging* 2005;15:254–60
 21. Brenner DJ, Hall EJ. **Computed tomography: an increasing source of radiation exposure.** *N Engl J Med* 2007;357:2277–84
 22. DeLong ER, DeLong DM, Clarke-Pearson DL. **Comparing the areas under two or more correlated receiver operating characteristic curves: a nonparametric approach.** *Biometrics* 1988;44:837–45
 23. Zhou X-H, Obuchowski NA, McClish DK. **Comparing the accuracy of two diagnostic tests.** In: *Statistical Methods in Diagnostic Medicine*, 2nd ed. Hoboken: John Wiley & Sons; 2011:165–92
 24. Barnhart HX, Williamson JM. **Weighted least-squares approach for comparing correlated kappa.** *Biometrics* 2002;58:1012–19
 25. Bezerra DC, Sharrett AR, Matsushita K, et al. **Risk factors for lacune subtypes in the Atherosclerosis Risk in Communities (ARIC) study.** *Neurology* 2012;78:102–08
 26. Mohr JP, Caplan LR, Melski JW, et al. **The Harvard Cooperative Stroke Registry: a prospective registry.** *Neurology* 1978;28:754–62
 27. Nakamura K, Saku Y, Ibayashi S, et al. **Progressive motor deficits in lacunar infarction.** *Neurology* 1999;52:29–33
 28. Tei H, Uchiyama S, Ohara K, et al. **Deteriorating ischemic stroke in 4 clinical categories classified by the Oxfordshire Community Stroke Project.** *Stroke* 2000;31:2049–54
 29. Shobha N, Fang J, Hill MD. **Do lacunar strokes benefit from thrombolysis? Evidence from the registry of the Canadian Stroke Network.** *Int J Stroke* 2013;8(suppl A100):45–49
 30. Mustanoja S, Meretoja A, Putaala J, et al. **Outcome by stroke etiology in patients receiving thrombolytic treatment: descriptive subtype analysis.** *Stroke* 2011;42:102–06
 31. Lee SJ, Saver JL, Liebeskind DS, et al. **Safety of intravenous fibrinolysis in imaging-confirmed single penetrator artery infarcts.** *Stroke* 2010;41:2587–91
 32. Murphy A, So A, Lee TY, et al. **Low dose CT perfusion in acute ischemic stroke.** *Neuroradiology* 2014;56:1055–62
 33. Wintermark M, Sanelli PC, Albers GW, et al. **Imaging recommendations for acute stroke and transient ischemic attack patients: a joint statement by the American Society of Neuroradiology, the American College of Radiology, and the Society of NeuroInterventional Surgery.** *AJNR Am J Neuroradiol* 2013;34:E117–27

Statin Therapy Does Not Affect the Radiographic and Clinical Profile of Patients with TIA and Minor Stroke

N. Asdaghi, J.I. Coulter, J. Modi, M.C. Camden, A. Qazi, M. Goyal, T. Rundek, and S.B. Coutts



ABSTRACT

BACKGROUND AND PURPOSE: Acute statin therapy improves neurologic outcome and diminishes infarct growth in animal models of stroke. Clinical studies suggest that premonitory and early statin use is associated with improved outcome after major stroke. We studied the association between statin therapy and radiographic and clinical outcomes in patients with high-risk TIA and minor stroke.

MATERIALS AND METHODS: Patients with high-risk TIA and minor stroke (NIHSS ≤ 3) were prospectively enrolled within 24 hours of symptom onset. Patients were followed clinically for 3 months, and a subset had a repeat MR imaging at 90 days.

RESULTS: Of 418 patients, 23% were prescribed statins before their stroke. Statins were continued in 20% and initiated in 42%. Patients on prior statin therapy were older and more hypertensive, treated with aspirin, and more likely to have symptomatic carotid disease compared with those not on statin. Adjusting for these differences, prior statin treatment was not associated with DWI positivity (adjusted OR = 1.3; 95% CI, 0.77–2.1; $P = .32$) or smaller median baseline infarct volume, 1.1 mL (interquartile range = 4) versus 1 mL (interquartile range = 2.5; $P = .56$). Early or continued treatment with statins did not improve the risk of clinical deterioration (adjusted OR = 0.66; 95% CI, 0.27–1.6; $P = .35$) or poor functional outcome at 3 months (adjusted OR = 0.66; 95% CI, 0.35–1.24; $P = .19$).

CONCLUSIONS: Prestroke or early-stroke statin therapy was not associated with a reduction in the number of DWI lesions, infarct volume, or improved clinical or functional outcome at 3 months. The effect of acute statin treatment in patients with ischemic stroke/TIA remains unclear and needs further investigation.

ABBREVIATIONS: CATCH = CT and MR Imaging in the Triage of TIA and Minor Cerebrovascular Events to Identify High Risk Patients; IQR = interquartile range

The benefit from 3-hydroxy-3-methylglutaryl coenzyme-A reductase inhibitors (statins) to prevent fatal and nonfatal stroke in patients with transient ischemic attack and all severity of strokes has been established in a randomized controlled trial.¹ Beyond their lipid-lowering property, these drugs have been shown to have a neuroprotective effect, with smaller infarct sizes and better functional outcome on pretreatment with statins in animal models of stroke.^{2–4} Nevertheless, the results of clinical

studies on the effects of early initiation, continuation, or withdrawal of statin therapy on clinical outcomes have been conflicting.^{5,6} In one study, acute discontinuation of statins after the ischemic event conferred a higher risk of early neurologic deterioration and increased death and dependency at 90 days.⁵ In contrast, the functional outcome of patients randomized to early statin treatment versus placebo was no different in a pilot randomized controlled trial.⁶ Observational studies have also shown conflicting reports, with some reporting a reduction in mortality⁷ and improvement in functional outcomes^{8–10} in patients with stroke pretreated or acutely treated with statins. Other studies have shown worse outcomes in patients on statins at stroke onset.¹¹ A recent meta-analysis found improved functional outcome in patients on statins at the time of stroke onset.¹⁰

Patients with TIA and minor stroke have an early unstable clinical course, with most recurrent ischemic events occurring in the first 48 hours after symptom onset.^{12–14} If statins have a neuroprotective effect, it would be important to see an effect in this population. However, the results of the Fast Assessment of Stroke and TIA to Prevent Early Recurrence trial did not support the

Received July 21, 2014; accepted after revision January 6, 2015.

From the Departments of Clinical Neurosciences (N.A., J.I.C., M.C.C., A.Q., M.G., S.B.C.) and Radiology (J.M., M.G., S.B.C.) and Hotchkiss Brain Institute (S.B.C.), University of Calgary, Calgary, Alberta, Canada; and Division of Cerebrovascular Disease (N.A., T.R.), Department of Neurology, Miller School of Medicine, University of Miami, Miami, Florida.

The CATCH study was funded by grants from the Canadian Institute of Health Research (MOP-89937) and a Pfizer Cardiovascular Research Award.

Please address correspondence to Negar Asdaghi, MD, FRCPC, Cerebrovascular Division, Department of Neurology, Miller School of Medicine, University of Miami, Clinical Research Building, 1120 NW 14th St, 13th floor, Miami, FL 33136; e-mail: nasdaghi@med.miami.edu

Indicates open access to non-subscribers at www.ajnr.org

<http://dx.doi.org/10.3174/ajnr.A4257>

hypothesis that acute statin therapy prevents early stroke recurrence.¹⁵ In fact, there was a nonsignificant trend toward higher 90-day ischemic events in the statin arm. A recent multicenter analysis of patients with TIA showed a decrease in the rate of stroke recurrence in patients with carotid stenosis with urgent treatment or pretreatment with statin therapy.¹⁶ However, the authors did not find a reduction in the recurrent stroke rate in patients without carotid stenosis. To date, a clinical study assessing the effects of statin therapy on acute MR imaging findings of patients with TIA and minor stroke has not been undertaken.

We therefore aimed to determine the effects of premorbid or early-initiated statin therapy on radiographic and clinical outcomes in a prospective cohort of patients with TIA and minor stroke.

MATERIALS AND METHODS

Patients

We included patients who underwent MR imaging in the study entitled CT and MR Imaging in the Triage of TIA and Minor Cerebrovascular Events to Identify High Risk Patients (CATCH).¹⁷ The methods of the CATCH study have previously been published. Briefly, patients with high-risk TIA (focal weakness or speech disturbance lasting ≥ 5 minutes) or minor ischemic stroke (with an initial National Institute of Health Stroke Scale score of ≤ 3) were prospectively enrolled. All patients presented to the Foothills Medical Centre, Calgary, Alberta, Canada. Informed consent was obtained before enrollment. All patients underwent MR imaging, standard clinical and demographic information was recorded, and secondary stroke-prevention measures were implemented in accordance with current practice guidelines.¹⁸

Baseline CT and MR Imaging Protocol

All patients underwent a noncontrast CT of the head, followed immediately by CT angiography of the circle of Willis and neck from the aortic arch to skull vertex. CT scans were performed on a 64-section scanner (Somatom Sensation 64; Siemens, Erlangen, Germany). Patients underwent MR imaging brain scans as soon as possible. Patients were imaged using either a 3T scanner ($n = 349$) (Discovery 750; GE Healthcare, Milwaukee, Wisconsin) or a 1.5T MR imaging scanner ($n = 69$) (Avanto; Siemens). Sequences included sagittal T1, axial T2, and axial fluid-attenuated inversion recovery. Acute ischemic lesions were identified on diffusion-weighted imaging. Follow-up MR imaging was performed in a subpopulation of patients who had their original MR imaging on the 3T scanner at day 90.

Image Analysis

Details of this assessment have been previously reported.¹⁹ Briefly, MR imaging sequences (DWI/ADC, FLAIR, and T2) were reviewed for the presence of ischemic lesions at each time point. DWI hyperintense lesion borders were defined by using a semi-automated threshold-intensity technique. We referenced these lesions to the corresponding areas on the apparent diffusion coefficient maps to avoid selecting regions of T2 shinethrough. The $b = 1000$ image was used as the primary template because quantitative ADC thresholds tend to vary depending on the time after stroke onset and concurrent perfusion status. Planimetric DWI and FLAIR lesion volume measurement was performed by using

Quantomo software.²⁰ CTAs were assessed for the presence of any intra- or extracranial vessel occlusion or stenosis of $\geq 50\%$ ipsilateral to the clinically relevant ischemic brain tissue (positive CTA finding). Symptomatic carotid disease was defined as a TIA or minor stroke referable to an extracranial carotid artery with $\geq 50\%$ stenosis. All images were assessed by a neuroradiologist who remained blinded to the results of the other imaging modalities and was given information regarding the clinical symptoms only.

Radiographic and Clinical Outcomes

Radiographic worsening was defined as evidence of either infarct growth (a priori defined as contiguous growth of the initial infarct by ≥ 2 mL)¹⁹ or infarct recurrence (development of a new ischemic lesion) on follow-up FLAIR imaging at day 90 with or without any clinical manifestations.

Poor functional outcome was defined as mRS ≥ 2 at day 90.²¹ Recurrent clinical events (stroke progression or a distinct recurrent stroke) were a priori defined²² as a functional deterioration in neurologic status of vascular origin lasting 24 hours or a new sudden focal neurologic deficit of vascular origin lasting at least 24 hours that was not thought to be secondary to other nonvascular factors such as drugs, fever, or infection.

Statistical Analysis

Statistical analyses were performed by using Statistical Package for Social Sciences, Version 20.0 (IBM, Armonk, New York). The primary outcome was the rate of DWI positivity and the median acute infarct volume in those with positive lesions on DWI. Secondary outcomes were the rate of recurrent stroke (imaging and clinical) and poor functional outcome. Outcomes were stratified by whether the patient was known to be on a statin at the time of the presenting event. Clinical outcomes (clinical deterioration, either progression of previous symptoms or a new recurrent stroke, and poor functional outcome) and radiographic outcomes (DWI positivity on baseline MR imaging, radiographic infarct progression, and radiographic recurrence) were reported by using multivariate regression analysis, adjusting for baseline differences in age, hypertension, diabetes, prior aspirin use, and symptomatic internal carotid artery disease. For the secondary outcomes, both statin use at the time of the presenting event and early initiation of a statin were assessed. Clinical and radiographic outcomes were reported by using multilevel regression analysis, adjusting for differences in age, sex, hypertension, and baseline positive CTA and DWI findings. Data are reported by using standard descriptive statistics. DWI volumes were log-transformed before analysis because the volumes were not normally distributed.

RESULTS

A total of 418 patients were included in this substudy during 29 months, of whom 98% completed the clinical follow-up at day 90. The median time from index event to CT/CTA was 5.2 hours (IQR = 6), and to MR imaging, it was 17.5 hours (12.3). At the time of the index event, 23% (96/418) of patients were on statin therapy, and this was continued in 89% (85/96). Patients on prior statin therapy were older and more hypertensive, had more diabetes mellitus, and were more likely to be on aspirin and have symptomatic extracranial carotid disease (Table 1).

Baseline MR Imaging Findings of Patients Based on Premorbid Statin Therapy

Fifty-seven percent (238/418) of patients had an acute ischemic lesion on a baseline DWI study, of whom 26% (61/238) were on statin therapy. Prior statin treatment was not associated with lower rates of DWI positivity (Adjusted OR = 1.3; 95% CI, 0.77–2.1; $P = .32$). The median DWI volume was 1.045 mL (interquartile range [IQR] = 3.55) in those with an acute infarct. Premorbid statin therapy was not associated with a smaller DWI lesion (median = 1 mL [IQR = 2.5], geometric mean = 1.1 mL versus median = 1.1 mL [IQR = 4], geometric mean = 1.3 mL, $P = .56$).

Clinical and Radiographic Outcome Based on Premorbid Statin Therapy

Ninety-eight percent (410/418) of patients had 90-day clinical follow-up. Clinical deterioration (progression of symptoms or a distinct recurrent stroke) occurred in 7% (29/410) by day 90. There was no difference in the rate of clinical deterioration in those on prior statin treatment (7.3%) versus those not on it (7%; adjusted OR = 1.13; 95% CI, 0.43–3.01; $P = .92$). A distinct recurrent stroke occurred in 3.2% (13/410), and symptom progression, in 4.1% (17/410). There was no difference in the rate of

symptom progression (adjusted OR = 0.44; 95% CI, 0.09–2.2; $P = .32$) or clinical stroke recurrence (adjusted OR = 2.06; 95% CI, 0.57–7.4; $P = .26$) in patients previously on versus those not on statins.

Poor functional outcome at 90 days was seen in 15% (62/410) of patients. Pretreatment with statins did not affect the rate of poor functional outcome (adjusted OR = 1.43; 95% CI, 0.77–2.67; $P = .25$).

Fifty-two percent (217/418) of patients had follow-up MR imaging at day 90 in this study. Radiographic deterioration (a new ischemic infarct or infarct growth) was seen in 13.4% (29/217) of patients. There was no difference in the rate of radiographic deterioration in those on premorbid statin (adjusted OR = 2.32; 95% CI, 0.88–6.13; $P = .89$).

The Effects of Continued or Early Initiation of Statin Therapy on Clinical and Radiographic Outcomes

Sixty percent (251/418) of patients in the study had acute statin treatment either initiated ($n = 166$) or continued ($n = 85$). The median time from symptom onset to statin initiation was 12 hours (IQR = 0–24 hours). Fifty percent of patients had statins initiated in the emergency department. The patients in the statin group were older, were a high percentage male, were more likely hypertensive, had more atherosclerotic disease (symptomatic relevant intra- or extracranial occlusion or stenosis $\geq 50\%$), and had a higher rate of DWI positivity at baseline (Table 2).

Poor functional outcome at 90 days was seen in 15.7% (39/249) of those on statin treatment versus 14.3% (23/161) in those without statin therapy (adjusted OR = 0.66; 95% CI, 0.35–1.24; $P = .19$). There was no difference in the rate of any clinical deterioration in the statin-treated group versus those not on statin treatment (adjusted OR = 0.66; 95% CI, 0.27–1.6; $P = .35$). The results did not change when the analysis was restricted to distinct recurrent stroke alone (adjusted OR = 0.47; 95% CI, 0.14–1.6; $P = .23$). Similarly, in patients who had follow-up MR imaging at 90 days, the rate of radiographic worsening (either new ischemic recurrence or infarct growth) was not different in patients who were treated with statin versus those who were not after the index event (adjusted OR = 1.59; 95% CI, 0.6–4.15; $P = .34$).

Effects of Statin Therapy on Ischemic Outcome Based on the Mechanism of Strokes

Patients were more likely to be treated with statins (either started or continued) if the mechanism of their event was large-artery atherosclerosis (adjusted OR = 5.24; 95% CI, 1.9–13.9; $P < .001$). A total of 48.5% (203/418) had some degree of carotid disease, and 9.3% (39/418) had a significant symptomatic extracranial carotid stenosis (stenosis of $\geq 50\%$) on CTA, 85% (33/39) of whom were treated with statins. Carotid revascularization was performed in 19/39 (8 endarterectomies and 11 stent placements). Treatment with statins did not affect the rate of clinical (relative risk = 0.3; 95% CI, 0.08–1.05; $P = .06$) or ra-

Table 1: Baseline clinical and radiographic characteristics of patients based on prior statin treatment

Baseline Characteristics	Prior Statin (n = 96)	No Prior Statin (n = 322)	P Value
Age (yr) (median) (IQR)	73 (14)	66 (24)	<.001
Sex (% male)	68% (65/96)	58% (187/322)	.09
Smoking	15% (14/96)	15% (49/322)	.87
Hypertension (%)	73% (70/96)	50% (159/322)	<.001
Diabetes mellitus (%)	19% (18/96)	12% (39/322)	.044
Prior ASA treatment (%)	65% (62/96)	22% (71/322)	<.001
Symptomatic carotid disease ^a	19% (18/96)	7% (21/322)	.001
Symptomatic intracranial disease ^b	12% (11/96)	21% (67/322)	.174
Positive CTA finding ^c	31% (30/96)	27% (88/322)	.45
DWI-positive	64% (61/96)	55% (177/322)	.08
DWI infarct volume (mL) (median) (IQR)	1.0 (2.5)	1.1 (4)	.56

Note:—ASA indicates aspirin.

^a Symptomatic carotid disease: extracranial carotid stenosis of $\geq 50\%$.

^b Symptomatic intracranial disease: symptomatic intracranial vascular occlusion or stenosis of $\geq 50\%$.

^c Positive CTA finding: relevant intra- or extracranial occlusion or stenosis of $\geq 50\%$.

Table 2: Baseline clinical and radiographic characteristics stratified by statin treatment (statin therapy either continued or acutely started) or not

Baseline Characteristics	On Statin Treatment ^a (n = 251)	No Statin Treatment (n = 167)	P Value
Age (yr) (median) (IQR)	70 (18)	62 (25)	<.001
Hypertension (%)	63% (159/251)	42% (70/167)	<.001
Sex (% male)	65% (163/251)	53% (89/167)	.01
Smoking	17% (42/251)	13% (21/167)	.24
Diabetes mellitus (%)	15% (38/251)	11% (19/167)	.38
Symptomatic extracranial carotid disease $\geq 50\%$ (%)	13% (33/251)	4% (6/167)	.001
Symptomatic intracranial vascular occlusion/ stenosis $\geq 50\%$ (%)	25% (63/251)	15% (25/167)	.013
Positive CTA finding ^b	36% (89/251)	17% (29/167)	<.001
DWI-positive on baseline MRI	69% (172/251)	40% (66/167)	<.001
DWI infarct volume (mL) (median) (IQR)	1.1 (3.8)	1.0 (2.9)	.48

^a Statin treatment either acutely started or continued.

^b Positive CTA finding: relevant intra- or extracranial occlusion or stenosis of $\geq 50\%$.

diographic (adjusted OR = 0.42; 95% CI, 0.06–2.69; $P = .36$) deterioration in this subgroup with symptomatic carotid disease. Similarly, the rate of poor functional outcome at day 90 was not different in this subgroup with or without statin therapy (adjusted OR = 0.67; 95% CI, 0.22–2.03; $P = .48$).

DISCUSSION

In this prospective study of patients with high-risk TIA and minor stroke, we did not find that pretreatment with statins reduced the rate of DWI positivity or the volume of acute ischemic lesions. Similarly, neither pretreatment nor acute statin initiation conferred a beneficial effect on functional, clinical, or radiographic outcome. In keeping with data from previous studies,¹⁶ patients on premorbid statin therapy were older and generally had more vascular risk factors than their statin-naïve counterparts. If one adjusted for these differences, premorbid or early statin initiation did not improve clinical or radiographic outcome in this population.

Early initiation of preventive measures is associated with a reduction of further vascular events and better clinical outcome in patients with TIA.^{23,24} Although statins were part of the treatment regimen in these studies, their specific effect was not studied in isolation. The effects of pretreatment with statins on recurrent vascular events were studied in a recent multicenter analysis of patients with TIA.¹⁶ In this study, statin pretreatment was associated with reduced stroke risk in the subtype of patients with TIA with symptomatic carotid stenosis. We did not find similar results in our study. However, this outcome may be due to the small number of patients with symptomatic carotid disease and the associated high rate of statin use in our population.

In rat models of stroke, pretreatment or acute treatment with statins has been shown to reduce the infarct size and improve neurologic outcome.^{25–27} It is postulated that in the acute ischemic phase, the pleiotropic effects of statins have a bigger role in prevention of recurrent vascular events rather than their effects on low-density lipoprotein reduction.²⁸ Some pleiotropic properties of statins include inhibition of the inflammatory response, plaque stabilization, improved cerebral vasoreactivity, improved endothelial function, and increased nitric oxide bioavailability.²⁹ The acute anti-inflammatory effects of statins resulting in plaque stabilization are thought to be the basis for prevention of recurrent vascular events in coronary artery disease.^{30,31}

The effects of statin therapy on infarct size have been previously reported in retrospective studies.^{32,33} In one study, a smaller infarct volume was associated with the interaction between statin pretreatment and the presence of diabetes in patients with stroke.³² A different study identified statin therapy, age, and a recent history of TIA as independent factors associated with smaller DWI volume.³³ In both studies, patients with TIA were excluded. In our study, pretreatment with statins did not improve the acute radiologic profile of patients with high-risk TIA/minor stroke either by reducing the rate of DWI positivity or the infarct volume. One possible explanation is that the infarct size in this population is so small to begin with that detecting a meaningful difference with statin pretreatment would be difficult.

Multiple groups have evaluated the association between statin pretreatment and the severity of stroke.^{7,34,35} Similar to ours,

findings in most studies do not suggest a beneficial role for statins in reducing the severity of clinical symptoms at presentation.^{7,35} Previous observations have shown a trend toward better functional outcomes^{34–36} and a reduction in ischemic progression/recurrent events⁷ or in-hospital mortality in patients pretreated with statins.⁷ Furthermore, a recent meta-analysis of observational and randomized studies looking only at patients receiving statins at the time of ischemic stroke versus those who were not, showed an improvement in the functional independence rate and survival in the statin-treated subgroup.¹⁰ In our study, however, statin therapy did not confer an improvement in functional outcome in patients with TIA and minor stroke. The previously reported results might have been confounded because in the meta-analysis,¹⁰ the observed benefit from acute statin therapy disappeared after adjusting for differences in age, severity of stroke, and vascular risk factors.

Our study is limited due to the lack of knowledge regarding the details of statin treatment at the time of presentation (duration of treatment and type and doses of medication). Pretreatment with statins was adjudicated on the basis of the patient having an active prescription at the time of their index event. In addition, our study is limited by inclusion of subjects in whom we were able to obtain an MR imaging, making our cohorts nonsequential. In addition, in our study, patients were assessed early and secondary preventive measures were implemented in a timely fashion, which may explain the low outcome rates in our population and this may have reduced our study power. However, these low outcome rates have also been reported in previous studies with similar rigorous and early treatment initiation in a TIA/minor stroke population and are not unique to our study.^{23,24}

CONCLUSIONS

In this prospective imaging study of high-risk TIA and minor stroke, we did not find a reduction in the rate or the size of acute infarct with pretreatment with statins. We also found no difference in recurrent stroke rates in patients either previously on statins or acutely started on statins at the time of their event. The effect of acute statin therapy in patients with TIA and minor stroke requires further study.

ACKNOWLEDGMENTS

The authors wish to thank Dr Michael D. Hill for his statistical support.

Disclosures: Negar Asdaghi—UNRELATED: Other: Supported by a fellowship from the Canadian Institutes for Health Research and a research allowance from the Vancouver General Hospital and University of British Columbia hospital foundation. Tatjana Rundek—UNRELATED: Grants/Grants Pending: National Institutes of Health,* American Heart Association*; Other: received support from the National Institute of Neurological Diseases and Stroke K24 award NS 062737. Mayank Goyal—UNRELATED: Consultancy: Covidien, Comments: for trial design and teaching activities; Grants/Grants Pending: Covidien,* Comments: partial funding of Endovascular Treatment for Small Core and Proximal Occlusion Ischemic Stroke trial. Shelagh B. Coutts—RELATED: Grant: Canadian Institute of Health Research,* Pfizer Cardiovascular Research Award,* Comments: grant funding for the CATCH study; UNRELATED: Grants/Grants Pending: Genome Canada,* Institute of Health Research,* Comments: grant funding for research. Spectrometry for TIA Rapid Assessment study, Institute of Health Research grant funding for Diagnosis Of Uncertain-origin Benign Transient neurological symptoms study; Other: salary support from the Alberta-Innovates-Health Solutions and the Heart and Stroke Foundation of the Distinguished Clinician Scientist Award of Canada, supported in partnership with the Ca-

REFERENCES

1. Amarenco P, Bogousslavsky J, Callahan A 3rd, et al. **High-dose atorvastatin after stroke or transient ischemic attack.** *N Engl J Med* 2006;355:549–59
2. Amin-Hanjani S, Stagliano NE, Yamada M, et al. **Mevastatin, an HMG-CoA reductase inhibitor, reduces stroke damage and up-regulates endothelial nitric oxide synthase in mice.** *Stroke* 2001;32:980–86
3. Kawashima S, Yamashita T, Miwa Y, et al. **HMG-CoA reductase inhibitor has protective effects against stroke events in stroke-prone spontaneously hypertensive rats.** *Stroke* 2003;34:157–63
4. Endres M, Laufs U, Huang Z, et al. **Stroke protection by 3-hydroxy-3-methylglutaryl (HMG)-CoA reductase inhibitors mediated by endothelial nitric oxide synthase.** *Proc Natl Acad Sci U S A* 1998;95:8880–85
5. Blanco M, Nombela F, Castellanos M, et al. **Statin treatment withdrawal in ischemic stroke: a controlled randomized study.** *Neurology* 2007;69:904–10
6. Montaner J, Chacon P, Krupinski J, et al. **Simvastatin in the acute phase of ischemic stroke: a safety and efficacy pilot trial.** *Eur J Neurol* 2008;15:82–90
7. Elkind MS, Flint AC, Sciacca RR, et al. **Lipid-lowering agent use at ischemic stroke onset is associated with decreased mortality.** *Neurology* 2005;65:253–58
8. Sacco S, Toni D, Bignamini AA, et al. **Effect of prior medical treatments on ischemic stroke severity and outcome.** *Funct Neurol* 2011;26:133–39
9. Moonis M, Kane K, Schwiderski U, et al. **HMG-CoA reductase inhibitors improve acute ischemic stroke outcome.** *Stroke* 2005;36:1298–300
10. Ní Chróinín D, Asplund K, Asberg S, et al. **Statin therapy and outcome after ischemic stroke: systematic review and meta-analysis of observational studies and randomized trials.** *Stroke* 2013;44:448–56
11. Pikiša S, Cvetko D, Malojčić B, et al. **A population-based prospective 24-month study of stroke: incidence and 30-day case-fatality rates of first-ever strokes in Croatia.** *Neuroepidemiology* 2012;38:164–71
12. Johnston SC, Gress DR, Browner WS, et al. **Short-term prognosis after emergency department diagnosis of TIA.** *JAMA* 2000;284:2901–06
13. Hill MD, Yiannakoulis N, Jeerakathil T, et al. **The high risk of stroke immediately after transient ischemic attack: a population-based study.** *Neurology* 2004;62:2015–20
14. Coutts SB, Hill MD, Campos CR, et al. **Recurrent events in transient ischemic attack and minor stroke: what events are happening and to which patients?** *Stroke* 2008;39:2461–66
15. Kennedy J, Hill MD, Ryckborst KJ, et al. **Fast assessment of stroke and transient ischaemic attack to prevent early recurrence (FASTER): a randomised controlled pilot trial.** *Lancet Neurol* 2007;6:961–69
16. Merwick A, Albers GW, Arsava EM, et al. **Reduction in early stroke risk in carotid stenosis with transient ischemic attack associated with statin treatment.** *Stroke* 2013;44:2814–20
17. Coutts SB, Modi J, Patel SK, et al. **CT/CT angiography and MRI findings predict recurrent stroke after transient ischemic attack and minor stroke: results of the prospective CATCH study.** *Stroke* 2012;43:1013–17
18. Lindsay P, Bayley M, McDonald A, et al. **Toward a more effective approach to stroke: Canadian Best Practice Recommendations for Stroke Care.** *CMAJ* 2008;178:1418–25
19. Asdaghi N, Hill MD, Coulter JI, et al. **Perfusion MR predicts outcome in high-risk transient ischemic attack/minor stroke: a derivation-validation study.** *Stroke* 2013;44:2486–92
20. Kosior JC, Idris S, Dowlatshahi D, et al. **Quantomo: validation of a computer-assisted methodology for the volumetric analysis of intracerebral haemorrhage.** *Int J Stroke* 2011;6:302–05
21. Coutts SB, Modi J, Patel SK, et al. **What causes disability after transient ischemic attack and minor stroke? Results from the CT And MRI in the Triage of TIA and Minor Cerebrovascular Events to Identify High Risk Patients (CATCH) Study.** *Stroke* 2012;43:3018–22
22. Horton M, Modi J, Patel SK, et al. **Refinement of imaging predictors of recurrent events following transient ischemic attack and minor stroke.** *PLoS One* 2013;8:e65752
23. Lavallée PC, Meseguer E, Abboud H, et al. **A transient ischaemic attack clinic with round-the-clock access (SOS-TIA): feasibility and effects.** *Lancet Neurol* 2007;6:953–60
24. Rothwell PM, Giles MF, Chandratheva A, et al. **Effect of urgent treatment of transient ischaemic attack and minor stroke on early recurrent stroke (EXPRESS study): a prospective population-based sequential comparison.** *Lancet* 2007;370:1432–42
25. Engelhorn T, Doerfler A, Heusch G, et al. **Reduction of cerebral infarct size by the AT1-receptor blocker candesartan, the HMG-CoA reductase inhibitor rosuvastatin and their combination: an experimental study in rats.** *Neurosci Lett* 2006;406:92–96
26. Saito T, Nito C, Ueda M, et al. **Continuous oral administration of atorvastatin ameliorates brain damage after transient focal ischemia in rats.** *Life Sci* 2014;94:106–14
27. Cui L, Zhang X, Yang R, et al. **Neuroprotection of early and short-time applying atorvastatin in the acute phase of cerebral ischemia: down-regulated 12/15-LOX, p38MAPK and cPLA2 expression, ameliorated BBB permeability.** *Brain Res* 2010;1325:164–73
28. Laufs U. **Beyond lipid-lowering: effects of statins on endothelial nitric oxide.** *Eur J Clin Pharmacol* 2003;58:719–31
29. Vaughan CJ, Murphy MB, Buckley BM. **Statins do more than just lower cholesterol.** *Lancet* 1996;348:1079–82
30. Kinlay S, Schwartz GG, Olsson AG, et al. **Effect of atorvastatin on risk of recurrent cardiovascular events after an acute coronary syndrome associated with high soluble CD40 ligand in the Myocardial Ischemia Reduction with Aggressive Cholesterol Lowering (MIRACL) study.** *Circulation* 2004;110:386–91
31. Ray KK, Cannon CP, McCabe CH, et al. **Early and late benefits of high-dose atorvastatin in patients with acute coronary syndromes: results from the PROVE IT-TIMI 22 trial.** *J Am Coll Cardiol* 2005;46:1405–10
32. Nicholas JS, Swearingen CJ, Thomas JC, et al. **The effect of statin pretreatment on infarct volume in ischemic stroke.** *Neuroepidemiology* 2008;31:48–56
33. Shook SJ, Gupta R, Vora NA, et al. **Statin use is independently associated with smaller infarct volume in nonlacunar MCA territory stroke.** *J Neuroimaging* 2006;16:341–46
34. Deplanque D, Masse I, Lefebvre C, et al. **Prior TIA, lipid-lowering drug use, and physical activity decrease ischemic stroke severity.** *Neurology* 2006;67:1403–10
35. Martí-Fàbregas J, Gomis M, Arboix A, et al. **Favorable outcome of ischemic stroke in patients pretreated with statins.** *Stroke* 2004;35:1117–21
36. Jonsson N, Asplund K. **Does pretreatment with statins improve clinical outcome after stroke? A pilot case-referent study.** *Stroke* 2001;32:1112–15

Optimal MRI Sequence for Identifying Occlusion Location in Acute Stroke: Which Value of Time-Resolved Contrast-Enhanced MRA?

A. Le Bras, H. Raoult, J.-C. Ferré, T. Ronzière, and J.-Y. Gauvrit



ABSTRACT

BACKGROUND AND PURPOSE: Identifying occlusion location is crucial for determining the optimal therapeutic strategy during the acute phase of ischemic stroke. The purpose of this study was to assess the diagnostic efficacy of MR imaging, including conventional sequences plus time-resolved contrast-enhanced MRA in comparison with DSA for identifying arterial occlusion location.

MATERIALS AND METHODS: Thirty-two patients with 34 occlusion levels referred for thrombectomy during acute cerebral stroke events were consecutively included from August 2010 to December 2012. Before thrombectomy, we performed 3T MR imaging, including conventional 3D-TOF and gradient-echo T2 sequences, along with time-resolved contrast-enhanced MRA of the extra- and intracranial arteries. The 3D-TOF, gradient-echo T2, and time-resolved contrast-enhanced MRA results were consensually assessed by 2 neuroradiologists and compared with prethrombectomy DSA results in terms of occlusion location. The Wilcoxon test was used for statistical analysis to compare MR imaging sequences with DSA, and the κ coefficient was used to determine intermodality agreement.

RESULTS: The occlusion level on the 3D-TOF and gradient-echo T2 images differed significantly from that of DSA ($P < .001$ and $P = .002$, respectively), while no significant difference was observed between DSA and time-resolved contrast-enhanced MRA ($P = .125$). κ coefficients for intermodality agreement with DSA (95% CI, percentage agreement) were 0.43 (0.3%–0.6; 62%), 0.32 (0.2%–0.5; 56%), and 0.81 (0.6%–1.0; 88%) for 3D-TOF, gradient-echo T2, and time-resolved contrast-enhanced MRA, respectively.

CONCLUSIONS: The time-resolved contrast-enhanced MRA sequence proved reliable for identifying occlusion location in acute stroke with performance superior to that of 3D-TOF and gradient-echo T2 sequences.

ABBREVIATIONS: ExCICA = cervical/extracranial ICA; GRE T2 = gradient-echo T2; IICA = intrapetrous plus intracavernous segment; IVT = intravenous thrombolysis; MET = mechanical endovascular therapy; SAA = supra-aortic artery; SCICA = supraclinoid segment; TR-CE MRA = time-resolved contrast-enhanced MRA

Precisely identifying occlusion location on initial imaging of acute cerebral ischemic stroke is a key challenge for establishing prognosis and the most appropriate therapeutic management approach. Intravenous thrombolysis (IVT) efficacy is lower for proximal than distal occlusions, ranging from 8.7% for ICA¹ to around 13%–30% for proximal MCA occlusions.² Accurate identification of occlusion location also enables candidate selection

for mechanical endovascular therapy (MET), which may be offered for large intracranial artery occlusions.^{3–5}

Digital subtraction angiography remains the criterion standard of imaging techniques for precisely determining occlusion location. When MR imaging is used as the first-line technique in patients with acute stroke, 3D-TOF is the recommended MRA sequence for depicting the level of intracranial occlusion. Some studies have demonstrated that the extra time needed to perform this additional sequence does not adversely affect outcomes.^{6,7} However, despite high sensitivity and specificity (85%–100% and 91%–100%, respectively) in identifying the absence of blood flow,^{8–11} 3D-TOF cannot provide direct visualization of the thrombus¹² and may misidentify the occlusion location due to its lack of sensitivity to slow flow.^{13,14} The gradient-echo T2 (GRE T2) sequence provides additional data at 77%–83% sensitivity for intracranial thrombus identification.^{15–17} Nevertheless, it may also misidentify the occlusion location because the associated susceptibility vessel sign depends on thrombus composition. Finally, none of these sequences provides supra-aortic artery (SAA) as-

Received September 12, 2014; accepted after revision December 21.

From the Departments of Neuroradiology (A.L.B., H.R., J.-C.F., J.-Y.G.) and Neurology (T.R.), Centre Hospitalier Universitaire Rennes, Rennes, France; and Unité VISAGE U746 INSERM-INRIA, IRISA UMR CNRS 6074 (H.R., J.-C.F., J.-Y.G.), University of Rennes, Rennes, France.

This work was supported by the Comité de la Recherche Clinique, Centre Hospitalier Universitaire Rennes (contact grant LOC/10–11).

Please address correspondence to A. Le Bras, MD, Department of Neuroradiology, 2 Rue Henri Le Guilloux, 35033 Rennes, France; e-mail: anthony.le.bras@chu-rennes.fr

Indicates article with supplemental on-line table.

<http://dx.doi.org/10.3174/ajnr.A4264>

Table 1: Acquisition parameters for MRA sequences

	TR-CE MRA	3D-TOF	GRE T2
Receive coil	Body coil	8-Channel brain coil	8-Channel brain coil
TR/TE (ms)	4.0/1.25	23/3.5	757/16.1
Flip angle	25°	15°	18°
Acquisition plane	Coronal	Axial	Axial
FOV (mm)	320 × 320	200 × 200	230 × 230
Acquisition matrix	268 × 267	312 × 206	512 × 512
Section thickness (after interpolation)	2.6 (1.3)	1.6 (0.8)	5
Acquired voxel size (mm)	1.2 × 1.2 × 2.6	0.64 × 0.97 × 1.6	0.45 × 0.45 × 5
Reconstructed voxel size (mm)	0.8 × 0.8 × 1.3	0.39 × 0.39 × 0.8	
No. of sections	77	87	24
Anteroposterior coverage (mm)	100		
k-t BLAST undersampling factor	4	—	—
No. of dynamics	12	1	—
Phase acquisition times	8.7 sec	—	—
Total acquisition times	1 minute 44 seconds	2 minutes 36 seconds	1 minute 37 seconds

essment, though some of the recent grade A recommendations highlighted its utility in steno-occlusive disease screening for etiologic evaluation and subsequent appropriate endovascular therapy.^{18,19}

Contrast-enhanced MRA can improve intracranial artery and SAA analysis. With improved contrast and less sensitivity to flow dynamics compared with 3D-TOF, this technique achieves optimal performance in detecting arterial diseases²⁰⁻²² and is being increasingly used in conjunction with brain imaging techniques for acute stroke cases.¹⁴ However, contrast-enhanced MRA is limited because it provides only a single static acquisition restricted to the early arterial phase, and slow-flow dynamics can cause pseudo-occlusions to appear upstream of the steno-occlusive lesion.^{23,24} Recent time-resolved contrast-enhanced MRA (TR-CE MRA) sequences appear to come closest to DSA imaging used in depicting arteriovenous malformations or dural arteriovenous fistulas^{25,26} and theoretically take advantage of arterial filling dynamics,²⁷ with the option of late phases, thus avoiding the lack of contrast filling of cervical arteries upstream of the intracranial occlusion.

This prospective study sought to assess the diagnostic performance of 3D-TOF, GRE T2, and TR-CE MRA in the identification of occlusion location, compared with DSA as the standard reference, in patients referred for MET in the acute phase of stroke.

MATERIALS AND METHODS

Patient Population

We obtained both institutional review board approval and informed consent for this study, which complied with the Health Insurance Portability and Accountability Act. From August 2010 to December 2012, 33 consecutive patients who fulfilled the eligibility criteria were prospectively enrolled.

The inclusion criteria were as follows: age older than 18 years, MR imaging diagnosis of acute cerebral ischemic stroke based on diffusion imaging, referral for MET within 6 hs of symptom onset for anterior circulation occlusion, proximal thrombus detected by MR imaging, and time between MRA sequences and DSA <3 hs 30 minutes. The exclusion criteria included hemorrhagic lesions that were visible on MR images or comorbidity with poor prognosis.

MET was performed for every patient. For eligible patients, IVT was completed before endovascular thrombectomy, either immediately after IVT (combined therapy) or 1 h after IVT initiation if no clinical improvement was observed (rescue therapy).²⁸

MR Imaging

Data acquisition was performed on a 3T MR imaging system (Achieva; Philips Healthcare, Best, the Netherlands), which is the first-line imaging technique available 24/7 in our center. It was therefore possible to initiate optimal management without delay.¹² The imaging protocol consisted of parenchymal brain imaging sequences (axial DWI, GRE T2, and FLAIR) and angiographic sequences (3D-TOF and TR-CE MRA). The MRA acquisition parameters are provided in Table 1. The total average acquisition time for all MR imaging sequences was 12 minutes.

The TR-CE MRA sequence was based on a k-t Broad-use Linear Acquisition Speed-up Technique (BLAST)-accelerated 3D sequence, performed without moving the patient, with a whole-body birdcage coil used as a receiver.^{29,30} This technique provided wide coverage, from the aortic arch to the M3–M4 segments of the MCAs, with high temporal and spatial resolution.³⁰ The acquisition slabs were positioned by using a low-resolution phase-contrast MRA that had been performed earlier. A fixed volume of a 15-mL bolus of gadoterate meglumine (Dotarem; Guerbet, Aulnay-sous-Bois, France) was administered intravenously at 1.5 mL/s with an automatic Spectris power injector (Medrad, Indianapolis, Pennsylvania), followed by a 30-mL saline flush, without a bolus-tracking acquisition. Maximum-intensity-projection images of angiographic sequences were automatically generated, as with 3D-TOF.

DSA Imaging

Diagnostic prethrombectomy DSA was performed as the standard of reference for SAA and intracranial artery analysis. All DSA examinations were performed by a neurointerventionalist with >5 years' experience on a biplanar system (Allura Xper; Philips Healthcare) with the patient under general anesthesia by using the femoral artery approach. Angiographic images were acquired at 2 frames per second by using an automatic iodinated contrast medium injector at 6–8 mL/s for intracranial arteries and 2–4 mL/s for SAA (fluoroscopic guidance).

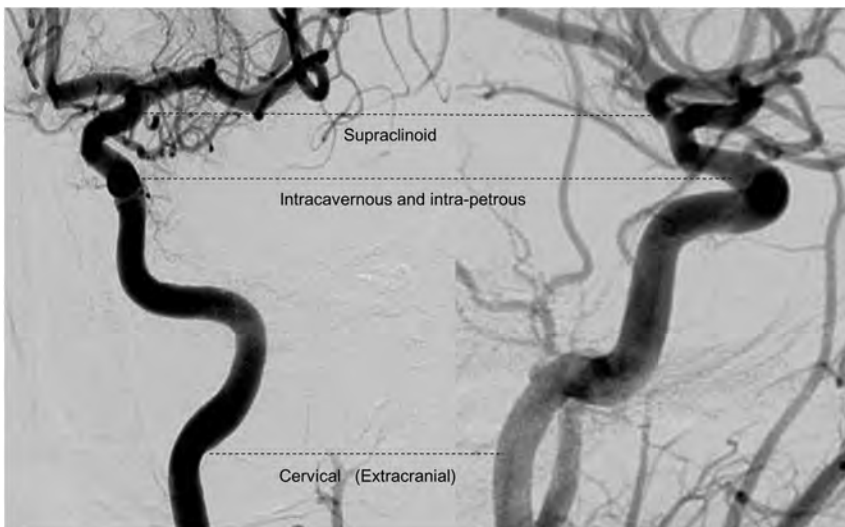


FIG 1. ICA segmentation used for the occlusion-level definition derived from Gibo et al, 1981.³¹ The internal carotid artery is divided into supraclinoid ICA, intracavernous and intrapetrous ICA, and cervical/extracranial ICA.

Image Analysis

The 3D-TOF, GRE T2, and TR-CE MRA sequences were reviewed on a specially designed imaging workstation (Extended MR Workspace 2.6.3; Philips Healthcare), which displayed native images and 3D MPR and MIP images. Two neuroradiologists, J.-C.F. and H.R., with 10 and 5 years' experience, respectively, were blinded to the DSA and clinical findings to independently evaluate the 3D-TOF and TR-CE MRA sequences. Any disagreements were discussed to reach a consensus. DSA was evaluated by 1 observer blinded to the other findings, by using frontal and lateral series on the target artery to define the standard of reference for the intracranial occlusion location and SAA stenosis quantification when applicable. In the event of tandem occlusion, both occlusion levels were reported. Patients were studied in randomized order. The diagnostic performance of both MRA sequences (TR-CE MRA and 3D-TOF) and the GRE T2 sequence was assessed and compared with DSA in terms of intracranial occlusion location. The diagnostic performance of TR-CE MRA was assessed and compared with DSA with regard to SAA stenosis detection. The images were assessed in terms of diagnostic performance and image quality.

The location of the intracranial occlusion caused by the thrombus was defined as follows: for both MRA (3D-TOF and TR-CE) sequences, the site of complete stoppage of the arterial flow; and for the GRE T2 sequence, the proximal portion of the susceptibility vessel sign. The ICA segmentation used for occlusion location was defined according to previous classifications,^{31,32} giving rise to the cervical/extracranial segment (Ex-CICA), intrapetrous plus intracavernous segment (IICA), and supraclinoid segment (SCICA) (Fig 1). The M1 and M2 segments of the MCA were defined by standard practice guidelines. Supra-aortic artery stenosis was classified according to the semiquantitative SAA stenosis severity scale that is typically used in symptomatic patients,^{33,34} namely, none or moderate (stenosis, <50%), severe (stenosis, >50%), and occluded (complete stoppage of the arterial flow without downstream flow).

The contribution of the dynamic nature of TR-CE MRA was

assessed by quantifying the number of phases that elapsed between the phase yielding maximum signal intensity within the nonpathologic arteries and the phase yielding maximum signal intensity directly upstream of the occlusion location.

The image diagnostic confidence index of both MRA sequences for SAA and intracranial arteries (Fig 1) was evaluated according to a modified diagnostic confidence index scale^{27,30,35}: nondiagnostic (vessel borders not definable), fair (vessel borders scarcely definable, inhomogeneous vessel signal), good (good delineation of vessel borders with slight irregularities, homogeneous vessel signal with slight artifacts), and excellent (sharp and complete delineation of vessel borders, homogeneous vessel signal without artifacts).

Statistical Analysis

The statistical analysis was performed by using SPSS software (IBM, Armonk, New York). After recoding categorical variables as ordinal variables, we evaluated occlusion level differences with MRA sequences and GRE T2 compared with the reference imaging standard (DSA) by using a 2-tailed Wilcoxon exact signed rank test, with a statistically significant difference assumed for $P < .05$. To quantify the intermodality agreement of MRA sequences, comparing GRE T2 with DSA, we calculated the κ coefficient, 95% confidence intervals, and percentage agreement.

Finally, interobserver agreement for MRA image diagnostic confidence indexes for the major intracranial arteries was determined.

RESULTS

Of the 33 patients initially included in this study, 1 patient was later excluded due to a technical problem that occurred on gadolinium administration during the TR-CE MRA sequence, resulting in nonopacification of the SAA and intracranial arteries. The final number of patients included was 32 (On-line Table), with 21 men and 11 women (mean age, 64.9 ± 14.8 years; age range, 29–88 years). This number included 19 (59.3%) who had previously undergone IVT, 12 of whom had MET as a rescue therapy (if no substantial clinical improvement was seen 1 h after IVT).²⁸ Two of these patients had a tandem occlusion. The mean time between MR imaging and DSA was 126 ± 35 minutes. For patients who underwent IVT, the mean time between IVT and DSA was 120 ± 33 minutes.

Intracranial Occlusion Location

Artery occlusion was diagnosed for all patients on the basis of the 3D-TOF and TR-CE MRA sequences, whereas GRE T2 only provided a diagnosis in 26 of the 32 patients (81.2%). Interobserver agreement for occlusion location was considered good for TR-CE MRA ($\kappa = 0.72$; 95% CI, 0.53–0.91) and excellent for 3D-TOF ($\kappa = 0.86$; 95% CI, 0.62–1).

A 2-tailed Wilcoxon exact signed rank test revealed significant

Table 2: Identification of intracranial occlusion location with 3D-TOF, GRE T2, and TR-CE MRA, compared with DSA as the standard reference^a

Occlusion Location	DSA (No.) (%)	3D-TOF MRA (No.) (%)	GRE T2 (No.) (%)	TR-CE MRA (No.) (%)
No occlusion (no susceptibility vessel sign for GRE T2)	0 (0%)	0 (0%)	6 (17.6%)	0 (0%)
ExCICA	3 (8.8%)	5 (14.7%)	0 (0%)	3 (8.8%)
IICA	0 (0%)	5 (14.7%)	0 (0%)	0 (0%)
SCICA	8 (23.5%)	3 (8.8%)	3 (8.8%)	9 (26.5%)
M1	17 (50.0%)	20 (58.8%)	22 (64.7%)	19 (55.9%)
M2	6 (17.6%)	1 (2.9%)	2 (5.9%)	3 (8.8%)
κ		0.43	0.31	0.81
95% CI		0.26–0.60	0.15–0.48	0.60–1
(% of agreement)		61.8%	55.9%	88.2%

^aIntracranial occlusion location with 3D-TOF, GRE T2, and TR-CE MRA, compared with DSA as the standard reference, showing the occlusion level detected as well as κ and percentage of agreement with DSA for each MRI sequence.

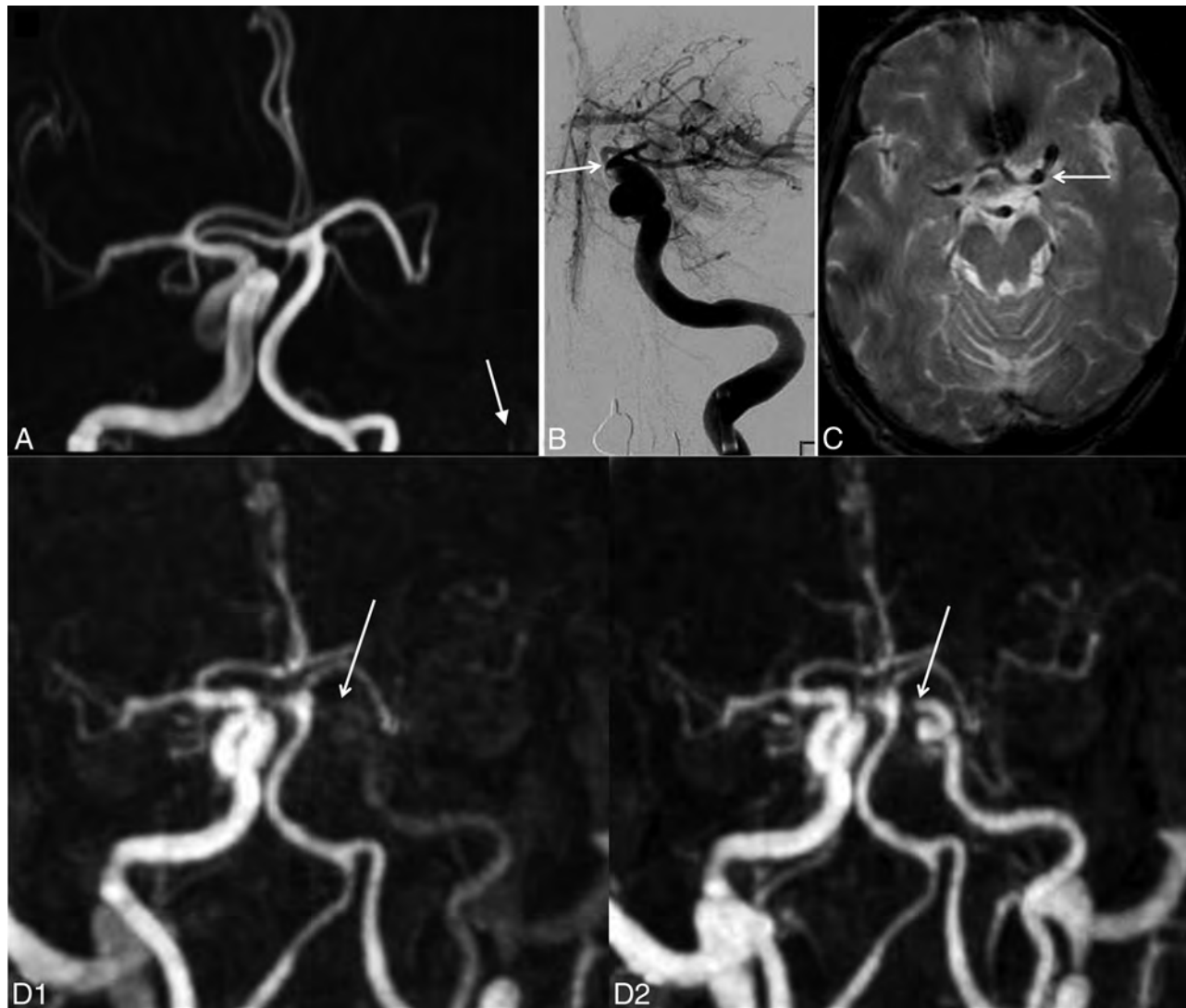


FIG 2. In patient 11, agreement between TR-CE MRA and DSA and discordance with TOF. A, 3D-TOF frontal MIP image shows complete occlusion of the left ICA from the IICA to distal segments of the left MCA. No data were available on the patency of the ICA proximal to the IICA segment (*white arrow*). B, Frontal DSA shows opacification of the left ICA up to the supraclinoid segment (*white arrow*). C, GRE T2 axial image displays a susceptibility vessel sign in the M1 segment of the left MCA. D, Frontal MIP TR-CE MRA shows patency of the left ICA up to the SCICA in the last phases (*white arrows*).

differences in the occlusion level among 3D-TOF, GRE T2, and DSA ($P < .001$ and $P = .002$, respectively), whereas there was no significant difference between DSA and TR-CE MRA ($P = .125$).

Agreement between both MRA sequences and the GRE T2

sequence with DSA is shown in Table 2. The primary discrepancies between 3D-TOF and DSA were found when the occlusion was within the SCICA or M1 segments when using DSA, as opposed to the more proximal location within the IICA or even

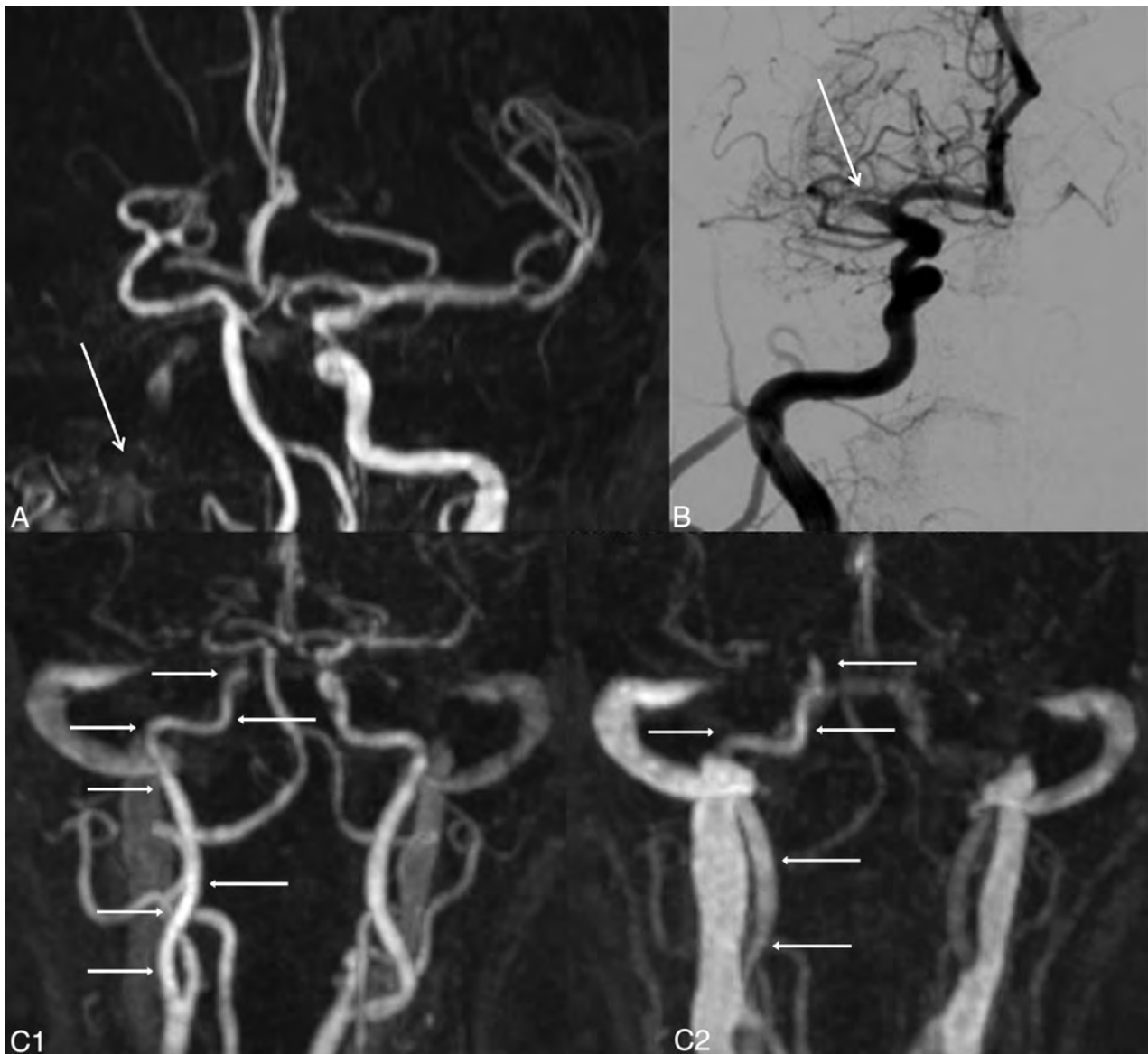


FIG 3. In patient 1, disagreement between TR-CE MRA and DSA and discordance with TOF. *A*, 3D-TOF frontal MIP image shows complete occlusion of the right ICA from the IICA to distal segments of the left MCA, with a doubt about the patency of the ICA proximal to the IICA segment (*white arrow*). *B*, Frontal DSA shows opacification of the right ICA up to the M1 segment (*white arrow*). *C*, Frontal MIP TR-CE MRA shows patency of the right ICA up to the SCICA in the last phases (*white arrows*).

cervical/extracranial segment seen with 3D-TOF (Fig 2). The few discrepancies observed between TR-CE MRA and DSA occurred when the occlusion was within the M1 or M2 segments of the MCA when using DSA, with TR-CE MRA showing the occlusion more within the M1 segment of the MCA or in the SCICA (Fig 3).

SAA Stenosis Detection

SAA stenosis was classified with DSA as follows: none or moderate in 28 patients (87.5%), severe in 1 (3.1%), and occlusion in 3 (9.4%). All cases were correctly classified on TR-CE MRA imaging (Fig 4).

Dynamic Nature of TR-CE-MRA

For 11 of the 32 patients (34.4%), there was a time difference of at least 1 phase between maximum opacification of nonpathologic

arteries and optimum opacification within the occluded segment. The difference was 1 phase for 6 patients, 2 phases for 3 patients, 3 phases for 1 patient, and 6 phases for 1 other patient. In 9 of these 11 patients (81.8%), the occlusion location was misidentified on 3D-TOF, in contrast to only 2 misidentified cases with TR-CE MRA.

Image Diagnostic Confidence Index

For intracranial artery evaluation, the diagnostic confidence index was significantly higher ($P = .013$) with the 3D-TOF sequences (mean, 3.0 ± 0.7) than with the TR-CE MRA sequences (mean, 2.6 ± 0.7).

Interobserver agreement was considered good for the intracranial arteries visualized with the TR-CE MRA and 3D-TOF sequences ($\kappa = 0.72$; 95% CI, 0.48–0.96; and $\kappa = 0.75$; 95% CI, 0.53–0.97, respectively) and moderate for SAAs visual-

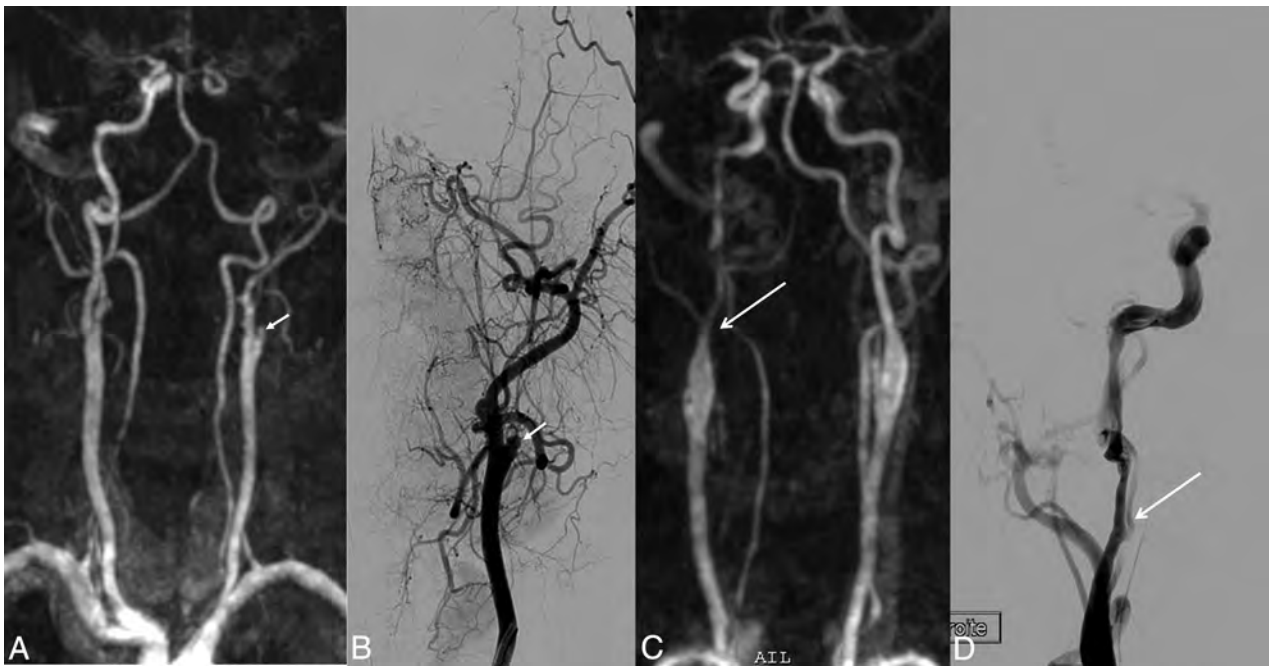


FIG 4. Examples of occlusion and stenosis of the extracranial arteries. TR-CE MRA and its corresponding frontal DSA image. In patient 7 (A and B), occlusion of the left ICA, probably of atheromatous etiology (white arrow) on TR-CE MRA (A) and DSA (B). In patient 24 (C and D), severe stenosis (>50%) of the right ICA, on TR-CE MRA (C) and DSA (D), presumed due to an arterial dissection (white arrow).

ized with the TR-CE MRA sequences ($\kappa = 0.41$; 95% CI, 0.20–0.62).

DISCUSSION

Our study showed TR-CE MRA to be more accurate than 3D-TOF and GRE T2 for identifying occlusion location, producing excellent agreement with DSA and offering a simultaneous and reliable SAA analysis with no additional time acquisition if substituted for the 3D-TOF sequence and entailing no delay in initiating optimal management.

The 3D-TOF showed low reliability for occlusion location, illustrated by its low 62% agreement with DSA ($\kappa = 0.43$). However, its sensitivity for thrombus detection was in line with the literature (100.0%).^{8,10} Previous studies have already reported the limitation of 3D-TOF in terms of occlusion depiction,^{10,22} with Korogi et al,¹⁰ for example, demonstrating that 21% of the intracranial segments occluded in the 3D-TOF sequence proved permeable in the contrast-enhanced 3D-TOF sequence. In our study, despite using 3T MR imaging with an optimal signal-to-noise ratio for 3D-TOF image quality, the discrepancies between the DSA and 3D-TOF sequences resulted in major misdiagnosis, especially when the occlusion was located in the ICA supraclinoid segment. The 3D-TOF sequence showed a tendency to locate the occlusion in a more proximal position than the DSA-located occlusions. This could be accounted for by the flow reduction upstream of the thrombus being erroneously detected by this flow-based technique. Similarly, GRE T2 achieved only 56% agreement with DSA ($\kappa = 0.31$), despite its expected high sensitivity for thrombus detection (81.2%).^{15–17}

In contrast, TR-CE MRA proved a reliable non-time-consuming tool for occlusion location, with 88% agreement with DSA ($\kappa = 0.81$). The superior diagnostic performance of TR-CE MRA

compared with 3D-TOF was not hampered by the lower image quality, probably due to the poorer spatial resolution, and may be the result of several factors: First, the T1 effect of gadolinium compensates for the signal loss caused by spin-dephasing that occurs in 3D-TOF when the flows are slow, turbulent, or oriented parallel to the section plane, in this case essentially upstream of the real occlusion site diagnosed on the DSA (standard of reference) image and especially within the IICA segment. Second, during the last phases, the dynamic nature of TR-CE MRA enables identification of the persistent slow-filling artery upstream of and closest to the occlusion. This flow can be missed on 3D-TOF, due to spin-dephasing,¹³ as well as on conventional CE-MRA, on account of only a single static arterial phase being available, a problem that has already been reported with CT in the setting of cerebral stroke.^{23,24} Both of these static conventional MRA contrast-enhanced or non-contrast-enhanced sequences, therefore, carry the risk of occlusion overestimation.

The advantage of dynamic imaging, as previously suggested in a study based on 4D CT,³⁶ was especially evident in our study. In some cases, we found that TR-CE MRA enabled rectification of the occlusion level that had been misdiagnosed on 3D-TOF due to its added advantage of late phases. Finally, the comparison of TR-CE MRA with the DSA technique in this study also confirmed its reliability for detecting SAA disease, a result that was previously reported.³⁰ The ability of TR-CE MRA to provide simultaneous accurate data in terms of intracranial thrombus location and SAA stenosis during the initial MR imaging in a short acquisition time (<2 minutes) is of particular significance. This advantage clearly means that TR-CE MRA may have the potential to improve patient triage and MET strategy planning. For example, identification of a tandem occlusion enables optimum MET preparation

through the use of a triaxial guide-catheter system for stent placement as needed.³⁷ Moreover, advanced knowledge of a critical case as tandem or a very proximal intracranial occlusion can determine the choice of general over local anesthesia. On the other hand, a single M1 occlusion can lead to single-catheter access and local anesthesia, thus resulting in a shorter procedure.³⁸ Last, although a more distal occlusion level in M2 or further is not recommended for MET, overestimation of the level of occlusion (in M1 or more proximally) caused by 3D-TOF may lead to the wrong therapeutic decision.

Our study has several limitations. First, due care should be taken when interpreting the results, given the moderate patient sample size, and a larger population should be assessed to confirm our data. Second, our study focused solely on the anterior circulation, and the presumed advantage of applying TR-CE MRA to the cerebral posterior circulation requires further investigation. Third, there was a time lapse between MR imaging and DSA. During this interval, arterial occlusion may spread or decrease regardless of ongoing thrombosis or fibrinolysis processes, resulting in discrepancies in the occlusion location between MR imaging and DSA. However, the high rate of concordance reported between TR-CE MRA and DSA suggests that this limitation did not influence our conclusions. Fourth, we did not compare TR-CE MRA with conventional contrast-enhanced MRA because it would have required time and a second injection; also, the agreement between the 2 sequences had been demonstrated previously.³⁰ Finally the TR-CE MRA sequence has a low spatial resolution, which obviously reduces image quality for intracranial arteries and hampers analysis beyond the M2 or M1 segments in some cases. This drawback could be easily remedied by using dedicated coils and parallel imaging.^{39,40}

CONCLUSIONS

Of all the MR imaging sequences we evaluated, TR-CE MRA proved to be the most reliable for identifying occlusion location in the setting of acute stroke, offering superior performance to 3D-TOF and T2 GRE, along with the added advantage of enabling SAA stenosis detection. Thus TR-CE MRA could replace 3D-TOF and so reduce the interval before optimal management, especially when endovascular treatment is considered. The GRE T2 sequence remains mandatory because it enables hemorrhage identification.

ACKNOWLEDGMENTS

The authors thank Aymeric Stamm, MD, for supervising the statistical analysis of this study.

REFERENCES

- del Zoppo GJ, Poeck K, Pessin MS, et al. **Recombinant tissue plasminogen activator in acute thrombotic and embolic stroke.** *Ann Neurol* 1992;32:78–86
- Bhatia R, Hill MD, Shobha N, et al. **Low rates of acute recanalization with intravenous recombinant tissue plasminogen activator in ischemic stroke: real-world experience and a call for action.** *Stroke* 2010;41:2254–58
- Mazighi M, Serfaty JM, Labreuche J, et al. **Comparison of intravenous alteplase with a combined intravenous-endovascular approach in patients with stroke and confirmed arterial occlusion (RECANALISE study): a prospective cohort study.** *Lancet Neurol* 2009;8:802–09
- Vendrell JF, Mernes R, Nagot N, et al. **Evaluation of an intravenous-endovascular strategy in patients with acute proximal middle cerebral artery occlusion.** *AJNR Am J Neuroradiol* 2013;34:603–08
- Leker RR, Eichel R, Gomori JM, et al. **Stent-based thrombectomy versus intravenous tissue plasminogen activator in patients with acute middle cerebral artery occlusion.** *Stroke* 2012;43:3389–91
- Breuer L, Schellinger PD, Huttner HB, et al. **Feasibility and safety of magnetic resonance imaging-based thrombolysis in patients with stroke on awakening: initial single-centre experience.** *Int J Stroke* 2010;5:68–73
- Köhrmann M, Schellinger PD. **Stroke-MRI: extending the time-window: recent trials and clinical practice.** *Int J Stroke* 2007;2:53–54
- Stock KW, Radue EW, Jacob AL, et al. **Intracranial arteries: prospective blinded comparative study of MR angiography and DSA in 50 patients.** *Radiology* 1995;195:451–56
- Stock KW, Wetzel S, Kirsch E, et al. **Anatomic evaluation of the circle of Willis: MR angiography versus intraarterial digital subtraction angiography.** *AJNR Am J Neuroradiol* 1996;17:1495–99
- Korogi Y, Takahashi M, Mabuchi N, et al. **Intracranial vascular stenosis and occlusion: diagnostic accuracy of three-dimensional, Fourier transform, time-of-flight MR angiography.** *Radiology* 1994;193:187–93
- Hirai T, Korogi Y, Ono K, et al. **Prospective evaluation of suspected stenooclusive disease of the intracranial artery: combined MR angiography and CT angiography compared with digital subtraction angiography.** *AJNR Am J Neuroradiol* 2002;23:93–101
- Wintermark M, Sanelli PC, Albers GW, et al. **Imaging recommendations for acute stroke and transient ischemic attack patients: a joint statement by the American Society of Neuroradiology, the American College of Radiology, and the Society of NeuroInterventional Surgery.** *AJNR Am J Neuroradiol* 2013;34:E117–27
- Ishimaru H, Ochi M, Morikawa M, et al. **Accuracy of pre- and post-contrast 3D time-of-flight MR angiography in patients with acute ischemic stroke: correlation with catheter angiography.** *AJNR Am J Neuroradiol* 2007;28:923–26
- Sohn CH, Sevicik RJ, Frayne R. **Contrast-enhanced MR angiography of the intracranial circulation.** *Magn Reson Imaging Clin N Am* 2003;11:599–614
- Flacke S, Urbach H, Keller E, et al. **Middle cerebral artery (MCA) susceptibility sign at susceptibility-based perfusion MR imaging: clinical importance and comparison with hyperdense MCA sign at CT 1.** *Radiology* 2000;215:476–82
- Rovira A, Orellana P, Alvarez-Sabin J, et al. **Hyperacute ischemic stroke: middle cerebral artery susceptibility sign at echo-planar gradient-echo MR imaging.** *Radiology* 2004;232:466–73
- Naggara O, Raymond J, Domingo Ayllon M, et al. **T2* “susceptibility vessel sign” demonstrates clot location and length in acute ischemic stroke.** *PLoS One* 2013;8:e76727
- Latchaw RE, Alberts MJ, Lev MH, et al. **Recommendations for imaging of acute ischemic stroke: a scientific statement from the American Heart Association.** *Stroke* 2009;40:3646–78
- Jauch EC, Saver JL, Adams HP, et al. **Guidelines for the early management of patients with acute ischemic stroke: a guideline for healthcare professionals from the American Heart Association/American Stroke Association.** *Stroke* 2013;44:870–947
- Anzalone N, Scomazzoni F, Castellano R, et al. **Carotid artery stenosis: intraindividual correlations of 3D time-of-flight MR angiography, contrast-enhanced MR angiography, conventional DSA, and rotational angiography for detection and grading.** *Radiology* 2005;236:204–13
- Yang CW, Carr JC, Futterer SF, et al. **Contrast-enhanced MR angiography of the carotid and vertebrobasilar circulations.** *AJNR Am J Neuroradiol* 2005;26:2095–101
- Yang JJ, Hill MD, Morrish WF, et al. **Comparison of pre- and post-contrast 3D time-of-flight MR angiography for the evaluation of**

- distal intracranial branch occlusions in acute ischemic stroke. *AJNR Am J Neuroradiol* 2002;23:557–67
23. Kim JJ, Dillon WP, Glastonbury CM, et al. **Sixty-four-section multi-detector CT angiography of carotid arteries: a systematic analysis of image quality and artifacts.** *AJNR Am J Neuroradiol* 2010;31:91–99
 24. Schreiber S, Schreiber F, Glaser M, et al. **Detecting artery occlusion and critical flow diminution in the case of an acute ischemic stroke: methodological pitfalls of common vascular diagnostic methods.** *Ultraschall Med* 1980 2011;32:274–80
 25. Meckel S, Maier M, Ruiz DSM, et al. **MR angiography of dural arteriovenous fistulas: diagnosis and follow-up after treatment using a time-resolved 3D contrast-enhanced technique.** *AJNR Am J Neuroradiol* 2007;28:877–84
 26. Unlu E, Temizoz O, Albayram S, et al. **Contrast-enhanced MR 3D angiography in the assessment of brain AVMs.** *Eur J Radiol* 2006;60:367–78
 27. Raoult H, Ferré JC, Morandi X, et al. **Quality-evaluation scheme for cerebral time-resolved 3D contrast-enhanced MR angiography techniques.** *AJNR Am J Neuroradiol* 2010;31:1480–87
 28. Costalat V, Machi P, Lobotesis K, et al. **Rescue, combined, and stand-alone thrombectomy in the management of large vessel occlusion stroke using the Solitaire device: a prospective 50-patient single-center study: timing, safety, and efficacy.** *Stroke* 2011;42:1929–35
 29. Kozerke S, Tsao J, Razavi R, et al. **Accelerating cardiac cine 3D imaging using k-t BLAST.** *Magn Reson Med* 2004;52:19–26
 30. Ferré JC, Raoult H, Breil S, et al. **Supra-aortic arteries: three-dimensional time-resolved k-t BLAST contrast-enhanced MRA using a nondedicated body coil at 3 Tesla in acute ischemic stroke.** *J Magn Reson Imaging* 2014;40:1056–63
 31. Gibo H, Lenkey C, Rhoton AL Jr. **Microsurgical anatomy of the supraclinoid portion of the internal carotid artery.** *J Neurosurg* 1981;55:560–74
 32. Shapiro M, Becske T, Riina HA, et al. **Toward an endovascular internal carotid artery classification system.** *AJNR Am J Neuroradiol* 2014;35:230–36
 33. Hinkmann FM, Voit HL, Anders K, et al. **Ultra-fast carotid CT-angiography: low versus standard volume contrast material protocol for a 128-slice CT-system.** *Invest Radiol* 2009;44:257–64
 34. Rerkasem K, Rothwell PM. **Carotid endarterectomy for symptomatic carotid stenosis.** *Cochrane Database Syst Rev* 2011;CD001081
 35. Kramer H, Runge VM, Morelli JN, et al. **Magnetic resonance angiography of the carotid arteries: comparison of unenhanced and contrast enhanced techniques.** *Eur Radiol* 2011;21:1667–76
 36. Frölich AM, Schrader D, Klotz E, et al. **4D CT angiography more closely defines intracranial thrombus burden than single-phase CT angiography.** *AJNR Am J Neuroradiol* 2013;34:1908–13
 37. Machi P, Lobotesis K, Maldonado IL, et al. **Endovascular treatment of tandem occlusions of the anterior cerebral circulation with Solitaire FR thrombectomy system: initial experience.** *Eur J Radiol* 2012;81:3479–84
 38. Soize S, Kadziolka K, Estrade L, et al. **Mechanical thrombectomy in acute stroke: prospective pilot trial of the Solitaire FR device while under conscious sedation.** *AJNR Am J Neuroradiol* 2013;34:360–65
 39. Parikh PT, Sandhu GS, Blackham KA, et al. **Evaluation of image quality of a 32-channel versus a 12-channel head coil at 1.5T for MR imaging of the brain.** *AJNR Am J Neuroradiol* 2011;32:365–73
 40. De Zwart JA, Ledden PJ, van Gelderen P, et al. **Signal-to-noise ratio and parallel imaging performance of a 16-channel receive-only brain coil array at 3.0 Tesla.** *Magn Reson Med* 2004;51:22–26

SWI or T2*: Which MRI Sequence to Use in the Detection of Cerebral Microbleeds? The Karolinska Imaging Dementia Study

S. Shams, J. Martola, L. Cavallin, T. Granberg, M. Shams, P. Aspelin, L.O. Wahlund, and M. Kristoffersen-Wiberg



ABSTRACT

BACKGROUND AND PURPOSE: Cerebral microbleeds are thought to have potentially important clinical implications in dementia and stroke. However, the use of both T2* and SWI MR imaging sequences for microbleed detection has complicated the cross-comparison of study results. We aimed to determine the impact of microbleed sequences on microbleed detection and associated clinical parameters.

MATERIALS AND METHODS: Patients from our memory clinic ($n = 246$; 53% female; mean age, 62) prospectively underwent 3T MR imaging, with conventional thick-section T2*, thick-section SWI, and conventional thin-section SWI. Microbleeds were assessed separately on thick-section SWI, thin-section SWI, and T2* by 3 raters, with varying neuroradiologic experience. Clinical and radiologic parameters from the dementia investigation were analyzed in association with the number of microbleeds in negative binomial regression analyses.

RESULTS: Prevalence and number of microbleeds were higher on thick-/thin-section SWI (20/21%) compared with T2*(17%). There was no difference in microbleed prevalence/number between thick- and thin-section SWI. Interrater agreement was excellent for all raters and sequences. Univariate comparisons of clinical parameters between patients with and without microbleeds yielded no difference across sequences. In the regression analysis, only minor differences in clinical associations with the number of microbleeds were noted across sequences.

CONCLUSIONS: Due to the increased detection of microbleeds, we recommend SWI as the sequence of choice in microbleed detection. Microbleeds and their association with clinical parameters are robust to the effects of varying MR imaging sequences, suggesting that comparison of results across studies is possible, despite differing microbleed sequences.

ABBREVIATIONS: CMB = cerebral microbleed; KIDS = Karolinska Imaging Dementia Study; TSWI = thick-section SWI; tSWI = thin-section SWI; WMH = matter hyperintensities

Cerebral microbleeds (CMBs) have lately become a focus of growing interest. Mainly related to small-vessel disease and seen as a result of hypertensive arteriopathy and cerebral amyloid angiopathy, CMBs have been proposed to have potentially important clinical implications.¹⁻³ Theories have proposed that CMBs have a possible important role in the dementia pathophysiology,

and additionally, CMBs have shown associations with intracerebral hemorrhage.⁴

Intracerebral hemorrhage and dementia share common characteristics with CMBs. The incidence of cerebral amyloid angiopathy in patients with Alzheimer disease is up to 98%,⁵ and hypertension has been related to the development of dementia.⁶ Additionally, cerebral amyloid angiopathy and hypertension are the 2 main pathologies behind spontaneous intracerebral hemorrhage, and CMBs are thereby hypothesized to be a possible predictor for intracerebral hemorrhage.⁷

Correct and validated detection is essential to determine and understand CMBs and their associated clinical implications. CMBs are, due to their microscopic appearance, not visualized on CT or conventional MR imaging.¹ Detection has, up until now, been with hemosiderin-sensitive sequences, T2* and SWI. Hemosiderin is a paramagnetic substance, causing inhomogeneity in the magnetic field surrounding the CMB, leading to quick decay of the MR imaging signal, called the "susceptibility effect." T2* is a

Received September 30, 2014; accepted after revision December 16.

From the Department of Clinical Science, Intervention, and Technology, Division of Medical Imaging and Technology (S.S., J.M., L.C., T.G., M.S., P.A., M.K.-W.), and Department of Neurobiology, Care Sciences, and Society (L.O.W.), Karolinska Institutet, Stockholm, Sweden; and Department of Radiology (S.S., J.M., L.C., T.G., M.S., P.A., M.K.-W.) and Division of Clinical Geriatrics (L.O.W.), Karolinska University Hospital, Stockholm, Sweden.

Please address correspondence to Sara Shams, MD, Department of Radiology, Karolinska University Hospital, SE-14186 Stockholm, Sweden; e-mail: sara.shams@ki.se

Indicates open access to non-subscribers at www.ajnr.org

Indicates article with supplemental on-line table.

<http://dx.doi.org/10.3174/ajnr.A4248>

gradient recalled-echo sequence, without a refocusing 180° radio-frequency pulse, thus making it sensitive to the susceptibility effect.⁸ The SWI sequence, in turn, is a technique that has recently been increasingly incorporated in clinical MRI protocols. SWI maximizes the susceptibility effect by combining a long TE, fully flow-compensated 3D gradient echo, and using both the magnitude and filtered phase information.^{9,10} On sequences sensitive to the susceptibility effect, CMBs are represented by round hypointense dots. Factors of importance in increasing the sensitivity of CMB detection include higher spatial resolution and field and increased TE, with a longer TE increasing the susceptibility effect.³ However, this increased sensitivity may come at a cost, possibly contributing to an increased number of false-positive CMBs. Mimics of CMBs include both calcium and iron deposits, flow voids in blood vessels, and cavernomas and partial volume artifacts.³ Other reasons for CMBs may be trauma, such as diffuse axonal injury.³

While both T2* and SWI have demonstrated good histopathologic correlation,¹¹⁻¹³ the use of the 2 different CMB sequences in CMB detection has complicated the comparison of results across studies. SWI has been shown to increase the number of CMBs detected,^{3,14,15} and studies using the SWI sequence rather than T2* show a higher number and, in some cases, prevalence of CMBs.^{14,16,17} The conventional SWI sequence has a thinner section thickness than the T2* sequence. A thin section thickness has been shown to increase CMB detection¹⁵; thus, this might contribute to the increased CMB detection seen with SWI. Furthermore, higher field strengths have been shown to increase the number of CMBs detected.¹⁵ However, whether the increased sensitivity for CMBs with SWI on 3T increases the association of CMBs with clinical parameters remains unknown.

In this study, we aimed to disentangle the effect of sequence from that of section thickness by comparing CMB detection on the conventional thick-section T2*, a reconstructed thick-section SWI (TSWI), and the conventional thin-section SWI (tSWI) at 3T. By doing so, we aimed to determine the impact on CMB rating of the different MR imaging sequences and their various effects on clinical associations.

MATERIALS AND METHODS

Patients

This study is part of the Karolinska Imaging Dementia Study (KIDS), a prospective cross-sectional study on the impact of CMBs on dementia. Patients were consecutively and prospectively recruited, and the inclusion criterion for this study was a dementia investigation or follow-up at the memory clinic, Karolinska University Hospital, Stockholm, Sweden. The exclusion criterion for recruitment was any contraindication to undergoing MR imaging. For this study, 246 patients (53% women; mean age, 62 ± 10 years) were recruited and had their brain scan performed on a 3T MR imaging scanner with both T2* and SWI added to the general dementia MR imaging protocol. The exclusion criterion for this study during image analysis was insufficient quality of the MR image; however, no patient was excluded for this reason. All patients underwent routine dementia assessment, including medical history; physical, neurologic, and cognitive examinations;

laboratory tests; and MR imaging of the brain with CMB sequences. Diagnosis was based on the International Classification of Diseases-10 criteria, by an experienced memory clinic team, consisting of geriatricians, neuropsychologists, neurophysiologists, and neuroradiologists after all aspects had been considered.

Clinical parameters were obtained during the dementia investigation. The presence of hypertension, hyperlipidemia, and diabetes was determined on the basis of prior medical history, diagnosis, and medications. The presence of anticoagulant medication was determined by the routine clinical assessment of each patient's current medications. Each patient was asked about current smoking or alcohol consumption and known hereditary dementia. Body mass index was calculated at the time of dementia investigation and was registered for 177 patients. Cognition was graded by the Mini-Mental State Examination and was registered for 239 patients. The status of hereditary dementia was unknown in 71 patients; current smoking and alcohol consumption status was unknown or missing in 60 and 54 patients, respectively.

Patients included in this study were divided in 4 subgroups, with the following accompanying International Classification of Diseases-10 codes: Alzheimer disease (*n* = 62): early onset, F00.0 (*n* = 20), late onset, F00.1 (*n* = 16), atypical disease with vascular components, F00.2 (*n* = 24), unspecified Alzheimer disease, F00.9 (*n* = 2); mild cognitive impairment (*n* = 80): F06.7; subjective cognitive impairment (*n* = 71): Z03.2A, Z03.3, and R41.8A; other dementias (*n* = 33): alcohol-related dementia, F10.6, F10.7a (*n* = 2), asymptomatic hereditary dementia (*n* = 4), Z31.5, frontotemporal lobe dementia (*n* = 4), F0.70, Parkinson dementia (*n* = 6), G31.8a, unspecified dementia (*n* = 10), F03.9, vascular dementia (*n* = 7), F01.2, F01.3.

Informed consent was obtained from each patient, and approval was obtained from the regional ethics review board.

MR Imaging Protocol

All patients (*n* = 246) underwent MR imaging on a 3T Magnetom Trio scanner (Siemens, Erlangen, Germany) with a 12-channel head coil at the radiology department, Karolinska University Hospital, Stockholm, Sweden. For each patient, axial tSWI and T2* sequences and conventional MR imaging sequences, such as T1, T2, and FLAIR, were performed. tSWI was reconstructed to TSWI, by performing a minimum-intensity-projection, by using postprocessing software in the PACS system, making it possible to adjust section thickness and setting it to the same section thickness as that in T2*. Parameters for the sequences in this study were the following: tSWI: TE, 20 ms; TR, 28 ms; flip angle, 15°; section thickness, 1.6 mm; intersection gap, 0.3 mm; FOV, 172 × 230 mm; in-plane voxel size, 0.8 × 0.7 mm; total acquisition time, 5 minutes; TSWI: TE, 20 ms; TR, 28 ms; flip angle, 15°; section thickness, 4.0 mm; intersection gap, 1.2 mm; FOV, 172 × 230 mm; in-plane voxel size, 0.8 × 0.7; T2*: TE, 20 ms; TR, 620 ms; flip angle, 20°; section thickness, 4.0 mm; intersection gap, 1.2 mm; FOV, 220 × 220 mm; in-plane voxel size, 1.1 × 0.9; FLAIR: TE, 89 ms; TR, 9000 ms; flip angle, 130°; TI, 2500 ms; section thickness, 4.0 mm; FOV, 199 × 220 mm; total acquisition time, 5.5 minutes.

Image Analysis

For image analysis, 3 raters were chosen on the basis of prior neuroradiologic experience. At the initial time of rating, the raters had the following background experience: Rater 1 was an MD/PhD student, with 2 years of training and experience in neuroradiology/MR imaging. Rater 2 had been a neuroradiologist for 10 years. Rater 3 had been a neuroradiologist for 21 years.

All CMB image analysis was performed according to the Microbleed Anatomical Rating Scale,¹⁸ with the number and topography of CMBs assessed, as reported before.¹⁹ Minor modifications were made to the scale to increase the accuracy of the CMB rating: CMBs were not rated as probable, only as definitive. Hypointensities in the globus pallidus were not rated, to reduce the risk of calcifications and physiologic iron deposition mimicking CMBs. Furthermore, if the patient had a deep venous anomaly in the vicinity of a CMB, the CMB was not rated as definitive because deep venous anomalies increase the risk of adjacent cavernomas that, in turn, can mimic a CMB. The T2-weighted images and the CMB sequences were analyzed simultaneously to better distinguish vessels and flow voids, which might mimic CMBs. The Microbleed Anatomical Rating Scale and the modifications to it were thoroughly discussed by all raters before analysis. A test cohort of patients ($n = 20$) from the original KIDS cohort, with CMBs varying on T2* or SWI, imaged with the same 3T scanner, was assessed by all raters to establish consensus, before initiating the real rating session.

Rater 1 first analyzed all patients ($n = 246$) for CMBs, as part of the original KIDS CMB analysis.¹⁹ Interrater agreement analysis with Rater 2 was reached on the initial CMB rating, on 50 patients with CMBs and an additional 50 patients without CMBs, showing an intraclass correlation coefficient of 0.988 for all patients with CMBs, and 0.987 when the 50 patients without CMBs were added to the analysis.¹⁹ Of all patients, 55 were designated as having CMBs. The 55 patients with CMBs and 20 randomly chosen patients without CMBs were then analyzed by Raters 1, 2, and 3 six months later. The rating procedure was the same for all raters: First CMBs on the T2* sequence were rated continuously on a single day. Three days later CMBs on the tSWI sequence were rated, continuously on a single day. Six months later the TSWI sequence was rated continuously on a single day. The MR images were mixed for each rating session, to randomize the order of CMB interpretation. The raters were blinded to all patient and clinical data; the CMB sequences were not supposed to be used for rating each other's ratings and their own previous ratings.

White matter hyperintensities (WMH) were graded according to the Fazekas scale, from 0 to 3 (none or single punctate; multiple punctate; early confluent; large confluent).¹¹ All images were rated with the rater blinded to clinical data, and other ratings performed. Rater 1 graded all images for WMH on axial FLAIR sequences. Rater 2 graded 50 of the images rated by Rater 1 for interrater agreement analysis. All images rated were randomly chosen with broad representation of the different WMH scores. The weighted κ value obtained was 0.94, which equals excellent agreement.

All radiologic ratings were performed on a PACS workstation with 2 radiologic monitors.

Statistical Analysis

McNemar and Wilcoxon signed rank tests were used to determine the difference between the prevalence and number of CMBs between sequences; analysis was performed separately between T2* and TSWI, T2* and tSWI, and TSWI and tSWI. Intraclass correlation analysis was made on the interrater agreement for CMB detection on the different sequences. κ -weighted analysis was performed on the interrater agreement on WMH and is presented under "Image Analysis." The limits for intraclass correlation and κ statistics were the following: 0.4–0.6, moderate agreement; 0.6–0.8, good agreement; >0.8, excellent agreement. All data were nonparametric; thus, for the univariate analysis of clinical data, χ^2 was used for categorical values and Mann-Whitney U tests, for continuous values. Due to the number of patients with zero CMBs, negative binomial regressions were performed to analyze the association between clinical parameters and the number of CMBs. Univariate negative binomial regression analysis was performed with the number of CMBs as a dependent variable and the clinical parameters separately added to the model as independent variables. Subsequently, each regression model was adjusted for age and sex. The univariate comparisons and the regression analyses were performed, as decided a priori, on the median value of CMBs, by all 3 raters. General values given represent the median value on all separate ratings, from all 3 raters for all patients, unless otherwise specified. Likewise, for general values on the prevalence of CMBs, the median prevalence was chosen (ie, if ≥ 2 raters considered a CMB present/absent, that became the value representing the median of all raters). The whole cohort ($n = 246$) was included in all statistical analyses. SPSS 22.0 (IBM, Armonk, New York) was used for statistical analysis. All P values presented were post hoc Bonferroni-corrected, and $P < .05$ was set as the threshold of statistical significance.

RESULTS

CMB Detection

The prevalence of CMBs for the whole cohort was 17% ($n = 43$) on T2*, 20% ($n = 50$) on TSWI, and 21% ($n = 51$) on tSWI (Table 1). tSWI ($P = .02$) led to a significant rise in CMB prevalence compared with T2*, but there was no significant difference between TSWI and T2* and TSWI and tSWI. Similarly, the increase in the number of CMBs detected was significant between T2* and TSWI ($P < .001$) and T2* and tSWI ($P < .001$), but not between TSWI and tSWI. All raters detected most CMBs on tSWI. Table 1 shows the CMB detection for the different sequences and raters.

The increase in CMB prevalence on TSWI and tSWI, compared with T2*, held true across the different dementia diagnoses (Table 2). There was no difference in prevalence between TSWI and tSWI. The number of CMBs detected increased with TSWI in Alzheimer disease ($P = .006$) and on tSWI in Alzheimer disease ($P = .006$) and mild cognitive impairment ($P = .006$), compared with T2*. There was no significant difference between TSWI and tSWI (Table 2). Table 2 shows the results of CMB detection in the different dementia diagnoses.

Interrater Agreement and Reasons for Disagreement

Interrater agreement was excellent throughout all sequences and raters (Table 3). Analysis of multiple CMBs (defined as >1 CMB)

still equaled excellent agreement across sequences and raters. The 20 patients without CMBs were classified as not having CMBs by all 3 raters on all sequences. Analyzing the agreement regarding the number of CMBs across all CMB sequences, for the median value of all raters, gave an intraclass correlation value of 0.897, which equals excellent agreement.

Throughout all ratings, 5 reasons for disagreement were identified. Multiple, pale, and small CMBs were the most frequent reason for disagreement. CMBs close to vessels and obvious CMBs not detected by 1 rater, explained as lack of attention, were other minor reasons for disagreement. Most disagreement was

noted between T2* and TSWI/tSWI, with minor disagreement between TSWI and tSWI. Figure 1 includes CMBs present on tSWI but not on T2*. Figure 2 shows CMBs present on tSWI and T2* with accompanying disagreements.

Clinical Relevance

For univariate comparisons between patients with and without CMBs on T2*, tSWI, and TSWI, there was an association between CMBs and older age (T2*, $P = .03$; TSWI, $P = .01$) and higher WMH scores (≥ 1 : T2*, $P = .006$; TSWI, $P < .001$; tSWI, $P = .04$) (≥ 2 : T2*, TSWI, and tSWI, $P < .0001$) (3: T2*, TSWI, and tSWI, $P < .0001$) (Table 4).

Analyzing the number of CMBs and the relationship to clinical parameters in regression models for each of the MR imaging sequences showed that patients with a higher number of CMBs more often had Alzheimer disease, mild cognitive impairment, other dementias, higher age, male sex, higher alcohol consumption, hereditary dementia, and higher WMH scores. These associations were seen for T2*, TSWI, and tSWI (On-line Table). Patients who smoked and had anticoagulant therapy had fewer CMBs, as seen separately on T2*, tSWI, and TSWI (On-line Table). Further regression coefficients and analyses are shown in the On-line Table.

Table 1: CMBs for each sequence and rater^a

	All Raters	1	2	3
Prevalence of CMBs on T2* (No.) (%)	43 (17) ^b	42 (17) ^b	45 (18)	38 (15) ^{b,c}
Prevalence of CMBs on TSWI (No.) (%)	50 (20)	49 (20)	46 (19)	51 (21) ^c
Prevalence of CMBs on tSWI (No.) (%)	51 (21) ^b	51 (21) ^b	50 (20)	51 (21) ^b
T2* sum CMBs (No.)	365 ^{b,c}	373 ^{b,c}	461 ^b	260 ^{b,c}
TSWI sum CMBs (No.)	528 ^c	570 ^c	450 ^d	576 ^c
tSWI sum CMBs (No.)	699 ^b	619 ^b	806 ^{b,d}	672 ^b
Times more CMBs on tSWI than T2*	1.5	1.5	1.0	2.2
Times more CMBs on tSWI than T2*	1.9	1.7	1.7	2.6
Times more CMBs on tSWI than TSWI	1.3	1.1	1.8	1.2

^a McNemar and Wilcoxon signed rank tests were used to determine the difference in prevalence and sum of CMBs, respectively; analysis was done separately between T2* and TSWI, T2* and tSWI, and TSWI and tSWI. "All Raters" represents the median value of all separate ratings for all patients (ie, not the final values). The whole cohort is included in the analysis ($N = 246$). For "Prevalence," values are given as the number of patients (percentage). All significant values are designated in the Table. All P values have been Bonferroni-corrected.

^b $P < .05$ between T2* and tSWI.

^c $P < .05$ between T2* and TSWI.

^d $P < .05$ between TSWI and tSWI.

Table 2: CMBs on T2*, TSWI, and tSWI in the separate dementia diagnoses^a

Diagnosis	AD (n = 62)	MCI (n = 80)	Other (n = 33)	SCI (n = 71)
Prevalence of CMBs on T2* (No.) (%)	20 (32)	13 (16)	6 (16)	4 (6)
Prevalence of CMBs on TSWI (No.) (%)	22 (32)	16 (20)	7 (22)	5 (7)
Prevalence of CMBs on tSWI (No.) (%)	22 (35)	16 (20)	7 (22)	6 (8)
T2* sum CMBs (No.)	258 ^{b,c}	69 ^c	47	6
TSWI sum CMBs (No.)	344 ^b	101	73	10
tSWI sum CMBs (No.)	459 ^c	116 ^c	79	12
Times more CMBs on tSWI than T2*	1.3	1.5	1.6	1.7
Times more CMBs on tSWI than T2*	1.8	1.7	1.7	2.0
Times more CMBs on tSWI than TSWI	1.3	1.1	1.1	1.2

Note:—AD indicates Alzheimer disease; Other, other dementias; MCI, mild cognitive impairment; SCI, subjective cognitive impairment.

^a Differences in prevalence and sum of CMBs were determined with the McNemar and Wilcoxon signed rank test, respectively; analysis was made between T2* and TSWI, T2* and tSWI, and TSWI and tSWI. Ratings represent the median value of all separate ratings for all patients. All significant values are designated in the Table. All P values have been Bonferroni-corrected.

^b $P < .05$ between T2* and TSWI.

^c $P < .05$ between T2* and tSWI.

Table 3: Interrater agreement for CMBs on T2*, TSWI, and tSWI^a

Sequence ^b	Patients (No.)	All Raters ^c	Raters 1 and 2	Raters 1 and 3	Raters 2 and 3
Analysis 1					
T2*	55	0.942 (0.915–0.961)	0.990 (0.981–0.994)	0.858 (0.758–0.917)	0.818 (0.689–0.894)
TSWI	55	0.982 (0.974–0.988)	0.963 (0.942–0.977)	0.994 (0.990–0.996)	0.959 (0.936–0.974)
tSWI	55	0.991 (0.986–0.994)	0.979 (0.964–0.988)	0.997 (0.995–0.998)	0.984 (0.972–0.991)
Analysis 2					
T2*	25	0.959 (0.795–0.944)	0.992 (0.982–0.996)	0.911 (0.798–0.961)	0.882 (0.733–0.948)
TSWI	37	0.984 (0.972–0.991)	0.968 (0.938–0.984)	0.994 (0.988–0.997)	0.963 (0.929–0.981)
tSWI	33	0.991 (0.985–0.995)	0.983 (0.966–0.992)	0.997 (0.994–0.999)	0.983 (0.966–0.992)

^a Interrater agreement was determined with the intraclass correlation coefficient, and the 95% confidence intervals are given in parenthesis.

^b Analysis was made twice: 1) for all patients ($n = 55$) with CMBs, on the basis of the initial KIDS CMB analysis; 2) for all patients with >1 CMB according to Rater 1.

^c "All Raters" represents analysis among Raters 1, 2, and 3.

DISCUSSION

SWI, both tSWI and TSWI, increased the prevalence and number of CMBs detected, compared with T2*. However, the difference between tSWI and TSWI was minor. Interrater agreement for all sequences was excellent. There were minor differences in clinical parameters among T2*, TSWI, and tSWI when only considering the presence of CMBs. Taking the number of CMBs in account showed further clinical associations with CMBs in the whole cohort and only minor differences between the sequences.

To the best of our knowledge, this is the first study on the impact of MR imaging sequences on CMB detection and accompanying clinical associations in dementia at 3T. Goos et al¹⁷ examined the effect of T2*, TSWI, and tSWI at 1.5T, showing a higher number and prevalence of CMBs detected on SWI and no difference in clinical associations among the sequences, after ad-

justment for age and sex. The higher prevalence and number of CMBs detected with SWI are in accordance with our results and suggest that the increase in CMB detection on SWI across 1.5T–3T is associated with the intrinsic processing of the SWI sequence. However, compared with Goos et al, we present more clinical associations with a high number of CMBs, even after ad-

justment for age and sex. This result may be due to our use of a higher field strength, further sharpening the diagnostic accuracy.

Previous studies investigating the impact of MR imaging sequences on CMB ratings, especially taking clinical parameters into account, are scarce. The prevalence of CMBs has been shown to be around 18% to 32% in Alzheimer disease, versus 3% to 11% in healthy aging populations.¹ The number and prevalence of CMBs have been shown to increase on SWI compared with T2*.¹ Regarding interrater agreement, Goos et al¹⁷ showed excellent interrater agreement for both T2* and SWI, which is in

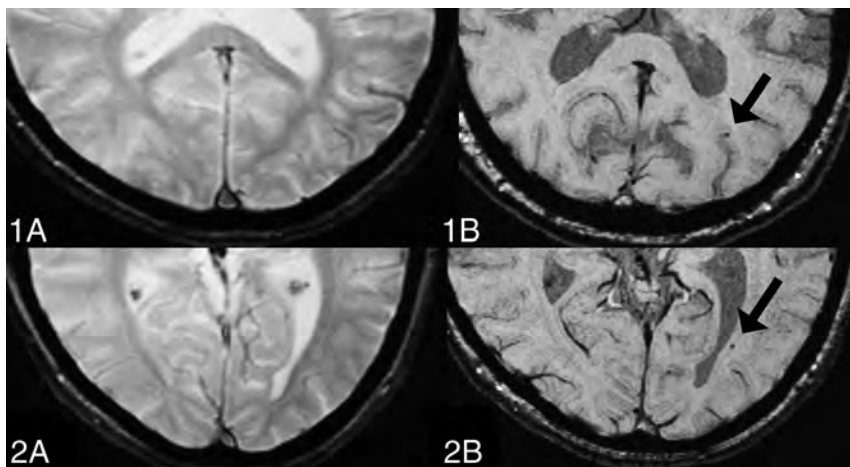


FIG 1. CMBs on tSWI but not T2*. For all images: A, T2*. B, tSWI. 1, Only Rater 1 identified the CMBs on tSWI. 2, Raters 1 and 2 identified the CMBs on tSWI.

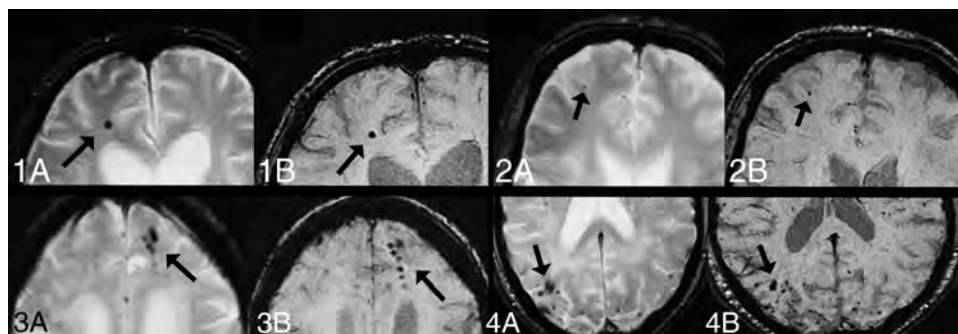


FIG 2. CMBs on both T2* and tSWI. For all images: A, T2*. B, tSWI. 1, All raters identified the single CMB on both T2* and tSWI. 2, The pale CMB on T2* was only identified by Rater 2. On tSWI, the CMB was clearly delineated and was identified by all raters. 3 and 4, Disagreement on the exact number of CMBs occurred on T2*. On tSWI, the CMBs are more clearly outlined.

Table 4: Clinical parameters and association with CMBs depending on sequence^a

Clinical Parameters	T2* CMB+ (n = 43)	T2* CMB- (n = 203)	TSWI CMB+ (n = 50)	TSWI CMB- (n = 196)	tSWI CMB+ (n = 51)	tSWI CMB- (n = 195)
Women (No.) (%)	19 (44)	113 (56)	22 (44)	110 (56)	22 (43)	109 (56)
Age (yr) (mean) (SD)	68 (11) ^b	63 (10) ^b	68 (11) ^b	63 (10) ^b	68 (11)	63 (10)
Hypertension (No.) (%)	20 (47)	74 (37)	23 (46)	71 (36)	24 (47)	70 (36)
Hyperlipidemia (No.) (%)	6 (14)	31 (16)	8 (16)	29 (15)	9 (18)	28 (15)
Diabetes (No.) (%)	7 (16)	21 (10)	8 (16)	20 (10)	7 (14)	21 (11)
Current smoking (No.) (%)	4 (12)	35 (23)	6 (15)	33 (22)	6 (15)	33 (23)
Alcohol (No.) (%)	30 (91)	131 (82)	35 (90)	126 (82)	36 (92)	125 (82)
Hereditary (No.) (%)	21 (72)	82 (56)	23 (67)	80 (57)	23 (68)	80 (57)
Anticoagulant medication (No.) (%)	11 (26)	36 (18)	14 (28)	33 (17)	13 (26)	34 (18)
MMSE (mean) (SD)	25 (4)	25 (5)	25 (4)	25 (5)	25 (4)	25 (5)
BMI (mean) (SD)	27 (5)	25 (3)	25 (4)	27 (5)	25 (4)	27 (5)
WMH ≥1 (No.) (%)	38 (88) ^b	138 (68) ^b	45 (90) ^b	131 (74) ^b	45 (88) ^b	130 (67) ^b
WMH ≥2 (No.) (%)	19 (44) ^c	20 (10) ^c	21 (42) ^c	18 (9) ^c	21 (41) ^c	18 (9) ^c
WMH = 3 (No.) (%)	12 (28) ^c	8 (4) ^c	14 (28) ^c	6 (3) ^c	14 (28) ^c	6 (3) ^c

Note:—MMSE indicates Mini-Mental State Examination; BMI, body mass index; CMB+, patients with CMBs; CMB-, patients without CMBs.

^a χ^2 and Mann-Whitney *U* tests were done to determine in-sequence differences; significance testing was only done within sequences, and significant values are designated in the Table. All analyses were made on the basis of the median rating value of all raters on all patients. All *P* values have been Bonferroni-corrected.

^b *P* < .05.

^c *P* < .001.

line with findings in our study, whereas Cheng et al¹⁴ showed better agreement for SWI. We also noted that our CMB ratings differed slightly between Raters 1/3 and 2. In contrast to Raters 1 and 3, Rater 2 detected fewer CMBs on TSWI than on tSWI. This finding may be due to the thinner section thickness of the tSWI, facilitating CMB detection.

We demonstrate that TSWI and tSWI both increase CMB detection, compared with T2*. tSWI leads to the largest increase in CMBs, possibly reflecting the impact of section thickness on CMB detection.¹⁵ The significant increase in CMB detection with both TSWI and tSWI is probably due to the innate properties of the SWI sequence. Furthermore, we show that TSWI and tSWI increase the prevalence/number of CMBs, with a minor impact on clinical associations, compared with T2*. This finding is of importance for future studies on CMBs and for the interpretation of studies regarding CMBs. Our results suggest that studies with T2* and/or SWI are comparable in clinical associations, implying that the exact number of CMBs may not be of major importance. However, further research is needed to outline the importance of the exact numbers of CMBs, especially in clinical routine neuro-radiologic analysis, and until then, the most sensitive sequence in CMB detection, the SWI, is recommended. Patients with multiple CMBs have been shown to demonstrate lower levels of CSF amyloid β 42 levels compared with patients without CMBs; thus, differentiating patients with single and multiple CMBs with the SWI sequence may provide additional information on the CSF biomarker level of patients.²⁰ The advantage of higher sensitivity may further contribute to increasing the power of studies, with possibly fewer subjects needed for analysis. Using SWI compared with T2* is of additional benefit due to its shorter acquisition time on our scanner, though the time difference when compared with T2* was minor.

In addition, we corroborate the known relationship between CMBs and small-vessel disease, by showing an increase in the number of CMBs with increased WMH. Most interesting, other further associations with CMBs, such as alcohol, smoking, and hereditary dementia, were discovered when considering the number of CMBs. This might imply the multifactorial existence of CMBs. The inverse relationship of a high number of CMBs with anticoagulants is surprising and warrants further research.

The strengths of our study include a large cohort, raters with variable neuroradiologic experience, and the use of rating scales for radiologic analyses, contributing to the generalizability of our results. In addition, we compared T2* and TSWI with the same section parameters, and tSWI; this comparison makes it possible to further disentangle the effects of sequence from that of section thickness. For additional clarification, T2* with thin-section thickness could have been used. The CMB rating was performed on the SWI and T2* sequences only, in accordance with other similar studies,^{14,17} and with the use of the Microbleed Anatomical Rating Scale.¹⁸ To minimize calcification mimics of CMBs, we excluded CMBs in the globus pallidus from the rating. However, the use of the phase or quantitative susceptibility maps would have provided additional information and could have helped in differentiating calcifications from CMBs.^{9,10}

CONCLUSIONS

On the basis of the increased number of CMBs detected, we recommend SWI as the sequence of choice for CMB detection. The difference in CMB prevalence/numbers between T2* and SWI does, however, not affect the association with clinical parameters, suggesting that studies with T2* and SWI are comparable.

ACKNOWLEDGMENTS

We would like to thank Helena Forssell and Karin Kjellsdotter for their administrative and technical assistance and Seyed-Mohammad Fereshtehnejad and Xiaozhen Li for their engagement in this project.

REFERENCES

1. Werring DJ, ed. *Cerebral Microbleeds: Pathophysiology to Clinical Practice*. Cambridge: Cambridge University Press; 2011
2. Cordonnier C, van der Flier WM. **Brain microbleeds and Alzheimer's disease: innocent observation or key player?** *Brain* 2011; 134(pt 2):335–44
3. Greenberg SM, Vernooij MW, Cordonnier C, et al. **Cerebral microbleeds: a guide to detection and interpretation.** *Lancet Neurol* 2009;8:165–74
4. Kakar P, Charidimou A, Werring DJ. **Cerebral microbleeds: a new dilemma in stroke medicine.** *JRSM Cardiovasc Dis* 2012;1: 2048004012474754
5. Jellinger KA. **Alzheimer disease and cerebrovascular pathology: an update.** *J Neural Transm* 2002;109:813–36
6. Skoog I, Lernfelt B, Landahl S, et al. **15-year longitudinal study of blood pressure and dementia.** *Lancet* 1996;347:1141–45
7. Lee SH, Bae HJ, Kwon SJ, et al. **Cerebral microbleeds are regionally associated with intracerebral hemorrhage.** *Neurology* 2004;62: 72–76
8. Chavhan GB, Babyn PS, Thomas B, et al. **Principles, techniques, and applications of T2*-based MR imaging and its special applications.** *Radiographics* 2009;29:1433–49
9. Haacke EM, Mittal S, Wu Z, et al. **Susceptibility-weighted imaging: technical aspects and clinical applications, part 1.** *AJNR Am J Neuroradiol* 2009;30:19–30
10. Mittal S, Wu Z, Neelavalli J, et al. **Susceptibility-weighted imaging: technical aspects and clinical applications, part 2.** *AJNR Am J Neuroradiol* 2009;30:232–52
11. Fazekas F, Kleinert R, Offenbacher H, et al. **The morphologic correlate of incidental punctate white matter hyperintensities on MR images.** *AJNR Am J Neuroradiol* 1991;12:915–21
12. Schrag M, McAuley G, Pomakian J, et al. **Correlation of hypointensities in susceptibility-weighted images to tissue histology in dementia patients with cerebral amyloid angiopathy: a postmortem MRI study.** *Acta Neuropathol* 2010;119:291–302
13. Shoamanesh A, Kwok CS, Benavente O. **Cerebral microbleeds: histopathological correlation of neuroimaging.** *Cerebrovasc Dis* 2011; 32:528–34
14. Cheng AL, Batool S, McCreary CR, et al. **Susceptibility-weighted imaging is more reliable than T2*-weighted gradient-recalled echo MRI for detecting microbleeds.** *Stroke* 2013;44:2782–86
15. Nandigam RNK, Viswanathan A, Delgado P, et al. **MR imaging detection of cerebral microbleeds: effect of susceptibility-weighted imaging, section thickness, and field strength.** *AJNR Am J Neuroradiol* 2009;30:338–43
16. Uetani H, Hirai T, Hashimoto M, et al. **Prevalence and topography of small hypointense foci suggesting microbleeds on 3T susceptibility-weighted imaging in various types of dementia.** *AJNR Am J Neuroradiol* 2013;34:984–89
17. Goos JDC, van der Flier WM, Knol DL, et al. **Clinical relevance of**

- improved microbleed detection by susceptibility-weighted magnetic resonance imaging. *Stroke* 2011;42:1894–900
18. Gregoire SM, Chaudhary UJ, Brown MM, et al. **The Microbleed Anatomical Rating Scale (MARS): reliability of a tool to map brain microbleeds.** *Neurology* 2009;73:1759–66
19. Shams S, Martola J, Granberg T, et al. **Cerebral microbleeds: different prevalence, topography and risk factors depending on dementia diagnosis—the Karolinska Imaging Dementia Study.** *AJNR Am J Neuroradiol* 2015;36:661–66
20. Goos JDC, Kester MI, Barkhof F, et al. **Patients with Alzheimer disease with multiple microbleeds: relation with cerebrospinal fluid biomarkers and cognition.** *Stroke* 2009;40:3455–60

Progression of Microstructural Damage in Spinocerebellar Ataxia Type 2: A Longitudinal DTI Study

M. Mascalchi, N. Toschi, M. Giannelli, A. Ginestroni, R. Della Nave, E. Nicolai, A. Bianchi, C. Tessa, E. Salvatore, M. Aiello, A. Soricelli, and S. Diciotti



ABSTRACT

BACKGROUND AND PURPOSE: The ability of DTI to track the progression of microstructural damage in patients with inherited ataxias has not been explored so far. We performed a longitudinal DTI study in patients with spinocerebellar ataxia type 2.

MATERIALS AND METHODS: Ten patients with spinocerebellar ataxia type 2 and 16 healthy age-matched controls were examined twice with DTI (mean time between scans, 3.6 years [patients] and 3.3 years [controls]) on the same 1.5T MR scanner. Using tract-based spatial statistics, we analyzed changes in DTI-derived indices: mean diffusivity, axial diffusivity, radial diffusivity, fractional anisotropy, and mode of anisotropy.

RESULTS: At baseline, the patients with spinocerebellar ataxia type 2, as compared with controls, showed numerous WM tracts with significantly increased mean diffusivity, axial diffusivity, and radial diffusivity and decreased fractional anisotropy and mode of anisotropy in the brain stem, cerebellar peduncles, cerebellum, cerebral hemisphere WM, corpus callosum, and thalami. Longitudinal analysis revealed changes in axial diffusivity and mode of anisotropy in patients with spinocerebellar ataxia type 2 that were significantly different than those in the controls. In patients with spinocerebellar ataxia type 2, axial diffusivity was increased in WM tracts of the right cerebral hemisphere and the corpus callosum, and the mode of anisotropy was extensively decreased in hemispheric cerebral WM, corpus callosum, internal capsules, cerebral peduncles, pons and left cerebellar peduncles, and WM of the left paramedian vermis. There was no correlation between the progression of changes in DTI-derived indices and clinical deterioration.

CONCLUSIONS: DTI can reveal the progression of microstructural damage of WM fibers in the brains of patients with spinocerebellar ataxia type 2, and mode of anisotropy seems particularly sensitive to such changes. These results support the potential of DTI-derived indices as biomarkers of disease progression.

ABBREVIATIONS: AD = axial diffusivity; FA = fractional anisotropy; MD = mean diffusivity; MO = mode of anisotropy; RD = radial diffusivity; SCA2 = spinocerebellar ataxia type 2; TBSS = tract-based spatial statistics; MNI = Montreal Neurological Institute

Spinocerebellar ataxia type 2 (SCA2) is the second most frequent autosomal dominant inherited ataxia worldwide, after SCA3.¹ It is caused by expansion in excess of 32 CAG repeats in the gene encoding the Ataxin-2 protein, which mainly targets several

pontine neurons and Purkinje cells in the cerebellum,² and it is associated with a pathologic pattern of pontocerebellar atrophy.^{1,3} MR T1-weighted imaging enables in vivo detection of brain stem and cerebellar atrophy in patients with SCA2 in cross-sectional⁴⁻⁶ and longitudinal⁷ studies.

Recently, DWI and DTI have enabled quantitative assessment of the microstructural changes in brain tissue that result from neurodegenerative diseases.^{5,8-21} In particular, in longitudinal studies, DTI may be a sensitive instrument for tracking the progression of neurodegeneration (namely, neuronal damage and loss, Wallerian degeneration, demyelination, and gliosis) and, we hope, for detecting the efficacy (or lack of thereof) of new thera-

Received July 29, 2014; accepted after revision November 21.

From the Quantitative and Functional Neuroradiology Research Unit (M.M.), Meyer Children and Careggi Hospitals of Florence, Florence, Italy; "Mario Serio" Department of Experimental and Clinical Biomedical Sciences (M.M., A.B.), University of Florence, Florence, Italy; Medical Physics Section (N.T.), Department of Biomedicine and Prevention, University of Rome "Tor Vergata," Rome, Italy; Department of Radiology (N.T.), Athinoula A. Martinos Center for Biomedical Imaging, Boston, Massachusetts; Harvard Medical School (N.T.), Boston, Massachusetts; Unit of Medical Physics (M.G.), Pisa University Hospital "Azienda Ospedaliero-Universitaria Pisana," Pisa, Italy; Neuroradiology Unit (A.G.), Careggi General Hospital, Florence, Italy; "San Giuseppe" Hospital (R.D.N.), Empoli, Italy; IRCSS SDN Foundation (E.N., M.A., A.S.), Naples, Italy; Unit of Radiology (C.T.), Versilia Hospital, Lido di Camaiore, Italy; Department of Neurological Sciences (E.S.), University of Naples Federico II, Naples, Italy; University of Naples Parthenope (A.S.), Naples, Italy; Department of Electrical, Electronic, and Information Engineering "Guglielmo Marconi" (S.D.), University of Bologna, Cesena, Italy.

Please address correspondence to Mario Mascalchi, MD, PhD, "Mario Serio" Department of Experimental and Clinical Biomedical Sciences, University of Florence, Viale Morgagni 50, Florence, Italy; e-mail: m.mascalchi@dfc.unifi.it

 Indicates article with supplemental on-line photo.

<http://dx.doi.org/10.3174/ajnr.A4343>

Table 1: Demographic, genetic, and clinical data of 10 patients with SCA2

Patient No.	Age (yr)	Sex	No. of Triplet Repeat Expansions	Disease Duration (yr)	IACRS at Baseline	IACRS at Follow-Up
1	60.6	M	38	20	20	23
2	28.4	M	39	2	9	14
3	31.5	M	43	7	16	16
4	46.5	F	41	7	17	21
5	47.4	F	41	10	19	27
6	43.7	M	41	8	15	15
7	67.8	M	41	23	14	18
8	54.5	F	42	23	25	31
9	56.9	M	40	14	20	27
10	37.7	F	40	14	17	21
Mean (SD)	47.5 (12.7)		40.6 (1.4)	12.8 (7.3)	17.2 (4.3)	21.3 (5.7)

Note:—IACRS indicates Inherited Ataxia Clinical Rating Scale.

peutic strategies. So far, relatively few studies have addressed this point,^{22–30} and none have addressed it in relation to autosomal dominant ataxias.

We performed a longitudinal DTI study in 10 patients with SCA2 and 16 age-matched healthy controls to explore the ability of DTI to detect and map the progression of microstructural damage reflecting advance of neurodegeneration. In particular, we analyzed several DTI-derived indices, including mean diffusivity (MD), axial diffusivity (AD), radial diffusivity (RD), fractional anisotropy (FA), and mode of anisotropy (MO), by using tract-based spatial statistics (TBSS), which enable a robust and unbiased voxelwise whole-brain analysis of the main white matter tracts.^{19,21,31,32}

MATERIALS AND METHODS

Subjects

Ten patients (4 women, 6 men; mean age, 47.5 ± 12.7 years) with a genetically determined diagnosis of SCA2³³ gave their consent to participate in this longitudinal study, which was approved by the local ethics committee. The cutoff number of triplet repeat expansions that qualified for diagnosis of SCA2 was 34 CAG repeats on 1 allele, and the mean number of abnormal triplets was 40.6 ± 1.4. Each patient underwent MR imaging twice on the same scanner and with the same acquisition protocol at an average of 3.6 ± 0.7 years apart (range, 2.2–4.1 years). At the time of both MR imaging examinations, each patient underwent evaluation by the same clinician (A.G.), who assessed the neurologic deficit by using the Inherited Ataxia Clinical Rating Scale.³⁴ This is a 0–38 scale (38 corresponds to maximum clinical deficit) that evaluates signs and symptoms related to ataxia and also pyramidal tract dysfunction and impaired vibration or position sense, which are frequently observed in SCA2.¹ At the time of baseline MR imaging, the mean disease duration from clinical onset in patients with SCA2 was 12.8 ± 7.3 years (range, 2–23 years), and the mean Inherited Ataxia Clinical Rating Scale score was 17.2 ± 4.3 (range, 9–25). Demographic, genetic, and clinical data of the patients with SCA2 are summarized in Table 1.

Sixteen age- and sex-matched healthy subjects (7 women, 9 men; mean age, 50.3 ± 18.8 years) were recruited as controls and provided written consent to participate in the study. They had no history of neurologic or psychiatric dysfunction, and results of their neurologic examinations at baseline and follow-up were negative. Control subjects also underwent MR imaging twice with

the same scanner and acquisition protocol at an average of 3.3 ± 1.0 years apart (range, 1.9–4.7 years).

The TBSS results from the baseline examinations of 9 of the patients with SCA2 and 10 of the healthy controls enrolled in the present study were reported previously.¹⁹

MR Imaging Protocol

The patients and controls underwent MR imaging in a single center on a 1.5T system (Intera; Philips, Best, the Netherlands) with a 33 mT/m maximum gradient strength. After scout imaging, axial

diffusion-weighted images were obtained with single-shot echo-planar imaging sequences (TR, 9394 ms; TE, 89 ms; FOV, 256 × 256 mm; matrix size, 128 × 128; number of sections, 50; section thickness, 3 mm; no intersection gap; number of excitations, 3; sensitivity encoding acceleration factor, 2) by using a 6-channel head coil. Diffusion-sensitizing gradients were applied along 15 noncollinear directions by using a b-value of 0 (B0 image) and 1000 s/mm². As part of the protocol, we also acquired sagittal 3D T1-weighted turbo gradient-echo images (TR, 8.1 ms; TE, 3.7 ms; flip angle, 8°; inversion time, 764 ms; FOV, 256 × 256 mm; matrix size, 256 × 256; contiguous sections, 160; section thickness, 1 mm). T1-weighted images were used in a longitudinal morphometry study.⁷

Image Processing and TBSS

Preliminary visual evaluations of all B0 and diffusion-weighted images revealed no motion artifacts in any patient with SCA2 or control subject. Diffusion-weighted images were corrected for head motion and eddy current distortions by using the FMRIB Diffusion Toolbox (2.0; <http://www.fmrib.ox.ac.uk/fsl/fdt/index.html>), part of the FMRIB Software Library (FSL 5.0.2; <http://www.fmrib.ox.ac.uk/fsl>),³⁵ after which brain tissue was segmented by using the FSL Brain Extraction Tool (<http://fsl.fmrib.ox.ac.uk/fsl/fslwiki/BET>). The b-matrix was subsequently reoriented by applying the rotational part of the affine transformation used in the eddy/motion-correction step.³⁶ A tensor model was then fitted to the raw data by using a constrained nonlinear least-squares procedure implemented in the software package Camino (www.camino.org.uk),³⁷ and residual nonpositive definite tensors (in regions in which the nonlinear algorithm failed to converge) were removed by tensor interpolation in the log-Euclidean domain.³⁸ Diffusion tensor invariants, MD, AD, RD, FA, and MO, were then computed from the estimated tensor field by using the DTI ToolKit software package (<http://software.incf.org/software/dti-toolkit-dti-tk>).³⁹ The MO is an adimensional tensor invariant (range, –1 to 1) that characterizes anisotropy type.⁴⁰ In particular, the MO specifies the type of anisotropy as a continuous measure reflecting differences in the shape of the diffusion tensor ranging from planar (eg, in regions of crossing fibers from 2 fiber populations of similar attenuation or regions of “kissing” fibers [low MO value]) to linear (eg, in regions in which 1 fiber population orientation predominates [high MO value]).⁴¹

Voxelwise statistical analyses of all tensor invariant data were carried out by using TBSS,³² also part of the FMRIB Software Library,

which involves 1) nonlinear registration of every FA image to every other one, 2) identification of the “most representative image” as the one that requires the least warping to align every other image to it, 3) affine alignment of this target image into Montreal Neurological Institute 152 (MNI152) space, 4) transformation of every other image into MNI space by combining the single nonlinear transforms into the target image with the affine transform into MNI space, 5) creation of a mean FA image, and 6) thinning to create a mean FA skeleton that represents the centers of all tracts common to the group. Each subject’s aligned FA data were then projected onto this skeleton, and previously computed warps were also successively applied to MD, AD, RD, and MO images, thereby transforming all images into MNI space for subsequent skeletonization as described above. The resulting data were then fed into voxelwise intersubject and intrasubject statistics. Each analysis included full correction for multiple comparisons over space by using permutation-based nonparametric inference within the framework of the general linear model. Specifically, a first general linear model included only group (“between” factor) to investigate the effect of group (patients versus controls) at baseline. A second general linear model included both group and time (“within” factor), which enabled us to investigate the group–time interaction (patient versus control differences in follow-up versus baseline changes). In another general linear model, we investigated within-patient correlation between changes in DTI-derived indices and changes of clinical variables. All the general linear model designs included age and sex as nuisance covariates. Also, with the aim of taking into account potential confounders resulting from longitudinal atrophy,⁷ every subject’s follow-up T1 scan was registered to the corresponding baseline T1 scan by using high-dimensional nonlinear registration, after which a Jacobian determinant image (which quantifies regional volume change) was computed for the inverse transformations. The baseline scans were all registered to a population-specific T1 template, which in turn was registered to the MNI152 T1 template. The Jacobian determinant image was then transformed into MNI152 space through a single interpolation step in which all the aforementioned transformations were combined. Full details about this procedure can be found in Mascalchi et al⁷ and Tessa et al.⁴² After masking out CSF, the whole-brain average of the Jacobian determinant image was inserted into the longitudinal general linear models as a subject-specific nuisance covariate of global atrophy.

To improve the confidence intervals on resulting *P*-value maps, in each comparison we used 50,000 permutations (as opposed to the commonly used value of 5000). *P* values were calculated and corrected for multiple comparisons by using the 2D parameter settings with threshold-free cluster enhancement, thereby avoiding the use of an arbitrary threshold for the initial cluster formation.⁴³

RESULTS

Baseline Evaluations

TBSS showed changes in all DTI-derived indices in several WM tracts of the brain in patients with SCA2 that were significant compared with those of the controls. These tracts included the cerebral and cerebellar WM, the corpus callosum, brain stem, cerebellar peduncle, and thalamus (On-line Fig 1) and consisted of increased MD and RD and decreased FA and MO. AD was increased in the brain stem, cerebellum, and cerebellar peduncles, and the WM was underlying

the right primary sensorimotor cortex, corpus callosum, and thalamus. However, AD was decreased in the right internal capsule and frontal WM. There were no significant decreases in MD or RD or significant increases in FA or MO.

Longitudinal Evaluations

TBSS revealed longitudinal AD and MO changes in patients with SCA2 that were significant compared with those of the controls (Fig 1).

Longitudinal AD changes were significantly greater (ie, increased) in patients with SCA2 than in controls in the right cerebral hemisphere and corpus callosum (Fig 1). The mean longitudinal changes in these regions are listed in Table 2.

Longitudinal MO changes were significantly lower (ie, decreased) in patients with SCA2 than in controls in many WM tracts, including bilateral hemispheric cerebral WM, corpus callosum, internal capsule, cerebral peduncle, pons, and left inferior, middle, and superior cerebellar peduncle tracts and in the WM of the left paramedian vermis (Fig 1). The mean longitudinal changes in these regions are listed in Table 2.

No WM tract showed significant differences in longitudinal MD, RD, or FA changes in patients with SCA2 versus those in controls.

MR Imaging Clinical Correlations

No significant correlations between clinical progression (modification of the Inherited Ataxia Clinical Rating Scale) and changes in the DTI-derived indices were observed.

DISCUSSION

In patients with SCA2, histopathologic studies have shown widespread neuronal loss, which is prominent in the cerebellar cortex and pontine nuclei, midbrain, medulla, and motor cortex.^{1,3,44} WM damage in patients with SCA2 consists of a loss of myelinated fibers and gliosis affecting the transverse pontine fibers, central cerebellum and cerebellar folia, middle and inferior cerebellar peduncles, medial lemniscus and trigeminal tracts, fasciculus gracilis and cuneatus, and spinocerebellar tracts.¹ Gliosis has been observed also in the thalamus, globus pallidus, and subthalamic region.¹

MR imaging shows loss of bulk of the brain stem and cerebellum in presymptomatic and early symptomatic SCA2 gene carriers^{4–6} and circumscribed atrophy of the frontal, parietal, and temporal cortex, the thalamus, and frontal and temporal WM in more advanced cases.^{19,45,46} MR imaging can also show diffuse high signal intensity of the brain stem and cerebellar WM with sparing of the corticospinal tracts in proton-attenuation and T2-weighted images.⁴⁷ Two studies evaluated patients with SCA2 with DTI using regions of interest¹⁶ or MD histogram analysis and TBSS.¹⁹ Both studies revealed a widespread decrease in FA and an increase in the apparent diffusion coefficient, MD, and RD, which are consistent with microstructural damage of WM tracts in the brain stem, cerebellar peduncles, and cerebellum and in the corpus callosum and several WM tracts in the cerebral hemispheres, including the corticospinal tracts, inferior longitudinal fasciculus, and inferior fronto-occipital fasciculus.

To the best of our knowledge, this is the first DTI study to have explored longitudinal changes of the brain regional microstructure in patients with SCA2 compared with those of healthy age-matched

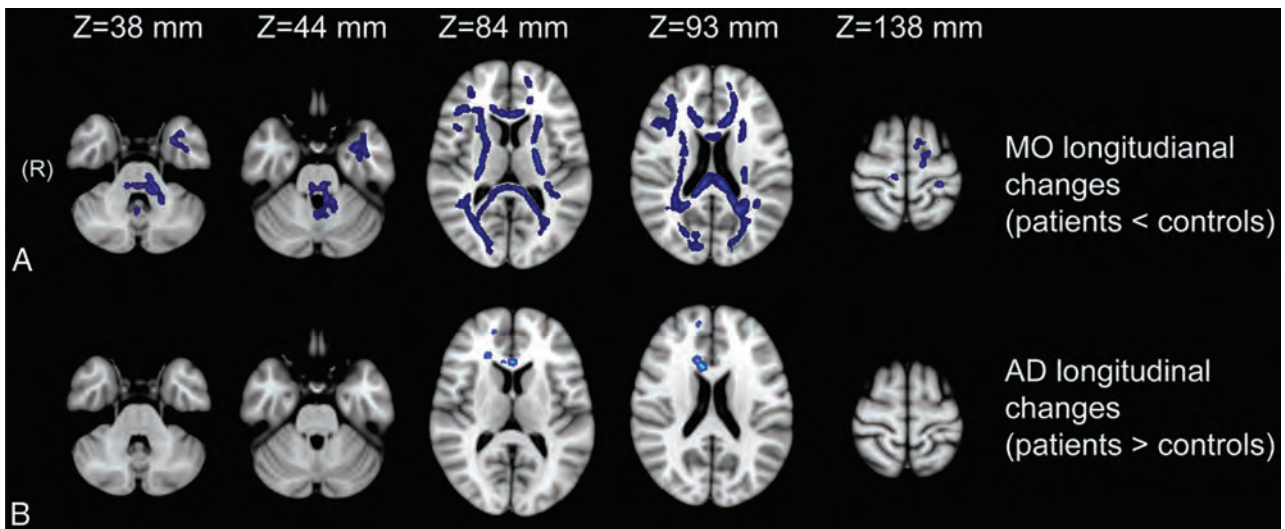


FIG 1. Longitudinal between-group TBSS analyses at different anatomic levels (z coordinate in Montreal Neurological Institute 152 space). TBSS revealed differences in longitudinal changes of some DTI-derived indices (AD and MO) in WM tracts in patients with SCA2 that were significant compared with those of the controls. *A*, Longitudinal MO changes were significantly greater in patients with SCA2 than in controls and extensively involved hemispheric cerebral WM, corpus callosum, internal capsules, cerebral peduncles, pons, and left cerebellar peduncles. Longitudinal AD changes were significantly greater in the right cerebral hemisphere and the corpus callosum of the patients with SCA2 than in the controls (*B*).

Table 2: Mean values of DTI-derived indices in regions in which the longitudinal AD and MO changes were significantly different between patients with SCA2 and controls

DTI-Derived Index	Patients with SCA2			Controls		
	Mean Value at Baseline	Mean Value at Follow-Up	Mean Value Change (Follow-Up - Baseline)	Mean Value at Baseline	Mean Value at Follow-Up	Mean Value Change (Follow-Up - Baseline)
AD ($\times 10^{-3}$ mm ² /s)	1.17	1.28	0.11	1.18	1.16	-0.02
MO	0.51	0.37	-0.14	0.56	0.62	0.06

controls. In particular, patients with SCA2 showed progression of WM damage in the hemispheric cerebral WM, corpus callosum, pons, and left cerebellar peduncles and in the WM of the left paramedian vermis. We noted a hemispheric asymmetry of some longitudinal DTI changes in our patients with SCA2, which may reflect either the relatively low sample size or a truly uneven distribution of the neurodegenerative process. Asymmetry of damage was previously reported from MR imaging studies of patients with Huntington disease, familial Alzheimer disease, and Friedreich ataxia^{21,48-51} and is not uncommon in pathologic studies of neurodegenerative diseases.⁵² In our opinion, the issue of the symmetric versus asymmetric distribution of microstructural changes revealed by DTI needs further investigation with larger sample sizes.

We believe that a thorough analysis of the cross-sectional and longitudinal changes of the various DTI-derived indices that were used in this study, and their interplay in a typical neurodegenerative disease such as SCA2, can be of interest. At baseline, TBSS showed widespread changes in DTI-derived indices in patients with SCA2 compared with those in the controls. These changes include increases in MD and RD and decreases in FA and MO. AD was increased in the brain stem, cerebellum and cerebellar peduncles, thalami, and WM underlying the (right) primary sensory cortex and decreased in the right internal capsule and frontal WM. The increases in MD and RD and decreases in FA are in line with those reported so far in cross-sectional studies of various neurodegenerative diseases.^{5,8-11,13-25,27-29,53} In our study, we observed areas of increased AD that are in line with those shown in

cross-sectional studies of patients with Alzheimer disease,⁵³⁻⁵⁶ Friedreich ataxia,²⁰ and Huntington disease.^{13,55} It is notable that an increase in AD per se is not inconsistent with a decrease in FA. In fact, it is sufficient for the increased AD to be accompanied by a more pronounced increase in RD to result in a decrease of FA in degenerating WM fibers.²⁰ Also, we observed an area of decreased AD in the right internal capsule and frontal WM. The coexistence of WM areas exhibiting increased and decreased AD was reported from a study of Alzheimer disease⁵³ and supports the view that AD may show time-dependent behavior related to a variable combination of factors determining either a decrease caused by Wallerian degeneration and gliosis or an increase caused by axonal damage and atrophy of WM fiber tracts with expanded extracellular space. In our opinion, the complex interplay of these processes should be addressed in animal-model studies.⁵⁷

To our knowledge, so far, only 1 cross-sectional study in patients with mild cognitive impairment and mild Alzheimer disease addressed MO changes in patients with a neurodegenerative disease.⁴¹ An initially counterintuitive increase in the MO was observed in a region of crossing fibers (ie, planar anisotropy) in the centrum semiovale of patients with mild cognitive impairment versus controls and was explained by selective preservation of motor-related projection fibers (at an early stage of the disease) crossing the degenerating association fibers of the superior longitudinal fasciculus, which results in more linear anisotropy.⁴¹ In our study, we observed at baseline a widespread decrease of the MO in patients with SCA2 versus that of controls, which included areas with crossing fibers such as cerebellar

hemispheric WM, centrum semiovale, lobar WM, and areas without crossing fibers such as the cerebellar peduncles, brain stem longitudinal tracts, external and internal capsules, and corpus callosum. Given that a decrease in the MO indicates a reduction of the degree of linear anisotropy, our results suggest a general disorganization of WM fibers in patients with SCA2.

The longitudinal data in our study reveal significantly more pronounced modifications of AD and MO in patients with SCA2 than in the controls. In the patients with SCA2, the increase in AD was circumscribed to the right frontal WM and corpus callosum, whereas the decrease in the MO involved symmetrically and extensively the hemispheric cerebral WM and internal capsules, the corpus callosum, the cerebellar peduncles, the pons, all 3 of the cerebellar peduncles, and the left paramedian vermis WM. No areas of significant difference in changes in MD, RD, or FA in patients with SCA2 were detected compared with those in controls.

The increase in AD at follow-up in the patients with SCA2 is in line with the data from a longitudinal study of symptomatic patients with Huntington disease and was interpreted as the reflection of increased extra-axonal space, resulting from reduced axonal caliber, which allows faster water-molecule movement parallel to axons.⁵⁵ The decrease in the MO at follow-up in patients with SCA2 is in line with the progressive WM fiber disorganization expected in a neurodegenerative disease. It is notable that the far more extensive longitudinal changes in the MO compared with the modifications in AD, including WM tracts in the brain stem and cerebellum, may support the potential use of the MO as an additional valuable and sensitive descriptor of microstructural changes.⁴¹ We submit the following non-mutually exclusive explanations for the lack of significant differences in longitudinal MD, FA, and RD modification in our group of patients with SCA2 compared with those in the control group: 1) the occurrence of a “ceiling” effect; 2) low statistical power (β error) (in this regard, a gain in the signal-to-noise ratio, which can be obtained at higher field strength [eg, 3T] or by using a head coil with a greater number of channels [eg, 32] for advanced neuroimaging) and the use of high angular resolution diffusion-weighted imaging acquisitions would have improved the sensitivity of our study in detecting any white matter changes in the brain stem and/or cerebellum.

Finally, we preliminarily explored whether longitudinal DTI changes were correlated with clinical progression in patients with SCA2. The lack of a significant correlation between longitudinal DTI changes and clinical deterioration in our study (which has been observed also for morphometry findings in patients with SCA2⁷ and those with SCA1, SCA3, or SCA6⁵⁸) might reflect the small sample size, but in our opinion, supports the role of DTI metrics as potential biomarkers of the progression of disease-related microstructural alterations that may precede the evolution of clinical disease manifestations.

However, we did not obtain a structured assessment of cognitive or behavioral changes in our patients. We therefore could not explore the possibility that DTI modifications are correlated with the evolution of nonmotor features. Given that a recent study indicated that a simple clinical examination can track disease progression in paucisymptomatic SCA2 gene carriers,⁵⁹ we feel that a tight comparative evaluation of clinical and MR techniques including DTI and morphometry in monitoring neurodegenera-

tion is advisable for ascertaining the optimal strategy in view of future trials, especially in patients in the early stages of disease.⁶⁰

CONCLUSIONS

DTI is capable of tracking the progression of microstructural brain damage and therefore represents a candidate biomarker of the progression of neurodegeneration in patients with SCA2.

REFERENCES

1. Auburger GW. **Spinocerebellar ataxia type 2.** *Handb Clin Neurol* 2012;103:423–36
2. Orr HT. **Cell biology of spinocerebellar ataxia.** *J Cell Biol* 2012;197:167–77
3. Seidel K, Siswanto S, Brunt ER, et al. **Brain pathology of spinocerebellar ataxias.** *Acta Neuropathol* 2012;124:1–21
4. Jacobi H, Reetz K, du Montcel ST, et al. **Biological and clinical characteristics of individuals at risk for spinocerebellar ataxia types 1, 2, 3, and 6 in the longitudinal RISCA study: analysis of baseline data.** *Lancet Neurol* 2013;12:650–58
5. Mascalchi M, Vella A. **Magnetic resonance and nuclear medicine imaging in ataxias.** *Handb Clin Neurol* 2012;103:85–110
6. Jacobi H, Hauser TK, Giunti P, et al. **Spinocerebellar ataxia types 1, 2, 3 and 6: the clinical spectrum of ataxia and morphometric brain-stem and cerebellar findings.** *Cerebellum* 2012;11:155–66
7. Mascalchi M, Diciotti S, Giannelli M, et al. **Progression of brain atrophy in spinocerebellar ataxia type 2: a longitudinal tensor-based morphometry study.** *PLoS One* 2014;9:e89410
8. Agosta F, Pievani M, Sala S, et al. **White matter damage in Alzheimer disease and its relationship to gray matter atrophy.** *Radiology* 2011;258:853–63
9. Teipel SJ, Grothe M, Lista S, et al. **Relevance of magnetic resonance imaging for early detection and diagnosis of Alzheimer disease.** *Med Clin North Am* 2013;97:399–424
10. Zhang Y, Tartaglia MC, Schuff N, et al. **MRI signatures of brain macrostructural atrophy and microstructural degradation in frontotemporal lobar degeneration subtypes.** *J Alzheimers Dis* 2013;33:431–44
11. Mascalchi M, Vella A, Ceravolo R. **Movement disorders: role of imaging in diagnosis.** *J Magn Reson Imaging* 2012;35:239–56
12. Tessa C, Giannelli M, Della Nave R, et al. **A whole-brain analysis in de novo Parkinson disease.** *AJNR Am J Neuroradiol* 2008;29:674–80
13. Della Nave R, Ginestroni A, Tessa C, et al. **Regional distribution and clinical correlates of white matter structural damage in Huntington disease: a tract-based spatial statistics study.** *AJNR Am J Neuroradiol* 2010;31:1675–81
14. Cosottini M, Giannelli M, Siciliano G, et al. **Diffusion-tensor MR imaging of corticospinal tract in amyotrophic lateral sclerosis and progressive muscular atrophy.** *Radiology* 2005;237:258–64
15. Guimaraes RP, D’Abreu A, Yasuda CL, et al. **A multimodal evaluation of microstructural white matter damage in spinocerebellar ataxia type 3.** *Mov Disord* 2013;28:1125–32
16. Mandelli ML, De Simone T, Minati L, et al. **Diffusion tensor imaging of spinocerebellar ataxias types 1 and 2.** *AJNR Am J Neuroradiol* 2007;28:1996–2000
17. Salvatore E, Tedeschi E, Mollica C, et al. **Supratentorial and infratentorial damage in spinocerebellar ataxia 2: a diffusion-weighted MRI study.** *Mov Disord* 2014;29:780–86
18. Kang JS, Klein JC, Baudrexel S, et al. **White matter damage is related to ataxia severity in SCA3.** *J Neurol* 2014;261:291–99
19. Della Nave R, Ginestroni A, Tessa C, et al. **Brain white matter damage in SCA1 and SCA2. An in vivo study using voxel-based morphometry, histogram analysis of mean diffusivity and tract-based spatial statistics.** *Neuroimage* 2008;43:10–19
20. Della Nave R, Ginestroni A, Diciotti S, et al. **Axial diffusivity is increased in the degenerating superior cerebellar peduncles of Friedreich’s ataxia.** *Neuroradiology* 2011;53:367–72
21. Della Nave R, Ginestroni A, Tessa C, et al. **Brain white matter tracts**

- degeneration in Friedreich ataxia. An in vivo MRI study using tract-based spatial statistics and voxel-based morphometry. *Neuroimage* 2008;40:19–25
22. Amlien IK, Fjell AM, Walhovd KB, et al. Mild cognitive impairment: cerebrospinal fluid tau biomarker pathologic levels and longitudinal changes in white matter integrity. *Radiology* 2013;266:295–303
 23. Keil C, Prell T, Peschel T, et al. Longitudinal diffusion tensor imaging in amyotrophic lateral sclerosis. *BMC Neurosci* 2012;13:141
 24. Pellicchia MT, Barone P, Vicidomini C, et al. Progression of striatal and extrastriatal degeneration in multiple system atrophy: a longitudinal diffusion-weighted MR study. *Mov Disord* 2011;26:1303–09
 25. Reginold W, Lang AE, Marras C, et al. Longitudinal quantitative MRI in multiple system atrophy and progressive supranuclear palsy. *Parkinsonism Relat Disord* 2014;20:222–25
 26. Teipel SJ, Meindl T, Wagner M, et al. Longitudinal changes in fiber tract integrity in healthy aging and mild cognitive impairment: a DTI follow-up study. *J Alzheimers Dis* 2010;22:507–22
 27. Vandenberghe W, Demaerel P, Dom R, et al. Diffusion-weighted versus volumetric imaging of the striatum in early symptomatic Huntington disease. *J Neurol* 2009;256:109–14
 28. Weaver KE, Richards TL, Liang O, et al. Longitudinal diffusion tensor imaging in Huntington's disease. *Exp Neurol* 2009;216:525–29
 29. Sritharan A, Egan GF, Johnston L, et al. A longitudinal diffusion tensor imaging study in symptomatic Huntington's disease. *J Neurol Neurosurg Psychiatry* 2010;81:257–62
 30. Seppi K, Schocke MF, Mair KJ, et al. Progression of putaminal degeneration in multiple system atrophy: a serial diffusion MR study. *Neuroimage* 2006;31:240–45
 31. Smith SM, Johansen-Berg H, Jenkinson M, et al. Acquisition and voxelwise analysis of multi-subject diffusion data with tract-based spatial statistics. *Nat Protoc* 2007;2:499–503
 32. Smith SM, Jenkinson M, Johansen-Berg H, et al. Tract-based spatial statistics: voxelwise analysis of multi-subject diffusion data. *Neuroimage* 2006;31:1487–505
 33. Pareyson D, Gellera C, Castellotti B, et al. Clinical and molecular studies of 73 Italian families with autosomal dominant cerebellar ataxia type I: SCA1 and SCA2 are the most common genotypes. *J Neurol* 1999;246:389–93
 34. Filla A, DeMichele G, Caruso G, et al. Genetic data and natural history of Friedreich's disease: a study of 80 Italian patients. *J Neurol* 1990;237:345–51
 35. Smith SM, Jenkinson M, Woolrich MW, et al. Advances in functional and structural MR image analysis and implementation as FSL. *Neuroimage* 2004;23(suppl 1):S208–19
 36. Leemans A, Jones DK. The B-matrix must be rotated when correcting for subject motion in DTI data. *Magn Reson Med* 2009;61:1336–49
 37. Cook PA, Bai Y, Nedjati-Gilani S, et al. Camino: open-source diffusion-MRI reconstruction and processing. In: *Proceedings of the 14th Scientific Meeting of the International Society for Magnetic Resonance in Medicine*, Seattle, Washington. May 6–12, 2006:2759
 38. Arsigny V, Fillard P, Pennec X, et al. Log-Euclidean metrics for fast and simple calculus on diffusion tensors. *Magn Reson Med* 2006;56:411–21
 39. Zhang H, Avants BB, Yushkevich PA, et al. High-dimensional spatial normalization of diffusion tensor images improves the detection of white matter differences: an example study using amyotrophic lateral sclerosis. *IEEE Trans Med Imaging* 2007;26:1585–97
 40. Ennis DB, Kindlmann G. Orthogonal tensor invariants and the analysis of diffusion tensor magnetic resonance images. *Magn Reson Med* 2006;55:136–46
 41. Douaud G, Jbabdi S, Behrens TE, et al. DTI measures in crossing-fibre areas: increased diffusion anisotropy reveals early white matter alteration in MCI and mild Alzheimer's disease. *Neuroimage* 2011;55:880–90
 42. Tessa C, Lucetti C, Giannelli M, et al. Progression of brain atrophy in the early stages of Parkinson's disease: a longitudinal tensor-based morphometry study in de novo patients without cognitive impairment. *Hum Brain Mapp* 2014;35:3932–44
 43. Smith SM, Nichols TE. Threshold-free cluster enhancement: addressing problems of smoothing, threshold dependence and localisation in cluster inference. *Neuroimage* 2009;44:83–98
 44. Rüb U, Seidel K, Ozerden I, et al. Consistent affection of the central somatosensory system in spinocerebellar ataxia type 2 and type 3 and its significance for clinical symptoms and rehabilitative therapy. *Brain Res Rev* 2007;53:235–49
 45. Brenneis C, Bosch SM, Schocke M, et al. Atrophy pattern in SCA2 determined by voxel-based morphometry. *Neuroreport* 2003;14:1799–802
 46. Goel G, Pal PK, Ravishankar S, et al. Gray matter volume deficits in spinocerebellar ataxia: an optimized voxel based morphometric study. *Parkinsonism Relat Disord* 2011;17:521–27
 47. Lee YC, Liu CS, Wu HM, et al. The "hot cross bun" sign in the patients with spinocerebellar ataxia. *Eur J Neurol* 2009;16:513–16
 48. Rosas HD, Liu AK, Hersch S, et al. Regional and progressive thinning of the cortical ribbon in Huntington's disease. *Neurology* 2002;58:695–701
 49. Kipps CM, Duggins AJ, Mahant N, et al. Progression of structural neuropathology in preclinical Huntington's disease: a tensor based morphometry study. *J Neurol Neurosurg Psychiatry* 2005;76:650–55
 50. Thieben MJ, Duggins AJ, Good CD, et al. The distribution of structural neuropathology in pre-clinical Huntington's disease. *Brain* 2002;125:1815–28
 51. Ginestroni A, Battaglini M, Della Nave R, et al. Early structural changes in individuals at risk of familial Alzheimer's disease: a volumetry and magnetization transfer MR imaging study. *J Neurol* 2009;256:925–32
 52. Stefanits H, Budka H, Kovacs GG. Asymmetry of neurodegenerative disease-related pathologies: a cautionary note. *Acta Neuropathol* 2012;123:449–52
 53. Huang H, Fan X, Weiner M, et al. Distinctive disruption patterns of white matter tracts in Alzheimer's disease with full diffusion tensor characterization. *Neurobiol Aging* 2012;33:2029–45
 54. Acosta-Cabronero J, Williams GB, Pengas G, et al. Absolute diffusivities define the landscape of white matter degeneration in Alzheimer's disease. *Brain* 2010;133:529–39
 55. Rosas HD, Lee SY, Bender AC, et al. Altered white matter microstructure in the corpus callosum in Huntington's disease: implications for cortical "disconnection." *Neuroimage* 2010;49:2995–3004
 56. Salat DH, Tuch DS, van der Kouwe AJ, et al. White matter pathology isolates the hippocampal formation in Alzheimer's disease. *Neurobiol Aging* 2010;31:244–56
 57. Kelp A, Koeppen AH, Petrasch-Parwez E, et al. A novel transgenic rat model for spinocerebellar ataxia type 17 recapitulates neuropathological changes and supplies in vivo imaging biomarkers. *J Neurosci* 2013;33:9068–81
 58. Reetz K, Costa AS, Mirzazade S, et al. Genotype-specific patterns of atrophy progression are more sensitive than clinical decline in SCA1, SCA3 and SCA6. *Brain* 2013;136:905–17
 59. Velazquez-Perez L, Rodriguez-Labrada R, Canales-Ochoa N, et al. Progression of early features of spinocerebellar ataxia type 2 in individuals at risk: a longitudinal study. *Lancet Neurol* 2014;13:482–89
 60. Klockgether T. Spinocerebellar ataxia type 2: progression before diagnosis. *Lancet Neurol* 2014;13:445–46

Usefulness of Quantitative Susceptibility Mapping for the Diagnosis of Parkinson Disease

Y. Murakami, S. Kakeda, K. Watanabe, I. Ueda, A. Ogasawara, J. Moriya, S. Ide, K. Futatsuya, T. Sato, K. Okada, T. Uozumi, S. Tsuji, T. Liu, Y. Wang, and Y. Korogi



ABSTRACT

BACKGROUND AND PURPOSE: Quantitative susceptibility mapping allows overcoming several nonlocal restrictions of susceptibility-weighted and phase imaging and enables quantification of magnetic susceptibility. We compared the diagnostic accuracy of quantitative susceptibility mapping and $R2^*$ ($1/T2^*$) mapping to discriminate between patients with Parkinson disease and controls.

MATERIALS AND METHODS: For 21 patients with Parkinson disease and 21 age- and sex-matched controls, 2 radiologists measured the quantitative susceptibility mapping values and $R2^*$ values in 6 brain structures (the thalamus, putamen, caudate nucleus, pallidum, substantia nigra, and red nucleus).

RESULTS: The quantitative susceptibility mapping values and $R2^*$ values of the substantia nigra were significantly higher in patients with Parkinson disease ($P < .01$); measurements in other brain regions did not differ significantly between patients and controls. For the discrimination of patients with Parkinson disease from controls, receiver operating characteristic analysis suggested that the optimal cutoff values for the substantia nigra, based on the Youden Index, were >0.210 for quantitative susceptibility mapping and >28.8 for $R2^*$. The sensitivity, specificity, and accuracy of quantitative susceptibility mapping were 90% (19 of 21), 86% (18 of 21), and 88% (37 of 42), respectively; for $R2^*$ mapping, they were 81% (17 of 21), 52% (11 of 21), and 67% (28 of 42). Pair-wise comparisons showed that the areas under the receiver operating characteristic curves were significantly larger for quantitative susceptibility mapping than for $R2^*$ mapping (0.91 versus 0.69, $P < .05$).

CONCLUSIONS: Quantitative susceptibility mapping showed higher diagnostic performance than $R2^*$ mapping for the discrimination between patients with Parkinson disease and controls.

ABBREVIATIONS: A_z = area under the receiver operating characteristic curve; PD = Parkinson disease; QSM = quantitative susceptibility mapping; ROC = receiver operating characteristic

The diagnosis of Parkinson disease (PD), a movement disorder with varying combinations of rest tremors, bradykinesia, rigidity, and postural instability, is based mainly on clinical assessments that do not yield great accuracy. One objective of noninvasive neuroimaging techniques in PD is to find markers that aid in the diagnosis, disease-progression monitoring, and long-term drug-impact evaluation.¹ MR imaging with rich tissue contrasts

and high spatial resolution offers a unique value for probing PD brain structure and function.

Particularly, there has been substantial interest in in vivo MR imaging of increased nigral iron content,^{2,3} a pathophysiologic feature involved in the selective dopaminergic neurodegeneration of the substantia nigra in patients with PD.⁴ Iron likely stored in ferritin⁵ is highly paramagnetic and can be sensitized in MR imaging by using relaxation contrast (such as T2-weighted imaging) and susceptibility contrasts (such as T2*-weighted imaging and $R2^*$ [$1/T2^*$] mapping).⁶ For quantitative study of brain iron, $R2^*$ mapping has been used,^{7,8} demonstrating increased iron in the substantia nigra in patients with PD,⁹⁻¹¹ and a recent postmortem correlation study has demonstrated that the relationship with $R2^*$ can be linear in regions of more uniform iron deposition.¹² However, $R2^*$ mapping depends on field strength,¹³ contains substantial blooming artifacts that increase with TE,¹⁴ and generally relates to iron concentration in a complex way, varying from linear to quadratic.¹⁵⁻¹⁷

Received August 8, 2014; accepted after revision November 24.

From the Departments of Radiology (Y.M., S.K., K.W., I.U., A.O., J.M., S.I., K.F., T.S., Y.K.) and Neurology (K.O., T.U., S.T.), University of Occupational and Environmental Health, School of Medicine, Kitakyushu, Japan; and Departments of Biomedical Engineering and Radiology (T.L., Y.W.), Cornell University, New York, New York.

Please address correspondence to Shingo Kakeda, MD, Department of Radiology, University of Occupational and Environmental Health, 1-1 Iseigaoka, Yahatanishi-ku, Kitakyushu 807-8555, Japan; e-mail: kakeda@med.uoeh-u.ac.jp

Indicates article with supplemental on-line appendix.

<http://dx.doi.org/10.3174/ajnr.A4260>

Recently, quantitative susceptibility mapping (QSM) has been developed to determine tissue magnetic susceptibility from gradient-echo data.^{18–20} Because ferritin susceptibility is much stronger than other tissues in brains free of hemorrhages and aggregates of other metals, QSM can be used to quantify brain iron distribution.^{21,22} Clinical data from patients with multiple sclerosis suggest that QSM is more sensitive than R2* mapping in detecting changes in multiple sclerosis brains.²³

According to a previously published study using QSM, a significant difference was not found between patients with PD and healthy control subjects for the susceptibility value of the substantia nigra.²⁴ However, because only 9 patients were available for the previous study, the clinical potential of QSM has not been fully elucidated. Furthermore, the difference between QSM and the standard method for studying iron change, including R2* mapping, has not been evaluated in patients with PD. In this study, we tested the hypothesis that QSM is more sensitive than R2* mapping to pathologies in PD brains by comparing QSM and R2* values in 6 brain structures (the thalamus, putamen, caudate nucleus, pallidum, substantia nigra, and red nucleus) in patients with PD and healthy controls.

MATERIALS AND METHODS

MR Imaging

All subjects underwent brain MR imaging with QSM. All studies were performed on a 3T MR imaging system (Signa Excite 3T; GE Healthcare, Milwaukee, Wisconsin) by using a dedicated 8-channel phased array coil (Invivo, Gainesville, Florida). QSM was obtained with a 3D flow-compensated multiecho spoiled gradient echo sequence.²⁵ The imaging parameters included the following: coronal planes covering the brain; number of TEs, 11; first TE, 4.5 ms; TE spacing, 5 ms; TR, 58.4 ms; flip angle, 15°; bandwidth per pixel, ±62.5 Hz; FOV, 22 × 16.5 cm; acquisition matrices, 320 × 416; section thickness, 1.5 mm; imaging time, 7 minutes 1 second. A parallel imaging method (the array spatial sensitivity encoding technique) was used with a reduction factor of 2. In this study, 56 coronal sections were used to capture the center of the brain that contains the deep gray nuclei structures. QSM was reconstructed from the complex data obtained during the gradient-echo sequence by using the morphology enabled dipole inversion technique.¹⁹ After the complex multiecho MR images were saved, a nonlinear fitting was performed to estimate the magnetic field inhomogeneity, followed by a magnitude-guided phase unwrapping.²⁰ The background field was further removed by applying the projection to the dipole fields method.²⁶ Finally, the remaining tissue field was inverted to generate a susceptibility map by using the morphology enabled dipole inversion method.²⁰ An empirically determined regularization parameter of 1000 was consistently applied to all cases. All 11 echoes were used with weightings proportional to their signal-to-noise ratios for reconstructing QSM and R2*.^{27,28} R2* mapping was reconstructed from the magnitude gradient-echo data with a monoexponential fit by using the log-linear method.

In addition, all patients underwent our standard brain MR imaging protocol, including T2-weighted imaging, FLAIR imaging, and T1-weighted imaging (spin-echo or 3D fast spoiled gradient-echo imaging). The imaging parameters (TR, ms/TE, ms/

Table 1: Demographic and clinical data of subjects studied

	Patients with PD (n = 21)	Controls (n = 21)	P
Sex (M/F)	9:12	9:12	1.00
Age (yr) (mean)	72.0 ± 7.5	69.7 ± 8.6	.54
Onset (yr) (mean)	69.0 ± 8.3		
Disease duration (mo) (mean)	32.7 ± 27.1		
H & Y stage (median) (range)	2 (1–3)		

Note:—H & Y stage indicates Hoehn and Yahr stage.

TI, ms/NEX/imaging time) were 4500/85/not applicable/1 time/2 minutes 10 seconds for T2-weighted imaging; 12,000/140/2600/2 times/3 minutes 20 seconds for FLAIR imaging; and 400/4/not applicable /2 times/2 minutes 40 seconds for spin-echo T1-weighted images. T2 and T1-weighted images and FLAIR images were acquired at a section thickness of 5 mm, an intersection gap of 2.5 mm, an FOV of 22 cm, and a matrix of 256 × 192. The following parameters were used for spoiled gradient-echo imaging: TR, ms/TE, ms, 10/4; flip angle, 10°; bandwidth, 42 kHz; section thickness, 1.2 mm; matrix, 256 × 256; FOV, 24 × 24 cm; imaging time, 3 minutes 56 seconds. Parallel imaging technique (a reduction factor of 2) was used for only T2-weighted imaging and spoiled gradient-echo imaging.

Patients and Controls

Our institutional review board approved this retrospective study analyzing existing patient data with patient information de-identified and waived informed consent. At our institution, the 3D flow-compensated multiecho spoiled gradient-echo sequence is part of routine brain MR imaging for indications including the following: 1) screening of minor hemorrhage; and 2) evaluation of vascular disease, movement disorder, or degenerative disease. From the patients who underwent brain MR imaging examinations, including the 3D flow-compensated multiecho spoiled gradient-echo sequence between May 2012 and December 2012, the study included 21 patients whose PD was diagnosed by 2 of the authors (K.O. and T.U. with 18 and 30 years of experience, respectively, in movement disorders). All fulfilled the UK Parkinson's Disease Brain Bank criteria for the diagnosis of idiopathic PD. At the time of testing, 19 patients were on antiparkinsonian medication. From this data base, we also selected the 21 age- and sex-matched subjects as controls, who had no history of neurologic or psychiatric diseases. Indications for their examination included headache, anterior communicating and middle cerebral artery aneurysms, bilateral upper extremity numbness, benign positional vertigo, and hemifacial spasm. In all patients with PD and controls, conventional imaging results were normal. Demographic and clinical data on all study subjects are shown in Table 1.

Image Analysis

Two neuroradiologists (S.K. and J.M. with 16 and 11 years of experience, respectively) who were blinded to the subject data manually traced ROIs by using Image J software (National Institutes of Health, Bethesda, Maryland). For the ROI measurements by the neuroradiologists, each image technique (QSM and R2* mapping) was analyzed separately, and only 1 technique was shown at a time. ROIs of the nuclei were drawn on the basis of the

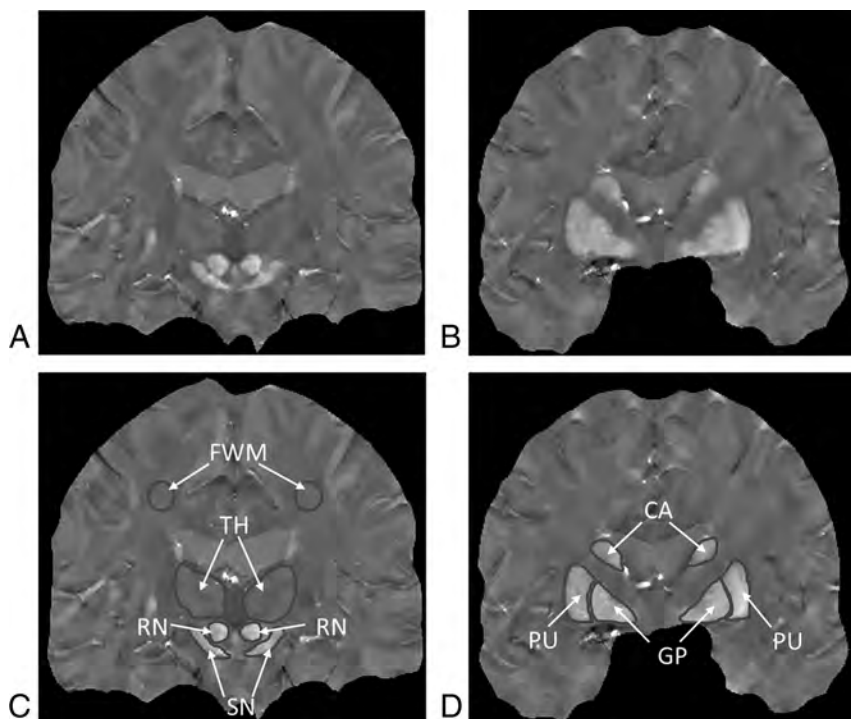


FIG 1. QSM images (A and B) and selected regions of interest (C and D). CA indicates caudate nucleus; GP, globus pallidus; PU, putamen; RN, red nucleus; SN, substantia nigra; TH, thalamus.

anatomic structures on the 3D QSM and $R2^*$ maps. The ROIs included the bilateral substantia nigra, red nuclei, globus pallidus, head of the caudate nuclei, putamina, and thalami (Fig 1). Data on each structure were obtained from all visible sections. We calculated the mean QSM and $R2^*$ values for each bilateral structure using all echoes according to their signal-to-noise ratio.^{27,28} To analyze the QSM and $R2^*$ values, we calculated the average of the value in the bilateral regions. For each subject (patients with PD and controls), we then used the mean QSM and $R2^*$ values obtained by 2 neuroradiologists as the final values and evaluated all the statistical analyses by using the final value. Data were used to calculate the sensitivity, specificity, and the area under the receiver operating characteristic (ROC) curve (A_z) of each method for discriminating patients with PD from controls.

In addition, 1 radiologist (Y.M. with 8 years of experience) measured the volume of the structures on QSM images. The volume was calculated by tracing the boundary of the structure manually from the head to its tail and then summing the cross-sectional areas of the entire structure and multiplying the sum by the section thickness.

Statistical Analysis

We used statistical software (StatView 5.0; SAS Institute, Cary, North Carolina). Differences of $P < .05$ were considered statistically significant. Differences in the sex- and age distribution of the patients with PD and controls were compared with the Fisher exact test for sex and the 2-tailed Student t test for age. Differences in the QSM and $R2^*$ values of the patients with PD and controls were analyzed with the Mann-Whitney U test. A computer program (ROC-kit, 1.1B2 β Version; Charles E. Metz, University of

Chicago, Chicago, Illinois) was used to compare the diagnostic performance of the different MR images and to compute the ROC curve and the A_z . To discriminate between patients with PD and controls, we established a cutoff value for the signal-intensity ratio based on the highest Youden Index (eg, QSM value of >0.210).²⁹ Sensitivity, specificity, and accuracy for discriminating patients with PD from the controls were calculated by using these cutoff values. Accuracies were compared with the Fisher exact test. To measure interobserver agreement with respect to the QSM and $R2^*$ values recorded by the radiologists, we used the Kendall W test, in which $W < 0.20$ = poor, 0.21–0.40 = fair, 0.41–0.60 = moderate, 0.61–0.80 = good, and 0.80–1.00 = excellent agreement.

RESULTS

As shown in Table 1, there were no statistically significant differences in the sex and age distribution of the patients with PD and controls. The median Hoehn

and Yahr stage of patients with PD was 2, and 20 of 21 patients with PD had lateralized motor symptoms.

The QSM and $R2^*$ values for the substantia nigra were significantly higher in patients with PD than in controls (QSM value 0.224 versus 0.199, $P < .01$; Table 2 and Fig 2). The QSM and $R2^*$ values of all other brain regions measured (the red nucleus, globus pallidus, head of caudate, putamina, and thalami) did not differ significantly between patients with PD and the controls. For the 20 patients with PD who had lateralized motor symptoms, we compared the QSM values of both sides (contralateral and ipsilateral to the clinically more affected side) and found that there was no significant difference between them (0.222 versus 0.225, $P = .13$).

For the mean total number of sections and the mean volume, there were no significant differences between the patients with PD and the controls (Table 3).

Specific Changes in the Bilateral Nigral Average Phase Values in Patients with PD

For the discrimination between patients with PD and controls, ROC analysis suggested optimal cutoff values of >0.210 for the QSM value and of >28.8 for the $R2^*$ value; these values were based on the Youden Index. The sensitivity, specificity, and accuracy of QSM and $R2^*$ are shown in Table 4. The accuracy was significantly higher for QSM than for $R2^*$ ($P < .05$).

The ROC curves are plotted in Fig 3. The A_z value was 0.91 for QSM and 0.69 for $R2^*$. Pair-wise comparisons showed that the A_z for QSM was significantly larger than that for $R2^*$ ($P < .05$).

Table 2: Regional QSM and R2* values

	QSM (ppm)			R2* Value (1/SE)		
	Patients with PD	Controls	P Value	Patients with PD	Controls	P Value
Substantia nigra	0.224 ± 0.014 ^a	0.199 ± 0.014	.01 × 10 ⁻³	30.1 ± 1.5 ^b	29.0 ± 2.0	.01
Red nucleus	0.188 ± 0.021	0.195 ± 0.019	.15	27.0 ± 1.7	27.8 ± 2.2	.08
Globus pallidus	0.200 ± 0.014	0.205 ± 0.029	.82	29.7 ± 1.8	29.5 ± 2.1	.36
Head of caudate	0.166 ± 0.013	0.166 ± 0.013	.97	25.2 ± 1.4	24.6 ± 1.7	.19
Putamen	0.168 ± 0.013	0.170 ± 0.009	.17	26.4 ± 0.9	26.7 ± 1.6	.44
Thalamus	0.127 ± 0.059	0.126 ± 0.007	.53	22.4 ± 1.0	22.8 ± 1.2	.25

Note:—SE indicates standard error.

^a Significantly different from controls ($P < .01$).

^b Significantly different from controls ($P < .05$).

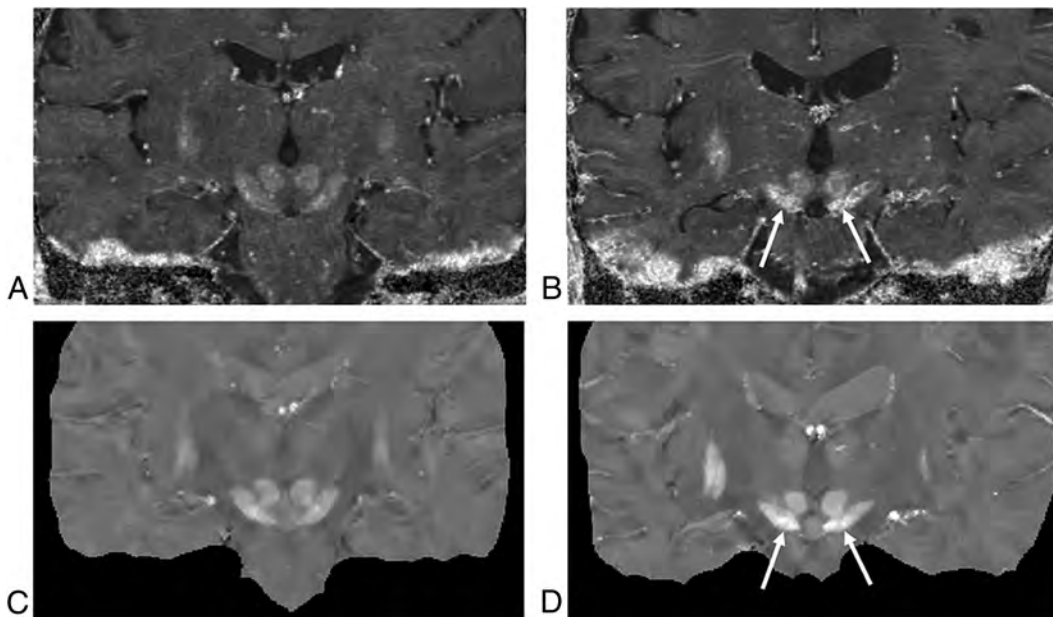


FIG 2. R2* (top row) and QSM maps (bottom row) of 2 subjects, a 68-year-old control subject (A and C) and a 66-year-old patient with PD (B and D). Both the R2* and the QSM maps show higher paramagnetic susceptibility in the substantia nigra of the patient with PD than in the control (arrows).

Table 3: Mean number of sections and mean volume for the ROI measurements

	Mean No. of Sections		Mean Volume (mm ³)		P Value
	Patients with PD	Controls	Patients with PD	Controls	
Substantia nigra	9.6	9.7	598.2 ± 88.0	612.5 ± 66.3	.59
Red nucleus	4.8	4.7	187.9 ± 15.3	189.3 ± 16.6	.87
Globus pallidus	19.0	19.1	2734.7 ± 263.0	2667.1 ± 241.6	.54
Head of caudate	14.9	14.8	1529.9 ± 115.7	1564.6 ± 121.5	.47
Putamen	18.4	18.4	4964.5 ± 505.2	5127.1 ± 718.4	.62
Thalamus	15.2	15.1	1770.4 ± 89.7	1750.5 ± 118.4	.63

Table 4: Sensitivity, specificity, accuracy, and A_z value of analyses of data in patients with PD and control subjects^a

	QSM Average	R2* Average
Sensitivity	90% (19/21)	81% (17/21)
Specificity	86% (18/21)	52% (11/21)
Accuracy	88% (37/42)	67% (28/42)
A _z value	0.91 ^b	0.69

^a Numbers in parentheses are raw data.

^b Significantly different from R2* ($P < .05$).

Interobserver Agreement

For evaluating QSM data, interobserver agreement was good and the Kendall W value was 0.685. For the R2* mapping, interobserver agreement was moderate and the Kendall W value was 0.415.

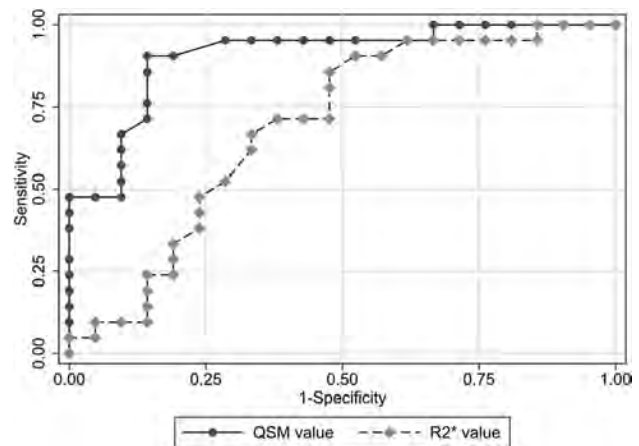


FIG 3. Graphs of the ROC curves for discriminating patients with PD and the controls. The A_z value was 0.91 for QSM_{average}, 0.90 for QSM_{maximum}, 0.69 for R2*_{average}, and 0.71 for R2*_{maximum}. Pair-wise comparisons showed that the A_z for QSM_{average} and QSM_{maximum} was significantly larger than that for R2*_{average} and R2*_{maximum} ($P < .05$).

DISCUSSION

Our MR imaging data on quantifying brain changes in patients with idiopathic PD demonstrated that the QSM values were in-

creased in the substantia nigra, but not in the red nucleus, globus pallidus, head of caudate, putamina, and thalami. The QSM value more accurately discriminated patients with PD and the controls than the $R2^*$ value for measuring the pathologic change in the substantia nigra. Moreover, for the assessment of interobserver agreement, the QSM measurement was also superior to the $R2^*$ measurement.

Identifying a sensitive MR imaging technique for studying substantia nigra change in patients with PD is highly valuable for a PD study because the substantia nigra is the location of dopaminergic cell death in PD. Although, in this study, the QSM values and $R2^*$ values of the substantia nigra were significantly higher in patients with PD, the analyses of the volume of the substantia nigra showed no significant difference between the patients with PD and controls. The susceptibility may therefore be a more sensitive marker for the detection of abnormalities of the substantia nigra. Highly paramagnetic iron can affect both relaxation and susceptibility contrasts in MR imaging. Accordingly, a wide range of MR imaging techniques has been used to study substantia nigra change in PD, including R2 (1/T2), $R2^*$, and susceptibility-weighted imaging.³⁰ Previously, $R2^*$ mapping was identified as being more sensitive than R2 mapping for measuring substantia nigra change in PD.⁹ As a result, $R2^*$ mapping has become the standard method for studying PD iron change.^{11,31-34} Our ROC and interobserver agreement results here show that QSM is more accurate than $R2^*$ mapping for measuring substantia nigra change in PD; this finding is consistent with that in a recent study showing that QSM is more accurate than $R2^*$ mapping in measuring basal ganglia change in multiple sclerosis.²³ Therefore, QSM may replace $R2^*$ mapping for MR imaging measurement of iron-associated change in the brain.

The physics of magnetic susceptibility may explain why QSM is more accurate than $R2^*$ mapping. According to the MR imaging signal equation, the exponential $R2^*$ decay rate reflecting the static dephasing by the inhomogeneous field plus the thermal random dephasing (R2) is, in general, not well-defined or, at most, is related to iron concentration in a geometry-dependent manner.¹⁷ Physics theory and experimental data¹² demonstrated that a good linear relationship between $R2^*$ and iron concentration may only be expected in regions of uniform iron deposition. On the other hand, the inhomogeneous field estimated from the MR imaging signal is the tissue susceptibility linearly convolving with the dipole kernel.^{28,35} Deconvolution of the field generates QSM,¹⁸⁻²⁰ which, divided by iron molar susceptibility, is the iron concentration map. Therefore, QSM is more accurate than $R2^*$ mapping for measuring iron content.

MR imaging phase has also been used to measure the increased nigral iron content in patients with PD.³⁶ It should be cautioned that in general, the phase depends on iron concentration in a convoluted way according to the Maxwell Equation, the law of magnetism. The phase value at a location reflects not the local tissue susceptibility property but the sum of effects (dipole field contributions) from all magnetic sources surrounding the observation point, resulting in no simple relation between phase in a voxel and its iron content as confirmed experimentally.¹³

In FDG-PET studies, 100% of patients with clinically moderate PD were identified,³⁷ and 85% of patients with early PD were

differentiated from the controls.³⁸ However, PET is limited by its rigid technical requirements and high cost.³⁹ In contrast, MR imaging is relatively noninvasive and does not require the use of radioactive tracers, suggesting that it may be more practical for longitudinal follow-up studies and repeat assessments.⁴⁰ A previous study reported that the measurement derived from diffusion tensor imaging has been significantly correlated with the number of dopaminergic neurons lost in the substantia nigra in patients with PD.⁴¹ The DTI is known to reflect local diffusion characteristics of water molecules, while the MR imaging parameters by QSM or $R2^*$ mapping are sensitive to iron deposits. The previous investigators have reported that $R2^*$ and fractional anisotropy values of the substantia nigra in patients with PD were not correlated,⁴² though it is known that iron deposition affects the measurement from DTI.⁴³ Consequently, these MR imaging parameters yield different but complementary information. According to Péran et al,³³ a combination of 3 MR imaging parameters (the $R2^*$ value, mean diffusivity, and fractional anisotropy) can yield 95% global accuracy (A_z value) for discriminating patients with PD from controls. To their observation, we add that the combination of MR imaging parameters, including QSM, whose discrimination power is superior to $R2^*$ mapping, discriminates accurately between patients with PD and controls.

Some patients with early-stage PD manifest asymmetric signs and symptoms, while the late stages of PD are characterized by a similar degree of bilateral symptoms. Therefore, we compared the QSM values of both sides (contralateral and ipsilateral to the clinically more affected side). However, our results demonstrated that there was no significant difference between them. Others³³ found that the ratio of the smaller-to-larger median values (symmetry ratio) for ROIs in the left and right deep gray matter regions was similar in patients with PD and controls. Their findings coincide with our observation that with respect to discriminating between patients with PD and controls, there was no significant difference between average and maximum values.

In the current study, the QSM and $R2^*$ values of all other brain regions measured did not differ significantly between patients with PD and the controls. Regarding the iron levels of the putamen in patients with PD, there seem to be inconsistent results among previous studies. For example, 1 postmortem study found no difference in putamen iron in PD tissue relative to controls,⁴⁴ which was consistent with the current findings. In contrast, another study that used the R2 parameter ($R2^*-R2$) demonstrated higher levels of iron not only in the substantia nigra but also in the putamen in the PD group relative to the controls⁴⁵; this discrepancy with the present study may be due to the difference in the severity of the disease (the median Hoehn and Yahr stage: 3 in the previous study, 2 in the current study). In addition, in a previous study, significant variation of $R2^*$ was longitudinally observed in the caudal putamen of patients with PD evolving during a 3-year period.⁴⁶ Therefore, additional longitudinal studies are needed to evaluate the relationship between the iron levels of the putamen and the severity of PD more comprehensively.

Our retrospective study has some limitations. First, this study was limited by a small sample size, which prevented us from exploring potential subgroup analyses such as a correlation between the average phase values of the bilateral substantia nigra and dis-

ease severity. Second, in this study, we used the clinical criteria for the diagnosis of PD because of difficulty in obtaining a histopathologic confirmation in patients with PD, which may impair the validity of our analyses, including sensitivity, specificity, and accuracy. Third, many patients had a long disease duration in this study. The detection of minimal nigral lesions is particularly challenging in that clinical signs at the early stage of disease are often subtle or ambiguous. Therefore, prospective studies on a larger number of patients with early-stage PD and unconfirmed PD are underway to determine whether QSM can accurately identify patients with PD. Fourth, the controls in this study were not healthy volunteers. Although they had no history of neurologic or psychiatric diseases, we could not exclude the possibility of existing pathology in the controls. Fifth, the reduced interobserver agreement for the R2* measures probably reflects reduced stability of R2* compared with QSM, affecting the results of the sensitivity, specificity, and accuracy of R2* values and thereby reducing the utility of R2* compared with QSM. Sixth, for the ROI measurements, we analyzed the QSM and R2* mapping separately to compare the diagnostic accuracy between them more precisely. Therefore, the exact same ROIs were not used in this study; this difference could affect the results of the accuracy of QSM and R2* values. Seventh, we did not evaluate DTI scans, which can provide an indirect measure of dopaminergic degeneration within the substantia nigra. Studies comparing DTI and QSM findings may help to identify underlying pathologic conditions in patients with PD. Eighth, in our assessments, we did not subdivide the substantia nigra into the pars compacta and pars reticulata.

Although others⁴⁷ evaluated the nigral subdivisions in controls on the basis of signal intensity and comparisons with the known anatomy, it is not clear that the nigral subdivisions can be evaluated separately in patients with PD. In our study, we evaluated the substantia nigra as a whole. Last, the FOV of QSM cannot cover the whole brain; it was set to cover the deep gray nuclei structures in this study. Therefore, we could not evaluate other important regions such as the dentate nuclei.

CONCLUSIONS

The sensitivity of QSM is superior to R2* mapping for the detection of pathologic changes in the substantia nigra of patients with PD. QSM can identify the nigrostriatal signature of PD, and its discrimination between patients with PD and controls is highly accurate. Thus, the increased susceptibility due to the higher iron content in the substantia nigra of patients with PD can be quantified more accurately with QSM. Our findings suggest that QSM may be valuable for the diagnosis and assessment of PD.

Disclosures: Tian Liu—UNRELATED: Employment: MedimageMetric; Patents (planned, pending or issued): Cornell University.* Comments: Tian Liu is listed as an inventor of the QSM technology. *Money paid to the institution.

REFERENCES

- Caslake R, Moore JN, Gordon JC, et al. **Changes in diagnosis with follow-up in an incident cohort of patients with parkinsonism.** *J Neurol Neurosurg Psychiatry* 2008;79:1202–07
- Drayer BP, Olanow W, Burger P, et al. **Parkinson plus syndrome: diagnosis using high field MR imaging of brain iron.** *Radiology* 1986;159:493–98
- Bizzi A, Brooks RA, Brunetti A, et al. **Role of iron and ferritin in MR imaging of the brain: a study in primates at different field strengths.** *Radiology* 1990;177:59–65
- Dexter DT, Wells FR, Lees AJ, et al. **Increased nigral iron content and alterations in other metal ions occurring in brain in Parkinson's disease.** *J Neurochem* 1989;52:1830–36
- Griffiths PD, Dobson BR, Jones GR, et al. **Iron in the basal ganglia in Parkinson's disease: an in vitro study using extended X-ray absorption fine structure and cryo-electron microscopy.** *Brain* 1999;122(pt 4):667–73
- Wang Y. *Principles of Magnetic Resonance Imaging: Physics Concepts, Pulse Sequences, and Biomedical Applications.* <https://www.create-space.com>: CreateSpace Independent Publishing Platform; 2012
- Ordidge RJ, Gorell JM, Deniau JC, et al. **Assessment of relative brain iron concentrations using T2-weighted and T2*-weighted MRI at 3 Tesla.** *Magn Reson Med* 1994;32:335–41
- Haacke EM, Cheng NY, House MJ, et al. **Imaging iron stores in the brain using magnetic resonance imaging.** *Magn Reson Imaging* 2005;23:1–25
- Gorell JM, Ordidge RJ, Brown GG, et al. **Increased iron-related MRI contrast in the substantia nigra in Parkinson's disease.** *Neurology* 1995;45:1138–43
- Graham JM, Paley MN, Grunewald RA, et al. **Brain iron deposition in Parkinson's disease imaged using the PRIME magnetic resonance sequence.** *Brain* 2000;123(pt 12):2423–31
- Martin WR, Wieler M, Gee M. **Midbrain iron content in early Parkinson disease: a potential biomarker of disease status.** *Neurology* 2008;70:1411–17
- Langkammer C, Krebs N, Goessler W, et al. **Quantitative MR imaging of brain iron: a postmortem validation study.** *Radiology* 2010;257:455–62
- Yao B, Li TQ, Gelderen P, et al. **Susceptibility contrast in high field MRI of human brain as a function of tissue iron content.** *Neuroimage* 2009;44:1259–66
- Wang S, Lou M, Liu T, et al. **Hematoma volume measurement in gradient echo MRI using quantitative susceptibility mapping.** *Stroke* 2013;44:2315–17
- Ogawa S, Menon RS, Tank DW, et al. **Functional brain mapping by blood oxygenation level-dependent contrast magnetic-resonance-imaging: a comparison of signal characteristics with a biophysical model.** *Biophys J* 1993;64:803–12
- Davis TL, Kwong KK, Weisskoff RM, et al. **Calibrated functional MRI: mapping the dynamics of oxidative metabolism.** *Proc Natl Acad Sci U S A* 1998;95:1834–39
- Yablonskiy DA, Haacke EM. **Theory of NMR signal behavior in magnetically inhomogeneous tissue: the static dephasing regime.** *Magn Reson Med* 1994;32:749–63
- de Rochefort L, Liu T, Kressler B, et al. **Quantitative susceptibility map reconstruction from MR phase data using bayesian regularization: validation and application to brain imaging.** *Magn Reson Med* 2010;63:194–206
- Liu J, Liu T, de Rochefort L, et al. **Morphology enabled dipole inversion for quantitative susceptibility mapping using structural consistency between the magnitude image and the susceptibility map.** *Neuroimage* 2012;59:2560–68
- Liu T, Wisnieff C, Lou M, et al. **Nonlinear formulation of the magnetic field to source relationship for robust quantitative susceptibility mapping.** *Magn Reson Med* 2013;69:467–76
- Bilgic B, Pfefferbaum A, Rohlfing T, et al. **MRI estimates of brain iron concentration in normal aging using quantitative susceptibility mapping.** *Neuroimage* 2012;59:2625–35
- Deistung A, Schafer A, Schweser F, et al. **Toward in vivo histology: a comparison of quantitative susceptibility mapping (QSM) with magnitude-, phase-, and R-2*-imaging at ultra-high magnetic field strength.** *Neuroimage* 2013;65:299–314
- Langkammer C, Liu T, Khalil M, et al. **Quantitative susceptibility mapping in multiple sclerosis.** *Radiology* 2013;267:551–59
- Lotfipour AK, Wharton S, Schwarz ST, et al. **High resolution mag-**

- netic susceptibility mapping of the substantia nigra in Parkinson's disease. *J Magn Reson Imaging* 2012;35:48–55
25. Liu T, Surapaneni K, Lou M, et al. Cerebral microbleeds: burden assessment by using quantitative susceptibility mapping. *Radiology* 2012;262:269–78
 26. Liu T, Khalidov I, de Rochefort L, et al. A novel background field removal method for MRI using projection onto dipole fields (PDF). *NMR Biomed* 2011;24:1129–36
 27. Kressler B, de Rochefort L, Liu T, et al. Nonlinear regularization for per voxel estimation of magnetic susceptibility distributions from MRI field maps. *IEEE Trans Med Imaging* 2010;29:273–81
 28. Pauling L, Coryell CD. The magnetic properties and structure of hemoglobin, oxyhemoglobin and carbonmonoxyhemoglobin. *Proc Natl Acad Sci U S A* 1936;22:210–16
 29. Youden WJ. Index for rating diagnostic tests. *Cancer* 1950;3:32–35
 30. Martin WR. Quantitative estimation of regional brain iron with magnetic resonance imaging. *Parkinsonism Relat Disord* 2009;15(suppl 3):S215–18
 31. Du G, Lewis MM, Shaffer ML, et al. Serum cholesterol and nigrostriatal R2* values in Parkinson's disease. *PLoS One* 2012;7:e35397
 32. Rossi M, Ruottinen H, Elovaara I, et al. Brain iron deposition and sequence characteristics in Parkinsonism: comparison of SWI, T(2)* maps, T(2)-weighted-, and FLAIR-SPACE. *Invest Radiol* 2010;45:795–802
 33. Péran P, Cherubini A, Assogna F, et al. Magnetic resonance imaging markers of Parkinson's disease nigrostriatal signature. *Brain* 2010;133:3423–33
 34. Baudrexel S, Nurnberger L, Rub U, et al. Quantitative mapping of T1 and T2* discloses nigral and brainstem pathology in early Parkinson's disease. *Neuroimage* 2010;51:512–20
 35. Jackson JD. *Classical Electrodynamics*. 3rd ed. New York: John Wiley and Sons; 1999
 36. Jin L, Wang J, Zhao L, et al. Decreased serum ceruloplasmin levels characteristically aggravate nigral iron deposition in Parkinson's disease. *Brain* 2011;134:50–58
 37. Hu MT, White SJ, Herlihy AH, et al. A comparison of (18)F-dopa PET and inversion recovery MRI in the diagnosis of Parkinson's disease. *Neurology* 2001;56:1195–200
 38. Morrish PK, Sawle GV, Brooks DJ. Clinical and [18F] dopa PET findings in early Parkinson's disease. *J Neurol Neurosurg Psychiatry* 1995;59:597–600
 39. Meyer GJ, Schober O, Stoppe G, et al. Cerebral involvement in systemic lupus erythematosus (SLE): comparison of positron emission tomography (PET) with other imaging methods. *Psychiatry Res* 1989;29:367–68
 40. Volkow ND, Rosen B, Farde L. Imaging the living human brain: magnetic resonance imaging and positron emission tomography. *Proc Natl Acad Sci U S A* 1997;94:2787–88
 41. Boska MD, Hasan KM, Kibuule D, et al. Quantitative diffusion tensor imaging detects dopaminergic neuronal degeneration in a murine model of Parkinson's disease. *Neurobiol Dis* 2007;26:590–96
 42. Du G, Lewis MM, Styner M, et al. Combined R2* and diffusion tensor imaging changes in the substantia nigra in Parkinson's disease. *Mov Disord* 2011;26:1627–32
 43. Zhang J, Tao R, Liu C, et al. Possible effects of iron deposition on the measurement of DTI metrics in deep gray matter nuclei: an in vitro and in vivo study. *Neurosci Lett* 2013;551:47–52
 44. Antonini A, Leenders K, Meier D, et al. T2 relaxation time in patients with Parkinson's disease. *Neurology* 1993;43:697–700
 45. Wallis LI, Paley MN, Graham JM, et al. MRI assessment of basal ganglia iron deposition in Parkinson's disease. *J Magn Reson Imaging* 2008;28:1061–67
 46. Ulla M, Bonny JM, Ouchchane L, et al. Is R2* a new MRI biomarker for the progression of Parkinson's disease? A longitudinal follow-up. *PLoS One* 2013;8:e57904
 47. Eapen M, Zald DH, Gatenby JC, et al. Using high-resolution MR imaging at 7T to evaluate the anatomy of the midbrain dopaminergic system. *AJNR Am J Neuroradiol* 2011;32:688–94

Evaluating the Effects of White Matter Multiple Sclerosis Lesions on the Volume Estimation of 6 Brain Tissue Segmentation Methods

S. Valverde,  A. Oliver, Y. Díez, M. Cabezas, J.C. Vilanova, L. Ramió-Torrentà, À. Rovira, and X. Lladó



ABSTRACT

BACKGROUND AND PURPOSE: The accuracy of automatic tissue segmentation methods can be affected by the presence of hypointense white matter lesions during the tissue segmentation process. Our aim was to evaluate the impact of MS white matter lesions on the brain tissue measurements of 6 well-known segmentation techniques. These include straightforward techniques such as Artificial Neural Network and fuzzy C-means as well as more advanced techniques such as the Fuzzy And Noise Tolerant Adaptive Segmentation Method, fMRI of the Brain Automated Segmentation Tool, SPM5, and SPM8.

MATERIALS AND METHODS: Thirty T1-weighted images from patients with MS from 3 different scanners were segmented twice, first including white matter lesions and then masking the lesions before segmentation and relabeling as WM afterward. The differences in total tissue volume and tissue volume outside the lesion regions were computed between the images by using the 2 methodologies.

RESULTS: Total gray matter volume was overestimated by all methods when lesion volume increased. The tissue volume outside the lesion regions was also affected by white matter lesions with differences up to 20 cm³ on images with a high lesion load (≈ 50 cm³). SPM8 and Fuzzy And Noise Tolerant Adaptive Segmentation Method were the methods less influenced by white matter lesions, whereas the effect of white matter lesions was more prominent on fuzzy C-means and the fMRI of the Brain Automated Segmentation Tool.

CONCLUSIONS: Although lesions were removed after segmentation to avoid their impact on tissue segmentation, the methods still overestimated GM tissue in most cases. This finding is especially relevant because on images with high lesion load, this bias will most likely distort actual tissue atrophy measurements.

ABBREVIATIONS: ANN = Artificial Neural Network; FANTASM = Fuzzy And Noise Tolerant Adaptive Segmentation Method; FAST = FMRI Automated Segmentation Tool; FCM = fuzzy C-means; H1 = Hospital Vall d'Hebron, Barcelona, Spain; H2 = Hospital Universitari Dr. Josep Trueta, Girona, Spain; H3 = Clinica Girona, Girona, Spain; WML = white matter lesion

During the past few years, MR imaging brain tissue segmentation techniques have become important tools in the clinical evaluation and progression of MS because they make it possible to measure the changes in brain atrophy and lesion load.¹⁻³ However, white matter lesions (WMLs) can significantly affect tissue volume measurements if these lesions are included in the segmentation process.⁴⁻⁶ Several studies have analyzed the effects of WMLs on brain tissue measurements of common segmentation

techniques such as SPM5 (<http://www.fil.ion.ucl.ac.uk/spm/>)⁷ and FMRI Automated Segmentation Tool (FAST, <http://fsl.fmrib.ox.ac.uk/fsl/fslwiki/FAST>).⁸ Chard et al⁵ studied the effect of synthetic lesions on SPM5 segmentations for different WML voxel intensities (from 30% to 90% of normal WM intensity) and lesion loads (from 10 to 20 cm³). The authors reported that GM volume was overestimated by $\approx 2.3\%$, whereas WM tissue was underestimated by $\approx 3.6\%$ in scans with 15 cm³ of simulated lesions. More recently, Battaglini et al⁴ also analyzed the effects of different WML intensities and lesion loads on tissue measurements obtained with FAST software. The authors showed again that total GM volume tended to increase with higher lesion loads in segmented images with generated simulated lesions. Gelineau-Morel et al⁶ performed a similar study on the effects of simulated and real WMLs but on tissue volume measurements outside lesion regions. The authors reported that on images with simulated lesions, FAST clearly underestimated GM outside lesion regions as long as lesion volume increased and lesion intensities approximated those of GM tissue. The incidence of

Received August 19, 2014; accepted after revision December 20.

From the Computer Vision and Robotics Group (S.V., A.O., Y.D., X.L.), University of Girona, Campus Montilivi, Girona, Spain; Girona Magnetic Resonance Center (J.C.V.), Girona, Spain; Multiple Sclerosis and Neuroimmunology Unit (L.R.-T.), Dr. Josep Trueta University Hospital, Institut d'Investigació Biomèdica de Girona, Girona, Spain; and Magnetic Resonance Unit (M.C., A.R.), Department of Radiology, Vall d'Hebron University Hospital, Barcelona, Spain.

Please address correspondence to Sergi Valverde, Ed. P-IV, Campus Montilivi, University of Girona, 17071 Girona, Spain; e-mail: svalverde@eia.udg.edu

 Indicates open access to non-subscribers at www.ajnr.org

<http://dx.doi.org/10.3174/ajnr.A4262>

WMLs on real scans was smaller, but FAST still tended to underestimate GM with increasing lesion loads.

On the other hand, various studies have also analyzed the correlation between brain tissue atrophy and MS disability progression.^{9,10} These studies showed a brain atrophy decrease rate between 0.3% and 0.5% of change in brain parenchyma per year in patients with MS,^{9,10} with a decrease in GM and WM volume of up to 0.4% and 0.2% per year, respectively.¹⁰ This statement along with study results such as those found by Battaglini et al⁴ and Gelineau-Morel et al⁶ indicates that a portion of brain atrophy could be hidden by the inclusion of WMLs on tissue segmentation.

In this study, we performed a quantitative evaluation of the effects of WMLs on brain tissue volume measurements to analyze the extent to which tissue estimations are affected by changes in WML volume and intensity. In contrast to other similar studies,⁴⁻⁶ our analysis extended the number of segmentation methods involved, offering a comparative evaluation of the effects of WMLs on the volume measurements of 6 segmentation methods. Furthermore, given the reported correlation between brain atrophy rates and disability progression,^{9,10} it can be clinically relevant for the MS community to extend the analysis of the effects of simulated WML to real data of patients with MS; hence, our analysis was focused exclusively on data from the T1-weighted images from patients with clinically confirmed MS.

MATERIALS AND METHODS

Image Acquisition

The dataset consisted of 30 MR images from patients with clinically confirmed MS at 3 different hospitals (Fig 1). Each patient underwent MR imaging by using the same protocol (T1-weighted, T2-weighted, proton-attenuation-weighted, and FLAIR images), though a different scanner was used at each hospital. Ten patient images from Hospital Vall d'Hebron, Barcelona, Spain, (H1) were acquired on a 1.5T Magnetom Symphony Quantum (Siemens, Erlangen, Germany), with 2D conventional spin-echo T1-weighted (TR, 450 ms; TE, 17 ms), dual-echo proton-attenuation T2-weighted sequences (TR, 3750 ms; TE, 14/86 ms), and FLAIR sequences (TR, 9000 ms; TE, 114 ms; and TI, 2500 ms). Ten patient images from Hospital Universitari Dr. Josep Trueta, Girona, Spain, (H2) were acquired on a 1.5T Intera scanner (R12) (Philips Healthcare, Best, the Netherlands) with 2D conventional spin-echo T1-weighted (TR, 653 ms; TE, 14 ms), dual-echo proton-attenuation T2-weighted (TR, 2800 ms; TE, 16/80 ms), and FLAIR sequences (TR, 8153 ms; TE, 105 ms; and TI, 2200 ms). Ten patient images from Clinica Girona, Girona, Spain, (H3) were acquired on a 1.5T Signa HDxt scanner (GE Healthcare, Milwaukee, Wisconsin) with 3D fast-spoiled gradient T1-weighted (TR, 30 ms; TE, 9 ms; flip-angle, 30°), fast spin-echo T2-weighted (TR, 5000–5600 ms; TE, 74–77 ms), proton-attenuation-weighted (TR, 2700 ms; TE, 11.9 ms), and FLAIR sequences (TR, 9002 ms; TE, 80 ms; and TI, 2250 ms). All images were acquired in the axial view with a section thickness of 3 mm.

Images of Patients with MS

WML masks were semiautomatically delineated from proton-attenuation-weighted images by using Jim software (Xinapse Systems,

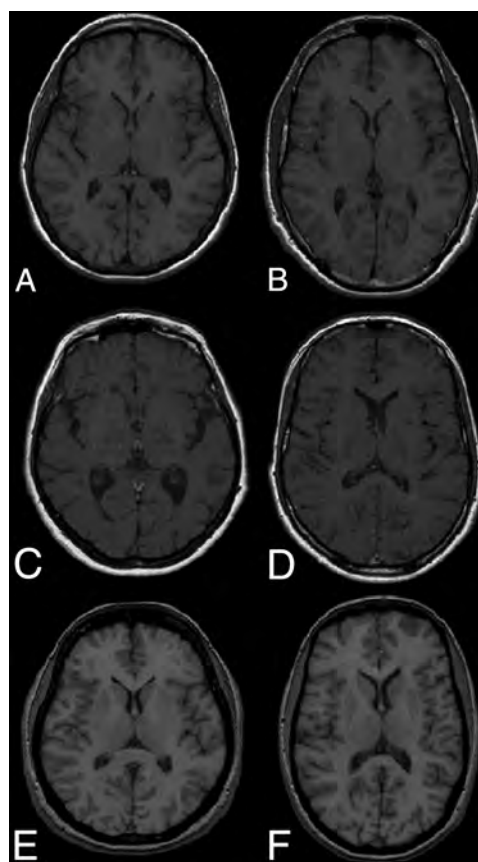


FIG 1. T1-weighted images from the 3 hospitals and scanners involved in the study: 1.5T Magnetom Symphony Quantum (Siemens) from H1 (first row), 1.5T Intera (R12) (Philips) from H2 (middle row), and 1.5T Signa HDxt (GE Healthcare) from H3 (last row).

<http://www.xinapse.com/home.php>) by expert radiologists at each hospital. Then, the proton-attenuation-weighted images and lesion masks were coregistered with T1-weighted images by affine registration.¹¹ The average means and SD lesion volumes for H1, H2, and H3 were $4.15 \pm 4.35 \text{ cm}^3$ (minimum = 0.11, maximum = 11.22 cm^3), $21.79 \pm 17.79 \text{ cm}^3$ (minimum = 0.18, maximum = 52.45 cm^3), and $4.78 \pm 4.60 \text{ cm}^3$ (minimum = 0.43, maximum = 16.34 cm^3).

All T1-weighted patient images were processed following the same pipeline (Fig 2). Internal skull-stripping and intensity-correction options were disabled on SPM5, SPM8 (<http://www.fil.ion.ucl.ac.uk/spm/software/>), and FAST. Instead, to reduce the differences in brain area and signal image intensity produced by different preprocessing tools, we skull-stripped all images by using the Brain Extraction Tool (<http://fsl.fmrib.ox.ac.uk/fsl/fslwiki/BET>)¹² and intensity-corrected them by using N3.¹³

As a second step, 2 sets were produced from preprocessed images: an original set that included WMLs as part of current tissue and a masked set in which the WMLs were masked out before tissue segmentation and relabeled as WM after, following the same procedure used by radiologists of the 3 hospitals.

Segmentation Methods

The set of methods was composed of 6 well-known automatic brain tissue segmentation techniques: Artificial Neural Network (ANN), fuzzy C-means (FCM), Fuzzy And Noise Tolerant Adaptive Segmentation Method (FANTASM), FAST, SPM5, and

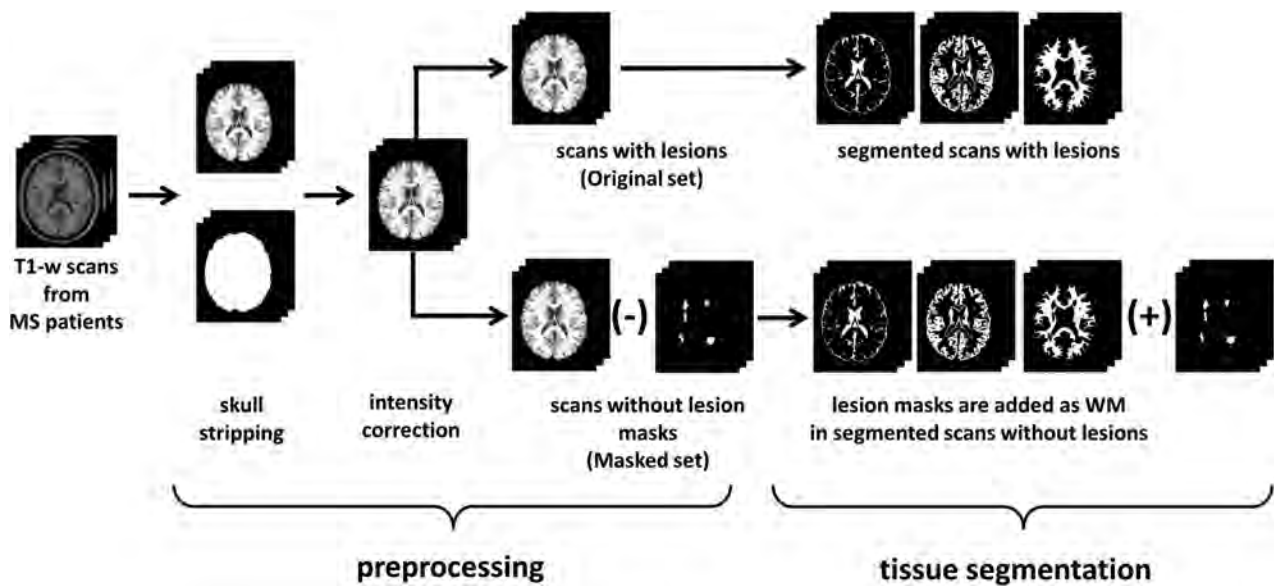


FIG 2. Our pipeline approach. From the 30 T1-weighted scans of patients with MS, nonbrain parts are stripped and brain voxels are corrected for intensity inhomogeneities. From the same corrected set (original), a new set is generated by removing WML masks from scans before segmentation (masked). The scans of both sets are segmented into 1 of the 3 tissue classes (GM, WM, and CSF). Lesion voxels are added as WM after segmentation on masked images.

SPM8. ANN and FCM were implemented for our study, while the rest of the methods were obtained from available repositories. The ANN method is based on self-organizing maps, also known as Kohonen networks.¹⁴ ANN was implemented for our study by using the Matlab 7.12 environment (MathWorks, Natick, Massachusetts) following the technique proposed by Tian et al.¹⁵ FCM¹⁶ and FANTASM¹⁷ are both based on fuzzy-clustering techniques. FCM implements the classic fuzzy-clustering approach, while FANTASM adds neighboring information to increment the robustness of the method to intensity inhomogeneity artifacts and noise. FCM was also implemented by using the Matlab environment and following the technique described in Pham,¹⁶ in which clusters were initialized according to Bezdek et al.¹⁸ FANTASM is included in the MIPAV toolbox (<http://mipav.cit.nih.gov>). FAST⁸ guides the segmentation with spatial information through the optimization of Hidden Markov Random Fields, and the method is included in the fMRI of the Brain Software Library toolbox (<http://fsl.fmrib.ox.ac.uk/fsl/fslwiki/>). SPM5 and SPM8⁷ are based on an iterative Gaussian Mixture Model optimization, weighting the probability of belonging to a certain tissue class with a priori spatial information from tissue-probability atlases. However, SPM8 comes with a set of different characteristics to improve registration and tissue segmentation. Both methods are included in the SPM8 toolbox (<http://www.fil.ion.ucl.ac.uk/spm/software/spm8>). All methods were run with default parameters.

Evaluation

Images from both the original and masked sets were segmented into GM, WM, and CSF tissue classes by using the 6 presented segmentation methods. Then, we computed the normalized tissue volumes as the number of voxels classified as GM, WM, and CSF, respectively, divided by the total number of voxels. Three different analyses were performed on these data. First, we analyzed how lesion voxels were classified by each segmentation

method to establish to what extent the tissue volumes reported by each algorithm on the original and masked images could be expected to be different. Second, we analyzed the direct effect of lesions in the global volume estimation by computing the differences in total tissue volume as the percentage of change between original and masked images. For example, in the case of GM tissue:

$$\%GM = \frac{NGMV_{Original} - NGMV_{Masked}}{NGMV_{Masked}} \times 100,$$

where $NGMV_{Original}$ and $NGMV_{Masked}$ stand for the normalized gray matter volumes of original and masked images, respectively. Third, we also investigated the indirect effects of lesions in the rest of the tissue volume outside lesion regions. These are tissue volume estimations that incorporate lesions in the segmentation process but do not consider them when the volume is evaluated.

Statistical Analysis

The correlation among factors (differences in tissue volume, lesion load, and lesion intensity) was calculated by using Pearson linear correlation coefficient (r). The significance level α was set at .05. This level was used both for confidence interval computation and 95% significance hypothesis 2-tailed t tests. All statistical analyses were calculated by using the Matlab environment.

RESULTS

Lesion Classification

Figure 3 depicts the percentage of WML voxels classified either as WM (Fig 3, top) or GM (Fig 3, bottom). Percentages are detailed for each segmentation method and hospital. The amount of WMLs that were classified as GM varied for each method, mostly due to the differences among algorithms. Figure 4 illustrates the differences among methods by showing the output classification performed by each of the 6 segmentation methods.

Observed differences in the percentage of classified WML vox-

els as GM and WM between hospitals can be attributed to each particular scanner acquisition configuration that defines the tissue signal-intensity distributions. The distance between WML and WM mean signal intensities was highest in H3 as computed by each of the 6 methods (range, from $89.2 \pm 4.45\%$ to $92.22 \pm 4.45\%$ of WML mean signal intensity with respect to WM) and was lowest in H2 (range, from $95.3 \pm 1.76\%$ to $100.34 \pm 6.39\%$). As shown in Fig 1, there is a better contrast between GM and WM tissue on the H3 images compared with the H1 and H2 images.

The correlation between the percentage of lesion classification and lesion size was not significant in all cases ($r < 0.33$, $P > .05$). In contrast, the percentage of WML classified as GM or WM and the distance between the mean WML and WM signal intensities showed a moderate correlation in all hospitals ($r > 0.6$, $P < .01$). On the basis of our data, the contrast between tissues computed as the normalized difference between the mean GM and WM signal intensity distributions was correlated with the distance between the WM and WML mean signal intensities ($r = 0.6$, $P < .001$).

Differences in Total Tissue Volume Estimation

The mean percentage differences in total tissue volume between the original and masked images are presented in Table 1. All methods overestimated GM tissue in original scans, regardless of

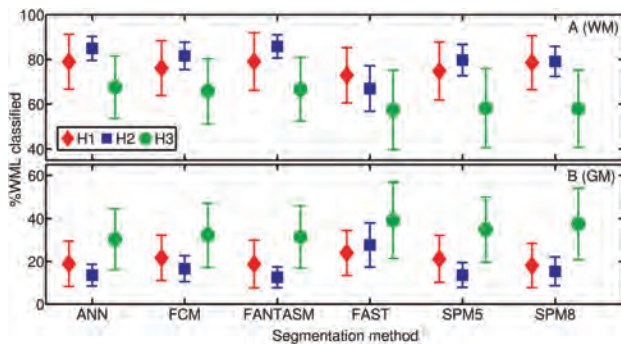


FIG 3. Percentage of voxels in WML regions having been classified as GM (top) and WM (bottom) for each segmentation method and hospital, H1 (◇), H2 (□) or H3 (○). Reported values are means and SDs.

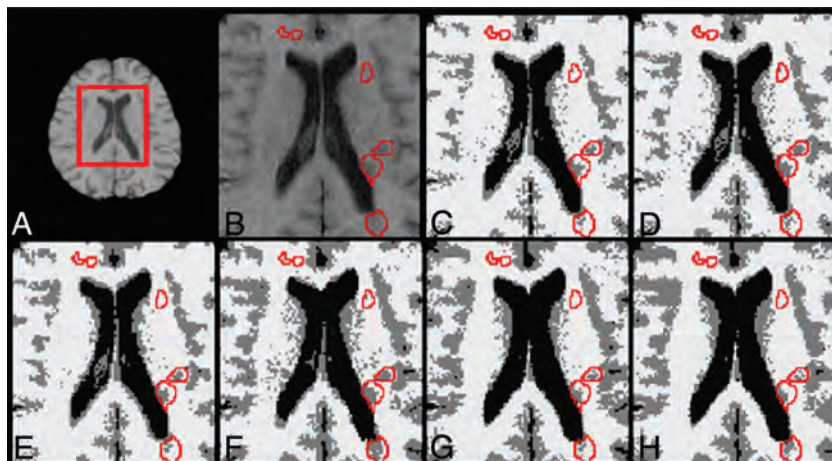


FIG 4. Classification output returned by each segmentation method on the same image. A, T1-weighted scan. B, Zoomed part of the scan with lesions outlined in red. Brain tissue segmentation outputs also with lesions outlined for ANN (C), FCM (D), FANTASM (E), FAST (F), SPM5 (G), and SPM8 (H). C–H, Segmented GM tissue is represented in gray; WM, in white; and CSF, in black.

the hospital, but the overestimation was increased in H2 compared with H1 and H3 due to greater lesion volumes in H2. The differences among methods for the same hospital and tissue were also significantly greater in H2 than in H1 and H3. Abnormally low mean and high SD values observed in SPM5 for both GM (0.10 ± 2.68) and WM (1.04 ± 3.01) in H2 were caused by 2 patients who exhibited very high opposite differences between their respective original and masked images, decreasing the overall mean difference and increasing the SD.

Correlation between the differences in total mean tissue volume and lesion size was significant in all hospitals: Lesion size had a direct effect on tissue segmentation. Table 2 shows the Pearson correlation values obtained between differences in tissue volume and lesion size across methods. All methods except SPM5 presented a positive correlation in GM and a negative correlation in WM in H1 and H2. SPM5 correlated in H1 but not in H2, where it was influenced by abnormal values in the 2 images with highest lesion load. In H3, only FCM, FANTASM, and FAST were positively correlated in GM and negatively correlated in WM. The correlation coefficients for ANN, SPM5, and SPM8 in H3 were weak and not significant in GM and WM.

Volume Estimation of Tissue Outside Lesion Regions

The mean percentage differences in tissue volume outside lesion regions between original and masked images are presented in Table 3. The differences between the images segmented with lesions and images in which the lesions were masked before tissue segmentation were again higher in H2, and the methods still substantially overestimated the GM outside the lesion regions to the detriment of WM, even though analyzed tissues were free of lesion regions. In contrast, only SPM5 and SPM8 reported a noticeable underestimation of GM in H3, also to the detriment of WM.

Differences in tissue volume outside the lesion regions correlated with lesion size for all tissues and hospitals, indicating an effect of lesion size not only on lesion voxels but also on tissue that is not affected by lesions. Table 4 presents the correlation values obtained across methods. In H1, there was a remarkable correlation for ANN, FCM, FANTASM, and FAST in all tissues. The obtained values for SPM8 were also significant in GM and CSF. In H2, the correlation was significant in ANN, FCM, and FANTASM in all tissues. In H3, only FCM and FAST showed a significant correlation in all tissues, whereas FCM, FAST, SPM5, and SPM8 correlated significantly only in WM. All methods except SPM5 and SPM8 reported a significant correlation for CSF.

DISCUSSION

Previous studies have shown that the range of voxel signal intensities composing each of the tissue distributions can be altered by WMLs if these voxels are included in the segmentation process.^{4,5} Lesion load and the apparent lesion signal intensity lead to observed changes in tissue segmentation in original images.

Table 1: Average percentage of change in total tissue volume estimation between original and masked images^a

Method	H1			H2			H3		
	GM	WM	CSF	GM	WM	CSF	GM	WM	CSF
ANN	0.33 ± 0.42	-0.23 ± 0.28	0.11 ± 0.11	1.59 ± 1.37	-0.56 ± 0.46	0.78 ± 0.76	0.25 ± 0.31	-0.16 ± 0.28	-0.09 ± 0.09
FCM	0.28 ± 0.37	-0.22 ± 0.29	0.09 ± 0.11	2.28 ± 2.26	-0.90 ± 0.83	0.94 ± 0.90	0.28 ± 0.23	-0.25 ± 0.20	0.08 ± 0.09
FANTASM	0.23 ± 0.26	-0.18 ± 0.21	0.08 ± 0.08	1.34 ± 1.13	-0.49 ± 0.37	0.80 ± 0.73	0.26 ± 0.22	-0.24 ± 0.19	0.07 ± 0.08
FAST	0.29 ± 0.36	-0.29 ± 0.36	0.12 ± 0.13	1.92 ± 1.59	-1.28 ± 1.03	0.47 ± 0.39	0.34 ± 0.28	-0.37 ± 0.31	0.12 ± 0.17
SPM5	0.20 ± 0.30	-0.21 ± 0.20	-0.14 ± 0.54	0.10 ± 2.68	-1.04 ± 3.01	0.53 ± 0.51	0.04 ± 0.17	-0.18 ± 0.36	0.15 ± 0.23
SPM8	0.08 ± 0.09	-0.08 ± 0.08	-0.04 ± 0.18	0.55 ± 0.34	-0.93 ± 0.55	0.54 ± 0.42	0.09 ± 0.15	-0.23 ± 0.25	0.17 ± 0.23

^a The results are divided by tissue and hospital. Reported values are the means ± SD. Positive values indicate a tissue overestimation on original images compared with masked.

Table 2: Pearson correlation coefficients between method differences in total volume estimation and WML size^a

Method	GM	WM	CSF
H1			
ANN	0.94	-0.90	0.89
FCM	0.93	-0.89	0.83
FANTASM	0.87	-0.80	0.78
FAST	0.97	-0.97	0.96
SPM5	0.58 ^b	-0.89	-0.21 ^b
SPM8	0.92	-0.63	-0.69
H2			
ANN	0.91	-0.88	0.93
FCM	0.92	-0.94	0.92
FANTASM	0.89	-0.87	0.84
FAST	0.95	-0.96	0.82
SPM5	-0.35 ^b	-0.06 ^b	0.72
SPM8	0.76	-0.79	0.57 ^b
H3			
ANN	0.56 ^b	-0.55 ^b	0.88
FCM	0.77	-0.84	0.88
FANTASM	0.74	-0.82	0.85
FAST	0.88	-0.94	0.92
SPM5	-0.06 ^b	-0.03 ^b	0.21 ^b
SPM8	0.56 ^b	-0.48 ^b	0.09 ^b

^a Correlation was computed for each method and hospital separately. All values were found to be significant (*P* value < .05) unless otherwise noted.

^b Not significant.

For instance, if a portion of the lesion voxels is classified as WM, the mean overall WM intensity decreases, shifts WM boundaries into darker intensities, and narrows GM tissue distribution.^{4,6} Voxels that should have been classified as GM are assigned to WM, increasing the WM volume estimation and decreasing GM volume. If some of the WML voxels are classified as GM, the apparent GM mean intensity increases and the WM tissue distribution narrows. This change occurs because voxels that are theoretically classified as WM are assigned to GM, increasing GM estimation against a lower WM volume estimation.

We compare our results with those in previous studies regarding the effects of WMLs on brain tissue volume measurements. However, given the differences in image data, criterion standards, simulated lesions, and lesion voxel intensities among studies, a direct comparison further than an analysis of trends with similar WML intensities and lesion loads should be carefully performed. Our experiments follow the same trend presented by Battaglini et al,⁴ and both studies show that FAST overestimates total GM volume on images segmented with lesions. Similarly, our results also coincide with those found by Chard et al⁵ in simulated data, and in both studies, SPM5 overestimated GM tissue on images with lesions. In contrast, our results appear to be inconsistent with those reported by Gelineau-Morel et al.⁶ These studies showed a significant correlation between WML intensity and an underesti-

ation of GM volume outside the lesions, especially when the lesions had intensities similar to those of the mean GM. The observed differences are caused by distinct signal-intensity profiles of WMLs in each study. In the case of Gelineau-Morel et al,⁶ the WML signal intensities were noticeably more hypointense compared with our data. The probability of voxels to be classified as GM dropped as a result of the influence of hypointense WML intensities in tissue distributions. Part of WML voxels with a signal intensity similar to that of GM were still classified as WM, reducing the signal intensity threshold between GM and WM. As a result, most of the partial volume voxels with signal intensity in the boundary between GM and WM were classified as WM, artificially reducing the overall number of GM voxels.

Our results show that the classification of WML regions is highly dependent on lesion voxel signal intensities and the variation of their signal intensity in terms of the WM signal distribution. Lesion segmentation is clearly determined by this variation because the probability of WML voxels being classified as WM will be higher as long as WML intensities resemble those of WM. However, the signal-intensity contrast among tissues also plays an important role because it can influence the amount of WML voxels that are classified as GM or WM. As long as the contrast among distributions increases, more lesion voxels will be added into the GM distribution. Although the main factor in the observed differences in tissue volume across methods is caused by lesion volume, the percentage of lesion voxels that are classified as GM and WM might also be a remarkable factor in the observed tissue-volume differences, especially in images with high lesion loads. Therefore, the relationship between image quality and lesion load also might have to be considered to explain the differences in tissue volume.

SPM8 was the method with the lowest difference in total tissue volume between original and masked images. In contrast, FAST was the method that was more affected by lesions. In general, all methods overestimated GM in original scans, though values were more significant in H2 than H1 and H3 due to higher lesion loads in H2. In H1 and H3, most of the underestimated WM was shifted into GM. The small percentage of lesions that were segmented as CSF, especially the low lesion volume, limited the impact of WML voxels on the overall CSF tissue distribution of original images.

SPM8 and FANTASM were the methods with the lowest incidence of WML in tissue volume measurements outside lesion regions, while FCM and FAST showed the largest differences among all methods. Lesion volume also explains the limited effect of WML on tissue segmentation outside lesion regions in H1 and H3, compared with images with higher lesion loads such as the H2 images. In H1 and H3, although the behavior differs slightly for

Table 3: Average percentage change in the volume estimation of tissue outside the lesion regions between original and masked scans^a

Method	H1			H2			H3		
	GM	WM	CSF	GM	WM	CSF	GM	WM	CSF
ANN	0.15 ± 0.26	-0.10 ± 0.18	0.07 ± 0.08	0.70 ± 0.61	-0.31 ± 0.24	0.67 ± 0.69	-0.01 ± 0.28	0.04 ± 0.24	-0.12 ± 0.08
FCM	0.09 ± 0.16	-0.07 ± 0.13	0.05 ± 0.08	1.27 ± 1.69	-0.56 ± 0.62	0.82 ± 0.81	0.01 ± 0.03	-0.03 ± 0.05	0.05 ± 0.07
FANTASM	0.06 ± 0.05	-0.05 ± 0.05	0.03 ± 0.05	0.48 ± 0.48	-0.25 ± 0.18	0.68 ± 0.63	0.00 ± 0.04	-0.02 ± 0.05	0.04 ± 0.07
FAST	0.08 ± 0.14	-0.09 ± 0.14	0.07 ± 0.08	0.56 ± 0.87	-0.45 ± 0.64	0.22 ± 0.33	0.02 ± 0.07	-0.06 ± 0.13	0.08 ± 0.16
SPM5	0.06 ± 0.25	0.02 ± 0.13	-0.19 ± 0.54	-0.29 ± 2.61	-0.47 ± 2.91	0.21 ± 0.32	-0.20 ± 0.24	0.23 ± 0.34	0.06 ± 0.15
SPM8	-0.03 ± 0.06	0.09 ± 0.15	-0.10 ± 0.23	0.13 ± 0.30	-0.29 ± 0.33	0.25 ± 0.26	-0.15 ± 0.12	0.14 ± 0.15	0.10 ± 0.20

^a The results are divided by hospital and tissue. Reported values are the means ± SD. Positive values indicate a tissue overestimation on original images compared with masked.

Table 4: Pearson correlation coefficients among method differences in volume estimation of tissue outside the lesion regions and WML size^a

Method	GM	WM	CSF
H1			
ANN	0.77	-0.74	0.83
FCM	0.82	-0.80	0.71
FANTASM	0.80	-0.73	0.66
FAST	0.86	-0.93	0.97
SPM5	0.11	0.51 ^b	-0.30 ^b
SPM8	-0.57 ^b	0.95	-0.77
H2			
ANN	0.85	-0.92	0.93
FCM	0.71	-0.84	0.94
FANTASM	0.66	-0.82	0.87
FAST	0.33 ^b	-0.46 ^b	0.62 ^b
SPM5	-0.43 ^b	0.18 ^b	0.65 ^b
SPM8	0.16 ^b	-0.37 ^b	0.30 ^b
H3			
ANN	0.07	-0.16 ^b	0.79
FCM	0.50	-0.77	0.89
FANTASM	0.17	-0.57 ^b	0.87
FAST	0.45	-0.73	0.89
SPM5	-0.78 ^b	0.72	0.14 ^b
SPM8	-0.64 ^b	0.72	-0.01 ^b

^a Correlation was computed for each method and hospital separately. All values were found to be significant (*P* value < .05) unless otherwise noted.

^b Not significant.

each method, the differences in tissues outside the lesion regions are very small.

The differences outside the lesion regions are especially important because they highlight the bias introduced by WMLs on the estimation of tissue volume that is not pathologically affected. If one compares the results between total tissue volume and tissue volume outside lesion regions, it can be observed that an important part of the overestimated total GM is essentially derived from the same hypointense WML voxels that are classified as GM. Moreover, it is important to highlight the differences in the algorithms. Methods such as FCM and ANN, which only rely on signal intensity, introduce more errors in tissue segmentation compared with methods such as SPM8 and SPM5, which incorporate spatial information. This reinforces the necessity for selecting a segmentation algorithm that does not depend on signal intensity only. However, even though WML voxels have not been considered for computing tissue volume outside the lesion regions, there is still a clear tendency toward overestimating GM. On images with a high lesion load, the observed differences in GM volume outside lesion regions reach values that are equivalent to the yearly expected GM atrophy.^{9,10} Following these assumptions, SPM8, FANTASM, and SPM5 are the methods with the lowest reported incidence of

WML on brain tissue volume measurements, especially on images with a high lesion load.

The present study is not free of limitations. The principal limitation is the lack of tissue expert annotations, given that the study incorporated a relatively large number of images from 3 different hospitals and this task was time-consuming. A second limitation of the study is the sensitivity of the tissue segmentation methods to changes in the skull-stripping mask. Errors in the brain mask may lead to the inclusion of blood vessels such as the internal carotid arteries with hyperintense signal intensity, which might bias the tissue distributions. A final limitation of the study is the inherent difficulty of comparing previous studies, given the differences in the scanner protocols used to acquire the images of patients with MS. The differences in the acquisition protocol may cause the observed differences in the lesion intensity profile compared with previous works.^{8,10} Our study shows that such an intensity profile introduces variations in GM and WM tissue distributions.

CONCLUSIONS

The results of this study indicate a direct relationship between the differences in brain tissue volume and changes in lesion load and WML intensity. Of the analyzed methods, SPM8 exhibited the lowest incidence of WMLs in volume estimation, whereas FCM yielded the highest GM overestimation. Furthermore, all methods were affected by WMLs in tissue volume outside the lesion regions. SPM8 and FANTASM exhibited the lowest differences in tissue volume outside the lesion regions, whereas the influence of WMLs outside the lesion regions is more important in methods such as FCM and FAST. The latter results are especially important because even when masking lesions after segmentation to avoid the inclusion of lesion voxels segmented as GM into the volume estimation, the methods tend to overestimate GM tissue on images segmented with lesions. On images with high lesion load, this bias might conceal or falsify part of the GM and WM tissue atrophy.

Disclosures: Sergi Valverde—RELATED: Grant: FI-DGR2013 research grant from the Generalitat de Catalunya. Mariano Cabezas—RELATED: holds a 2014 European Committee for Treatment and Research in Multiple Sclerosis—Magnetic Resonance Imaging in MS research fellowship.

REFERENCES

- Lladó X, Oliver A, Cabezas M, et al. Segmentation of multiple sclerosis lesions in brain MRI: a review of automated approaches. *Information Sciences* 2012;186:164–85
- Lladó X, Ganiler O, Oliver A, et al. Automated detection of multiple sclerosis lesions in serial brain MRI. *Neuroradiology* 2012;54:787–807

3. Zivadinov R, Bergsland N, Dolezai O, et al. **Evolution of cortical and thalamus atrophy and disability progression in early relapsing-remitting MS during 5 years.** *AJNR Am J Neuroradiol* 2013;34:1931–39
4. Battaglini M, Jenkinson M, De Stefano N. **Evaluating and reducing the impact of white matter lesions on brain volume measurements.** *Hum Brain Mapp* 2012;33:2062–71
5. Chard DT, Jackson JS, Miller DH, et al. **Reducing the impact of white matter lesions on automated measures of brain gray and white matter volumes.** *J Magn Reson Imaging* 2010;32:223–28
6. Gelineau-Morel R, Tomassini V, Jenkinson M, et al. **The effect of hypointense white matter lesions on automated gray matter segmentation in multiple sclerosis.** *Hum Brain Mapp* 2012;33:2802–14
7. Ashburner J, Friston K. **Unified segmentation.** *Neuroimage* 2005;26:839–51
8. Zhang Y, Brady M, Smith S. **Segmentation of brain MR images through a hidden Markov random field model and the expectation-maximization algorithm.** *IEEE Trans Med Imaging* 2001;20:45–57
9. Horsfield MA, Rovaris M, Rocca MA, et al. **Whole-brain atrophy in multiple sclerosis measured by two segmentation processes from various MRI sequences.** *J Neurol Sci* 2003;216:169–77
10. Rudick RA, Lee JC, Nakamura K, et al. **Gray matter atrophy correlates with MS disability progression measured with MSFC but not EDSS.** *J Neurol Sci* 2009;282:106–11
11. Rueckert D, Sonoda LI, Hayes C, et al. **Nonrigid registration using free-form deformations: application to breast MR images.** *IEEE Trans Med Imaging* 1999;18:712–21
12. Smith SM. **Fast robust automated brain extraction.** *Hum Brain Mapp* 2002;17:143–55
13. Sled JG, Zijdenbos AP, Evans CP. **A nonparametric method for automatic correction of intensity nonuniformity in MRI data.** *IEEE Trans Med Imaging* 1997;17:87–97
14. Kohonen T. **The self-organizing map.** *Proceedings of the IEEE* 1990;78:1464–80
15. Tian D, Fan L. **A brain MR images segmentation method based on SOM neural network.** In: *Proceedings of the 1st International Conference on Bioinformatics and Biomedical Engineering ICBBE*, Wuhan, People's Republic of China. July 6–8, 2007:686–89
16. Pham DL. **Spatial models for fuzzy clustering.** *Computer Vision and Image Understanding* 2001;84:285–97
17. Pham DL. **Robust fuzzy segmentation of magnetic resonance images.** In: *Proceedings of the Fourteenth IEEE Symposium on Computer-Based Medical Systems*, Bethesda, Maryland. July 26–27, 2001:127–31
18. Bezdek, JC, Keller J, Krishnapuram R, et al. *Fuzzy Models and Algorithms for Pattern Recognition and Image Processing.* Norwell: Kluwer Academic Publishers; 1999:1650.F89

Enhanced Axonal Metabolism during Early Natalizumab Treatment in Relapsing-Remitting Multiple Sclerosis

O.T. Wiebenga, A.M. Klauser, M.M. Schoonheim, G.J.A. Nagtegaal, M.D. Steenwijk, J.A. van Rossum, C.H. Polman, F. Barkhof, P.J.W. Pouwels, and J.J.G. Geurts



ABSTRACT

BACKGROUND AND PURPOSE: The considerable clinical effect of natalizumab in patients with relapsing-remitting multiple sclerosis might be explained by its possible beneficial effect on axonal functioning. In this longitudinal study, the effect of natalizumab on absolute concentrations of total *N*-acetylaspartate, a marker for neuronal integrity, and other brain metabolites is investigated in patients with relapsing-remitting multiple sclerosis by using MR spectroscopic imaging.

MATERIALS AND METHODS: In this explorative observational study, 25 patients with relapsing-remitting multiple sclerosis initiating natalizumab treatment were included and scanned every 6 months for 18 months. Additionally 18 matched patients with relapsing-remitting multiple sclerosis continuing treatment with interferon- β or glatiramer acetate were included along with 12 healthy controls. Imaging included short TE 2D-MR spectroscopic imaging with absolute metabolite quantification of total *N*-acetylaspartate, creatine and phosphocreatine, choline-containing compounds, myo-inositol, and glutamate. Concentrations were determined for lesional white matter, normal-appearing white matter, and gray matter.

RESULTS: At baseline in both patient groups, lower concentrations of total *N*-acetylaspartate and creatine and phosphocreatine were found in lesional white matter compared with normal-appearing white matter and additionally lower glutamate in lesional white matter of patients receiving natalizumab. In those patients, a significant yearly metabolite increase was found for lesional white matter total *N*-acetylaspartate (7%, $P < .001$), creatine and phosphocreatine (6%, $P = .042$), and glutamate (10%, $P = .028$), while lesion volumes did not change. In patients receiving interferon- β /glatiramer acetate, no significant change was measured in lesional white matter for any metabolite, while whole-brain normalized lesion volumes increased.

CONCLUSIONS: Patients treated with natalizumab showed an increase in total *N*-acetylaspartate, creatine and phosphocreatine, and glutamate in lesional white matter. These increasing metabolite concentrations might be a sign of enhanced axonal metabolism.

ABBREVIATIONS: GA = glatiramer acetate; Glu = glutamate; IFN β = interferon β ; LWM = lesional white matter; NAWM = normal-appearing white matter; MRSI = MR spectroscopic imaging; PVE = partial volume estimation; tCr = total creatine (creatine and phosphocreatine); tNAA = total *N*-acetylaspartate; RRMS = relapsing-remitting multiple sclerosis

Multiple sclerosis is an inflammatory and neurodegenerative disease of the central nervous system. The acute pathology of the disease is characterized by focal lesions in the white matter,¹ while accumulation of gray matter damage is more prominent in the progressive stage of the disease.²

Previous spectroscopy studies found that lesional WM (LWM) (ie, only lesions or WM directly surrounding lesions) is

characterized by decreased levels of total *N*-acetylaspartate (tNAA), a marker of neuronal integrity, and decreased total creatine (tCr), a marker of energy metabolism, combined with higher levels of choline-containing compounds, a marker of cell membrane turnover.^{3,4} In the WM, an increased Cho/tCr ratio has been detected before the lesions are visible on conventional

Received September 11, 2014; accepted after revision December 19.

From the Departments of Radiology and Nuclear Medicine (O.T.W., G.J.A.N.[†], M.D.S., F.B.), Anatomy and Neurosciences (O.T.W., A.M.K., M.M.S., G.J.A.N.[†], J.J.G.G.), Neurology (J.A.v.R., C.H.P.), and Physics and Medical Technology (P.J.W.P.), Neuroscience Campus Amsterdam and VU University Medical Center, Amsterdam, the Netherlands.

[†] Deceased.

O.T. Wiebenga and A.M. Klauser contributed equally to this article.

This work was sponsored by the Dutch MS Research Foundation, grant number 09-358d. MR imaging was partly sponsored by Biogen Idec. Biogen Idec did not participate in any aspect of the design or performance (including data collection, data management, data analysis and interpretation, or preparation) of this investigator initiated study. Final approval for the work and manuscript was given by the authors.

Please address correspondence to Oliver T. Wiebenga, MD, VU University Medical Center, Department of Radiology and Nuclear Medicine, PO Box 7057, 1007 MB, Amsterdam, the Netherlands; e-mail: o.wiebenga@vumc.nl

Indicates article with supplemental on-line appendix.

<http://dx.doi.org/10.3174/ajnr.A4252>

Table 1: Baseline variables of patients and controls^a

	Natalizumab (n = 25)	IFNb/GA (n = 18)	Healthy Controls (n = 12)	P Value
Age (yr)	36.0 ± 8.9	38.2 ± 5.0	37.6 ± 8.7	.619
Sex (male/female)	9:16	9:9	3:9	.368
EDSS ^{b,c}	3.0 (1.5–6.5)	2.5 (1.0–6.5)		.589
Duration since onset (yr)	7.9 ± 6.1	8.8 ± 5.3		.550
Prior IFNb/GA duration at baseline (yr)	2.6 ± 3.0	4.4 ± 3.9		.121
Brain volumes				
NGMV (L)	0.75 ± 0.04	0.73 ± 0.05	0.77 ± 0.04	.063
NWMV (L)	0.70 ± 0.03	0.69 ± 0.03	0.72 ± 0.04	.061
NBV (L)	1.45 ± 0.05	1.42 ± 0.08	1.49 ± 0.07	.020 ^d
T2 lesion volume (mL) ^e	6.1 (2.4–14.3)	4.9 (2.4–11.9)		.599

Note:—EDSS indicates Expanded Disability Status Scale; NGMV, normalized total GM volume; NWMV, normalized total WM volume; NBV, normalized whole-brain volume.

^aData are mean ± SD. When normally distributed, a multivariate general linear model was used with age and sex included as covariates. Nonparametric testing was performed using Kruskal-Wallis and post hoc Mann-Whitney *U* tests.

^b χ^2 test.

^cMedian and range.

^dOnly significant between patients treated with IFNb/GA and healthy controls.

^eMedian and interquartile range.

MR imaging.⁵ In the normal-appearing WM (NAWM), decreased tNAA and increased mIns, a marker of gliosis, have been found^{6–8} and have shown correlations with clinical disability scores.^{9,10}

The anti-inflammatory effect of natalizumab,¹¹ second-line therapy for relapsing-remitting MS (RRMS) in most countries, leads to a dramatic reduction in the formation of WM lesions, a decrease in the whole-brain atrophy rate, and improved rates of clinical progression and relapses.^{12,13} Previous studies have shown that interferon β -1b (IFNb) and glatiramer acetate (GA) increase tNAA concentrations in MS,^{14,15} but the effect of natalizumab remains unclear.

We, therefore, performed MR spectroscopic imaging (MRSI) in patients starting natalizumab treatment and repeated measurements every 6 months in LWM, NAWM, and GM. Measurements were compared with those in healthy controls. Additionally, patients with RRMS continuing on IFNb/GA were followed during the same period.

MATERIALS AND METHODS

Subjects

Three groups of subjects were investigated in this observational study: patients with RRMS starting natalizumab at baseline, those continuing IFNb/GA, and healthy controls (Table 1), as described separately (O.T.W. et al, unpublished data, 2015). The study was approved by the ethics review board of the VU University Medical Center, and all subjects gave written informed consent before participation.

Inclusion criteria for the study were an age between 18 and 65 years and a diagnosis of clinically definite MS (for patients only).¹⁶ Exclusion criteria were a history of psychiatric or neurologic disease (other than MS for patients), contraindications for MR imaging, and a history of alcohol or drug abuse.

Patients starting natalizumab ($n = 25$; 300 mg intravenously every 4 weeks) had at least 1 prior period of IFNb/GA treatment with breakthrough disease or rapidly evolving active RRMS before starting treatment. These patients were included after the decision to start natalizumab had already been made. At baseline,

6 patients were treatment-naïve for natalizumab, 14 patients had received 1, and 3 patients had received 2 infusions. Two patients who had already received 6 infusions when they joined the study were only analyzed at the 6-month visit and onward. All patients continued natalizumab treatment for the duration of the study.

Patients receiving IFNb/GA ($n = 18$) continued this treatment at baseline. Twelve patients used IFN-b, the dose and route of administration dependent on type, and 6 patients used GA, 20 mg subcutaneously, daily. Patients receiving IFNb/GA were matched to those receiving natalizumab for age, sex, disability (Expanded Disability Status Scale), and duration of therapy. Two patients discontinued IFNb/GA treatment but remained in the study. One discontinued GA after baseline because of side effects (necrosis and scarring of skin at injection sites) combined with stable disease; another discontinued IFNb at month 12 due to conversion to secondary-progressive MS.

Healthy controls ($n = 12$) were age- and sex-matched to patients receiving natalizumab at baseline.

MR Imaging Acquisition

MR imaging was performed on a 1.5T whole-body scanner (Sonata; Siemens, Erlangen, Germany) with an 8-channel receiver head coil. Sequences included a 3D T1-weighted MPRAGE sequence (TR, 2700 ms; TE, 5 ms; TI, 950 ms; 176 sagittal sections; 1.3-mm section thickness; $1.3 \times 1.3 \text{ mm}^2$ in-plane resolution), and a proton-attenuation/T2-weighted turbo spin-echo sequence (TR, 3130 ms; TE, 24 and 85 ms; 46 contiguous 3-mm axial sections; $1 \times 1 \text{ mm}^2$ in-plane, aligned to the pituitary-fastigium line as outlined in Fig 1A).

2D-MRSI included a point-resolved spectroscopy sequence (TR/TE, 3000/30 ms) on a single 15-mm slab aligned to the sections of the proton-attenuation/T2 sequence, with the center touching the top of the corpus callosum.¹⁷ Depending on head size, the FOV was 160×160 or 140×160 mm and the corresponding volume of interest was 70×100 or 80×100 mm. The use of 16×16 phase-encodings resulted in a voxel size of 1.3 or 1.5 mL. Reference 2D-MRSI datasets without water suppression were measured by using both head and body coils as a receiver.

Brain and Lesion Volumes

T2-hyperintense WM lesions were quantified by using an automated segmentation method.¹⁸ Normalized whole-brain WM and GM volumes were computed by using the 3D-T1 images and SIENAX (part of fMRI of the Brain Software Library 5.02; <http://www.fmrib.ox.ac.uk/fsl>) after lesion filling, by using automated lesion-filling (Lesion Automated Preprocessing).¹⁹ The partial volume segmentation masks of WM, GM, CSF, and lesions, produced by SIENAX, was summed to compute a partial volume

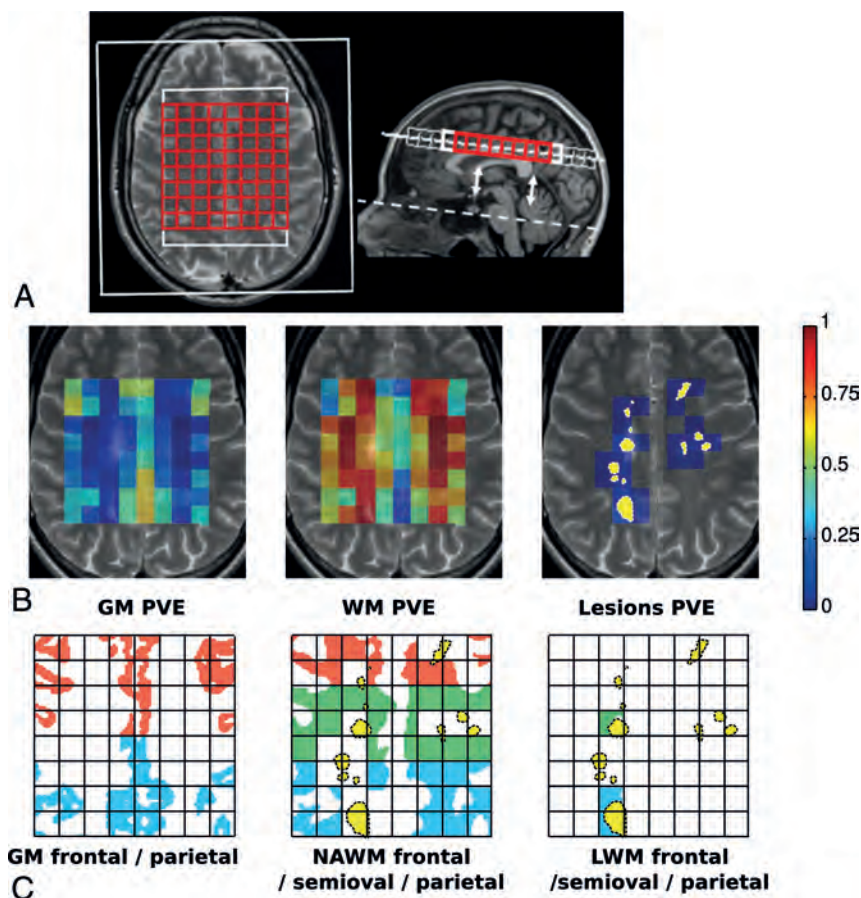


FIG 1. A, The illustration shows axial T2-weighted and sagittal T1-weighted MR images. The pituitary-fastigium axis (*dashed line*) is used to position the grid (in red) with 64 voxels. B, An example of the WM, GM, and lesion PVE calculated on the MRSI grid and superimposed with the T2 image of the center of the slab. The yellow in the lesion PVE image represents the projection of the lesion content of the slab. C, The allocation of the different regions of GM, NAWM, and LWM based on the rows of the grid and the lesion content is seen.

estimate (PVE) for every tissue type in every voxel in the VOI (Fig 1B).

Metabolite Segmentation

The absolute concentrations of the metabolites tNAA, tCr, Cho, mIns, and glutamate (Glu) were quantified for each voxel of the MRSI slab by using LCModel (<http://www.lcmmodel.com>),²⁰ as reported previously.¹⁷ Although the chemical shift artifacts are not very large at 1.5T, there are distinct differences between the first and last rows. They were therefore discarded in the analysis to avoid additional variation due to this effect (Fig 1A).

A segmentation based on existing methods^{21,22} was then applied to determine the specific metabolite concentrations for each tissue type and region. This approach accounts for the partial volume effects of GM, WM, and CSF by using the respective PVE values of the MRSI voxels and accounts for change in brain volume with time. Therefore, the variation of the concentrations is reduced by the distinction between WM and GM contributions. Moreover, inaccurate repositioning of the MRSI slab is partially compensated by the method, correcting for the change in the tissue content of every voxel.²¹⁻²³ On the basis of the PVE, we determined 3 tissue types: GM, NAWM, and LWM. NAWM was defined as the WM content of voxels that contain <1% lesion

PVE, whereas LWM was defined as the WM volume of voxels that contain >5% lesion PVE. The WM of voxels containing a lesion PVE between 1% and 5% was discarded for the sake of specificity. Metabolite concentrations in the CSF were considered negligible. The MRSI slab was divided in 3 regions (frontal, centrum semiovale, and parietal) to take into account regional differences in concentrations (Fig 1C).²¹ Metabolite concentrations were then extrapolated for the 3 tissue types in each region (see the On-line Appendix for details).

The quality of the spectral acquisition was assessed with the average SNR and full width at half maximum over the 64 voxels for every subject and measurement, as estimated by LCModel. Spectra representing the quality of the acquisition have been published previously.¹⁷ We excluded the 2D-MRSI acquisition when the whole-grid average of the full width at half maximum exceeded 2 SDs above the group mean value.

The conservation of the metabolite quantities through the segmentation was verified with the concentration conservation factor (On-line Appendix).

Statistical Analysis

Multilevel modeling was performed with MLwiN, Version 2.18 (<http://www.bristol.ac.uk/cmm/software/mlwin/>); the threshold for significance was $P =$

.05. To longitudinally assess any metabolite change with time, we applied a multilevel model with random intercepts and slopes to the data for each metabolite and tissue type (LWM, NAWM, GM). The results of the analysis were Bonferroni-corrected for multiple comparisons across tissue types; then, they were multiplied by 3 (or 2 for healthy controls without LWM). The model included 3 levels: 1) subject, 2) time point (baseline, month 6, month 12, month 18), and 3) region (frontal, centrum semiovale, parietal). The longitudinal rate of metabolite change was assessed by random slopes associated with the number of days elapsed since the baseline visit. Age, sex, group, and regions were included as covariates in this model. Additionally, mean lesional PVE was added as a covariate for the LWM model only.

For the baseline characterization, a multilevel analysis was performed for every metabolite including age and sex as covariates and including an interaction term between tissue region and group to assess the baseline difference between NAWM and LWM in both patient groups.

In the tissue types revealing no time evolution, we performed a cross-sectional analysis including all the time points as repeated measures, comparing patients receiving natalizumab with healthy controls. This was done with a multilevel analysis for every me-

tabolite and tissue, with age and sex as covariates, with an interaction term between group and region that tests regional group differences for all time points. The significance of the effects was assessed with a Wald test and was Bonferroni-corrected for multiple-tissue-type comparisons.

RESULTS

Subjects

The groups did not differ in age and sex. Additionally, the patient groups did not differ in disease duration, disability (Expanded Disability Status Scale), brain volumes, and T2 lesion volume at baseline (Table 1). No serious or unanticipated adverse events attributed to MS medication developed in the patient groups.

Four MRSI acquisitions (1 of a patient receiving natalizumab, 2 of patients receiving IFN β /GA, and 1 of a healthy control) displayed insufficient spectral quality and were excluded from analysis.

Lesion and Brain Volumes

The patient groups did not differ on T2 lesion volumes at baseline ($P = .730$; Table 1). No change in lesion volume in the VOI (the MRSI slab) was observed with time in the patients receiving natalizumab or in those receiving IFN β /GA (Fig 2, bottom row). Whole-brain normalized lesion volumes increased with time in the patients receiving IFN β /GA ($+0.47 \pm 0.15$ mL/year, $P = .002$), whereas there was no significant change for the patients receiving natalizumab ($+0.32 \pm 0.33$ mL/year, $P = .33$).

The evolution of normalized total white matter and gray matter volumes and normalized whole-brain volumes of part of this cohort was presented in a separate study, showing reduced normalized whole-brain white matter during 12 months in both patient groups (O.T.W. et al, unpublished data, 2015).

Baseline Metabolite Concentrations in LWM and Corresponding NAWM

At baseline, patients receiving natalizumab had lower tNAA for all 3 LWM regions (between 10% and 16%, $P < .008$), lower tCr for 2 LWM regions (10% for frontal and 11% for semiovale, $P = .006$), lower Glu for 3 LWM regions (between 12% and 15%, $P < .049$), and higher mIns in the parietal LWM (10%, $P = .008$) compared with the corresponding regional NAWM (all comparisons were corrected for age and sex in the model; for absolute concentrations, see Table 2). Reduced tNAA and tCr and increased mIns in LWM compared with corresponding NAWM were also seen in patients receiving IFN β /GA. This finding was significant for LWM semiovale tNAA (14%, $P < .001$) and tCr (9%, $P = .02$) and for mIns in frontal LWM (18%, $P < .001$).

Metabolite Evolution with Time

Only patients receiving natalizumab showed metabolite changes with time and an increase in only LWM (frontal, centrum semiovale, and parietal LWM combined) for tNAA, tCr, and Glu. The estimated increase in LWM for tNAA was 0.51 ± 0.13 mmol/L/year (7%, $P < .001$); for tCr, it was 0.26 ± 0.11 mmol/L/year (6%, $P = .045$); and for Glu, it was 0.49 ± 0.19 mmol/L/year (10%, $P = .033$) (Fig 2).

All metabolite concentrations remained statistically stable in

the LWM of patients receiving IFN β /GA. Additionally, no concentration change was detected with time in NAWM or in GM in any group for any metabolite.

NAWM and GM Metabolite Concentrations

NAWM and GM were analyzed cross-sectionally in patients receiving natalizumab, because these regions did not evolve with time, including all the time points as repeated measures (Table 2).

We observed lower NAWM tNAA compared with healthy controls in parietal regions (-7% , $P = .043$), with a trend in frontal regions (-7% , $P = .079$). Higher concentrations of mIns were found in patients receiving natalizumab for all 3 NAWM regions compared with healthy controls (approximately 22%, $P < .001$). No difference was found in GM for any metabolite between patients receiving natalizumab and healthy controls.

Quality Parameters

For the MRSI datasets, which were included in the analysis, the mean full width at half maximum and SNR were respectively 5.12 ± 0.65 Hz and 10.9 ± 1.7 for the patients receiving natalizumab, 5.15 ± 0.67 Hz and 10.7 ± 1.2 for those receiving IFN β /GA, and 5.10 ± 0.68 Hz and 12.0 ± 1.7 for the healthy controls.

DISCUSSION

In patients with RRMS treated with natalizumab, we observed an increase of the tNAA concentration in LWM (7%/year) combined with an increase of tCr (6%/year) and Glu (10%/year) during 18 months of treatment, while lesion volumes remained stable. In contrast, there were no metabolite changes with time in the LWM of patients continuing IFN β /GA, while whole-brain normalized lesion volumes increased in this group (however, there was no change with time in lesion volume in the VOI [the MRSI slab] in the patients receiving IFN β /GA).

The longitudinal increase of tNAA, tCr, and Glu in the LWM of patients treated with natalizumab, independent of change in lesion volume, might be a sign of enhanced mitochondrial axonal metabolism²⁴ elicited by the anti-inflammatory effect of natalizumab. This effect is especially relevant for tNAA, which is synthesized in neuronal mitochondria. Higher levels of tNAA might, therefore, reflect increased mitochondrial activity. Recent studies have found that reactive oxygen species and reactive nitrogen species cause mitochondrial dysfunction and energy failure, which might be a mechanism for neuronal degeneration.²⁵ By prevention of reactive oxygen species and reactive nitrogen species producing macrophages in the CNS, natalizumab might indirectly enhance mitochondrial axonal metabolism. Additionally, in animals models, axon damage has already been shown to be reversible by neutralization of reactive oxygen species and reactive nitrogen species.²⁶ Our results corroborate a previous study that found that natalizumab suppressed the evolution of enhancing (active) lesions into T1-hypointense lesions, thereby preventing more severe axonal loss.²⁷ This interpretation is in accordance with a study using diffusion tensor imaging that found an increase of fractional anisotropy in initially enhancing lesions after 12 months of natalizumab treatment.²⁸

There are only a few pharmacologic MR spectroscopy studies in patients with RRMS, and 2 of these followed metabolite inten-

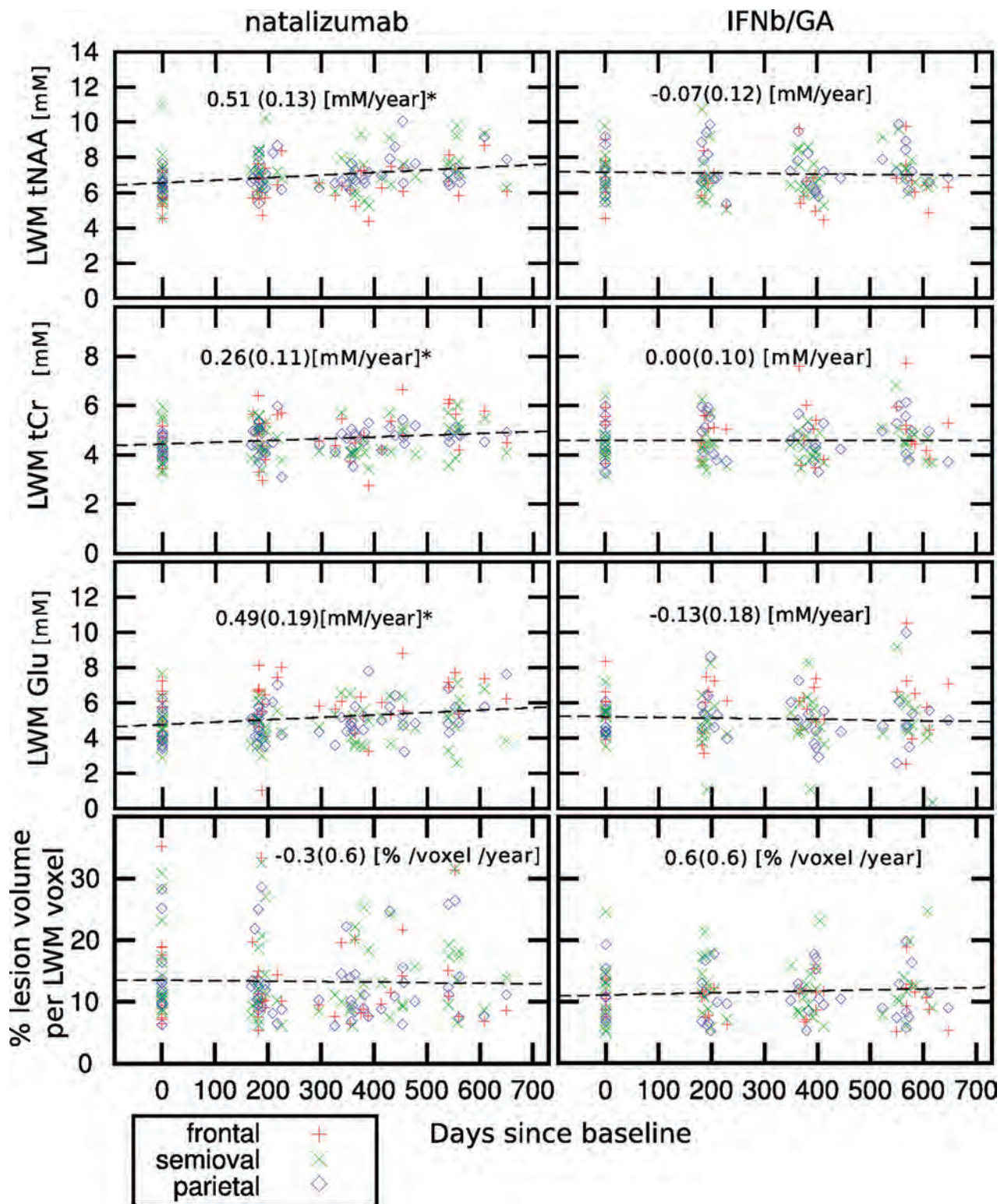


FIG 2. Scatterplot of individual measurements of tNAA, tCr, and Glu in LWM (mmol/L) (upper 3 rows) and percentage of lesion volume per LWM voxel (lower row) as a function of the days elapsed since the baseline for the patients treated with natalizumab and IFNβ/GA. The *asterisk* indicates that patients treated with natalizumab show a significant increase of tNAA, tCr, and Glu in the LWM (mmol/L/year \pm SD). At each time point (baseline, month 6, month 12, and month 18), the number of subjects in the natalizumab group was, respectively, 18, 25, 23, and 15; in the IFNβ/GA group, it was 15, 17, 18, and 16; and in the healthy control group, it was 11, 12, 11, and 8.

sity ratios in a 2D section positioned in the center of the brain.^{14,15} One study investigating GA treatment in 18 patients with RRMS, compared with 4 untreated patients with RRMS, found a 7.1%

increase in NAA/Cr in the GA-treated group during 24 months in NAWM.¹⁴ Another study in 10 patients with RRMS found a 5.5% increase of NAA/Cr among patients treated with IFNβ during a

Table 2: Baseline absolute metabolite concentrations in NAWM, LWM, and GM^a

	Natalizumab (n = 25)			IFNb/GA (n = 18)			Controls (n = 12)	
	NAWM	LWM	GM	NAWM	LWM	GM	WM	GM
tCr								
Frontal	4.86 ± 0.71	4.35 ^c ± 0.58	8.70 ± 1.89	4.93 ± 0.92	4.95 ± 0.90	8.70 ± 1.41	4.93 ± 0.64	8.48 ± 1.31
Semiovale	4.67 ± 0.63	4.30 ^c ± 0.81		4.83 ± 0.75	4.41 ^b ± 0.77		4.72 ± 0.60	
Parietal	4.52 ± 0.62	4.42 ± 0.52	7.78 ± 0.88	4.72 ± 0.69	4.57 ± 0.93	8.24 ± 1.02	4.58 ± 0.45	7.48 ± 0.99
tNAA								
Frontal	7.17 ± 1.20	5.89 ^c ± 0.81	11.1 ± 1.74	7.06 ± 1.16	6.75 ± 1.54	10.93 ± 1.61	7.62 ± 0.96	11.66 ± 1.37
Semiovale	7.96 ± 0.87	6.70 ^c ± 1.51		8.25 ± 1.56	7.05 ^c ± 1.17		8.51 ± 0.94	
Parietal	7.43 ^d ± 1.05	6.55 ^c ± 0.74	10.51 ± 1.08	7.59 ± 0.98	7.08 ± 1.24	11.52 ± 1.46	8.22 ± 0.81	10.89 ± 1.30
Cho								
Frontal	1.50 ± 0.20	1.51 ± 0.25	2.16 ± 0.49	1.59 ± 0.28	1.64 ± 0.29	2.11 ± 0.45	1.62 ± 0.25	2.08 ± 0.39
Semiovale	1.44 ± 0.19	1.42 ± 0.28		1.53 ± 0.21	1.49 ± 0.28		1.49 ± 0.16	
Parietal	1.13 ± 0.24	1.36 ± 0.19	1.31 ± 0.22	1.34 ± 0.23	1.39 ± 0.27	1.36 ± 0.24	1.37 ± 0.17	1.13 ± 0.20
mIns								
Frontal	4.82 ^e ± 1.18	5.29 ± 1.01	7.49 ± 1.57	4.44 ± 0.92	5.45 ^c ± 1.51	7.30 ± 1.11	3.90 ± 0.65	7.00 ± 1.16
Semiovale	4.47 ^e ± 1.18	4.76 ± 0.91		4.27 ± 0.69	4.71 ± 1.01		3.56 ± 0.44	
Parietal	4.79 ^e ± 0.64	5.59 ^b ± 1.07	6.47 ± 0.91	4.98 ± 0.93	5.32 ± 1.42	6.47 ± 0.83	4.01 ± 0.62	5.85 ± 0.52
Glu								
Frontal	6.34 ± 1.46	5.36 ^b ± 1.13	12.96 ± 2.98	5.86 ± 1.18	6.03 ± 1.48	12.71 ± 2.57	6.25 ± 0.96	14.01 ± 2.40
Semiovale	5.38 ± 1.08	4.73 ^b ± 1.16		5.50 ± 0.91	5.11 ± 0.96		5.49 ± 0.72	
Parietal	5.17 ± 1.34	4.22 ^b ± 0.94	12.99 ± 3.87	5.37 ± 1.57	4.80 ± 0.68	12.68 ± 1.44	5.31 ± 0.67	11.81 ± 1.85

^a In mmol/L tissue, mean ± SD. Absolute metabolite concentrations (mmol/L) of NAWM, GM, WM, and LWM in the frontal, centrum semiovale, and parietal regions averaged over the subjects at the baseline measurement.

^b Significant difference within the group between NAWM and LWM in the same region of the baseline measurement ($P < .05$).

^c Significant difference within the group between NAWM and LWM in the same region of the baseline ($P < .01$).

^d Significant differences between patients treated with natalizumab and healthy controls including all the time points ($P < .05$).

^e Significant differences between patients treated with natalizumab and healthy controls including all the time points ($P < .01$).

treatment period of 12 months, compared with 6 untreated patients, in the entire 2D section.¹⁵ Whether the increases in NAA/Cr in the studies mentioned above are caused by increased NAA or reduced Cr remains unclear. The results of studies assessing metabolite ratios are difficult to compare with studies quantifying absolute concentrations. Because the presumed stability of tCr is questioned⁶ and has to be further investigated, the study of absolute concentrations, as in this study, is more enlightening. We did not observe any change in tNAA and tCr in NAWM in patients receiving IFNb/GA; this might be explained by differences in demographics and methodology.

No change with time was found in metabolite concentrations in NAWM and GM in both patient groups or in the healthy controls. In agreement with our results, a previous pharmacologic MR spectroscopy study that followed the effect of natalizumab on absolute metabolite concentrations in NAWM by using single-voxel spectroscopy did not find evolution of any metabolite during 12 months in 27 patients with RRMS.²⁹ During a longer follow-up time, we would speculate that further enhanced effects of natalizumab on metabolite evolution in NAWM might be seen, given the slow rate of tNAA change with time of NAWM in patients with RRMS.

At baseline, significantly lower tNAA, tCr, and Glu was found in the LWM of frontal, parietal, and centrum semiovale WM (except for parietal tCr) compared with corresponding NAWM in the patients receiving natalizumab. Lower tNAA, tCr, and Glu were also found in the LWM of patients receiving IFNb/GA, which was only significant for tNAA and tCr in the semiovale LWM. The reduced concentration of tNAA found in the current study in LWM compared with NAWM in patients at baseline is in line with that in previous studies.⁶ We found lower tCr in LWM, where conflicting results about tCr have been published.⁶ While

in acute lesions, elevated Glu concentrations have been found, possibly due to inflammatory infiltrates of leukocytes, macrophages, and glial cells,³⁰ lower Glu concentrations in LWM have, to our knowledge, never been described before. Several studies reported elevated concentrations of Cho in LWM,^{3,31} which were not observed in the current study. A possible explanation for these conflicting results could be the heterogeneity of the groups across studies. Some surveys specifically investigated active and/or chronic lesions. The lesion types were not differentiated in this study.

The metabolite segmentation method we used, in which we account for the tissue compartments of every voxel, is advantageous because most voxels contain different tissue types and because NAWM, GM, and LWM are known to differ in metabolite concentrations.⁶ Differences in metabolite concentrations also exist between frontal and parietal tissue, especially for GM.³² Higher concentrations are found in GM compared with WM, and mismatch in repositioning could have a great impact on the signal of voxels containing mixed tissues.^{33,34} With the current methodology, the extracted concentrations of GM, NAWM, or LWM are independent of the individual voxel composition. The results are, therefore, less affected by inaccuracies in section repositioning and intersubject anatomic differences in comparison with a voxel-by-voxel analysis method. The quality parameters full width at half maximum and SNR were in line with those in a previous reproducibility study in healthy controls, indicating reliable measurements in patients with MS.¹⁷

The multilevel mixed model used for the statistical analysis provides greater power than a 2-way ANOVA and can cope with nonorthogonal predictors and missing values. The approach used is particularly conservative by correcting the results of the regres-

sion models by the number of tissues (3 for the patient groups and 2 for the healthy controls).

Apart from the relatively short follow-up time and the small sample size, the nonrandomized study design is a limitation of the study. Because natalizumab is second-line therapy at our center, only patients with active and breakthrough disease can receive treatment with natalizumab. As a result, these patients are more likely to have enhancing (active) lesions, compared with patients treated with IFN β /GA, who are relatively stable. Patients treated with natalizumab could possibly show higher normalization of LWM compared with LWM of stable MS; therefore, a direct comparison of the metabolite concentrations between the MS groups cannot be made. Unfortunately, we do not have gadolinium scans available for all patients; hence, the number of enhancing lesions between patient groups could not be compared. Nevertheless, there was no baseline difference in lesion volume, brain volume, and other disease characteristics such as disease duration and Expanded Disability Status Scale score, suggesting comparable disease severity of the patient groups.

The MRSI methodology used in this study might be especially informative in monitoring therapeutic effects with drugs specifically targeting neurodegeneration. This can mainly be expected at higher field strengths, which may allow a distinction between glutamate and glutamine, and which, due to a higher SNR, may allow a higher spatial resolution of the MRSI grid. It is recommended that additional quantitative MR imaging methods also be acquired, such as DTI or magnetic transfer ratio, to gain additional information about myelin integrity with time.

CONCLUSIONS

The possible beneficial effect of natalizumab on axonal functioning in patients with RRMS was assessed by using MRSI because natalizumab has a substantial clinical response. Patients treated with natalizumab showed an increase in tNAA, tCr, and Glu in lesional white matter. No change in NAWM and GM was found in any group for any metabolite. The increasing metabolite concentrations in LWM might be a sign of enhanced axonal metabolism. These findings may aid in explaining the large clinical effect of natalizumab. Larger studies with longer follow-up time are needed to assess the long-term effect of natalizumab on metabolite concentrations in LWM and NAWM and to monitor clinical evolution.

Disclosures: Oliver T. Wiebenga—RELATED: Grant: Dutch MS Research Foundation,* Biogen Idec.* Antoine M. Klauser—RELATED: Grant: Multiple Sclerosis Scientific Research Foundation.* Menno M. Schoonheim—UNRELATED: Consultancy: Genzyme*; Grants/Grants Pending: Dutch MS Research Foundation.* Comments: Research supported by grant 08–650; Payment for Lectures (including service on Speakers Bureaus): Novartis,* Serono.* Comments: Postgraduate education on MS. Martin D. Steenwijk—RELATED: Grant: Dutch MS Research Foundation*; UNRELATED: Grants/Grants Pending: Dutch MS Research Foundation, Comments: Research sponsored through a program grant to the VU University Medical Center/MS Center Amsterdam, grant number 09–358d. Gijsbert J.A. Nagtegaal—RELATED: Grant: Dutch MS Research Foundation*, Biogen Idec*; UNRELATED: Grants/Grants Pending: Merck Serono*; Travel/Accommodations/Meeting Expenses Unrelated to Activities Listed: Bayer Healthcare Pharmaceuticals.* *Money paid to the institution.

REFERENCES

1. Compston A, Coles A. Multiple sclerosis. *Lancet* 2008;372:1502–17
2. Geurts JJ, Calabrese M, Fisher E, et al. Measurement and clinical

- effect of grey matter pathology in multiple sclerosis. *Lancet Neurol* 2012;11:1082–92
3. He J, Inglese M, Li BS, et al. Relapsing-remitting multiple sclerosis: metabolic abnormality in nonenhancing lesions and normal-appearing white matter at MR imaging: initial experience. *Radiology* 2005;234:211–17
4. van Walderveen MA, Barkhof F, Pouwels PJ, et al. Neuronal damage in T1-hypointense multiple sclerosis lesions demonstrated in vivo using proton magnetic resonance spectroscopy. *Ann Neurol* 1999;46:79–87
5. Tartaglia MC, Narayanan S, DeStefano N, et al. Choline is increased in pre-lesional normal appearing white matter in multiple sclerosis. *J Neurol* 2002;249:1382–90
6. Caramanos Z, Narayanan S, Arnold DL. 1H-MRS quantification of tNA and tCr in patients with multiple sclerosis: a meta-analytic review. *Brain* 2005;128:2483–506
7. Geurts JJ, Reuling IE, Vrenken H, et al. MR spectroscopic evidence for thalamic and hippocampal, but not cortical, damage in multiple sclerosis. *Magn Reson Med* 2006;55:478–83
8. Vrenken H, Barkhof F, Uitdehaag BM, et al. MR spectroscopic evidence for glial increase but not for neuro-axonal damage in MS normal-appearing white matter. *Magn Reson Med* 2005;53:256–66
9. Bellmann-Strobl J, Stiepani H, Wuerfel J, et al. MR spectroscopy (MRS) and magnetisation transfer imaging (MTI), lesion load and clinical scores in early relapsing remitting multiple sclerosis: a combined cross-sectional and longitudinal study. *Eur Radiol* 2009;19:2066–74
10. Chard DT, Griffin CM, McLean MA, et al. Brain metabolite changes in cortical grey and normal-appearing white matter in clinically early relapsing-remitting multiple sclerosis. *Brain* 2002;125:2342–52
11. Yednock TA, Cannon C, Fritz LC, et al. Prevention of experimental autoimmune encephalomyelitis by antibodies against alpha-4-beta-1 integrin. *Nature* 1992;356:63–66
12. Miller DH, Soon D, Fernando KT, et al. MRI outcomes in a placebo-controlled trial of natalizumab in relapsing MS. *Neurology* 2007;68:1390–401
13. Polman CH, O'Connor PW, Havrdova E, et al. A randomized, placebo-controlled trial of natalizumab for relapsing multiple sclerosis. *N Engl J Med* 2006;354:899–910
14. Khan O, Shen Y, Caon C, et al. Axonal metabolic recovery and potential neuroprotective effect of glatiramer acetate in relapsing-remitting multiple sclerosis. *Mult Scler* 2005;11:646–51
15. Narayanan S, DeStefano N, Francis GS, et al. Axonal metabolic recovery in multiple sclerosis patients treated with interferon beta-1b. *J Neurol* 2001;248:979–86
16. Polman CH, Reingold SC, Edan G, et al. Diagnostic criteria for multiple sclerosis: 2005 revisions to the “McDonald Criteria.” *Ann Neurol* 2005;58:840–46
17. Wiebenga OT, Klauser AM, Nagtegaal GJ, et al. Longitudinal absolute metabolite quantification of white and gray matter regions in healthy controls using proton MR spectroscopic imaging. *NMR Biomed* 2014;27:304–11
18. Steenwijk MD, Pouwels PJ, Daams M, et al. Accurate white matter lesion segmentation by k nearest neighbor classification with tissue type priors (kNN-TTPs). *Neuroimage Clin* 2013;3:462–69
19. Chard DT, Jackson JS, Miller DH, et al. Reducing the impact of white matter lesions on automated measures of brain gray and white matter volumes. *J Magn Reson Imaging* 2010;32:223–28
20. Provencher SW. Estimation of metabolite concentrations from localized in vivo proton NMR spectra. *Magn Reson Med* 1993;30:672–79
21. Maudsley AA, Domenig C, Govind V, et al. Mapping of brain metabolite distributions by volumetric proton MR spectroscopic imaging (MRSI). *Magn Reson Med* 2009;61:548–59
22. Tal A, Kirov II, Grossman RI, et al. The role of gray and white matter segmentation in quantitative proton MR spectroscopic imaging. *NMR Biomed* 2012;25:1392–400

23. Gasparovic C, Yeo R, Mannell M, et al. **Neurometabolite concentrations in gray and white matter in mild traumatic brain injury: an 1H-magnetic resonance spectroscopy study.** *J Neurotrauma* 2009; 26:1635–43
24. Ciccarelli O, Altmann DR, McLean MA, et al. **Spinal cord repair in MS: does mitochondrial metabolism play a role?** *Neurology* 2010; 74:721–27
25. Witte ME, Geurts JJ, de Vries HE, et al. **Mitochondrial dysfunction: a potential link between neuroinflammation and neurodegeneration?** *Mitochondrion* 2010;10:411–18
26. Nikić I, Merkle D, Sorbara C, et al. **A reversible form of axon damage in experimental autoimmune encephalomyelitis and multiple sclerosis.** *Nat Med* 2011;17:495–99
27. Dalton CM, Miszkil KA, Barker GJ, et al. **Effect of natalizumab on conversion of gadolinium enhancing lesions to T1 hypointense lesions in relapsing multiple sclerosis.** *J Neurol* 2004;251: 407–13
28. Fox RJ, Cronin T, Lin J, et al. **Measuring myelin repair and axonal loss with diffusion tensor imaging.** *AJNR Am J Neuroradiol* 2011; 32:85–91
29. Mellergård J, Tisell A, Dahlqvist LO, et al. **Association between change in normal appearing white matter metabolites and intrathecal inflammation in natalizumab-treated multiple sclerosis.** *PLoS One* 2012;7:e44739
30. Srinivasan R, Sailasuta N, Hurd R, et al. **Evidence of elevated glutamate in multiple sclerosis using magnetic resonance spectroscopy at 3 T.** *Brain* 2005;128:1016–25
31. Mader I, Roser W, Kappos L, et al. **Serial proton MR spectroscopy of contrast-enhancing multiple sclerosis plaques: absolute metabolic values over 2 years during a clinical pharmacological study.** *AJNR Am J Neuroradiol* 2000;21:1220–27
32. Pouwels PJ, Frahm J. **Regional metabolite concentrations in human brain as determined by quantitative localized proton MRS.** *Magn Reson Med* 1998;39:53–60
33. Chard DT, McLean MA, Parker GJ, et al. **Reproducibility of in vivo metabolite quantification with proton magnetic resonance spectroscopic imaging.** *J Magn Reson Imaging* 2002;15:219–25
34. Kreis R. **Issues of spectral quality in clinical 1H-magnetic resonance spectroscopy and a gallery of artifacts.** *NMR Biomed* 2004;17: 361–81

Quiet PROPELLER MRI Techniques Match the Quality of Conventional PROPELLER Brain Imaging Techniques

I. Corcuera-Solano, A. Doshi, P.S. Pawha, D. Gui, A. Gaddipati, and L. Tanenbaum

ABSTRACT

BACKGROUND AND PURPOSE: Switching of magnetic field gradients is the primary source of acoustic noise in MR imaging. Sound pressure levels can run as high as 120 dB, capable of producing physical discomfort and at least temporary hearing loss, mandating hearing protection. New technology has made quieter techniques feasible, which range from as low as 80 dB to nearly silent. The purpose of this study was to evaluate the image quality of new commercially available quiet T2 and quiet FLAIR fast spin-echo PROPELLER acquisitions in comparison with equivalent conventional PROPELLER techniques in current day-to-day practice in imaging of the brain.

MATERIALS AND METHODS: Thirty-four consecutive patients were prospectively scanned with quiet T2 and quiet T2 FLAIR PROPELLER, in addition to spatial resolution-matched conventional T2 and T2 FLAIR PROPELLER imaging sequences on a clinical 1.5T MR imaging scanner. Measurement of sound pressure levels and qualitative evaluation of relative image quality was performed.

RESULTS: Quiet T2 and quiet T2 FLAIR were comparable in image quality with conventional acquisitions, with sound levels of approximately 75 dB, a reduction in average sound pressure levels of up to 28.5 dB, with no significant trade-offs aside from longer scan times.

CONCLUSIONS: Quiet FSE provides equivalent image quality at comfortable sound pressure levels at the cost of slightly longer scan times. The significant reduction in potentially injurious noise is particularly important in vulnerable populations such as children, the elderly, and the debilitated. Quiet techniques should be considered in these special situations for routine use in clinical practice.

ABBREVIATIONS: C = conventional; Δ L = SPL difference; Q = quiet; SPL = sound pressure level

Acoustic noise generated during MR imaging contributes to patient discomfort. Problems associated with high levels of acoustic noise include annoyance, anxiety, and verbal communication difficulties between the patient and operator.^{1,2} In addition, the very high noise pressure levels can cause hearing loss. Temporary shifts in hearing thresholds have been reported in 43% of the patients scanned without ear protection and with improperly fitted earplugs.³ In extreme cases, permanent hearing

impairment can occur.³⁻⁵ Noise is of particular concern in populations vulnerable to hearing loss such as the very young and elderly and those who may not be able to manage the effectiveness of earplug placement such as patients with psychiatric disorders or reduced levels of consciousness.⁵ Fetal noise exposure is also a concern.⁶

The primary source of acoustic noise in MR imaging procedures is the pulsed currents generated in gradient coils for spatial encoding of the MR signal.⁷ These currents, in the presence of the strong static magnetic field of the MR imaging system, induce significant (Lorentz) forces that cause vibrations in the gradient coils, which, in turn, generate a compression wave in the air perceived as the scanner noise.⁸⁻¹⁰ Previous methods used to ameliorate the high acoustic noise levels of clinical MR imaging include acoustic insulation of the scanner bore, resulting in reduced bore diameter and gradient waveform shaping/filtering^{11,12}; bandwidth limiting¹³; and restricting gradient performance—each trading image quality and acquisition speed for only modest noise reduction. More recent studies have demonstrated that innovative pulse-sequence modifications can be applied to achieve

Received October 8, 2014; accepted after revision December 5.

From the Neuroradiology Section, Department of Radiology (I.C.-S., A.D., P.S.P., L.T.), Icahn School of Medicine at Mount Sinai Hospital, Radiology, New York, New York; and GE Healthcare (D.G., A.G.), Milwaukee, Wisconsin.

Dr Idoia Corcuera-Solano was supported by a grant from the Spanish foundation: Fundación Alfonso Martín Escudero.

Paper previously presented in part at: Annual Meeting of the American Society of Neuroradiology and the Foundation of the ASNR Symposium, May 18–23, 2013; San Diego, California.

Please address correspondence to Lawrence N. Tanenbaum, MD, Mount Sinai Medical Center, Department of Radiology B1234, One Gustave L. Levy Pl, New York, NY 10029; e-mail: nuromri@gmail.com; @nuromri

<http://dx.doi.org/10.3174/ajnr.A4235>

substantial reductions of acoustic noise while maintaining image quality. Novel, almost silent sequences have recently become available.¹⁴⁻¹⁷ Before these new techniques can be widely adopted, validation against traditional techniques must be performed.

In this study, we evaluated the image quality of new commercially available quiet T2 PROPELLER (Q-T2) and quiet T2 FLAIR PROPELLER (Q-FLAIR) sequences in comparison with our standard of care conventional T2 PROPELLER (C-T2) and T2 FLAIR PROPELLER (C-FLAIR) techniques. To our knowledge, this is the first study to assess the performance of quiet T2 and quiet T2 FLAIR MR imaging applications in day-to-day clinical practice.

MATERIALS AND METHODS

Study Design and Patients

This prospective single-center study followed the Health Insurance Portability and Accountability Act guidelines, and its protocol was approved by the institutional review board. Written informed consent was obtained from subjects or, in the case of noncompetent patients, their respective parents or next of kin for all procedures, in accordance with the local institutional review board protocol.

Thirty-four consecutive inpatients undergoing routine brain MR imaging between February 2013 and March 2014 were included. Eighteen men and 16 women with a mean age of 54 years (range, 21–96 years) were prospectively enrolled in this intraindividual comparative study and evaluated. All patients were given standard clinical ear protective equipment and underwent brain MR imaging examinations for a variety of clinical purposes. The clinical conditions were stroke ($n = 6$), persistent headache ($n = 6$), demyelinating disease ($n = 5$), mental disorder ($n = 3$), vertigo ($n = 2$), seizure ($n = 2$), brain tumor ($n = 3$), metastatic disease ($n = 2$), infectious disease ($n = 2$), recurrent falls ($n = 2$), and CSF leak ($n = 1$).

MR Imaging Protocol

MR imaging included all sequences in routine use for each clinical indication, including axial PROPELLER T2 and T2 FLAIR. Added were spatial resolution–matched quiet PROPELLER T2 and quiet T2 FLAIR in the transverse plane. All scans were obtained on a clinical 1.5T MR imaging system (Optima 450W; GE Healthcare, Milwaukee, Wisconsin) by using a 32-channel head coil (24 elements are activated). Section locations were identical across comparison scans. MR imaging data acquisition parameters are summarized in Table 1.

Acoustic Noise Measurements

Acoustic noise measurements were conducted onsite with the scanner unoccupied by using imaging parameters identical to those in use with patients. The sound pressure level (SPL) values were measured by using a sound level meter (Type 2250; Bruel and Kjaer, Naerum, Denmark), which has an accuracy of ± 1 dBA, and a microphone (Type 4189; Bruel and Kjaer). The device was placed inside the head coil close to where the ears would be, and measurements were averaged for 20 seconds. The SPL was mea-

Table 1: MR Imaging data-acquisition parameters

	C-T2	Q-T2	C-T2 FLAIR	Q-T2 FLAIR
TR (ms)	3066	6380	9500	9500
TE (ms)	99	98	190	105
TI (ms)	NA	NA	2250	2250
FOV (cm)	22 × 22	22 × 22	23 × 23	23 × 23
Matrix	320 × 320	320 × 320	288 × 288	288 × 288
Section thickness (mm)	5	5	5	5
Section spacing (mm)	0	0	0	0
No. of sections	30	30	30	30
Bandwidth (kHz)	50	41	62.5	41
Refocus flip angle	160°	160°	160°	160°
Echo-train length	28	16	32	18
NEX	1.7	1.5	1.7	1.5
Acceleration factor	2	2	2	2
Scan time (min)	1.26	2.16	3.10	5.20

Note:—NA indicates not applicable.

sured for each sequence by using the same apparatus. We calculated the following parameters:

- SPL difference between conventional and quiet sequences: $\Delta L = C - Q$
- Comparison of power level or sound intensity factor: $I = 10^{\Delta L/10}$
- Comparison of sound pressure or sound pressure factor: $SP = 10^{\Delta L/20}$
- Loudness factor: $LF = 10^{\Delta L/33.22} = 2^{\Delta L/10}$.

Image Quality Assessment

A qualitative comparison of images acquired with quiet and conventional approaches was performed. Matched image sets were gathered from each patient: Q-T2 ($n = 34$) was compared with C-T2 ($n = 34$); and Q-FLAIR ($n = 31$), with C-FLAIR ($n = 31$). Three patients were not eligible for the T2 FLAIR comparison because both scans were not obtained.

A total of 130 image sets presented in the same order were independently assessed by 2 neuroradiologists (with 10 and 25+ years of experience) blinded to the acquisition technique. The images were evaluated qualitatively on an analysis and viewing workstation (Advantage Workstation 4.6; GE Healthcare) for overall quality and gray matter–white matter differentiation, by using a 3-point scale: 3 being better than expected, 2 being as expected, and 1 being worse than expected. Because alterations in multiecho sequence scan acquisition parameters such as echo spacing and echo-train length can manifest as a blur, perceived blurring (yes/no) was evaluated. All scans benefited from inherent PROPELLER motion resistance; thus, this was not measured. Additionally, readers were asked to rank the 2 pair sets for preference and declare images as better, worse, or equivalent (overall preference). Image quality scores were averaged across both readers for analysis and were presented as mean value and SD.

Statistical Analysis

Interobserver agreement for assessment of image quality was quantified by weighted κ statistics.¹⁸ A nonparametric paired Wilcoxon test was used to compare the qualitative parameters between the quiet and conventional image pairs. Image quality scores for each set of MR images were analyzed. Qualitative results were expressed as mean and SD. Statistical analysis was performed by using commercially available software (SPSS, Version 20; IBM,

Armonk, New York). Difference was considered statistically significant at $P < .05$.

RESULTS

Acoustic Noise Reduction

The respective average SPL measurements for C-T2, C-FLAIR, and Q-T2 and Q-FLAIR protocols are shown in Table 2. Repeated measurements showed no variation in average and peak SPL; therefore, no SD is reported.

The average SPL difference between C-T2 sequences and Q-T2 was found to be 26.4 dB (26% reduction). This represents a sound intensity factor difference of 436.5, a sound pressure factor difference of 21, and a loudness factor difference of 6.2. The SPL difference between C-FLAIR sequences and Q-FLAIR was found to be 28.5 dB (27% reduction), which corresponds to differences in a sound intensity factor of 708, a sound pressure factor of 27, and a loudness factor of 7.2.

Qualitative Analysis

Interrater reliability was good (Cohen κ weighted = 0.67). No significant difference in image quality was found between conventional and quiet sequences ($P > .05$). Readers expressed no preference between quiet and conventional T2 sequences, and in all cases, gray matter–white matter differentiation and overall quality were rated “as expected.” Similarly, image quality scores of the Q-FLAIR and C-FLAIR protocols were comparable. In 1 case, Q-FLAIR was preferred over the conventional technique regarding overall quality, while in another case, C-FLAIR protocol was preferred over Q-FLAIR regarding gray matter–white matter differentiation. In all other cases, the quiet and conventional sets were rated “as expected.” When the perceived blurring was assessed, no evidence of blur was noted in any case. Image examples are provided in Figs 1 and 2.

Table 2: Comparison of acoustic noise

	Conventional Avg SPL	Quiet Avg SPL	$\Delta L = C - Q$	$I = 10^{\Delta L/10}$	$SP = 10^{\Delta L/20}$	$LF = 10^{\Delta L/33.22} = 2^{\Delta L/10}$
T2	101.5	75.1	26.4	436.5	21	6.2
T2 FLAIR	104.4	75.9	28.5	708	27	7.2

Note:—Avg indicates average; I, intensity factor; SP, sound pressure factor; LF, loudness factor.

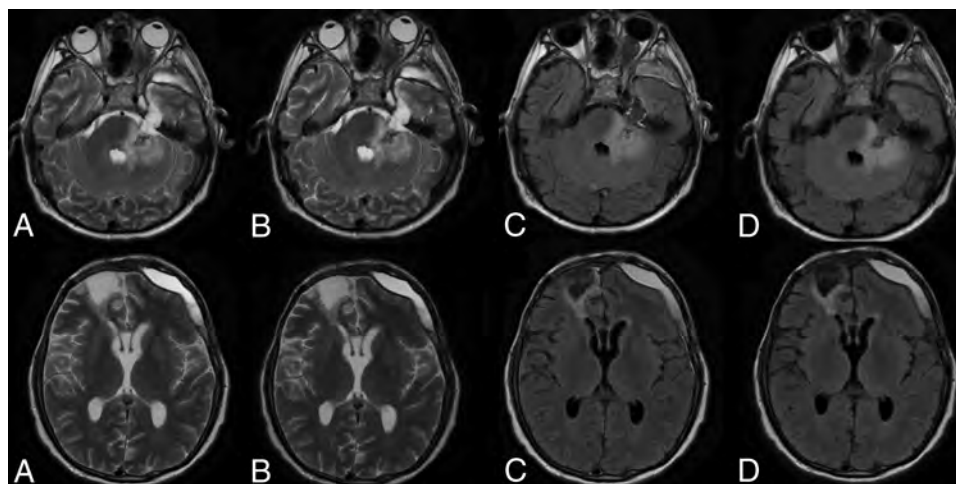


FIG 1. A 58-year-old man with post-craniofacial recurrent tumor resection with postsurgical changes. Comparison of C-T2 (A), Q-T2 (B), C-FLAIR (C), and Q-FLAIR (D).

DISCUSSION

Acoustic noise associated with MR imaging procedures is primarily due to pulsed-current-related vibration of the gradient coil support structure. The sounds made by the scanner vary in volume and tone with the type of pulse sequence performed.^{5,19} The acoustic noise varies due to the alteration of the gradient output (rise time or amplitude) with variation of MR imaging parameters. Noise tends to be enhanced by decreases in section thickness, FOV, TR, and TE.⁵

Noise levels for clinical MR imaging pulse sequences run as high as 100–120 dB,^{19–22} levels capable of causing temporary or even permanent hearing loss if hearing protection is not properly applied.

The commercially available quiet sequences used in this study drastically reduce noise levels to approximately 75 dB, a reduction in average SPL of up to 28.5 dB. Quiet PROPELLER uses a standard 2D modified radial sampling scheme with an acoustic noise model to optimize gradient waveforms.²³ The k -space trajectory and data sampling can be optimized so that gradient steps are smaller than those in conventional PROPELLER, resulting in a scan with noise levels < 6 dBA above ambient levels.

At a penalty of only slightly longer scan times, Q-T2 and Q-FLAIR provided high-quality images comparable with conventional acquisitions. Spatial-resolution-matched quiet sequences had similar scores for overall quality and gray matter–white matter differentiation without an increase in image blur.

To the best of our knowledge, this is the first report in the literature assessing the performance of quiet T2 and quiet T2 FLAIR PROPELLER imaging in the day-to-day practice of clinical imaging. Our results complement the recent previously reported data regarding the use of new quiet scanning approaches. Pierre et al¹⁵ compared, in a group of 10 volunteers, a quiet T2 TSE sequence prototype with its equivalent standard T2 TSE sequence and

demonstrated that overall image quality remained above acceptable while reducing SPL. Two other recent studies assessed unique 3D T1-weighted silent scan technology in clinical practice, obtaining similarly acceptable results.^{16,17}

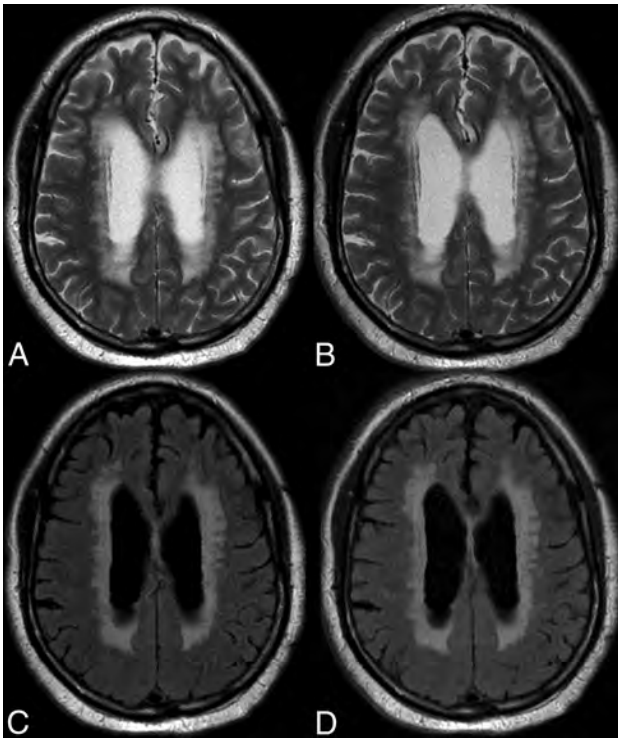


FIG 2. An 82-year-old man with extensive periventricular T2 and T2 FLAIR white matter foci suggesting ischemic small vessel changes. Comparison of C-T2 (A), Q-T2 (B), C-FLAIR (C), and Q-FLAIR (A).

We acknowledge several study limitations. Differences in k -space trajectory and overall performance of the quiet techniques required fixed alterations in parameter choices such as TR, echo train, and TE to match spatial resolution and section numbers of the conventional acquisition, potentially contributing to subtle variations in image appearance. While representative of a new class of MR images, these results apply only to the specific approach to noise-reduced imaging and the specific parameter choices made and will not translate exactly to other scanners, techniques, and parameter choices. The small sample size requires a confirmation of our findings in a larger population. As this technology evolves, additional studies will be required in a large population with a variety of disease states.

CONCLUSIONS

Quiet FSE provides equivalent image quality at comfortable sound pressure levels at the cost of slightly longer scan times. The significant reduction in potentially injurious noise is particularly important in vulnerable populations such as children, the elderly, and the debilitated. Quiet techniques should be used in these special situations and considered for routine use in clinical practice.

ACKNOWLEDGMENTS

The authors acknowledge Maggie Fung for her assistance.

Disclosures: Idoia Corcuera-Solano—RELATED: Grant: Fundación Alfonso Martín Escudero, Comments: At the time of that research, I was supported by a grant from the Spanish foundation Fundación Alfonso Martín Escudero. Ajeet Gaddipati—UNRELATED: Employment: GE Healthcare, Comments: This work was done as part of my employment at GE Healthcare MR Imaging Department; Patents (planned, pending or issued): pending patent through GE Healthcare, Comments: GE Docket No. 265701 (ZPS 8081.704), Comfortable Acoustic Level Techniques for MRI Pulse Sequences. Dawei Gui—UNRELATED: Employment: GE Healthcare; Patents (planned, pending or issued): GE Healthcare, Comments: GE Doc No. 265701-1. Lawrence Tanenbaum—RELATED: Consulting Fee or Honorarium: GE Healthcare; UNRELATED: Payment for Lectures (including service on Speakers Bureaus): GE Healthcare, Siemens.

REFERENCES

1. Moelker A, Maas RA, Pattynama PM. Verbal communication in MR environments: effect of MR system acoustic noise on speech understanding. *Radiology* 2004;232:107–13
2. Quirk ME, Letendre AJ, Ciottone RA, et al. Anxiety in patients undergoing MR imaging. *Radiology* 1989;170:463–66
3. Brummett RE, Talbot JM, Charuhas P. Potential hearing loss resulting from MR imaging. *Radiology* 1988;169:539–40
4. Radomskij P, Schmidt MA, Heron CW, et al. Effect of MRI noise on cochlear function. *Lancet* 2002;359:1485
5. McJury M, Shellock FG. Auditory noise associated with MR procedures: a review. *J Magn Reson Imaging* 2000;12:37–45
6. Reeves MJ, Brandreth M, Whitby EH, et al. Neonatal cochlear function: measurement after exposure to acoustic noise during in utero MR imaging. *Radiology* 2010;257:802–09
7. Hedeem RA, Edelstein WA. Characterization and prediction of gradient acoustic noise in MR imagers. *Magn Reson Med* 1997;37:7–10
8. Mansfield P, Haywood B, Coxon R. Active acoustic control in gradient coils for MRI. *Magn Reson Med* 2001;46:807–18
9. Bowtell RW, Mansfield P. Quiet transverse gradient coils: Lorentz force balanced designs using geometrical similitude. *Magn Reson Med* 1995;34:494–97
10. Mansfield P, Glover PM, Beaumont J. Sound generation in gradient coil structures for MRI. *Magn Reson Med* 1998;39:539–50
11. Cho ZH, Chung ST, Chung JY, et al. A new silent magnetic resonance imaging using a rotating DC gradient. *Magn Reson Med* 1998;39:317–21
12. Segbers M, Rizzo Sierra CV, Duifhuis H, et al. Shaping and timing gradient pulses to reduce MRI acoustic noise. *Magn Reson Med* 2010;64:546–53
13. Hennel F, Girard F, Loenneker T. “Silent” MRI with soft gradient pulses. *Magn Reson Med* 1999;42:6–10
14. Heismann B, Ott M, Grodzki D. Sequence-based acoustic noise reduction of clinical MRI scans. *Magn Reson Med* 2015;73:1104–09
15. Pierre EY, Grodzki D, Aandal G, et al. Parallel imaging-based reduction of acoustic noise for clinical magnetic resonance imaging. *Invest Radiol* 2014;49:620–26
16. Alibek S, Vogel M, Sun W, et al. Acoustic noise reduction in MRI using Silent Scan: an initial experience. *Diagn Interv Radiol* 2014;20:360–63
17. Ida M, Wakayama T, Nielsen ML, et al. Quiet T1-weighted imaging using PETRA: initial clinical evaluation in intracranial tumor patients. *J Magn Reson Imaging* 2015;41:447–53
18. Landis JR, Koch GG. The measurement of observer agreement for categorical data. *Biometrics* 1977;33:159–74
19. Shellock FG, Morisoli SM, Ziarati M. Measurement of acoustic noise during MR imaging: evaluation of six “worst-case” pulse sequences. *Radiology* 1994;191:91–93
20. Moelker A, Wielopolski PA, Pattynama PM. Relationship between magnetic field strength and magnetic-resonance-related acoustic noise levels. *MAGMA* 2003;16:52–55
21. Hurwitz R, Lane SR, Bell RA, et al. Acoustic analysis of gradient-coil noise in MR imaging. *Radiology* 1989;173:545–48
22. Moelker A, Maas RA, Lethimonnier F, et al. Interventional MR imaging at 1.5 T: quantification of sound exposure. *Radiology* 2002;224:889–95
23. Pipe JG, Gibbs WN, Li Z, et al. Revised motion estimation algorithm for PROPELLER MRI. *Magn Reson Med* 2014;72:430–37

Proton Resonance Frequency Chemical Shift Thermometry: Experimental Design and Validation toward High-Resolution Noninvasive Temperature Monitoring and In Vivo Experience in a Nonhuman Primate Model of Acute Ischemic Stroke

S. Dehkharghani, H. Mao, L. Howell, X. Zhang, K.S. Pate, P.R. Magrath, F. Tong, L. Wei, D. Qiu, C. Fleischer, and J.N. Oshinski



ABSTRACT

BACKGROUND AND PURPOSE: Applications for noninvasive biologic temperature monitoring are widespread in biomedicine and of particular interest in the context of brain temperature regulation, where traditionally costly and invasive monitoring schemes limit their applicability in many settings. Brain thermal regulation, therefore, remains controversial, motivating the development of noninvasive approaches such as temperature-sensitive nuclear MR phenomena. The purpose of this work was to compare the utility of competing approaches to MR thermometry by using proton resonance frequency chemical shift. We tested 3 methodologies, hypothesizing the feasibility of a fast and accurate approach to chemical shift thermometry, in a phantom study at 3T.

MATERIALS AND METHODS: A conventional, paired approach (difference [DIFF]-1), an accelerated single-scan approach (DIFF-2), and a new, further accelerated strategy (DIFF-3) were tested. Phantom temperatures were modulated during real-time fiber optic temperature monitoring, with MR thermometry derived simultaneously from temperature-sensitive changes in the water proton chemical shift (~ 0.01 ppm/ $^{\circ}\text{C}$). MR thermometry was subsequently performed in a series of in vivo nonhuman primate experiments under physiologic and ischemic conditions, testing its reproducibility and overall performance.

RESULTS: Chemical shift thermometry demonstrated excellent agreement with phantom temperatures for all 3 approaches (DIFF-1: linear regression $R^2 = 0.994$; $P < .001$; acquisition time = 4 minutes 40 seconds; DIFF-2: $R^2 = 0.996$; $P < .001$; acquisition time = 4 minutes; DIFF-3: $R^2 = 0.998$; $P < .001$; acquisition time = 40 seconds).

CONCLUSIONS: These findings confirm the comparability in performance of 3 competing approaches to MR thermometry and present in vivo applications under physiologic and ischemic conditions in a primate stroke model.

ABBREVIATIONS: DIFF = difference; PRF = proton resonance frequencies

Brain temperature regulation is a poorly understood physiologic process at the intersection of complex metabolic and hemodynamic phenomena.¹⁻⁵ The importance of temperature dysregulation as a driving force in various mechanisms of neuronal injury has been highlighted in past reports, and the exquisite

sensitivity of neuronal substrate to even modest hypothermia is well-described.⁶⁻¹⁰ Direct brain temperature measurements, however, remain difficult, and reports are limited in number; specifically, the cost and invasiveness of implantable temperature probes limit their applicability in clinically relevant models for characterization of either physiologic or pathologic cerebral spatial temperature gradients.¹¹⁻¹⁴ Similarly, systemic surrogates of brain temperature, such as tympanic or rectal probes, may be inaccurate as estimates of brain temperature, particularly during dysregulation, and furthermore unable to address the presence of spatial cerebral temperature gradients directly.¹⁵⁻¹⁹

Noninvasive imaging approaches to brain temperature monitoring have thus been explored.²⁰ Among these, the use of MR

Received September 23, 2014; accepted after revision November 27.

From the Department of Radiology and Imaging Sciences (S.D., H.M., K.S.P., F.T., D.Q., J.N.O.), Emory University Hospital, Atlanta, Georgia; Yerkes National Primate Research Center (L.H., X.Z.), Emory University, Atlanta, Georgia; Department of Biomedical Engineering (P.R.M.), Northwestern University, Evanston, Illinois; and Department of Biomedical Engineering (L.W., C.F.), Emory University-Georgia Institute of Technology, Atlanta, Georgia.

This work was supported by the American Society of Neuroradiology Scholar Award in Neuroradiology Research (2012–2013, 2013–2014) and an Emory University Research Committee (2013–2014) grant awarded to the lead author; in part the National Center for Research Resources; and currently by the Office of Research Infrastructure Programs of the National Institutes of Health (P51RR000165, OD P51OD011132).

Portions of these data previously presented as oral scientific abstracts at: Annual Meeting of the American Society of Neuroradiology and the Foundation of the ASNR Symposium, May 10–23, 2013; San Diego, California.

Please address correspondence to Seena Dehkharghani, MD, Neuroradiology Division, Attention: Mary Davis, Department of Radiology and Imaging Sciences, Emory University Hospital, 1364 Clifton Rd, NE, Atlanta, GA 30322; e-mail: seena.dehkharghani@emory.edu

Indicates open access to non-subscribers at www.ajnr.org

<http://dx.doi.org/10.3174/ajnr.A4241>

spectroscopy to measure temperature-dependent fluctuations in the relative difference between proton resonance frequencies (PRF), such as the chemical shift difference of water and *N*-acetylaspartate, has gained interest for its theoretic ability to generate quantitative cerebral temperature maps as demonstrated in recent human cerebral thermometry by Karaszewski et al²¹⁻²⁴ and Marshall et al.²⁵ Briefly, the PRF method of thermometry is predicated on the identification of a static, non-temperature-dependent resonance frequency (eg, the methyl resonance of NAA at approximately 2.01 ppm) to serve as an internal reference for the temperature-sensitive water proton resonance (nominally assigned at 4.7 ppm), which, by comparison, exhibits frequency shifts due to changes in hydrogen bonding equilibrium and electron shielding.²⁶ The robust presence of both NAA and water within brain tissues facilitates detection and measurement, making this technique practical as an approach to cerebral thermometry. Accurate determination of the chemical shift difference between the water and NAA resonance frequencies ($\Delta\delta_{\text{water-NAA}}$) has been shown to correlate well with changes in temperature (0.01 ppm/°C) and to correlate uniformly across physiologic ranges of pH and protein concentration.²⁷ PRF thermometry may be acquired with single-voxel spectroscopy or the more time-consuming multivoxel techniques known commonly as chemical shift imaging or MR spectroscopic imaging. The latter, despite several limitations, has the potential for generation of chemical shift grids and maps for simultaneous measurement of temperature distribution across brain regions.^{26,28,29}

Initial studies by Corbett et al²⁷ used a paired acquisition strategy, consisting first of a non-water-suppressed proton spectrum, allowing the detection of the large water peak in the hydrogen PRF spectrum, followed by a water-suppressed spectrum, in which suppression/reduction of the water signal augments the detectability of lower amplitude hydrogen metabolites such as NAA. In doing so, the water-NAA chemical shift is measured from paired spectra, introducing potential errors related to interscan temperature changes or motion between the 2 acquisitions. It has been proposed that a single, partially water-suppressed spectrum may provide sufficient residual water signal for an “internally referenced” water-NAA chemical shift measurement, and subsequent studies adopted this strategy, albeit without report of direct experimental validation.^{15,30}

Distortion of the water peak with water-suppression techniques could impart errors in center frequency estimation and thus impose pitfalls in such a single-scan approach to PRF thermometry; the rigorous and detailed direct comparison of competing approaches is therefore lacking. This work presents the comparative utility of competing approaches to PRF thermometry under reproducible experimental conditions, with primary attention to speed and accuracy by using a flow-modulated and temperature-controlled phantom and a clinical 3T scanner. In vivo experience with single- and multivoxel MR thermometry is then presented in 2 nonhuman primate experiments during physiologic and ischemic conditions.

MATERIALS AND METHODS

Phantom Model

All imaging experiments for this study were performed on a 3T Tim Trio whole-body system (Siemens, Erlangen, Germany). The phantom model in use for this study consists of the following:

- 1) an aqueous brain cytosol spectroscopy phantom prepared in our laboratory with varying compositions of selected, known cerebral metabolites, including NAA, lactate, glutamate, choline, and creatine; 2) a circulating water bath created specifically for use in the following series of MR thermometry experiments; and 3) a 4-channel MR imaging-compatible fiber optic thermometry system. The design and validation of the circulating water bath are detailed subsequently.

For the purposes of the following thermometry calibration experiments, NAA (the nonwater metabolite of interest for PRF thermometry conducted herein) was maintained at approximately 20 mmol/L. Paramagnetic agents (gadolinium) were used in the iterative calibration and optimization of relaxation times and resonance line widths.

An MR imaging-compatible, circulating water bath coupled to a temperature control system was built for temperature regulation in these experiments, modulated by a proportional-integral-derivative controller connected to a 1000-W heating element and optimized to control brain cytosol phantom temperatures during ¹H-spectroscopy experiments. The accuracy of the model and circulating water bath was tested before spectroscopy experiments; a proportional-integral-derivative input sequence steadily increasing phantom temperatures from approximately 18 to 45°C for 2 hours was prescribed. The phantom was then placed in the MR imaging scanner where actual reference temperatures were recorded during simultaneous MR spectroscopy. Additional system testing confirmed excellent stability and control of temperature over the prescribed range ($\pm 0.1^\circ\text{C}$).

Fiber optic thermometry was performed in real-time during all phantom experiments and was monitored by an MR imaging-compatible high-resolution ($\pm 0.01^\circ\text{C}$, 3-second temporal update) 4-channel bandgap gallium arsenide system (OTG-M series; OpSens, Quebec, Quebec, Canada).

PRF Thermometry

A series of experiments was undertaken to compare the existing and proposed approaches to PRF thermometry using $\Delta\delta_{\text{water-NAA}}$. The metabolite solution was secured in a bottle within the phantom and monitored at room temperature ($\sim 18\text{--}19^\circ\text{C}$) in the preliminary experience with the system. Despite the cold forced air within the scanner, only minimal fluctuations ($< 0.3^\circ\text{C}$) in equilibrium temperatures were observed preceding thermometry experiments with simultaneous probe and MR spectroscopy thermometry acquired as detailed below.

Techniques. Three approaches to PRF thermometry were investigated, denoted hereafter as difference (DIFF) 1, DIFF 2, and DIFF 3 (Fig 1A). The initial experiment (DIFF 1) used a traditional paired-scan technique as described by Corbett et al.²⁷ Briefly, pairs of single-voxel spectroscopy interleaving non-water-suppressed and water-suppressed spectra were sequentially acquired across modulated temperatures ranging between ~ 18 and 45°C . These paired spectra were repeatedly acquired in succession, both by using a point-resolved spectroscopy sequence, and collected during approximately 140 minutes with real-time fiber optic temperature monitoring.

Past investigations have used an accelerated, single-scan prescription for PRF thermometry, and this approach (DIFF 2) was

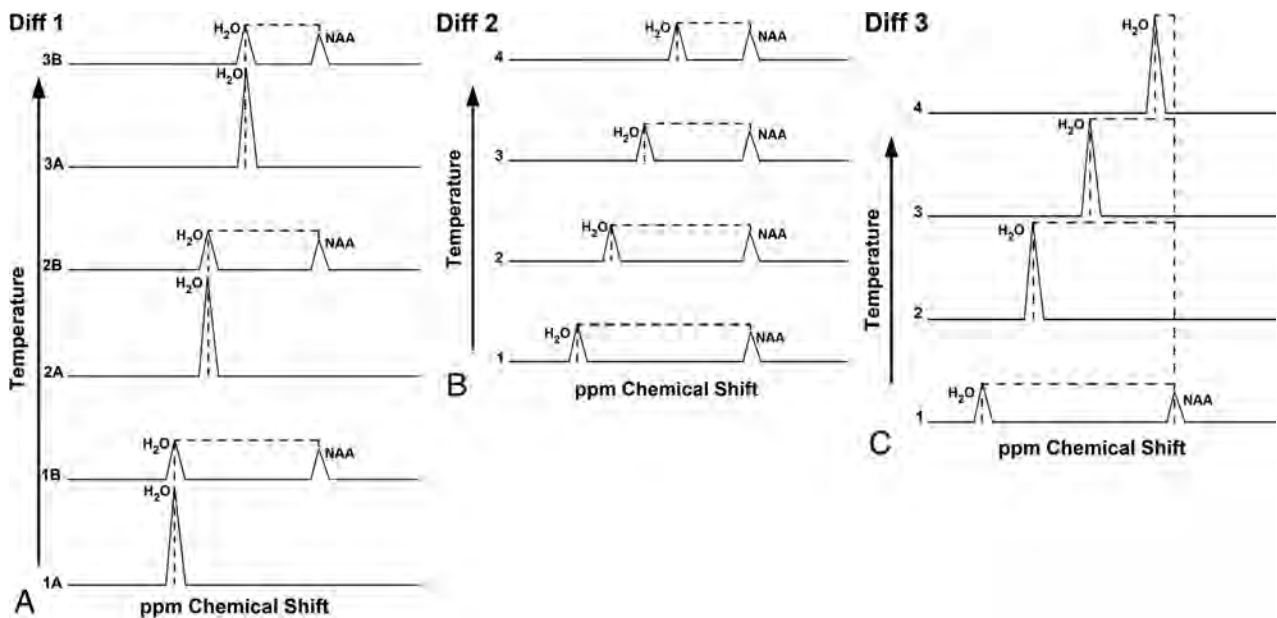


FIG 1. Schematic representation of methodologies for PRF thermometry: DIFF 1, DIFF 2, and DIFF 3 (see text). With increasing temperatures, the water resonance frequency is observed to shift at approximately 0.01 ppm/°C toward the lower resonance. **A**, DIFF 1, representing the initial-approach interleaving pairs of non-water-suppressed and water-suppressed proton spectra during increasing temperatures. Alphanumeric combinations denote the pair number, followed by either A for non-water-suppressed or B for water-suppressed spectra. The shifting water-resonance frequency is thus measured against the static NAA resonance, the latter obtained from B in each pair. **B**, DIFF 2 partially water-suppressed spectrum used for the simultaneous measurement of both water and NAA frequencies. **C**, DIFF 3, newly proposed accelerated methodology, wherein the NAA reference frequency is obtained from an initial water-suppressed spectrum and is followed by a high-temporal-resolution series of non-water-suppressed spectra, measured against the initial NAA reference frequency.

tested in a subsequent experiment (Fig 1B).¹⁵ Specifically, given the stationary resonance of the methyl NAA reference frequency (~2.01 ppm), this approach uses only partial suppression of the water resonance, allowing simultaneous water and NAA peak assignments from a given spectrum, theoretically obviating the less time-efficient paired strategy in DIFF 1. Simultaneous assignment of both water and NAA peaks may therefore mitigate potential concerns over interscan motion or temperature changes inherent to the paired approach in DIFF 1. In this manner, DIFF 2 was measured and plotted against probe reference temperatures under otherwise similar experimental conditions as described in DIFF 1.

As an alternative to either preceding methodology, given our observation of stability in the NAA reference frequency as previously reported, we tested a new, third approach with further predicted improvements in temporal resolution.²⁷ This hybridized approach (DIFF 3) was tested using a single initial NAA reference frequency, followed by a series of rapid (~40-second) non-water-suppressed metabolite scans, under conditions similar to those described in DIFF 1 and DIFF 2 with temperatures steadily increased to 35°C (Fig 1C).

MR Spectroscopy Postprocessing and Analysis. Scanner acquisition parameters were optimized for 3T imaging and designed to approximate conditions for future in vivo and clinical applications to the extent achievable. T1-weighted images were first obtained by using a T1 MPRAGE sequence (TR = 2300 ms, TE = 3.68 ms, TI = 900 ms, flip angle = 9°, voxel size = 1 × 1 × 1 mm³) for localization. All spectra were acquired as follows: 8-mL single-voxel point-resolved spectroscopy sequence with TR = 2 seconds;

TE = 30 ms; signal averages = 16 (without water suppression) and 64 (with water suppression), giving an acquisition time of 40 seconds (non-water-suppressed) and ~4 minutes (water-suppressed), respectively. Water suppression used for metabolite frequency assignments was achieved by a standard 3-pulse chemical shift selective water suppression technique (35- to 50-Hz suppression bandwidth). Center frequency was set on the water resonance initially. Following the advanced automated shimming protocol equipped on the scanner, manual shimming was applied to further refine the shimming conditions.

Spectroscopic data were analyzed with the jMRUI (http://www.mrui.uab.es/mrui/_download) package. All MR spectroscopy data were zero-filled to 4096 data points and preprocessed with manual zero-order phase correction and 2-Hz exponential apodization. The frequency of the water signal acquired at the onset was set to 4.7 ppm and thereafter as the reference for all other spectral data. The residual water signal in water-suppressed scans was removed by using the Hanckel-Lanczos Singular Value Decomposition method. Spectroscopic data were Fourier-transformed for display and visual quality control purposes by using the Advanced Method for Accurate Robust and Efficient Spectral Fitting algorithm within the jMRUI package. Gaussian components were modeled in the frequency domain of the metabolites of interest, including choline, creatine, *N*-acetylaspartate, and glutamate/glutamine. The chemical shifts (ie, frequencies) of the fitted metabolite peaks were reported to a precision of 0.001 ppm. Spectra were automatically discarded if the fitted line widths were <1 Hz or >10 Hz. During analysis of all spectra, with the tempera-

ture-dependent water resonance nominally assigned to a 4.7-ppm chemical shift, the apparent “shift” is paradoxically imparted to the NAA peak, ostensibly bringing the NAA peak further toward high resonance by a range accounted for by the true water frequency shift.

Temperature-dependent changes in the relative frequency shift between H₂O and NAA were analyzed by a simple linear regression model in SAS 9.3 (SAS Institute, Cary, North Carolina) for derivation of the temperature-dependent coefficient of the water-NAA frequency shift relative to temperature change. The computed correlation coefficient was compared with the reported/expected results from past studies and used for comparison of the 3 approaches detailed above. The slope of regression and intercept was determined, and the strength of correlation and accuracy were determined from the coefficient of determination (R^2) and root-mean-square error, respectively. Statistical significance was established at $P < .05$.

In Vivo Thermometry

Two adult rhesus macaques were sourced from the Yerkes National Primate Research Center for noninvasive thermometry; rhesus macaques were selected for their phylogenetic similarities to humans in a parallel investigation of a nonhuman primate model of inducible stroke under investigation in our institution. All animal studies were performed under approval of the Institutional Animal Care and Use Committee providing for the entirety of the experimental protocol. Briefly, irreversible endovascular occlusion was achieved by tandem deployable suture embolus delivered under superselective angiographic guidance to the right MCA by using a minimal interventional approach.^{31,32}

Imaging was performed on a clinical 3T whole-body system identical to that described for in vitro experiments and using a dedicated 8-channel phased array head coil for local signal reception. Baseline MR thermometry was performed with single- or multivoxel techniques, both using a paired approach acquiring separate non-water-suppressed and water-suppressed spectra (DIFF 1 approach). Single-voxel spectroscopy was acquired with the same parameters as described for the preceding in vitro experiments. Multivoxel spectroscopy was acquired with a 2D 8-cm² point-resolved spectroscopy sequence acquisition with the following sequence parameters: water spectrum: TR = 1500 ms; TE = 30 ms; NEX = 1; metabolite spectrum: TR = 1500 ms; TE = 30 ms; NEX = 7; acquisition time = 10 minutes 31 seconds. Eight outer volume suppression bands were placed with specific effort to exclude areas of potential contamination. For both single- and multivoxel thermometry, baseline scanning was performed across 6 repetitions during a 3-hour scanning session of healthy adult macaques under 1%–1.5% isoflurane with continuous physiologic monitoring and maintenance of the rectal temperature at approximately 37°C.³³ In separate experimental sessions, single- or multivoxel spectra were subsequently acquired at approximately 6 hours following endovascular MCA occlusion during a continuous MR imaging session focused on infarct evolution. Voxels were excluded on the basis of spectral corruption as defined for the in vitro methodology.

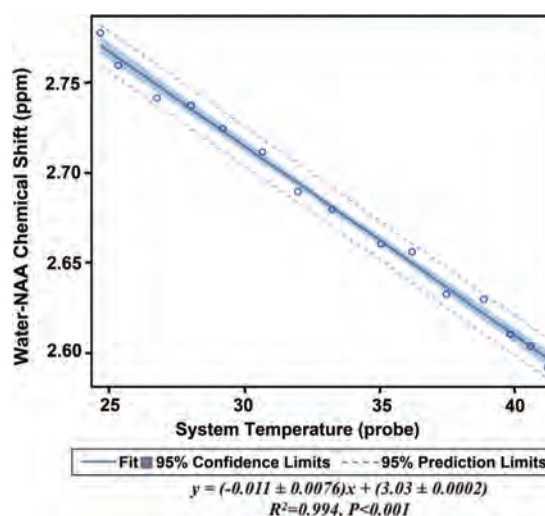


FIG 2. Linear regression from the DIFF 1 experiment. The y-axis represents the water-NAA chemical shift difference, plotted against continuous fiber optic measured temperatures from approximately 18 to 45°C. The slope of regression, 0.01 ppm/°C, is in agreement with the expected temperature dependency of the temperature-dependent proton chemical shift.

RESULTS

Phantom Thermometry

Before dynamic temperature measurements, minor fluctuations in phantom temperatures were observed due to equilibration and cold forced air within the scanner, varying between 18.8 and 19.0°C; temperatures measured from $\Delta\delta_{\text{water-NAA}}$ varied from the probe temperature by <0.3°C across 6 successive measures during this period. On temperature change with the flow-modulated phantom, $\Delta\delta_{\text{water-NAA}}$ demonstrated an expected linear decrease with increasing temperature for all 3 approaches. Phantom experiments for the 3 different methodologies demonstrated excellent agreement between probe and chemical shift thermometry.

For DIFF 1 (Fig 2), linear regression demonstrated the expected slope and intercept for the temperature-dependent proton chemical shift, $y = (-0.011 \pm 0.0076)x + (3.03 \pm 0.0002)$ ($R^2 = 0.994$, root-mean-square error = 0.005, $P < .001$).

In an initial series of experiments using the DIFF 2 protocol, errors relating to apparent overestimation of temperatures were observed. Specifically, the process of repeated water suppression in successive spectra imparted distortions on the observed water peak, because the chemical shift selective suppression pulse is rendered increasingly askew during the course of temperature change. To address this error, in a subsequent experiment, we repeatedly refocused the center frequency on the shifting water resonance before acquisition of each DIFF 2 spectrum, eliminating the distortions (see “Discussion”). Using the DIFF 2 approach with the addition of this refocusing step, we observed excellent agreement with measured probe temperatures (Fig 3), $y = (-0.010 \pm 0.0002)x + (3.00 \pm 0.0066)$ ($R^2 = 0.996$, root-mean-square error = 0.004, $P < .001$).

The DIFF 3 approach, proposed to further accelerate the existing methodologies, demonstrated excellent correlation with temperatures (Fig 4), at 7× temporal resolution, $y = (-0.014 \pm 0.0001)x + (3.12 \pm 0.0016)$ ($R^2 = 0.998$, root-mean-square error = 0.00577, $P < .001$).

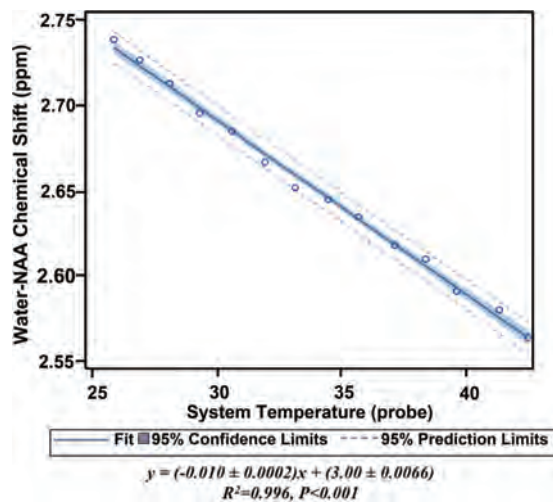


FIG 3. Linear regression from the DIFF 2 experiment. Similar correlation as noted in DIFF 1. By comparison with DIFF 1, approximately 15%–20% time savings is achieved by eliminating the paired approach used in Fig 2.

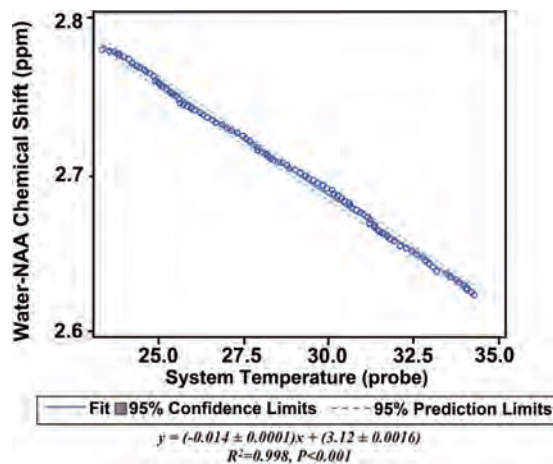


FIG 4. DIFF 3 versus temperature change. Excellent correlation is again noted between measured temperatures and the water-NAA chemical shift. Frequency shifts are measured from sequential, non-water-suppressed spectra against an initial NAA reference frequency. Elimination of the repeated metabolite spectra in DIFF 1 and DIFF 2 permits increasing temporal resolution, with collection of 102 data points between approximately 18 and 35°C, compared with <15 measures across a similar experimental session.

In Vivo Thermometry

Single-voxel spectroscopy (Fig 5) acquired across 6 repeated acquisitions during a single 3-hour imaging session demonstrated excellent spectral quality with fitted line widths all <0.04 ppm (approximately 5 Hz) permitting reproducible determination of the water-NAA chemical shift difference. Mean and computed temperatures during maintenance of rectal temperatures at approximately 37°C were $36.94 \pm 0.22^\circ\text{C}$.

Multivoxel spectroscopy (Fig 6) demonstrated similarly robust findings, though with corruption of peripheral-most voxels likely affected both by lipid contamination and chemical shift misregistration, despite meticulous outer volume suppression. An inner volume of 8×4 voxels was suitable for water-NAA chemical shift determination and demonstrated distinct zonality in computed temperatures, with relatively symmetric regions of

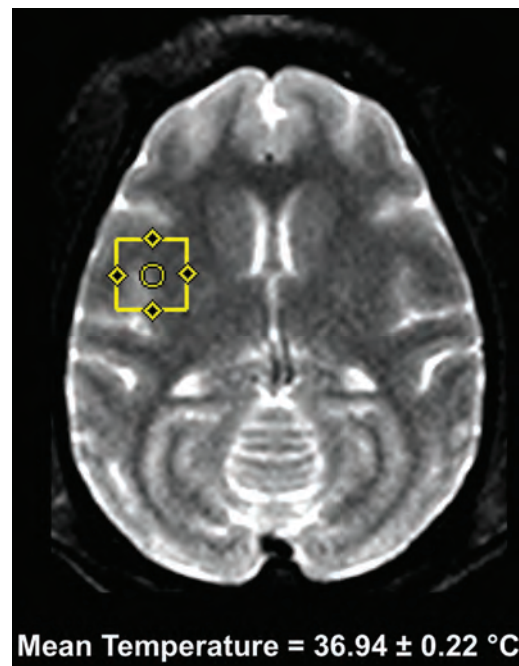


FIG 5. Single-voxel MR spectroscopy in a healthy nonhuman primate during physiologic monitoring under general anesthesia, with maintenance of rectal temperatures at approximately 37°C. Six repeated MR spectroscopy scans were acquired from the right operculum by using a standard point-resolved spectroscopy sequence across an approximately 3-hour imaging session. Temperatures were computed from the temperature-dependent water-NAA chemical shift difference (see text), with mean computed temperatures of $36.94 \pm 0.22^\circ\text{C}$. Spectral fitted full width at half maximum varies between 4 and 5 Hz.

mean temperature variation ranging from a minimum of 36.3°C to a maximum of 39.3°C .

Delayed single-voxel thermometry obtained 6 hours following right MCA occlusion (Fig 7) demonstrated slightly lower temperatures within the infarct territory compared with the contralateral normal hemisphere (36.66 versus 37.06°C , respectively). Multivoxel spectroscopy 6 hours following induced ischemia (Fig 8) demonstrated evolution of the zonal thermal gradients observed during physiologic imaging conditions, also with generally lower temperatures throughout the infarct territory.

DISCUSSION

These findings establish the comparability of 3 competing approaches to PRF thermometry and introduce a fixed-NAA approach (DIFF 3), mitigating some of the speed limitations inherent to most PRF thermometry, without adverse effects on accuracy. Among the 2 commonly used approaches to chemical shift thermometry, denoted herein as DIFF 1 and DIFF 2, we observed excellent correlation for both, confirming that the conventional use of paired water and metabolite spectra (DIFF 1) could be supplanted by a more efficient single-scan approach (DIFF 2) as recently proposed.²⁷ While such an approach offers improved temporal resolution without concern for interscan motion (ie, between the paired water and metabolite spectra), implementation is not without potential pitfalls. Specifically, simply acquiring successive partially water-suppressed spectra for $\Delta\delta_{\text{water-NAA}}$ may engender distortions of the observed water peak. The chemical shift selective suppression pulse intended for water

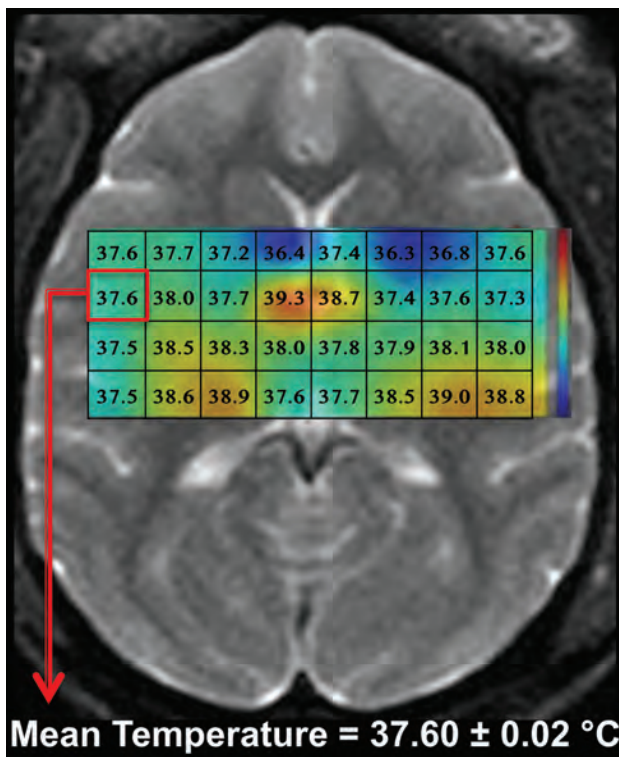


FIG 6. Multivoxel MR thermometry in a healthy nonhuman primate during physiologic monitoring under general anesthesia, with maintenance of rectal temperatures at approximately 37°C. Six repeated MR spectroscopy scans were acquired by using 2D chemical shift imaging spectroscopy (see text) across an approximately 3-hour imaging session. Computed temperatures are derived from the water-NAA proton chemical shift and color thermal grid overlaid on the axial T2-weighted reference image for display purposes. A relatively symmetric, zonal distribution of temperatures is noted across repeated studies; a representative peripheral voxel demonstrates the repeatability of in vivo imaging, with mean computed temperatures of $37.6 \pm 0.02^\circ\text{C}$. Spectral-fitted full widths at half maximum vary between 4 and 5 Hz across voxels.

saturation is rendered increasingly askew during the course of temperature change during heating/cooling, and the consequent distortions on the water peak could confound measurements. This error relates to the nominal assignment of the water resonance at 4.7 ppm at the onset, albeit with an unaccounted for temperature-dependent frequency shift, which, during heating, moves downstream and increasingly off-resonance. The suppression pulse, now off-resonance, may deform the water peak during curve-fitting and increasingly so with greater temperature change.

The DIFF 3 protocol offers further enhancements to the temporal resolution achievable in either DIFF 1 or DIFF 2. The basis for this approach can be understood in the context of water resonance taken in isolation; one may consider the possibility of acquiring simply a succession of high temporal resolution (~40-second) non-water-suppressed scans, from which the changes of water resonance frequency relative to baseline could be used to derive relative temperature change, vis-à-vis phase-contrast thermometry techniques in widespread use. Such an approach would, however, eliminate the primary advantage of $\Delta\delta_{\text{water-NAA}}$ thermometry, specifically, the “internally referenced” nature of PRF, which allows comparing the temperature-dependent water resonance against a static reference frequency

such as NAA. The NAA reference frequency thus accounts for non-temperature-related field drifts and other sources of error as detailed in past reports.²⁶ We thus proposed that accelerated PRF thermometry might instead be achieved by the acquisition of a baseline hydrogen metabolite spectrum for NAA assignment, followed, in close succession, by serial non-water-suppressed spectra. By taking advantage of a baseline reference frequency provided by the initial metabolite spectrum, one can observe the benefits of $\Delta\delta_{\text{water-NAA}}$ thermometry in a more efficient protocol and without detriment to accuracy. The benefits of $>7\times$ data collection speed could offset potential shortcomings with this approach, and indeed DIFF 3 demonstrated accuracy comparable with that of DIFF 1 and DIFF 2 in this experimental protocol.

The 0.004 difference between slopes of regression for the DIFF 3 methodology cannot be readily explained and could relate to partially uncompensated field drifts during the experimental session. In this respect, the benefits of acceleration may be balanced by the potential for errors and therefore, lesser accuracy as a method approaching absolute thermometry. Alternatively, the NAA (or other non-hydrogen-bound metabolite signatures) could be sampled periodically relative to water scans, hence still providing some relative acceleration while potentially mitigating any unaccounted for frequency drift.

Despite promising results for all 3 approaches, it must be noted that $\Delta\delta_{\text{water-NAA}}$, while superior as an approximation of absolute thermometry compared with competing techniques, several inherent limitations exist for $\Delta\delta_{\text{water-NAA}}$ as an absolute thermometer.²⁶ These relate principally to errors in the detection of the frequency of the signal and arise largely from inter- and intravoxel inhomogeneity; while errors from intervoxel inhomogeneities are considerably ameliorated by using an internal reference frequency such as NAA, intravoxel inhomogeneities may induce smearing of spectra and impart inaccuracies during estimation of resonance frequencies, particularly when SNR is limited. These and other limitations have been significantly addressed by the use of spectral estimation techniques, which prove valuable in achieving the frequency resolution necessary to make chemical shift thermometry clinically relevant.

In the present study, an aqueous brain cytosol model was selected for the temperature validation experiments, building on prior experimental models described by Corbett et al,²⁷ and ensuring and facilitating a predictable, controlled temperature response during heating.

$\Delta\delta_{\text{water-NAA}}$ represents the only thermometry technique determined purely from the frequency of proton resonance, in contrast to other techniques derived from amplitudes. In this respect, robust thermometry can be achieved even in disorders wherein neuronal injury may lessen detectable NAA, as shown from in vivo stroke thermometry conducted by Corbett et al.^{27,30,34} Furthermore, unique to this technique is its tissue-type insensitivity, owing to the predictability of the proton chemical shift with changing temperatures, an attribute shared only with the other PRF technique, water phase-contrast thermometry. By comparison with phase-contrast techniques however, chemical shift thermometry can potentially be performed without baseline scanning, while allowing the correction of non-temperature-related changes in the proton phase such as susceptibility variations.²⁶

We further acknowledge several limitations in the study design, including, primarily, those obstacles precluding validation of primate MR spectroscopy temperatures with absolute probe measurements. Resource and technical limitations complicate the collection of temporospatial cerebral thermal gradients in the nonhuman primate model, and insofar as the rectal temperatures reflect brain temperatures, they must be considered an approximation. Applications of MR thermometry in the setting of neurovascular ischemia have been explored preliminarily, including initial reports by Marshall et al²⁵ and Karaszewski et al,²³ operationally describing a theoretic formalism for the evolving temperature gradients observed in the setting of ischemia. Technical obstacles preclude absolute measurement of cerebral spatio-temporal gradients, motivated by the development of noninvasive approaches as described here. Corbett et al²⁷ observed gradients of 0.5–1.0°C across the superficial 1 cm of the brain in a small

piglet stroke model and excellent agreement between localized probe and MR spectroscopy-derived temperatures. A theoretic framework of brain temperature regulation further highlights the potential for basal thermal gradients, relating to differences in blood flow, metabolism, and evaporative heat loss, with increasing variation predicted in functionally active regions.⁵

While the in vivo experiments herein represent only an initial experience with MR spectroscopy thermometry in the setting of a controlled, inducible primate stroke model, the diminished temperatures observed are consistent with predicted phenomena in their prior studies. Phantom experiments using multivoxel techniques were generally challenging in our model, due to the relatively small dimensions of the phantom, designed to ensure a uniform and predictable temperature response but limiting the use of multivoxel acquisition uncorrupted by the boundaries of the phantom. We have recently shown the comparability and lack

of significant differences in multivoxel and single-voxel thermometry at static room temperatures; however, the phantom design in that protocol did not permit real-time probe temperature collection.³⁵ We, however, maintain that application of the same spectral quality-control measures as are in place for single-voxel spectroscopy and the excellent spectral quality in multivoxel experiments support the robustness of the spectra in those experiments. The potential impact of isoflurane on blood flow, metabolism, and thus potentially brain temperature could not be directly assessed within the experimental model in place. We aimed primarily to exhibit the feasibility of MR spectroscopy ther-

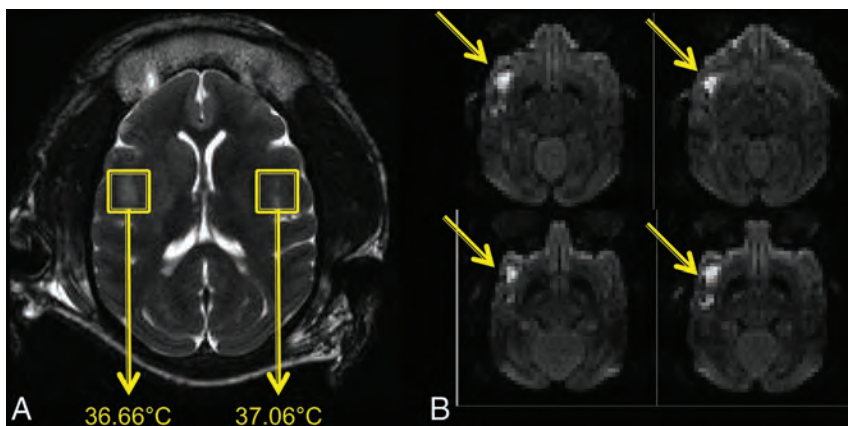


FIG 7. A, Single-voxel MR thermometry in an adult nonhuman primate 6 hours following endovascular MCA occlusion. Axial T2-weighted image (right) with symmetric 1.5-mL voxels placed in the bilateral opercular region. B, Area of infarction in the right hemisphere demonstrated on diffusion-weighted images (yellow arrows). Computed temperatures within the region of infarction are noted approaching 0.5°C less than those in the contralateral hemisphere.

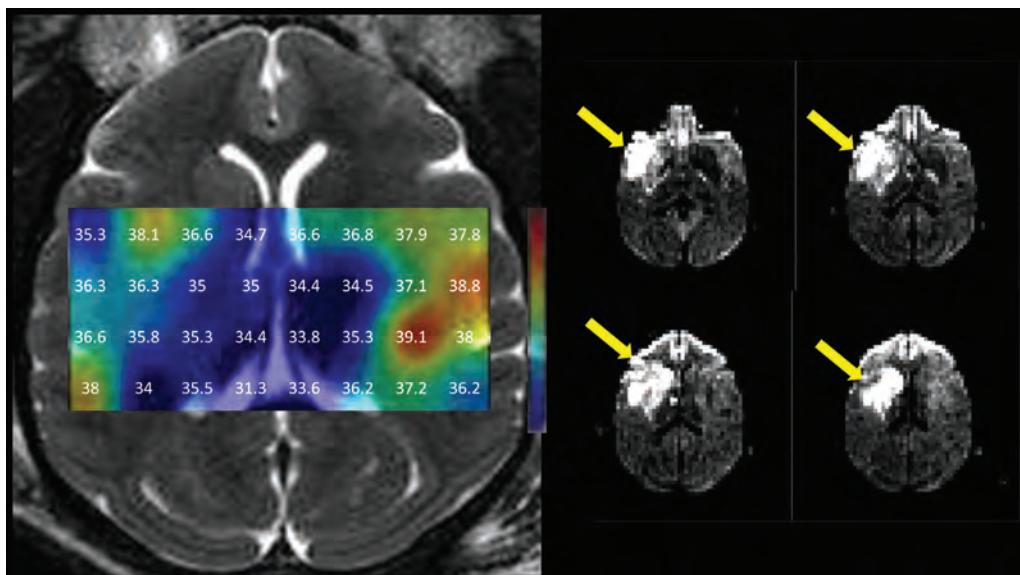


FIG 8. Multivoxel MR thermometry in an adult rhesus macaque obtained approximately 6 hours following endovascular MCA occlusion. Symmetric gradients observed under physiologic, preischemic conditions in Fig 6 were replaced by generally lower temperatures throughout the infarction territory of the right MCA seen on diffusion-weighted imaging (yellow arrows). Temperatures throughout the right hemispheric infarct territory generally diminish by comparison with the contralateral normal left hemisphere.

mometry in the healthy and ischemic primate brain, and in this respect, the conditions of administration and monitoring and control of physiologic temperatures were preserved across experiments.

CONCLUSIONS

The potential applications of brain thermometry in normal physiology and disease are widespread, but characterization of cerebral temperatures has traditionally been limited by the costly and invasive nature of implantable thermometry systems.

Disclosures: Seena Dehkharghani—RELATED: Grant: Foundation of the American Society of Neuroradiology.* Hui Mao—UNRELATED: Grants/Grants Pending: National Institutes of Health.* *Money paid to the institution.

REFERENCES

1. Baker MA. A brain-cooling system in mammals. *Scientific American* 1979;240:130–39
2. Brengelmann GL. Specialized brain cooling in humans? *FASEB J* 1993;7:1148–52; discussion 1152–53
3. Cabanac M. Selective brain cooling in humans: “fancy” or fact? *FASEB J* 1993;7:1143–46; discussion 1146–47
4. Hayward JN, Baker MA. Role of cerebral arterial blood in the regulation of brain temperature in the monkey. *Am J Physiol* 1968; 215:389–403
5. Sukstanskii AL, Yablonskiy DA. Theoretical model of temperature regulation in the brain during changes in functional activity. *Proc Natl Acad Sci U S A* 2006;103:12144–49
6. Busto R, Dietrich WD, Globus MY, et al. Small differences in intracerebral brain temperature critically determine the extent of ischemic neuronal injury. *J Cereb Blood Flow Metab* 1987;7:729–38
7. Erecinska M, Thoresen M, Silver IA. Effects of hypothermia on energy metabolism in mammalian central nervous system. *J Cereb Blood Flow Metab* 2003;23:513–30
8. Hammer MD, Krieger DW. Acute ischemic stroke: is there a role for hypothermia? *Cleve Clin J Med* 2002;69:770, 773–74, 776–77
9. Liu L, Yenari MA. Therapeutic hypothermia: neuroprotective mechanisms. *Front Biosci* 2007;12:816–25
10. Wolfe KB. Effect of hypothermia on cerebral damage resulting from cardiac arrest. *Am J Cardiol* 1960;6:809–12
11. Minamisawa H, Møllergaard P, Smith ML, et al. Preservation of brain temperature during ischemia in rats. *Stroke* 1990;21:758–64
12. Minamisawa H, Nordstrom CH, Smith ML, et al. The influence of mild body and brain hypothermia on ischemic brain damage. *J Cereb Blood Flow Metab* 1990;10:365–74
13. Schwab S, Spranger M, Aschoff A, et al. Brain temperature monitoring and modulation in patients with severe MCA infarction. *Neurology* 1997;48:762–67
14. Verlooy J, Heytens L, Veeckmans G, et al. Intracerebral temperature monitoring in severely head injured patients. *Acta Neurochir (Wien)* 1995;134:76–78
15. Cady EB, D’Souza PC, Penrice J, et al. The estimation of local brain temperature by in vivo 1H magnetic resonance spectroscopy. *Magn Reson Med* 1995;33:862–67
16. Kiyatkin EA. Brain temperature fluctuations during physiological and pathological conditions. *Eur J Appl Physiol* 2007;101:3–17
17. Modi J, Bai HD, Menon BK, et al. Enhancing acute ischemic stroke interpretation with online aspects training. *Can J Neurol Sci* 2012; 39:112–14
18. Simon E. Tympanic temperature is not suited to indicate selective brain cooling in humans: a re-evaluation of the thermophysiological basics. *Eur J Appl Physiol* 2007;101:19–30
19. Soukup J, Rieger A, Holz C, et al. Temperature gradient between brain tissue and arterial blood mirrors the flow-metabolism relationship in uninjured brain: an experimental study. *Acta Anaesthesiol Scand* 2007;51:872–79
20. Rieke V, Butts Pauly K. MR thermometry. *J Magn Reson Imaging* 2008;27:376–90
21. Karaszewski B, Carpenter TK, Thomas RG, et al. Relationships between brain and body temperature, clinical and imaging outcomes after ischemic stroke. *J Cereb Blood Flow Metab* 2013;33:1083–89
22. Karaszewski B, Thomas RG, Dennis MS, et al. Temporal profile of body temperature in acute ischemic stroke: relation to stroke severity and outcome. *BMC Neurol* 2012;12:123
23. Karaszewski B, Wardlaw JM, Marshall I, et al. Measurement of brain temperature with magnetic resonance spectroscopy in acute ischemic stroke. *Ann Neurol* 2006;60:438–46
24. Karaszewski B, Wardlaw JM, Marshall I, et al. Early brain temperature elevation and anaerobic metabolism in human acute ischaemic stroke. *Brain* 2009;132:955–64
25. Marshall I, Karaszewski B, Wardlaw JM, et al. Measurement of regional brain temperature using proton spectroscopic imaging: validation and application to acute ischemic stroke. *Magn Reson Imaging* 2006;24:699–706
26. Kuroda K. Non-invasive MR thermography using the water proton chemical shift. *Int J Hyperthermia* 2005;21:547–60
27. Corbett RJ, Laptook AR, Tollefsbol G, et al. Validation of a noninvasive method to measure brain temperature in vivo using 1H NMR spectroscopy. *J Neurochem* 1995;64:1224–30
28. Kuroda K, Mulkern RV, Oshio K, et al. Temperature mapping using the water proton chemical shift: self-referenced method with echo-planar spectroscopic imaging. *Magn Reson Med* 2000;43:220–25
29. Kuroda K, Suzuki Y, Ishihara Y, et al. Temperature mapping using water proton chemical shift obtained with 3D-MRSI: feasibility in vivo. *Magn Reson Med* 1996;35:20–29
30. Corbett R, Laptook A, Weatherall P. Noninvasive measurements of human brain temperature using volume-localized proton magnetic resonance spectroscopy. *J Cereb Blood Flow Metab* 1997;17:363–69
31. Zhang X, Tong F, Li CX, et al. A fast multiparameter MRI approach for acute stroke assessment on a 3T clinical scanner: preliminary results in a non-human primate model with transient ischemic occlusion. *Quant Imaging Med Surg* 2014;4:112–22
32. de Crespigny AJ, D’Arceuil HE, Maynard KI, et al. Acute studies of a new primate model of reversible middle cerebral artery occlusion. *J Stroke Cerebrovasc Dis* 2005;14:80–87
33. Li CX, Patel S, Auerbach EJ, et al. Dose-dependent effect of isoflurane on regional cerebral blood flow in anesthetized macaque monkeys. *Neurosci Lett* 2013;541:58–62
34. Corbett RJ, Purdy PD, Laptook AR, et al. Noninvasive measurement of brain temperature after stroke. *AJNR Am J Neuroradiol* 1999;20:1851–57
35. Dehkharghani S, Wei L, Mao H, et al. Multivoxel proton spectroscopy for non-invasive MR thermometry: phantom comparison of PRESS and semiLASER-localized chemical shift imaging for temperature monitoring. In: *Proceedings of the International Society for Magnetic Resonance in Medicine*, Milan, Italy. May 10–16, 2014

HydroCoils Reduce Recurrence Rates in Recently Ruptured Medium-Sized Intracranial Aneurysms: A Subgroup Analysis of the HELPS Trial

W. Brinjikji, P.M. White, H. Nahser, J. Wardlaw, R. Sellar, H.J. Cloft, and D.F. Kallmes

ABSTRACT

BACKGROUND AND PURPOSE: The HydroCoil Endovascular Aneurysm Occlusion and Packing Study (HELPS) was a randomized, controlled trial comparing HydroCoils with bare-platinum coils. The purpose of this study was to perform a subgroup analysis of angiographic and clinical outcomes of medium-sized aneurysms in the HELPS trial.

MATERIALS AND METHODS: Patients with medium-sized aneurysms (5–9.9 mm) were selected from the HELPS trial. Outcomes compared between the HydroCoil and bare-platinum groups included the following: 1) any recurrence, 2) major recurrence, 3) retreatment, and 4) mRS score of ≤ 2 . Subgroup analysis by rupture status was performed. Multivariate logistic regression analysis adjusting for aneurysm neck size, shape, use of adjunctive device, and rupture status was performed.

RESULTS: Two hundred eighty-eight patients with medium-sized aneurysms were randomized (144 in each group). At 15–18 months posttreatment, the major recurrence rate was significantly lower in the HydroCoil group than in controls (18.6% versus 30.8%, $P = .03$, respectively). For patients with recently ruptured aneurysms, the major recurrence rate was significantly lower for the HydroCoil group than for controls (20.3% versus 47.5%, $P = .003$), while rates were similar between groups for unruptured aneurysms (16.7% versus 14.8%, $P = .80$). Multivariate analysis of patients with recently ruptured aneurysms demonstrated a lower odds of major recurrence with HydroCoils (OR = 0.27; 95% CI, 0.12–0.58; $P = .0007$). No difference in retreatment rates or mRS of ≤ 2 was seen between groups.

CONCLUSIONS: HydroCoils were associated with statistically significant and clinically relevant lower rates of major recurrence for recently ruptured, medium-sized aneurysms in the HELPS trial. Because this was not a prespecified subgroup analysis, these results should not alter clinical practice but, rather, provide insight into the design of future clinical trials comparing bare platinum with second-generation coils.

ABBREVIATION: HELPS = HydroCoil Endovascular Aneurysm Occlusion and Packing Study

Coil embolization of intracranial aneurysms is prone to recurrence rates of up to 20% within 18 months of treatment.¹ Up to 10% of coiled aneurysms require retreatment, usually with additional coil embolization. The costs and risks of monitoring aneurysms for recurrences and retreating them, when necessary, are not negligible.² Many modified coils have been developed aimed at decreasing aneurysm recurrence and retreatment rates. Hydrogel coils (HydroCoil; MicroVention, Tustin, California) are designed with an expansile hydrogel that fills more of the aneurysm

lumen than standard platinum coils.³ By doing so, these coils are thought to achieve increased packing density thus accelerating aneurysm healing and decreasing recurrence and retreatment rates.⁴

The HydroCoil Endovascular Aneurysm Occlusion and Packing Study (HELPS) was a randomized, controlled trial comparing HydroCoils with bare platinum coils.⁵ This study compared the rate of a composite primary outcome, which included both angiographic and clinical outcomes, between groups. The trial demonstrated a 7.0% reduction in the proportion of adverse composite primary outcomes with HydroCoils ($P = .13$), with significantly higher rates of adverse outcomes in the control group when only ruptured aneurysms were considered. In addition, the investigators found a statistically significant, but not clinically meaningful, difference in major angiographic recurrences between the HydroCoil and bare platinum groups.

While the HELPS trial represents level 1 evidence, the clinical

Received September 22, 2014; accepted after revision December 11.

From the Department of Radiology (W.B., H.J.C., D.F.K.), Mayo Clinic, Rochester, Minnesota; Institute for Ageing and Health (P.M.W.), Newcastle University, Newcastle-upon-Tyne, United Kingdom; Department of Clinical Neuroscience (H.N.), University of Edinburgh, Edinburgh, United Kingdom; and Walton Centre (J.W., R.S.), Liverpool, United Kingdom.

Please address correspondence to Waleed Brinjikji, MD, 200 1st St SW, Rochester, MN 55905; e-mail: brinjikji.waleed@mayo.edu

<http://dx.doi.org/10.3174/ajnr.A4266>

applicability of the findings of the trial may be difficult to apply in clinical practice.⁶ While the composite analysis has definite benefits over exclusive focus on recurrence and treatment rates, this composite end point has not been the usual metric used to evaluate the efficacy of aneurysm treatment. In addition, small aneurysms have very low recurrence rates, and large aneurysms have high recanalization rates, regardless of the device used.⁷ As such, inclusion of small or large aneurysms may mask benefits isolated to medium-sized aneurysms.^{8,9} Furthermore, ruptured aneurysms have a different biology from unruptured ones as evidenced by elevated recurrence rates in many series.¹⁰ To fully characterize potential differences in “usual” outcomes between HydroCoil and bare platinum coils, we performed a subgroup analysis of angiographic and clinical outcomes of medium-sized aneurysms in the HELPS trial, stratifying outcomes by rupture status. We hypothesized that treatment with the HydroCoil would result in significantly improved recurrence rates among medium-sized aneurysms.

MATERIALS AND METHODS

Patient Population

Patients were enrolled in the HELPS trial from 24 centers in 7 countries. Patients were eligible for inclusion if they presented with a previously untreated cerebral aneurysm measuring 2–25 mm in maximum diameter, were 18–75 years of age, were deemed by the neurovascular team to need coiling, were not pregnant, had a World Federation of Neurosurgical Societies grade between 0 and III, had anatomy in which endovascular occlusion was judged possible, had not previously been enrolled in the trial, and the neurointerventionalist who would perform the procedure was content to randomize to bare platinum coils or HydroCoils. Patients were excluded if they had >1 aneurysm requiring treatment at 1 procedure. For the purposes of this subgroup analysis, only the subset of patients with medium-sized (5.0–9.9 mm) aneurysms were included. All patients gave written informed consent. If they could not give consent, then informed consent was provided by a surrogate or legally authorized representative. This trial had UK Multicenter Research Ethics Committee approval, and all centers had local ethics approval. Detailed information about the coiling procedure, randomization techniques, baseline demographics, data handling, and coiling is shown elsewhere.^{5,11}

Outcomes

The following baseline characteristics were compared between the HydroCoil and control groups: sex, age, dome-to-neck ratio, rupture status, use of assist device, aneurysm shape, aneurysm location (anterior versus posterior), and baseline World Federation of Neurosurgical Societies score. For the purposes of this subgroup analysis, we studied the following individual outcomes: any recurrence, major recurrence, mRS of ≤ 2 , and retreatment. A major recurrence was defined as a recurrence sufficiently large enough to technically allow placement of further coils as defined by the core laboratory assessing the angiograms.¹² Retreatment was classified as any further treatment on the target aneurysm. mRS assessment was performed by a postal questionnaire completed by the patients or by their main caretaker and was independent of the interventional team. The above outcomes were studied at 2 sepa-

rate periods: 3–6 months postcoiling and 15–18 months postcoiling. Analyses were performed comparing the rate of these outcomes between patients randomized to the HydroCoil group and those randomized to the control group (bare platinum coils). The analyses included the following patient subgroups: 1) all patients with medium aneurysms, 2) all patients with recently ruptured aneurysms, and 3) all patients with non-recently ruptured/unruptured aneurysms. Recently ruptured aneurysms were defined as those that had ruptured within 30 days of treatment.

Statistical Analysis

All means are presented with their corresponding SDs. Comparison between groups of these categorical outcomes was performed by using the Fisher exact test. Multivariate logistic regression analyses were performed to determine whether differences between the HydroCoil and control groups existed for the following outcomes: 1) any recurrence at last follow-up, 2) major recurrence at last follow-up, 3) mRS of ≤ 2 at last follow-up, and 4) retreatment at last follow-up. Multivariate logistic regression analyses, including all patients with medium-sized aneurysms, were adjusted for neck size, rupture status, aneurysm shape, and the use of an assist device. When we performed subgroup analyses by rupture status, the above-mentioned variables were included with the exception of rupture status. Statistical analysis was performed by using JMP 10.0 Pro (www.jmp.com; SAS Institute, Cary, North Carolina).

Role of Funding Source

The sponsor/funder (MicroVention) had no part in the trial design, data collection, analysis, or reporting. These were organized by the steering committee, which was independent of the sponsor. The corresponding author had full access to all the data and had final responsibility for the decision to submit the publication.

RESULTS

Patient and Aneurysm Characteristics

A total of 288 patients with medium-sized aneurysms were randomized. There were no significant differences in any of the baseline characteristics studied between groups. Of 144 patients in the HydroCoil group, 74 (51.4%) had recently ruptured aneurysms; and of the 144 patients in the control group, 75 (52.1%) had recently ruptured aneurysms ($P = 1.00$). Sixty-six aneurysms in the HydroCoil group were treated with assist devices (46.2%) versus 63 patients in the control group (44.4%) ($P = .81$). There were no differences in the usage rate of balloon assistance ($P = .50$) or stent assistance ($P = .63$) between groups. Aneurysm shape did not differ between groups because 43 patients (29.9%) in the HydroCoil group had irregular-shaped aneurysms compared with 38 patients (26.4%) in the control group ($P = .60$). There was no difference in aneurysm location ($P = .13$). These data are summarized in Table 1.

Outcomes: All Patients with Medium-Sized Aneurysms

At 3–6 months posttreatment, 114 patients (79.2%) in the HydroCoil group and 115 patients (79.9%) in the control group had angiographic follow-up. There was a lower rate of any recurrence in the HydroCoil group compared with the control group (23 patients, 20.2%, versus 35 patients, 33.3%; $P = .03$). Major recur-

rence rates did not differ between groups, however, as 11 patients (9.6%) in the HydroCoil group had major recurrences versus 17 patients (16.2%) in the control group ($P = .16$). At 15–18 months posttreatment, 113 patients (78.5%) in the HydroCoil group and 120 patients (83.3%) in the control group had angiographic fol-

low-up. There was a similar rate of any recurrence between groups (40 patients, 35.4%, versus 55 patients, 45.8%; $P = .11$). However, the rate of major recurrence was significantly lower in the HydroCoil group than in the control group (21 patients, 18.6%, versus 37 patients, 30.8%; $P = .03$). No difference in retreatment rates or mRS of ≤ 2 was seen between groups at either time point. These data are summarized in Table 2.

Table 1: Baseline characteristics of medium-sized aneurysms

	HydroCoil	Control	P
Total patients (No.)	144	144	–
Sex			
Female	100 (69.4)	102 (70.8)	.90
Male	44 (30.6)	42 (29.2)	
Age (yr)			
45 or younger	42 (29.2)	49 (34.0)	.57
46–55	43 (29.9)	44 (30.6)	
Older than 55	59 (41.0)	51 (35.4)	
Dome-to-neck ratio			
<1.5	43 (29.9)	50 (34.7)	.45
>1.5	101 (70.1)	94 (65.3)	
Rupture status			
Recently ruptured	74 (51.4)	75 (52.1)	1.0
Unruptured/not recently ruptured	70 (48.6)	69 (47.9)	
Use of assist device ^a			
Yes	66 (46.2)	63 (44.4)	.81
No	77 (53.9)	79 (55.6)	
Balloon	39 (27.1)	33 (22.9)	.50
Stent	27 (18.8)	31 (21.5)	.66
Aneurysm shape			
Irregular (multilobulated)	43 (29.9)	38 (26.4)	.60
Not multilobulated	101 (70.1)	106 (73.6)	
Aneurysm location			
Anterior circulation	119 (82.6)	127 (88.2)	.13
Posterior circulation	25 (17.4)	17 (11.8)	
Baseline WFNS			
0	67 (46.5)	64 (44.4)	.76
I	66 (45.8)	64 (44.4)	
II	9 (6.3)	14 (9.7)	
III	2 (1.4)	2 (1.4)	

Note:—WFNS indicates World Federation of Neurosurgical Societies.

^a Data on assist device use were not available for 1 patient in the HydroCoil group and 2 patients in the control group.

Twelve patients in the medium aneurysm cohort died during follow-up (6 in the bare platinum group and 6 in the HydroCoil group). Of these, 8 died within 1 month of the procedure. Four died because of subarachnoid hemorrhage; 1 death was due to cardiac arrest and multiorgan failure; 1, due to bleeding of a treated unruptured aneurysm; and 2, from ischemic complications secondary to vasospasm or intracranial hypertension. Of the other 4 deaths, 1 was from gastric cancer, 1 was from bacterial meningitis, 1 was due to a post-SAH stroke that resulted in the patient being in a vegetative state, and 1 was from rebleed of a treated ruptured aneurysm.

Outcomes: Patients with Recently Ruptured, Medium-Sized Aneurysms

Among patients with recently ruptured aneurysms, at 3–6 months posttreatment, 56 patients in the HydroCoil group and 50 patients in the control group had angiographic follow-up. The rate of any recurrence was lower in the HydroCoil group (14 patients, 25.0%, versus 24 patients, 38.0%; $P = .02$), as was the rate of major recurrence (4 patients, 7.1%, versus 13 patients, 26.0%; $P = .02$). At 15–18 months posttreatment, 59 patients in each group had angiographic follow-up. The rate of any recurrence was significantly lower in the HydroCoil group (22 patients, 37.3%, versus 38 patients, 64.4%; $P = .006$), as was the rate of major recurrence (12 patients, 20.3%, versus 28 patients, 47.5%; $P = .003$). There was no difference in retreatment or mRS of ≤ 2 at either time point. These data are summarized in Table 3.

Table 2: Angiographic and clinical results of all patients with medium-sized aneurysms

	3–6 Months			15–18 Months		
	HydroCoil (No.) (%)	Bare Platinum (No.) (%)	P	HydroCoil (No.) (%)	Bare Platinum (No.) (%)	P
No. of patients with angiographic follow-up	114	115	–	113	120	–
No. of patients with clinical follow-up	124	119	–	128	129	–
Any recurrence	23 (20.2)	35 (33.3)	.03 ^a	40 (35.4)	55 (45.8)	.11
Major recurrence	11 (9.6)	17 (16.2)	0.16	21 (18.6)	37 (30.8)	.03 ^a
Retreatment	1 (0.9)	2 (1.7)	1.0	3 (2.7)	5 (4.2)	.72
mRS ≤ 2	107 (86.3)	106 (89.1)	.56	113 (88.3)	116 (89.9)	.69

^a Significant.

Table 3: Angiographic and clinical results of patients with recently ruptured medium-sized aneurysms

	3–6 Months			15–18 Months		
	HydroCoil (No.) (%)	Bare Platinum (No.) (%)	P	HydroCoil (No.) (%)	Bare Platinum (No.) (%)	P
No. of patients with angiographic follow-up	56	50	–	59	59	–
No. of patients clinical follow-up	63	64	–	65	65	–
Any recurrence	14 (25.0)	24 (48.0)	.02 ^a	22 (37.3)	38 (64.4)	.006 ^a
Major recurrence	4 (7.1)	13 (26.0)	.02 ^a	12 (20.3)	28 (47.5)	.003 ^a
Retreatment	0 (0.0)	0 (0.0)	1.0	0 (0.0)	2 (3.4)	.50
mRS ≤ 2	54 (85.7)	56 (87.5)	.80	56 (86.2)	59 (90.8)	.58

^a Significant.

Table 4: Angiographic and clinical results of patients with non-recently ruptured medium-sized aneurysms

	3–6 Months			15–18 Months		
	HydroCoil (No.) (%)	Bare Platinum (No.) (%)	<i>P</i>	HydroCoil (No.) (%)	Bare Platinum (No.) (%)	<i>P</i>
No. of patients with angiographic follow-up	58	55	–	54	61	–
No. of patients with clinical follow-up	61	55	–	63	64	–
Any recurrence	9 (15.5)	11 (20.0)	.62	18 (33.3)	17 (27.9)	.55
Major recurrence	7 (12.1)	4 (7.3)	.53	9 (16.7)	9 (14.8)	.80
Retreatment	1 (1.7)	2 (3.6)	.61	3 (5.6)	3 (4.9)	1.0
mRS ≤ 2	53 (86.9)	50 (90.9)	.57	57 (90.5)	57 (89.1)	1.0

Table 5: Multivariate logistic regression analysis^a

	All Patients (OR) (95% CI) ^b	<i>P</i>	Recently Ruptured (OR) (95% CI) ^c	<i>P</i>	Non-Recently Ruptured (OR) (95% CI) ^c	<i>P</i>
Any recurrence	0.72 (0.43–1.20)	.21	0.37 (0.18–0.76)	.006	1.58 (0.73–3.47)	.25
Major recurrence	0.54 (0.30–0.98)	.04	0.27 (0.12–0.58)	.0007	1.55 (0.58–4.29)	.38
mRS ≤ 2	1.08 (0.51–2.32)	.83	0.96 (0.35–2.68)	.94	1.23 (0.38–4.06)	.73
Retreatment	0.51 (0.07–2.78)	.44	0.00 (0.00–2.01)	.12	0.97 (0.11–8.81)	.98

^a Odds of HydroCoil versus the control group.

^b Adjusted for neck size, use of adjunctive device, aneurysm shape, and rupture status.

^c Adjusted for neck size, use of adjunctive device, and aneurysm shape.

Outcomes: Patients with Non-Recently Ruptured Aneurysms

Fifty-eight patients in the HydroCoil group and 55 patients in the control group had angiographic follow-up at 3–6 months. The rate of any recurrence was similar between groups as 15.5% of patients treated with HydroCoil (9 patients) and 20.0% of controls (11 patients) had a recurrence ($P = .62$). The same was true for major recurrences (7 patients, 12.1%, versus 4 patients, 7.3%, respectively; $P = .53$). At 15–18 months, 54 patients treated with HydroCoils and 61 control patients had follow-up angiograms. The recurrence rate was 33.3% for patients treated with HydroCoils (18 patients) and 27.9% for controls (17 patients) ($P = .55$). No difference in major recurrence rates was seen between groups (16.7%, 9 patients, versus 14.8%, 9 patients, respectively; $P = .80$). These data are summarized in Table 4.

Multivariate Analysis

On multivariate logistic regression analysis, when considering the aneurysms of all patients (unruptured/non-recently ruptured and recently ruptured), HydroCoil was associated with lower odds of major recurrence (OR = 0.54; 95% CI, 0.30–0.98; $P = .04$). For patients with recently ruptured aneurysms, HydroCoil was associated with lower odds of any recurrence (OR = 0.37; 95% CI, 0.18–0.76; $P = .006$) and major recurrence (OR = 0.27; 95% CI, 0.12–0.58; $P = .0007$). There was a trend toward lower retreatment rates in the recently ruptured group treated with HydroCoils (OR = 0.00; 95% CI, 0.00–2.01; $P = .12$). No difference in recurrence rates was seen between coil types in the non-recently ruptured/unruptured group. There were no differences in mRS of ≤2 between groups. These data are summarized in Table 5.

DISCUSSION

This subgroup analysis of patients in the HELPS trial found that HydroCoil is associated with statistically significant and clinically relevant lower rates of recurrence compared with bare platinum, specifically for major recurrence, among patients with medium-sized, recently ruptured aneurysms. In addition, multivariate

analysis found lower rates of major recurrence with the HydroCoil group for all aneurysms, even when adjusting for rupture status. Subgroup analyses of patients with non-recently ruptured/unruptured aneurysms found no difference in recurrence rates between the HydroCoil and control groups. Overall, these data strongly suggest that hydrogel coils, such as the HydroCoil, are superior to bare platinum coils in the treatment of ruptured medium-sized aneurysms. These findings could have substantial therapeutic implications if validated in future trials because medium-sized aneurysms accounted for nearly half of the patients with ruptured aneurysms treated in the International Subarachnoid Aneurysm Trial.¹³ This was not a prespecified subgroup analysis; thus, these results should not serve to alter clinical practice at this time and need to be validated in future studies.

There are a few potential explanations for the association of HydroCoils with superior occlusion rates compared with bare platinum coils, specifically in ruptured aneurysms. The biology of ruptured aneurysms differs substantially from that of unruptured aneurysms. Ruptured aneurysms are, by definition, unstable and more prone to growth and recurrence than unruptured aneurysms.¹⁰ Hydrogel coils are designed with an expansile hydrogel that fills more of the aneurysm lumen than standard platinum coils. HydroCoils provide substantially improved volumetric packing of the aneurysm lumen compared with standard bare platinum coils.^{4,14} By expanding to fill the aneurysm lumen, these coils may be more effective at sealing the aneurysm rupture point, a point of growth within the aneurysm. Furthermore, in an in vitro study, Watanabe et al¹⁵ found that HydroCoils were more effective than bare platinum coils in stopping outflow from the rupture point of experimental aneurysms. These coils may also be more effective at sealing the aneurysm neck as supported by histologic studies in both rabbits and humans.^{16,17} In a study comparing the efficacy of HydroCoil, HydroSoft (MicroVention), platinum, and Cerecyte coils (Codman Neurovascular, Raynham, Massachusetts) in angiographic and histologic occlusion of aneurysms in a rabbit model, Killer et al¹⁸ found that hydrogel devices (ie, HydroCoil and HydroSoft) had significantly

higher rates of histologic and angiographic occlusion, which increased with time. Increased healing was seen at both the aneurysm neck and dome.

A number of previously published studies have compared the efficacy of bare platinum and modified coils. In a meta-analysis of 82 studies, Rezek et al¹⁹ compared the efficacy of bare platinum coils with Matrix (Stryker, Kalamazoo, Michigan), HydroCoil, and Cerecyte coils. They found no difference in the rate of unfavorable angiographic outcomes among groups. This study was limited in that they did not perform subgroup analyses by aneurysm size and rupture status. Furthermore, a vast majority of the included studies were noncontrolled case series, thus limiting the level of evidence of these findings. Several single-center studies have demonstrated that HydroCoils are associated with decreased recurrence rates compared with bare platinum coils; however, none were randomized, controlled trials, and many were too small for subgroup analyses to define which patients may benefit the most from HydroCoil treatment.^{20,21} A number of single-arm studies have demonstrated high aneurysm-occlusion rates with HydroCoils.^{22–24} The largest of these, the HydroCoil for Endovascular Aneurysm Occlusion study, found high rates of initial and long-term occlusion in a series of 191 aneurysms treated with HydroCoils.²⁵ The authors found relatively low rates of minor and major recurrences among aneurysms of <10 mm, similar to the findings of our study.²⁶ Our subgroup analysis of patients in HELPS is the largest comparative analysis to date examining clinical and angiographic results of medium-sized aneurysms, to our knowledge.

Limitations

Our study has limitations. Subgroup analyses can be misleading for a number of reasons.²⁷ For example, if the overall result of a trial is significant, then on the basis of chance, some subgroups will have a positive result and some will have a negative result. Also, if the overall result of a study is negative, on the basis of chance alone, some subgroups may have a larger treatment effect. Subgroup analyses should be based on hypotheses that make sense biologically.²⁷ On the basis of prior preclinical studies, we thought that it was biologically plausible that HydroCoils would be more effective in the treatment of ruptured aneurysms. Ultimately, subgroup analyses are most helpful when they are prespecified in the trial design. Ours was not a prespecified subgroup analysis for the HELPS trial; therefore, these data should not necessarily alter clinical practice but rather serve as a guide for the design of future trials comparing second-generation coils with bare platinum coils. Another major flaw in subgroup analyses in general is overemphasis of *P* values rather than the treatment effect. Therefore, readers should examine the results of subgroup analyses closely to determine whether the differences between groups are clinically meaningful.²⁸

No follow-up data on aneurysm recurrence and retreatment were available beyond 18 months. Given the significantly higher rate of major recurrence in the control group with medium-sized ruptured aneurysms, it is conceivable that more of these patients would go on to retreatment during the long-term follow-up. The combination of low power and lack of consistent follow-up beyond 18 months likely contributes to the lack of statistical signif-

icance in the aneurysm retreatment rates between groups, despite the higher rates of major recurrence in the control group. Not all patients received angiographic and clinical follow-up. Of the 288 initially randomized patients with medium-sized aneurysms, only 229 had angiographic follow-up at 3–6 months and 233 had angiographic follow-up at 15–18 months. Last, we did not study differences in packing attenuation between groups. Baseline factors, such as hypertension, which may be associated with aneurysm recurrence, were not assessed in our analysis. In addition, we did not study the types of recurrence (recurrence due to recanalization, regrowth, coil compaction, or coil migration through the aneurysm wall).

The aneurysm recanalization rate in our study was much higher than that reported in other clinical studies and meta-analyses studying postcoiling recanalization rates.⁹ The most likely reason is that we used a core laboratory in the assessment of unfavorable outcome, whereas in most clinical studies, clinical and angiographic outcomes are not assessed by an independent core laboratory. For example, in the Cerecyte Coil Trial, unfavorable angiographic outcomes were noted twice as frequently by the independent core laboratory compared with the operators that performed the procedure.²⁹ In addition, in a meta-analysis of >15,000 treated aneurysms in 104 studies, Rezek et al³⁰ found that core laboratory studies reported statistically significant and clinically meaningful higher rates of unfavorable outcomes than self-reported studies.

CONCLUSIONS

Our subgroup analysis of patients with medium-sized aneurysms in the HELPS trial found that treatment with HydroCoils resulted in significantly lower rates of major recanalization in this population. The benefits of HydroCoils were most marked in the medium-sized, recently ruptured population. Because this was not a prespecified subgroup analysis, these results should not serve to alter clinical practice but, rather, provide insight into the design of future clinical trials comparing bare platinum with second-generation coils.

Disclosures: Waleed Brinjikji—UNRELATED: Grants/Grants Pending: Brain Aneurysm Foundation.* Philip M. White—RELATED: Grant: MicroVention.* Comments: HELPS trial was funded by MicroVention; Consulting Fee or Honorarium: Codman, MicroVention, Comments: for educational Stroke and Institute for Natural Resources meetings organized by me but funded by industry support; Support for Travel to Meetings for the Study or Other Purposes: MicroVention, Comments: standard class airfare only. Hans Nahser—RELATED: Support for Travel to Meetings for the Study or Other Purposes: Lothian National Health Service, Comments: mainly for being present at the steering committee meetings; Travel/Accommodations/Meeting Expenses Unrelated to Activities Listed: Stryker Target, ev3, Covidien, Codman, NeuroLogic, Comments: infrequently, by various companies. Joanna Wardlaw—RELATED: Grant: MicroVention.* Comments: funded the HELPS trial; UNRELATED: Consultancy: ReNeuron.* Comments: expenses for work on Data Monitoring Committee of PISCES (Pilot Investigation of Stem Cells in Stroke) and PISCES 2 trials. Harry J. Cloft—UNRELATED: Grants/Grants Pending: Cordis Endovascular.* Comments: Site Principal Investigator at enrolling site for Stenting and Angioplasty with Protection in Patients and High Risk for Endarterectomy registry sponsored by Cordis Endovascular. David F. Kallmes—UNRELATED: Board Membership: GE Healthcare, Comments: Cost-Effectiveness Board; Consultancy: ev3,* Medtronic.* Comments: planning and implementing clinical trials; Grants/Grants Pending: MicroVention,* SurModics,* Sequent,* NeuroSigma,* ev3,* Codman.* Comments: preclinical research and clinical trials; Royalties: University of Virginia Patent Foundation, Comments: Spine Fusion. *Money paid to the institution.

REFERENCES

1. Crobeddu E, Lanzino G, Kallmes DF, et al. **Review of 2 decades of aneurysm-recurrence literature. Part 2. Managing recurrence after endovascular coiling.** *AJNR Am J Neuroradiol* 2013;34:481–85
2. Ringer AJ, Rodriguez-Mercado R, Veznedaroglu E, et al. **Defining the risk of retreatment for aneurysm recurrence or residual after initial treatment by endovascular coiling: a multicenter study.** *Neurosurgery* 2009;65:311–15; discussion 315
3. Kallmes DF, Fujiwara NH. **New expandable hydrogel-platinum coil hybrid device for aneurysm embolization.** *AJNR Am J Neuroradiol* 2002;23:1580–88
4. Cloft HJ, Kallmes DF. **Aneurysm packing with HydroCoil embolic system versus platinum coils: initial clinical experience.** *AJNR Am J Neuroradiol* 2004;25:60–62
5. White PM, Lewis SC, Gholkar A, et al. **Hydrogel-coated coils versus bare platinum coils for the endovascular treatment of intracranial aneurysms (HELPS): a randomised controlled trial.** *Lancet* 2011; 377:1655–62
6. Brinjikji W, Kallmes DF. **Back to the tower of Babel: comparing outcomes from aneurysm trials.** *AJNR Am J Neuroradiol* 2012;33: 995–98
7. Brinjikji W, Lanzino G, Cloft HJ, et al. **Endovascular treatment of very small (3 mm or smaller) intracranial aneurysms: report of a consecutive series and a meta-analysis.** *Stroke* 2010;41:116–21
8. Chalouhi N, Tjoumakaris S, Gonzalez LF, et al. **Coiling of large and giant aneurysms: complications and long-term results of 334 cases.** *AJNR Am J Neuroradiol* 2014;35:546–52
9. Ferns SP, Sprengers ME, van Rooij WJ, et al. **Coiling of intracranial aneurysms: a systematic review on initial occlusion and reopening and retreatment rates.** *Stroke* 2009;40:e523–29
10. Crobeddu E, Lanzino G, Kallmes DF, et al. **Review of 2 decades of aneurysm-recurrence literature. Part 1. Reducing recurrence after endovascular coiling.** *AJNR Am J Neuroradiol* 2013;34:266–70
11. White PM, Lewis SC, Nahser H, et al. **HydroCoil Endovascular Aneurysm Occlusion and Packing Study (HELPS trial): procedural safety and operator-assessed efficacy results.** *AJNR Am J Neuroradiol* 2008;29:217–23
12. Raymond J, Guilbert F, Weill A, et al. **Long-term angiographic recurrences after selective endovascular treatment of aneurysms with detachable coils.** *Stroke* 2003;34:1398–403
13. Molyneux AJ, Kerr RS, Yu LM, et al. **International subarachnoid aneurysm trial (ISAT) of neurosurgical clipping versus endovascular coiling in 2143 patients with ruptured intracranial aneurysms: a randomised comparison of effects on survival, dependency, seizures, rebleeding, subgroups, and aneurysm occlusion.** *Lancet* 2005;366:809–17
14. Gaba RC, Ansari SA, Roy SS, et al. **Embolization of intracranial aneurysms with hydrogel-coated coils versus inert platinum coils: effects on packing density, coil length and quantity, procedure performance, cost, length of hospital stay, and durability of therapy.** *Stroke* 2006;37:1443–50
15. Watanabe K, Sugiu K, Tokunaga K, et al. **Packing efficacy of HydroCoil embolic system: in vitro study using ruptured aneurysm model.** *Neurosurg Rev* 2007;30:127–30; discussion 130
16. Killer M, Arthur AS, Barr JD, et al. **Histomorphology of thrombus organization, neointima formation, and foreign body response in retrieved human aneurysms treated with HydroCoil devices.** *J Biomed Mater Res B Appl Biomater* 2010;94:486–92
17. Ding YH, Dai D, Lewis DA, et al. **Angiographic and histologic analysis of experimental aneurysms embolized with platinum coils, Matrix, and HydroCoil.** *AJNR Am J Neuroradiol* 2005;26:1757–63
18. Killer M, Hauser T, Wenger A, et al. **Comparison of experimental aneurysms embolized with second-generation embolic devices and platinum coils.** *Acta Neurochir (Wien)* 2009;151:497–505; discussion 505
19. Rezek I, Mousan G, Wang Z, et al. **Coil type does not affect angiographic follow-up outcomes of cerebral aneurysm coiling: a systematic review and meta-analysis.** *AJNR Am J Neuroradiol* 2013; 34:1769–73
20. Wei D, Wei C, Huang S, et al. **Comparison between effects of HydroCoil embolic system and ordinary coil on large- and medium-sized intracranial aneurysms.** *Pak J Med Sci* 2013;29:1334–37
21. Lee JY, Seo JH, Lee SJ, et al. **Mid-term outcome of intracranial aneurysms treated with HydroSoft coils compared to historical controls treated with bare platinum coils: a single-center experience.** *Acta Neurochir (Wien)* 2014;156:1687–94
22. Arthur AS, Wilson SA, Dixit S, et al. **Hydrogel-coated coils for the treatment of cerebral aneurysms: preliminary results.** *Neurosurg Focus* 2005;18:E1
23. Berenstein A, Song JK, Niimi Y, et al. **Treatment of cerebral aneurysms with hydrogel-coated platinum coils (HydroCoil): early single-center experience.** *AJNR Am J Neuroradiol* 2006;27:1834–40
24. Fanning NF, Berentei Z, Brennan PR, et al. **HydroCoil as an adjuvant to bare platinum coil treatment of 100 cerebral aneurysms.** *Neuroradiology* 2007;49:139–48
25. Cloft HJ. **HydroCoil for Endovascular Aneurysm Occlusion (HEAL) study: periprocedural results.** *AJNR Am J Neuroradiol* 2006;27:289–92
26. Cloft HJ. **HydroCoil for Endovascular Aneurysm Occlusion (HEAL) study: 3–6 month angiographic follow-up results.** *AJNR Am J Neuroradiol* 2007;28:152–54
27. Assmann SF, Pocock SJ, Enos LE, et al. **Subgroup analysis and other (mis)uses of baseline data in clinical trials.** *Lancet* 2000;355: 1064–69
28. Motulsky HJ. **Common misconceptions about data analysis and statistics.** *J Pharmacol Exp Ther* 2014;351:200–05
29. Rezek I, Lingineni RK, Sneade M, et al. **Differences in the angiographic evaluation of coiled cerebral aneurysms between a core laboratory reader and operators: results of the Cerecyte Coil Trial.** *AJNR Am J Neuroradiol* 2014;35:124–27
30. Rezek I, Mousan G, Wang Z, et al. **Effect of core laboratory and multiple-reader interpretation of angiographic images on follow-up outcomes of coiled cerebral aneurysms: a systematic review and meta-analysis.** *AJNR Am J Neuroradiol* 2013;34:1380–84

Evaluation of 4D Vascular Flow and Tissue Perfusion in Cerebral Arteriovenous Malformations: Influence of Spetzler-Martin Grade, Clinical Presentation, and AVM Risk Factors

C. Wu, S.A. Ansari, A.R. Honarmand, P. Vakil, M.C. Hurley, B.R. Bendok, J. Carr, T.J. Carroll, and M. Markl



ABSTRACT

BACKGROUND AND PURPOSE: The role of intracranial hemodynamics in the pathophysiology and risk stratification of brain AVMs remains poorly understood. The purpose of this study was to assess the influence of Spetzler-Martin grade, clinical history, and risk factors on vascular flow and tissue perfusion in cerebral AVMs.

MATERIALS AND METHODS: 4D flow and perfusion MR imaging was performed in 17 patients with AVMs. Peak velocity and blood flow were quantified in AVM feeding and contralateral arteries, draining veins, and the straight sinus. Regional perfusion ratios (CBF, CBV, and MTT) were calculated between affected and nonaffected hemispheres.

RESULTS: Regarding flow parameters, high-grade AVMs (Spetzler-Martin grade of >2) demonstrated significantly increased peak velocity and blood flow in the major feeding arteries ($P < .001$ and $P = .004$) and straight sinus ($P = .003$ and $P = .012$) and increased venous draining flow ($P = .001$). The Spetzler-Martin grade significantly correlated with cumulative feeding artery flow ($r = 0.85$, $P < .001$) and draining vein flow ($r = 0.80$, $P < .001$). Regarding perfusion parameters, perinidal CBF and CBV ratios were significantly lower ($P < .001$) compared with the remote ratios and correlated negatively with cumulative feeding artery flow ($r = -0.60$, $P = .014$ and $r = -0.55$, $P = .026$) and draining vein flow ($r = -0.60$, $P = .013$ and $r = -0.56$, $P = .025$). Multiple regression analysis revealed no significant association of AVM flow or perfusion parameters with clinical presentation (rupture and seizure history) and AVM risk factors.

CONCLUSIONS: Macrovascular flow was significantly associated with increasing Spetzler-Martin grade and correlated with perinidal microvascular perfusion in cerebral AVMs. Future longitudinal studies are needed to evaluate the potential of comprehensive cerebral flow and perfusion MR imaging for AVM risk stratification.

ABBREVIATIONS: c = contralateral hemisphere; H = hemisphere excluding the nidus; i = ipsilateral hemisphere; P = perinidal; PCA = posterior cerebral artery; R = remote area; SMG = Spetzler-Martin grade

Cerebral arteriovenous malformations are associated with an increased risk of intracranial hemorrhage, accounting for 2%–4% of all hemorrhagic strokes annually.¹ Previous studies have demonstrated the potential risk of hemorrhage following

AVM embolization, presumably due to acute alterations in AVM or cerebral hemodynamics.² However, the Spetzler-Martin grade (SMG), widely used for surgical risk stratification in cerebral AVMs, does not provide insight into local or global hemodynamics.³ Quantitative assessment of AVM feeding and draining flow, combined with whole-brain tissue perfusion, can potentially characterize both AVM macro- and microvascular pathophysiology. In addition, the relationships between quantitative AVM hemodynamic parameters and the SMG or clinical history (rupture/seizures) and other risk factors (eg, presence of flow-induced aneurysms or venous stenosis, deep AVM location, and single or deep venous drainage) remain unclear.

In this study, a comprehensive MR imaging and analysis protocol based on 4D flow and DSC perfusion MR imaging was applied for the characterization of 3D AVM macrovascular flow and microvascular brain tissue perfusion. 4D flow MR imaging can measure the 3-directional velocity field with full volumetric coverage of the vessels of interest.^{4,5} Previous studies have shown that

Received August 5, 2014; accepted after revision December 11.

From the Department of Biomedical Engineering (C.W., T.J.C., M.M.), McCormick School of Engineering, Northwestern University, Evanston, Illinois; and Departments of Radiology (C.W., S.A.A., A.R.H., P.V., M.C.H., B.R.B., J.C., T.J.C., M.M.), Neurological Surgery (S.A.A., M.C.H., B.R.B.), Neurology (S.A.A.), and Otolaryngology (B.R.B.), Feinberg School of Medicine, Northwestern University, Chicago, Illinois.

This work was supported by an American Heart Association Predoctoral Fellowship 14PRE18370014, National Institutes of Health—T32-EB005170, National Institutes of Health—R01-HL088437, and Radiological Society of North America Research Seed Grant/Toshiba America Systems RSD1207.

Please address correspondence to Can Wu, MS, Department of Biomedical Engineering and Radiology, Northwestern University, 737 N Michigan Ave, Suite 1600, Chicago, IL 60611; e-mail: canwu2016@u.northwestern.edu

Indicates open access to non-subscribers at www.ajnr.org

Indicates article with supplemental on-line videos.

<http://dx.doi.org/10.3174/ajnr.A4259>

Demographics and AVM features of the 17 patients with AVMs included in the study

AVM (No.)	Age (yr)	Sex	Nidal Size (cm ³)	Drainage	Eloquence	SMG (1–5)	Major Feeding Arteries
1	43	M	5.6 × 4.1 × 5.1	D+S	N	3	LMCA, LACA, RACA
2	29	M	4.0 × 3.5 × 3.4	D+S	N	3	RPcomA, RPCA
3	43	M	2.7 × 3.1 × 3.1	D+S	Y	3	RPcomA, RPCA
4	21	F	4.0 × 3.4 × 3.8	D+S	Y	4	LMCA, LPCA, LMMA
5	22	M	2.5 × 2.3 × 2.4	D+S	N	2	RMCA
6	68	F	4.0 × 3.0 × 2.5	D+S	Y	4	LACA, RACA, RMCA
7 ^a	34	M	3.3 × 2.3 × 2.5	S	N	1	RACA
8	40	F	3.0 × 2.0 × 4.0	D+S	N	2	LMCA, LPCA
9	25	F	2.3 × 2.3 × 1.7	D+S	N	2	RMCA
10	52	F	2.4 × 2.1 × 2.6	S	N	1	LPICA
11 ^a	16	F	2.3 × 2.8 × 2.8	S	Y	2	LACA, LMCA
12	55	M	2.1 × 3.6 × 2.6	S	N	2	LMCA, LPCA
13	49	M	1.9 × 2.4 × 2.4	S	N	1	RMCA
14	41	F	6.6 × 3.7 × 5.2	D+S	Y	4	LMCA, LPCA, LACA
15	29	M	5.4 × 3.7 × 5.5	D+S	Y	4	RMCA, RPCA
16 ^a	36	M	3.6 × 3.4 × 3.2	S	N	2	RACA, RMCA
17	66	M	2.6 × 2.3 × 1.7	D+S	Y	3	LMCA, LPCA

Note:—D indicates deep; S, superficial; L, left; R, right; Y, yes; N, no; LPICA, left posterior inferior cerebellar artery; LACA, left anterior cerebral artery; RACA, right anterior cerebral artery; RPcomA, right posterior communicating artery; LMMA, left middle meningeal artery.

^a Contralateral arteries not visible in the 4D flow data.

4D flow MR imaging is highly promising in the evaluation of intracranial hemodynamics in cerebral AVMs.^{6–8} To gain additional information on the impact of AVMs on cerebral tissue perfusion, we used DSC PWI based on a fast spin-echo EPI acquisition during the first pass of contrast agent through the brain vasculature to quantify microvascular perfusion biomarkers.^{9,10} The AVM nidus has relatively low resistance and thus often causes high-flow transnidus shunts, which may result in hypoperfusion in the cerebral parenchyma immediately adjacent to AVMs. However, this so-called “steal effect” with diversion of blood from the adjacent tissue to the AVM nidus is still controversial, and it is unclear whether it should be considered a mechanism for the clinical presentation of cerebral AVMs.¹¹

The purpose of this study was to quantitatively evaluate macrovascular flow in AVM arterial and venous networks and microvascular perfusion of the peripheral cerebral parenchyma. We investigated relationships between these quantitative hemodynamic parameters and SMG classification followed by correlation with various AVM symptomatic and anatomic risk factors.

MATERIALS AND METHODS

Patient Population

We studied 17 patients with pretreatment AVMs (7 women; mean age, 39 ± 15 years) who were identified by institutional neurologists/neurosurgeons and referred for MR imaging between May 2011 and March 2013. Demographics and clinical characteristics of the patients with AVMs are summarized in the Table. The SMG of all AVMs was evaluated on the basis of conventional DSA by experienced neuroradiologists, and ranged from 1 to 4 (1, *n* = 3; 2, *n* = 6; 3, *n* = 4; 4, *n* = 4). Quantitative analysis of macrovascular flow parameters (peak velocities and mean flow) and microvascular perfusion was performed in all patients with AVMs and was correlated with respect to SMG classification, clinical presentation (history of hemorrhagic events, seizures), and other AVM risk factors (deep AVM location, presence of flow-induced aneurysms or venous stenosis, and single or deep venous drainage). The study was approved by the local institutional review board

and was conducted in accordance with Health Insurance Portability and Accountability Act guidelines.

MR Imaging

All MR imaging measurements were performed on 1.5T (Magnetom Avanto) and 3T (Magnetom Trio) MR imaging scanners (Siemens, Erlangen, Germany) equipped with standard 12-channel head coils. A single dose (4 mL/s, 0.1 mmol/kg bodyweight) of Gd-DTPA contrast agent (Magnevist; Bayer HealthCare Pharmaceuticals, Wayne, New Jersey) was administered before DSC PWI (spin-echo EPI), followed by a 15-mL saline flush at a rate of 4 mL/s. Imaging parameters for DSC PWI were as follows: TR/TE = 1100/34 ms, FOV = 220 × 220 mm², spatial resolution = 1.7 × 1.7 × 5.0 mm³, acquisition time = 2 minutes and 30 seconds. 4D flow imaging with 3D volumetric coverage of the AVM vasculature was applied, and data were acquired with prospective electrocardiogram synchronization. Typical sequence parameters for 4D flow MR imaging were the following: TR/TE = 5.2/2.8 ms, flip angle = 15°, velocity sensitivity = 100 cm/s, FOV = 220 × 160 mm², temporal resolution = 42 ms, spatial resolution = 1.1 × 1.1 × 1.5 mm³, acquisition time = 15–20 minutes depending on the heart rate of the patient during the scan.

4D Flow Data Preprocessing and 3D Blood Flow Visualization

4D flow data were preprocessed by using a customized software programmed in Matlab (MathWorks, Natick, Massachusetts) to filter out background noise and correct for Maxwell terms, eddy current phase offset errors, and velocity aliasing.¹² In addition, a 3D phase-contrast MR angiogram was created on the basis of the magnitude and phase difference images. Finally, the preprocessed data were imported into software for 3D blood flow visualization and quantification (EnSight; CEI, Apex, North Carolina). 3D vascular visualization was based on time-resolved 3D pathlines that depict the temporal evolution of blood flow over the cardiac cycle (On-line Videos). Pathlines were emitted from the entire intracranial vasculature provided by the 3D phase-contrast MR angio-

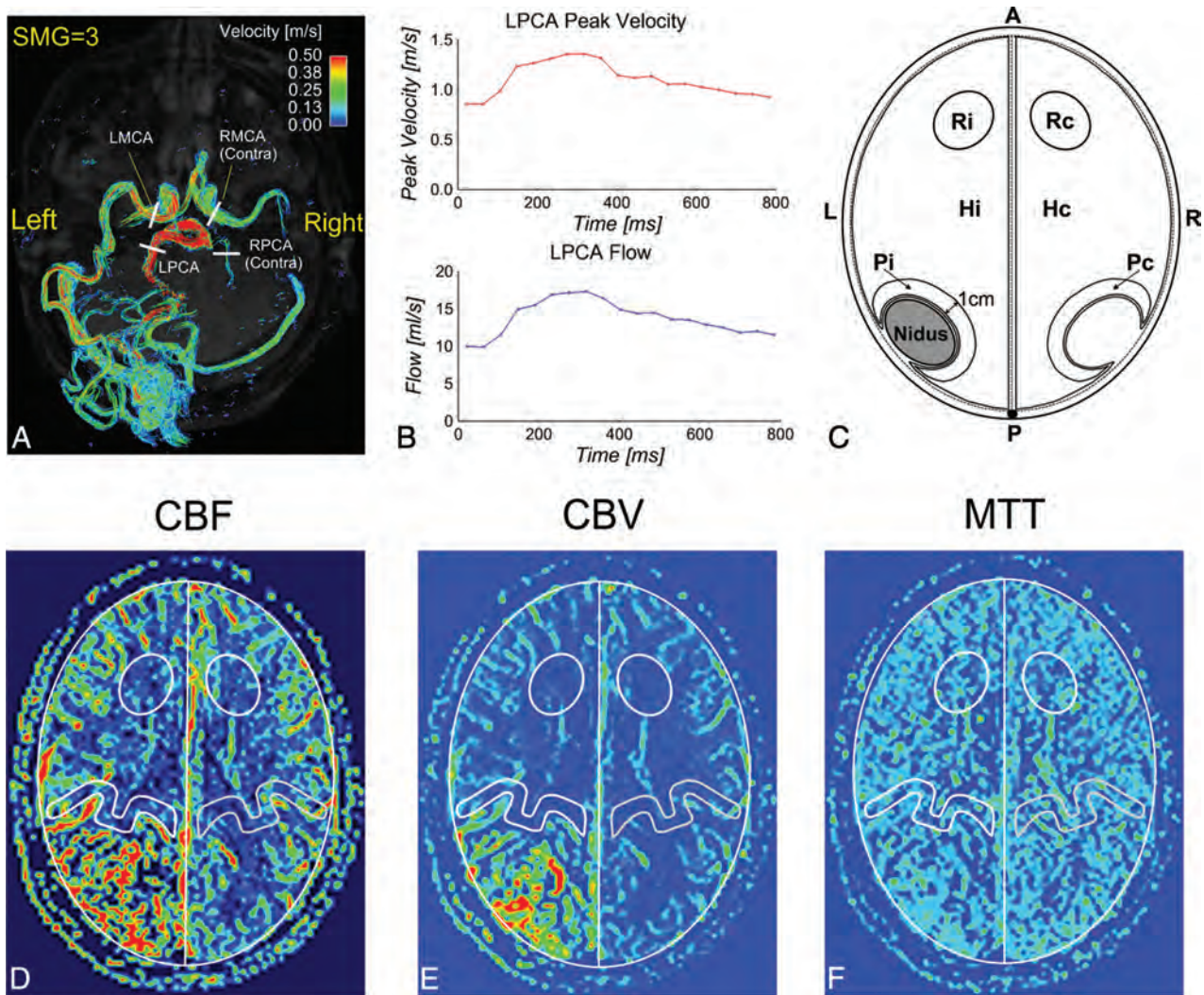


FIG 1. 3D blood flow visualization in a left medial occipital AVM (AVM-17) with time-integrated pathlines (A) and quantification of the peak velocity and blood flow in the major feeding arteries (B, example for LPCA) and a perfusion model (C), including 3 pairs of ROIs (Pi/Pc, Hi/Hc, and Ri/Rc) used for perfusion analysis in CBF (D), CBV (E), and MTT (F) images (example for AVM-4). LMCA indicates left MCA; LPCA, left PCA; RMCA, right MCA; RPCA, right PCA; Contra, contralateral artery; Pc, Hc, and Rc, corresponding ROIs in the contralateral hemisphere.

gram data (total virtual particles = 25,000). The color-coding of the time-integrated traces reflects the velocities of blood traveling along the pathlines during 1 cardiac cycle and illustrates the range and magnitude of blood flow velocities within the cardiac cycle (Fig 1A).

Flow Quantification

For each AVM, 2D analysis planes were manually positioned perpendicularly in all identified feeding and contralateral arteries, draining veins, and the straight sinus by the same observer. The planes were placed consistently across all patients with AVMs (ie, M1 for MCA and P2 for posterior cerebral artery [PCA]) (Fig 1A, example for AVM-17). For each analysis plane, peak velocity (meter/second) and time-averaged blood flow (milliliter/second) over the cardiac cycle were quantified (Fig 1B, for the left PCA).

Tissue Perfusion Quantification

Perfusion maps (CBF, CBV, and MTT) were calculated on-line by using a method described previously, including automatic deter-

mination of the arterial input function and deconvolution with the concentration–time curve based on singular value decomposition.^{9,13} Similar to the model proposed by Guo et al,¹⁴ 3 pairs of ROIs at the ipsilateral (i) and contralateral (c) hemispheres were defined as follows (Fig 1C): perinidal (P) area for the detection of potential AVM steal (Pi/Pc), hemisphere (H) excluding the nidus for global perfusion evaluation (Hi/Hc), and remote area (R) as an internal control (Ri/Rc). The ROIs were manually delineated by 2 independent observers on a selected CBF map including the largest AVM nidal dimension. ROIs were drawn ipsilateral to the AVM nidus without inclusion of visible vascular territories, and paired contralateral ROIs were automatically created (Fig 1D–F, example for AVM-4). Perinidal ROIs were defined consistently for all patients (ie, 1-cm perimeter adjacent to the nidus). The mean values of the ipsilateral-to-contralateral perfusion ratios from the 2 observations were used for subsequent perfusion analysis. ROI selection and calculation of the perfusion parameters were implemented by using an in-house program in Matlab.

Statistical Analysis

Flow parameters were compared between AVM feeding and contralateral arteries (2-tailed paired *t* test). Flow parameters in the major feeding arteries, draining veins, and straight sinus were compared between the low-grade (SMG-A: SMG = 1 and 2) and high-grade (SMG-B: SMG = 3 and 4) AVM groups (2-tailed *t* test). The intraclass correlation coefficient (0.00–0.20, poor; 0.21–0.40, fair; 0.41–0.60, moderate; 0.61–0.80, good; and 0.81–1.00, excellent) was used to evaluate the interobserver agreement for perfusion measurements, and perfusion ratios were compared in the 3 ROIs (2-tailed paired *t* test). In addition, correlation analysis was performed between the SMG and AVM hemodynamics (Spearman correlation), between the AVM nidal volume calculated by $V = \pi/6 \times a \times b \times c$ (*a*, *b*, *c* are 3D nidal diameters measured by experienced neuroradiologists on the basis of conventional DSA)¹⁵ and AVM hemodynamics (Pearson correlation), and between AVM flow parameters and perfusion ratios (Pearson correlation). Multiple regression analysis (stepwise) was performed to identify the potential association of AVM flow or perfusion parameters with clinical presentation and risk factors. All statistical analyses were performed by using the software package SPSS (IBM, Armonk, New York). $P < .05$ was considered statistically significant.

RESULTS

4D flow and perfusion MR imaging were successfully acquired in all except for 1 patient (AVM-3) whose perfusion acquisition failed due to a technical error (no injection of contrast agent). Patient demographics including SMG and 33 identified feeding arteries are summarized in the Table. Patients with high-grade AVMs (SMG-B, $n = 8$) had more feeding arteries (at least 2) compared with patients with low-grade AVMs (SMG-A, $n = 9$). Of the 17 patients in this study, 7 had seizure history; 3, a previous intracranial hemorrhage; 8, a deep nidal location; 12, a flow-induced aneurysm; 3, a draining venous stenosis; 5, a single draining vein; and 11, a deep venous drainage. Note that 3 patients (AVM-3, AVM-5, and AVM-7) presented with overt hemorrhage, but they were clinically stable during the scans.

Visualization of AVM Flow and Perfusion

Figure 2 shows the 3D phase-contrast MR angiogram (top row) and 3D blood flow visualization (middle row) for 4 representative AVMs with varying SMGs ranging from 1 to 4. Arterial feeding (solid white arrows) and venous draining (open white arrows) patterns of all AVMs can be clearly appreciated. Perfusion images (Fig 2, bottom row) illustrate corresponding microvascular CBF in the brain capillary bed.

Quantitative Arterial and Venous Flow

Twenty AVM feeding and corresponding contralateral artery pairs could be identified. Both peak velocities (1.21 ± 0.39 m/s versus 0.62 ± 0.23 m/s, $P < .001$) and blood flow (9.06 ± 3.05 mL/s versus 2.99 ± 1.59 mL/s, $P < .001$) in the AVM feeding arteries were significantly higher compared with the contralateral arteries (Fig 3A, -E). Additionally, major feeding artery peak velocities (Fig 3B) and blood flow (Fig 3F) for the SMG-B group were significantly increased compared with the SMG-A group

(1.57 ± 0.33 m/s versus 0.89 ± 0.26 m/s, $P < .001$, and 12.31 ± 2.60 mL/s versus 7.68 ± 2.99 mL/s, $P = .004$), indicating elevated feeding artery flow in high-grade AVMs. For draining veins, the high-grade AVM group demonstrated significantly higher blood flow (17.54 ± 8.47 mL/s versus 5.24 ± 1.57 mL/s, $P = .001$, Fig 3G). Differences in peak velocities (0.67 ± 0.27 m/s versus 0.30 ± 0.07 m/s, $P = .003$) and blood flow (6.34 ± 4.87 mL/s versus 1.71 ± 0.37 mL/s, $P = .012$) were also found in the straight sinus (Fig 3D, -H).

Microvascular Perfusion Ratios

Interobserver agreement for the perfusion measurement was good to excellent (CBF: intraclass correlation coefficient = 0.78; CBV: intraclass correlation coefficient = 0.86; MTT: intraclass correlation coefficient = 0.76). A significantly lower perinidal CBF ratio was identified compared with the remote ratio (0.85 ± 0.12 versus 0.99 ± 0.07 , $P < .001$) in agreement with the lower perinidal CBV ratio compared with the remote ratio (0.83 ± 0.13 versus 1.00 ± 0.08 , $P < .001$), indicating the presence of perinidal hypoperfusion (AVM steal) (Fig 4A). However, perinidal and remote MTT ratios were not significantly different (0.98 ± 0.09 versus 1.03 ± 0.10 , $P = .110$). In addition, no significant difference was observed between remote and hemispheric perfusion ratios (CBF: $P = .231$, CBV: $P = .481$, and MTT: $P = .635$). Perfusion ratios were also not significantly different between low- and high-grade AVM subgroups (Fig 4B–D).

Relationships among SMG, Nidal Volume, Arterial and Venous Flow, and Perfusion Ratios

Strong and significant relationships were observed between SMG and maximum peak velocities in the feeding arteries ($r = 0.78$, $P < .001$), cumulative blood flow in all feeding arteries ($r = 0.85$, $P < .001$), and blood flow in the major draining vein ($r = 0.80$, $P < .001$) and in the straight sinus ($r = 0.67$, $P = .003$). Further analysis revealed significant relationships of AVM nidal volume with cumulative blood flow in all feeding arteries ($r = 0.82$, $P < .001$) and draining veins ($r = 0.66$, $P = .004$). Moreover, the perinidal CBF ratio correlated negatively with cumulative feeding artery flow ($r = -0.60$, $P = .014$) and draining vein flow ($r = -0.60$, $P = .013$). A similar negative correlation was observed between the perinidal CBV ratio and cumulative flow in the feeding arteries ($r = -0.55$, $P = .026$) and draining veins ($r = -0.56$, $P = .025$).

Relationship between AVM Hemodynamics and Risk Factors

Multiple regression analysis revealed no significant association of AVM vascular flow or perfusion parameters with clinical presentation (rupture and seizure history) and AVM risk factors (deep AVM location, presence of flow-induced aneurysms or venous stenosis, and single or deep venous drainage).

DISCUSSION

The results of this study demonstrate the potential of 4D flow and DSC perfusion MR imaging for the comprehensive evaluation of macro- and microvascular hemodynamics in cerebral AVMs. 4D flow MR imaging provided 3D visualization of complex AVM

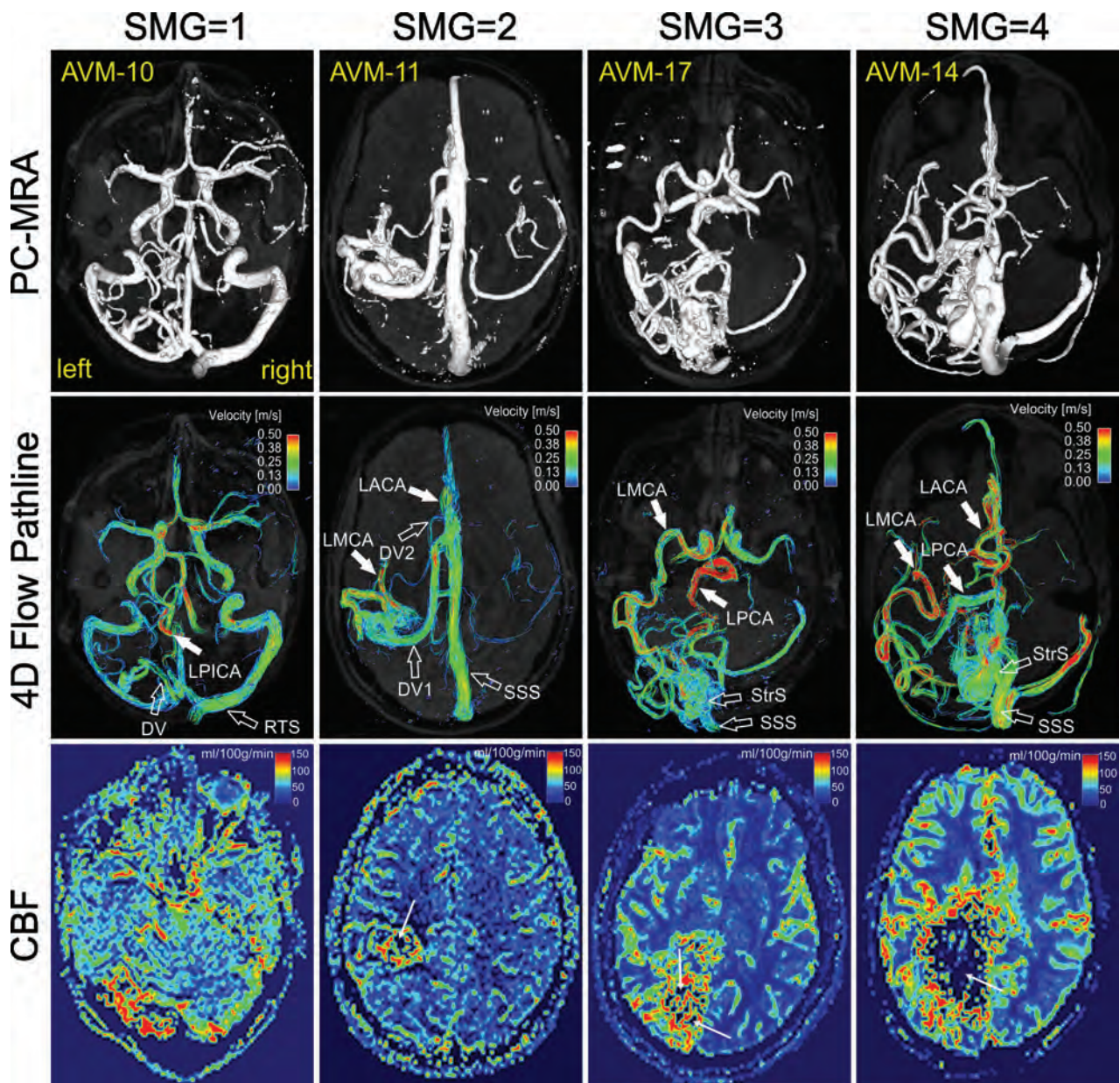


FIG 2. Phase-contrast MRA (PC-MRA), time-integrated 3D pathlines, and perfusion (CBF) for 4 patients with AVMs (SMG = 1–4). AVM arterial feeding (*solid white arrows*) and venous draining patterns (*open white arrows*) can be clearly appreciated in the PC-MRA and 4D flow pathlines. The draining veins of AVM-17 and AVM-14 are obscured by pathlines and are not shown. 4D flow pathlines also illustrate the distribution of blood flow velocities in the entire brain. Note the flow voids (*thin white arrows*) within the nidus for AVM-11, AVM-17, and AVM-14 due to high transnidus shunt flow. LPICA indicates left posterior inferior cerebellar artery; LACA, left anterior cerebral artery; DV, draining vein; RTS, right transverse sinus; StrS, straight sinus; SSS, superior sagittal sinus.

arterial feeding and venous draining patterns and offered quantitative flow characterization of large intracranial AVM vessels. DSC PWI was used to characterize the relative differences in microvascular perfusion parameters. Our findings demonstrate the association of the SMG classification with flow parameters and also reveal significant relationships between macrovascular flow and perinidal tissue perfusion but indicate no significant association of AVM flow or perfusion parameters with symptomatic and anatomic risk factors.

Cerebral AVMs are highly heterogeneous and complex lesions that preclude standardized clinical protocols and uniform paradigms for risk stratification and treatment planning. Initial results

from A Randomized trial of Unruptured Brain Arteriovenous malformations (ARUBA) have questioned the benefit-to-risk ratio of interventional therapy versus medical management in unruptured AVMs.¹⁶ Previous studies indicated that perinidal tissue perfusion and flow dynamics in the AVM feeding and draining systems play an important role in assessing the intra- and postoperative hemorrhagic risk.^{17,18} Hence, patient- and AVM-specific risk stratification with individualized AVM hemodynamic evaluation may be an increasingly important analysis required to demonstrate a benefit of embolization or surgical treatment in high-risk AVMs.

A growing number of AVM risk factors have been demon-

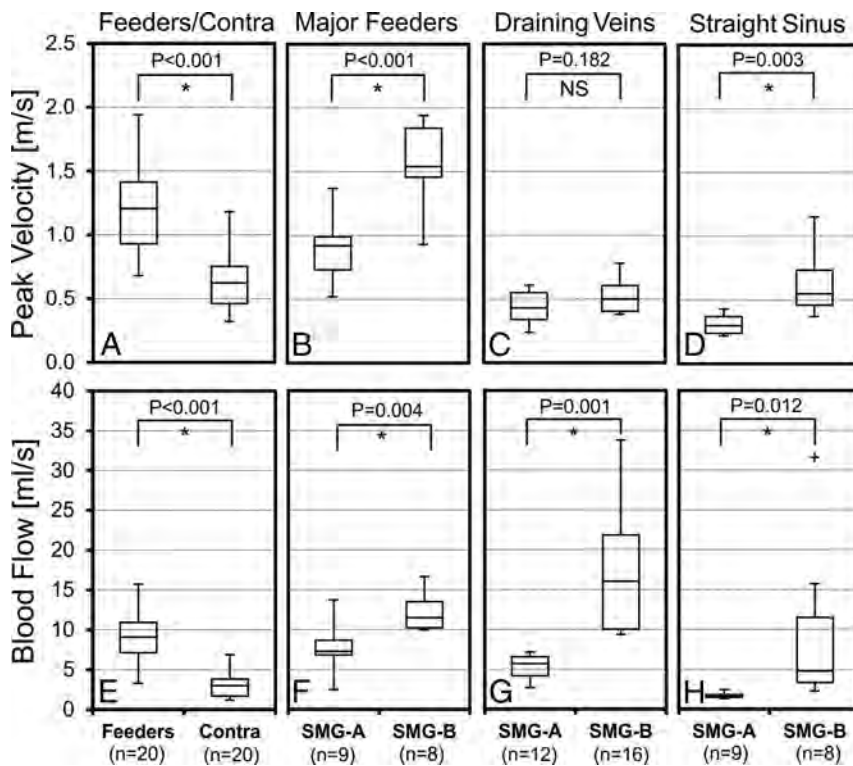


FIG 3. Distribution of peak velocities and blood flow in the AVM feeding (Feeders) and corresponding normal contralateral arteries (Contra) (A and E), as well as in the major feeding arteries (B and F), draining veins (C and G), and the straight sinus (D and H) for the low (SMG-A) and high (SMG-B) grade AVM groups. The feeding arteries had significantly higher peak velocity and blood flow compared with the normal contralateral arteries. The high-grade AVM group (SMG-B) had significantly higher peak velocity and blood flow in the major feeding arteries and the straight sinus and significantly higher blood flow in the draining veins compared with the low-grade group (SMG-A). The asterisk indicates significant difference with $P < .05$; NS, not significant.

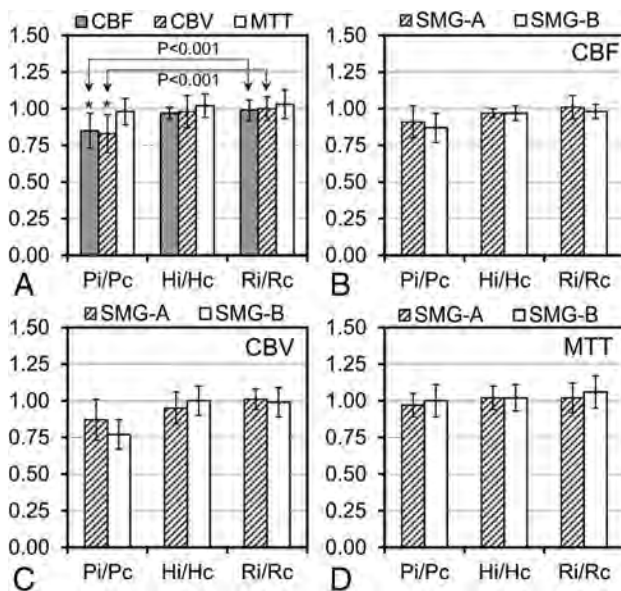


FIG 4. Ipsilateral-to-contralateral perfusion ratios (CBF, CBV, and MTT ratios) in the 3 pairs of ROIs (Pi/Pc, Hi/Hc, and Ri/Rc) for 16 AVMs (A) and perfusion ratios in the low (SMG-A, $n = 9$) and high (SMG-B, $n = 7$) grade AVM groups for CBF (B), CBV (C), and MTT (D). The asterisk indicates a significant difference between perinidal (Pi/Pc) and remote (Ri/Rc) perfusion ratios.

strated to be associated with increased risk of future hemorrhage, such as prior intracranial hemorrhage,^{1,19} a single draining vein,¹⁹ flow-induced aneurysms,²⁰ and deep location.^{1,21} However, the mechanisms of how these factors confer increased hemorrhagic risk remain unclear, with a paucity of data on the role of quantitative AVM hemodynamics. Illies et al²² reported that a previous intracranial hemorrhage was the only risk factor associated with a significant increase of the relative transit time. In our study, we observed no direct connection between AVM hemodynamic parameters and a history of intracranial hemorrhage based on a relatively small sample size. In addition, our findings revealed no significant association of AVM flow or perfusion parameters with seizure history and other anatomic risk factors.

An early 4D flow study by Chang et al⁷ identified significantly higher time-averaged flow and velocity in the ipsilateral arteries compared with normal contralateral vessels. Similar to their findings, our results demonstrate significantly higher peak velocity and blood flow in the feeding arteries compared with normal contralateral arteries. In addition, our results demonstrate that the SMG directly correlates with arterial

flow parameters: The major feeding arteries in high-grade AVMs had significantly higher peak velocities and blood flow in comparison with low-grade AVMs. In addition to SMG, correlations were also identified between AVM nidal volume and cumulative arterial/venous blood flow, indicating that nidal size in the SMG grading system is presumably the dominating factor responsible for different AVM hemodynamics.

A subset of the patients enrolled in this study (AVM 1–14) have been included in a previously reported pilot 4D flow MR imaging study.⁶ The present study included additional recruited patients, refined flow-quantification analysis, and a combination with DSC perfusion MR imaging that was not described in the previous study. In the previous study, a direct relationship between SMG and increased blood flow velocities was found only for draining veins by visual grading of time-integrated pathlines on a 3-point scale (0: <0.25 m/s, 1: <0.5 m/s, 2: >0.5 m/s).⁶ Reanalysis of these data by using regional flow quantification as used in this study demonstrated the following arterial feeding and venous draining peak velocities in 3 SMG groups: SMG = 1 (0.68 ± 0.29 m/s; 0.32 ± 0.13 m/s), SMG = 2 (0.79 ± 0.23 m/s; 0.38 ± 0.16 m/s), and SMG > 3 (0.97 ± 0.54 m/s; 0.50 ± 0.24 m/s). In comparison, the previously used visual velocity grading resulted in SMG = 1 (1.7 ± 0.6 ; 0.6 ± 0.6), SMG = 2 (1.4 ± 0.5 ; 0.8 ± 0.8), and SMG > 3 (1.6 ± 0.5 ; 1.2 ± 0.6). These results

indicate that visual grading analysis agreed with quantitative measures for venous velocities but resulted in lower arterial velocities in group SMG = 2 compared with group SMG = 1. In contrast, quantitative analysis showed consistently increased arterial velocities with increasing SMG. The discrepancy may be caused by a different magnitude of velocities in the arterial (0.88 ± 0.44 m/s) and venous (0.43 ± 0.21 m/s) systems. The previously used visual grading method may thus not have allowed accurate arterial velocity measurement for arterial velocities of >0.5 m/s.

Fast arterial-to-venous blood flow velocities in cerebral AVMs present a great challenge for the quantification of arteriovenous shunting with conventional imaging techniques. It is problematic to quantify arteriovenous shunting simply on the basis of absolute arterial or venous blood flow velocities without consideration of the complex and heterogeneous nidal vascular network. DSA, time-resolved contrast-enhanced MRA, and arterial spin-labeled MR imaging have been shown to provide improved quantification of arteriovenous shunting measured with venous arrival time or arterial-to-venous transit time.^{15,23,24}

A previous DSC PWI study demonstrated AVM steal based on significantly higher Hi/Hc ratios of CBF and CBV in 19 patients with AVMs in comparison with healthy subjects.¹⁴ Fiehler et al²⁵ reported decreased perfusion ratios between affected and nonaffected hemispheres in the MCA and PCA territories accounting for AVM steal. In our study, there were significantly lower perinidal CBF and CBV ratios compared with the remote ratios indicating presence of perinidal hypoperfusion ("AVM steal"). Our perfusion imaging findings were not affected if the 2 ruptured AVMs (AVM-5 and AVM-7) were excluded from the analysis. Flow voids were observed within a high-flow AVM nidus (Fig 2, thin white arrows) due to spin-echo PWI. The signal voids may be alleviated by increasing section thickness and shortening the TR.

A major limitation of this study is the small number of patients with AVMs ($n = 17$), which underlines the relatively rare pathology of cerebral AVMs. Nevertheless, to our knowledge, this is the largest cohort to date for quantitative evaluation of flow parameters in both AVM arterial and venous systems as well as microvascular brain tissue perfusion. Future studies with larger patient cohorts and healthy control groups are warranted to increase the statistical power and further clarify the relevance of macrovascular flow and microvascular tissue perfusion in cerebral AVMs.

Another limitation related to 4D flow MR imaging is its inability to capture the wide range of velocities in cerebral AVMs (ie, fast feeding artery flow versus slow venous flow). Dual velocity encoding is promising to improve the velocity-to-noise ratio for vascular flow quantification.²⁶ In addition, small vessels (eg, feeding arteries and draining veins with diameters of <3 mm) were difficult to visualize and quantify with the current 4D flow technique due to limited spatial resolution, which may be improved by advanced imaging accelerating techniques to increase spatial resolution while keeping total scan times at acceptable levels.²⁷ Moreover, the AVMs included in this study had a different number of feeding and draining vessels, which may bias the statistical results for the peak velocities and blood flow.

The perfusion method used in this study has been successfully applied in the evaluation of brain tumor,¹⁰ but it was only validated against the reference standard (PET) for gradient-echo

PWI.²⁸ In addition, a wide variability in contralateral white matter CBF values was reported in the presence of vascular pathology.²⁹ Thus, we were cautious to use the values in our study as quantitative perfusion measurement in cerebral AVMs without further validation. Instead, the relative perfusion ratios between the affected and nonaffected hemispheres were calculated to characterize the potential perfusion disturbance. Moreover, although a single section with the largest nidal dimension was considered to represent the most significant hemodynamics in cerebral AVMs,¹⁴ 3D assessment of brain tissue perfusion would provide better characterization of microvascular hemodynamic disturbance in cerebral AVMs.²²

CONCLUSIONS

4D flow and DSC perfusion MR imaging enabled quantitative hemodynamic assessment of cerebral AVMs in both AVM arterial feeding and venous drainage systems as well as the capillary microperfusion of peripheral brain tissue. Our results demonstrate the association of SMG with AVM arterial and venous flow as well as significant relationships between macrovascular flow and changes in cerebral perfusion parameters. Future studies in larger patient cohorts including longitudinal follow-up are needed to evaluate the potential of comprehensive MR imaging for the assessment of both cerebral flow and perfusion for improved AVM risk stratification.

Disclosures: Can Wu—RELATED: Grant: American Heart Association,* Comments: American Heart Association Predoctoral Fellowship 14PRE18370014. Bernard R. Bendok—RELATED: Grant: MicroVention (research grant),* James Carr—UNRELATED: Consultancy: Guerbet; Grants/Grants Pending: Bayer,* Astellas,* Siemens*; Payment for Lectures (including service on Speakers Bureaus): Siemens. *Money paid to the institution.

REFERENCES

1. Hernesniemi JA, Dashti R, Juvela S, et al. **Natural history of brain arteriovenous malformations: a long-term follow-up study of risk of hemorrhage in 238 patients.** *Neurosurgery* 2008;63:823–29; discussion 829–31
2. Heidenreich JO, Hartlieb S, Stendel R, et al. **Bleeding complications after endovascular therapy of cerebral arteriovenous malformations.** *AJNR Am J Neuroradiol* 2006;27:313–16
3. Spetzler RF, Martin NA. **A proposed grading system for arteriovenous malformations.** *J Neurosurg* 1986;65:476–83
4. Bammer R, Hope TA, Aksoy M, et al. **Time-resolved 3D quantitative flow MRI of the major intracranial vessels: initial experience and comparative evaluation at 1.5T and 3.0T in combination with parallel imaging.** *Magn Reson Med* 2007;57:127–40
5. Markl M, Frydrychowicz A, Kozerke S, et al. **4D flow MRI.** *J Magn Reson Imaging* 2012;36:1015–36
6. Ansari SA, Schnell S, Carroll T, et al. **Intracranial 4D flow MRI: toward individualized assessment of arteriovenous malformation hemodynamics and treatment-induced changes.** *AJNR Am J Neuroradiol* 2013;34:1922–28
7. Chang W, Loecher MW, Wu Y, et al. **Hemodynamic changes in patients with arteriovenous malformations assessed using high-resolution 3D radial phase-contrast MR angiography.** *AJNR Am J Neuroradiol* 2012;33:1565–72
8. Hope MD, Purcell DD, Hope TA, et al. **Complete intracranial arterial and venous blood flow evaluation with 4D flow MR imaging.** *AJNR Am J Neuroradiol* 2009;30:362–66
9. Srouf JM, Shin W, Shah S, et al. **SCALE-PWI: A pulse sequence for absolute quantitative cerebral perfusion imaging.** *J Cereb Blood Flow Metab* 2011;31:1272–82

10. Carroll TJ, Horowitz S, Shin W, et al. **Quantification of cerebral perfusion using the “bookend technique”: an evaluation in CNS tumors.** *Magn Reson Imaging* 2008;26:1352–59
11. Mast H, Mohr JP, Osipov A, et al. **‘Steal’ is an unestablished mechanism for the clinical presentation of cerebral arteriovenous malformations.** *Stroke* 1995;26:1215–20
12. Bock J, Kreher BW, Hennig J, et al. **Optimized pre-processing of time-resolved 2D and 3D phase contrast MRI data.** In: *Proceedings of the 15th Scientific Meeting of the International Society for Magnetic Resonance in Medicine*, Berlin, Germany. May 19–25, 2007:3138
13. Carroll TJ, Rowley HA, Houghton VM. **Automatic calculation of the arterial input function for cerebral perfusion imaging with MR imaging.** *Radiology* 2003;227:593–600
14. Guo WY, Wu YT, Wu HM, et al. **Toward normal perfusion after radiosurgery: perfusion MR imaging with independent component analysis of brain arteriovenous malformations.** *AJNR Am J Neuroradiol* 2004;25:1636–44
15. Todaka T, Hamada J, Kai Y, et al. **Analysis of mean transit time of contrast medium in ruptured and unruptured arteriovenous malformations: a digital subtraction angiographic study.** *Stroke* 2003;34:2410–14
16. Mohr JP, Parides MK, Stapf C, et al. **Medical management with or without interventional therapy for unruptured brain arteriovenous malformations (ARUBA): a multicentre, non-blinded, randomised trial.** *Lancet* 2014;383:614–21
17. Ogasawara K, Yoshida K, Otawara Y, et al. **Cerebral blood flow imaging in arteriovenous malformation complicated by normal perfusion pressure breakthrough.** *Surg Neurol* 2001;56:380–84
18. Young WL, Prohovnik I, Ornstein E, et al. **Monitoring of intraoperative cerebral hemodynamics before and after arteriovenous malformation resection.** *Anesth Analg* 1988;67:1011–14
19. Pollock BE, Flickinger JC, Lunsford LD, et al. **Factors that predict the bleeding risk of cerebral arteriovenous malformations.** *Stroke* 1996;27:1–6
20. Redekop G, TerBrugge K, Montanera W, et al. **Arterial aneurysms associated with cerebral arteriovenous malformations: classification, incidence, and risk of hemorrhage.** *J Neurosurg* 1998;89:539–46
21. Stefani MA, Porter PJ, terBrugge KG, et al. **Large and deep brain arteriovenous malformations are associated with risk of future hemorrhage.** *Stroke* 2002;33:1220–24
22. Illies T, Forkert ND, Saering D, et al. **Persistent hemodynamic changes in ruptured brain arteriovenous malformations.** *Stroke* 2012;43:2910–15
23. Raoult H, Ferre JC, Morandi X, et al. **Quality-evaluation scheme for cerebral time-resolved 3D contrast-enhanced MR angiography techniques.** *AJNR Am J Neuroradiol* 2010;31:1480–87
24. Wolf RL, Wang J, Detre JA, et al. **Arteriovenous shunt visualization in arteriovenous malformations with arterial spin-labeling MR imaging.** *AJNR Am J Neuroradiol* 2008;29:681–87
25. Fiehler J, Illies T, Piening M, et al. **Territorial and microvascular perfusion impairment in brain arteriovenous malformations.** *AJNR Am J Neuroradiol* 2009;30:356–61
26. Nett EJ, Johnson KM, Frydrychowicz A, et al. **Four-dimensional phase contrast MRI with accelerated dual velocity encoding.** *J Magn Reson Imaging* 2012;35:1462–71
27. Jung B, Honal M, Ullmann P, et al. **Highly k-t-space-accelerated phase-contrast MRI.** *Magn Reson Med* 2008;60:1169–77
28. Vakil P, Lee JJ, Mouannes-Srour JJ, et al. **Cerebrovascular occlusive disease: quantitative cerebral blood flow using dynamic susceptibility contrast MR imaging correlates with quantitative H2[15O] PET.** *Radiology* 2013;266:879–86
29. Mukherjee P, Kang HC, Videen TO, et al. **Measurement of cerebral blood flow in chronic carotid occlusive disease: comparison of dynamic susceptibility contrast perfusion MR imaging with positron emission tomography.** *AJNR Am J Neuroradiol* 2003;24:862–71

Endovascular Treatment of Wide-Neck Anterior Communicating Artery Aneurysms Using WEB-DL and WEB-SL: Short-Term Results in a Multicenter Study

D.N. Gherasim, B. Gory, R. Sivan-Hoffmann, L. Pierot, H. Raoult, J.-Y. Gauvrit, H. Desal, X. Barreau, D. Herbreteau, R. Riva, F. Ambesi Impiombato, X. Armoiry, and F. Turjman

ABSTRACT

BACKGROUND AND PURPOSE: Endovascular treatment of wide-neck anterior communicating artery aneurysms can often be challenging. The Woven EndoBridge (WEB) device is a recently developed intrasaccular flow disrupter dedicated to endovascular treatment of intracranial aneurysms. The aim of this study was to investigate the feasibility, safety, and efficacy of the WEB Dual-Layer and WEB Single-Layer devices for the treatment of wide-neck anterior communicating artery aneurysms.

MATERIALS AND METHODS: Patients with anterior communicating artery aneurysms treated with the WEB device between June 2013 and March 2014 in 5 French centers were analyzed. Procedural success, technical complications, clinical outcome at 1 month, and immediate and 3- to 6-month angiographic follow-up results were analyzed.

RESULTS: Ten patients with unruptured anterior communicating artery aneurysms with a mean neck diameter of 5.4 mm were treated with the WEB. Treatment failed in 3 of the 10 aneurysms without further clinical complications. One patient developed a procedural thromboembolic event, and the other 6 had normal neurologic examination findings at 1-month follow-up. Immediate anatomic outcome evaluation showed adequate occlusion (total occlusion or neck remnant) in 6 of 7 patients. Angiographic control was obtained in all patients, including 6 adequate aneurysm occlusions (3 complete occlusions and 3 neck remnants) at short-term follow-up.

CONCLUSIONS: In our small series, treatment of wide-neck anterior communicating artery aneurysms with the WEB device was feasible and safe. However, patient selection based on the aneurysm and initial angiographic findings in the parent artery is important due to the limitations of the WEB device navigation.

ABBREVIATIONS: WEB = Woven EndoBridge; WEB-DL = WEB Dual-Layer; WEB-SL = WEB Single-Layer

Coiling of intracranial aneurysms is now a well-established endovascular treatment option.^{1,2} Nevertheless, in cases of wide-neck aneurysms, coiling alone has often been proved unsuitable. Balloon-assisted and stent-assisted coiling may be therapeutic options.³⁻⁵ However, low rates of initial angiographic occlusion and high rates of recurrence are reported in such situations.⁵⁻⁷ In

addition, bifurcation aneurysms often require an X- or Y-configuration double-stent treatment technique that carries a higher rate of procedural complications⁸⁻¹³ in addition to the complications linked to the mandatory use of dual antiplatelet therapy.¹¹⁻¹³

The Woven EndoBridge (WEB) aneurysm embolization system (Sequent Medical, Aliso Viejo, California) is a recently developed intrasaccular flow disrupter dedicated to intracranial wide-neck aneurysm management; to date, WEB Dual-Layer (WEB-DL) feasibility, safety, and short-term angiographic findings have only been reported in a few studies, mostly in aneurysms of the middle cerebral artery, while its feasibility and results in treatment of anterior communicating artery aneurysms are not well-known.¹⁴⁻¹⁸ The characteristics of the WEB device combining a large-diameter microcatheter and a relatively stiff device may hamper its placement in this location.

The goal of this study was to analyze the feasibility, safety, and efficacy of WEB-DL and WEB Single-Layer (WEB-SL) flow disruptors for the treatment of wide-neck anterior communicating artery aneurysms.

Received July 11, 2014; accepted after revision December 14.

From the Department of Interventional Neuroradiology (D.N.G., B.G., R.S.-H., F.A.I., R.R., F.T.) and Direction de la Recherche Clinique et de l'Innovation (X.A.), Hôpital Neurologique Pierre Wertheimer, Hospices Civils de Lyon, Lyon, France; Department of Radiology (L.P.), Hôpital Maison Blanche, Reims, France; Department of Neuroradiology (H.R., J.-Y.G.), Centre Hospitalier Universitaire Rennes, Rennes, France; Department of Neuroradiology (H.D.), Centre Hospitalier Universitaire Nantes, Nantes, France; Department of Neuroradiology (X.B.), Pellegrin Hospital, Bordeaux, France; and Department of Neuroradiology (D.H.), Centre Hospitalier Universitaire Tours, Tours, France.

D.N.G. and B.G. contributed equally to this work.

Please address correspondence to Benjamin Gory, MD, MSc, Department of Interventional Neuroradiology, Hôpital Neurologique Pierre Wertheimer, Hospices Civils de Lyon, 59 Bd Pinel, 69677 Bron, France; e-mail: benjamin.gory@chu-lyon.fr

<http://dx.doi.org/10.3174/ajnr.A4282>

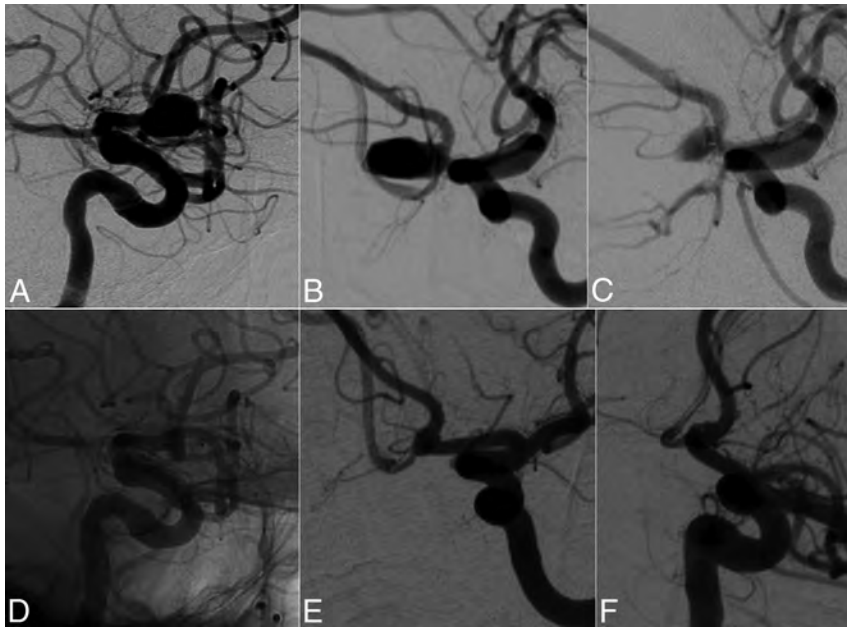


FIG 1. A 65-year-old man with an unruptured anterior communicating artery aneurysm. *A* and *B*, Angiography shows a wide-neck anterior communicating artery aneurysm. *C*, End-procedure angiography shows satisfactory occlusion of the aneurysm with a neck remnant. *D*, Unsubtracted lateral view shows the WEB device. *E* and *F*, Follow-up angiography at 6 months shows complete aneurysm occlusion.

MATERIALS AND METHODS

Population

Between June 2013 and March 2014, patients with anterior communicating artery aneurysms in 5 French centers were treated by using a WEB device. Patient selection was made by the interventional neuroradiologists of each center according to the aneurysm location, size, and neck diameter. Patients were selected for the WEB device when their wide-neck aneurysms necessitated an adjunctive technique such as Y-stent placement. In these situations, we chose to use an intrasaccular device rather than other techniques. Ethics committee approval from each center was obtained for this prospective study. All patients signed an informed consent.

Characteristics of the WEB Device

We used 2 types of WEB devices: the DL and SL. The WEB-DL is composed of inner and outer nitinol braids held together by proximal, middle, and distal radiopaque markers, thereby obtaining 2 separate compartments, 1 distal and 1 proximal (Fig 1A). The WEB-SL is composed of only 1 nitinol braid held together by 2 markers (Fig 1B). The WEB device is deployed in a manner similar to that of endovascular coils via the use of a ≥ 0.027 -inch internal-diameter microcatheter. The detachment system is electrothermal and instantaneous. The WEB device is CE-approved for use in unruptured and ruptured intracranial aneurysms.

Endovascular Procedure

All procedures were performed with the patient under general anesthesia and systemic heparinization. Unilateral femoral access was performed, and the tip of the long sheath was placed in the left or right common carotid artery. A coaxial system was assembled,

and the aneurysm was catheterized with a Rebar 27 (Covidien, Irvine, California), Marksman 27 (Covidien), or DAC 038 (Concentric Medical, Mountain View, California). The WEB device chosen according to the aneurysm diameters was then deployed into the sac. After deployment, a control angiogram was performed to check the position of the device in the aneurysm. If the position or the size was not satisfactory, the device was then resheathed and repositioned or resheathed and replaced by another, more suitable device.

Outcome Evaluation

Clinical outcomes were assessed at discharge and 1 month by using the modified Rankin Scale.¹⁹ Morbidity was defined as an mRS score of 2–5.

Angiographic images were obtained in anteroposterior, lateral, and working projections before, immediately after treatment, and at 3 or 6 months' follow-up according to the center. A simplified 3-point Raymond scale (total occlusion, neck remnant, aneurysm remnant) was used to assess the results of the procedure.⁶

RESULTS

Ten patients (4 women and 6 men; mean age, 59.3 years) with unruptured anterior communicating artery aneurysms were included. The mean width size was 6.2 mm (range, 3.5–8.1 mm), the mean dome size was 5.8 mm (range, 3.8–8.2-mm), and mean neck size was 5.4 mm (range, 3.6–8-mm) (Table 1). Successful deployment of the WEB was obtained in 7 patients (with 2 WEB-DLs and 5 WEB-SLs). In all successful cases, the aneurysms were treated with a single device.

Treatment Failure

In 3 patients (patients 1, 4, and 5), WEB deployment failed. In case 1, the device could not be advanced beyond the carotid bifurcation due to unfavorable vascular anatomy conditions, which led to instability of the microcatheter; the aneurysm was then successfully coiled. In case 4, correct WEB deployment was achieved, but on control angiograms, suboptimal positioning of the device was seen with its base protruding through the neck of the aneurysm inside the parent artery. A second, 6 × 3 mm, WEB-DL device was then deployed, again with suboptimal positioning. The aneurysm was then treated with a balloon-assisted coiling technique. In case 5, WEB-deployment failure occurred due to difficult microcatheter navigation through the A1 segment of the anterior cerebral artery; the aneurysm was later coiled successfully.

Procedural Complications

No intraoperative aneurysm rupture was observed during WEB deployment. In 1 patient (patient 2), the base of the WEB protruded into the lumen of the left A2 segment through the aneu-

Table 1: Clinical presentation and aneurysm characteristics in 10 patients with 10 anterior communicating artery aneurysms

No.	Age (yr) Sex	Aneurysm Status	Aneurysm Characteristics			WEB Size (mm), Type
			Neck (mm)	Width (mm)	Dome (mm)	
1	56, F	Unruptured	6.6	6.3	6.9	7 × 5, DL (failure)
2	56, M	Unruptured	8	8.1	5.6	8 × 5, DL
3	65, F	Unruptured	5.6	6.2	5.1	7 × 4, DL
4	54, F	Unruptured	4.8	6	4	6 × 3, DL (failure)
5	52, M	Unruptured	3.6	3.5	3.8	4 × 3, SL (failure)
6	56, M	Unruptured	3.9	6.7	6.4	7 × 5, SL
7	65, M	Unruptured	5.3	5.9	8.2	7 × 6, SL
8	68, F	Unruptured	5.4	6.5	5.3	7 × 3, SL
9	75, M	Unruptured	5.4	7.5	6.3	8 × 4, SL
10	46, M	Unruptured	5.4	5.5	6.1	7 × 5, SL

Table 2: Clinical and anatomic outcomes

No.	Clinical		Anatomic		
	Initial Symptoms	mRS at 1 Mo	Immediate	Time (mo)	Short-Term
1	Headaches	0	WEB failure	–	–
2	Asymptomatic	1	Neck remnant	3	Aneurysm remnant
3	Asymptomatic	0	Complete occlusion	3	Complete occlusion
4	Asymptomatic	0	WEB failure	–	–
5	Headaches	0	WEB failure	–	–
6	Asymptomatic	0	Aneurysm remnant	6	Neck remnant
7	Headaches	0	Neck remnant	6	Complete occlusion
8	Seizures	0	Complete occlusion	–	Neck remnant
9	Severe headaches	0	Neck remnant	3	Complete occlusion
10	Vertigo	0	Neck remnant	6	Neck remnant

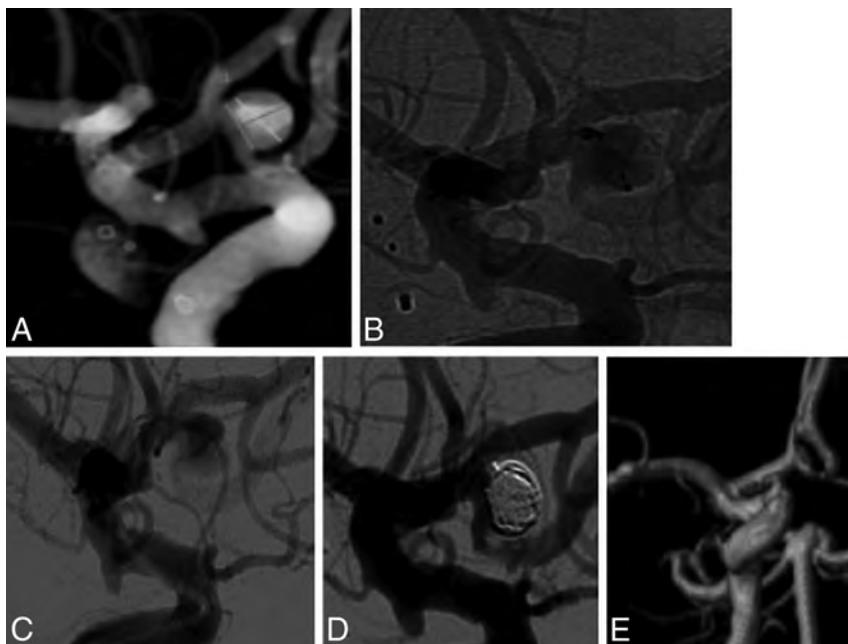


FIG 2. A 54-year-old woman with unruptured anterior communicating artery aneurysm. *A*, 3D angiography shows a 4.8-mm wide-neck 6-mm-long anterior communicating artery aneurysm. *B* and *C*, Unsuccessful deployment of a WEB-DL device occluding the origin of the left anterior cerebral artery. *D*, Complete aneurysm occlusion after coiling. *E*, Follow-up MRA at 3 months shows complete occlusion of the anterior communicating artery aneurysm.

rysm neck, a balloon was used to push the WEB inside the aneurysm, and a distal thromboembolic event later occurred in branches of the ipsilateral anterior cerebral artery. At 1 month, the patient had an mRS score of 1.

injections again revealed suboptimal positioning (Fig 2*B*, *-C*). A decision was made to coil the aneurysm (Fig 2*D*), and 3-month MRA follow-up showed complete aneurysm occlusion (Fig 1*E*).

Clinical Outcome

Clinical outcomes are summarized in Table 2. Six (85.7%) of 7 patients with successful WEB deployment were asymptomatic at 1-month follow-up (mRS 0). One patient presented with posttreatment right-sided hemiparesis (patient 2) due to a distal left A2 thromboembolism found later on follow-up MR imaging. At 1 month, the patient recovered most of the deficit with a mild brachial deficit remnant (mRS 1).

No treatment-related mortality was observed (0.0%); posttreatment permanent morbidity was 0.0%.

Anatomic Outcome

At the end of procedure, 6 of the 7 patients (85.7%) achieved satisfactory occlusion (complete occlusion or neck remnant). Two patients had complete occlusion, and 4 were found to have a neck remnant. All of the 7 patients with successful WEB deployment were assessed at short-term follow-up (3–6 months) by using either conventional angiography (6 cases) or CTA (1 case); satisfactory occlusion was seen in 6 patients (85.7%).

Illustrative Cases

Case 1. A 65-year-old man (patient 7) presented with a 8.2-mm wide-neck anterior communicating artery aneurysm seen at angiography (Fig 1*A*, *-B*). Endovascular treatment with a 7 × 6 mm WEB-SL device was performed (Fig 1*C*, *-D*). Good clinical outcome was recorded after treatment, and a 6-month follow-up angiogram showed complete occlusion of the aneurysm (Fig 1*E*, *-F*).

Case 2. A 54-year-old woman (patient 4) presented with an incidental finding of a 4.8-mm wide-neck anterior communicating artery aneurysm (Fig 2*A*). Endovascular 6 × 3 mm WEB deployment was performed, and postprocedure angiography showed suboptimal positioning of the device with protrusion of its base through the neck of the aneurysm and residual contrast filling of the sac. A second 6 × 3 mm WEB-DL was deployed, but control



FIG 3. A 46-year-old man with an anterior communicating artery aneurysm. *A*, Angiography shows a 6-mm wide-neck 8-mm-long anterior communicating artery aneurysm. *B* and *C*, A 7 × 5 mm WEB-SL device is successfully deployed. *D* and *E*, Six-month follow-up angiography shows a significant neck remnant.

Case 3. A 46-year-old man (patient 10) presented with an incidental anterior communicating artery aneurysm. Angiography revealed a 5.4-mm wide-neck anterior communicating artery aneurysm (Fig 3A). Endovascular treatment was performed by using a WEB-SL device with final incomplete aneurysm occlusion (Fig 3B, -C). Angiographic follow-up at 6 months revealed incomplete occlusion of the neck (Fig 3D, -E).

DISCUSSION

This small series shows that endovascular treatment with WEB-DL and WEB-SL devices is feasible in wide-neck anterior communicating artery aneurysms, with very low morbidity and mortality and a high adequate occlusion rate at short-term follow-up.

Feasibility and Patient Selection

We show that treatment of anterior communicating artery aneurysms with a WEB device is feasible; however, selection of patients should be taken into account before deciding on a WEB treatment. In this series, the rate of failure was not negligible (30%). WEB treatment of anterior communicating artery aneurysms requires a favorable angle between the long axis of the aneurysm and that of the parent vessel (A1 segment of the anterior cerebral artery) as reported by Lubicz et al.¹⁵ An unfavorable anatomy may lead to prolonged interventional timing and/or impossible WEB deployment. We observed 1 deployment failure (patient 4) because the long axis of the aneurysm was not in line with that of the parent vessel, and after several failed attempts to place the microcatheter, it was decided to coil the aneurysm.

In addition, a favorable angle between the centerline of the A1 segment of the anterior cerebral artery and the terminal internal

carotid artery is also important (patient 5). The use of a much larger and stiffer microcatheter for the WEB device than usually used for coiling is currently mandatory.

Safety of the WEB Device

The safety of this device seems very good. In our small series, there was neither device-related mortality nor permanent morbidity, despite the specific anatomy (wide-neck anterior communicating artery aneurysms). Our results compare well with other studies on the WEB device. In the series of Pierot et al¹⁶ dealing with 34 middle cerebral artery aneurysms with unfavorable anatomy, the rate of mortality was 0.0% and morbidity was 3.1% (1 intraoperative aneurysm rupture with mRS 3 at 1 month follow-up). In the recent large multicenter series of 85 patients, morbidity and mortality at 1 month were 1.3% and 0.0%, respectively.¹⁸

Wide-neck intracranial aneurysms can be treated with stent-assisted coiling^{4,5}; however, in case of bifurcation

aneurysms such as anterior communicating artery aneurysms, the stent placement procedure requires a Y- or X-configuration, which has a high incidence of adverse events and outcomes.¹¹⁻¹³ Compared with intracranial stent placement, the major advantage of using a WEB device is the absence of antiplatelet therapy. In our series, no antiplatelet premedication was performed except in 1 patient with an iliac artery stent placement. The use of antiplatelet therapy is known to increase the risk of hemorrhagic complications.^{7,11,13} In a survey that included 1517 patients treated with stents, Shapiro et al⁷ reported an overall procedure complication rate of 19% and a periprocedural mortality of 2.1%.

Due to the particular anatomy of anterior communicating artery aneurysms, the use of flow diverters should be limited²⁰; moreover, the safety of flow diversion should be assessed in larger series.^{21,22}

Efficacy of the WEB Device

Satisfactory aneurysm occlusion was achieved in most cases (85.7%). Our results are close to those of other series; however, to date, few results of the treatment with the WEB-SL device have been published.¹⁴⁻¹⁸ In Pierot et al,¹⁶ adequate occlusion (total occlusion or neck remnant) was observed in 83.3% of 33 treated aneurysms. In Lubicz et al,¹⁵ in a series of 19 treated wide-neck bifurcations aneurysms, 2 complete occlusions, 15 near-complete occlusions (89.5% adequate occlusion), and 2 incomplete occlusions were reported at 6-month angiographic follow-up. Similar findings were also reported in the large prospective French series of 85 patients (92.3%).¹⁸

However, the rate of neck remnants is not negligible, and the concave base of the WEB device could explain these findings. This

high rate of neck remnants could also be explained by the compaction of the device toward the dome. Further technical improvements may be needed to ameliorate the occlusion caused by the device. Long-term follow-up of these patients is mandatory to verify its efficacy precisely. In addition, the efficacy of the WEB-device treatment in terms of aneurysm recanalization according to the type used (WEB-DL or WEB-SL) is not well-known; therefore, mid- and long-term follow-up are needed.

The limitations of our study were the small number of patients and a follow-up period that was too short to evaluate the efficacy of the WEB device. However, it is important to have a preliminary evaluation for this new endovascular treatment device for anterior communicating artery aneurysms.

CONCLUSIONS

In this small series, we found that the WEB device may be a new treatment option for wide-neck bifurcation anterior communicating artery aneurysms. Angiographic findings of the aneurysms and the parent artery are crucial to improve the feasibility of the WEB device. Nevertheless, the rate of neck remnants is not negligible and necessitated improvements of the device technology.

Disclosures: Laurent Pierot—RELATED: Consulting Fee or Honorarium: Sequent Medical; UNRELATED: Consultancy: Codman, Covidien, MicroVention, Balt, Stryker Neurovascular. Xavier Barreau—RELATED: Consulting Fee or Honorarium: Sequent Medical. Comments: honorarium for filling my Web case data base. Denis Herbreteau—RELATED: Consulting Fee or Honorarium: Sequent Medical (proctoring); Support for Travel to Meetings for the Study or Other Purposes: Sequent Medical. Francis Turjman—UNRELATED: Consultancy: Codman,* Balt, Covidien; Payment for Lectures (including service on Speakers Bureaus): Codman,* Covidien*; Payment for Development of Educational Presentations: Codman, Balt*; Travel/Accommodations/Meeting Expenses Unrelated to Activities Listed: Covidien, Codman. *Money paid to the institution.

REFERENCES

- Pierot L, Spelle L, Vitry F; for the ATENA Investigators. **Immediate clinical outcome of patients harboring unruptured intracranial aneurysms treated by endovascular approach: results of the ATENA study.** *Stroke* 2008;39:2497–504
- Gory B, Turjman F. **Endovascular treatment of 404 intracranial aneurysms treated with Nexus detachable coils: short-term and mid-term results from a prospective, consecutive, European multicenter study.** *Acta Neurochir* 2014;156:831–37
- Gory B, Kessler I, Seizem Nekiri G, et al. **Initial experience of intracranial aneurysm embolization using the balloon remodeling technique with Scepter C, a new double-lumen balloon.** *Interv Neuroradiol* 2012;18:284–87
- Gory B, Klisch J, Bonafé A, et al. **Solitaire AB stent-assisted coiling of wide-necked intracranial aneurysms: short-term results from a prospective, consecutive, European multicentric study.** *Neuroradiology* 2013;55:1373–78
- Gory B, Klisch J, Bonafé A, et al. **Solitaire AB stent-assisted coiling of wide-necked intracranial aneurysms: mid-term results from the SOLARE study.** *Neurosurgery* 2014;75:215–19
- Raymond J, Guilbert F, Weill A, et al. **Long-term angiographic recurrences after selective endovascular treatment of aneurysms with detachable coils.** *Stroke* 2003;34:1398–403
- Shapiro M, Beckske T, Sahlein D, et al. **Stent-supported aneurysm coiling: a literature survey of treatment and follow-up.** *AJNR Am J Neuroradiol* 2012;33:159–63
- Spiotto AM, Gupta R, Fiorella D, et al. **Mid-term results of endovascular coiling of wide-necked aneurysms using double stents in a Y configuration.** *Neurosurgery* 2011;69:421–29
- Jankowitz BT, Thomas A, Jovin T, et al. **Y stenting using kissing stents for the treatment of bifurcation aneurysms.** *J Neurointerv Surg* 2012;4:16–21
- Saatci I, Geyik S, Yavuz K, et al. **X-configured stent-assisted coiling in the endovascular treatment of complex anterior communicating artery aneurysms: a novel reconstructive technique.** *AJNR Am J Neuroradiol* 2011;32:E113–17
- Bartolini B, Blanc R, Pistocchi S, et al. **“Y” and “X” stent-assisted coiling of complex and wide-neck intracranial bifurcation aneurysms.** *AJNR Am J Neuroradiol* 2014;35:2153–58
- Gory B, Rouchaud A, Saleme S, et al. **Endovascular treatment of middle cerebral artery aneurysms for 120 nonselected patients: a prospective cohort study.** *AJNR Am J Neuroradiol* 2014;35:715–20
- Piotin M, Blanc R, Spelle L, et al. **Stent-assisted coiling of intracranial aneurysms: clinical and angiographic results in 216 consecutive aneurysms.** *Stroke* 2010;41:110–15
- Pierot L, Liebig T, Sychra V, et al. **Intrasaccular flow-disruption treatment of intracranial aneurysms: preliminary results of a multicenter clinical study.** *AJNR Am J Neuroradiol* 2012;33:1232–38
- Lubicz B, Mine B, Collignon L, et al. **WEB device for endovascular treatment of wide-neck bifurcation aneurysms.** *AJNR Am J Neuroradiol* 2013;34:1209–14
- Pierot L, Klisch J, Cognard C, et al. **Endovascular WEB flow disruption in middle cerebral artery aneurysms: preliminary feasibility, clinical, and anatomical results in a multicenter study.** *Neurosurgery* 2013;73:27–34; discussion 34–35
- Klisch J, Sychra V, Strasilla C, et al. **The Woven EndoBridge cerebral aneurysm embolization device (WEB II): initial clinical experience.** *Neuroradiology* 2011;53:599–607
- Papagiannaki C, Spelle L, Januel AC, et al. **WEB intrasaccular flow disruptor—prospective, multicenter experience in 83 patients with 85 aneurysms.** *AJNR Am J Neuroradiol* 2014;35:2106–11
- Bonita R, Beaglehole R. **Recovery of motor function after stroke.** *Stroke* 1988;19:1497–500
- Darsaut T, Bing F, Salazkin I, et al. **Flow diverters failing to occlude experimental bifurcation or curved sidewall aneurysms: an in vivo study in canines.** *J Neurosurg* 2012;117:37–44
- Gory B, Bonafé A, Pierot L, et al. **Safety and efficacy of flow-diverter stents in endovascular treatment of intracranial aneurysm: interest of the prospective DIVERSION observational study.** *J Neuroradiol* 2014;41:93–96
- Turjman F, Levrier O, Combaz X, et al. **EVIDENCE Trial: design of a phase 2, randomized, controlled, multicenter study comparing flow diversion and traditional endovascular strategy in unruptured saccular wide-necked intracranial aneurysms.** *Neuroradiology* 2015; 57:49–54

The FRED Flow-Diverter Stent for Intracranial Aneurysms: Clinical Study to Assess Safety and Efficacy

M.A. Möhlenbruch, C. Herweh, L. Jestaedt, S. Stampfl, S. Schönenberger, P.A. Ringleb, M. Bendszus, and M. Pham



ABSTRACT

BACKGROUND AND PURPOSE: Flow-diverter stents are emerging for the endovascular treatment of difficult-to-treat or otherwise untreatable cerebral aneurysms (wide-neck, fusiform, dissecting, blisterlike, or giant). We assessed the clinical safety and efficacy of the Flow-Redirection Endoluminal Device.

MATERIALS AND METHODS: This was an institutional review board–approved single-center observational clinical study in 29 patients with 34 aneurysms elected to be treated by endovascular intervention. After providing informed consent, patients were included according to the following criteria: aneurysm fundus-to-neck ratio <2 or neck diameter >4 mm, fusiform, dissecting, or giant aneurysms. The primary end point for clinical safety was the absence of death, absence of major or minor stroke, and absence of transient ischemic attack. The primary end point for treatment efficacy was complete angiographic occlusion according to the O'Kelly Marotta grading scale immediately after the procedure and at follow-up after 3 and 6 months (O'Kelly Marotta D: complete occlusion).

RESULTS: The Flow-Redirection Intraluminal Device deployment was technically successful in all cases. In 26/29 (89%) of patients, the primary end point of safety was reached; in the 3 remaining patients, 1 disabling ischemic stroke and 2 minor strokes with complete recovery at follow-up were observed. Angiographic (DSA and MRA) and clinical follow-up were available after 3 months in 29/29 (100%) and after 6 months in 25/29 (86%) patients (after 6 months, only MRA follow-up was performed according to our study protocol and institutional standard). At 3-month follow-up, complete occlusion was reached in 19/34 aneurysms (O'Kelly Marotta D: 19/34; 56%). At 6-month follow-up, aneurysm occlusion was complete in 22/30 aneurysms (O'Kelly Marotta D: 22/30; 73%).

CONCLUSIONS: Deployment of the Flow-Redirection Intraluminal Device flow-diverter stent is safe and effective in the treatment of difficult-to-treat or otherwise untreatable intracranial aneurysms.

ABBREVIATIONS: FD = flow-diverter; FRED = Flow-Redirection Intraluminal Device; LTA = light transmission aggregometry; OKM = O'Kelly Marotta grading scale; PTA = percutaneous transluminal angioplasty

Endovascular treatment of intracranial aneurysms by coiling has become an accepted alternative to surgical clipping, with increasing evidence for lower morbidity and mortality rates, especially in clinical equipoise.¹⁻³ However, especially in wide-neck, fusiform, dissecting, and giant aneurysms, incomplete coiling and reperfusion are still a major limitation preventing stable long-term occlusion. Aneurysm recanalization and/or neck remnants may be observed despite

further refinement in coil technology such as coated platinum coils⁴ and/or procedural modification such as the balloon-remodeling technique⁵ or stent-assisted coil embolization.⁶

The development of flow-diverter (FD) stents has offered the potential of aneurysm occlusion through thrombosis triggered by the disruption of flow into the aneurysm sac.⁷⁻¹⁶ As a key element of construction, these stents have a braided mesh with a densely covered surface. Once the FD is expanded to cover the aneurysm neck, thrombosis is induced by stasis of flow within the aneurysmal sac. The porosity of the FD mesh and the pressure gradient between parent and smaller adjacent branch vessels preserve flow and patency of the latter even if covered. The Flow-Redirection Endoluminal Device (FRED; MicroVention, Tustin, California) is a new generation of FDs for reconstruction of the parent artery and aneurysm occlusion. Its unique dual-layer design composed of a low-porosity inner mesh and a high-porosity outer stent may provide potential advantages over other available FDs in safe deliverability and effective occlusion

Received August 7, 2014; accepted after revision December 3.

From the Departments of Neuroradiology (M.A.M., C.H., L.J., S. Stampfl, M.B., M.P.) and Neurology (S. Schönenberger, P.A.R.); University of Heidelberg Medical Center, Heidelberg, Germany.

Please address correspondence to Markus A. Möhlenbruch, MD, Department of Neuroradiology, University of Heidelberg Medical Center, Im Neuenheimer Feld 400, 69120 Heidelberg, Germany; e-mail: markus.moehlenbruch@med.uni-heidelberg.de

Indicates article with supplemental on-line tables.

<http://dx.doi.org/10.3174/ajnr.A4251>

of the target lesion. We report our analysis of the clinical safety and efficacy of the FRED in 29 patients with 34 aneurysms.

MATERIALS AND METHODS

Patient Selection

Approval for prospective data collection of all interventional procedures reported in this study was given by the institutional review board of the medical faculty. Informed consent for study inclusion was obtained from the patients or their legal representatives. Patients were enrolled between February 2013 and July 2014.

Criteria of Inclusion/Exclusion

Patients with intracranial aneurysms were included in the study and treated with the FRED if the aneurysms satisfied the following morphologic and morphometric criteria of inclusion: 1) wide-neck saccular (fundus-to-neck ratio <2 or neck diameter >4 mm), 2) fusiform or circumferential, 3) dissecting, 4) blisterlike (broad-based at a typical location, eg, the supraclinoid side wall of the ICA and ≤ 2 mm), and 5) giant (defined as ≥ 25 -mm maximum diameter) or those presenting with mass effect. We considered these aneurysms to have a high likelihood of technical failure and/or recurrence with conventional endovascular techniques. Five patients (5/29, 17%) with recanalization after previous coiling were enrolled. Exclusion criteria were consensus about clipping as the appropriate treatment option in cases with unfavorable branch configuration with an acute angle in relation to the parent vessel or an unfavorably small diameter of the parent artery of ≤ 2.0 mm.

FRED

The FRED is an FD designed for the treatment of intracranial aneurysms. The device consists of a braided self-expandable closed-cell dual-layer stent (also referred to a “stent within a stent”) with a low-porosity inner mesh of higher pore attenuation (48 nitinol wires) and an outer stent with high porosity (16 nitinol wires). This dual-layer design is restricted to the midsection of the stent and encompasses 80% of its total length. An interwoven double helix of radiopaque tantalum strands attaches the inner mesh to the outer stent and improves visibility over its full length of dual-layer coverage. Each end of the stent is flared and marked by 4 radiopaque tips. Currently, the FRED is available in 5 different diameters (3.5, 4.0, 4.5, 5.0, and 5.5 mm) recommended for vessel diameters from 2.5 to 5.5 mm and at working lengths (dual-layer coverage) from 7 to 56 mm. The FRED is attached to a delivery microwire with a radiopaque distal tip and a proximal marker. If the device is not correctly positioned across the aneurysm neck, the pusher allows resheathing and repositioning of the stent as long as $\leq 80\%$ of its length has been unsheathed/deployed. As soon as the 0.027-inch delivery-microcatheter (Headway 27; MicroVention) is fully withdrawn over the delivery microwire, the coupling wire releases and the stent is deployed.

Description of Technique

Every procedure was performed via a transfemoral approach with the patient under general anesthesia. A 6F–8F guiding catheter was introduced through a femoral sheath into the carotid or ver-

tebral artery. The radiologic examination of the target vessel was performed by using a biplane angiographic system (Artis zee biplane; Siemens, Erlangen, Germany) and 3D rotational angiography. FD length was chosen according to the length of the aneurysm neck with the procedural goal to ensure arterial wall coverage with the inner mesh extending to at least 2 mm beyond both the distal and proximal limits of the neck. For FD delivery, a Headway 27 microcatheter was navigated past the aneurysm neck with a microguidewire, Traxcess (MicroVention) or Radiofocus Guide Wire GT 16 (Terumo, Tokyo, Japan). Under roadmap guidance, the FD was unsheathed by slowly withdrawing the delivery microcatheter for 2–3 minutes while the delivery wire was gently pushed on to facilitate complete opening and wall apposition of the FD. An in-stent percutaneous transluminal angioplasty (PTA) was performed with a balloon microcatheter (HyperGlide or HyperForm; Covidien, Irvine, California) if incomplete opening was observed on 2D angiography or 3D DynaCT (Siemens). In those cases in which additional aneurysm coiling was performed, a microcatheter was initially positioned inside the aneurysmal sac followed by jailing of the microcatheter between the parent vessel wall and the FD at deployment.

Anticoagulation/Antiplatelet Regimen

Patients were prepared with aspirin, 100 mg, and clopidogrel, 75 mg (loading dose of 300 mg), 5 days before treatment. During the procedure, anticoagulation was initiated with a bolus of standard heparin (70–100 IU/kg) followed by intravenous administration to maintain an activated clotting time of ≥ 250 seconds. After the procedure, a daily dose of clopidogrel (75 mg) and aspirin (100 mg) was given for 3 and 6 months, respectively. Platelet inhibition was tested by using the light transmission aggregometry (LTA) method on the day before or immediately before starting the procedure. If according to this test, the patient was considered a non-responder (LTA result of $<6 \Omega$), an LTA test with 2-MeS-AMP (selective P2Y₁₂-adenosine diphosphate receptor antagonist) was performed. In case of an LTA result with 2-MeS-AMP $\leq 5 \Omega$, a pharmacokinetic nonresponse was suspected and a reloading dose of clopidogrel (300 mg) was administered. In the case of repeated test failure even after reloading or an LTA result with 2-MeS-AMP $>5 \Omega$, pharmacodynamic resistance was assumed and prasugrel was substituted for clopidogrel. In patients with ruptured aneurysms, tirofiban was administered intravenously during the endovascular procedure before FD deployment and aspirin and clopidogrel were started after the procedure.

Evaluation of End Points

Safety. Clinical evaluation by detailed neurologic examination was performed immediately after the procedure, at 2 hours after the procedure, and during the clinical visit on the following day and was finally scored by the mRS at discharge and follow-up by a board-certified neurologist not blinded to treatment. Technical safety, including navigation, visibility, deployment, opening, and vessel wall apposition of the FD, were rated by 2 senior neurointerventionalists (M.A.M., M.P.).

Efficacy. Each angiographic result was categorized according to the O’Kelly Marotta (OKM) grading scale for assessment of cere-

bral aneurysms treated by flow diversion.¹⁷ Each aneurysm was assigned an occlusion grade according to the initial degree of filling (A = total filling, B = subtotal filling, C = entry remnant, D = no filling) and the degree of stasis (prolongation of stasis into 1 = arterial, 2 = capillary, 3 = venous phase). Detailed follow-up examinations were performed with both DSA and MR imaging (3T, Magnetom Trio or Magnetom Verio; Siemens; TOF MRA with and without contrast agent) at 3 months. After 6 months, MRA was exclusively performed. To evaluate thrombosis of the aneurysm and shrinkage of the aneurysm sac, we measured the maximum diameters of all lesions on preprocedural MR images in the axial plane with 2 additional orthogonal planes and compared them with MR imaging at 3 and 6 months. Aneurysm morphometry on MR imaging was categorized into 3 groups: 1) complete or partial ($\geq 20\%$) decrease, 2) stable, 3) progressive ($\geq 10\%$).

RESULTS

Twenty-nine patients (14 female, 15 male; mean age, 58 years; age range, 32–80 years) with 34 aneurysms fulfilled the criteria of inclusion. Patient demographics and aneurysm features are shown in On-line Table 1, and clinical and angiographic details are listed in On-line Table 2.

After preparation with aspirin and clopidogrel, a pharmacokinetic resistance was suspected in 1 patient. Following a reloading dose of clopidogrel, responder status was confirmed. In another patient, pharmacodynamic resistance was assumed on the basis of LTA results and prasugrel was substituted for clopidogrel. Twenty-three aneurysms originated from the ICA/posterior communicating artery; 3, from the anterior cerebral artery; and 8 were located in the posterior circulation. We included 17 wide-neck saccular aneurysms, 3 fusiform/dissecting aneurysms, 4 blisterlike aneurysms, and 10 large/giant aneurysms (including 2 partially thrombosed aneurysms). Nine aneurysms were symptomatic, and 5 aneurysms were in acute/subacute stages of SAH. In all patients and for all aneurysms, the FRED could be navigated to the target area and was deployed successfully across the aneurysm neck with complete neck coverage.

Thirty-two of 34 (94%) aneurysms were treated by deployment of a single FD. Two patients had undergone previous endovascular treatment with stents for the same target lesion: One patient with reperfusion was previously treated by stent-assisted coiling (LEO+ stent; Balt Extrusion, Montmorency, France); the other patient with a 16.3-mm large-neck cavernous ICA aneurysm was pretreated with 2 overlapping LEO+ stents (3.5×50 mm). Median diameters of the stented parent vessel segments were proximally 3.8 mm (range, 2.0–5.3 mm) and distally 3.4 mm (range, 1.9–5.7 mm). In 10 cases, bioactive coils (Cerecyte; Codman Neurovascular, Raynham, Massachusetts) were used with a median packing attenuation of 20% (range, 9%–43%). A PTA before FD deployment was performed in 1 patient with a 50% stenosis directly proximal to a fusiform vertebral aneurysm. PTA after FD deployment was performed in 5 patients with paraophthalmic or supraclinoid ICA aneurysms. In all of these 5 patients, near-complete ($\geq 90\%$) wall apposition of the FD had been achieved before PTA; however, PTA was elected to further improve wall apposition and opening of the vessel diameter. At termination of the procedure, an immediate change of angiographic

filling (OKM grading scale) was achieved in 33/34 (97%) aneurysms with complete or near-complete early occlusion (OKM C or D) occurring in 9/34 (26%) within 30 minutes after FD deployment.

Clinical Safety and Procedure-Related Complications

The primary end point of safety (absence of any new transient or permanent neurologic deficit or death) was reached in 26/29 (90%) patients. A new permanent neurologic deficit by major stroke occurred in 1 of the treated patients after the procedure. Minor strokes were observed in 2 patients (1 immediately post-procedural and 1 after 2 months [see below]) who recovered completely and were each asymptomatic after 3 months of follow-up (NIHSS = 0, mRS = 0). Neither mortality nor transient ischemic symptoms occurred in any of the treated patients after the procedure and throughout follow-up.

The major stroke occurred in a patient with a ruptured aneurysm of a short paramedian circumferential perforator branch emerging from the basilar trunk. This very small aneurysm measured 1.6 mm and arose from the midsection of the basilar trunk just distal to the AICA offspring. It was unmasked only on the repeat angiogram 12 days after SAH and was not visible on the initial angiogram obtained on the day of SAH. Weight-adapted tirofiban was started intravenously with heparin after femoral access and was maintained for 12 hours. The shortest available FRED (3.5×7 mm) was successfully deployed to cover the midsection of the basilar trunk, and the control angiogram demonstrated immediate contrast stasis within the dome with preserved flow through the perforator. Nine hours after FRED deployment, the patient developed a right-sided high-grade hemiparesis and dysarthria. DWI MR imaging was performed immediately and confirmed a left paramedian pontine ischemic infarction at the level of the aneurysm. At discharge, the patient had a Glasgow Coma Scale score of 15 with substantially improved motor strength on her right side.

One minor stroke occurred in a patient with a superior cerebellar artery aneurysm 1 day after FRED deployment. DWI MR imaging confirmed a few microembolic infarcts in the ipsilateral superior cerebellar artery territory. Immediate control DSA showed intact duplicated superior cerebellar arteries and contrast stasis within the dome without any evidence of local thrombus formation inside the FD or thromboembolic branch occlusion distal to it. The patient was discharged home with a residual mild unsteadiness of gait, which had completely resolved at 3-month follow-up.

The second above-mentioned minor stroke occurred in a patient with a giant partially thrombosed ICA aneurysm 2 months after FD deployment. Because of infection of his ventriculoperitoneal shunt, which required conversion to a ventriculoatrial shunt, prasugrel (the patient was a nonresponder to aspirin and clopidogrel) was terminated. After 1 week of anticoagulation on heparin only, the patient developed sudden hemiparesis due to complete FD in-stent thrombosis with complete ICA occlusion confirmed by Doppler sonography and emergency DSA. Resolution of symptoms could be observed clinically during emergency DSA in the awake state after pharmacologic induction of controlled hypertension with DSA documentation of sufficient col-

lateral circulation through the circle of Willis and leptomeningeal anastomoses. MR imaging the next day showed development of only microembolic watershed infarcts and absence of any cortical or basal territorial infarction. Full resolution of symptoms was observed in this patient at discharge, and stable ICA occlusion without any evidence of residual antegrade flow was documented by Doppler sonography and MR imaging. None of the other patients developed any new transient or permanent neurologic deficits during follow-up.

An asymptomatic in-stent thrombosis in the acute stage after SAH Hunt and Hess 3° was observed in 1 other patient with a dissecting aneurysm of AICA origin. Appositional clot formation occurred within the FD at the level of the aneurysm neck 5 minutes after FD deployment. This patient had received prior weight-adapted tirofiban (30 minutes before deployment) and heparin, and the clot dissolved after pharmacologic induction of controlled hypertension. Subsequently, DWI MR imaging ruled out brain stem infarction, and the patient did not develop any new symptoms.

Routine Follow-Up (Clinical, DSA, MRA)

Complete angiographic (DSA and MRA) and clinical follow-up could be performed after 3 months in 29/29 (100%) and after 6 months in 25/29 (86%) patients (after 6 months only MRA was performed according to our study protocol and institutional standard). At 3-month follow-up, a complete occlusion (OKM D) was achieved in 19/34 (56%) aneurysms. A near-complete occlusion (OKM C) was reached in 12/34 (35%) aneurysms. Reduction of aneurysmal sac filling and prolongation of stasis were noted in 27/34 (79%) aneurysms from the initial postprocedural control DSA to the 3-month follow-up control DSA. At 6-month follow-up, 7/30 (23%) aneurysms showed a decrease of residual inflow, and none developed recurrence with enlargement of the aneurysm at the base. At 6-month follow-up, aneurysm occlusion was complete (OKM D) in 22/30 (73%) aneurysms. A near-complete occlusion (OKM C) was detected in another 8/30 (27%) aneurysms. On follow-up angiograms, in no case was any in-stent stenosis, in-stent thrombosis, or migration of the FRED implant observed.

MR imaging analysis at 3 months showed shrinkage or complete disappearance of the thrombosed aneurysm in 59% (20/34 aneurysms) and no change in size in 41% (14/34 aneurysms including 10 additional aneurysm coilings). On MR imaging at 6 months, shrinkage or complete disappearance was observed in 70% (21/30 aneurysms) with no change in 30% (9/30 of aneurysms, including 8 that were additionally coiled).

Two illustrative cases are demonstrated in Figs 1 and 2.

DISCUSSION

In this single-center prospective clinical study, the FRED was evaluated for the treatment of otherwise untreatable or difficult-to-treat intracranial aneurysms (ie, wide-neck, fusiform, dissecting, blisterlike, or giant). This new generation of intracranial FD appeared to be a promising safe and effective alternative treatment to other FDs for these complex aneurysms. The primary end point for clinical safety (ie, absence of death and major or minor stroke

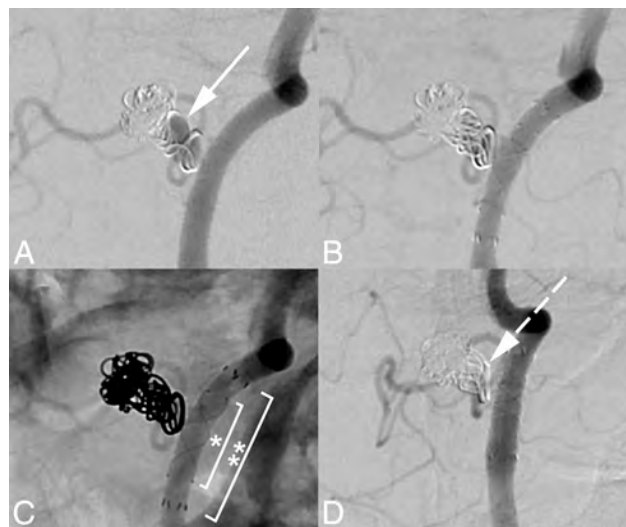


FIG 1. Patient 1 with a 4.4-mm residual aneurysm of the initial posterior inferior cerebellar artery segment close to its origin from the V4 segment of the left vertebral artery (solid white arrow, A). After recoiling, we implanted a FRED 3.5 × 13 mm to cover the orifice of the posterior inferior cerebellar artery origin (B). The flow-diverting working zone (inner stent) is centrally positioned over the posterior inferior cerebellar artery origin (solid white bracket marked with 1 asterisk, C). The outer stent, which provides stable vessel anchorage symmetrically, overlaps the proximal and distal edge of the inner flow-diverting stent. Its distal flared ends are marked with solid white brackets and 2 asterisks (C). At 3-month follow-up, complete occlusion of the residual aneurysm was observed, with no residual inflow (D), which was also verified on different projections and 3D DSA. At the base of the coil basket, the overprojection of a proximal posterior inferior cerebellar artery loop (dashed white arrow, D) simulates residual aneurysm filling, but contrast washes out rapidly at this position after the arterial phase (not shown). Complete occlusion was also confirmed by nonenhanced and enhanced TOF-MRA at 3 and 6 months.

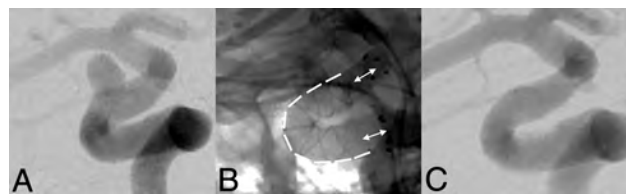


FIG 2. Patient 7 with a 6.5-mm supraclinoid ICA aneurysm (A). In this case, a FRED 4.5 × 25 mm could be placed to cover the aneurysm neck with the inner stent mesh having the flow-diverting effect (dashed white line). Complete wall apposition can be appreciated along the entire carotid siphon (B). The outer stent ensuring stable vessel wall anchorage overlaps the inner flow-diverting stent over 3.5 mm at its proximal and distal ends (double-headed white arrows, B). At its termination, 4 radiopaque tips mark the flared ends. At 3-month follow-up, complete occlusion of the aneurysm could be confirmed on DSA (C) with no residual inflow, which was also confirmed by MR imaging at that time and remained stable at 6-month follow-up.

and absence of transient ischemic attack) was reached in 26/29 (90%) treated patients.

The observed overall permanent morbidity of 3.4% and mortality of 0% in our study was low. In other prospective clinical studies on different intracranial FDs (Pipeline Embolization Device; Covidien, Irvine, California; Silk+, Balt Extrusion; Surpass stent; Stryker Neurovascular, Fremont, California), similar end points occurred with 0%–15% permanent neurologic deficits and 0%–8% mortality.^{7–16}

Altogether, we report in this study that the end point of clinical safety was not achieved in 2 patients with minor ischemic stroke, in whom complete resolution of symptoms was observed after 3-month follow-up and in 1 patient with major ischemic stroke. In the latter patient, the only one with a permanent neurologic deficit, an exceptionally rare and difficult-to-treat aneurysm was targeted. Only repeat DSA but not initial DSA revealed a ruptured aneurysm of a perforator branch of the trunk of the basilar artery. In the literature, only 13 cases were reported with this type of aneurysm.^{18,19} Because this aneurysm was not amenable to any coiling or neck-clipping technique, we decided in favor of treatment with flow diversion by using the FRED. Despite sufficiently effective antiplatelet therapy according to platelet function tests, however, the patient's symptoms, consistent with a delayed perforator stroke 9 hours after FRED deployment, were confirmed by DWI. The exact location and anatomic extension of the ischemic pontine DWI lesion was consistent with delayed occlusion of the perforator branch harboring the aneurysm and was likely the inevitable effect of decreased flow in this vessel.²⁰

In one patient who had microembolic infarcts in the superior cerebellar artery territory, from which she recovered completely at 3-month follow-up, a similar flow-related pathogenesis seems most plausible. In a larger series, only observing 32 posterior circulation aneurysms treated with FDs, Phillips et al¹² reported a permanent neurologic complication rate of 9.4%, with perforator territory infarctions occurring in 14% of the subgroup of patients with basilar artery aneurysms. These authors concluded that treatment with an FD is safe and effective but should be reserved for cases not easily or effectively treatable with conventional endovascular techniques, owing to the high rate of ischemic perforator infarcts following FD use in the posterior circulation and the basilar artery trunk in particular.¹²

Two cases (2/29 patients, 6.9%) of in-stent thrombosis occurred in our study: one appositional clot formation in the acute stage of SAH, which was fully reversible on angiography and without clinical consequences under controlled hypertension together with weight-adapted tirofiban and heparin; and the other at 2 months after termination of prasugrel because of infection of his ventriculoperitoneal shunt requiring surgical intervention for conversion into a ventriculoatrial shunt. No further delayed thromboembolic events after the procedure were detected in any other patient by occurrence of clinical symptoms or by follow-up MR imaging.

In the present trial, FD deployment was technically successful in all cases. Insufficient opening of the FD, which is reported for other available FDs to occur in up to 10% of cases, was not observed in any case for the FRED in our study.^{8,9,16} We elected to perform in-stent PTA of the FRED if the slightest suspicion of incomplete wall apposition arose on the immediate postdeployment control angiograms (5/29 patients, 17%). This operation standard was chosen because we consider the risk of thrombus formation and subsequent parent artery occlusion to be high if suboptimal wall apposition is tolerated.^{11,15} In those 5 cases in which we performed PTA within the FD stent (all were paraophthalmic or supraclinoid ICA aneurysms with sharp angulation of the carotid siphon), opening of the stent before PTA was still near-complete with at least 90% of the stent diameter and was

further improved to 100% after PTA. To ensure proper opening and full deployment of the FRED, we ensured that unsheathing and release of the FRED occurred in a slow and controlled fashion during several minutes by gentle application of the push/pull technique with the delivery microcatheter tip properly held in a central position within the central vessel lumen. However, the operator should be aware that even if these precautions are taken, incomplete opening still may occur, which should prompt complete retrieval of the device by simply resheathing it into the delivery microcatheter.

On follow-up DSA at 3 months, no in-stent stenosis or changes in stent morphology such as "fish mouth" (ie, inward crimping of 1 or both ends of FD) or "foreshortening" phenomena were observed, which were described in an early series by Kocer et al²¹ in 5 cases with a FRED. In our series of 29 patients, we exclusively used the second-generation version of the FRED, which obtained approval for human clinical use within the European community by CE marking in December 2012. Evaluation of the efficacy of occlusion showed promising results for the FRED in otherwise untreatable or difficult-to-treat aneurysms during early follow-up until 3 and 6 months postoperatively. Diagnostic follow-up was achieved not only by invasive angiographic but also MR angiographic evaluation, including contrast-enhanced TOF-MR angiography considered to be sensitive for residual aneurysmal inflow, especially when nonenhanced TOF-MR angiography source images are used for subtraction. At 3-month follow-up, complete occlusion (OKM D) was achieved in 19/34 (56%) aneurysms. At 6-month follow-up, aneurysm occlusion was complete in 22/30 (73%) aneurysms defined as an OKM grade of "D" (complete occlusion), which, on the Raymond and Roy scale, would correspond to grade 1.²²

Compared with other prospective clinical studies on different intracranial FDs (the Pipeline Embolization Device, SILK+, and Surpass), our efficacy rate of 86% in aneurysms of <10 mm was similar to the reported complete occlusion rate at 6 months of 49%–93%.^{7-16,23} However, in aneurysms of >10 mm, our occlusion rates were lower than the rates reported in the Pipeline Embolization Device for Uncoilable or Failed Aneurysms trial¹⁵ and in the recent meta-analysis from Brinjikji et al.²³ One possible explanation is that the low number of aneurysms of >10 mm in our study ($n = 11$) might have led to deviations from the population mean, which, due to the larger group size, might have been estimated more accurately in a larger study such as the Pipeline Embolization Device for Uncoilable or Failed Aneurysms trial, for example. Another possible explanation is that we required the 6-month follow-up to include TOF-MRA and applied rigorous aneurysm evaluation of nonenhanced TOF, contrast-enhanced TOF and, importantly, also on subtracted TOF images on which we rated any suspicion of residual inflow or very slow inflow as noncomplete occlusion.

In experimental aneurysm models and also in human studies, it could be regularly observed that FD stents can induce complete and stable occlusion of the aneurysm sac by stasis of flow and subsequent thrombosis, even without additional introduction of coils. In 10 patients, aneurysm occlusion was observed after adjunctive use of coils, introduced by a jailed microcatheter during the same treatment session before FD deployment. In our current

practice, we use adjunctive coiling if aneurysms are large or giant, in the acute stage of SAH, or in cases of retreatment/recurrence of previously ruptured aneurysms pretreated by coiling. The primary rationale for adjunctive coiling in our view is to prevent aneurysm rupture and to enhance stable long-term occlusion.²⁴ Additional coiling may not only prevent early or delayed rupture but also, especially for extremely wide-neck aneurysms, provide good mechanical support and stabilization for FD deployment and a stable long-term position, in that (partial) herniation or bulging of the FD into the aneurysm sac can be avoided.

The recently introduced FRED may offer several potential advantages over other currently available intracranial FDs: 1) Due to its dual-layer design and availability in long sizes of up to 56 mm, the scaffolding effect of the stent for obtaining outward stability toward the wall of the parent vessel seems to be enhanced and, most important, is achievable in a single treatment session, which makes this device especially useful in fusiform or giant aneurysms, whereas 2 sequential procedures might have been necessary before (scaffolding stent first followed by FD implantation). 2) The outer stent is woven with 16 wires leading to lower friction within the delivery microcatheter, thus facilitating deployment especially of longer stents—other available FDs, for example, are composed of 48 wires (Silk+ and Pipeline Embolization Device) or 96 wires (Surpass). 3) The additive radial force vectors of the inner and outer stent provide a high degree of reliability of stent opening, a feature especially critical when deployment includes ICA segments around the carotid siphon. 4) There is improved lamination of blood flow through its dual-layer design and higher pore attenuation with 16 + 48 wires compared with 48 wires of the Pipeline Embolization Device and Silk.^{16,25,26} 5) There is lower vessel wall coverage in the longitudinal direction because of the shorter inner stent (shortest available on the market), which is designed to limit the working layer mainly to the neck of the aneurysm and to spare adjacent branches or perforator arteries, to maintain the patency of these vessels. 6) There is enhanced visibility of the central stent segment and of its distal and proximal ends.

We acknowledge that the major limitations of this prospective study include the limited number of 29 patients, a short follow-up period, MRA only after 6 months, and lack of randomized comparisons with other potentially efficacious therapies. Furthermore, most aneurysms were located at the paraophthalmic segment of the ICA, the mean aneurysm size was relatively small, and not all cases were treated solely by FDs but additional coiling was performed in some cases. However, recruitment followed clearly defined criteria of inclusion/exclusion, and clinical/radiologic follow-up was rigorous, including not only invasive angiography but also MR imaging to measure accurately the shrinkage of the aneurysm sac and also nonenhanced and contrast-enhanced TOF-MR angiography to detect even small amounts of slow residual inflow that may be silent on invasive angiography. Furthermore, our cohort is the largest so far in which the safety and efficacy profile of this new generation of intracranial FDs has been investigated and may serve as a basis for subsequent larger and multicenter studies.

CONCLUSIONS

The FRED for treatment of difficult-to-treat or otherwise untreatable intracranial aneurysms was prospectively observed in this clinical study to provide a high degree of safety and efficacy, measured as complete aneurysm occlusion on DSA and MR imaging during 6-month follow-up. Long-term durability and safety still remain to be proved by larger series and after prolonged follow-up. We report that it is reasonable, safe, and effective to use intracranial FDs such as the FRED, especially for targeting otherwise untreatable or difficult-to-treat complex intracranial aneurysms.

Disclosures: Christian Herweh—UNRELATED: *Travel/Accommodations/Meeting Expenses Unrelated to Activities Listed*: Microvention, *Comments*: Brain AVM Congress 2014 (Nancy, France), travel expenses and registration fee. Peter A. Ringelb—UNRELATED: *Consultancy*: Boehringer Ingelheim, Bayer; *Grants/Grants Pending*: German Research Foundation; *Payment for Lectures (including service on Speakers Bureaus)*: Boehringer Ingelheim, Bayer, Bristol-Myers Squibb, Pfizer, PAION; *Payment for Development of Educational Presentations*: Boehringer Ingelheim; *Travel/Accommodations/Meeting Expenses Unrelated to Activities Listed*: Bayer. Martin Bendszus—UNRELATED: *Board Membership*: data and safety monitoring board Vascular Dynamics; *Consultancy*: Codman, Roche, Guerbet; *Payment for Lectures (including service on Speakers Bureaus)*: Roche, Novartis, Guerbet, Codman. Mirko Pham—UNRELATED: *Other*: Memorial Stipend from Else-Kröner-Fresenius-Foundation.

REFERENCES

1. Alshekhlee A, Mehta S, Edgell RC, et al. **Hospital mortality and complications of electively clipped or coiled unruptured intracranial aneurysm.** *Stroke* 2010;41:1471–76
2. Brinjikji W, Rabinstein AA, Nasr DM, et al. **Better outcomes with treatment by coiling relative to clipping of unruptured intracranial aneurysms in the United States, 2001–2008.** *AJNR Am J Neuroradiol* 2011;32:1071–75
3. Molyneux A, Kerr R, Stratton I, et al. **International Subarachnoid Aneurysm Trial (ISAT) of neurosurgical clipping versus endovascular coiling in 2143 patients with ruptured intracranial aneurysms: a randomized trial.** *Lancet* 2002;360:1267–74
4. White PM, Lewis SC, Gholkar A, et al. **Hydrogel-coated coils versus bare platinum coils for the endovascular treatment of intracranial aneurysms (HELPS): a randomised controlled trial.** *Lancet* 2011;377:1655–62
5. Moret J, Cognard C, Weill A, et al. **The “Remodelling Technique” in the treatment of wide neck intracranial aneurysms: angiographic results and clinical follow-up in 56 cases.** *Interv Neuroradiol* 1997;3:21–35
6. Shapiro M, Becske T, Sahlein D, et al. **Stent-supported aneurysm coiling: a literature survey of treatment and follow-up.** *AJNR Am J Neuroradiol* 2012;33:159–63
7. Lylyk P, Miranda C, Ceratto R, et al. **Curative endovascular reconstruction of cerebral aneurysms with the Pipeline embolization device: the Buenos Aires experience.** *Neurosurgery* 2009;64:632–42; discussion 642–43; quiz N6
8. Lubicz B, Collignon L, Raphaeli G, et al. **Flow-diverter stent for the endovascular treatment of intracranial aneurysms: a prospective study in 29 patients with 34 aneurysms.** *Stroke* 2010;41:2247–53
9. Byrne JV, Beltechi R, Yarnold JA, et al. **Early experience in the treatment of intra-cranial aneurysms by endovascular flow diversion: a multicentre prospective study.** *PLoS One* 2010;5. pii: e12492
10. Nelson PK, Lylyk P, Szikora I, et al. **The Pipeline embolization device for the intracranial treatment of aneurysms trial.** *AJNR Am J Neuroradiol* 2011;32:34–40
11. McAuliffe W, Wycoco V, Rice H, et al. **Immediate and midterm results following treatment of unruptured intracranial aneurysms with the Pipeline embolization device.** *AJNR Am J Neuroradiol* 2012;33:164–70
12. Phillips TJ, Wenderoth JD, Phatouros CC, et al. **Safety of the Pipeline**

- embolization device in treatment of posterior circulation aneurysms.** *AJNR Am J Neuroradiol* 2012;33:1225–31
13. Pistocchi S, Blanc R, Bartolini B, et al. **Flow diverters at and beyond the level of the circle of Willis for the treatment of intracranial aneurysms.** *Stroke* 2012;43:1032–38
 14. Yu SC, Kwok CK, Cheng PW, et al. **Intracranial aneurysms: midterm outcome of Pipeline embolization device: a prospective study in 143 patients with 178 aneurysms.** *Radiology* 2012;265:893–901
 15. Becske T, Kallmes DF, Saatci I, et al. **Pipeline for uncoilable or failed aneurysms: results from a multicenter clinical trial.** *Radiology* 2013;267:858–68
 16. De Vries J, Boogaarts J, Van Norden A, et al. **New generation of flow diverter (Surpass) for unruptured intracranial aneurysms: a prospective single-center study in 37 patients.** *Stroke* 2013;44:1567–77
 17. O’Kelly CJ, Krings T, Fiorella D, et al. **A novel grading scale for the angiographic assessment of intracranial aneurysms treated using flow diverting stents.** *Interv Neuroradiol* 2010;16:133–37
 18. Gross BA, Puri AS, Du R. **Basilar trunk perforator artery aneurysms: case report and literature review.** *Neurosurg Rev* 2013;36:163–68
 19. Chalouhi N, Jabbour P, Starke RM, et al. **Treatment of a basilar trunk perforator aneurysm with the Pipeline embolization device: case report.** *Neurosurgery* 2014;74:E697–701
 20. Roszelle BN, Babiker MH, Hafner W, et al. **In vitro and in silico study of intracranial stent treatments for cerebral aneurysms: effects on perforating vessel flows.** *J Neurointerv Surg* 2013;5:354–60
 21. Kocer N, Islak C, Kizilkilic O, et al. **Flow Re-direction Endoluminal Device in treatment of cerebral aneurysms: initial experience with short-term follow-up results.** *J Neurosurg* 2014;120:1158–71
 22. Raymond J, Guilbert F, Weill A, et al. **Long-term angiographic recurrences after selective endovascular treatment of aneurysms with detachable coils.** *Stroke* 2003;34:1398–403
 23. Brinjikji W, Murad MH, Lanzino G, et al. **Endovascular treatment of intracranial aneurysms with flow diverters: a meta-analysis.** *Stroke* 2013;44:442–47
 24. Kulcsár Z, Houdart E, Bonafé A, et al. **Intra-aneurysmal thrombosis as a possible cause of delayed aneurysm rupture after flow-diversion treatment.** *AJNR Am J Neuroradiol* 2011;32:20–25
 25. Kim M, Levy EI, Meng H, et al. **Quantification of hemodynamic changes induced by virtual placement of multiple stents across a wide-necked basilar trunk aneurysm.** *Neurosurgery* 2007;61:1305–12; discussion 1312–13
 26. Crowley RW, Evans AJ, Kassell NF, et al. **Endovascular treatment of a fusiform basilar artery aneurysm using multiple “in-stent stents.”** *J Neurosurg Pediatr* 2009;3:496–500

Retrieval of Migrated Coils with Stent Retrievers: An Animal Study

O. Nikoubashman, R. Pjontek, M.-A. Brockmann, R. Tolba, and M. Wiesmann

ABSTRACT

BACKGROUND AND PURPOSE: Coil migration is a potentially serious complication of endovascular aneurysm treatment. The aim of the study was to systematically investigate the effectiveness of coil retrieval with a stent retriever in an animal model.

MATERIALS AND METHODS: A total of 148 coils of various types and sizes were placed into arteries of varying diameters in a porcine in vivo model. Coil retrieval was performed by placing a Trevo ProVue stent retriever over the coil and trying to trap a part of the platinum coil within the stent mesh by advancing the microcatheter over the stent or simply by retrieving the stent without trying to trap the coil by advancing the microcatheter.

RESULTS: Coil retrieval was successful in 101 of 102 cases (99%), in which trapping of the coil within the stent retriever by advancing the microcatheter was applied. When we only pulled back the stent without trapping the coil, retrieval was successful in only 5 of 46 cases (11%). Coil type, coil structure (2D versus 3D), actual coil shape in the affected vessel, investigator experience, aspiration, coil localization, and vessel diameter had no significant influence on retrieval outcome. There was no case of vessel perforation.

CONCLUSIONS: Retrieval of migrated platinum coils with a stent retriever is an effective treatment option for migrated coils when the correct technique is applied.

ABBREVIATION: GDC = Guglielmi detachable coil

Brain aneurysms are the most common cause of severe and potentially lethal subarachnoid hemorrhage. Endovascular treatment with detachable coils has become a common option for both ruptured and unruptured cerebral aneurysms, especially if surgery is challenging.¹⁻⁴ Coil migration is a potentially serious complication of endovascular treatment that has been reported in up to 2%–6% of cases.^{5,6} Various rescue devices have been suggested for retrieval of migrated platinum coils. However, data in the literature dealing with the effectiveness and complication rates of the respective methods are restricted to a few case reports and small case series.⁵⁻⁷ Our aim was to systematically investigate the effectiveness and complication rates of coil retrieval with a stent retriever in an animal model.

MATERIALS AND METHODS

Proof of Concept

Proof of concept was first verified in a small in vitro study, consisting of 10 coil retrievals with a stent retriever in an in-house glass model.

Animal Preparation

All experiments were performed on 4 female German Landrace swine (weight, ~60 kg). The experiments were performed in accordance with the German legislation governing animal studies following the “Guide for the Care and Use of Laboratory Animals” (National Research Council, 8th edition, 2011) and the “Directive 2010/63/EU on the Protection of Animals Used for Scientific Purposes” (*EU Official Journal*, 2010). Official permission was granted from the governmental animal care and use office (Landesamt für Natur, Umwelt und Verbraucherschutz Nordrhein-Westfalen, Recklinghausen, Germany).

All animals received premedication with atropine (1.5 mL, 1%; Atropin), azaperone (0.1 mL/kg; Stresnil), and ketamine (0.1 mL/kg, 10%; Ketamin) followed by intubation and mechanical ventilation with an oxygen-air mixture. Anesthesia was maintained with propofol (2%, 8–12 mg/kg/hour), fentanyl (45–90 µg/kg/hour), and pentobarbital (160 mg/mL; Narcoren). All an-

Received September 22, 2014; accepted after revision December 11.

From the Department of Neuroradiology (O.N., R.P., M.-A.B., M.W.) and Institute for Laboratory Animal Science and Experimental Surgery (R.T.), University Hospital Aachen, Aachen, Germany; and Medical Imaging Physics (O.N.), Institute of Neuroscience and Medicine 4, Forschungszentrum Jülich, Jülich, Germany.

Please address correspondence to Martin Wiesmann, MD, PhD, Klinik für Diagnostische und Interventionelle Neuroradiologie, Universitätsklinikum Aachen, Pauwelsstr 30, 52074 Aachen, Germany; e-mail: mwiesmann@ukaachen.de

<http://dx.doi.org/10.3174/ajnr.A4240>

imals received heparin (5000 IU), acetylsalicylic acid (500 mg; aspirin), and nimodipine intravenously (2–4 mg, Nimotop). Constant saline infusion was performed in all animals to prevent dehydration. All animals had a normal vascular status.

Protocol

One experienced neurointerventionalist (M.W., 15 years of interventional experience) and 1 less experienced neurointerventionalist (O.N., 1 year of interventional experience) performed all procedures in random order. The type of coil and the target vessels were randomly assigned. When coils were placed in a target vessel, final coil localization was left to blood flow and was not manipulated by the investigators. Every coil type was retrieved by using the standard retrieval technique and the advanced retrieval technique with intentional trapping of the coil as described in detail below. Experiments were performed with and without aspiration via the guide catheter during retrieval in alternating order according to a predefined protocol. Consequently, every coil type was retrieved with and without aspiration and with and without intentional trapping, respectively.

Procedure

All procedures were performed under fluoroscopy by using a single-plane angiography system (Axiom Artis dFC; Siemens, Erlangen, Germany). Iopamidol (Solutrast, 300 mg/mol, diluted in an 8:2 ratio with a saline solution; Bracco Imaging, Konstanz, Germany) was used as a contrast agent.

The target vessels (subclavian artery and its first branches) were reached by using a 6F Envoy MPD guiding catheter with an angled tip (Codman & Shurtleff, Raynham, Massachusetts) supported by a 0.035-inch standard angled Radifocus Guide wire (Terumo, Tokyo, Japan).

Target vessels were catheterized with an Excelsior SL-10 microcatheter (Boston Scientific, Natick, Massachusetts) over a Synchro-2 soft 14 microguidewire (Boston Scientific). A coil was placed and detached by using its respective detaching mechanism. We applied the following coils: Guglielmi detachable coil (GDC)-10 360 Standard (4 mm × 7 cm), GDC-10 3D Standard (4 mm × 8 cm), GDC-10 Soft 2D SR (3 mm × 6 cm and 6 mm × 8 cm), GDC-10 Soft SR (3 mm × 6 cm, 3 mm × 14 cm, and 6 mm × 11 cm), GDC-10 UltraSoft (3 mm × 6 cm and 4 mm × 8 cm), Matrix² 2D Soft SR (6 mm × 10 mm), and Matrix² 3D Standard (3 mm × 6 cm and 4 mm × 8 cm) (all Stryker, Kalamazoo, Michigan).

After a coil migrated to its final position, retrieval was performed by using a Trevo ProVue (4-mm-diameter) stent retriever (Stryker) in combination with its supplied microcatheter (Trepo MC18; Stryker). The basic steps were as follows: The coil was passed with the microwire, over which the microcatheter was advanced. After removal of the microwire, the stent retriever was advanced and positioned so that the coil was located in the first two-thirds of the stent retriever. Next, the stent retriever was unsheathed. Retrieval was performed in 2 different manners: 1) Standard thrombectomy technique: the microcatheter and stent retriever were simultaneously pulled into the guiding catheter, without intentional trapping of the coil. 2) A retrieval technique as described by O'Hare et al⁸: the microcatheter and stent re-

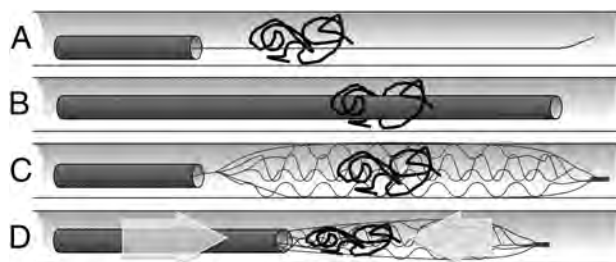


FIG 1. Illustration of the advanced retrieval technique with intentional trapping of the coil: The coil is passed with the microwire (A) followed by the microcatheter (B). Note that displacement of the coil might be encountered. The stent retriever should cover the coil with its distal two-thirds (C). The microcatheter is pushed forward while gently pulling back the stent retriever at the same time (D) to trap the coil. A resistance signals that the coil has been locked within the stent. At this point, both the microcatheter and the stent retriever are carefully withdrawn under fluoroscopic control.

triever were simultaneously pulled into the guiding catheter, with intentional trapping of the coil (see below).

Retrieval was considered successful only when complete coil retrieval was achieved. Retrieval duration was defined as the time between positioning of the microwire and retrieval of the system. An aspiration pump (Penumbra, Alameda, California) connected to the guiding catheter provided constant aspiration during retrieval in selected cases (see above). After each extraction, the vessels were examined for occlusion, vasospasm, and perforation in DSA.

Advanced Coil-Retrieval Technique

While delivery and unsheathing of the stent retriever are identical to the technique used for thrombectomy in stroke, there are important differences. When one unsheathes the stent retriever, the coil should be positioned within the first two-thirds of the stent retriever (Fig 1C). Note that displacement of the coil may be encountered when positioning the microcatheter (Fig 1A, -B). After one unsheathes the stent retriever (Fig 1A–C), the aim is to lock parts of the coil within the stent retriever. Therefore, the stent retriever is partially resheathed by carefully pushing the microcatheter and slightly pulling the stent retriever at the same time (Fig 1D). A resistance, which might be elastic at first, signals that parts of the coil have been caught within the stent, making further resheathing impossible. If there is no resistance, the procedure should be repeated because the coil is most likely not sufficiently locked within the stent. Although trapping the coil usually fixates the stent retriever within the microcatheter, the stent retriever should be secured against movement in relation to the microcatheter.

Sometimes it might be difficult (and sometimes impossible) to pass the coil with the microcatheter. In these cases, we placed the microcatheter proximal to the coil and carefully pushed the stent retriever into the coil (Fig 2). Even though we used this technique 16 times without complications, it most probably is associated with an increased perforation risk. Therefore, it should only be performed after careful risk-benefit analysis.

Once the coil is trapped, both microcatheter and stent retriever should be carefully withdrawn under fluoroscopic control (Fig 3).

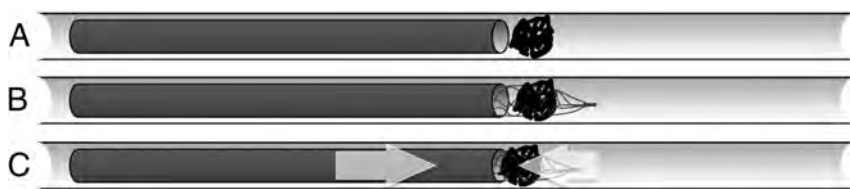


FIG 2. Illustration of the retrieval technique applied if passage of the coil with the microcatheter is not possible. In this case, the microcatheter should be positioned directly proximal to the coil (A). The stent retriever is carefully pushed into the coil (B) and the microcatheter is pushed forward while gently pulling back the stent retriever at the same time (C) to trap the coil. A resistance signals that the coil has been locked within the stent. The microcatheter and the stent retriever are then withdrawn as described in Fig 1. Note that this technique is likely to be associated with an increased risk of vessel perforation and thus should only be performed after careful risk-benefit analysis.

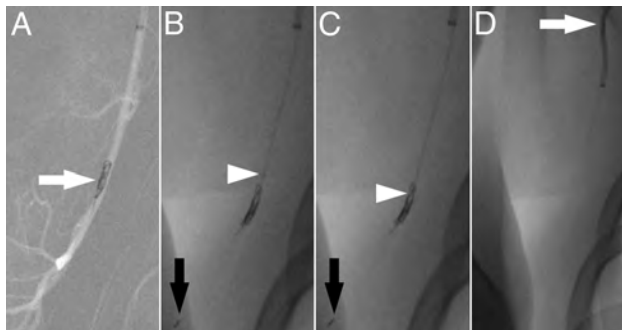


FIG 3. A GDC-10 Soft SR coil (3 mm × 6 cm) migrated into a musculoskeletal branch of the axillary artery (A, arrow). The stent retriever is unsheathed with the distal two-thirds of the stent retriever covering the coil (B). The distal tip of the stent retriever is marked with a black arrow (B and C). The microcatheter is being pushed (B and C, white arrowhead) while slightly pulling the stent retriever backward until a resistance is felt to trap the coil. Once the coil is locked, both the microcatheter and the stent retriever are carefully withdrawn into the guiding catheter (D, arrow).

Statistical Analyses

Standard statistical tests (Student *t* test, Pearson χ^2 test, Fisher exact test) were performed when applicable. *P* values under the α level of .05 were significant. All statistical analyses were performed with SPSS 20 software (IBM, Armonk, New York).

RESULTS

Preliminary In Vitro Experiment

In a preliminary experiment, a GDC-10 Soft SR (3 mm × 6 cm) coil was retrieved 5 times with a Solitaire stent (Covidien, Irvine, California) and 5 times with a Trevo ProVue stent retriever in an in-house glass model. The coil was intentionally trapped and successfully retrieved in all 10 experiments.

Animal Study

A total of 148 extractions were performed in 4 swine. Each investigator performed 74 retrievals. The advanced retrieval technique with intentional trapping of the coil was applied in 102 experiments (69%). Retrieval was assisted by aspiration in 71 of 148 cases (48%). In 132 cases (89%), it was possible to pass the coil with the microcatheter, and the stent retriever was unsheathed over the coil by pulling back the microcatheter. In 16 cases (11%), it was not possible to pass the coil with the microcatheter, and the stent retriever was carefully pushed over the coil (Fig 2). Mean

duration of retrieval was 1.35 ± 0.637 minutes (range, 1–3 minutes).

Retrieval was successful in 106 (72%) of all 148 cases. Overall, retrieval failed in 42 cases. More precisely, retrieval was not possible at all in 22 of 42 unsuccessful cases (15%), while a coil was initially captured but lost in the remaining 20 of 42 unsuccessful cases (14%). Retrieval was successful in 101 of 102 cases (99%) when the advanced retrieval technique with intentional trapping of the coil was applied (Fig 3). One of the 20 cases with loss of an initially captured coil occurred

when intentional trapping of the coil failed to fixate the coil sufficiently. When applying the standard retrieval technique (ie, retrieval without trapping of the coil), retrieval was successful in only 5 of 46 cases (11%).

There was no case of vessel perforation, vasospasm, or occlusion.

Localization and Specification of Used Coils

Coil localization was in the distal subclavian artery in 52 cases (35%), in the internal thoracic artery in 34 cases (23%), in the vertebral artery in 12 cases (8%), and in musculoskeletal branches of the axillary artery in 50 cases (34%). Mean vessel diameter was as follows—subclavian artery: 3.4 ± 1.2 mm; internal thoracic artery: 2.2 ± 0.39 mm; vertebral artery: 2.8 ± 0.45 mm; and musculoskeletal branches of the axillary artery: 2.7 ± 0.72 mm. Mean vessel diameter of all arteries was 2.8 ± 0.95 mm (range, 1.6–5.5 mm).

The frequency of coil retrieval was as follows—GDC-10 Standard 360: 20 times; GDC-10 3D Standard: 22 times; GDC-10 Soft 2D SR: 22 times; GDC-10 Soft SR: 20 times; GDC-10 ULTRASOFT: 22 times; Matrix² 2D Soft SR: 22 times; and Matrix² 3D Standard: 22 times.

Coil diameter was larger than the arterial diameter in 126 cases (85%) and equal to the arterial diameter in the remaining 22 cases (15%). Coils were in their respective designated shape in 33 cases (22%) and elongated in the remaining 115 cases (78%). Mean coil diameter was 4.3 ± 1.252 mm (range, 3–6 mm) and mean coil length was 7.9 ± 1.7 cm (range, 6–14 cm).

Retrieval Rates and Confounding Factors

Retrieval was significantly more likely when the advanced retrieval technique with intentional trapping of the coil was applied ($P < .001$, Pearson χ^2 test). Considering all 148 experiments, successful retrieval was more likely for small and short coils ($P = .041$ and $.014$, respectively, Student *t* test). However, coil size and length had no significant influence, when applying the advanced retrieval technique ($P = .828$ and $P = .638$, respectively; Student *t* test).

Coil type ($P = .476$, Pearson χ^2 test), coil structure (2D versus 3D) ($P = .828$, Pearson χ^2 test), actual coil configuration (designated shape versus elongated shape) ($P = .142$, Pearson χ^2 test), investigator experience ($P = 1.00$, Pearson χ^2 test), aspiration ($P = .155$, Pearson χ^2 test), coil localization ($P = .218$, Pearson χ^2

test), and mean vessel diameter ($P = .508$, Student t test) had no significant influence on retrieval success rates.

DISCUSSION

Coiling of wide-neck, giant, or very small aneurysms can be challenging. Even though stent or balloon-assisted techniques reduce the risk of complications, coil migration has been reported to occur in up to 2%–6% of cases.^{5,6} Whereas marginally herniated coils in an otherwise sufficiently embolized aneurysm are usually treated with temporary oral antiplatelet therapy until endothelialization of the herniated coil segment is complete, more prominently herniated coils can be adapted to the vessel wall by using a stent and likewise need to be treated with temporary oral antiplatelet therapy.^{9,10} Migrated coils, however, usually need to be retrieved immediately because they pose a high risk for subsequent vessel occlusion causing cerebral ischemia or death. This is why neurointerventionalists should always be prepared for immediate retrieval of migrated coils. However, many neurointerventionalists lack sufficient experience with dedicated retrieval devices (eg, “snare” devices or Alligator Retrieval Device; Chestnut Medical Technologies, Menlo Park, California). Moreover, dedicated retrieval devices may not be available in all neurovascular centers. Most neurointerventionalists, however, have become familiar with stent retrievers that are being used in acute stroke treatment. Thus, the results of our investigation might prove helpful and could be a viable way for most neurointerventionalists to retrieve a migrated coil.

There is no established standard procedure for the retrieval of migrated coils. Data dealing with endovascular coil retrieval consist of case reports and small case series.

Common retrieval techniques involve endovascular retrieval devices, namely the Alligator device or so-called snare devices, which have also been referred to as “lasso” devices (eg, Amplatz goose neck snares and microsnare; Covidien, Irvine, California).^{5,7,11–16} Coil retrieval with a snare or lasso device was successful in 28 of 33 (85%) cases.^{5,7,11–19} Coil retrieval with an Alligator device was successful in 1 of 2 reported cases.^{14,20} In past years, coil retrieval with stent retrievers, namely the Solitaire, the Trevo, and the Catch system (Balt, Montmorency, France) was reported.^{7,20,21} All 18 reported coil retrievals with these devices were successful.^{7,20,21} Coil retrieval with a Merci retriever (Concentric Medical, Mountain View, California) was successful in all 3 reported cases.^{22–24} Less common techniques involve trapping of a migrated coil between 2 wires,^{17,25} manual aspiration,²⁶ and coil retrieval with an Enterprise self-expanding stent (Codman & Shurtleff).²⁷

Overall, coil retrieval with a stent retriever device appears to be an effective treatment option, regardless of the stent retriever design.^{7,19–21} Consistent with our own experience, coil retrieval with a stent retriever is reported to be less challenging and to require less manipulation than coil retrieval with snare devices and the Alligator device.⁷ Especially, access to distal or curved vessels with the Alligator device can be very challenging, given its relatively stiff tip.

In our series, coil retrieval was successful in 101 of 102 cases (99%) when trapping of the coil within the stent was applied, regardless of coil type, coil structure (2D versus 3D), actual coil

shape in the affected vessel, investigator experience, additional aspiration, coil localization, and the diameter of the affected artery. When intentional trapping was desired, the only case with a lost coil occurred when the investigator noticed no resistance when the stent retriever and microcatheter were moved against each other.

There was no case of vasospasm or immediate vessel occlusion, which is most likely due to premedication with acetylsalicylic acid and nimodipine in our experiments. Because our swine model does not allow the detection of small thrombotic emboli during coil withdrawal, we recommend constant proximal aspiration during coil withdrawal and we advise the administration of acetylsalicylic acid or a glycoprotein IIb/IIIa antagonist to minimize the risk of local thrombosis and/or thrombotic embolism. In addition, intravenous administration of nimodipine should be considered if vasospasms are encountered. Furthermore, hypertension should be induced whenever possible to counteract reduced blood flow in the occluded territory. We also found that it is usually not possible to fully resheath the stent retriever due to the trapped coil. The exposed end of the stent retriever might get stuck during withdrawal when the treated aneurysm or a pre-existing stent have to be passed. A distal-access guiding catheter covering the stent retriever should be considered in these cases.

Limitations

Coil retrieval is an emergency procedure that cannot be examined systematically in humans. Even though data from an animal model cannot be transferred to humans without restrictions (eg, that peripheral swine vessels might be less susceptible to perforations compared with human cerebral vessels or that our swine model did not allow detection of thrombotic emboli), swine represent an established animal model for endovascular procedures, given their comparable vascular anatomy and coagulation.²⁸ To anticipate differences between humans and swine, we examined coil retrieval in vessels that are comparable with affected human vessels with regard to size, blood flow, and accessibility. A further limitation is that an experiment that involves all possible combinations of coils, vessels, and stent retrievers is practically impossible. Conscious of this limitation, we decided to retrieve various coils in various settings while keeping the rest of the study standardized to maximize statistical validity.

CONCLUSIONS

The results from our systematic animal study imply that stent retrievers can be considered an effective treatment option for retrieval of migrated coils in a vast variety of settings.

ACKNOWLEDGMENTS

The authors thank Anna Woitok and Thaddäus Stopinski for their skillful technical assistance during the animal studies.

Disclosures: Martin Wiesmann—UNRELATED: Consultancy: Stryker Neurovascular, Philips Healthcare; Payment for Lectures (including service on Speakers Bureaus): Boston Scientific, Bracco, Siemens, Stryker; Payment for Development of Educational Presentations: Abbott,* ab medica,* Acandis,* Bayer,* Bracco,* B. Braun,* Codman Neurovascular,* Covidien,* Dahlhausen,* MicroVention,* Penumbra,* Phenox,* Philips Healthcare,* St. Jude,* Stryker.* *Money paid to the institution.

REFERENCES

1. Molyneux AJ, Kerr RS, Yu LM, et al. **International Subarachnoid Aneurysm Trial (ISAT) of neurosurgical clipping versus endovascular coiling in 2143 patients with ruptured intracranial aneurysms: a randomised comparison of effects on survival, dependency, seizures, rebleeding, subgroups, and aneurysm occlusion.** *Lancet* 2005;366:809–17
2. van Gijn J, Kerr RS, Rinkel GJ. **Subarachnoid haemorrhage.** *Lancet* 2007;369:306–18
3. Chalouhi N, Tjoumakaris S, Gonzalez LF, et al. **Coiling of large and giant aneurysms: complications and long-term results of 334 cases.** *AJNR Am J Neuroradiol* 2014;35:546–52
4. Huang Q, Liu J, Zhao R, et al. **The safety and efficacy of stenting in the treatment of complex posterior cerebral artery aneurysms: a seven-case report and literature review.** *Clin Neuroradiol* 2013;23:175–87
5. Lampmann LE, Sluzewski M, Van Rooij WJ. **Retrieval of malpositioned, dislocated or fractured Guglielmi detachable coils from intracranial vessels: a report of seven cases.** *Interv Neuroradiol* 2000;6:251–56
6. Ding D, Liu KC. **Management strategies for intraprocedural coil migration during endovascular treatment of intracranial aneurysms.** *J Neurointerv Surg* 2014;6:428–31
7. Leslie-Mazwi TM, Heddier M, Nordmeyer H, et al. **Stent retriever use for retrieval of displaced microcoils: a consecutive case series.** *AJNR Am J Neuroradiol* 2013;34:1996–99
8. O'Hare AM, Rogopoulos AM, Stracke PC, et al. **Retrieval of displaced coil using a Solitaire(R) stent.** *Clin Neuroradiol* 2010;20:251–54
9. Schütz A, Solymosi L, Vince GH, et al. **Proximal stent fixation of fractured coils: technical note.** *Neuroradiology* 2005;47:874–78
10. Luo CB, Chang FC, Teng MM, et al. **Stent management of coil herniation in embolization of internal carotid aneurysms.** *AJNR Am J Neuroradiol* 2008;29:1951–55
11. Dinc H, Kuzeyli K, Kosucu P, et al. **Retrieval of prolapsed coils during endovascular treatment of cerebral aneurysms.** *Neuroradiology* 2006;48:269–72
12. Fiorella D, Albuquerque FC, Deshmukh VR, et al. **Monorail snare technique for the recovery of stretched platinum coils: technical case report.** *Neurosurgery* 2005;57(1 suppl):E210; discussion E210
13. Koseoglu K, Parildar M, Oran I, et al. **Retrieval of intravascular foreign bodies with goose neck snare.** *Eur J Radiol* 2004;49:281–85
14. Henkes H, Lownes S, Preiss H, et al. **A new device for endovascular coil retrieval from intracranial vessels: Alligator retrieval device.** *AJNR Am J Neuroradiol* 2006;27:327–29
15. Prestigiacomo CJ, Fidlow K, Pile-Spellman J. **Retrieval of a fractured Guglielmi detachable coil with use of the Goose Neck snare 'twist' technique.** *J Vasc Interv Radiol* 1999;10:1243–47
16. Watanabe A, Hirano K, Mizukawa K, et al. **Retrieval of a migrated detachable coil: case report.** *Neurol Med Chir (Tokyo)* 1995;35:247–50
17. Lee CY. **Use of wire as a snare for endovascular retrieval of displaced or stretched coils: rescue from a technical complication.** *Neuroradiology* 2011;53:31–35
18. Raftopoulos C, Goffette P, Billa RF, et al. **Transvascular coil hooking procedure to retrieve an unraveled Guglielmi detachable coil: technical note.** *Neurosurgery* 2002;50:912–14; discussion 914–15
19. Zoarski GH, Bear HM, Clouston JC, et al. **Endovascular extraction of malpositioned fibered platinum microcoils from the aneurysm sac during endovascular therapy.** *AJNR Am J Neuroradiol* 1997;18:691–95
20. Liu KC, Ding D, Starke RM, et al. **Intraprocedural retrieval of migrated coils during endovascular aneurysm treatment with the Trevo Stentriever device.** *J Clin Neurosci* 2014;21:503–06
21. Hopf-Jensen S, Hensler HM, Preiss M, et al. **Solitaire(R) stent for endovascular coil retrieval.** *J Clin Neurosci* 2013;20:884–86
22. Kung DK, Abel TJ, Madhavan KH, et al. **Treatment of endovascular coil and stent migration using the Merci retriever: report of three cases.** *Case Report Med* 2012;2012:242101
23. O'Hare A, Brennan P, Thornton J. **Retrieval of a migrated coil using an X6 MERCI device.** *Interv Neuroradiol* 2009;15:99–102
24. Vora N, Thomas A, Germanwala A, et al. **Retrieval of a displaced detachable coil and intracranial stent with an L5 Merci retriever during endovascular embolization of an intracranial aneurysm.** *J Neuroimaging* 2008;18:81–84
25. Standard SC, Chavis TD, Wakhloo AK, et al. **Retrieval of a Guglielmi detachable coil after unraveling and fracture: case report and experimental results.** *Neurosurgery* 1994;35:994–98; discussion 999
26. Stidd DA, Johnson AK, Lopes DK. **Manual aspiration technique to retrieve a prematurely detached coil during cerebral aneurysm embolization.** *Neurointervention* 2014;9:21–25
27. Wakhloo AK, Gounis MJ. **Retrievable closed cell intracranial stent for foreign body and clot removal.** *Neurosurgery* 2008;62(5 suppl 2):ONS390–93; discussion ONS393–94
28. Bouzeghrane F, Naggara O, Kallmes DF, et al. **In vivo experimental intracranial aneurysm models: a systematic review.** *AJNR Am J Neuroradiol* 2010;31:418–23

Fenestrations of Intracranial Arteries

S.B.T. van Rooij, R.S. Bechan, J.P. Peluso, M. Sluzewski, and W.J. van Rooij

ABSTRACT

BACKGROUND AND PURPOSE: Few data are available on the frequency and location distribution of fenestrations of intracranial arteries. We used 3D rotational angiography of all intracranial arteries in a cohort of 179 patients with suspected intracranial aneurysms to assess the prevalence and location of fenestrations and the relation of fenestrations to aneurysms.

MATERIALS AND METHODS: Of 179 patients with subarachnoid hemorrhage admitted between March 2013 and June 2014, 140 had 3D rotational angiography of all cerebral vessels. The presence and location of aneurysms and fenestrations were assessed. In patients with both aneurysms and fenestrations, we classified the relation of the location of the aneurysm as remote from the fenestration or on the fenestration.

RESULTS: In 140 patients, 210 aneurysms were present. In 33 of 140 patients (24%; 95% confidence interval, 17.2%–31.3%), 45 fenestrations were detected with the following locations: anterior communicating artery in 31 (69%), A1 segment of the anterior cerebral artery in 4 (9%), middle cerebral artery in 4 (9%), basilar artery in 4 (9%), vertebral artery in 1 (2%), and anterior inferior cerebellar artery in 1 (2%). Of 56 patients with anterior communicating artery aneurysms, 14 had a fenestration on the anterior communicating artery complex. The remaining 31 fenestrations had no anatomic relation to aneurysms. In 140 patients with 210 aneurysms, 14 aneurysms (7%) were located on a fenestration and 196 were not.

CONCLUSIONS: In patients with a suspected ruptured aneurysm, fenestrations of intracranial arteries were detected in 24% (33 of 140). Most fenestrations were located on the anterior communicating artery. Of 45 fenestrations, 14 (31%) were related to an aneurysm.

ABBREVIATION: AcomA = anterior communicating artery

Fenestrations of intracranial arteries are segmental duplications of the lumen into 2 distinct channels, each comprising endothelial and muscular layers with or without a shared adventitia. Fenestrations are anatomic variants and can range from a small focus of divided tissue to duplication of a long vessel segment.^{1,2}

Fenestrations result from partial failure of fusion of paired primitive embryologic vessels or from incomplete obliteration of anastomosis in a primitive vascular network.²

The association of fenestrations with aneurysms and other neurovascular disorders has been noted. Some suggest that altered flow dynamics in the presence of fenestrations may promote aneurysm development, though the exact relationship is not well-defined.

Surgical and anatomic studies suggest that fenestrations are common in intracranial arteries with the highest prevalence in the

anterior communicating artery (AcomA) complex.^{3–5} Demonstration of fenestrations with imaging is uncommon.^{6,7} Most fenestrations are only visible from a specific viewing angle that is often not provided by conventional angiography or reconstructed cross-sectional imaging. With 3D imaging, especially 3D rotational angiography, the detection rate of fenestrations has improved.⁸ Scant data are available on the frequency and location distribution of fenestrations of intracranial arteries, to our knowledge. We used 3D rotational angiography of all intracranial arteries in a cohort of 179 patients with suspected intracranial aneurysms to assess the prevalence and location of fenestrations and the relation of fenestrations with aneurysms.

MATERIALS AND METHODS

Patient Population

The institutional review board approved this prospective study with a waiver for informed consent. Between March 2013 and June 2014, 179 patients with acute SAH were admitted. The diagnosis of SAH was established with a native CT scan or lumbar puncture. Of 179 patients, 177 had CTA as the first diagnostic imaging technique, and 2 patients proceeded to angiography without CTA because of poor renal function. CTA was not followed

Received November 13, 2014; accepted December 1.

From the Department of Radiology (S.B.T.v.R.), Medisch Centrum Alkmaar, Alkmaar, the Netherlands; and Department of Radiology (R.S.B., J.P.P., M.S., W.J.v.R.), St. Elisabeth Ziekenhuis, Tilburg, the Netherlands.

Please address correspondence to W.J. van Rooij, MD, Department of Radiology, St. Elisabeth Ziekenhuis, Hilvarenbeekseweg 60, 5022GC Tilburg, the Netherlands; e-mail: wjvanrooij@gmail.com

<http://dx.doi.org/10.3174/ajnr.A4236>



FIGURE. Examples of fenestrations of intracranial arteries. *A*, Double-fenestrated anterior communicating artery with 2 small aneurysms. *B*, Fenestration on the anterior communicating artery (arrow). Note the aberrant origin of a duplicated middle cerebral artery from A2 (double arrow). *C*, A small fenestration on the middle cerebral artery. *D*, A proximal basilar fenestration.

by angiography in 37 patients because of a perimesencephalic hemorrhage pattern ($n = 18$), a moribund clinical condition ($n = 10$), or trauma and SAH ($n = 9$). In the remaining 140 patients, CTA was followed within 24 hours by 3D rotational angiography of 3 vessels. These 140 patients form the present study group.

3D Rotational Angiography

Angiography was performed on a biplane angiographic system (Allura Xper FD20/10; Philips Healthcare, Best, the Netherlands) by 1 of 3 interventional neuroradiologists (W.J.v.R., M.S., and J.P.P. with 26, 24, and 8 years of experience, respectively). In 80 (57%) uncooperative or intubated patients, angiography was performed with the patient under general anesthesia. A single 3D rotational angiographic run was acquired of both internal carotid arteries and 1 vertebral artery with a hand injection of 12–20 mL of contrast material. When the contralateral distal vertebral artery was not visualized, an additional 2D biplane run was performed of this vessel. The tube rotation arc was 240° with a rotation time of approximately 4.0 seconds. The rotational angiographic data were transferred to an independent workstation (Integris 3DRA Workstation; Philips Healthcare) for instant generation of 3D reformatted images in a 256³ matrix.

When possible, angiography was followed immediately by endovascular treatment with the patient under general anesthesia. Patients with aneurysms not suitable for coiling were scheduled for surgery.

Image Analysis

3D reformatted images were reviewed on the workstation by 2 observers in consensus (W.J.v.R. and S.B.T.v.R. with 26 and 3 years' experience in neuroradiology). Presence, location, and size of the aneurysms were recorded in a database. Other vascular disorders that might be responsible for the subarachnoid hemorrhage, such as arterial dissections, arteriovenous malformations, dural fistula, Moyamoya phenomenon, or reversible vasospasm syndrome, were separately recorded.

The presence and location of fenestrations was assessed. In patients with both aneurysms and fenestrations, we classified the relation of the location of the fenestration with the location of the aneurysm as remote from the fenestration or on the fenestration itself.

Data Analysis

Descriptive statistics were used for the presence, size, and locations of aneurysms and the frequency and locations of fenestrations. The sex distribution in patients with and without fenestrations was compared. In patients with and without intracranial aneurysms, the proportion of patients with a fenestration was compared with those without a fenestration. For comparison of proportions, the χ^2 test was used.

RESULTS

Patients

Of 140 patients with SAH and 3D rotational angiography of 3 vessels, 100 were women (71%) and 40 were men (29%), with a mean age of 58.0 years (median, 59 years; range, 27–84 years).

Aneurysms

In 140 patients, 213 aneurysms were detected. Twenty patients (14%) had no aneurysms; 68 patients had 1 aneurysm; 24 patients, 2 aneurysms; 16 patients, 3 aneurysms; 11 patients, 4 aneurysms; and 1 patient, 5 aneurysms. Of 120 patients with aneurysms, 52 (43%) had multiple aneurysms.

Aneurysm locations were the anterior communicating artery in 56, middle cerebral artery in 51, posterior communicating artery in 29, basilar tip in 15, carotid cavernous sinus in 12, superior cerebellar artery in 10, posterior inferior cerebellar artery in 8, internal carotid bifurcation in 7, pericallosal artery in 5, anterior choroidal artery in 4, supraclinoid carotid dissection in 4, vertebral junction in 3, posterior cerebral artery in 2, carotid ophthalmic artery in 2, anterior cerebral artery in 1, and anterior inferior cerebellar artery in 1.

Fenestrations

On 3D rotational angiography, 45 fenestrations were detected in 33 of 140 patients (24%; 95% confidence interval, 17.2%–31.3%). Examples are provided in the Figure. Eleven patients had 2 fenest-

trations, and 1 patient had 3 fenestrations. Location distribution was as follows: the AcomA in 31 (69%), A1 segment of the anterior cerebral artery in 4 (9%), middle cerebral artery in 4 (9%), basilar artery in 4 (9%), vertebral artery in 1 (2%), and anterior inferior cerebellar artery in 1 (2%). Of 45 fenestrations, 39 (87%) were located in the anterior circulation, and 6 (13%), in the posterior circulation. Of 33 patients with fenestrations, 7 were men (21%) and 26 were women (79%). Sex distribution did not differ between patients with and without fenestrations.

Relation of Fenestrations to Aneurysms

Of 56 patients with an AcomA aneurysms, 14 (25%) had a fenestration on the AcomA complex. The remaining 31 fenestrations had no anatomic relation with aneurysms. In 140 patients with 210 aneurysms, 14 aneurysms (7%) were located on or adjacent to a fenestration and 196 (93%) were not.

Forty-one fenestrations were present in 30 of the 120 patients (25%) with aneurysms, and 4 fenestrations were present in 3 of the 20 patients (15%) without aneurysms. This difference was not significant ($P = .49$).

DISCUSSION

We found that fenestrations are common anatomic variations of intracranial arteries with a frequency of 24% in a cohort of 140 patients with suspected ruptured aneurysms. There was no significant difference in the occurrence of fenestrations in 120 patients with and 20 patients without aneurysms. We used optimal 3D rotational angiography imaging of all cerebral vessels in the clinical setting of patients with subarachnoid hemorrhage with intended endovascular treatment of aneurysms. Most 3D angiography was performed with the patient under general anesthesia, thereby eliminating image degradation by patient motion. These 3D images acquired under optimal circumstances were scrutinized by 2 experienced readers for the presence of fenestrations. Thus, data are robust, and the assessed frequency of fenestrations is likely to be realistic.

The only limitation of the study is that the patient population is a selection of those with subarachnoid hemorrhage with a much higher incidence of intracranial aneurysms than that in the general population. The high frequency of fenestrations may, therefore, not be generalized. Postmortem studies with a large sample size may resolve this issue but are currently not available.

Although almost a third of fenestrations had an anatomic relation to an aneurysm, these were all AcomA aneurysms on AcomA fenestrations. This observation may be expected in the given patient population with suspected aneurysms because most fenestrations and most aneurysms occurred on the AcomA. A definite association between aneurysms and fenestrations on this location remains unclear from our data.

This study confirms the common occurrence of fenestrations that was found in a previous study using 3D rotational angiography in patients with intracranial aneurysms.⁸ In that study, 3D rotational angiography was performed in only 1 cerebral vessel territory following detection of an aneurysm with 2D angiography. In the present study, all cerebral vessels were imaged in 3D, so data are more robust. Despite this methodologic difference, fenestrations were more frequent in the previous study than in the

present study (28%, 59 of 208 patients versus 24%, 33 of 140 patients). With the relatively small sample sizes of both studies, the difference might be within the confidence limits. In both studies, the AcomA complex was the most common location of fenestrations and most fenestrations occurred in the anterior circulation.

Until recently, before the era of 3D imaging, fenestrations were considered a rarity. This might be because fenestrations are only visible from specific viewing angles that are mostly not available on 2D angiograms. In a recent study of almost 11,000 angiograms, fenestrations were identified in 2.1%, with the highest prevalence in the posterior circulation, especially the basilar artery.⁷ Also in another recent review of intracranial fenestrations with associated aneurysms, the most common single fenestration location was the basilar artery.⁹ With modern 3D reconstructions of axial images of CT and MR angiography, the prevalence was somewhat higher, up to 13%.¹⁰⁻¹⁴ Large-vessel fenestrations such as those on the proximal basilar artery are readily depicted with 2D angiograms or CT and MR angiography, but resolution is insufficient to detect subtle small-vessel fenestrations such as in the AcomA complex.¹⁵

Many studies have noted the presence of fenestrations in the setting of a variety of neurovascular pathology apart from aneurysms, such as dissections, arteriovenous malformations, dural fistula, and even ischemic stroke. This may not be surprising because cerebral angiography is performed exclusively in patients with suspected intracranial vascular disease. A causative relation of fenestrations with neurovascular disorders has never been firmly established. On the contrary, recent studies with more frequent depiction of fenestrations including the present study suggest that a relation to aneurysms or other vascular pathology is not very likely.^{7,8,10} Only large postmortem studies can provide a definite answer to this issue.

CONCLUSIONS

In patients with a suspected ruptured aneurysm, fenestrations of intracranial arteries were detected in 24% (33 of 140). Most fenestrations were located on the AcomA. Of 45 fenestrations, 14 (31%) were related to an aneurysm.

REFERENCES

1. Padgett DH. **The development of the cranial arteries in the human embryo.** *Contrib Embryol* 1948;212:207-61
2. Kathuria S, Gregg L, Chen J, et al. **Normal cerebral arterial development and variations.** *Semin Ultrasound CT MR* 2011;32:242-51
3. Wollschlaeger G, Wollschlaeger PB, Lucas FV, et al. **Experience and result with post-mortem cerebral angiography performed as routine procedure of the autopsy.** *Am J Roentgenol Radium Ther Nucl Med* 1967;101:68-87
4. Gomes FB, Dujovny M, Umansky F, et al. **Microanatomy of the anterior cerebral artery.** *Surg Neurol* 1986;26:129-41
5. Serizawa T, Saiki N, Yamaura A. **Microsurgical anatomy and clinical significance of the anterior communicating artery and its perforating branches.** *Neurosurgery* 1997;40:1211-16
6. Sanders WP, Sorek PA, Mehta BA. **Fenestration of intracranial arteries with special attention to associated aneurysms and other anomalies.** *AJNR Am J Neuroradiol* 1993;14:675-80
7. Cooke DL, Stout CE, Kim WT, et al. **Cerebral arterial fenestrations.** *Interv Neuroradiol* 2014;20:261-74
8. van Rooij SB, van Rooij WJ, Sluzewski M, et al. **Fenestrations of**

- intracranial arteries detected with 3D rotational angiography. *AJNR Am J Neuroradiol* 2009;30:1347–50
9. Patel MA, Caplan JM, Yang W, et al. **Arterial fenestrations and their association with cerebral aneurysms.** *J Clin Neurosci* 2014;21:2184–88
 10. Bayrak AH, Senturk S, Akay HO, et al. **The frequency of intracranial arterial fenestrations: a study with 64-detector CT-angiography.** *Eur J Radiol* 2011;77:392–96
 11. Bharatha A, Aviv RI, White J, et al. **Intracranial arterial fenestrations: frequency on CT angiography and association with other vascular lesions.** *Surg Radiol Anat* 2008;30:397–401
 12. Tanaka M, Kikuchi Y, Ouchi T. **Neuroradiological analysis of 23 cases of basilar artery fenestration based on 2280 cases of MR angiographies.** *Interv Neuroradiol* 2006;12(suppl 1):39–44
 13. Sogawa K, Kikuchi Y, Ouchi T, et al. **Fenestrations of the basilar artery demonstrated on magnetic resonance angiograms: an analysis of 212 cases.** *Interv Neuroradiol* 2013;19:461–65
 14. Uchino A, Saito N, Okada Y, et al. **Fenestrations of the intracranial vertebrobasilar system diagnosed by MR angiography.** *Neuroradiology* 2012;54:445–50
 15. Uchino A, Nomiya K, Takase Y, et al. **Anterior cerebral artery variations detected by MR angiography.** *Neuroradiology* 2006;48:647–52

MR Imaging–Detected Carotid Plaque Hemorrhage Is Stable for 2 Years and a Marker for Stenosis Progression

R.J. Simpson, S. Akwei, A.A. Hosseini, S.T. MacSweeney, D.P. Auer, and N. Altaf



ABSTRACT

BACKGROUND AND PURPOSE: MR imaging–detected carotid plaque hemorrhage is associated with an increased risk of recurrent ischemic cerebrovascular events and could be an indicator of disease progression; however, there are limited data regarding the dynamics of the MR imaging–detected carotid plaque hemorrhage signal. We assessed the temporal change of this signal and its impact on carotid disease progression.

MATERIALS AND METHODS: Thirty-seven symptomatic patients with 54 carotid stenoses of >30% on sonography underwent serial MR imaging during 24 months. A signal-intensity ratio of >1.5 between the carotid plaque and adjacent muscle was defined as plaque hemorrhage, and a change in signal-intensity ratio of >0.31 between time points was considered significant. Sixteen patients underwent ≥ 2 carotid sonography scans to determine the peak systolic velocities and degree of stenosis with time.

RESULTS: Of the 54 carotids, 28 had the presence of hyperintense signal on an MR imaging sequence (PH+) and 26 had the absence of hyperintense signal on an MR imaging sequence (PH–) at baseline. The signal-intensity ratio was stable in 33/54 carotid plaques, but 39% showed a change. Plaque hemorrhage classification did not change in 87% of carotid plaques, but 4 became PH+, and 3, PH–. As a group, PH+ carotids did not change significantly in signal-intensity ratio ($P = .585$), whereas PH– showed an increased signal-intensity ratio at 24.5 months ($P = .02$). In PH+ plaques, peak systolic velocities significantly increased by 22 ± 39.8 cm/s from baseline to last follow-up sonography ($Z = 2.427$, $P = .013$).

CONCLUSIONS: During 2 years, MR imaging–detected carotid plaque hemorrhage status remained stable in most (87%) cases with 4 (7%) incident plaque hemorrhages. PH+ plaques were associated with increased flow velocity during the follow-up period.

ABBREVIATIONS: MR imaging-PH = MR imaging–detected plaque hemorrhage; PH = plaque hemorrhage; PH+ = presence of hyperintense signal on an MR imaging sequence; PH– = absence of hyperintense signal on an MR imaging sequence; PSV = peak systolic velocity; SIR = signal-intensity ratio

Currently, the degree of ICA stenosis is the principal criterion on the basis of which the decision for carotid intervention is made. This is based on strong evidence from randomized con-

trolled trials that carotid endarterectomy reduces stroke risk in patients with severe carotid artery stenosis.^{1,2} However, those studies also showed that a significant proportion of patients with symptomatic carotid disease will not have a recurrence. Subsequently, much research is focused on the identification of high-risk subgroups,³ especially for those with moderate or asymptomatic carotid stenosis.

Plaque hemorrhage (PH) is implicated in carotid plaque vulnerability⁴ and is detectable by MR imaging.^{5,6} A recent longitudinal follow-up study and meta-analysis⁷ demonstrated that MR imaging–detected plaque hemorrhage (MR imaging-PH) strongly predicts recurrent ischemic events. The MR imaging-PH

Received October 14, 2014; accepted after revision November 12.

From the Radiological Sciences Group (R.J.S., S.A., A.A.H., D.P.A., N.A.), Division of Clinical Neurosciences, University of Nottingham, Nottingham, United Kingdom; and Department of Vascular and Endovascular Surgery (R.J.S., S.T.M., N.A.), Nottingham University Hospitals National Health Service Trust, Nottingham, United Kingdom.

R.J.S. and S.A. contributed equally to this work.

This work was supported by the National Institute for Health Research under its Research for Patient Benefit Programme (grant reference number PB-PG-0107-11438). Financial support was also provided by the Stroke Association Junior Research Training Fellowship, London, United Kingdom; the Nottingham Vascular Surgery Research Fund, Nottingham, United Kingdom; and The Health Foundation, London, United Kingdom.

The views expressed are those of the authors and not necessarily those of the National Health Service, the National Institute for Health Research, or the Department of Health.

Paper previously presented at: UK Stroke Forum 2011, November 29–December 1, 2011; Glasgow, United Kingdom.

Please address correspondence to Richard J. Simpson, Radiological Sciences, Division of Clinical Neurosciences, University of Nottingham, B Floor, West Block, Queens Medical Centre, Nottingham, NG7 2UH, UK; e-mail: msxrs@nottingham.ac.uk

Indicates open access to non-subscribers at www.ajnr.org

<http://dx.doi.org/10.3174/ajnr.A4267>

Table 1: Velocity grading criteria based on the NASCET angiographic method^{13,14}

Stenosis	ICA PSV (cm/s)	ICA EDV (cm/s)	CCA/ICA PSV Ratio
0–29	<100	<40	<3.2
30–49	110–130	<40	<3.2
50–59	>130	<40	<3.2
60–69	>130	40–110	3.2 to <4.0
70–79	>210	120–140	≤4.0
80–95	>210	>140	≤4.0
96–99	String flow	String flow	String flow
100	Occluded	Occluded	Occluded

Note:—CCA indicates common carotid artery; EDV, end diastolic velocity.

signal seems to be stable for 12 months,⁸ but stability of MR imaging-PH features beyond 12 months remains unclear. Knowledge of longer term stability of MR imaging-PH would be helpful if it is to be used to assist decision-making in interventions and to determine the need for follow-up imaging.

Plaque volume progression on sonography recently has been shown to predict cerebrovascular events⁹; however, this measure was not used in the current study. Carotid stenosis progression has been suggested to be a better predictor of subsequent TIA/stroke than a single measurement.¹⁰ Although general carotid sonography surveillance may not be cost-effective,¹¹ this situation may well be different for a subgroup of patients with a higher risk for stenosis progression. It is conceivable that MR imaging-PH is also an indicator of disease progression¹² and, therefore, may be useful in this regard.

The aim of this study was to determine MR imaging signal changes in the carotid artery plaque during 2 years and whether the presence of MR imaging-PH at baseline is associated with stenosis progression.

MATERIALS AND METHODS

Eligible patients presenting with a recent history of nondisabling stroke, hemispheric transient ischemic attack, or amaurosis fugax and ipsilateral carotid stenosis of >30% measured by sonography were recruited into this study from a TIA clinic. Peak systolic velocity (PSV) and end diastolic velocity measurements were recorded from the common, internal, and external carotids bilaterally. Established grading criteria were used to assess the percentage stenosis (Table 1), which was taken from the Carotid and Vertebral Artery Transluminal Angioplasty Study^{13,14} and was based on the NASCET angiographic method.² A planned carotid intervention and atrial fibrillation were exclusion criteria. In addition, contralateral carotid plaques were included if a stenosis of >30% was observed. Patients were scheduled to undergo serial MR imaging and sonography. MRI and clinical assessment to determine evidence of recurrence were performed at baseline and at 4, 12, and 24 months.

All patients continued to receive routine clinical care independent of their MR imaging findings. The local research ethics committee approved the study, and all patients gave written informed consent at the point of recruitment. The data regarding recurrence have been published previously.^{15,16}

MR Imaging Protocol and Image Analysis

MR carotid imaging was undertaken on a 1.5T Magnetom Vision scanner (Siemens, Erlangen, Germany) by using a receive-only

quadrature neck array coil. The MR imaging, previously described,⁶ was a coronal T1-weighted magnetization-prepared 3D gradient-echo sequence incorporating a selective number of partitions, a water-excitation pulse, and a TI chosen to null the signal from blood and fat (TR, 10.3 ms; TE, 4.0 ms; flip angle, 15°; TI, 20 ms; FOV, 350 × 300 mm; matrix, 256 × 140; 140 partitions; volume thickness, 120–150 mm). This sequence detects subacute-to-chronic hemorrhage because methemoglobin has a hyperintense signal.

MR imaging analysis was performed on standard reformatted axial images by using Java imaging software (www.xinapse.com), by 3 reviewers with 1- to 3-years' carotid image-analysis experience, blinded to clinical data and images from other time points. As previously described,^{15–17} the highest intensity in the carotid artery wall within 1 cm from the bifurcation was compared with all of the immediately adjacent sternocleidomastoid muscle (signal-intensity [SI] ratio [SIR] = $SI_{\text{plaque}}/SI_{\text{muscle}}$). The presence of MR imaging-PH was diagnosed if the normalized SIR between the 2 was at least 1.5 (PH+). Inter- and intraobserver agreements were assessed by analyzing all the images 5 months after the initial analysis. The minimum detectable change applied to the SIR is considered the minimal amount of change in SIR to exceed an estimated error due to variation in measurement. Thus a change in SIR is only considered a real change if it is larger than the threshold set at ±0.31, defined as twice the pooled SD of intraobserver test-retest data. A change in PH status from PH– (normalized SIR of <1.5) to PH+ was noted only when the SIR rose above the 1.5 threshold and vice versa.

Sonography

All carotid sonography (baseline and follow-up) was performed by 1 of 2 accredited Clinical Vascular Scientists by using a Logiq 9 sonography machine (GE Healthcare, Milwaukee, Wisconsin). The ultrasound grading criteria in the follow-up stage were identical to that of the recruitment stage, as detailed above. Change in peak systolic velocity in the internal carotid artery from baseline to the last follow-up sonography scan was used as the primary marker of progressive carotid disease.¹⁸ Categorical progression of stenosis, where there was an increase by at least 1 category, was also reported.

Statistical Analysis

SIR inter-/intraobserver agreement was analyzed by using the Cronbach α . The SIR at different time points was analyzed with repeated-measures analysis of variance, in which if the Mauchly test of sphericity was not significant, then the Geenhouse-Geisser adjustment was reported. The χ^2 test was used to compare the prevalence of PH+ at baseline between symptomatic and asymptomatic carotids. The Fisher exact test was used to determine the association between disease progression and both the presence of PH and the recurrence of symptoms. The Wilcoxon signed rank test was used to test the effect of PH on PSV of the ICA. All analyses were performed with SPSS Statistics for Windows, Version 19.0 (IBM, Armonk, New York). $P < .05$ was considered statistically significant.

RESULTS

Sixty-four participants were recruited during a 2-year period, but 27 were excluded because they did not undergo subsequent MR imaging (18 with claustrophobia, 3 with bilateral stenosis <30%, 6 “other”). Therefore, 37 patients were included in this study; their demographics can be seen in Table 2, and carotid stenosis at baseline, in Table 3.

At baseline, 28/54 (52%) carotid arteries were PH+ (mean SIR, 2.02 ± 0.39). The mean SIR of those without MR imaging-PH was 1.31 ± 0.13 . PH was detected in 22/37 (59%)

Table 2: Patient characteristics

Characteristic	
Age (yr) (mean) (SD)	70.5 (9.24)
Male	87%
Smoking history	
Never	8 (22%)
Previous smoker	16 (43%)
Current smoker	13 (35%)
Ischemic heart disease	6 (16%)
Diabetes	8 (22%)
High cholesterol	20 (54%)
Hypertensive	29 (78%)
Statin use	
None	12 (32%)
Commenced after TIA/stroke	25 (68%)

Table 3: Degree of carotid stenosis at baseline^a

Degree of stenosis	Ipsilateral ICA	Contralateral ICA
0%–30%	–	20 (54.1)
30%–49%	10 (27.0)	4 (10.8)
50%–59%	4 (10.8)	1 (2.7)
60%–69%	19 (51.4)	3 (8.1)
70%–79%	1 (2.7)	–
80%–95%	1 (2.7)	4 (10.8)
95%–99%	2 (5.4)	–
100%	–	5 (13.5)

Note: – indicates none.

^a Values are counts (percentages). “Ipsilateral” and “Contralateral” are used to describe the carotid artery in relation to presenting symptoms.

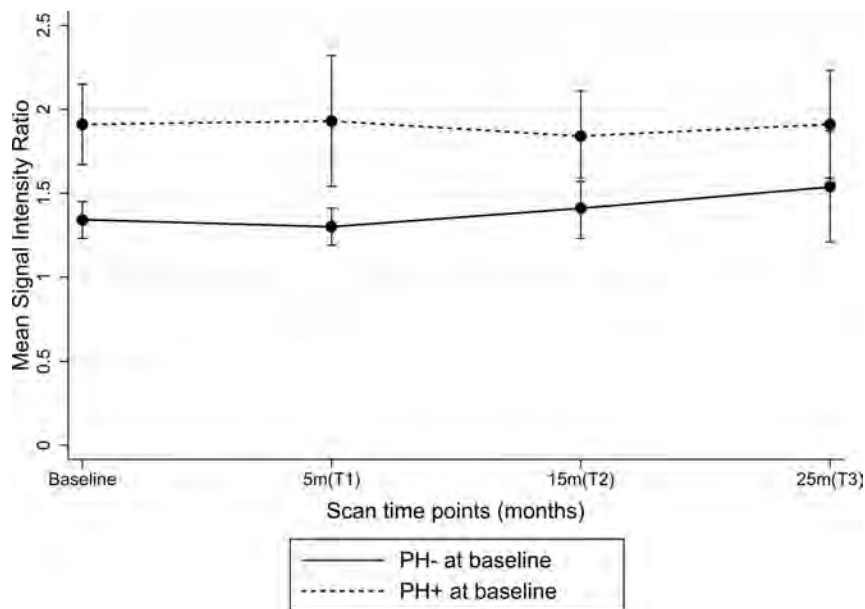


FIGURE. Trend of SIR during 24.5 months based on baseline PH status.

symptomatic carotid arteries, compared with 6/17 (35%) in the asymptomatic group; however, this difference was not significant ($\chi^2 = 2.7, P = .1$).

Thirty-seven patients with 54 carotid plaques with >30% stenosis (37 symptomatic and 17 asymptomatic) underwent serial MR imaging. The mean times for follow-up scans from baseline were T1 (4.5 ± 3.1 months), T2 (14.5 ± 3.1 months), and T3 (24.6 ± 2.6 months). Suitable images were available for all carotid arteries at T0 (baseline), but only 46, 47, and 34 at T1, T2, and T3, respectively, due to loss to follow-up and uninterpretable images. Thus, 84% (181/216) of the potential images were included in the analysis.

Temporal Stability of MR Imaging PH

The carotid muscle SIR was stable with time in 33 of the 54 carotid arteries (61%). Thus, 21 carotid plaques (16 PH+ and 5 PH–) underwent a detectable change in SIR of >0.31 absolute difference at some point during follow-up. Most of the detectable changes (14/21) resulted in an increase in SIR; of these, 13 PH+ plaques remained PH+ (SIR > 1.5), while 1 PH– plaque remained PH– (SIR < 1.5), despite the change. This means that PH status remained the same in 47/54 plaques (87%). The 7 plaques demonstrating categoric change included 4 of 26 (7%) previously PH– plaques that became PH+, while 3 of 28 (5%) with PH+ reverted to PH–.

At the group level, SIR change did not differ with symptom status at baseline. SIR significantly increased during a mean of 24.5 ± 2.56 months ($P = .02$, repeated-measures ANOVA) in PH– plaques (Figure). However, SIR did not significantly increase during the follow-up period in PH+ plaques ($P = .585$). Quantitative assessment of SIR showed excellent reliability on both interobserver (Cronbach $\alpha = 0.99$) and intraobserver (Cronbach $\alpha = 0.99$) assessment.

Recurrent Events

As previously reported,¹⁵ 11 patients (30%) had recurrent symptoms (stroke, 7; amaurosis fugax, 2; TIA, 2) during follow-up or within 6 months of their final scan. Most, 9/11 (82%), recurrent symptoms occurred in the previously symptomatic carotid artery. Five events occurred in carotid plaques that had undergone detectable positive change in SIR. No events occurred in plaques with new PH+. There was, however, a significant association between recurrent events and baseline plaque hemorrhage status. Nine (82%) events occurred in the 28 carotid arteries that were PH+ at baseline compared with 2 events in the 26 PH– carotid arteries at baseline, ($\chi^2, P = .026$).

Carotid Stenosis Progression

A subgroup of 16 patients with $\geq 30\%$ ipsilateral stenosis and variable contralateral disease were followed up with carotid sonography during a mean of

40.2 months (range, 20–91 months; 46 sonograms). However, due to limited access to the sonography machine, it was not possible to scan all patients. The mean scan intervals from baseline were the following: T1 (26.1 ± 13.01 months), T2 (34.1 ± 10.19 months), and T3 (55.3 ± 26.85 months). At the group level, there was a significant progression of ICA-PSV in PH+ carotid arteries, with a mean increase of 22 ± 39.8 cm/s from baseline (147 cm/s) to last follow-up (169 cm/s) sonogram ($Z = 2.427, P = .013$). No such association was seen in plaques without MR imaging-PH (-5.5 ± 55.4 cm/s). Symptomatic carotid stenoses were not associated with an increase in ICA PSV.

Stenosis progression according to predefined grades was seen in 9 of the 32 carotid arteries (28%), giving an annualized progression rate of 8.4%. However, no significant differences were seen in the grade progression between symptomatic (5/16) and asymptomatic (4/16) plaques or between PH+ (6/22) and PH- (3/10) disease.

DISCUSSION

MR imaging-PH-positive carotid plaques showed no change in SIR during 24 months but demonstrated a significant increase in peak systolic velocities. In contrast, there was no progression of velocities but a mild increase in MR imaging signal intensity in PH- plaques.

In 28 PH+ plaques, there was no change in relative MR imaging signal intensity during 24 months, providing further evidence of the stability of PH. The observed prolonged elevation of signal suggests persistence of methemoglobin, in line with previous reports on MR imaging-PH for up to 18 months.^{8,19,20} We also showed stable plaque signal in asymptomatic plaques, which corroborates a small study in 14 asymptomatic patients with PH signs for 54 months.²¹ However, selection bias in that study should be noted because only those plaques with MR imaging-PH on the most recent scan were included.

Quantitative assessment of plaque intensities revealed a small but significant increase in previously plaque hemorrhage-negative plaques. In contrast to our findings, Wang et al²² recently reported a reduction in SIR during 19 months in asymptomatic plaques. These differences may be explained by differences in the selection of asymptomatic patients with carotid disease between studies. We defined an asymptomatic plaque as contralateral to the symptomatic artery and symptom-free for >6 months, whereas Wang et al²² selected patients who had never had any symptoms of cerebrovascular disease. Evidence suggests that differences exist between these 2 groups, in that truly asymptomatic plaques appear to be more stable.²³ Conversely, the overall SIR increase in PH plaques is corroborated by the individual classification showing that 15% of PH plaques converted during the follow-up of 2 years. The most likely explanation is the incident plaque hemorrhage in a higher risk patient group than in a completely asymptomatic patient cohort.

Although the MR imaging signal intensity due to intracranial hemorrhage is subject to rapid change,²⁴ carotid MR imaging-PH and thus methemoglobin have been shown to be more persistent.¹⁹ The temporal stability of MR imaging-PH may be due to the inherent stability of methemoglobin or because its breakdown is balanced by continued production of methemoglobin from

continued hemorrhage from a fragile plaque vasa vasorum.²⁵ Our results indicating temporal stability of the MR imaging-PH signal, together with previous work that reported MR imaging-PH, strongly predict recurrent stroke/TIA⁷ and raise the possibility that all plaques found to be PH+ reflect a cumulative high risk regardless of how recent the PH may have been. This is particularly pertinent for delayed presentations of TIA and stroke. The evidence of incident PH certainly suggests that carotid disease merits surveillance; however, the natural history of newly formed PH in carotid plaques remains uncertain.

We found an increase in PSV in PH+ but not in PH- carotid arteries, which did, however, not translate into a preferential progression in the categoric degree of stenosis. Although clinically useful, the categorization of blood flow velocities and ratios (Table 1) has the effect of reducing the statistical power to detect the relationship among variables.²⁶ Thus, plaque area/volume, PSV, and other continuous variables may be more sensitive to changes in disease progression than grades of stenosis. Our findings, while preliminary, suggest that PH may be a maker of stenosis progression. This would be in line with a previous study that showed²¹ that the presence of MR imaging-PH increased the rate of plaque progression determined by wall volume. Histologic evidence from coronary artery plaques also supports the notion that the presence of PH increases atheroma progression.¹²

Study Limitations

Our study is limited by its sample size; thus, there were a relatively small number of carotid plaques that changed PH status or progressed during the follow-up. This finding was further confounded by the exclusion bias for patients scheduled for carotid intervention, meaning that our cohort either had minor carotid disease or those with more severe disease had declined or were turned down for surgery. The small sample size has resulted in wide SD for the mean changes in internal carotid artery peak systolic velocity. A number of scans were not available for analysis due to loss to follow-up and poor-quality images, despite multiple invitations for the non-attenders. In this study, we used a single T1-weighted imaging sequence to detect PH, to optimize its clinical applicability. This has meant that we did not use multi-sequence imaging to determine the age of the PH, as used by Chu et al²⁷ and Wang et al.²² We also did not measure the volume of the MR imaging-PH with time, due to the limited resolution of the images at 1.5T. Although sonography-derived plaque volume is also a marker of vulnerability,⁹ no measurement of volume was made in our study. In addition, quantification of plaque volume has been demonstrated recently by using serial CT angiography.²⁸

CONCLUSIONS

These results demonstrate the temporal stability of carotid MR imaging-PH, supporting its value as a risk marker beyond the acute presentation. We also provide preliminary evidence that PH may be a marker for stenosis progression as measured by PSV.

Disclosures: Richard J. Simpson—RELATED: Grant: Stroke Association,* National Institute for Health Research,* Comments: Junior Research Training Fellowship, National Institute for Health Research—Research for Patient Benefit program. Solomon Akwei—UNRELATED: Travel/Accommodations/Meeting Expenses Unrelated to Activities Listed: Nottingham Vascular Research Fund, Comments: covered expenses

incurred for attending the Vascular Society Meeting, Brighton, UK, November 2010. Akram A. Hosseini—RELATED: Grant: National Institute for Health Research,* Comments: National Institute for Health Research Clinical Research Fellowship. Dorothee P. Auer—RELATED: Grant: Stroke Association, UK,* Comments: paid for Richard Simpson's fellowship; Support for Travel to Meetings for the Study or Other Purposes: Stroke Association, UK,* Comments: travel and consumables for Richard Simpson; UNRELATED: Grants/Grants Pending: National Institute of Health Research—Research for Patient Benefit program,* MS Society,* Parkinson's UK,* Medical Research Council,* Engineering and Physical Sciences Research Council,* Arthritis Research UK,* Cancer Research UK.* *Money paid to the institution.

REFERENCES

- European Carotid Surgery Trialists' Collaborative Group. MRC European Carotid Surgery Trial: interim results for symptomatic patients with severe (70–99%) or with mild (0–29%) carotid stenosis. *Lancet* 1991;337:1235–43
- North American Symptomatic Carotid Endarterectomy Trial Collaborators. Beneficial effect of carotid endarterectomy in symptomatic patients with high-grade carotid stenosis. *N Engl J Med* 1991; 325:445–53
- U-King-Im J, Young V, Gillard JH. Carotid-artery imaging in the diagnosis and management of patients at risk of stroke. *Lancet Neurol* 2009;8:569–80
- Sary HC, Chandler AB, Dinsmore RE, et al. A definition of advanced types of atherosclerotic lesions and a histological classification of atherosclerosis: a report from the Committee on Vascular Lesions of the Council on Arteriosclerosis, American Heart Association. *Circulation* 1995;92:1355–74
- Moody AR, Allder S, Lennox G, et al. Direct magnetic resonance imaging of carotid artery thrombus in acute stroke. *Lancet* 1999;353:122–23
- Moody AR, Murphy RE, Morgan PS, et al. Characterization of complicated carotid plaque with magnetic resonance direct thrombus imaging in patients with cerebral ischemia. *Circulation* 2003;107: 3047–52
- Hosseini AA, Kandiyil N, Macsweeney ST, et al. Carotid plaque hemorrhage on magnetic resonance imaging strongly predicts recurrent ischemia and stroke. *Ann Neurol* 2013;73:774–84
- Kwee RM, van Oostenbrugge RJ, Mess WH, et al. Carotid plaques in transient ischemic attack and stroke patients: one-year follow-up study by magnetic resonance imaging. *Invest Radiol* 2010;45:803–09
- van Engelen A, Wannarong T, Parraga G, et al. Three-dimensional carotid ultrasound plaque texture predicts vascular events. *Stroke* 2014;45:2695–701
- Bertges DJ, Muluk V, Whittle J, et al. Relevance of carotid stenosis progression as a predictor of ischemic neurological outcomes. *Arch Intern Med* 2003;163:2285–89
- Cull DL, Cole T, Miller B, et al. The value of a carotid duplex surveillance program for stroke prevention. *Ann Vasc Surg* 2011;25:887–94
- Kolodgie FD, Gold HK, Burke AP, et al. Intraplaque hemorrhage and progression of coronary atheroma. *N Engl J Med* 2003;349:2316–25
- McCabe DJ, Pereira AC, Clifton A, et al. Restenosis after carotid angioplasty, stenting, or endarterectomy in the Carotid and Vertebral Artery Transluminal Angioplasty Study (CAVATAS). *Stroke* 2005;36:281–86
- Sidhu PS, Allan PL. Ultrasound assessment of internal carotid artery stenosis. *Clin Radiol* 1997;52:654–58
- Altaf N, Daniels L, Morgan PS, et al. Detection of intraplaque hemorrhage by magnetic resonance imaging in symptomatic patients with mild to moderate carotid stenosis predicts recurrent neurological events. *J Vasc Surg* 2008;47:337–42
- Kandiyil N, Altaf N, Hosseini AA, et al. Lower prevalence of carotid plaque hemorrhage in women, and its mediator effect on sex differences in recurrent cerebrovascular events. *PLoS One* 2012;7:e47319
- Altaf N, MacSweeney ST, Gladman J, et al. Carotid intraplaque hemorrhage predicts recurrent symptoms in patients with high-grade carotid stenosis. *Stroke* 2007;38:1633–35
- Schillinger M, Exner M, Mlekusch W, et al. Inflammation and Carotid Artery—Risk for Atherosclerosis Study (ICARAS). *Circulation* 2005;111:2203–09
- Takaya N, Yuan C, Chu B, et al. Presence of intraplaque hemorrhage stimulates progression of carotid atherosclerotic plaques: a high-resolution magnetic resonance imaging study. *Circulation* 2005; 111:2768–75
- Saam T, Yuan C, Chu B, et al. Predictors of carotid atherosclerotic plaque progression as measured by noninvasive magnetic resonance imaging. *Atherosclerosis* 2007;194:e34–42
- Sun J, Underhill HR, Hippe DS, et al. Sustained acceleration in carotid atherosclerotic plaque progression with intraplaque hemorrhage: a long-term time course study. *JACC Cardiovasc Imaging* 2012;5:798–804
- Wang Q, Wang Y, Cai J, et al. Differences of signal evolution of intraplaque hemorrhage and associated stenosis between symptomatic and asymptomatic atherosclerotic carotid arteries: an in vivo high-resolution magnetic resonance imaging follow-up study. *Int J Cardiovasc Imaging* 2010;26:323–32
- van Lammeren GW, den Hartog AG, Pasterkamp G, et al. Asymptomatic carotid artery stenosis: identification of subgroups with different underlying plaque characteristics. *Eur J Vasc Endovasc Surg* 2012;43:632–36
- Bradley WG Jr. MR appearance of hemorrhage in the brain. *Radiology* 1993;189:15–26
- Virmani R, Kolodgie FD, Burke AP, et al. Atherosclerotic plaque progression and vulnerability to rupture: angiogenesis as a source of intraplaque hemorrhage. *Arterioscler Thromb Vasc Biol* 2005; 25:2054–61
- Altman DG, Royston P. The cost of dichotomising continuous variables. *BMJ* 2006;332:1080
- Chu B, Kampschulte A, Ferguson MS, et al. Hemorrhage in the atherosclerotic carotid plaque: a high-resolution MRI study. *Stroke* 2004;35:1079–84
- van Gils MJ, Vukadinovic D, van Dijk AC, et al. Carotid atherosclerotic plaque progression and change in plaque composition over time: a 5-year follow-up study using serial CT angiography. *AJNR Am J Neuroradiol* 2012;33:1267–73

Changes of Time-Attenuation Curve Blood Flow Parameters in Patients with and without Carotid Stenosis

C.-J. Lin, F.-C. Chang, W.-Y. Guo, S.-C. Hung, C.-B. Luo, J. Beilner, M. Kowarschik, and W.-F. Chu

ABSTRACT

BACKGROUND AND PURPOSE: From the time-attenuation curves of DSA flow parameters, maximal intensity, maximal slope, and full width at half maximum of selected vascular points are defined. The study explores the reliability of defining the flow parameters by the time-attenuation curves of DSA.

MATERIALS AND METHODS: Seventy patients with unilateral carotid artery stenosis (group A) and 56 healthy controls (group B) were retrospectively enrolled. Fixed contrast injection protocols and DSA acquisition parameters were used with all patients. The M1, sigmoid sinus, and internal jugular vein on anteroposterior view DSA and the M2, parietal vein, and superior sagittal sinus on lateral view DSA were chosen as ROI targets for measuring flow parameters. The difference of time of maximal intensity between 2 target points was defined as the circulation time between the target points.

RESULTS: The maximal intensity difference of 2 selected points from the ICA to the M1, sigmoid sinus, internal jugular vein, M2, parietal vein, and superior sagittal sinus was significantly longer in group A than in group B. The maximum slope of M1, M2, and the superior sagittal sinus was significantly lower in group A than in group B. The full width at half maximum of M1 and M2 was significantly larger in group A than in group B. The maximal slope of M1 demonstrated the best diagnostic performance.

CONCLUSIONS: The maximal intensity difference of 2 selected points derived from DSA can be used as a definitive alternative flow parameter for intracranial circulation time measurement. Maximal slope and full width at half maximum complement the maximal intensity difference of 2 selected points in defining flow characteristics of healthy subjects and patients with carotid stenosis.

ABBREVIATIONS: FWHM = full width at half maximum; MS = maximal slope; PV = parietal vein; SSS = superior sagittal sinus; TDC = time-attenuation curve; Tmax = time of maximal intensity; rTmax = Tmax difference of 2 selected points

DSA is the standard reference for diagnosing cerebrovascular diseases with its superior temporal and spatial resolution compared with other imaging methods.¹⁻³ Using different approaches, a number of recent studies have demonstrated the feasibility of quantitative flow parameter measurement by using flat detector DSA.⁴⁻⁷ Compared with optical flow methods and computer fluid dynamics simulations, flow parameter analysis with

the time-attenuation curve (TDC) of DSA images is less demanding in terms of computer power and processing time.^{8,9} Clinically, TDCs are used to assess the “real-time” peritherapeutic hemodynamics of various vascular disorders in an angiography suite.¹⁰⁻¹² The TDC represents the dynamic intensity changes of a contrast bolus passing an ROI. It is affected by the bolus characteristics and physiologic and anatomic conditions (eg, arterial stenosis or arteriovenous shunts).^{11,13} From the TDC, we may measure the time of maximal intensity (Tmax), maximal slope (MS), and full width at half maximum (FWHM) of any selected vascular point on the DSA image. The time difference to reach maximum intensity (rTmax) of 2 selected vascular points indicates the circulation time between these 2 points. Accordingly, cerebral circulation time is defined as the rTmax between the internal carotid artery and the parietal vein (PV). The PV is closer to the brain parenchyma compared with the transverse sinus or jugular vein and thus better represents the time for blood flow to travel through the brain parenchyma.¹⁴ Circulation time is an objective flow parameter for various vascular disorders (eg, carotid stenosis, carotid

Received August 10, 2014; accepted after revision December 1.

From the Department of Radiology (C.-J.L., F.-C.C., W.-Y.G., S.-C.H., C.-B.L., W.-F.C.), Taipei Veterans General Hospital, Taipei, Taiwan; School of Medicine (C.-J.L., F.-C.C., W.-Y.G., S.-C.H., C.-B.L.), National Yang-Ming University, Taipei, Taiwan; Angiography and Interventional X-Ray Systems (J.B.), Siemens Ltd China, Healthcare Sector, Shanghai, P.R. China; and Angiography and Interventional X-Ray Systems (M.K.), Siemens AG, Healthcare Sector, Erlangen, Germany.

This work was cosponsored by the Taipei Veterans General Hospital and Siemens (grant No: T1100200).

Please address correspondence to Wan-Yuo Guo, MD, PhD, Department of Radiology, Taipei Veterans General Hospital No. 201, Shipai Rd, Section 2, Taipei, 11217, Taiwan; e-mail: wyguo@vghtpe.gov.tw

<http://dx.doi.org/10.3174/ajnr.A4239>

cavernous fistula, and peritherapeutic assessment).^{10,12,15,16} The aim of the present study was to compare the diagnostic accuracy of rTmax, MS, and FWHM for detecting blood flow property changes by using a large sample of healthy subjects and patients with carotid stenosis.

MATERIALS AND METHODS

Patient Selection

The institutional review board of the hospital approved this retrospective study, and patient consent forms were waived. From October 2011 to December 2013, 546 patients were consecutively referred to our institution for DSA. Patients with poor heart function present with polymorphic TDC waveforms and thus make identification of Tmax and subsequent measurement of MS and FWHM difficult. After we excluded patients with poor renal and/or heart functions and previous large territorial infarct and those whose imaging did not follow the standard DSA acquisition protocol, 126 patients eligible for analysis were retrospectively recruited for the current study. Seventy of 126 patients (mean age, 73.6 years; 59 men and 11 women) with unilateral extracranial internal carotid artery stenosis (>70%, based on the NASCET criteria) were classified as group A. The other 56 patients (mean age, 65.6 years; 26 men and 30 women) referred for DSA with nonarterial occlusive disorders (namely, post-aneurysm clipping/coiling follow-up and suspected vascular lesions with negative angiography findings) were classified as group B.

Imaging Protocol and Data Analysis

DSA acquisitions with a standard, clinically routine protocol were performed in all 126 cases. A power injector (Liebel-Flarsheim Angiomat; Illumena, San Diego, California) was used to create a contrast bolus after placing a 4F angiocatheter in the common carotid artery at the C4 vertebral body level. A bolus of 12 mL of 60% diluted contrast medium (340 mg I/mL) was administered within 1.5 seconds. Neither extra contrast medium nor extra radiation was used. The acquisition parameters were 7.5 frames/s for the first 5 seconds, followed by 4 frames/s for 3 seconds, 3 frames/s for 2 seconds, and finally 2 frames/s for 2 seconds. The entire DSA acquisition time was 12 seconds. However, it might be manually tailored to be shortened or prolonged for optimized internal jugular vein opacification.¹⁰ The mean and range of irradiation parameters and dosage were the following: 91.4 (88–97) kV, 287.8 (268–318) mA, 29.1 (29.1–29.2) ms, and 1.21 (0.7–1.78) mGy/frame for anteroposterior views and 73.4 (70–92) kV, 402.5 (283–426) mA, 29.1 (29.1–29.2) ms, and 1.30 (0.68–1.86) mGy/frame for lateral views.

DSAs of contralateral (normal) sides in group A were not evaluated, mainly due to different FOVs routinely used in our institution for the contralateral (normal) side of patients with unilateral internal carotid artery stenosis. There were 24 patients with hypoplasia or aplasia of the anterior communicating artery in group A. The same biplane angiography suite (Axiom Artis dBA; Siemens, Erlangen, Germany) was used for DSA throughout the entire study. The degree of arterial stenosis was determined by the more severe degree on anteroposterior lateral views according to the NASCET criteria.¹⁷ All DSA analyses were performed on a workstation equipped with prototype software, DSA Analyzer

(Siemens). DSA Analyzer is a software package for analyzing 2D DSA image series. It represents an extended version of the commercially available software tool syngo iFlow (Siemens). On the basis of the TDC, DSA Analyzer extracts flow parameters (eg, Tmax, MS, and FWHM) of user-selected vascular points or ROIs on DSA.

Selection of ROIs

Parametric color-coding of DSA according to the Tmax of individual pixels was displayed instantly.⁴ On the basis of previous research, we placed ROIs on the first segment of the middle cerebral artery, sigmoid sinus, and ipsilateral internal jugular vein on anteroposterior view DSA and on the second branch of the middle cerebral artery, parietal vein, and superior sagittal sinus (SSS) on lateral view DSA for flow parameter analyses (Fig 1).^{10,14} The ROI placement was standardized to avoid overlapping anatomic structures and inhomogeneous areas and to use the caliber of the target vessel as the diameter of an ROI.¹⁰ One neuroradiologist with 8 years' experience and 1 angiographic technician performed the ROI placements by consensus. Both were unaware of the clinical conditions of the studied subjects.

Definition of Flow Parameters

After ROI placements, 3 flow parameters (Tmax, MS, and FWHM) were immediately extracted from the respective TDCs. "Tmax" was defined as the time point at which the pixel reached its maximum concentration during the angiographic series. "MS" was defined as the maximum tangential slope between the arrival time of the contrast medium and the Tmax on the TDC. "FWHM" was defined as the width of the 2 time points on the TDC when the concentration reached half of the maximum concentration (Fig 2). Tmax of the ROIs was normalized by subtraction of the Tmax of the cervical ICA on the anteroposterior view or cavernous ICA on the lateral view. The normalized time difference was defined as rTmax—that is, the circulation time between 2 selected vascular points. Accordingly, rTmax ICA-PV was referred to as "cerebral circulation time," the time for blood flow to travel through the brain parenchyma.¹⁴

Statistical Analysis

All statistical analyses were performed by using SPSS 20 (2010; IBM, Armonk, New York). The correlation between the stenotic degree and TDC flow parameters (rTmax, MS, and FWHM) was explored by using the Pearson correlations. The differences of rTmax, MS, and FWHM between groups A and B were compared by using a Student *t* test. We used receiver operating characteristic curves to evaluate the diagnostic performance of the above-mentioned flow parameters in carotid stenosis. The maximum area under the curve of the receiver operating characteristic was used to determine the optimal cutoff value. Significance was set to $P < .05$ for all statistical tests.

RESULTS

No subjects in group A had acute stroke peritherapeutically evidenced by MR imaging. The patient demographic data are listed in Table 1. The average age in group A (73.6 ± 11.6 years) was older than that for group B (65.6 ± 10.2 years). Stenotic degree

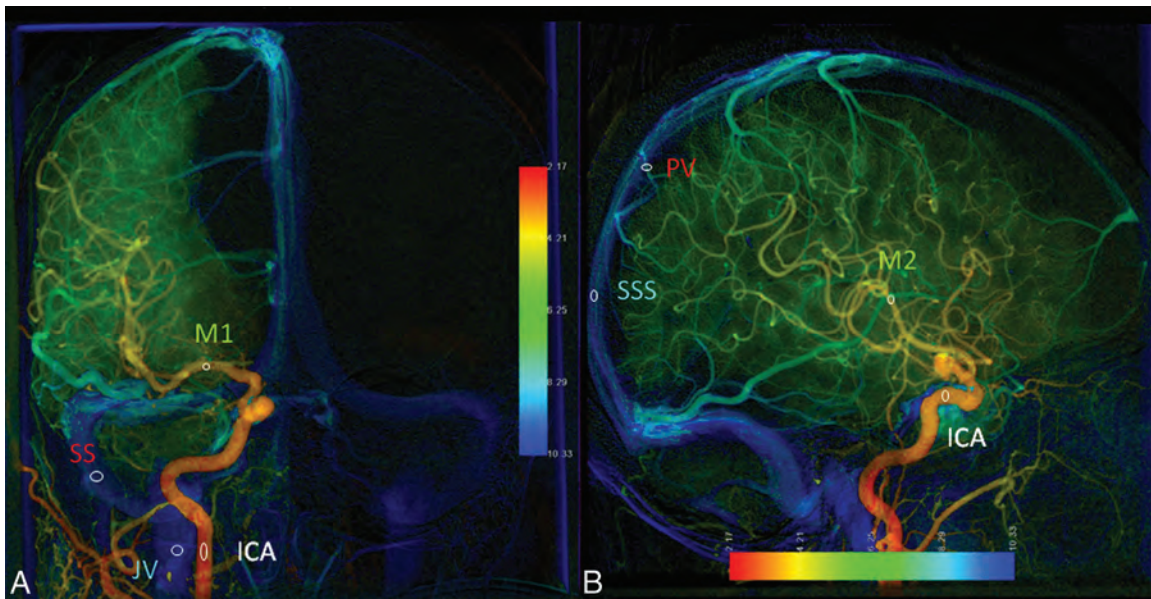


FIG 1. Anteroposterior (A) and lateral (B) views of parametric color-coding of quantitative DSA. A, The ROI of the ICA is located at the midpoint of the cervical portion of the ICA. The ROI of M1 is located at the midpoint of the first segment of the middle cerebral artery. The sigmoid sinus ROI is located at the midpoint of the ipsilateral sigmoid sinus. The jugular vein ROI is located in the internal jugular vein at the same level as the ICA ROI. B, The ICA ROI is located in the cavernous portion of the ICA. The M2 ROI is located in the insular branch of the MCA. The PV ROI is located in the outlet of the parietal vein. The SSS ROI is located 2 cm above the confluence of the SSS.

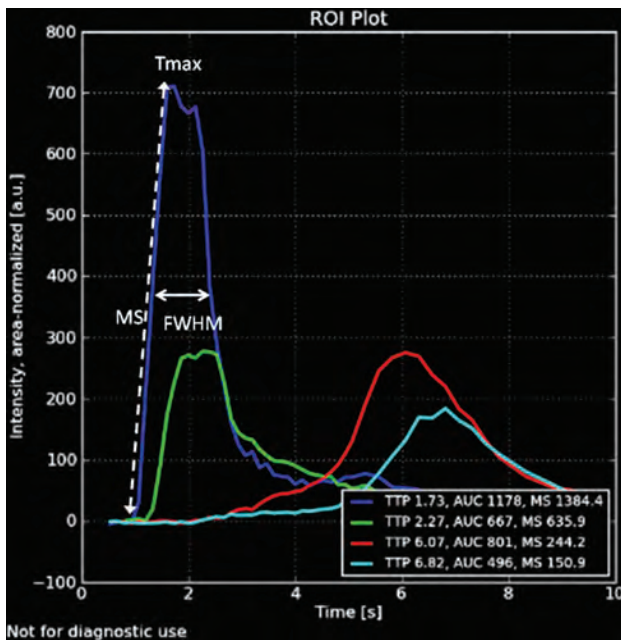


FIG 2. Time-attenuation curves of lateral view DSA in a healthy subject. The blue curve represents the TDC of the ROI in the cavernous portion of the ICA. Tmax is the time point at which the ROI reaches maximal intensity. The MS of an ROI is defined by the maximal tangential slope located between arrival time and Tmax. FWHM is the width of the waveform at the level of half maximum concentration.

had a mild positive correlation with rTmax in M2 ($r = 0.380$) and M1 ($r = 0.486$) and FWHM in M2 ($r = 0.34$) and a mild negative correlation with MS in PV (-0.448) (Table 2). MS of the PV was the only venous ROI showing a negative correlation with stenotic degree.

The comparison of rTmax, MS, and FWHM in 6 ROIs between groups A and B is shown in Table 3. All rTmax values were

Table 1: Patient characteristics for groups A and B

	Group A (Stenosis)	Group B (Healthy)	P Value
No.	70	56	
Age (yr)	73.6 ± 11.6	65.6 ± 10.2	<.001 ^a
Heart rate (beats/min)	69.9 ± 17.2	72.6 ± 12.3	0.312
Blood pressure (mm Hg)	92.8 ± 19.9	97.6 ± 18.5	0.124
Stenotic degree (%)	81.4%	NA	NA
Prior minor stroke	19 (27%)	1 (1.7%)	<.001 ^a

Note:—NA indicates not applicable.

^aStatistically significant (t test, $P < .05$). There was no measurable stenosis in the healthy (control) population.

Table 2: Correlation of degree of stenosis with rTmax, MS, and FWHM^a

	rTmax	MS	FWHM
Degree of stenosis (%)	M2 (0.380)	M1 (0.486) ^b	PV (-0.448) ^b
	PV (0.280)	SS (0.222)	SSS (-0.238)
	SSS (0.272)	JV (0.264)	M1 (-0.305)

Note:—SS indicates sigmoid sinus; JV, internal jugular vein.

^aROIs demonstrating statistically significant Pearson correlations are listed in each cell (correlations are given in parentheses).

^bThese 2 parameters were mildly correlated ($r > 0.4$).

significantly longer in group A than in group B. For MS, only the M1, M2, and SSS of group A demonstrated flatter slopes than in group B. For FWHM, only M1 and M2 demonstrated significantly wider waveforms in group A than in group B. None of the venous ROIs demonstrated significantly wider waveforms in group A.

M1 and M2 are the only ROIs with all 3 flow parameters demonstrating significant differences between 2 groups. SSS is the only venous ROI with 2 flow parameters (rTmax and MS) showing significant differences between the 2 groups.

Figure 3 illustrates the receiver operating characteristic curves of the flow parameters (6 rTmax, 3 MS, and 2 FWHM) to compare their diagnostic performance in detecting carotid stenosis.

Table 3: Comparison of group A and B values for rTmax, MS, and FWHM for 6 different ROIs

ROI	Group A		P Value
	Stenosis (n = 70)	Group B Healthy (n = 56)	
rTmax			
M2	0.77 ± 0.52	0.58 ± 0.32	.005 ^a
PV	5.08 ± 1.32	4.38 ± 1.38	.001 ^a
SSS	6.35 ± 1.79	5.44 ± 1.44	.001 ^a
M1	0.66 ± 0.31	0.46 ± 0.46	.001 ^a
SS	6.71 ± 1.91	5.91 ± 1.67	.004 ^a
JV	7.29 ± 1.77	6.60 ± 1.62	.008 ^a
MS			
M2	337.15 ± 166.18	390.39 ± 166.98	.03 ^a
PV	159.34 ± 73.36	170.56 ± 99.95	.43
SSS	103.78 ± 57.8	134.38 ± 111.07	.03 ^a
M1	331.59 ± 144.43	454.44 ± 320.48	.003 ^a
SS	100.32 ± 58.22	97.02 ± 47.17	.699
JV	116.78 ± 63.13	136.22 ± 109.63	.185
FWHM			
M2	2.54 ± 1.14	2.09 ± 0.70	<.001 ^a
PV	2.84 ± 2.37	2.74 ± 1.65	.74
SSS	3.49 ± 2.38	3.86 ± 0.75	.607
M1	3.57 ± 1.90	2.78 ± 0.92	.002 ^a
SS	4.33 ± 1.83	3.72 ± 1.17	.61
JV ^b	NA	NA	NA

Note:—SS indicates sigmoid sinus; JV, internal jugular vein.

^a Statistically significant difference (t test, $P < .05$).

^b The FWHM of the JV was not applicable because the DSA acquisition terminated before the waveform of the JV dropped in most cases.

The 4 best diagnostic flow parameters were MS in M1 (cutoff value, 378.3; sensitivity, 66.7%; specificity, 60.0%), followed by FWHM in M1 (cutoff value, 3.40; sensitivity, 57.1%; specificity, 78.4%), rTmax of M1 (cutoff value, 0.45; sensitivity, 81%; specificity, 58.2%), and rTmax of SSS (cutoff value, 6.895; sensitivity, 55.2%; specificity, 73.7%) (Table 4).

DISCUSSION

Within normal physiologic conditions, the degree of carotid stenosis has greater impact on rTmax than on MS and FWHM. Carotid stenosis makes the waveform of the poststenotic arterial segment delayed (prolonged rTmax in group A) and wider (larger FWHM values in group A) (Fig 4). This effect has also been observed as delay and dispersion effects in MR imaging and CT perfusion studies.^{18,19} Doppler sonography illustrates the phenomenon, known as “tardus parvus,” due to the widened and flatter poststenotic waveform.^{20,21}

rTmax values of arteries and veins (artery-vein) were prolonged in group A (defined by the presence of carotid stenosis). Proximal arterial stenosis may transit the slowdown effects on blood flow to the downstream areas of the brain parenchyma. Poststenting normalization of rTmax artery-vein in carotid occlusive arterial disease indicates restoration of both arterial and venous blood flows.^{14,22} Patients who have ipsilateral stenotic and hypoplastic venous outlets are prone to develop hyperperfusion syndrome after stent placement.²²⁻²⁴

MS was considered a surrogate marker for intravascular velocity because it represents the maximum gradient of x-ray attenuation and therefore reflects the speed of contrast medium (ie, the blood flow velocity).^{11,25} Theoretically, MS should be more sensitive to flow changes compared with rTmax. Nevertheless, only 2 arterial ROIs (M1, M2) and 1 venous ROI (SSS) demonstrated a

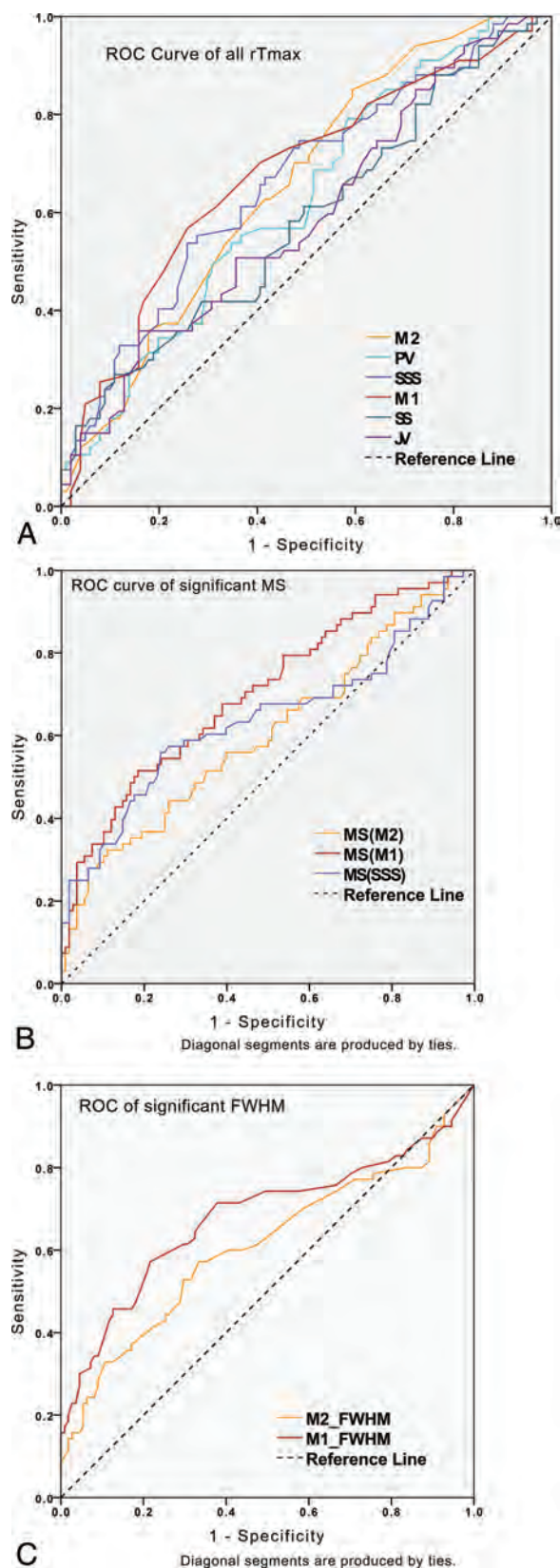


FIG 3. Receiver operating characteristic curves of all significantly different rTmax values (A), all significantly different MS values (B), and all significantly different FWHM values (C) in differentiating patients with stenosis from control groups.

significant decrease in MS in group A. As for FWHM, values were wider only in M2 and M1 in group A but not in any venous ROIs. If we take the receiver operating characteristic curves into consideration, M1 was the best location for detecting stenosis because its 3 flow parameters all showed reasonably high diagnostic performance. rTmax is still the best flow parameter among the 3 because the rTmax of all ROIs was prolonged and therefore demonstrated delayed reach of wave peaks in the TDC chart in group A (Fig 4). MS and FWHM illustrated less impact on venous flows. One plausible explanation would be that the smaller amplitude of the waveform and the en-

countering of more anatomic variation in the intracranial venous system make venous flow more complicated and MS and FWHM less sensitive. Additionally, the unpredictable inflow of blood without contrast from other vascular territories changes the attenuation of TDC and makes analysis of venous ROIs challenging.

Optical flow methods and computer fluid dynamics simulations quantify flows with an alternative approach, and both are highly demanding in terms of computer power and processing time. Until now, they have been available mainly in research institutes, and their roles in clinical applications are still limited. Nevertheless, computer fluid dynamics measures exclusively in vivo flow information in aneurysmal and juxta-aneurysmal areas.^{26,27} Its role in stenotic cerebrovascular disease is not clear. The current study results showed that MS and FWHM were only clinically significant in limited ROIs and were complementary to rTmax in describing flows.

Several limitations exist in our study. The DSA series was 2D; therefore, the overlapping of anatomic structures mixed and distorted the TDCs. Future research by using 3D DSA datasets would resolve this issue.^{5,28-31} Curve fitting or using the average slopes of ascending parts of the TDC would improve the reliability of MS and FWHM. Other potential flow parameters (eg, arrival time, kurtosis, and skewness) can describe bolus characteristics. The size and location of previous infarction might affect the measurements of the TDC but were not explored in the current study. According to our initial experience, those with old small lacunar infarcts or subterritorial infarct usually develop collateral circulation. Therefore, chronic ischemic insults might influence the rTmax or circulation, but stenotic degree still dominates in terms of TDC changes.

Table 4: Cutoff values of 10 significant TDC parameters for detecting stenosis flow with optimized sensitivity and specificity

ROI Variable	AUC	P Value	Cutoff Value	Sensitivity	Specificity
rTmax					
M2	0.638 (0.555–0.722)	.002	0.415	83.6%	37.6%
PV	0.615 (0.53–0.701)	.011	4.905	55.2%	63.4%
SSS	0.655 (0.57–0.74) ^a	.001	6.895	55.2%	73.7%
M1	0.663 (0.58–0.746) ^a	.001	0.45	81.0%	58.2%
SS	0.582 (0.495–0.669)	.045	7.42	73.5%	91.2%
JV	0.589 (0.503–0.676)	.045	7.77	63.7%	84.9%
MS					
M2	0.606 (0.517–0.695)	.02	511.5	89.6%	21.8%
M1	0.689 (0.608–0.77) ^a	.041	378.3	66.7%	60.0%
SSS	0.636 (0.547–0.725)	.002	90.5	55.1%	75.5%
FWHM					
M2	0.609 (0.52–0.699)	.013	3.45	57.1%	67.7%
M1	0.679 (0.59–0.77) ^a	.001	3.40	57.1%	78.4%

Note:—SS indicates sigmoid sinus; JV, internal jugular vein.

^aThe best 4 parameters for detecting stenotic flow.

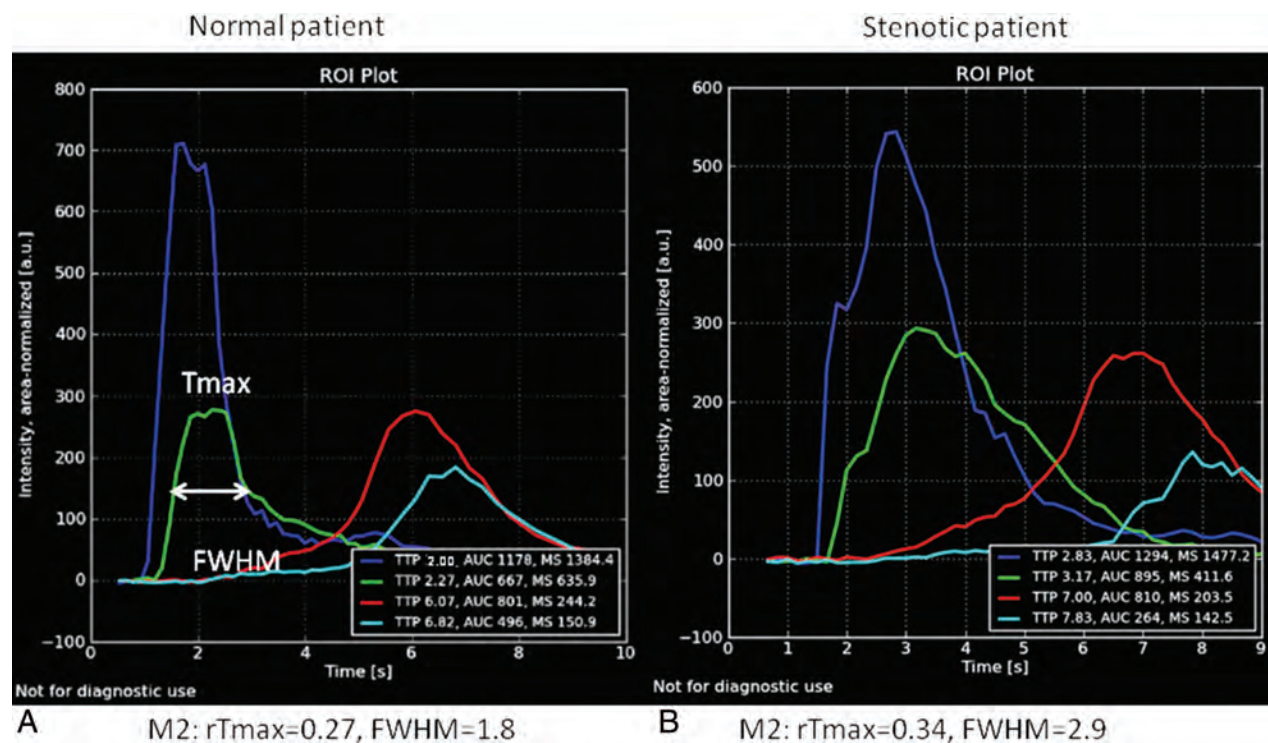


FIG 4. TDC of lateral views of angiography are from a healthy individual (A) and a patient with 80% carotid stenosis (B). Both green lines are TDCs of M2. The rTmax of M2 in the patient with stenosis is 0.34 seconds, which was more prolonged than that (0.27 seconds) in the healthy individual. The FWHM of M2 (2.9 seconds) in the patient with stenosis is longer than that (1.8 seconds) in the healthy individual. The ICA (dark blue curves), sigmoid sinus (red curves), and internal jugular vein (light blue curves) all demonstrate prolonged rTmax and are right-shifted in the patient with stenosis. These delayed and dispersed phenomena of angiographic TDCs are consistent with those observed in MR imaging and CT perfusion imaging.

Our study offers reassurance about the reliability of evaluating intravascular flows by TDC and offers a real-time clinically diagnostic tool to tailor endovascular treatment within the angiography suite.^{26,32} Currently, the ROIs are placed manually. Future work on automation in ROI placement based on selecting the best-described waveform of flows may further shorten the assessment time and broaden the clinical application of color-coded quantitative DSA.

CONCLUSIONS

Our study confirmed that rT_{max} remains the preferred measurement for all ROIs when a single-flow parameter is used. MS and FWHM demonstrated equivalent diagnostic performance in differentiating carotid stenosis and thus can serve as complementary diagnostic parameters because neither alone achieves excellent sensitivity or specificity.

ACKNOWLEDGMENTS

We thank Josephe Lavalle for manuscript preparation and C.S. Lin for statistical support.

Disclosures: Wan-Yuo Guo—UNRELATED: Grant: collaboration between Institution and Siemens*; Support for Travel to Meetings for the Study or Other Purposes: Taipei Veterans General Hospital,* Comments: to present the study results; Provision of Writing Assistance, Medicines, Equipment, or Administrative Support: software provided by Siemens under the collaboration contract. Janina Beilner—OTHER RELATIONSHIPS: In this study, Siemens software was used. I am a Siemens employee. Markus Kowarschik—OTHER RELATIONSHIPS: Employee of Siemens.*Money paid to the institution.

REFERENCES

- Raney R, Raney AA, Sanchez-Perez JM. **The role of complete cerebral angiography in neurosurgery.** *J Neurosurg* 1949;6:222–37
- Luo Z, Wang D, Sun X, et al. **Comparison of the accuracy of subtraction CT angiography performed on 320-detector row volume CT with conventional CT angiography for diagnosis of intracranial aneurysms.** *Eur J Radiol* 2012;81:118–22
- Petkova M, Gauvrit J-Y, Trystram D, et al. **Three-dimensional dynamic time-resolved contrast-enhanced MRA using parallel imaging and a variable rate k-space sampling strategy in intracranial arteriovenous malformations.** *J Magn Reson Imaging* 2009;29:7–12
- Strother CM, Bender F, Deuerling-Zheng Y, et al. **Parametric color coding of digital subtraction angiography.** *AJNR Am J Neuroradiol* 2010;31:1919–24
- Pereira V, Ouaed R, Brina O, et al. **Quantification of internal carotid artery flow with digital subtraction angiography: validation of an optical flow approach with Doppler ultrasound.** *AJNR Am J Neuroradiol* 2014;35:156–63
- Xiang J, Tutino VM, Snyder KV, et al. **CFD: computational fluid dynamics or confounding factor dissemination? The role of hemodynamics in intracranial aneurysm rupture risk assessment.** *AJNR Am J Neuroradiol* 2014;35:1849–57
- Kefayati S, Poepping TL. **Transitional flow analysis in the carotid artery bifurcation by proper orthogonal decomposition and particle image velocimetry.** *Med Eng Phys* 2013;35:898–909
- Pasta S, Cho JS, Dur O, et al. **Computer modeling for the prediction of thoracic aortic stent graft collapse.** *J Vasc Surg* 2013;57:1353–61
- Huang TC, Wu TH, Lin CJ, et al. **Peritherapeutic quantitative flow analysis of arteriovenous malformation on digital subtraction angiography.** *J Vasc Surg* 2012;56:812–15
- Lin CJ, Hung SC, Guo WY, et al. **Monitoring peri-therapeutic cerebral circulation time: a feasibility study using color-coded quantitative DSA in patients with steno-occlusive arterial disease.** *AJNR Am J Neuroradiol* 2012;33:1685–90
- Shpilfoygel SD, Close RA, Valentino DJ, et al. **X-ray videodensitometric methods for blood flow and velocity measurement: a critical review of literature.** *Med Phys* 2000;27:2008–23
- Gölitiz P, Struffert T, Lücking H, et al. **Parametric color coding of digital subtraction angiography in the evaluation of carotid cavernous fistulas.** *Clin Neuroradiol* 2013;23:113–20
- Wilcox BR, Coulter NA, Rackley CE, et al. **The effect of changing heart rate on blood flow, power dissipation, and resistance in the common carotid artery of man.** *Ann Surg* 1970;171:24–30
- Greitz T. **A radiologic study of the brain circulation by rapid serial angiography of the carotid artery.** *Acta Radiol Suppl* 1956;1–123
- Lin CJ, Luo CB, Hung SC, et al. **Application of color-coded digital subtraction angiography in treatment of indirect carotid-cavernous fistulas: initial experience.** *J Chin Med Assoc* 2013;76:218–24
- Gado M, Eichling J, Grubb R, et al. **Appraisal of the angiographic circulation time as an index of cerebral blood flow.** *Radiology* 1975;115:107–12
- North American Symptomatic Carotid Endarterectomy Trial Collaborators. **Beneficial effect of carotid endarterectomy in symptomatic patients with high-grade carotid stenosis.** *N Engl J Med* 1991;325:445–53
- Calamante F. **Arterial input function in perfusion MRI: a comprehensive review.** *Prog Nucl Magn Reson Spectrosc* 2013;74:1–32
- Kudo K, Sasaki M, Ogasawara K, et al. **Difference in tracer delay-induced effect among deconvolution algorithms in CT perfusion analysis: quantitative evaluation with digital phantoms.** *Radiology* 2009;251:241–49
- Withers CE, Gosink BB, Keightley AM, et al. **Duplex carotid sonography: peak systolic velocity in quantifying internal carotid artery stenosis.** *J Ultrasound Med* 1990;9:345–49
- Blackshear WM, Phillips DJ, Chikos PM, et al. **Carotid artery velocity patterns in normal and stenotic vessels.** *Stroke* 1980;11:67–71
- Lin CJ, Chang FC, Tsai FY, et al. **Stenotic transverse sinus predisposes to poststenting hyperperfusion syndrome as evidenced by quantitative analysis of peritherapeutic cerebral circulation time.** *AJNR Am J Neuroradiol* 2014;35:1132–36
- Narita S, Aikawa H, Nagata S, et al. **Intraprocedural prediction of hemorrhagic cerebral hyperperfusion syndrome after carotid artery stenting.** *J Stroke Cerebrovasc Dis* 2013;22:615–19
- Aikawa H, Kazekawa K, Tsutsumi M, et al. **Intraprocedural changes in angiographic cerebral circulation time predict cerebral blood flow after carotid artery stenting.** *Neurol Med Chir (Tokyo)* 2010;50:269–74
- Levitt MR, Morton RP, Haynor DR, et al. **Angiographic perfusion imaging: real-time assessment of endovascular treatment for cerebral vasospasm.** *J Neuroimaging* 2014;24:387–92
- Rhode KS, Lambrou T, Hawkes DJ, et al. **Novel approaches to the measurement of arterial blood flow from dynamic digital x-ray images.** *IEEE Trans Med Imaging* 2005;24:500–13
- Shobayashi Y, Tateshima S, Kakizaki R, et al. **Intra-aneurysmal hemodynamic alterations by a self-expandable intracranial stent and flow diversion stent: high intra-aneurysmal pressure remains regardless of flow velocity reduction.** *J Neurointerv Surg* 2013;5(suppl 3):iii38–42
- Waechter I, Bredno J, Hermans R, et al. **Model-based blood flow quantification from rotational angiography.** *Med Image Anal* 2008;12:586–602
- Waechter I, Bredno J, Weese J, et al. **Using flow information to support 3D vessel reconstruction from rotational angiography.** *Med Phys* 2008;35:3302–16
- Bogunović H, Lončarić S. **Blood flow and velocity estimation based on vessel transit time by combining 2D and 3D X-ray angiography.** *Med Image Comput Assist Interv* 2006;9(pt 2):117–24
- Davis B, Royalty K, Kowarschik M, et al. **4D digital subtraction angiography: implementation and demonstration of feasibility.** *AJNR Am J Neuroradiol* 2013;34:1914–21
- Hung SC, Lin CJ, Guo WY, et al. **Toward the era of a one-stop imaging service using an angiography suite for neurovascular disorders.** *Biomed Res Int* 2013;2013:873614

Imaging Appearance of Dextranomer/Hyaluronic Acid Copolymer Implant Injections for Treatment of Velopharyngeal Insufficiency

W. Brinjikji, S.A. Cofer, and J.I. Lane

ABSTRACT

BACKGROUND AND PURPOSE: Dextranomer/hyaluronic acid copolymer implants are used in treating velopharyngeal insufficiency. These posterior nasopharyngeal implants can be mistaken for pathologic conditions such as retropharyngeal abscess on imaging. We studied the imaging appearance of dextranomer/hyaluronic acid copolymer implants in patients treated for velopharyngeal insufficiency.

MATERIALS AND METHODS: A consecutive series of patients with velopharyngeal insufficiency treated with dextranomer/hyaluronic acid copolymer were included in this study. Data on patient characteristics and volume of dextranomer/hyaluronic acid copolymer injected were obtained. Postoperative imaging characteristics on plain radiography, CT, and MR imaging were assessed. The imaging appearance of postoperative complications was determined.

RESULTS: Sixteen patients were included in this study. Seven patients underwent postoperative plain radiographs, 5 patients underwent CT, and 9 patients underwent MR imaging. Plain radiographs demonstrated soft-tissue swelling in the retropharyngeal space, which resolved at 1 month. On CT, dextranomer/hyaluronic acid copolymer implants appeared as bilateral nasopharyngeal soft-tissue masses isoattenuated to hypoattenuated relative to muscle in 80% (4/5) of patients. On MR imaging, dextranomer/hyaluronic acid copolymer implants appeared as bilateral nasopharyngeal soft-tissue masses that were isointense to muscle on T1 (8/9, 88.9%) and hyperintense to muscle on T2 (8/9, 88.9%) and demonstrated no restricted diffusion (4/4, 100.0%) or peripheral enhancement (7/7, 100.0%).

CONCLUSIONS: The normal postoperative findings of posterior nasopharyngeal dextranomer/hyaluronic acid copolymer injection on MR imaging is characterized by the presence of bilateral nasopharyngeal soft-tissue masses that are isointense to muscle on T1 and hyperintense on T2, with no restricted diffusion or peripheral enhancement. Velopharyngeal dextranomer/hyaluronic acid copolymer implants are iso- to hypoattenuated to muscle on CT and are not visible radiographically once associated implantation-related swelling has resolved.

ABBREVIATION: VPI = velopharyngeal insufficiency

Posterior pharyngeal wall augmentation is a promising technique for the treatment of velopharyngeal insufficiency (VPI).¹ By augmenting the posterior pharyngeal wall so it extends more anteriorly, an easily reached contact point for the soft palate is created, allowing velopharyngeal closure. Numerous implant materials have been used, including cartilage, fat, paraffin, and calcium hydroxyapatite.¹⁻⁷ Injection of dextranomer/hyaluronic acid has emerged as an effective technique for treating vocal cord dysfunction and laryngeal insufficiency, and augmenting the pos-

terior pharyngeal wall in the treatment of VPI.⁸⁻¹² Because many patients receiving these implants will undergo imaging studies unrelated to VPI, characterization of the normal imaging appearance of hyaluronic acid implants in the posterior pharyngeal wall is important to avoid confusion with pathologic processes.

MATERIALS AND METHODS

Patient Population

After institutional review board approval, a retrospective series of patients who received posterior pharyngeal wall augmentation with hyaluronic implants (dextranomer/hyaluronic acid copolymer or hyaluronic acid) between April 1, 2010, and August 31, 2012, and who underwent follow-up imaging was reviewed. For all patients, data on age, sex, underlying disease, and volume of polymer injected were collected.

Received September 23, 2014; accepted after revision November 17.

From the Departments of Radiology (W.B., J.I.L.) and Otorhinolaryngology (S.A.C.), Mayo Clinic, Rochester, Minnesota.

Please address correspondence to Waleed Brinjikji, MD, Department of Radiology, Mayo Clinic, 200 1st St SW, Rochester, MN 55905; e-mail: brinjikji.waleed@mayo.edu

<http://dx.doi.org/10.3174/ajnr.A4246>

Procedural Details

All surgical procedures were performed by an otorhinolaryngologist. Preoperative nasoendoscopy was used to determine the level of velopharyngeal closure. Patients were treated under general endotracheal anesthesia. A catheter was inserted into each nostril and withdrawn through the oral cavity and clamped to itself to retract the palate. Mirror visualization of the nasopharynx was correlated with the findings of the nasoendoscopy. Following identification of the level of velopharyngeal closure, dextranomer/hyaluronic acid copolymer or hyaluronic acid solution was injected to augment the posterior nasopharyngeal wall. Careful aspiration before the injection was performed to avoid placement

Clinical characteristics of patients treated for velopharyngeal insufficiency

Characteristics	
No. of patients	15
Mean age (SD) (yr)	21.3 (21.9)
Median age (yr) (minimum, maximum)	10 (3, 68)
No. (%) female	8 (53.3)
Comorbidities (No.) (%)	
Velocardiofacial syndrome	3 (20.0)
Neurofibromatosis type 1	3 (20.0)
Postsurgical complication	3 (20.0)
Collet-Sicard syndrome	1 (6.7)
Pierre-Robin sequence	1 (6.7)
Oculopharyngeal muscular dystrophy	1 (6.7)
Chiari II	1 (6.7)
Cleft palate	1 (6.7)
Sensorineural hearing loss	1 (6.7)
Injection agent	
No. dextranomer/hyaluronic acid copolymer (%)	14 (93.3)
No. hyaluronic acid (%)	1 (6.7)
Mean (SD) volume of implant injected (mL)	3.2 ± 1.2



FIG 1. Postoperative radiographs following dextranomer/hyaluronic acid copolymer injection. Images obtained at 2 days (A) and 3 months (B) post-dextranomer/hyaluronic acid copolymer injection demonstrate soft-tissue swelling at 2 days posttreatment (A) and no soft-tissue swelling on the 3-month radiograph (B).

within a vessel. Irrigation was then performed, and all hardware was removed from the patient's mouth. Procedural success was generally evaluated with a postoperative endoscopic evaluation and/or a video swallow study.

Imaging Characteristics

Neck MR imaging was generally performed on 1.5T scanners. Fast spin-echo T1 and T2 images were obtained. Imaging parameters for T2 sequences were the following: TR = 3000 ms, TE = 100 ms, section thickness = 4–5 mm, matrix size = 256 × 256 pixels. Imaging parameters for T1 sequences were the following: TR = 467 ms, TE = 10 ms. Postgadolinium imaging was generally performed by using fat-saturated echo-spoiled gradient-echo imaging (TR = 170 ms, TE = 3.2 ms) or fat-saturated spin-echo sequences (TR = 483 ms, TE = 20 ms). Diffusing-weighted imaging was performed by using TR = 10,050 ms and TE = 72 ms. Section thickness was 5 mm for axial images and 4 mm for sagittal images. Matrix size was 256 × 256 pixels. In general, images were obtained from the orbits to the superior mediastinum. For CT neck imaging, the parameters were the following: kVP = 120, mA = 400, kernel = H41s, section thickness = 2 mm. Image matrix size was 512 × 512 pixels, and FOV was 250 × 250 mm.

In addition to imaging patients following injection of hyaluronic acid, we imaged a vial of dextranomer/hyaluronic acid copolymer adjacent to a vial of water as a reference standard with both T1- and T2-weighted sequences. T2-weighted image parameters were the following: TR = 4000 ms, TE = 110 ms, section thickness = 4 mm, matrix size = 256 × 256 pixels. Imaging parameters for the T1 images were the following: TR = 500 ms, TE = 11 ms, section thickness = 4 mm, matrix size = 256 × 256 pixels.

All imaging was reviewed by a board-certified neuroradiologist with 22 years' experience (J.I.L.). Imaging characteristics studied included postoperative x-ray findings, postoperative CT findings, and postoperative MR imaging findings. For patients receiving postoperative CT studies, data were obtained on the attenuation of the implant relative to surrounding muscle and the appearance of the posterior pharyngeal wall in cases in which contrast was used. For patients undergoing postoperative MR imaging studies, data were obtained on the imaging appearance of the dextranomer/hyaluronic acid copolymer implants relative to surrounding muscle on T1-weighted sequences, T2-weighted sequences, diffusion-weighted sequences, and postcontrast T1-weighted sequences. Data on time to imaging were also obtained.

For patients who experienced complications related to dextranomer/hyaluronic acid copolymer injection (ie, retropharyngeal abscess), the appearance

of these complications on both CT and MR imaging was studied and compared with the normal imaging appearance of dextranomer/hyaluronic acid copolymer implants.

RESULTS

Patient Population

Fifteen patients were included in our study. The median age of these patients was 10 years (minimum age = 3 years, maximum age = 68 years). Five patients were adults (33.3%), and 10 patients (66.6%) were children. Eight patients were female (53.3%), and 7 patients were male (46.7%). Among the patients included in our study, the most common underlying causes of VPI were postsurgical complications after treatment of a malignancy (3/15, 20.0%), neurofibromatosis 1 (3/15, 20.0%), and velocardiofacial syndrome (3/15, 20.0%). The mean volume of hyaluronic acid injected was 3.2 ± 1.2 mL (minimum = 1 mL, maximum = 6 mL). Fourteen patients were injected with dextranomer/hyaluronic acid copolymer, and 1 patient was injected with hyaluronic acid. The patient injected with hyaluronic acid alone underwent only CT. Clinical data for the patients included in our study are summarized in the Table.

Imaging Appearance of Hyaluronic Acid Implants

Plain Radiographs. Seven patients in this study (46.7%) were studied with plain radiographs at some point in their postoperative period (range = 2 days to 15 months). Four patients had plain radiographs within 1 month of the procedure. Of these, 3 patients (75.0%) had prevertebral soft-tissue swelling. Three patients (20%) had plain radiographs after 1 month, and the plain radiograph findings were normal in all 3 cases. The dextranomer/hyaluronic acid copolymer implants were not specifically visible in any patients on plain radiography. The postoperative radiographic appearance of patients receiving these implants is shown in Fig 1.

CT Appearance. Five patients (33.3%) underwent CT during the postoperative period (minimum = 2 months, maximum = 9 months). Four of the patients received dextranomer/hyaluronic acid copolymer injection, and 1 patient received hyaluronic acid implants. On CT, both hyaluronic acid copolymer and hyaluronic acid implants appeared as bilateral nasopharyngeal soft-tissue masses that were isoattenuated to hypoattenuated relative to muscle in 80% (4/5) of patients. The CT appearance of these implants is demonstrated in Fig 2.

One patient presented with a ring-enhancing retropharyngeal mass with central low attenuation consistent with a large retropharyngeal abscess at 8 months after the procedure. The CT imaging appearance of this retropharyngeal abscess is demonstrated in Fig 3. The abscess was surgically aspirated and grew Gram-positive anaerobic bacilli.

MR Imaging Appearance. Nine patients (60.0%) underwent MR imaging during the postoperative period (minimum = 0 days, maximum = 18 months). On MR imaging, dextranomer/hyaluronic acid copolymer implants appeared as bilateral submucosal nasopharyngeal soft-tissue masses that were isointense to muscle on T1 (8/9, 88.9%) and hyperintense to muscle on T2 (8/9, 88.9%) and demonstrated no restricted diffusion (4/4, 100.0%).



FIG 2. Normal imaging characteristics of dextranomer/hyaluronic acid copolymer injections on CT. A, Contrast-enhanced CT in a 56-year-old woman 2 months postinjection of dextranomer/hyaluronic acid copolymer. The *white arrow* points to a small amount of hypoattenuated fluid in the retropharyngeal space consistent with the injection site. B, Noncontrast CT in a 3-year-old boy 3 months status post dextranomer/hyaluronic acid copolymer injection. Hypoattenuation in the right retropharyngeal space (*white arrow*) indicates the implant. Sagittal images of the patient better demonstrate the hypoattenuation corresponding to the implant (C). D, Contrast-enhanced CT in a 53-year-old woman 9 months post dextranomer/hyaluronic acid copolymer injection demonstrates hypoattenuation in the retropharyngeal space consistent with the implant.

No peripheral enhancement was observed in patients who received gadolinium (7/7, 100.0%). The MR imaging appearance remained stable with time. The MR imaging appearance of these dextranomer/hyaluronic acid copolymer implants is demonstrated in Fig 4. One patient developed a retropharyngeal abscess at the injection site, which was characterized by T2 hyperintensity, mild T1 hyperintensity, restricted diffusion, and peripheral enhancement. This is demonstrated along with the CT appearance in Fig 3.

MR imaging of the ex vivo dextranomer/hyaluronic acid copolymer vial by using T2 imaging parameters demonstrated that the dextranomer/hyaluronic acid copolymer was hyperintense with a signal intensity similar to that of water. Using T1 imaging parameters, the ex vivo dextranomer/hyaluronic acid copolymer was hyperintense with a higher signal intensity than that of water. These findings are demonstrated in Fig 5.

DISCUSSION

We have demonstrated that on MR imaging, posterior nasopharyngeal hyaluronic acid injection is characterized by the presence of bilateral nasopharyngeal soft-tissue masses that are isointense

to muscle on T1 and hyperintense on T2, with no restricted diffusion or peripheral enhancement. On CT, hyaluronic acid injections are generally iso- to hypoattenuated to adjacent muscle. On plain radiographs, the normal imaging appearance is soft-tissue fullness within 1 month of the procedure, which normalizes

thereafter. Dextranomer/hyaluronic acid copolymer implants are not radiodense on plain radiography or CT.

These findings are important to recognize to distinguish the normal postoperative imaging appearance of dextranomer/hyaluronic acid copolymer injections from nasopharyngeal pathology.

Because VPI is associated with so many diseases in which imaging is involved in the diagnosis and follow-up, it is highly likely that patients with VPI will undergo imaging in which the posterior nasopharynx is included. In our series of patients with VPI who underwent imaging, 3 had undergone surgical treatment for a head and neck/brain malignancy, 3 had neurofibromatosis type 1, and 3 had velocardiofacial syndrome. Several previous studies have demonstrated a strong association between neurofibromatosis type 1, velocardiofacial syndrome and postradiation, and surgical treatment for head and neck malignancies and VPI.¹³⁻¹⁷

In our series, 1 patient developed a retropharyngeal abscess at the injection site. The imaging appearance of this abscess is clearly distinct from the normal postoperative imaging of hyaluronic acid implants by its increased size, restricted diffusion, and peripheral enhancement. It is important for clinicians and radiologists to be able to distinguish

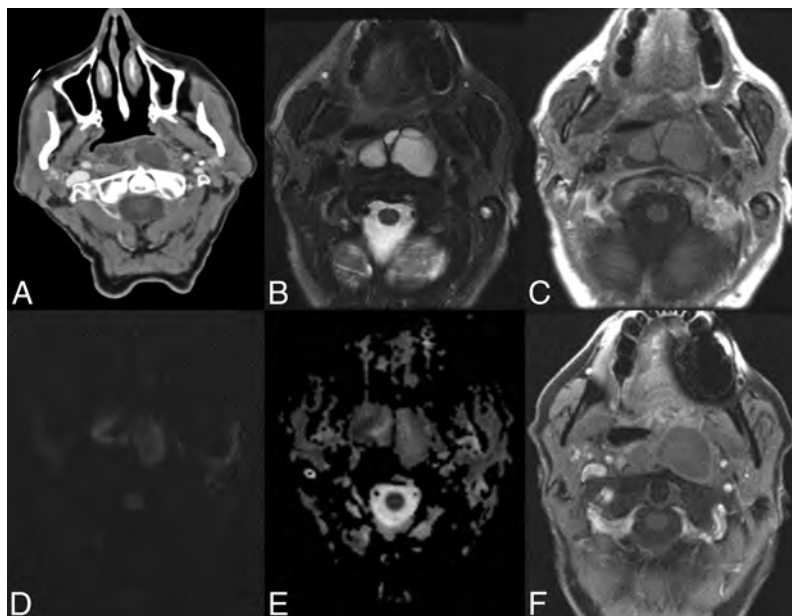


FIG 3. Retropharyngeal abscess 8 months after dextranomer/hyaluronic acid copolymer injection in a 68-year-old man. Retropharyngeal abscess following dextranomer/hyaluronic acid copolymer injection demonstrates mild peripheral enhancement on contrast-enhanced CT (A), internal T2 hyperintensity (B), and mild T1 hyperintensity (C). There are areas of restricted diffusion within the abscess seen on the DWI (D) and ADC (E) images. Peripheral enhancement on postgadolinium echo-spoiled gradient echo is demonstrated as well (F).

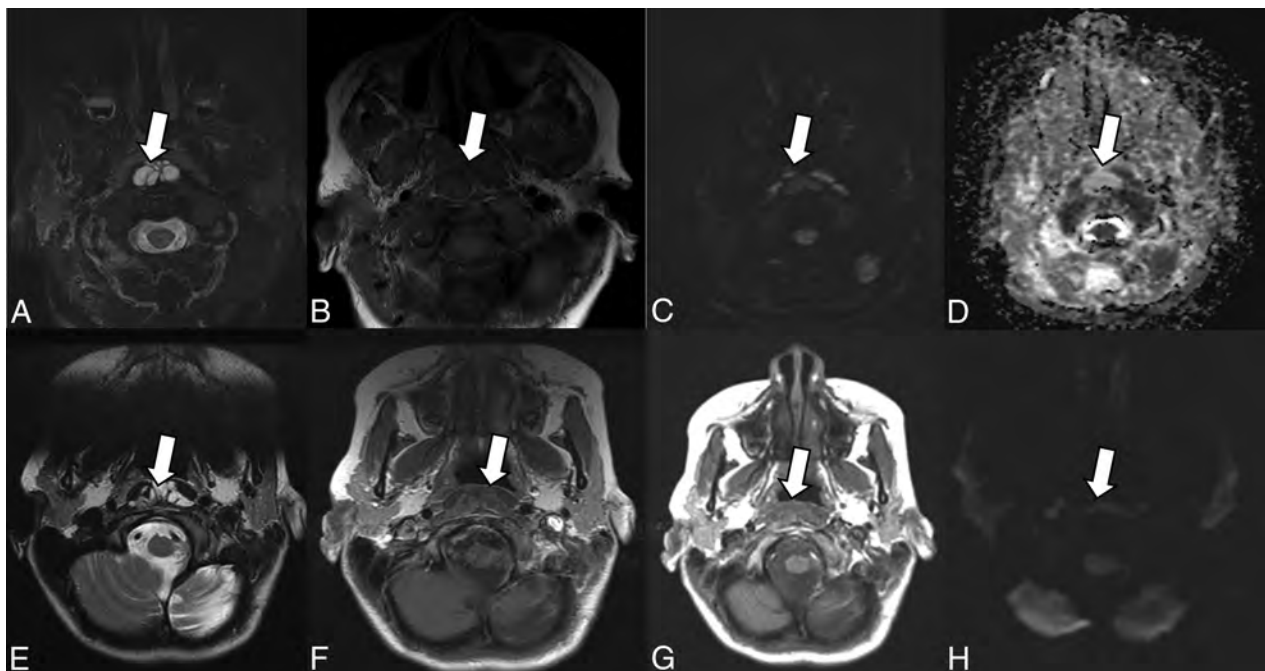


FIG 4. Normal imaging characteristics of dextranomer/hyaluronic acid copolymer injection on MR imaging. MR images in a 71-year-old man status post dextranomer/hyaluronic acid copolymer injection demonstrate a multiloculated T2 hyperintense (A) and T1 isointense lesion (B) on axial images. DWI (C) and ADC (D) images demonstrate no evidence of restricted diffusion. MR images in a 13-year-old girl 1 month status post injection demonstrate a multiloculated T2 hyperintense (E) and a T1 isointense lesion on axial images (F). No evidence of peripheral enhancement is seen on postgadolinium T1-weighted images (G). No evidence of restricted diffusion (H) is seen.

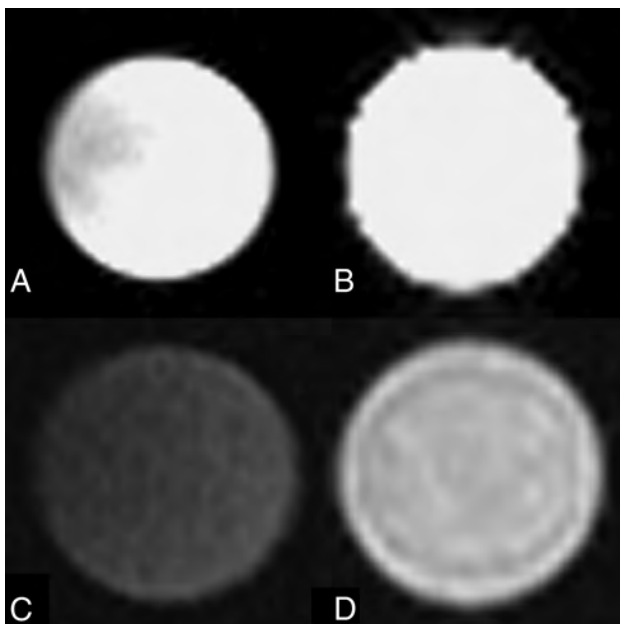


FIG 5. MR imaging characteristics of an ex vivo sample of dextranomer/hyaluronic acid copolymer compared with water. T2 imaging by using a water vial (A) and a vial of dextranomer/hyaluronic acid copolymer solution (B) demonstrates that the dextranomer/hyaluronic acid copolymer solution is hyperintense with a signal intensity similar to that of water. T1 imaging by using a water vial (C) and a vial of dextranomer/hyaluronic acid copolymer (D) demonstrates that the dextranomer/hyaluronic acid copolymer solution is hyperintense to water.

the appearance of a retropharyngeal abscess from the normal appearance of hyaluronic acid to avoid misdiagnosis and unnecessary intervention.

To our knowledge, no studies currently exist on the postoperative imaging findings of patients undergoing posterior pharyngeal wall augmentation with dextranomer/hyaluronic acid copolymer implants. However, the imaging appearance of dextranomer/hyaluronic acid copolymer implants in patients treated for vesicoureteral reflux has been previously described. Similar to our study, hyaluronic acid implants have been shown to have a CT and radiographic attenuation comparable with that of soft tissue.^{18,19} Some studies have demonstrated that these implants can calcify after 24 months.^{18,19} In our study, no evidence of calcification of these implants was seen, but no patients received follow-up radiography or CT after 24 months. On MR imaging, these implants have been shown to be hyperintense on T2-weighted imaging and isointense on T1-weighted imaging. No contrast enhancement is seen.^{18,20} The diffusion characteristics of these implants have not been previously characterized.

Limitations

There are a number of limitations to our study. Because this was a retrospective study, the use of the various imaging modalities could not be standardized. There is a wide range of follow-up times for postoperative imaging, which limits our ability to determine any temporal changes to the imaging appearance of hyaluronic acid implants. Furthermore, no patients who received dextranomer/hyaluronic acid copolymer implants for

VPI have yet been followed beyond 2 years, the period beyond which calcifications have been reported in the urologic literature.

CONCLUSIONS

The normal postoperative findings of posterior nasopharyngeal dextranomer/hyaluronic acid copolymer injection are characterized by the presence of bilateral nasopharyngeal soft-tissue masses that are isointense to muscle on T1 and hyperintense on T2, with no restricted diffusion or peripheral enhancement on MR imaging and are iso- to hypoattenuated with adjacent muscle on CT. Familiarity with this appearance is critical in distinguishing the normal postoperative state from nasopharyngeal pathology.

Disclosures: Waleed Brinjikji—UNRELATED: Grants/Grants Pending: Brain Aneurysm Foundation.* *Money paid to the institution.

REFERENCES

1. Brigger MT, Ashland JE, Hartnick CJ. **Injection pharyngoplasty with calcium hydroxylapatite for velopharyngeal insufficiency: patient selection and technique.** *Arch Otolaryngol Head Neck Surg* 2010;136:666–70
2. Bluestone CD, Musgrave RH, McWilliams BJ, et al. **Teflon injection pharyngoplasty.** *Cleft Palate J* 1968;5:19–22
3. Cao Y, Ma T, Wu D, et al. **Autologous fat injection combined with palatoplasty and pharyngoplasty for velopharyngeal insufficiency and cleft palate: preliminary experience.** *Otolaryngol Head Neck Surg* 2013;149:284–91
4. Hagerty RF, Hill MJ. **Cartilage pharyngoplasty in cleft palate patients.** *Surg Gynecol Obstet* 1961;112:350–56
5. Lando RL. **Transplant of cadaveric cartilage into the posterior pharyngeal wall in treatment of cleft palate** [article in undetermined language]. *Stomatologija (Mosk)* 1950;4:38–39
6. Remacle M, Bertrand B, Eloy P, et al. **The use of injectable collagen to correct velopharyngeal insufficiency.** *Laryngoscope* 1990;100:269–74
7. Sipp JA, Ashland J, Hartnick CJ. **Injection pharyngoplasty with calcium hydroxyapatite for treatment of velopalatal insufficiency.** *Arch Otolaryngol Head Neck Surg* 2008;134:268–71
8. Cakli H, Ozudogru E, Cingi E, et al. **Near total laryngectomy: the problems influencing functions and their solutions.** *Eur Arch Otorhinolaryngol* 2005;262:99–102
9. Hallén L, Testad P, Sederholm E, et al. **DiHA (dextranomers in hyaluronan) injections for treatment of insufficient closure of the vocal folds: early clinical experiences.** *Laryngoscope* 2001;111:1063–67
10. Hertegård S, Hallén L, Laurent C, et al. **Cross-linked hyaluronan used as augmentation substance for treatment of glottal insufficiency: safety aspects and vocal fold function.** *Laryngoscope* 2002;112:2211–19
11. Peterson KL, Fenn J. **Treatment of dysphagia and dysphonia following skull base surgery.** *Otolaryngol Clin North Am* 2005;38:809–17, xi
12. Rickert D. **Polymeric implant materials for the reconstruction of tracheal and pharyngeal mucosal defects in head and neck surgery.** *GMS Curr Top Otorhinolaryngol Head Neck Surg* 2009;8:Doc06
13. Jaber JJ, Greenbaum ES, Sappington JM, et al. **Postlaryngectomy dysphagia masking as velopharyngeal insufficiency: a simple solution for an anterior neopharyngeal diverticulum.** *Am J Otolaryngol* 2012;33:367–69
14. Oberoi S, Huynh L, Vargervik K. **Velopharyngeal, speech and dental characteristics as diagnostic aids in 22q11.2 deletion syndrome.** *J Calif Dent Assoc* 2011;39:327–32

15. Rosenthal DI, Lewin JS, Eisbruch A. **Prevention and treatment of dysphagia and aspiration after chemoradiation for head and neck cancer.** *J Clin Oncol* 2006;24:2636–43
16. Ruda JM, Krakovitz P, Rose AS. **A review of the evaluation and management of velopharyngeal insufficiency in children.** *Otolaryngol Clin North Am* 2012;45:653–69, viii
17. Zhang I, Husein M, Dworschak-Stokan A, et al. **Neurofibromatosis and velopharyngeal insufficiency: is there an association?** *J Otolaryngol Head Neck Surg* 2012;41:58–64
18. Cerwinka WH, Kaye JD, Scherz HC, et al. **Radiologic features of implants after endoscopic treatment of vesicoureteral reflux in children.** *AJR Am J Roentgenol* 2010;195:234–40
19. Cerwinka WH, Qian J, Easley KA, et al. **Appearance of dextranomer/hyaluronic acid copolymer implants on computerized tomography after endoscopic treatment of vesicoureteral reflux in children.** *J Urol* 2009;181:1324–28; discussion 1329
20. Cerwinka WH, Grattan-Smith JD, Scherz HC, et al. **Appearance of Deflux implants with magnetic resonance imaging after endoscopic treatment of vesicoureteral reflux in children.** *J Pediatr Urol* 2009;5:114–18

Comparison of Fine-Needle Aspiration and Core Needle Biopsy under Ultrasonographic Guidance for Detecting Malignancy and for the Tissue-Specific Diagnosis of Salivary Gland Tumors

H.-J. Eom, J.H. Lee, M.-S. Ko, Y.J. Choi, R.G. Yoon, K.J. Cho, S.Y. Nam, and J.H. Baek

ABSTRACT

BACKGROUND AND PURPOSE: Diagnostic test accuracy studies for ultrasonography-guided fine-needle aspiration and ultrasonography-guided core needle biopsy have shown inconclusive results due to their heterogeneous study designs. Our aim was to compare the diagnostic accuracy of ultrasonography-guided fine-needle aspiration versus ultrasonography-guided core needle biopsy for detecting malignant tumors of the salivary gland and for the tissue-specific diagnosis of salivary gland tumors in a single tertiary hospital.

MATERIALS AND METHODS: This retrospective study was approved by our institutional review board and informed consent was waived. Four hundred twelve patients who underwent ultrasonography-guided fine-needle aspiration ($n = 155$) or ultrasonography-guided core needle biopsy ($n = 257$) with subsequent surgical confirmation or clinical follow-up were enrolled. We compared the diagnostic accuracy of ultrasonography-guided fine-needle aspiration and ultrasonography-guided core needle biopsy regarding malignant salivary gland tumors and the correct tissue-specific diagnosis of benign and malignant tumors. We also tested the difference between these procedures according to the operator's experience and lesion characteristics.

RESULTS: The inconclusive rates of ultrasonography-guided fine-needle aspiration and ultrasonography-guided core needle biopsy were 19% and 4%, respectively ($P < .001$). The overall accuracy of ultrasonography-guided core needle biopsy for diagnosing malignant tumors was significantly higher than that of ultrasonography-guided fine-needle aspiration ($P = .024$). The correct tissue-specific diagnosis rates of ultrasonography-guided fine-needle aspiration and ultrasonography-guided core needle biopsy were 95% versus 97% for benign tumors ($P = .648$) and 67% versus 80% for malignant tumors ($P = .310$). Trainees showed significantly lower accuracy with ultrasonography-guided fine-needle aspiration than with ultrasonography-guided core needle biopsy for diagnosing malignant tumors ($P = .021$). There was no difference between the diagnostic accuracy of ultrasonography-guided fine-needle aspiration and ultrasonography-guided core needle biopsy according to the internal composition of the lesions. There were no complications requiring intervention or hospitalization in our patients.

CONCLUSIONS: Ultrasonography-guided core needle biopsy is superior to ultrasonography-guided fine-needle aspiration in detecting and characterizing malignant tumors of the salivary gland and could emerge as the diagnostic method of choice for patients presenting with a salivary gland mass.

ABBREVIATIONS: CNB = core needle biopsy; FNA = fine-needle aspiration; US = ultrasonography; USCNB = ultrasonography-guided core needle biopsy; USFNA = ultrasonography-guided fine-needle aspiration

The preoperative diagnosis of salivary gland masses is important for avoiding unnecessary surgery for nonmalignant lesions, and for therapeutic planning for malignant tumors. Fine-needle aspiration (FNA) is a well-accepted and widely used technique for the preoperative diagnosis of salivary gland masses, showing an average specificity for detecting malignant tumors

among these masses of up to 96% with little variation from study to study.^{1,2} Remarkable variation is seen in the sensitivity of FNA, however, which ranges from 33% to 100%, with an average of 79%.¹⁻⁷ A recently published meta-analysis has suggested the influence of verification bias on the reported diagnostic accuracies of FNA, leading to an underestimation of its sensitivity and overestimation of its specificity in previous articles.⁸ In addition to verification bias, differences in test conditions have a major effect

Received September 28, 2014; accepted after revision November 25.

From the Department of Radiology and Research Institute of Radiology (H.-J.E., J.H.L., Y.J.C., R.G.Y., J.H.B.) and Departments of Health Medicine (M.-S.K.), Pathology (K.J.C.), and Otolaryngology (S.Y.N.), Asan Medical Center, University of Ulsan College of Medicine, Seoul, Korea.

Paper previously presented at: Annual Meeting of the Radiological Society of North America, November 30–December 5, 2014; Chicago, Illinois.

Please address correspondence to Jeong Hyun Lee, MD, PhD, Department of Radiology and Research Institute of Radiology, University of Ulsan College of Medicine, Asan Medical Center, 86 Asanbyeongwon-Gil, Songpa-Gu, Seoul 138-736, Republic of Korea; e-mail: jeonghlee@amc.seoul.kr

<http://dx.doi.org/10.3174/ajnr.A4247>

on the diagnostic performance of FNA. These test conditions include the use of ultrasonography (US) guidance, the presence of a pathologist on site, the experience level of the operator and the pathologist, and the internal composition of the biopsied masses. For example, US guidance can increase the diagnostic performance of FNA compared with palpation guidance, as evidenced in the diagnosis of thyroid nodules.⁹

Core needle biopsy (CNB) under US guidance is used frequently for masses in the head and neck area¹⁰⁻¹² and has several advantages over either palpation-guided or US-guided FNA, including the ability to obtain a larger specimen with preserved tissue architecture for possible immunohistochemical staining. This potentially contributes to the low nondiagnostic rate and high average sensitivity (92%) and specificity (100%) of this procedure, with little variation in its ability to detect malignant tumors in salivary glands.¹³ Despite the advantages of CNB, its routine use for salivary gland tumors has been debated due to potential morbidity, such as facial nerve damage, use of local anesthesia, and patient discomfort.

A recent meta-analysis was performed to compare the diagnostic performance of FNA and CNB. The authors of that study could not reach a definitive conclusion, however, due to the significant heterogeneity regarding FNA findings in the literature, even with a systematic review.^{11,14} Therefore, a study with a large series that considers different test conditions and minimizes any verification bias is still required for comparing the diagnostic performance of FNA and CNB and ultimately suggesting some clinical guidelines. Accordingly, we designed our current retrospective study to evaluate the diagnostic performance of FNA and CNB, both performed under US guidance, for detecting malignancy and undertaking tissue-specific diagnoses of salivary gland tumors in a large series of patients in our tertiary hospital. We also evaluated the factors influencing the diagnostic performance of both techniques, including the experience level of the operator and the internal composition of the biopsied mass.

MATERIALS AND METHODS

Patient Population

From 2003 to 2012, 474 consecutive patients underwent ultrasonography-guided fine-needle aspiration (USFNA) ($n = 192$) or ultrasonography-guided core needle biopsy (USCNB) ($n = 282$) for a salivary gland mass at our hospital. We retrospectively reviewed the medical records, US images, and the radiologic, cytologic, and/or histologic reports of USFNA and USCNB in all of these patients. After the exclusion of 62 patients (37 from the USFNA group and 25 from the USCNB group) due to limited medical records beyond 1-year clinical follow-up, we finally enrolled 155 patients who underwent USFNA and 257 who underwent USCNB in our study cohorts. There were 217 males and 195 females with an age range of 9–86 years in this series (mean, 53 years).

USFNA and USCNB

US examinations were performed by using 1 of 3 systems: an iU22 or HDI-5000 U (Philips Healthcare, Best, the Netherlands) or an EUB-7500 (Hitachi Medical Systems, Tokyo, Japan). Each system was equipped with a linear high-frequency probe (5–14 MHz).

After the US examination, the operator performed USFNA or USCNB in accordance with the operator's discretion or clinician's preferences. During image analysis, masses were classified as solid or predominantly solid (proportion of solid component >50%) and cystic or predominantly cystic (proportion of cystic change >50%) according to their internal architecture. All of the examinations, including US-guided biopsy, were performed by one of the faculty members (J.H.L. with US-guided biopsy experience of 14 years or J.H.B. with 18 years' experience) or by a trainee with <5 years of US-guided biopsy experience.

Before the procedures, written consent was obtained from the patient. USFNA was performed by using a 23-ga needle attached to a 10-mL disposable plastic syringe with a combination of capillary action and suction-aspiration techniques, depending on the lesion characteristics. Specimens were immediately fixed in 95% ethanol. USCNB was performed by using disposable 18-ga double-action spring-activated needles (1.1- or 1.6-cm excursion; AceCut; TSK, Tochigi, Japan) or 18-ga dual-action semiautomatic needles (1.0- or 2.0-cm excursion; Stericut with a coaxial guide; TSK Laboratory) after local anesthesia with 2% lidocaine. Local anesthetic was injected slowly into the subcutaneous fat and just beneath the capsule. Operators selected biopsy needles with adequate throw lengths compared with the maximum length of the target lesions. They were cautioned to put the specimen notch of the inner stylet within the target to minimize the risk of facial nerve damage. When the target was smaller than the length of the specimen notch, the needle was inserted in a caudocranial direction and the superior end of the specimen notch did not pass through the upper top of the target. In cases of cystic or predominantly cystic masses, lesions were biopsied after aspiration of cystic content, and targeting was directed at the solid component inside the mass. Specimens were immediately fixed in a 10% formalin solution. A freehand technique was used throughout the procedure to achieve accurate mass targeting. A coaxial technique was not used in all cases. All biopsy specimens were evaluated with the naked eye immediately after the procedure for the presence of whitish tissue material to assess the adequacy of the material. If the specimen was insufficient, the USFNA or USCNB was repeated. After the biopsy, firm local compression of the biopsy site with an ice pack was applied for 10–20 minutes.

Histologic Diagnosis and Statistical Analysis

Biopsy specimens were sent to the pathology department and reviewed by an experienced cytopathologist. A final diagnosis was established on the basis of surgical histologic findings for the surgical group or the USFNA result combined with clinical and/or radiologic follow-up results of >1 year in patients who did not undergo surgery. We strictly defined the inconclusive results of USFNA and USCNB. In addition to the commonly used definition of inadequate FNA results (6 groups each with ≥ 10 epithelial cells),¹⁵ we included indeterminate cytologic results of both USFNA and USCNB among the inconclusive findings when they were insufficient to determine whether the lesion was neoplastic or malignant.

Statistical analysis was performed to compare any difference in the inconclusive rates between USFNA and USCNB. We calculated the sensitivities, specificities, positive and negative predic-

Table 1: Demographic data and results of US image analysis^a

	Total (N = 412)	FNA (n = 155)	CNB (n = 257)	P Value
Age (yr) ^b	53 ± 16	55 ± 15	52 ± 16	.084
Size (cm) ^b	2.2 ± 1.1	2.2 ± 1.2	2.2 ± 1.1	.694
Sex				.374
Male	217	86 (55)	131 (51)	
Female	195	69 (45)	126 (49)	
Location				.637
Parotid gland	311	119 (77)	192 (75)	
Submandibular gland	101	36 (23)	65 (25)	
No. of needle passes				.052
1	267	112 (72)	155 (60)	
2	132	37 (24)	95 (37)	
3	13	6 (4)	7 (3)	

^a Unless otherwise indicated, data show the number of lesions, with percentages in parentheses.

^b Data show means.

Table 2: Summary of inconclusive results of USFNA and USCNB

	Total	Benign	Malignant	FU loss
USFNA	30			
Inadequate specimen	14	8	1	5
Others ^a	16	11	5	0
USCNB	10			
Inadequate specimen	1	0	1	0
Others ^a	9	3	4	2

Note:—FU indicates follow-up.

^a "Others" include inconclusive results for differential diagnoses between benign and malignant salivary gland tumors.

tive values, and overall diagnostic accuracies of USFNA and USCNB for detecting malignant tumors of the salivary gland and for correct tissue-specific diagnoses. We also tested any difference in the diagnostic profile of USFNA and USCNB. For comparison of tissue-specific diagnosis rates between 2 modalities, we excluded false-positive and false-negative results of USFNA and USCNB and those confirmed as benign by clinical and/or radiologic follow-up from the statistical analysis. Statistical testing was also performed to identify any differences between USFNA and USCNB according to the experience level of the operator and the internal composition of the biopsied lesions.

Statistical analysis was performed by using the SPSS software package (Version 19.0 for Windows; IBM, Armonk, New York). Continuous variables were compared by using an unpaired Student *t* test or Mann-Whitney *U* test, depending on the data distribution. Categorical variables were expressed by using frequencies and percentages and were tested by using a χ^2 or Fisher exact test. A *P* value of < .05 was statistically significant.

RESULTS

Patient demographic data and the results of the US image analysis are summarized in Table 1. There were no significant differences between the USFNA and USCNB groups with respect to demographic data, the location and size of the lesions, internal composition on US, and the number of needle passes. The inconclusive rates were 19% (30/155) for USFNA and 4% (10/257) for USCNB, which was a significant difference ($P < .001$). The summary of inconclusive results of USFNA and USCNB is shown in Table 2. The final diagnoses of USFNA and USCNB are detailed in Fig 1. Among the tumors that were classified as benign ($n = 76$) and malignant ($n = 19$) by USFNA, there were 5 false-negative and 3

false-positive results for the diagnosis of a malignant tumor of the salivary gland. Among the tumors that were classified as benign ($n = 177$) and malignant ($n = 53$) by USCNB, there were 4 false-negative results and 1 false-positive result. The false-positive and false-negative results are detailed in Table 3. There were no major complications among our study patients needing medication or hospitalization according to a review of the electronic medical records and radiologic reports.

The diagnostic accuracies of USFNA and USCNB in our current evaluation are summarized in Table 4. The sensitivity, specificity, accuracy, and positive and negative predictive values of USCNB for detecting malignant salivary gland tumors tended to be higher than those of USFNA. However, our statistical analysis revealed significance only for diagnostic accuracy ($P = .024$). The tissue-specific diagnosis rates of USFNA were 95% (39/41) in benign tumors and 67% (10/15) in malignant tumors; those of USCNB were 97% (142/147) in benign tumors and 80% (32/40) in malignant tumors. There were no significant differences in the tissue-specific diagnosis rates of either benign ($P = .648$) or malignant ($P = .310$) tumors between the USFNA and USCNB groups.

Regarding the experience level of the operators, the sensitivity, specificity, accuracy, and positive and negative predictive values of USCNB for diagnosing malignant tumors tended to be higher than those of USFNA for both faculty members and trainees. However, when the diagnostic procedures were performed by trainees, the diagnostic accuracy of USFNA was significantly lower than that of USCNB ($P = .021$). The sensitivity, specificity, accuracy, and positive and negative predictive values of USCNB for diagnosing malignant tumors were not significantly higher than those of USFNA, regardless of the internal composition. These results are summarized in Tables 5 and 6.

DISCUSSION

The results of our current study can be summarized as follows: First, USCNB shows significantly better diagnostic performance—expressed as diagnostic accuracy and inconclusive rates—than USFNA for detecting malignant salivary gland tumors; second, the diagnostic accuracy of USFNA is significantly affected by the operator's experience level, whereas that of USCNB is not; third, USFNA and USCNB do not show significantly different tissue-specific diagnosis rates; and finally, the diagnostic performances of these methods are not affected by the internal architecture of a biopsied lesion.

Our current study findings confirm the superiority of USCNB over USFNA in terms of diagnostic accuracy and inconclusive rates for detecting malignant salivary gland tumors. The inconclusive rates of USFNA and USCNB in our study were 19% and 4%, respectively. The cytologic results were considered inconclusive when the specimen was deemed inadequate for making a diagnosis or as indeterminate for the presence of malignant tumor or neoplasm when the USFNA or USCNB results were insufficient to make a clinical decision and management plan, both of which are crucial for proper patient management. It is quite disappointing that nearly one-fifth of USFNA examination findings were inconclusive from a practical point of view.

The variability in the diagnostic accuracy of previously re-

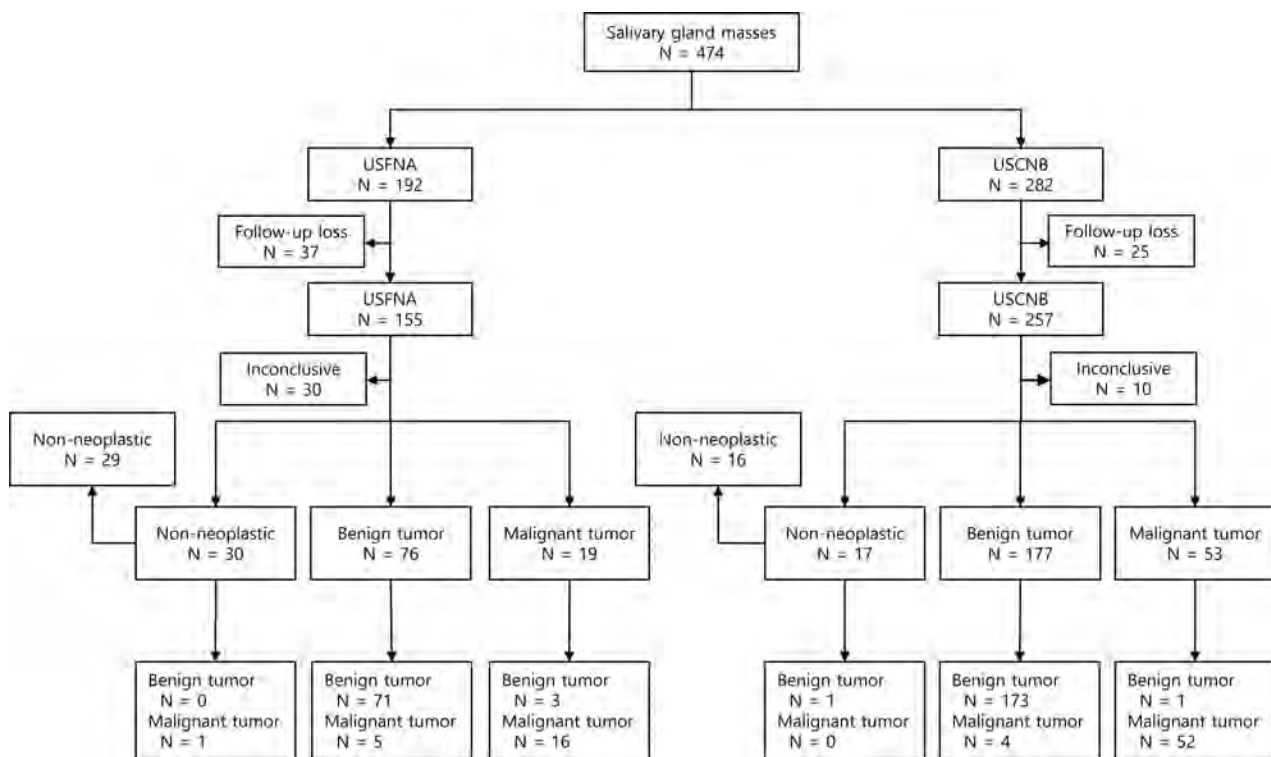


FIG 1. The results of USFNA and USCNB in all patients.

Table 3: False-positive and false-negative results of USFNA and USCNB in salivary gland tumors

Biopsy Results	Final Pathologies
USFNA	
False-negative	
Warthin tumor	Mucoepidermoid carcinoma
Pleomorphic adenoma	Mucoepidermoid carcinoma
Pleomorphic adenoma	Mucoepidermoid carcinoma
Pleomorphic adenoma	Carcinoma ex pleomorphic adenoma
Basal cell adenoma	Basal cell adenocarcinoma
False-positive	
Squamous cell carcinoma	Warthin tumor with squamous metaplasia
Acinic cell carcinoma	Oncocytoma
Acinic cell carcinoma	Oncocytoma
USCNB	
False-negative	
Pleomorphic adenoma	Epithelial-myoepithelial carcinoma
Pleomorphic adenoma	Carcinoma ex pleomorphic adenoma
Pleomorphic adenoma	Carcinoma ex pleomorphic adenoma
Basal cell adenoma	Basal cell adenocarcinoma
False-positive	
Low-grade mucoepidermoid carcinoma	Pleomorphic adenoma

ported FNA results is a well-known problem.¹⁶ This variability was evident in recent studies that evaluated the sensitivity of FNA for distinguishing benign from malignant salivary gland tumors, with sensitivities ranging from 38% to 87.8%.^{2,16-18} These reports did not state whether US was used for guidance during the biopsy. Our current study suggests that US guidance could yield better diagnostic accuracy than palpation-guided biopsy, given the relatively high diagnostic sensitivity that we observed. On the other hand, a recently published meta-analysis study found that USCNB has an overall sensitivity of 0.92 (95% CI, 0.77–0.98) and an overall specificity of 1.00 (95% CI, 0.76–1.00), with no signif-

icant heterogeneity.¹⁴ The results of USCNB in our study are comparable with those of this latter report.

Our study results also demonstrated that even with US guidance, the diagnostic accuracy of FNA is significantly lower than that of USCNB. This lower diagnostic accuracy could have resulted from the histologic diversity of the salivary gland tumors and could suggest that cytologic examination alone is not sufficient for diagnosing malignant tumors of the salivary glands, thus necessitating a larger specimen with preserved histologic architecture. Schmidt et al^{11,14} tried to compare the diagnostic performances of FNA and CNB for detecting malignant salivary gland tumors in 2 separate meta-analyses. However, the authors stated that a direct comparison of FNA and CNB was not possible be-

cause of an unexpected significant heterogeneity in the findings of studies regarding FNA, and they concluded that CNB could be reserved for special clinical settings, such as cases that were not diagnosed with FNA, given the theoretic drawbacks of CNB, such as facial nerve damage or use of local anesthesia.^{1,14}

Our present data demonstrate that USCNB can be safely performed because none of our 282 patients experienced facial nerve injury, and it has a significantly higher diagnostic accuracy for malignant salivary gland tumors. Another disadvantage of USCNB is that it uses larger bore needles compared with USFNA, which might increase the potential risk for tumor seeding along

Table 4: Comparison of diagnostic accuracies of USFNA and USCNB in salivary gland tumors^a

Diagnostic Accuracy	USFNA	USCNB	P Value
Sensitivity	76 (16/21)	93 (52/56)	.057
Specificity	96 (71/74)	99 (173/174)	.081
Accuracy	92 (87/95)	98 (225/230)	.024 ^b
Positive predictive value	84 (16/19)	98 (52/53)	.054
Negative predictive value	93 (71/76)	98 (173/177)	.133

^a Data show percentages, with patient numbers in parentheses.

^b Significant.

Table 5: Comparison of diagnostic accuracies of USFNA and USCNB in salivary gland tumors according to operator experience level^a

Diagnostic Values	FNA (%)	CNB (%)	P Value
Sensitivity			
Faculty	79 (15/19)	89 (32/36)	.426
Trainee	50 (1/2)	100 (20/20)	.091
Specificity			
Faculty	97 (57/59)	99 (96/97)	.557
Trainee	93 (14/15)	100 (77/77)	.163
Accuracy			
Faculty	92 (72/78)	96 (128/133)	.336
Trainee	88 (15/17)	100 (97/97)	.021 ^b

^a Data show percentages, with numbers in parentheses.

^b Significant.

Table 6: Comparison of diagnostic accuracies of USFNA and USCNB according to the internal component of salivary gland tumors^a

Diagnostic Values	FNA (%)	CNB (%)	P Value
Sensitivity			
Solid/predominantly solid	82 (14/17)	94 (46/49)	.172
Cystic/predominantly cystic	50 (2/4)	86 (6/7)	.491
Specificity			
Solid/predominantly solid	97 (66/68)	99 (154/155)	.221
Cystic/predominantly cystic	83 (5/6)	100 (19/19)	.240
Accuracy			
Solid/predominantly solid	94 (80/85)	98 (200/204)	.130
Cystic/predominantly cystic	70 (7/10)	96 (25/26)	.057

^a Data show percentages, with numbers in parentheses.

the needle tract.¹⁶ In this regard, besides a potential risk of malignant tumor seeding, benign tumors such as pleomorphic adenomas can have problematic recurrences, which may not even be evident until many years after the initial surgery. Although Novoa et al¹⁹ recently reviewed the safety of USCNB in the work-up of 438 head and neck lesions with 7 years of clinical follow-up and found no evidence of tumor cell seeding, further clinical investigation of tumor recurrence following USCNB is necessary in a large population during a long time course before the safety of USCNB can be verified and widely accepted.

Another interesting result of our current study is that the diagnostic accuracy of USFNA performed by trainees was significantly lower than that of USCNB performed by trainees. This result suggests that USFNA might be more dependent on the experience level of the operator than USCNB. It also suggests that USFNA is technically more demanding than USCNB and needs accurate localization of a lesion by using both the US probe and the needle, repeated continuous to-and-fro motions of the needle under real-time US monitoring, and an adequate combination of capillary action and suction-aspiration techniques according to the lesion characteristics.^{1,2,20,21}

The biopsy of salivary gland lesions carries a risk of complications such as hematoma, infection, or facial nerve injury. The retromandibular vein and external carotid artery are the major intraparotid vessels that are well-visualized with US imaging and can be easily avoided.²² However, the facial nerve is not readily identified with US.^{22,23} It has been suggested in previous reports that USFNA carries a lower risk of complications than USCNB.^{13,24,25} In our current investigation, which included 282 patients who underwent USCNB, there were no major complications observed such as facial nerve injury. Our suggestions for reducing the risk of potential facial nerve damage with USCNB are to select a core needle device with an adequate throw length compared with the maximum length of the targets and to obtain the specimen while carefully keeping the specimen notch within the target without passing through the upper margin of the target. Our study results confirm that facial nerve damage can generally be avoided by performing USCNB with caution.

In addition to the inherent limitations related to a retrospective study, our study had several other limitations. The use of USFNA and USCNB was not randomized (randomization would have been ideal), and the operator performed USFNA or USCNB in accordance with his or her discretion or the clinician's preferences. However, because our study showed no significant differences in evaluated clinical and US imaging data between USFNA and USCNB lesions, we think that bias by operators/clinicians as to whether USFNA or USCNB was used is limited. Additionally, although we demonstrated that USCNB is a safe procedure without major complications for the histologic diagnosis of salivary gland tumors, we did not compare the degree of patient discomfort from the use of lidocaine anesthesia or the larger bore needle used for USCNB with that used for USFNA. Patient discomfort might thus be the subject of future prospective studies.

CONCLUSIONS

USCNB is superior to USFNA in that it has a lower inconclusive rate and higher diagnostic accuracy for detecting malignant salivary gland tumors. USCNB could be considered the US-guided biopsy procedure of choice for evaluating patients with a salivary gland mass because it can aid in appropriate therapeutic planning and minimize unnecessary repeat biopsies.

REFERENCES

- Schmidt RL, Hall BJ, Wilson AR, et al. **A systematic review and meta-analysis of the diagnostic accuracy of fine-needle aspiration cytology for parotid gland lesions.** *Am J Clin Pathol* 2011;136:45–59
- Balakrishnan K, Castling B, McMahon J, et al. **Fine needle aspiration cytology in the management of a parotid mass: a two centre retrospective study.** *Surgeon* 2005;3:67–72
- Aversa S, Ondolo C, Bollito E, et al. **Preoperative cytology in the management of parotid neoplasms.** *Am J Otolaryngol* 2006;27:96–100
- Seethala RR, LiVolsi VA, Baloch ZW. **Relative accuracy of fine-needle aspiration and frozen section in the diagnosis of lesions of the parotid gland.** *Head Neck* 2005;27:217–23
- Al Salamah SM, Khalid K, Khan IA, et al. **Outcome of surgery for parotid tumours: 5-year experience of a general surgical unit in a teaching hospital.** *ANZ J Surg* 2005;75:948–52
- Al-Khafaji BM, Nestok BR, Katz RL. **Fine-needle aspiration of 154 parotid masses with histologic correlation: ten-year experience at**

- the University of Texas M.D. Anderson Cancer Center. *Cancer* 1998;84:153–59
7. Schelkun PM, Grundy WG. **Fine-needle aspiration biopsy of head and neck lesions.** *J Oral Maxillofac Surg* 1991;49:262–67
 8. Schmidt RL, Jedrziewicz JD, Allred RJ, et al. **Verification bias in diagnostic accuracy studies for fine- and core needle biopsy of salivary gland lesions in otolaryngology journals: a systematic review and analysis.** *Head Neck* 2014;36:1654–61
 9. Izquierdo R, Arekat MR, Knudson PE, et al. **Comparison of palpation-guided versus ultrasound-guided fine-needle aspiration biopsies of thyroid nodules in an outpatient endocrinology practice.** *Endocr Pract* 2006;12:609–14
 10. Hakala T, Kholova I, Sand J, et al. **A core needle biopsy provides more malignancy-specific results than fine-needle aspiration biopsy in thyroid nodules suspicious for malignancy.** *J Clin Pathol* 2013;66:1046–50
 11. Samir AE, Vij A, Seale MK, et al. **Ultrasound-guided percutaneous thyroid nodule core biopsy: clinical utility in patients with prior nondiagnostic fine-needle aspirate.** *Thyroid* 2012;22:461–67
 12. Burke C, Thomas R, Inglis C, et al. **Ultrasound-guided core biopsy in the diagnosis of lymphoma of the head and neck: a 9-year experience.** *Br J Radiol* 2011;84:727–32
 13. Taki S, Yamamoto T, Kawai A, et al. **Sonographically guided core biopsy of the salivary gland masses: safety and efficacy.** *Clin Imaging* 2005;29:189–94
 14. Schmidt RL, Hall BJ, Layfield LJ. **A systematic review and meta-analysis of the diagnostic accuracy of ultrasound-guided core needle biopsy for salivary gland lesions.** *Am J Clin Pathol* 2011;136:516–26
 15. Goellner JR, Gharib H, Grant CS, et al. **Fine needle aspiration cytology of the thyroid, 1980 to 1986.** *Acta Cytol* 1987;31:587–90
 16. Douville NJ, Bradford CR. **Comparison of ultrasound-guided core biopsy versus fine-needle aspiration biopsy in the evaluation of salivary gland lesions.** *Head Neck* 2013;35:1657–61
 17. Pitts DB, Hilsinger RL Jr, Karandy E, et al. **Fine-needle aspiration in the diagnosis of salivary gland disorders in the community hospital setting.** *Arch Otolaryngol Head Neck Surg* 1992;118:479–82
 18. Jayaram N, Ashim D, Rajwanshi A, et al. **The value of fine-needle aspiration biopsy in the cytodiagnosis of salivary gland lesions.** *Diagn Cytopathol* 1989;5:349–54
 19. Novoa E, Gurtler N, Arnoux A, et al. **Role of ultrasound-guided core-needle biopsy in the assessment of head and neck lesions: a meta-analysis and systematic review of the literature.** *Head Neck* 2012;34:1497–503
 20. Huang YC, Wu CT, Lin G, et al. **Comparison of ultrasonographically guided fine-needle aspiration and core needle biopsy in the diagnosis of parotid masses.** *J Clin Ultrasound* 2012;40:189–94
 21. Colella G, Cannavale R, Flamminio F, et al. **Fine-needle aspiration cytology of salivary gland lesions: a systematic review.** *J Oral Maxillofac Surg* 2010;68:2146–53
 22. Howlett DC, Menezes LJ, Lewis K, et al. **Sonographically guided core biopsy of a parotid mass.** *AJR Am J Roentgenol* 2007;188:223–27
 23. Verma K, Kapila K. **Role of fine needle aspiration cytology in diagnosis of pleomorphic adenomas.** *Cytopathology* 2002;13:121–27
 24. Wan YL, Chan SC, Chen YL, et al. **Ultrasonography-guided core-needle biopsy of parotid gland masses.** *AJNR Am J Neuroradiol* 2004;25:1608–12
 25. Kesse KW, Manjaly G, Violaris N, et al. **Ultrasound-guided biopsy in the evaluation of focal lesions and diffuse swelling of the parotid gland.** *Br J Oral Maxillofac Surg* 2002;40:384–88

Different Spectral Hounsfield Unit Curve and High-Energy Virtual Monochromatic Image Characteristics of Squamous Cell Carcinoma Compared with Nonossified Thyroid Cartilage

R. Forghani, M. Levental, R. Gupta, S. Lam, N. Dadfar, and H.D. Curtin



ABSTRACT

BACKGROUND AND PURPOSE: The attenuation of normal nonossified thyroid cartilage can be similar to that of head and neck squamous cell carcinoma on CT. We compared dual-energy CT spectral Hounsfield unit attenuation characteristics of nonossified thyroid cartilage with that of squamous cell carcinoma to determine the optimal virtual monochromatic image reconstruction energy levels for distinguishing tumor from normal nonossified thyroid cartilage.

MATERIALS AND METHODS: Dual-energy CT scans from 30 patients with histopathology-proved squamous cell carcinoma at different primary sites (laryngeal and nonlaryngeal) and 10 healthy patients were evaluated. Patients were scanned with a 64-section single-source scanner with fast-kilovolt (peak) switching, and scans were reconstructed at different virtual monochromatic energy levels ranging from 40 to 140 keV. Spectral attenuation curves of tumor and nonossified thyroid cartilage were quantitatively evaluated and compared. Any part of the tumor invading the cartilage, when present, was excluded from ROI analysis to avoid cross-contamination from areas where there could be a mixture of cartilage and invading tumor.

RESULTS: Normal nonossified thyroid cartilage had a characteristic, predictable spectral attenuation curve that was different from that of tumors. The greatest difference in attenuation of nonossified cartilage compared with tumor was on virtual monochromatic images of ≥ 95 keV ($P < .0001$), with sharp contrast between the relatively high attenuation of nonossified cartilage compared with that of tumor.

CONCLUSIONS: Head and neck squamous cell carcinoma has significantly different attenuation on virtual monochromatic images of ≥ 95 keV, compared with nonossified thyroid cartilage.

ABBREVIATIONS: CNR = contrast-to-noise ratio; DECT = dual-energy CT; HNSCC = head and neck squamous cell carcinoma; NOTC = nonossified thyroid cartilage; SHUAC = spectral Hounsfield unit attenuation curve; VMI = virtual monochromatic image

Head and neck squamous cell carcinoma (HNSCC) is a common malignancy of the larynx and hypopharynx. Imaging plays a key role in staging of laryngeal and hypopharyngeal cancers, and accurate staging is necessary to help determine whether a patient will undergo organ-preserving treatment or laryngectomy.

An important aspect of staging is to determine whether there is thyroid cartilage invasion.^{1,2,4-9} CT is typically the first-line technique for evaluation of laryngeal cancer, but evaluation of thyroid cartilage invasion remains a challenge on CT, in large part due to variable ossification of the thyroid cartilage. Although tumor has a different appearance from both the cortex and the fat-filled medullary space of ossified cartilage, the attenuation values of tumor and nonossified thyroid cartilage (NOTC) are very similar.^{1,10,11} Several criteria have been evaluated and proposed to improve the accuracy of CT for detection of cartilage invasion, but none are perfect.^{1,2,11-14}

Dual-energy CT (DECT) evaluates tissues at different x-ray energies, enabling spectral evaluation and material tissue characterization.¹⁵ With DECT, projection data are typically obtained simultaneously or near-simultaneously at 80 and 140 kilovolts (peak) (kV[p]).^{16,17} The measured values at the different acquisition energies can then be normalized to specific combinations of 2 different reference materials, such as iodine, water, or calcium. Furthermore, with sophisticated reconstruction algorithms, the

Received October 13, 2014; accepted after revision December 14.

From the Department of Radiology (R.F., M.L., S.L.), Jewish General Hospital, McGill University, Montreal, Quebec, Canada; Department of Radiology (R.G.), Massachusetts General Hospital, and Department of Radiology (N.D., H.D.C.), Massachusetts Eye and Ear Infirmary, Harvard Medical School, Boston, Massachusetts.

Abstract previously presented at: Annual Meeting of the American Society of Head and Neck Radiology, September 10–14, 2014; Seattle, Washington.

Please address correspondence to Reza Forghani, MD, PhD, Department of Radiology, Jewish General Hospital, Room C-212.1, 3755 Cote Ste-Catherine Rd, Montreal, QC, Canada, H3T 1E2; e-mail: rforghani@jg.mcgill.ca

 Indicates open access to non-subscribers at www.ajnr.org

 Indicates article with supplemental on-line appendix and tables.

 Indicates article with supplemental on-line photo.

<http://dx.doi.org/10.3174/ajnr.A4253>

Summary of primary HNSCC tumor sites evaluated

Primary Site	No. of Patients
Untreated tumors (<i>n</i> = 22)	
Larynx	7 ^a
Hypopharynx	1
Retromolar trigone, anterior tonsillar pillar	3
Oral cavity, other	5
Oropharynx, other	3
Sinuses, nose	3
Recurrent or metastatic tumors (<i>n</i> = 8)	
HNSCC invading parotid (<i>n</i> = 2), parapharyngeal space metastasis, oral cavity (<i>n</i> = 2), base of tongue, cheek, neopharynx	

^a Three of 7 laryngeal tumors had pathologically proven thyroid cartilage invasion.

information obtained from the different acquisitions can be combined to generate image sets at different predicted energy levels (kiloelectron volt [keV]), referred to as virtual monochromatic images (VMI). Depending on their elemental properties, different tissues have distinct attenuation, signal to noise, and contrast at different VMI energy levels, enabling spectral evaluation of tissue attenuation.^{16,17} Although currently there is only limited evidence, emerging data demonstrate advantages of DECT for head and neck imaging, with the potential for improved tumor visualization and material characterization.¹⁸⁻²¹ Kuno et al²² have also demonstrated that the addition of iodine overlay maps can increase interobserver reproducibility and improve the specificity of CT for determination of cartilage invasion without decreasing sensitivity compared with conventional CT images alone.

On contrast-enhanced CT, NOTC has relatively high intrinsic attenuation without measurable blood supply or iodine, whereas HNSCC demonstrates increased attenuation secondary to increased iodine content after administration of IV contrast. Therefore, because of their different compositions, we hypothesized that DECT virtual monochromatic images reconstructed at different energy levels may be useful in distinguishing tumor from nonossified thyroid cartilage, and in this investigation, we compared the spectral Hounsfield unit attenuation curve (SHUAC) characteristics of HNSCC with those of NOTC. The objective of our study was to evaluate the differences in spectral attenuation and determine the optimal virtual monochromatic image reconstruction energy levels for distinguishing tumor from NOTC. This study compared the enhancing part of tumor with normal nonossified thyroid cartilage. Any part of the tumor potentially invading the cartilage, when present, was excluded from quantitative ROI analysis to avoid cross-contamination from areas where there could potentially be a mixture of cartilage and invading tumor.

MATERIALS AND METHODS

Patients

The study was approved by the institutional review board. Thirty patients with proved HNSCC (by biopsy and/or surgery) and 10 healthy patients who had undergone DECT between June 2013 and July 2014 were retrospectively evaluated. Tumors from different primary sites were evaluated and are summarized in the Table. They included 7 patients with laryngeal carcinoma and 1 patient with hypopharyngeal carcinoma. Healthy patients were selected ad hoc from the same period (please refer to On-line Appendix for additional details on patient selection).

Image Acquisition

All patients were scanned with the same 64-section dual-energy scanner (Discovery CT750 HD; GE Healthcare, Milwaukee, Wisconsin). All examinations were acquired after administration of IV contrast. Eighty milliliters of iopamidol (Isovue 300; Bracco, Princeton, New Jersey) was injected at a rate of 2 mL/s, and the patient was scanned after a delay of 65 seconds. Scans were acquired in dual-energy rapid 80- to 140-kV(p) switching mode by using the Gemstone Spectral Imaging (GE Healthcare) protocol. These were acquired with a Gemstone Spectral Imaging preset 15, with a large scan FOV (≤ 50 cm), 40-mm beam collimation, 0.6-second rotation time, and 0.984:1 helical pitch. Images were reconstructed into 1.25-mm sections in a 25-cm display FOV and 512×512 matrix. The average CT dose index volume for the main acquisition (entire neck to the carina) was 17.3 mGy.

Image Postprocessing and Analysis

Quantitative image analysis was performed at the Advantage Workstation 4.6 (GE Healthcare). Scans were retrospectively reconstructed into different VMI energy levels ranging from 40 to 140 keV in 5-keV increments. Tumor and NOTC evaluation was performed by measuring mean CT attenuation (in Hounsfield unit \pm SD) within ROIs across the entire range of VMI energy levels.

First, NOTC was evaluated in healthy patients. Eighteen ROIs were placed in the NOTC in each patient, 9 on each side, to compare and confirm similarity of the 2 sides. Thereafter, normal NOTC and tumors were evaluated in 30 patients with HNSCC. In this population, the NOTC and tumor were each evaluated with 9 ROIs placed on at least 3 separate sections. For tumors, the ROIs were placed in the homogeneous-appearing enhancing part of the tumor, avoiding areas of cystic change or necrosis. For NOTC, ROIs were placed in the nonossified part of the thyroid cartilage, avoiding the area immediately adjacent to a site of ossification. In healthy patients and in patients with tumor who had primary tumors outside the larynx, ROIs were placed bilaterally within the NOTC. In patients with laryngeal cancers, ROIs were placed in either the contralateral normal NOTC, or if placed in the ipsilateral NOTC, they were placed in an area separated by at least 5 sections (6 mm) from any area of contact between tumor and cartilage. For evaluation of tumor in patients with laryngeal cancer, any part of the tumor adjacent to or invading the cartilage, when present, was excluded from quantitative ROI analysis to avoid cross-contamination from areas where there could potentially be a mixture of cartilage and invading tumor.

A total of 693 ROIs were evaluated. The sizes of the ROIs varied because of differences in thickness of the NOTC, tumor size, and tumor homogeneity among patients. The minimum individual ROI diameter used was 1.5 mm (corresponding to a sampled area per ROI of 1.77 mm²), and the maximum diameter used was 5.5 mm (corresponding to a sampled area per ROI of 23.76 mm²). As discussed earlier, multiple, at least 9, ROIs were used per structure, and the average ROI area evaluated per structure (normal cartilage or tumor) was 86.8 mm² (range, 21.2–212.1 mm²). The ROIs were averaged for each structure. So that the results are not biased toward larger structures (eg, larger tumors),

the average ROI for each patient's NOTC or tumor was given equal weight when pooling data from multiple patients. Care was taken to avoid overlap of the ROI with adjacent tissues or necrotic parts of tumor to avoid volume averaging. All ROIs were placed by an attending physician with fellowship training and 4 years' postfellowship experience in neuroradiology and head and neck radiology (R.F.). Additional information on the ROI analysis is provided in the On-line Appendix.

For each patient, the mean tumor and/or normal NOTC attenuation was determined on the basis of the average Hounsfield unit of the respective ROIs in that patient. Image noise was calculated as the SD in the ROI, and the average noise for each tumor or NOTC was calculated by obtaining the average SD in their respective ROIs.¹⁷ Comparisons of tumor and NOTC attenuation were performed by obtaining the average Hounsfield unit in all patients across the VMI range (40–140 keV). Tumor and NOTC contrast-to-noise ratios (CNRs) were calculated individually for each patient by using the following formula: $CNR = (\text{Average Tumor Attenuation} - \text{Average Cartilage Attenuation}) / \text{Square Root} [\text{Variance (Tumor)} + \text{Variance (Cartilage)}]$.¹⁷ In 3 patients with HNSCC, the thyroid cartilage was completely ossified. In this subgroup, the CNR calculation was performed by using the average normal NOTC attenuation from the other 37 patients (27 with HNSCC and 10 healthy patients).

Statistical Analysis

Results were reported as mean \pm SD. Pooled average SHUAC curves were generated from 40 to 140 keV, in 5-keV increments for comparison of NOTC and tumor. For comparison of means from 2 different groups, an unpaired 2-tailed *t* test was used. For comparison of multiple (>2) groups, 1-way ANOVA with the Tukey multiple comparison test was used. Variance was calculated by using the standard formula: $\text{variance} = \text{SD}^2$. A *P* value < .05 was statistically significant. We used GraphPad Prism software, Version 6.005, for statistical analysis (GraphPad Software, San Diego, California).

RESULTS

We first evaluated the spectral Hounsfield unit characteristics of normal NOTC in a group of 10 healthy patients (Fig 1A). The NOTC attenuation was highest at 40 keV and progressively decreased on higher kiloelectron volt VMIs (Fig 1A). There was no significant difference in the spectral Hounsfield unit characteristics of the right compared with the left NOTC. We then evaluated normal or unaffected NOTC in 30 patients with HNSCC (average age, 72 years; range, 56–97 years; 15 men, 15 women). Their primary tumor sites are summarized in the Table. Of the patients from the tumor group, 27 normal (or unaffected) NOTCs were included. In 3 patients, the entire thyroid cartilage was ossified and, therefore, was excluded from the analysis. There was no significant difference in NOTC between healthy subjects and those with normal or unaffected NOTC in the group of patients with HNSCC (Fig 1B). Subgroup analysis of normal/unaffected NOTC in the healthy patient group, patients with laryngeal cancer, those with untreated primaries outside the larynx, and those with recurrent/metastatic tumors was also performed with 1-way ANOVA with Tukey multiple comparison tests. There was no significant

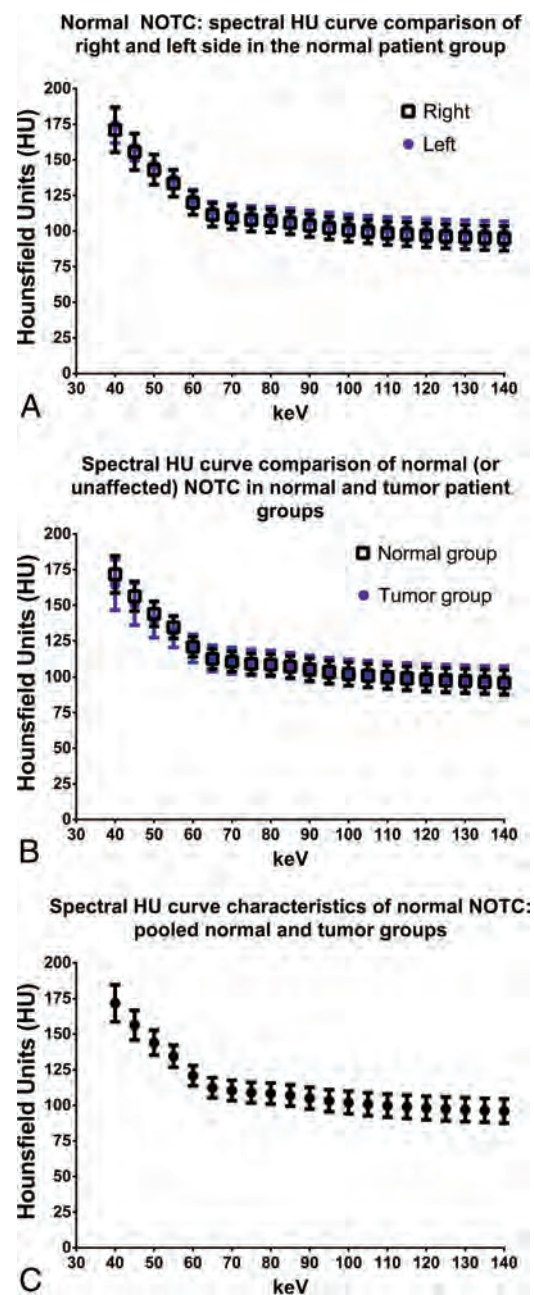


FIG 1. Comparison of spectral Hounsfield unit characteristics of normal nonossified thyroid cartilage in healthy subjects and patients with tumors. A, Baseline characteristics of NOTC evaluated in 10 healthy subjects is shown. For each patient, NOTC was evaluated with 9 ROIs on each side, corresponding to 18 ROIs total per patient, and 180 ROIs (90 ROIs for each side of the NOTC/curve). There was no significant difference in NOTC attenuation between the right and left sides across the virtual monochromatic range of 40–140 keV. B, Comparison of normal NOTC in healthy patients (right and left combined; $n = 10$, by using 180 ROIs) and normal or unaffected NOTC in the tumor group ($n = 27$, by using 243 ROIs). C, Pooled spectral Hounsfield unit curve demonstrating characteristics of normal NOTC in the entire patient population ($n = 37$). Values shown are mean \pm SD.

difference in the attenuation of normal NOTC between any of the groups, at any of the kiloelectron volts evaluated between 40 and 140 keV. The normal and unaffected NOTC spectral Hounsfield unit attenuation measurements from healthy patients and those

with tumor were combined and pooled from hereon for other comparative analyses (Fig 1C).

We next evaluated and compared the spectral attenuation characteristics of HNSCC and NOTC. Untreated primaries from the larynx ($n = 7$), extralaryngeal sites ($n = 15$), and recurrent/

metastatic tumors ($n = 8$) were evaluated (Fig 2). All tumor subgroups had overall similar SHUAC characteristics (Fig 2). As expected, the attenuation of tumors was highest at 40-keV VMI, the kiloelectron volt closest to the k-edge of iodine. Given the similarity in their SHAUCs, the tumors were all combined and compared with NOTC (Fig 3A). The SHUAC of tumors differed from that of NOTC, with a statistically significant difference in the mean attenuation of all tumors combined compared with NOTC at all kiloelectron volts except 50, 55, and 60 keV (Fig 3A, $P < .001$).

At 70 keV, the VMI energy level typically considered to be similar to that obtained with conventional single-energy CT,²³ there was a small difference between mean tumor and NOTC attenuation, with overlap between the 2 groups on the scatterplot (Fig 3B). At the lowest extreme of the curve, at 40 keV, both tumor and NOTC had the highest average attenuation. However, the difference between tumor and NOTC was best seen on the higher kiloelectron volt VMIs, due to a combination of differences in attenuation and reduced variation (SD) of the measured values in different patients (Fig 3A, -B). Indeed, in the groups evaluated in this study, there was no overlap between individual mean tumor and NOTC attenuation on VMIs reconstructed at ≥ 95 keV (Fig 3B).

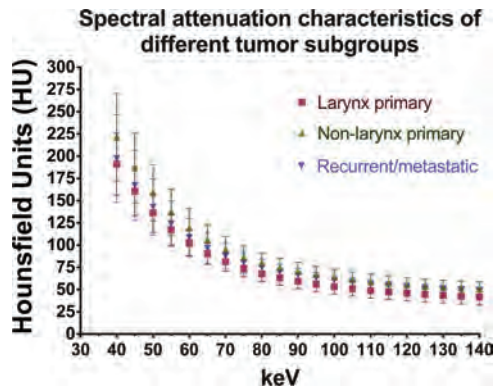


FIG 2. Comparison of spectral Hounsfield unit characteristics of different tumor subgroups: untreated larynx primaries ($n = 7$), untreated nonlarynx primaries ($n = 15$), and recurrent/metastatic tumors ($n = 8$). Note that the spectral Hounsfield unit attenuation curves of all the HNSCC tumor groups follow a similar trend, with increased attenuation of enhancing tumor at lower kiloelectron volts and decreased attenuation at higher kiloelectron volts. Values shown are mean \pm SD.

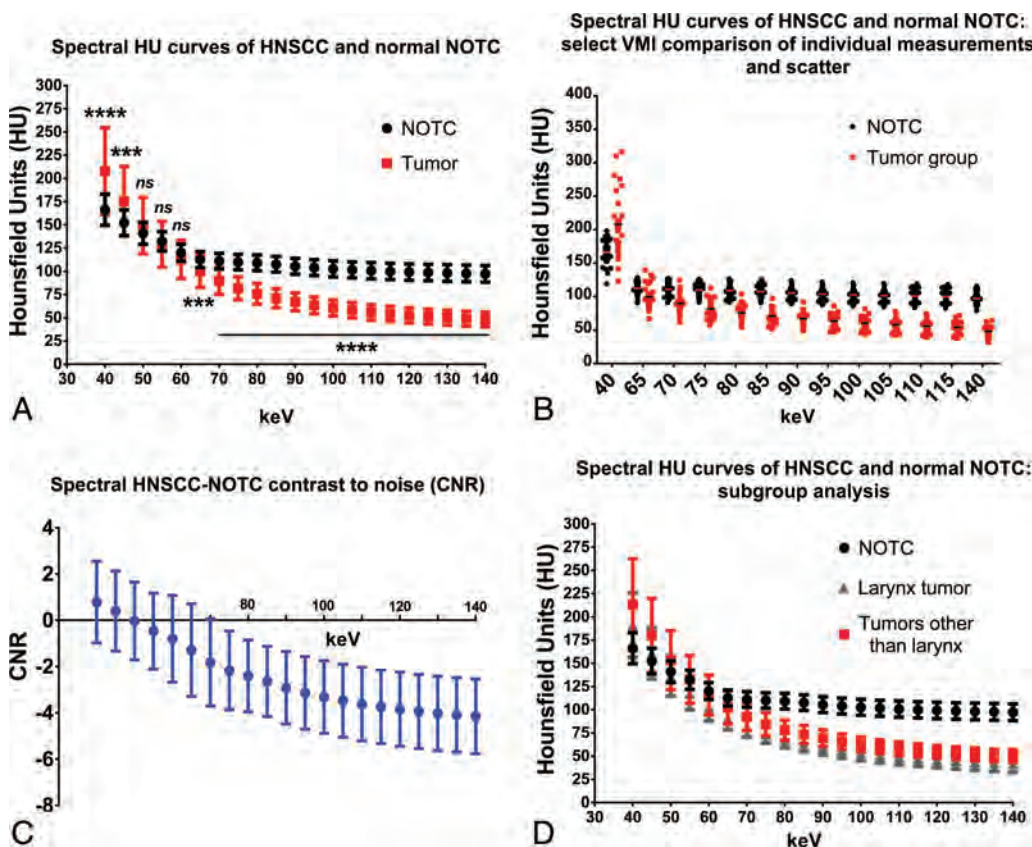


FIG 3. Spectral Hounsfield unit characteristics of head and neck squamous cell carcinoma compared with normal nonossified thyroid cartilage. A, Spectral Hounsfield unit curve of HNSCC at different primary sites ($n = 30$) compared with normal (or unaffected) NOTC ($n = 37$; 27 normal/unaffected NOTCs from the patients with tumor group and 10 NOTCs from healthy patients). B, Scatterplot of individual tumor densities at selected VMIs shows overlap between tumor and NOTC densities at many VMIs but complete separation at high-energy VMIs. C, Contrast-to-noise analysis performed at different kiloelectron volt VMIs demonstrating the higher absolute CNR at high-energy VMIs. D, Subgroup analysis of the laryngeal ($n = 7$) and nonlaryngeal (including a case of hypopharyngeal tumor, $n = 23$) primary sites. Three asterisks denotes $P < .001$; 4 asterisks denotes $P < .0001$; and ns, not significantly different.

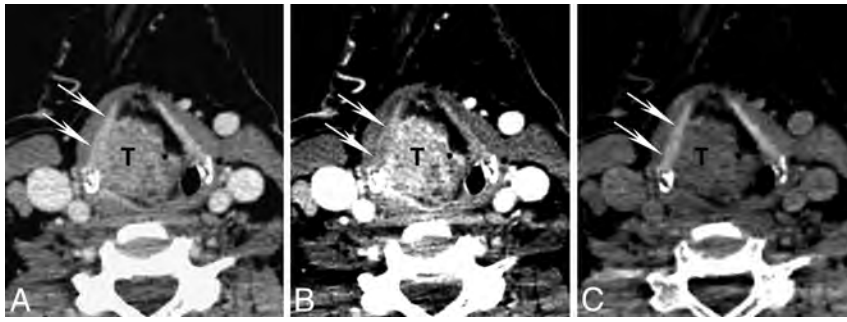


FIG 4. Differences in attenuation of NOTC (arrows) and tumor (T) on different kiloelectron volt VMIs. Axial contrast-enhanced CT images are shown from a patient with a supraglottic squamous cell carcinoma with the same section reconstructed as a virtual monochromatic images at 70, 40, and 140 keV. A, Seventy-kiloelectron volt VMI shows tumor abutting the inner surface of the right NOTC. B, Forty-kiloelectron volt VMI shows greater attenuation of the tumor than on the 70-keV VMI due to iodine content, increased contrast between tumor and NOTC, and somewhat better depiction of tumor-NOTC interface. C, One hundred forty-kiloelectron volt VMI shows suppression of tumor attenuation but preserved high attenuation in the NOTC. Note the qualitative contrast improvement with clear distinction of tumor-NOTC interface.

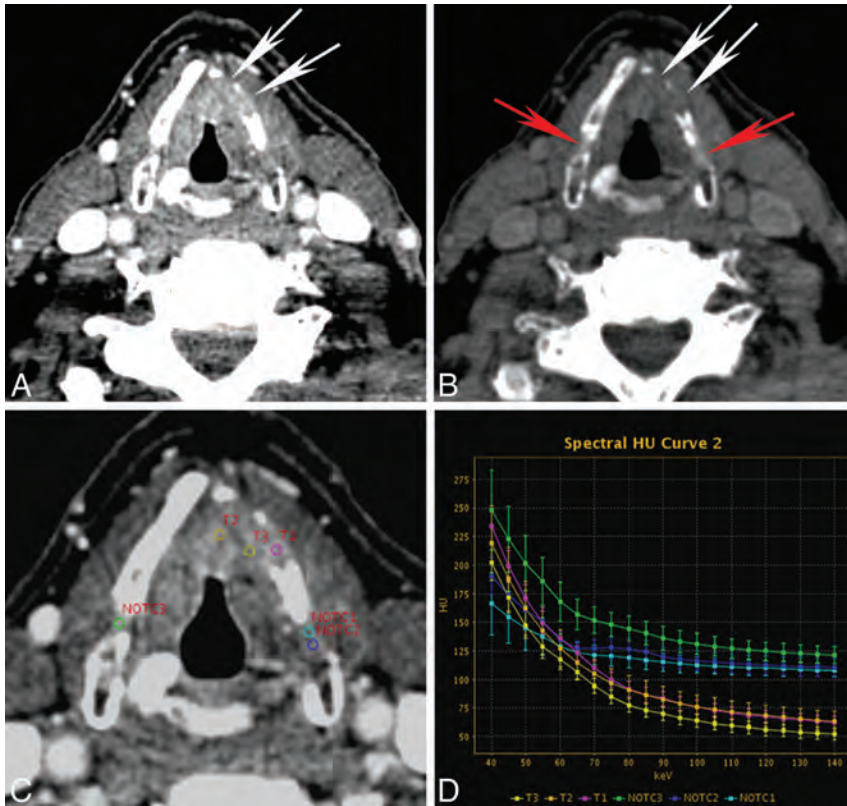


FIG 5. Quantitative spectral Hounsfield unit attenuation characterization of tumor and NOTC in a patient with pathologically proved tumor invasion into the thyroid cartilage. VMIs reconstructed at 40 keV (A) and 140 keV (B) demonstrate tumor invasion into the anterior left thyroid cartilage (white arrows). Note variable ossification of the left thyroid cartilage and minimal focal nonossification of the right thyroid cartilage. On the 140-keV VMI, attenuation due to invasion of the left thyroid cartilage (white arrows) is suppressed, appearing as a defect, compared with the normal ipsilateral NOTC and contralateral NOTC (red arrows). C and D, An example of quantitative analysis is shown, demonstrating individual spectral Hounsfield unit attenuation curves for different ROIs. Note the differences in spectral attenuation characteristics of tumor (T) compared with normal ipsilateral and contralateral NOTC. The spectral curve shows clear attenuation separation in the higher kiloelectron volt range. Please note that the curves shown in this figure are those for individual ROIs. In earlier figures, the average from multiple ROIs (at least 9) per structure, per patient, was used to calculate pooled mean attenuation for each group or subgroup (in addition, areas of invasion were not included in the earlier pooled analysis).

Subgroup analysis of the laryngeal ($n = 7$) primaries demonstrated similar trends in SHUAC, with persistent clear separation from the normal NOTC curve in the high kiloelectron volt range (Fig 3D). Subgroup analysis comparing NOTC with the untreated laryngeal primaries, untreated primaries outside the larynx, and recurrent/metastatic tumors also demonstrated a statistically significant difference between NOTC and all tumor subgroups on VMIs reconstructed at ≥ 70 KeV ($P < .0001$, 1-way ANOVA), with the greatest difference at of ≥ 95 KeV.

We also calculated the CNR to factor in differences in noise levels at different VMI energy levels. As in the previous observations, the absolute CNR was highest on high kiloelectron volt images (Fig 3C). Note that the negative values in Fig 3C indicate that tumor has a lower attenuation than NOTC at these kiloelectron volts. Therefore, tumor invasion of NOTC would be expected to appear as a low-attenuation defect in the otherwise high-attenuation NOTC (Figs 4 and 5).

DISCUSSION

Accurate determination of thyroid cartilage invasion is important for proper staging and treatment planning of laryngeal and hypopharyngeal cancers.¹⁻⁸ Evaluation of thyroid cartilage invasion on imaging remains a challenge because of variable ossification and appearance of thyroid cartilage and similarities in attenuation of tumor and NOTC on CT.^{1,2,10,11} While tumor preferentially invades the ossified part of the cartilage, the similarity in appearance of NOTC and tumor can make definitive assessment for invasion challenging in cases in which tumor abuts the nonossified part of thyroid cartilage. Clear distinction of invasive tumor and focal nonossification of the cartilage may not be possible.

Kuno et al²² demonstrated that DECT iodine overlay images improved the specificity of detection of laryngeal cartilage invasion. In our investigation, we compared the spectral Hounsfield unit characteristics of tumor and NOTC by using a single-source DECT with rapid kiloelectron volt switching to determine the utility of VMIs reconstructed at var-

ious kiloelectron volt levels for distinguishing tumor from NOTC. Our study expands on observations by Kuno et al that DECT can be helpful in the evaluation of laryngeal cartilage in patients with HNSCC. In our study, we evaluated another aspect of DECT, VMIs reconstructed at different kiloelectron volt energy levels, to characterize and compare HNSCC and unaffected NOTC.

Although in this investigation we did not directly evaluate thyroid cartilage invasion, the observations in this study are a step toward application of VMIs and SHUAC analysis for assessment of NOTC and proceeding to studies evaluating NOTC invasion. We demonstrate that HNSCC has a very different spectral Hounsfield unit attenuation curve than normal NOTC. Although there was some difference in mean attenuation between NOTC and tumor at 70 keV, the VMI energy level similar to that of a standard single-energy CT acquisition,²³ the difference was small and there was overlap between individual tumor and NOTC attenuation. This finding reflects the challenges that can be encountered in distinguishing NOTC from tumor on conventional CT.

On the other hand, there were significant differences in attenuation at either extreme of the VMI energy curve, with the distinction between tumor and NOTC best achieved on VMIs of ≥ 95 keV. On high kiloelectron volt VMIs, iodine attenuation in enhancing tumor is partially suppressed, whereas the normal NOTC retains a relatively high and fairly uniform attenuation and would therefore be distinct from adjacent tumor (Fig 4). Against the high-attenuation background of NOTC, tumor would be expected to appear as a relatively low-attenuation defect that stands out from the normal thyroid cartilage (Fig 5). Normal NOTC has uniform attenuation without gaps or defects.²⁴ On the basis of the results of our study, one would expect that VMIs may be used qualitatively to assess NOTC integrity (Figs 4 and 5). In cases where there is ambiguity, supplemental evaluation with quantitative ROI analysis and SHUAC analysis may also be helpful. A potential example of such application, demonstrating individual ROI curves, is shown in Fig 5. On the basis of the observations in this study, we believe that future investigations directly evaluating applications of high-energy VMI and SHUAC for thyroid cartilage invasion are warranted. Because many patients without thyroid cartilage invasion or with minor invasion may not be treated surgically, such studies will be designed to correlate imaging findings with long-term patient outcome rather than on the basis of histopathologic correlation alone.

Compared with iodine overlay maps, high kiloelectron volt-reconstructed VMIs are similar to standard sequences to which radiologists are accustomed, possibly providing an advantage for implementation and user acceptance. In addition, high kiloelectron volt VMIs can result in decreased artifacts associated with metallic implants and other materials.^{25,26} At this time, both high-energy kiloelectron volt VMIs and iodine overlay maps are likely to be useful for increasing the accuracy of CT for determination of laryngeal cartilage invasion, and a comparison of the 2 and evaluation of potential complementary application in thyroid cartilage assessment is an interesting topic for future research.

Because this work is a general characterization of HNSCC, we used both primary laryngeal tumors and tumors outside the larynx. In addition, we evaluated recurrent/metastatic tumors. Although there were small differences in mean attenuation among

the different tumor subgroups, all of the tumor groups had similar spectral attenuation characteristics (Fig 2). Furthermore, similar differences in NOTC and tumor attenuation with the greatest difference on high kiloelectron volt VMIs were observed when NOTC was compared with either the entire group of 30 tumors and specific subgroups.

Limitations of this study include the retrospective design and small number of cases. In addition, there was no pathologic confirmation of uninvaded NOTC. Nonetheless, our study demonstrates clear qualitative and quantitative differences in spectral Hounsfield unit attenuation curves of HNSCC compared with NOTC. We believe that our investigation and that by Kuno et al²² provide the basis for future, ideally prospective, studies to evaluate the advantages of DECT, including high kiloelectron volt VMIs, for detecting thyroid cartilage invasion and predicting patient outcome.

CONCLUSIONS

HNSCC has different spectral Hounsfield unit attenuation characteristics with significantly different attenuation on VMIs of ≥ 95 keV compared with nonossified thyroid cartilage. Therefore, DECT has the potential to improve accuracy for distinguishing tumor and NOTC and to improve evaluation of cartilage invasion by laryngeal cancer.

ACKNOWLEDGMENTS

We thank Veronika Glyudza for her assistance in data preparation and processing.

Disclosures: Reza Forghani—UNRELATED: Consultancy: Biogen Idec, Collège des Médecins du Québec, Comments: no relation to submitted work; one time honorarium for the "Neuroradiology Scientific Exchange Program: Focus on the Role of MRI in the Detection, Diagnosis and Monitoring of Natalizumab-Associated Progressive Multifocal Leukoencephalopathy in Patients with Multiple Sclerosis," Montreal, Quebec, Canada, February 22, 2014; expert consultant for Collège des Médecins du Québec (Telemedicine Committee, quality assurance); Expert Testimony: Collège des Médecins du Québec, Comments: quality assurance reviews (no relation to current work); Payment for Lectures (including service on Speakers Bureaus): no relation to submitted work; "Peer Review for Departmental QA and Audits: Essentials of a Successful Program, Benchmarks for Evaluation, and Challenges," Ontario Association of Radiologists Continuing Medical Education Peer Review Course, Ontario Bar Association, Toronto, Ontario, Canada, June 7, 2014; "Sinus Anatomy: Normal and Postoperative," Ontario Association of Radiologists Continuing Medical Education Head and Neck Imaging Course, Part I, Ontario Bar Association, Toronto, Ontario, Canada, May 24, 2014; Visiting Professor, McMaster University Health Sciences Center; Radiology Grand Rounds, St. Joseph's Healthcare Hamilton ("Applications of Diffusion-Weighted MR Imaging in the Evaluation of Acute Ischemia and Non-Ischemic Neurological Disorders"), Hamilton, Ontario, Canada, January 22, 2013; Stock/Stock Options: Real Time Medical Inc, Comments: no relation to submitted work; member, Medical and Quality Assurance Committee. Mark Levental—UNRELATED: Consultancy: Biogen Idec; Payment for Lectures (including service on Speakers Bureaus): Biogen Idec, Comments: member of speakers bureau. Rajiv Gupta—UNRELATED: Board Membership: Actelion, Comments: advising the company on the use of imaging in their drug trials; Grants/Grants Pending: Siemens,* Comments: research grant to the institution; Travel/Accommodations/Meeting Expenses Unrelated to Activities Listed: Siemens, Comments: travel support for a symposium organized by Siemens. Hugh D. Curtin—UNRELATED: Royalties: Elsevier, Comments: royalties for textbook, not related to this article. *Money paid to the institution.

REFERENCES

1. Hermans R. Staging of laryngeal and hypopharyngeal cancer: value of imaging studies. *Eur Radiol* 2006;16:2386–400
2. Kuno H, Onaya H, Fujii S, et al. Primary staging of laryngeal and hypopharyngeal cancer: CT, MR imaging and dual-energy CT. *Eur J Radiol* 2014;83:e23–35

3. Ferlito A, Silver CE, Howard DJ, et al. **The role of partial laryngeal resection in current management of laryngeal cancer: a collective review.** *Acta Otolaryngol* 2000;120:456–65
4. Hartl DM, Landry G, Hans S, et al. **Organ preservation surgery for laryngeal squamous cell carcinoma: low incidence of thyroid cartilage invasion.** *Laryngoscope* 2010;120:1173–76
5. Jenckel F, Knecht R. **State of the art in the treatment of laryngeal cancer.** *Anticancer Res* 2013;33:4701–10
6. Knab BR, Salama JK, Solanki A, et al. **Functional organ preservation with definitive chemoradiotherapy for T4 laryngeal squamous cell carcinoma.** *Ann Oncol* 2008;19:1650–54
7. Lefebvre JL. **Larynx preservation.** *Curr Opin Oncol* 2012;24:218–22
8. Edge SB, Byrd DR, Compton CC, et al. *AJCC Cancer Staging Manual.* New York: Springer-Verlag; 2010
9. Becker M, Zbaren P, Delavelle J, et al. **Neoplastic invasion of the laryngeal cartilage: reassessment of criteria for diagnosis at CT.** *Radiology* 1997;203:521–32
10. Archer CR, Yeager VL. **Evaluation of laryngeal cartilages by computed tomography.** *J Comput Assist Tomogr* 1979;3:604–11
11. Mafee MF, Schild JA, Michael AS, et al. **Cartilage involvement in laryngeal carcinoma: correlation of CT and pathologic macrosection studies.** *J Comput Assist Tomogr* 1984;8:969–73
12. Becker M. **Neoplastic invasion of laryngeal cartilage: radiologic diagnosis and therapeutic implications.** *Eur J Radiol* 2000;33:216–29
13. Beitler JJ, Muller S, Grist WJ, et al. **Prognostic accuracy of computed tomography findings for patients with laryngeal cancer undergoing laryngectomy.** *J Clin Oncol* 2010;28:2318–22
14. Zbäre P, Becker M, Lang H. **Pretherapeutic staging of laryngeal carcinoma: clinical findings, computed tomography, and magnetic resonance imaging compared with histopathology.** *Cancer* 1996;77:1263–73
15. Johnson TR, Fink C, Schönberg SO, et al, eds. *Dual Energy CT in Clinical Practice.* Berlin: Springer-Verlag; 2011
16. Johnson TR. **Dual-energy CT: general principles.** *AJR Am J Roentgenol* 2012;199:S3–8
17. Pomerantz SR, Kamalian S, Zhang D, et al. **Virtual monochromatic reconstruction of dual-energy unenhanced head CT at 65–75 keV maximizes image quality compared with conventional polychromatic CT.** *Radiology* 2013;266:318–25
18. Tawfik AM, Kerl JM, Bauer RW, et al. **Dual-energy CT of head and neck cancer: average weighting of low- and high-voltage acquisitions to improve lesion delineation and image quality: initial clinical experience.** *Invest Radiol* 2012;47:306–11
19. Vogl TJ, Schulz B, Bauer RW, et al. **Dual-energy CT applications in head and neck imaging.** *AJR Am J Roentgenol* 2012;199:S34–39
20. Tawfik AM, Kerl JM, Razek AA, et al. **Image quality and radiation dose of dual-energy CT of the head and neck compared with a standard 120-kVp acquisition.** *AJNR Am J Neuroradiol* 2011;32:1994–99
21. Srinivasan A, Parker RA, Manjunathan A, et al. **Differentiation of benign and malignant neck pathologies: preliminary experience using spectral computed tomography.** *J Comput Assist Tomogr* 2013;37:666–72
22. Kuno H, Onaya H, Iwata R, et al. **Evaluation of cartilage invasion by laryngeal and hypopharyngeal squamous cell carcinoma with dual-energy CT.** *Radiology* 2012;265:488–96
23. Patel BN, Thomas JV, Lockhart ME, et al. **Single-source dual-energy spectral multidetector CT of pancreatic adenocarcinoma: optimization of energy level viewing significantly increases lesion contrast.** *Clin Radiol* 2013;68:148–54
24. Dadfar N, Seyyedi M, Forghani R, et al. **Computed tomography appearance of normal nonossified thyroid cartilage: implication for tumor invasion diagnosis.** *J Comput Assist Tomogr* 2015;39:240–43
25. Srinivasan A, Hoeffner E, Ibrahim M, et al. **Utility of dual-energy CT virtual keV monochromatic series for the assessment of spinal transpedicular hardware-bone interface.** *AJR Am J Roentgenol* 2013;201:878–83
26. Stolzmann P, Winklhofer S, Schwendener N, et al. **Monoenergetic computed tomography reconstructions reduce beam hardening artifacts from dental restorations.** *Forensic Sci Med Pathol* 2013;9:327–32

American Society of Neuroradiology: Laurie A. Loevner

Dr. Loevner is the 54th President of the American Society of Neuroradiology (ASNR) and its fifth female one. Laurie obtained her MD from the University of Pennsylvania and trained in radiology at the University of Michigan before returning for her neuroradiology fellowship to Penn. Thereafter, she remained at that prestigious institution, attaining the rank of Professor in 2005 and now serving as Chief of Neuroradiology. It is simply

impossible to summarize her achievements here. Briefly, she is the author of 120 peer-reviewed articles, 100 abstracts, 40 reviews, and 8 books. Laurie has served as a principal or co-investigator on more than 20 funded projects. A fantastic speaker and teacher, she has delivered nearly 1000 invited lectures. Her service record is on a par with her other activities: She has held prestigious positions in most scientific imaging societies, notably President of the American Society of Head and Neck Radiology and of the Eastern Neuroradiological Society. A member of 5 editorial boards, she also serves as Neuroradiology Editor for *Radiographics*. A testimony to her dedication to ASNR and of her hard work was her splendid program for the 2015 Annual ASNR meeting. This program reflected her personality: energetic, modern, and multifaceted, but more important, it let us glimpse her warmth and humanity.

American Society of Functional Neuroradiology: Pratik Mukherjee

Dr. Mukherjee received his MD from Cornell University and his radiology training, including his fellowship in neuroradiology, from Washington University in St. Louis. He also received a doctorate in neuroscience from Rockefeller University. He currently serves as Professor of Radiology and Director of the Center for Imaging and Neurodegenerative Disorders at the University of California, San

Francisco. Among the most important of his academic activities are serving as a member/reviewer on 15 National Institutes of Health study panels, mentoring 45 individuals (from medical students to full-time faculty), currently serving as an investigator on 9 funded projects (18 in the past), and publishing nearly 110 articles.

American Society of Head and Neck Radiology: Richard H. Wiggins

Dr. Wiggins completed his medical training at the University of Texas in Houston, his radiology residency at the University of Mississippi, and his fellowships in head and neck and neuroradiology at the universities of Florida and Utah, respectively. He



holds certifications not only from the American Board of Radiology but also from the American Board of Imaging Informatics. Currently a Professor of Radiology in Salt Lake City, he has served as editor of 25 books and authored 11 others. He is also the author of nearly 60 articles. Dr. Wiggins is an excellent educator and speaker who has delivered more than 330 invited lectures. In addition to all of these achievements, he has been involved as an investigator in 14 funded projects.

American Society of Pediatric Neuroradiology: Erin Simon Schwartz

The new President of the American Society of Pediatric Neuroradiology (ASPNR) is Dr. Erin Simon Schwartz, who serves as Associate Professor of Radiology and attending radiologist at the Children's Hospital of Philadelphia, where she is also the director of the magnetoencephalography training at the University of Maryland and finished a neuroradiology fellowship at the University of California, San Francisco. Apart from her long service history with ASPNR, she has been a member of 17 committees for ASNR and is Past President of the American Society of Spine Radiology and of the Eastern Neuroradiological Society. In the past 5 years, she has delivered nearly 70 invited lectures and published close to 80 articles. She is a member of the editorial boards of 3 journals, including the *American Journal of Neuroradiology*.

American Society of Spine Radiology: Gregory J. Lawler

Dr. Lawler is this year's new American Society of Spine Radiology President. Before achieving this position, he served the society as Vice President, Member-at-Large, and a member of 12 of its committees. He is the president of his private practice located in Ridgefield, Connecticut. Notwithstanding the busy nature of his clinical practice, he has published in *Radiology* and other journals and has trained fellows from academic programs in invasive spinal procedures. During his presidency, he has pledged to strengthen partnerships and alliances with related scientific societies; advocate for the interests of neuroradiologists in Washington, DC; increase the number of sessions dedicated to spine interventions at the annual meeting; and create focus groups that will assess the outcomes of these procedures.

<http://dx.doi.org/10.3174/ajnr.A4389>

Go Green!

AJNR urges American Society of Neuroradiology members to reduce their environmental footprint by voluntarily suspending their print subscription.

The savings in paper, printing, transportation, and postage not only help members cut down on clutter, but go to fund new electronic enhancements and expanded content.

The digital edition of *AJNR* presents the print version in its entirety, along with extra features including:

- Publication Preview
- Case of the Week
- Podcasts
- Special Collections
- The *AJNR* Blog
- Weekly Poll

It also **reaches subscribers much faster than print**. An **electronic table of contents** will be sent directly to your mailbox to notify you as soon as it publishes.

Readers can **search, reference, and bookmark** current and archived content 24 hours a day on www.ajnr.org, rather than thumb through stacks of accumulated paper issues for articles and images they need.



<http://www.ajnr.org/cgi/feedback>

ASNR members who wish to opt out of print can do so by using the Feedback form on the *AJNR* Website (<http://www.ajnr.org/cgi/feedback>). Just type "Go Green" in the subject line to stop print and spare our ecosystem.



Simplify

the MOC Process



Manage

your CME Credits Online

CMEgateway.org

Available to Members of Participating Societies

American Board of Radiology (ABR)
American College of Radiology (ACR)
American Roentgen Ray Society (ARRS)
American Society of Neuroradiology (ASNR)
Commission on Accreditation of Medical
Physics Educational Programs, Inc. (CAMPEP)
Radiological Society of North America (RSNA)
Society of Interventional Radiology (SIR)
SNM
The Society for Pediatric Radiology (SPR)

It's Easy and Free!

- Log on to CME Gateway to:
- View or print reports of your CME credits from multiple societies from a single access point.
 - Print an aggregated report or certificate from each participating organization.
 - Link to SAMs and other tools to help with maintenance of certification.

American Board of Radiology (ABR) participation!

By activating ABR in your organizational profile, your MOC-fulfilling CME and SAM credits can be transferred to your own personalized database on the ABR Web site.

Sign Up Today!

go to CMEgateway.org

Trevo® XP ProVue Retrievers

See package insert for complete indications, complications, warnings, and instructions for use.

INDICATIONS FOR USE

The Trevo Retriever is intended to restore blood flow in the neurovasculature by removing thrombus in patients experiencing ischemic stroke within 8 hours of symptom onset. Patients who are ineligible for intravenous tissue plasminogen activator (IV t-PA) or who fail IV t-PA therapy are candidates for treatment.

COMPLICATIONS

Procedures requiring percutaneous catheter introduction should not be attempted by physicians unfamiliar with possible complications which may occur during or after the procedure. Possible complications include, but are not limited to, the following: air embolism; hematoma or hemorrhage at puncture site; infection; distal embolization; pain/headache; vessel spasm, thrombosis, dissection, or perforation; emboli; acute occlusion; ischemia; intracranial hemorrhage; false aneurysm formation; neurological deficits including stroke; and death.

COMPATIBILITY

3x20 mm retrievers are compatible with Trevo® Pro 14 Microcatheters (REF 90231) and Trevo® Pro 18 Microcatheters (REF 90238). 4x20 mm retrievers are compatible with Trevo® Pro 18 Microcatheters (REF 90238). Compatibility of the Retriever with other microcatheters has not been established. Performance of the Retriever device may be impacted if a different microcatheter is used. The Merci® Balloon Guide Catheters are recommended for use during thrombus removal procedures. Retrievers are compatible with the Abbott Vascular DOC® Guide Wire Extension (REF 22260)

WARNINGS

- Contents supplied STERILE, using an ethylene oxide (EO) process. Nonpyrogenic.
- To reduce risk of vessel damage, adhere to the following recommendations:
 - Take care to appropriately size Retriever to vessel diameter at intended site of deployment.
 - Do not perform more than six (6) retrieval attempts in same vessel using Retriever devices.
 - Maintain Retriever position in vessel when removing or exchanging Microcatheter.
- To reduce risk of kinking/fracture, adhere to the following recommendations:
 - Immediately after unsheathing Retriever, position Microcatheter tip marker just proximal to shaped section. Maintain Microcatheter tip marker just proximal to shaped section of Retriever during manipulation and withdrawal.
 - Do not rotate or torque Retriever.
 - Use caution when passing Retriever through stented arteries.
- Do not resterilize and reuse. Structural integrity and/or function may be impaired by reuse or cleaning.
- The Retriever is a delicate instrument and should be handled carefully. Before use and when possible during procedure, inspect device carefully for damage. Do not use a device that shows signs of damage. Damage may prevent device from functioning and may cause complications.
- Do not advance or withdraw Retriever against resistance or significant vasospasm. Moving or torquing device against resistance or significant vasospasm may result in damage to vessel or device. Assess cause of resistance using fluoroscopy and if needed resheath the device to withdraw.

- If Retriever is difficult to withdraw from the vessel, do not torque Retriever. Advance Microcatheter distally, gently pull Retriever back into Microcatheter, and remove Retriever and Microcatheter as a unit. If undue resistance is met when withdrawing the Retriever into the Microcatheter, consider extending the Retriever using the Abbott Vascular DOC guidewire extension (REF 22260) so that the Microcatheter can be exchanged for a larger diameter catheter such as a DAC® catheter. Gently withdraw the Retriever into the larger diameter catheter.
- Administer anti-coagulation and anti-platelet medications per standard institutional guidelines.

PRECAUTIONS

- Prescription only – device restricted to use by or on order of a physician.
- Store in cool, dry, dark place.
- Do not use open or damaged packages.
- Use by “Use By” date.
- Exposure to temperatures above 54°C (130°F) may damage device and accessories. Do not autoclave.
- Do not expose Retriever to solvents.
- Use Retriever in conjunction with fluoroscopic visualization and proper anti-coagulation agents.
- To prevent thrombus formation and contrast media crystal formation, maintain a constant infusion of appropriate flush solution between guide catheter and Microcatheter and between Microcatheter and Retriever or guidewire.
- Do not attach a torque device to the shaped proximal end of DOC® Compatible Retriever. Damage may occur, preventing ability to attach DOC® Guide Wire Extension.



Concentric Medical
301 East Evelyn
Mountain View, CA 94041



EMERGO Europe
Molenstraat 15
2513 BH, The Hague
The Netherlands



Stryker Neurovascular
47900 Bayside Parkway
Fremont, CA 94538

stryker.com/neurovascular
stryker.com/emea/neurovascular

Date of Release: JUN/2014

EX_EN_GL



THE FOUNDATION OF THE ASNR 

**THE FOUNDATION OF THE ASNR SYMPOSIUM 2016:
EMERGENCY NEURORADIOLOGY
MAY 21-22**

**ASNR 54TH ANNUAL MEETING
MAY 23-26**



Howard A. Rowley, MD, ASNR 2016 Program Chair/President-Elect
Programming developed in cooperation with ...

American Society of Functional Neuroradiology (ASFNR)
Christopher G. Filippi, MD

American Society of Head and Neck Radiology (ASHNR)
Lindell R. Gentry, MD

American Society of Pediatric Neuroradiology (ASPNR)
Erin Simon Schwartz, MD

American Society of Spine Radiology (ASSR)
Gregory J. Lawler, MD

Society of NeuroInterventional Surgery (SNIS)
Charles J. Prestigiacomo, MD

American Society of Neuroradiology (ASNR) Health Policy Committee
Robert M. Barr, MD, FACR

Computer Science and Informatics (CSI) Committee
John L. Go, MD

Research Scientists Committee
Dikoma C. Shungu, PhD

ASNR 54TH ANNUAL MEETING
c/o American Society of Neuroradiology
800 Enterprise Drive, Suite 205
Oak Brook, Illinois 60523-4216
Phone: 630-574-0220
Fax: 630 574-0661
www.asnr.org/2016

**SCAN NOW
TO VISIT
OUR WEBSITE**

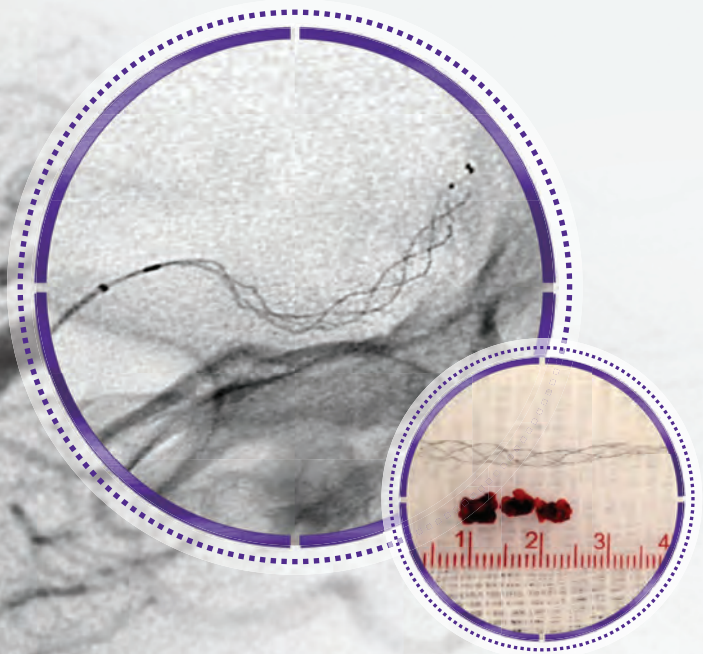


SAVE THE DATE... MAY 21-26, 2016
WASHINGTON MARRIOTT WARDMAN PARK • WASHINGTON DC

Stent Retrievers:

The evidence is clear

stryker[®]
Neurovascular



Images courtesy of Joey English, MD – used with permission.

Trial	Number of Patients	Statistically Superior Result for Endovascular Therapy
MR CLEAN ¹	500	
ESCAPE ²	316	
EXTEND-IA ³	70	
SWIFT PRIME ⁴	196	

Stent retrievers ± IV-tPA gave patients up to **3x higher likelihood** of an mRS 0-2 at 90 days than IV-tPA alone^{1,2,3,4}

1. O.A. Berkhemer et al. A Randomized Trial for Intraarterial Treatment for Acute Ischemic Stroke. *N Eng J Med* December 2014.

2. M. Goyal et al. Randomized Assessment of Rapid Endovascular Treatment of Ischemic Stroke. *N Eng J Med* published on February 11, 2015.

3. B.C.V. Campbell et al. Endovascular Therapy for Ischemic Stroke with Perfusion-Imaging Selection. *N Eng J Med* published on February 11, 2015.

4. Results of the SWIFT PRIME Trial were presented by Dr. Jeffrey Saver at the International Stroke Conference in Nashville, TN on Wednesday, February 11, 2015.